Special Issue

1st International Conference on

Sciences and Techniques for Renewable Energy and the Environment STR2E 2025

MAY 06-08, 2025

Faculty of Sciences and Techniques
Al Hoceima, Morocco

DOI: https://doi.org/10.51646/jsesd.v14iSTR2E

WEBSITE: https://str2e.com/
str2e.conference@gmail.com

Scopus Preview
Solar Energy
And Sustainable Development
Refereed, biannual scientific journal issued by:
The Libyan Center for Solar Energy Research and Studies.

Solar Energy And Sustainable Development

ISSN: 2411-9536 (P)
ISSN: 2434-6013 (e)

Issusd by the Libyan Center for Solal Energy Research and Studies

1st International Conference on

Sciences and Techniques for Renewable Energy and the Environment STR2E 2025

MAY 06-08, 2025

Faculty of Sciences and Techniques
Al Hoceima, Morocco

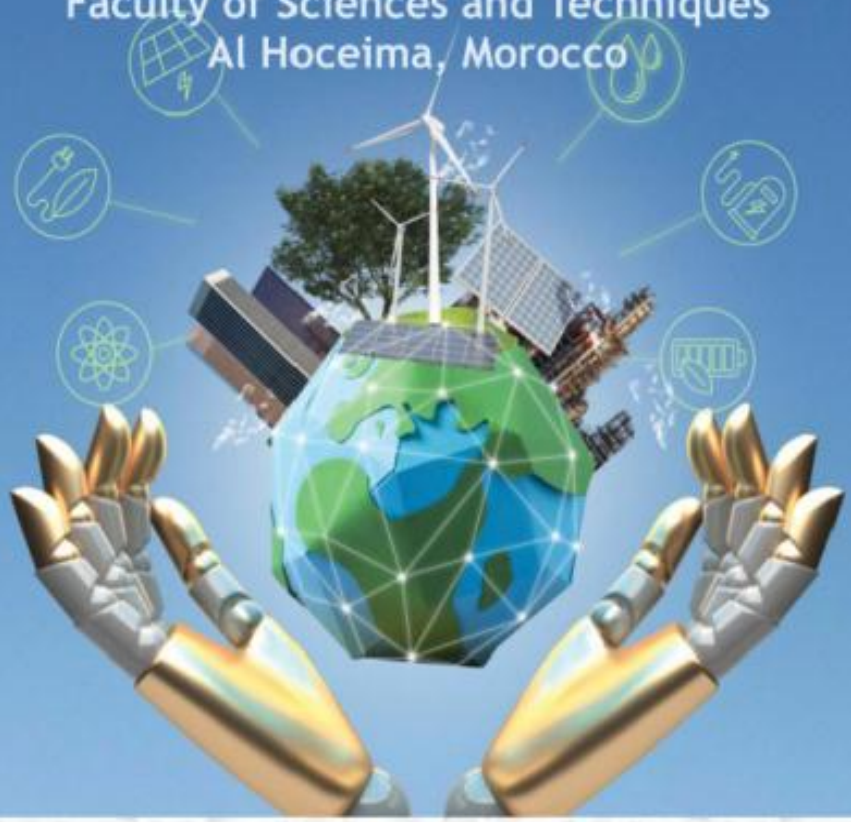

https://str2e.com

str2e.conference@gmail.com

Preface_STR2E2025

The 1st International Conference on Sciences and Techniques for Renewable Energy and the Environment (STR2E 2025), which was held from May 6 to 8, 2025, at the Faculty of Sciences and Techniques of Al Hoceima, Morocco.

STR2E 2025 was jointly organized by the **Chemistry, Computer Science and Artificial Intelligence Research Team (ERCI2A)** of **Abdelmalek Essaadi University, Tetouan, Morocco,** and the **Moroccan Association of Sciences and Techniques for Sustainable Development (MASTSD)**, based in Beni Mellal, Morocco), in collaboration with **Higher School of Technology**, Beni Mellal, Morocco, the Journal of "***Solar Energy and Sustainable Development***", and the **Libyan Center for Research and Studies in Solar Energy**

This special issue brings together very interesting articles related to recent scientific and technological advances in the fields of renewable energy and environmental sustainability, offering a multidisciplinary platform for exchanging ideas, by highlighting cutting-edge research cuts, and fostering collaborations aimed at developing innovative and sustainable solutions to current urgent energy and environmental challenges.

The aim of ***this Special Issue*** is to promote and publish recent studies on renewable energy and environmental sustainability. The scope of this ***Special Issue includes*** (but is not limited to) the following topics:

Topics:

T1: Advanced Technologies for the Electrochemical Production of Hydrogen and Protection Of The Environment.

T2: Photovoltaic, Grid, Solar Energy Materials And Wind Energy For Green Hydrogen T2: Energy, Smart Materials And Smart Cities.

T3: Green Chemistry Technology; Integration Of Renewable Energy In The Chemical Production.

T4: Internet Of Things, Artificial Intelligence (IoT & AI) And Robotics In Energy.

T5: Theoretical And Computational Chemistry For The Renewable Energy And Protection Of Environment T6: Embedded System In Energy T7: Sustainable Agricultural Systems and Technology.

T8: White hydrogen: sustainable energy from the depths of the earth T9: Biomass and Geothermal Energy Engineering.

Lead Guest Editor:

Pr. Charaf Laghlimi

Affiliation: ERCI2A, FSTH, Abdelmalek Essaadi University, Tetouan, Morocco. And the Moroccan Association of Sciences and Techniques for Sustainable Development (MASTSD), Beni Mellal, Morocco.

Institutional e-mail address:

charaf.cac.fbs@gmail.com ; c.laghlimi@uae.ac.ma

ORCID: 0000-0002-5022-5238

Scopus: https://www.scopus.com/authid/detail.uri?authorId=57207915986

Guest Editors:

1- Pr. Younes Ziat

Affiliation: Engineering and Applied Physics Team (EAPT), Superior School of Technology, Sultan Moulay Slimane University, Beni Mellal, Morocco. And the Moroccan Association of Sciences and Techniques for Sustainable Development (MASTSD), Beni Mellal, Morocco.

Institutional e-mail address: ziat.estbm@gmail.com

ID Scopus: https://www.scopus.com/authid/detail.uri?authorId=56074431200

2- Pr. Zakaryaa Zarhri

Affiliation : CONAHCYT- Faculty of Chemical Sciences and Engineering, The Autonomous University of

Morelos State, Av Universidad 1001, C.P. 62209, Cuernavaca, Morelos, Mexico.

Institutional e-mail address: zakaryaa.zarhri@docentes.uaem.edu.mx

IDScopus: https://www.scopus.com/authid/detail.uri?authorId=55944455700

3- Pr. Noureddine Lakouari

Affiliation : National Institute of Astrophysics, Optics and Electronics (INAOE), Puebla, Mexico. Secretariat of Science, Humanities, Technology and Innovation (Secihti), Mexico.

Institutional e-mail address: n.lakouari@inaoep.mx

ID Scopus:

https://www.scopus.com/authid/detail.uri?authorId=55861806500

TABLE OF CONTENT

1. **Investigation of Thermoelectric and Structural Properties of $BeAlH_3$, $BeGaH_3$, and $BeInH_3$ perovskite Hydrides for Energy Applications**

   DOI: https://doi.org/10.51646/jsesd.v14iSTR2E.786

   Ayoub Koufi, Younes Ziat, Hamza Belkhanchi , Abdellah Bouzaid

   Pages : 1-14

2. **Forecasting Energy Consumption on a Microgrid using ARIMA-GRU Model**

   DOI: https://doi.org/10.51646/jsesd.v14iSTR2E.791

   Lahoucine Oumiguil, Ali Nejmi

   Pages : 15-26

3. **Role of Embedded Systems in Smart Energy Management:**Challenges, Innovations, and Future Trends

   DOI: https://doi.org/10.51646/jsesd.v14iSTR2E.797

   Sachin Srivastava, G. Sai Satyanarayana, Abhay Dhasmana, Vineet Rawat, Aditya Singh Rana, Yashwant Singh Bisht

   Pages : 27-50

4. **DFT Approach for Improving the Electronic and Optical Properties of Kznf3 Perovskite:**Impact of Copper Doping

   DOI: https://doi.org/10.51646/jsesd.v14iSTR2E.798

   Noureddine Elmeskini, Younes Ziat, Hamza Belkhanchi, Ayoub Koufi

   Pages : 51-66

5. **First-Principles Study of Ge-Doped $CH_3NH_3PbI_3$ Perovskite:**Optical and Electronic Properties

   DOI: https://doi.org/10.51646/jsesd.v14iSTR2E.799

   Lhouceine Moulaoui, Abdelhafid Najim, Abdlmounaim Laassouli, Omar Bajjou, Khalid Rahmani, Bouzid Manaut

   Pages : 67-78

6. **Industrial Rock Packed-Bed Heat Storage System:**Thermal Behavior and Performance Assessment

DOI: https://doi.org/10.51646/jsesd.v14iSTR2E.800

Aicha Eddemani, Omar Achahour, Hayat El Baamrani, Ahmed Aharoune, Lahcen Bouirden , Ahmed Ihlal

Pages : 79-90

7. **Comprehensive Analysis of Optoelectronic Properties and Photovoltaic Performance of Rb2CuAsZ6 (Z = Br and Cl) Double Perovskites Using DFT and SCAPS-1D Modelling**

DOI: https://doi.org/10.51646/jsesd.v14iSTR2E.802

Kamal Assiouan, Hanan Ziani, Jamal EL Khamkhami, Abdelfattah Achahbar

Pages : 91-104

8. **Impact of Thermal Insulation on Vehicle Cabin Heat Loads and Energy Use**

DOI: https://doi.org/10.51646/jsesd.v14iSTR2E.803

Hasnaa Oubnaki , Charifa Haouraji , Ilham Mounir, Badia Mounir, Abdelmajid Farchi

Pages : 105-113

9. **Robust Control for DFIG-Based WECS with ANN-Based MPPT**

DOI: https://doi.org/10.51646/jsesd.v14iSTR2E.894

Achraf El Ouali, Yassine Lakhal, Mohamed Benchagra, Hamid Chojaa, Mohamed Vall Ould Mohamed

Pages : 114-122

10. **Analysis of the Thermal Response of a Floor Heating System Incorporating a Phase Change Material**

DOI: https://doi.org/10.51646/jsesd.v14iSTR2E.895

Afaf Charraou, Mohamed Errebii, Amina Mourid, Rachid Saadani, Miloud Rahmoune, Mustapha El Alami

Pages : 123-133

11. Optoelectronic Properties of Doped $CaTiO_3$ (C, N, Si and P): A DFT Study for Photovoltaic Applications

DOI: https://doi.org/10.51646/jsesd.v14iSTR2E.982

Abdellah Bouzaid , Younes Ziat, Hamza Belkhanchi, Ayoub Koufi , Mohammed Miri , Hmad Fatihi , Charaf Laghlimi

Pages : 134-150

12. Improving PEM Water Electrolysis Efficiency with ANN-Based Control to Handle Rapid Photovoltaic Power Fluctuations

DOI: https://doi.org/10.51646/jsesd.v14iSTR2E.985

Abdellah EL IDRISSI, Belkasem IMODANE, Hamid HAMDANI, M'hand OUBELLA, Mohamed BENYDIR, Mohamed AJAAMOUM

Pages : 151-163

13. Optimization of Adobe and Sawdust-Based Bricks for Improved Energy Efficiency in Construction

DOI: https://doi.org/10.51646/jsesd.v14iSTR2E.983

Mohammed Benfars, Abdelmounaim Alioui, Youness Azalam, Mourad Kaddiri, Mustapha Mabrouki

Pages : 164-179

14. Theoretical Insights into a High-Performance Optical Absorption in GaSeS/InSeS 2D van der Waals Heterostructure for Photovoltaic Applications

DOI: https://doi.org/10.51646/jsesd.v14iSTR2E.986

Hanan Ziani, Kamal Assiouan, Fatima Zohra Ben Abdelouahab, El Hassan El Harouny , Mustapha El Hadri , Farid Ben Abdelouahab

Pages : 180-197

15. Geometry-Dependent Thermal Transport in Porous Silicon: A Computational Study of Pore Geometry and Porosity Effects

DOI: https://doi.org/10.51646/jsesd.v14iSTR2E.1180

Othman Soubai, Younes Abouelhanoune, Mohammed Taibi

Pages : 198-215

16. **Parametric study of the impact of insulation and wall thickness in straw-reinforced adobe structures on energy performance in a Moroccan desert climate: A case study of Errachidia city**

DOI: https://doi.org/10.51646/jsesd.v14iSTR2E.1060

Abdelmounaim Alioui, Youness Azalam, Mohammed Benfars, Mustapha Mabrouki

Pages : 216-229

17. **DFT Analysis of Structural, Elastic and Optoelectronic Enhancements in $LiGeCl_3$ Under Pressure for Photovoltaic Applications**

DOI: https://doi.org/10.51646/jsesd.v14iSTR2E.1181

Mohammed Miri , Younes Ziat, Hamza Belkhanchi , Abdellah Bouzaid, Youssef Jouad , Youssef Ait El Kadi

Pages : 230-252

Solar Energy
And Sustainable Development
Refereed, biannual scientific journal issued by:
The Libyan Center for Solar Energy Research and Studies

Investigation of Thermoelectric and Structural Properties of $BeAlH_3$, $BeGaH_3$, and $BeInH_3$ perovskite Hydrides for Energy Applications

Ayoub Koufi[1]*, Younes Ziat[2], Hamza Belkhanchi[3], Abdellah Bouzaid[4].

[1,2,3,4]Engineering and Applied Physics Team, Sultan Moulay Slimane University, Beni Mellal, Morocco.
[1,2,3,4]The Moroccan Association of Sciences and Techniques for Sustainable Development, Beni Mellal, Morocco.

E-*mail:* [1] ayoub.koufi@usms.ma.

SPECIAL ISSUE ON:

The 1St International Conference on Sciences and Techniques for Renewable Energy and the Environment.
(STR2E 2025)
May 6-8, 2025 at FST-Al Hoceima-Morocco.

KEYWORDS

DFT; $BeAlH_3$, $BeGaH_3$, and $BeInH_3$; Gravimetric; Hydrogen; Thermal.

ABSTRACT

This study explores the structural, electrical, and thermoelectric properties of crystalline beryllium hydrides $BeXH_3$ (X = Al, Ga, In) using the generalized gradient approximation (GGA) within the framework of density functional theory (DFT). The analysis is performed using the BoltzTrap package, integrated with the Wien2k code, and the Murnaghan equation of state to determine total energy and atomic volume while providing detailed information on band structure and electronic densities of states.

Key thermoelectric properties, including power factor (PF), figure of merit (Zt), thermal conductivity (κ), and electrical conductivity (σ), were investigated over a temperature range from 300 to 900 K. The results show that BeGaH3 exhibits the best thermoelectric performance over the entire temperature range, with a maximum electrical conductivity of $3.5x10^{20}$ (.s) at 900 K. In contrast, BeAlH3 and BeInH3 show interesting thermoelectric behaviors with an increase in efficiency at higher temperatures. Thermal conductivity increases with temperature, influenced by electron vibrations, while Zt and PF factors show material-specific variations, highlighting the optimization potential of these compounds for thermoelectric devices.

*Corresponding author.

DOI: https://doi.org/10.51646/jsesd.v14iSTR2E.786

This is an open access article under the CC BY-NC license (http://Attribution-NonCommercial 4.0 (CC BY-NC 4.0)).

دراسة الخواص الحرارية الكهربائية والبنيوية لهيدريدات البيروفسكايت $BeXH_3$ لتطبيقات الطاقة $BeInH_3$ و $BeGaH_3$ $BeAlH_3$

أيوب كوفي، يونس زيات، حمزة بلخنشي، عبد الله بوزيد.

ملخص: تستكشف هذه الدراسة الخصائص التركيبية والكهربائية والحرارية الكهربائية لهيدريدات البيريليوم البلورية $BeXH_3$ (X = Al, Ga, In) باستخدام تقريب التدرج المعمم (GGA) في إطار نظرية الوظيفة الكثيفة (DFT). تم إجراء التحليل باستخدام حزمة BoltzTrap المدمجة مع كود Wien2k، ومعادلة الحالة لـ Murnaghan لتحديد الطاقة الكلية وحجم الذرة، مع توفير معلومات مفصلة عن بنية النطاقات وكثافة الحالات الإلكترونية. تم التحقيق في الخصائص الحرارية الكهربائية الرئيسية، بما في ذلك معامل القدرة (PF)، ومعامل الجودة (Zt)، والتوصيلية الحرارية (k)، والتوصيلية الكهربائية (σ) ضمن نطاق درجات حرارة من300 إلى 900 كلفن. أظهرت النتائج أن $BeGaH_3$ يتمتع بأفضل أداء حراري كهربائي عبر نطاق درجات الحرارة بالكامل، حيث يصل الحد الأقصى للتوصيلية الكهربائية إلى (3.5×10^{20} .s) عند 900 كلفن. في المقابل، أظهر كل من $BeAlH_3$ و$BeInH_3$ سلوكيات حرارية كهربائية مثيرة للاهتمام مع زيادة الكفاءة عند درجات حرارة أعلى. تزداد التوصيلية الحرارية مع ارتفاع درجة الحرارة، متأثرة باهتزازات الإلكترونات، بينما تظهر عوامل Zt وPF اختلافات تعتمد على المادة، مما يبرز إمكانيات تحسين هذه المركبات لتطبيقات الأجهزة الحرارية الكهربائية.

الكلمات المفتاحية: DFT؛ $BeGaH_3$، $BeAlH_3$، و $BeInH_3$؛ الجاذبية النوعية؛ الهيدروجين؛ الحراري .

1. INTRODUCTION

Hydrogen is one of the most abundant elements on Earth [1] and possesses unique properties that make it particularly interesting in the energy field. Compared with traditional fossil fuels, hydrogen releases far more heat when it reacts with oxygen [2, 3, 4]. The gas is considered a clean and sustainable energy source, as it is carbon-free, meaning it emits no CO_2 during combustion [5, 6]. This makes it a promising alternative for environmentally friendly energy solutions [7, 8, 9]. Hydrogen's applications are vast, ranging from fuel cells, employed in vehicles and some power plants, to internal combustion engines, notably in hybrid cars [10]. However, to enable wider adoption of hydrogen, two major challenges remain mass production and storage [11, 12, 13]. Current methods, such as steam methane reforming or electrolysis fueled by non-renewable sources, are proving costly and pose environmental problems [14, 15, 16]. Hydrogen storage also represents a technical challenge, due to its low energy density per unit volume [17, 18, 19]. This calls for specific solutions, such as storage in the form of chemical compounds, at very low temperatures or under high pressure, which entails risks in terms of safety and technological feasibility [20, 21, 22]. To make hydrogen accessible in a safe, economical, and efficient way, advances in production and storage technologies are crucial [23, 24]. With alternative energy sources such as hydrogen, wind, nuclear, and solar power, it becomes possible to mitigate the negative effects associated with fossil fuels and reduce our dependence on them [13, 25, 26].
This scientific discussion aims to highlight the growing importance of perovskite-type hydrides, emphasizing their unique properties and crucial role in the search for new materials for energy storage [27]. The crystalline structure of perovskite, with its ABH3 composition, is renowned for its malleability and modification potential, making it an ideal material for a variety of applications [28, 29]. In particular, perovskite hydrides show great promise as high-capacity hydrogen storage materials [30]. Thanks to the hydride ions embedded in their lattice, these materials enable reversible absorption and release of hydrogen, a valuable feature for meeting storage challenges in clean energy technologies [31, 32]. Interactions between hydride ions and the intrinsic structure of perovskites pave the way for advanced energy conversion technologies,

including catalytic functions that could enhance electrochemical and photoelectrochemical processes [33, 34]. A study of perovskite hydrides, including $MgCrH_3$ and $MgFeH_3$, revealed that $MgFeH_3$ is a very promising candidate due to its balance between conductivity, storage capacity, and stability [35]. Storage capacity is decreased when transition metal dopants are added, even though this speeds up processes and lowers desorption temperatures [36]. Density functional theory (DFT)-based methods are crucial for optimizing these materials because they allow for the prediction of structural and optoelectronic properties [37, 38]. Researchers can predict important characteristics, including thermal and electrical conductivity, Seebeck coefficient, and thermoelectric figure of merit by using DFT to simulate perovskites at the atomic scale [39]. New opportunities for thermal energy conversion and the creation of more efficient and sustainable energy technologies are made feasible by these developments, which enable the design of materials with the best thermoelectric qualities. In this work on the electronic gravimetric and thermoelectric properties of beryllium hydrides $BeXH_3$ (X = Al, Ga, and In) based on DFT, we use the generalized gradient approximation (GGA) integrated into the BoltzTrap program. This approach enables us to model atomic interactions and assess the ability of these materials to convert thermal energy into electrical energy. The following sections describe in detail the computational techniques deployed, present the data obtained, and discuss conclusions regarding the thermoelectric performance of beryllium hydrides as a function of temperature. This work thus contributes to our understanding of the potential of thermoelectric materials and their optimization for advanced energy applications. $BeXH_3$ compounds, particularly those with Al, Ga, and In, are of interest for a variety of applications. For instance, these hydrides could have potential uses in hydrogen storage, catalysis, or even in the development of novel materials for energy-related technologies. Their properties may also be relevant in the development of new types of batteries, sensors, and other electronic devices, owing to their lightweight nature and possible stability in specific conditions.

2. CALCULATION METHOD

This study utilizes theoretical calculations to evaluate the hydrogen storage capabilities and other properties of $BeXH_3$ (X = Al, Ga, and In) using the GGA, within the framework of DFT [40, 41], which elucidates the exchange and correlation potentials in these calculations. To do this, we use the BoltzTrap package implemented in the Wien2k code [42, 43]. Birch Murnaghan's equation of state is used for structural optimization [44]. During the self-consistent field (SCF), the convergence of total energy and charge was set at 0.0001 (Ry) and 0.001 (e). Using octahedral integration, a 1000 k-point mesh is used to sample the Brillouin zone in detail.

The Murnaghan-equation of state was used to obtain the ground state volume (V_0), mass modulus (B_0), and their derivatives (B_0') during optimization. Also, the Murnaghan-equation is used to calculate the pressure-dependent volume. To achieve network constants, the bulk modulus (B_0), pressure derivative (B_0'), and structural parameters were optimized over the volume of the unit cell, with the compressibility modulus (B) as a measure of a material's resistance to uniform compression, expressed in terms of change in volume under pressure. It is often used to characterize materials in terms of their ability to resist changes in volume under pressure. The mass modulus (B_0), on the other hand, is a term sometimes used in specific models to describe a relationship between mechanical properties and material density, although it is conceptually similar to the compressibility modulus. The pressure derivative (B') refers to the variation of the compressibility modulus as a function of pressure, providing a measure of the material's sensitivity to increasing pressure. This parameter is crucial to understanding how materials react under different pressure conditions and is commonly used in studies of high-pressure material properties.

The postulated equilibrium lattice constants are obtained by fitting the total energy as a function of the normalized volume to the Murnaghan equation of state (EOS). The equilibrium lattice parameters (a0) that we estimated reasonably agree with the experimental ones. Figure 1 shows the volumes extracted as a function of the expected energy using the Birch-Murnaghan depression.

$$E = E_0 + \frac{B_0}{B_0'}\left(V - V_0\right) - \frac{B_0 V_0}{B_0'\left(1 - B_0'\right)}\left[\left(\frac{V}{V_0}\right)^{1-B_0'} - 1\right] \qquad (1)$$

Where E_0 is taken as the minimum energy, which is the ground state energy corresponding to the volume V_0 of the unit cell.

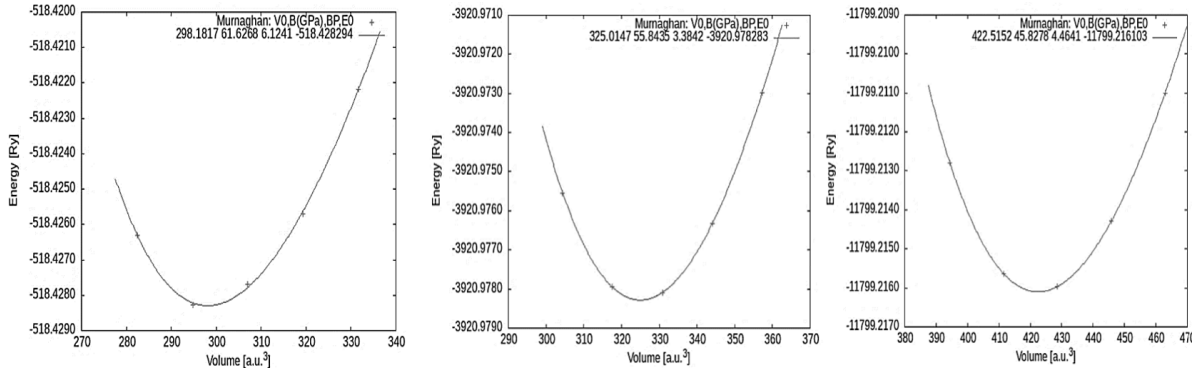

a) b) c)

Figure 1. Variation of total energy as a function of volume for: a) $BeAlH_3$; b) $BeGaH_3$; and c) $BeInH_3$.

3. RESULTS AND DISCUSSION

3.1. Structural properties

The central element of the $BeXH_3$ hydride perovskite structure (X = Al, Ga, and In) is based on a precise arrangement of atoms: beryllium (Be) atoms are placed at the corners (0, 0, 0) of the cube, while three hydrogen atoms occupy octahedral positions located at the face centers (0, 1/2, 1/2), (1/2, 0, 1/2) and (1/2, 1/2, 0). The X atoms (Al, Ga, and In) are located at the heart of the center (1/2, 1/2, 1/2) [45].

The lattice parameters for $BeXH_3$ (see Table 1) confirm the accuracy of our computations and the reliability of the obtained data. This structure corresponds to a face-centered cubic (fcc) lattice with a space group of $Pm\bar{3}m$ (No. 221).

Figure 2 depicts this arrangement, which is exactly in line with the structures reported in earlier research. Thus, it offers a strong foundation for analyzing this intriguing class of materials.

Table 1. Lattice parameters of $BeXH_3$.

Element	Lattice parameter
$BeAlH_3$	$a_0=b_0=c_0$=3.5353 Å (This work) 3.57 Å [45]
$BeGaH_3$	$a_0=b_0=c_0$= 3.6522 Å (This work) 3.66 Å [45]
$BeInH_3$	$a_0=b_0=c_0$= 3.9708 Å (This work) 3.99 Å [45]

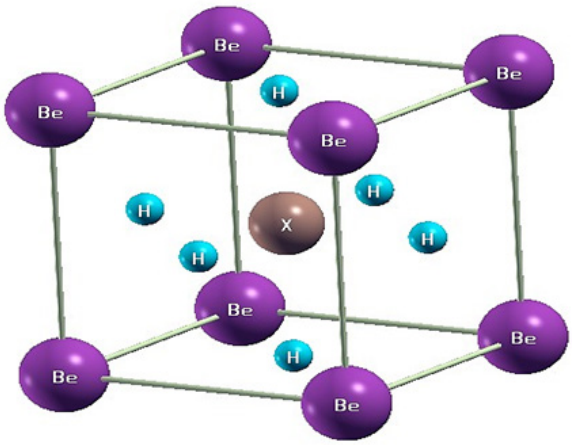

Figure 2. Structure of $BeXH_3$ (X = Al, Ga, and In).

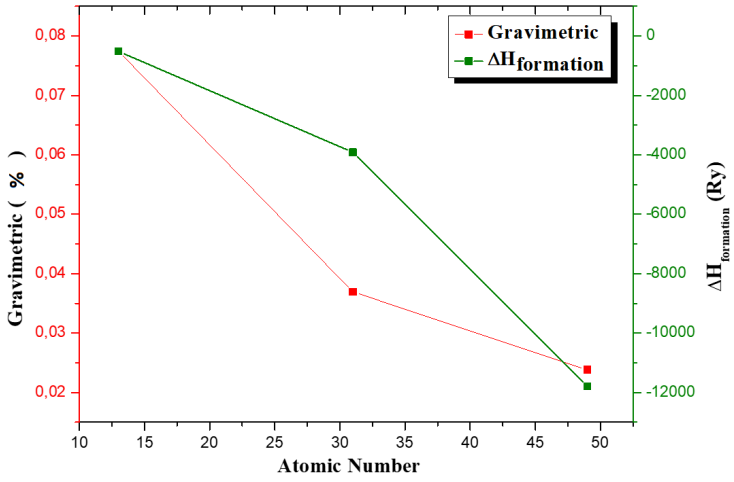

(a)

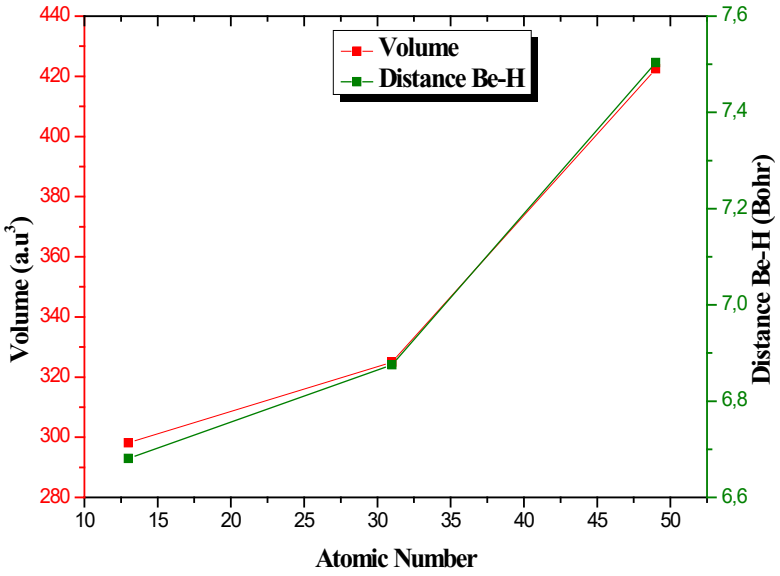

(b)

Figure 3. a) Gravimetric and $\Delta H_{formation}$ as a function of Atomic Number for $BeXH_3$ (X = Al, Ga, and In); b) Volume and distance Al-H as a function of Atomic Number for $BeXH_3$ (X = Al, Ga, and In).

Figure 3(a) illustrates a key observation: the gravimetric values and enthalpy of formation ($\Delta H_{formation}$) of the compounds studied decrease systematically with increasing atomic number of the central element (Al, Ga, In), this decrease in gravimetric values means that, as the central atom becomes heavier, the mass proportion of hydrogen in the compound decreases, directly affecting the energy density of the material. Furthermore, the decrease in $\Delta H_{formation}$ indicates that the thermodynamic stability of compounds is lower for elements with a higher atomic number, an effect attributable to differences in size and nuclear charge between atoms [46, 47]. Aluminum (Al, atomic number 13) has a gravimetric value of 0.077 and a $\Delta H_{formation}$ of -518.42829 Ry, showing good energy density and stability among the three compounds. The element Ga atomic number 31 has a gravimetric value of 0.036 and a $\Delta H_{formation}$ of -3920.9782 Ry. Conversely, indium (In, atomic number 49) displays a gravimetric value of 0.023 and a $\Delta H_{formation}$ of -11799.2161 Ry, signifying lower energy density and stability, making it "softer" than the other compounds. These trends can be partly explained by quantum phenomena such as the electron-shielding effect, which reduces the effective attraction of the nucleus to valence electrons in larger atoms [48, 49, 50]. As a result, bonds are weaker, and less energy is required to form compounds of heavier elements, resulting in a lower enthalpy of formation. This interpretation of the $\Delta H_{formation}$ and gravimetric values suggests that, of the $BeXH_3$ compounds, $BeInH_3$ has the least dense and most malleable structure, while $BeAlH_3$ remains the most stable and dense. Finally, as shown in Figure 3(b), a correlation can be deduced between the atomic number and the physical and chemical properties of these hydrides. The higher the atomic number, the greater the atomic volume, which directly influences the material's stability and gravimetric density.

3.2. Electronic properties

In our study, we used the GGA to analyze the electrical characteristics of $BeXH_3$ perovskite-type hydrides (X = Al, Ga, and In). The results obtained, shown in Figure 4, clearly demonstrate the metallic behavior of these compounds. The crossing of valence band maxima and conduction band minima over the fixed Fermi level (EF) at 0 eV indicates this intermetallic property. This crossover suggests that these materials are very conductive due to their non-zero density of electronic states at the EF.

Total density of states (TDOS) and Partial density of states (PDOS) analysis (see Figure 5) explores the individual contribution of each atom type to the overall electronic properties of the compound. Hydrogen s-states (H), X p-states (Al, Ga, and In), and Be s-states play a notable role around the Fermi level, each making significant contributions to the material's conductivity. However, it is the d states of the X atom (Al, Ga, and In) that dominate the valence band in the energy range between -12 and -6 eV, reflecting a major influence of these elements on the electronic stability of the material. This complex interaction between the electronic states p of X, s of Be, and s of H creates hybridization around the EF, a distinctive feature of metals, which explains their high conductivity. It is also relevant to note that this metallic conductivity confers on perovskite-type hydrides a hydrogen storage capacity superior to that of non-metallic compounds. Indeed, high conductivity facilitates charge transfer during hydrogen absorption and release processes, which is crucial for optimizing hydrogen storage reversibility. Furthermore, owing to their unique electronic structure, metals provide favorable adsorption sites for hydrogen molecules, thereby enhancing their storage capacity [51].

As a result, $BeXH_3$ perovskite-type hydrides seem to be viable options for storing hydrogen. Their electronic structure ensures high conductivity and favorable interaction with hydrogen molecules, essential qualities for storage technologies. It should also be noted that the subtle differences in electronic structure between the compounds $BeAlH_3$, $BeGaH_3$, and $BeInH_3$, due to the specific properties of the elements Al, Ga, and In, could enable fine-tuning of storage

properties, offering additional flexibility in the development of materials optimized for industrial applications [52]. This possibility paves the way for further research into the manipulation of electronic characteristics to further improve hydrogen storage efficiency in perovskites.

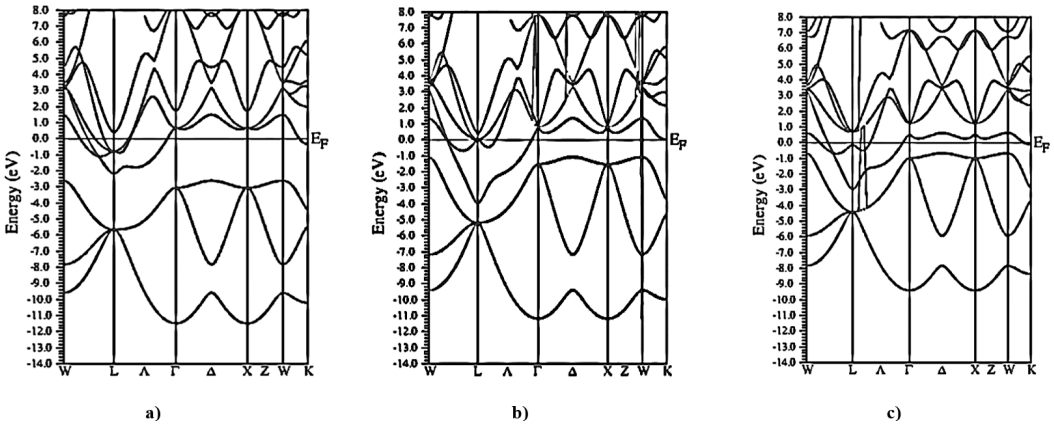

Figure 4. Band Structures of: a) $BeAlH_3$; b) $BeGaH_3$; and c) $BeInH_3$.

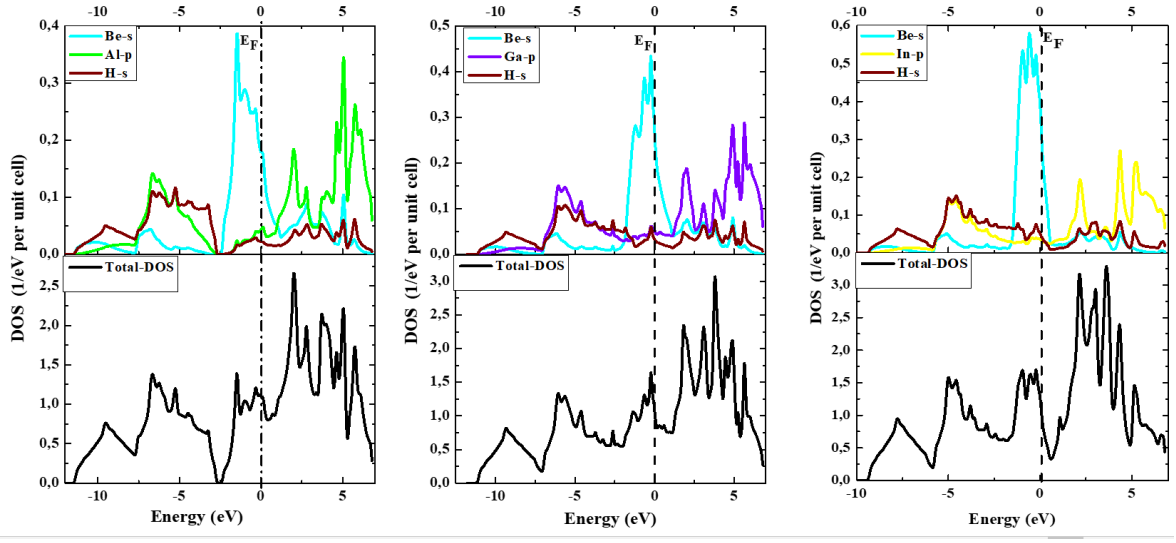

Figure 5. The density of states and partial density of states of a) $BeAlH_3$; b) $BeGaH_3$; and c) $BeInH_3$.

3.3. Thermoelectrical Properties

The behavior of electron transport properties is closely linked to the structure of the electron band, calculated here by applying the semi-classical Boltzmann transport theory and the rigid band model, implemented in BoltzTrap software. Since thermal dissipation is a frequent loss in energy-intensive processes, materials such as $BeXH_3$ (where X = Al, Ga, and In) are of crucial importance in renewable energy devices [53].

The efficiency of thermoelectric devices depends on the ratio between electrical and thermal conductivity, making this a key parameter to optimize [53]. $BeXH_3$ compounds (X = Al, Ga, and In) are of particular interest for their thermoelectric properties, and their electrical conductivity (σ), thermal conductivity (κ), figure of merit (Zt) and power factor (PF) have been studied for temperatures ranging from 300 K to 900 K. Although the electrical conductivity of $BeXH_3$ perovskite, expressed as the flux of free charge carriers, is a fundamental element, it has been little explored in the literature to date. As with most materials, factors such as chemical composition, crystal structure, and impurities significantly influence this conductivity.

The measurements shown in Figure 6(a) demonstrate the evolution of electrical conductivity with temperature: it increases between 300 and 500 K before gradually decreasing from 500 to 900 K. For $BeGaH_3$, conductivity reaches a maximum of $3.5x10^{20}$ (1/Ω.m.s) at 900 K, while for $BeAlH_3$ and $BeInH_3$ it drops to $2x10^{20}$ (1/Ω.m.s) and $7.5x10^{20}$ (1/Ω.m.s) respectively under the same conditions. Furthermore, temperature and pressure conditions during the evaluation of $BeXH_3$ (X = Al, Ga, In) also significantly influence the electronic characteristics and, by extension, the electrical conductivity of these materials. These data highlight the importance of physical properties engineering to improve material performance in thermoelectric applications.

Thermal conductivity, which governs heat transfer in a material, shows a linear increase with temperature in the absence of significant variations. Thermal conductivity values (κ) for $BeXH_3$ compounds (X = Al, Ga, and In) are shown in Figure 6(b): they increase progressively with temperature, reaching $14x10^{15}$ W/(K.m.s), $7x10^{15}$ W/(K.m.s), and $3x10^{15}$ W/(K.m.s) respectively for $BeAlH_3$, $BeGaH_3$, and $BeInH_3$ at 900 K. This increase in thermal conductivity is mainly due to vibrations of free electrons within the compounds, which intensify with increasing temperature. Thus, it can be concluded that temperature increase amplifies molecular vibrations in $BeXH_3$ structures (X = Al, Ga, and In), contributing substantially to the thermal conductivity of these materials. The Seebeck coefficient, thermal conductivity, and electrical resistivity all contribute to the dimensionless merit factor (Zt), which thermoelectric materials use to generate energy from temperature gradients [53]. The merit factor (Zt) is explained by the equation that follows:

$$Zt = \frac{\sigma S^2 T}{\kappa} \qquad (2)$$

where σ is the electrical conductivity, T is the temperature, S is the Seebeck coefficient, and κ is the thermal conductivity [54]. A high Zt value indicates effective thermoelectric performance in a material with low thermal conductivity, high electrical conductivity, and a significant Seebeck coefficient. The Merit factor (Zt), illustrated in Figure 6(c), shows a distinct variation for each $BeXH_3$ compound (X = Al, Ga, and In) as a function of temperature. For $BeAlH_3$, Zt initially decreases between 300-600 K, then increases from 600 to 900 K with increasing temperature. For $BeGaH_3$, on the other hand, Zt rises steadily over the entire temperature range. For $BeInH_3$, Zt falls slightly between 300 and 400 K before rising steadily from 400 to 900 K. At 900 K, maximum Zt values reach $2.5x10^{-2}$, $35x10^{-2}$, and $19.8x10^{-2}$ for $BeAlH_3$, $BeGaH_3$, and $BeInH_3$, respectively. These variations in merit factors highlight the specific thermal responses of each material and their potential for optimization in thermoelectric applications.

The material efficiency in thermoelectric devices is measured by the power factor, which is derived from electrical conductivity and the Seebeck coefficient [53]. For the production of energy, high power factor materials are desired, especially those with a power factor larger than unity, especially in the high-temperature thermoelectric sectors. The following formula explains the PF:

$$Power\ factor(PF) = \sigma S^2 \qquad (3)$$

The power factor (PF), as shown in Figure 6(d), varies differently for each $BeXH_3$ compound (X = Al, Ga, and In) as a function of temperature. For $BeAlH_3$, the power factor first decreases from 300 to 600 K, then increases from 600 to 900 K with rising temperature. For $BeGaH_3$, on the other hand, the power factor rises continuously over the entire temperature range. For $BeInH_3$, the power factor decreases slightly between 300 and 400 K, before resuming an increasing trend from 400 to 900 K. Around 900 K, maximum power factor values reach $2.5x10^{10}$ W/(K².m.s), $27x10^{10}$ W/(K².m.s), and $7x10^{10}$ W/(K².m.s) for $BeAlH_3$, $BeGaH_3$, and $BeInH_3$, respectively. These trends reveal specific variations in each material's response to thermal conditions, highlighting their distinct potential for optimization in thermoelectric applications where a high-power factor is

essential. The ability to control and optimize temperature gradients could help maintain the ideal conditions for hydrogen storage, potentially enhancing the performance and efficiency of storage systems. This synergy between thermoelectric properties and hydrogen storage could contribute to more sustainable, energy-efficient solutions for hydrogen-based energy systems.

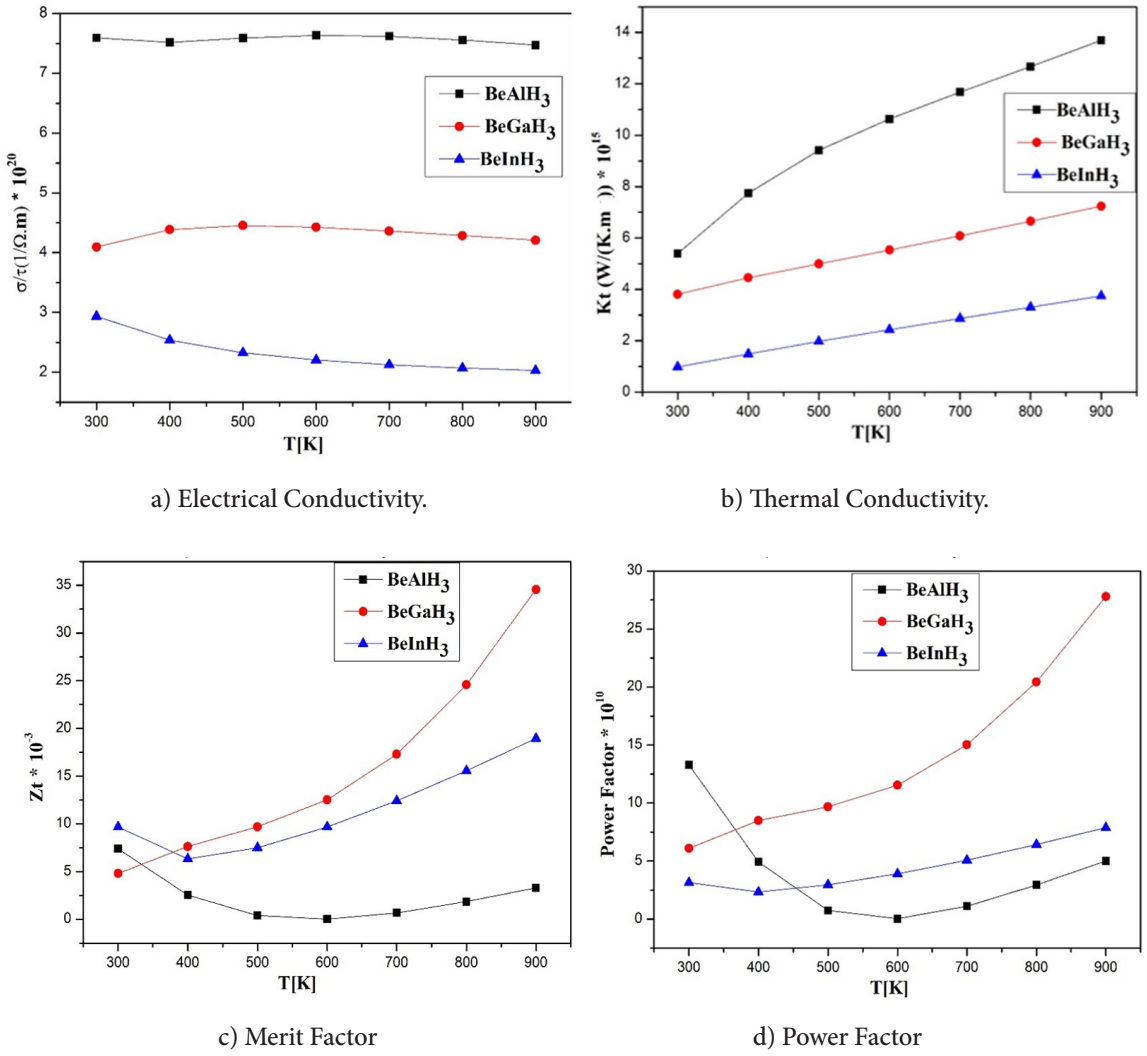

a) Electrical Conductivity. b) Thermal Conductivity.

c) Merit Factor d) Power Factor

Figure 6. Thermoelectric Properties of $BeXH_3$ (X = Al, Ga, and In).

To evaluate the thermoelectric performance of $BeXH_3$ (X = Al, Ga, In), we compared its properties with those of well-known candidates such as $MgFeH_3$ and $MgCrH_3$ [35]. Our findings reveal that $BeGaH_3$ exhibits significantly superior performance. At 900 K, $BeGaH_3$ shows an electrical conductivity of $3.5x10^{20}$ (1/Ω.m.s), which is considerably higher than that of $MgFeH_3$ 7.75×10^{19} (1/Ω.m.s) and $MgCrH_3$ 7.74×10^{19} (1/Ω.m.s). Additionally, the figure of merit (Zt) for $BeGaH_3$ reaches 0.35, outperforming $MgFeH_3$ (0.09) and $MgCrH_3$ 0.27 at 300 K. This enhancement is attributed to the unique combination of its high electrical conductivity, moderate thermal conductivity, and a power factor of 27×10^{10} W/(K².m.s). These results underline the potential of $BeGaH_3$ as a highly efficient thermoelectric material and hydrogen storage candidate, surpassing the limitations of Mg-based hydrides such as $MgFeH_3$ and $MgCrH_3$, which typically exhibit lower Zt values and higher thermal conductivity.

As a result, metallic behavior, such as that observed in $BeGaH_3$, significantly contributes to hydrogen storage efficiency through improved charge transport and enhanced hydrogen

adsorption. High electrical conductivity facilitates the rapid movement of electrons during hydrogen absorption and desorption, improving the kinetics of these processes. This leads to faster hydrogen uptake and release, which is essential for efficient storage. Additionally, the metallic nature of $BeGaH_3$ allows for better hydrogen adsorption at the metal-hydrogen interface, where the availability of delocalized electrons promotes the dissociation and absorption of hydrogen molecules, thus increasing storage capacity. Moreover, the high thermal conductivity of metallic hydrides helps manage the heat generated or absorbed during these cycles, further optimizing the hydrogen storage process. In comparison to non-metallic materials, $BeGaH_3$'s metallic conductivity ensures faster, more efficient hydrogen storage and release, improving both the storage capacity and the overall kinetics of the process.

4. CONCLUSION

In the present study, we have used the BoltzTrap software package, integrated with the Wien2k code, to perform a theoretical analysis and predict the structural, electrical, and thermal properties of $BeXH_3$ (X = Al, Ga, and In) using the (GGA) within the framework of (DFT). Our results reveal that the band structures of $BeAlH_3$, $BeGaH_3$, and $BeInH_3$ behave like conductors, with the valence band and conduction band overlapping with no energy gap (0 eV). Thermoelectric properties, such as electrical conductivity (σ), thermal conductivity (κ), figure of merit (Zt), and power factor (PF), indicate that $BeGaH_3$ outperforms $BeAlH_3$ and $BeInH_3$, particularly in terms of high-temperature stability and efficiency. Thermal conductivity increases linearly with temperature, influenced by electron vibrations, while electrical conductivity and merit and power factors vary with thermal conditions, with distinct optimization potential for each material. These discoveries offer promising prospects, not only for scientific advances but also for practical applications that could transform industry and everyday life, particularly in solid-state energy storage devices. The use of compounds such as $BeXH_3$ metal hydrides (X = Al, Ga, and In) looks promising for more compact and safer energy storage. However, further studies will be needed to improve the kinetics and storage capacity of these materials, supported by rigorous scientific efforts and organizational coordination to maximize their impact in thermoelectric and energy applications. The development of advanced materials for hydrogen storage, including efficient thermoelectric systems, is crucial for improving the performance, energy efficiency, and sustainability of future hydrogen-based energy technologies.

Author Contributions: Ayoub Koufi: Writing – original draft, visualization, validation, investigation, formal analysis, data curation, and conceptualization. Younes Ziat: Supervision. Hamza Belkhanchi: Writing – original draft, visualization, validation, investigation, formal analysis, data curation, and conceptualization. Abdellah Bouzaid: Visualization.

Funding: The authors are warmly grateful to the support of "The Moroccan Association of Sciences and Techniques for Sustainable Development (MASTSD), Beni Mellal, Morocco.

Data Availability Statement: Not applicable.

Acknowledgments: A special thank you to Professor Hanane Reddad from Sultan Moulay Slimane University, Beni Mellal, Morocco, for her technical and scientific support, as well as her full collaboration and discussion during the different steps of the present investigation.

Conflicts of Interest: The authors declare that they have no conflict of interest.

REFERENCES

[1] M. Newborough, & G. Cooley. Developments in the global hydrogen market: The spectrum of hydrogen colours. Fuel Cells Bulletin, 2020(11), 16-22 (2020).

[2] E. Jiaqiang, B. Luo, D. Han, J. Chen, G. Liao, F. Zhang, & J. Ding. A comprehensive review on performance improvement of micro energy mechanical system: Heat transfer, micro combustion and energy conversion. Energy, 239, 122509 (2022).

[3] I. S. Anufriev. Review of water/steam addition in liquid-fuel combustion systems for NOx reduction: Waste-to-energy trends. Renewable and Sustainable Energy Reviews, 138, 110665 (2021).

[4] S. Ozgen, S. Cernuschi, & S. Caserini. An overview of nitrogen oxides emissions from biomass combustion for domestic heat production. Renewable and Sustainable Energy Reviews, 135, 110113 (2021).

[5] N. S. Veeramalli, S. S. Vasamsetti, J. Aravind Kumar, S. Sathish, D. Prabu, & T. Krithiga. Sustainable Environment with Green Energy Options: Advantages and Disadvantages. In Green Hydrogen Economy for Environmental Sustainability., Volume 1: Fundamentals and Feedstocks (pp. 287-303). American Chemical Society (2024).

[6] Z. Hammi, N. Labjar, M. Dalimi, Y. El Hamdouni, & S. El Hajjaji. Green hydrogen: A holistic review covering life cycle assessment, environmental impacts, and color analysis. International Journal of Hydrogen Energy, 80, 1030-1045 (2024).

[7] C. Ghenai, M. Albawab, & M. Bettayeb. Sustainability indicators for renewable energy systems using multi-criteria decision-making model and extended SWARA/ARAS hybrid method. Renewable Energy, 146, 580-597 (2020).

[8] M. Majid. Renewable energy for sustainable development in India: current status, future prospects, challenges, employment, and investment opportunities. Energy, Sustainability and Society, 10(1), 1-36 (2020).

[9] Laghlimi, C., Moutcine, A., Ziat, Y., Belkhanchi, H., Koufi, A., & Bouyassan, S. (2024). Hydrogen, chronology and electrochemical production. Solar Energy and Sustainable Development, 22-37. https://doi.org/10.51646/jsesd.v14iSI_MSMS2E.405.

[10] V. Arun, R. Kannan, S. Ramesh, M. Vijayakumar, P. S. Raghavendran, M. Siva Ramkumar, ... & V. P. Sundramurthy. Review on Li-Ion Battery vs Nickel, Metal Hydride Battery in EV. Advances in Materials Science and Engineering, 2022(1), 7910072 (2022).

[11] M. G. Rasul, M. A. Hazrat, M. A. Sattar, M. I. Jahirul, & M. J. Shearer. The future of hydrogen: Challenges on production, storage and applications. Energy Conversion and Management, 272, 116326 (2022).

[12] B. C. Tashie-Lewis, & S. G. Nnabuife. Hydrogen production, distribution, storage and power conversion in a hydrogen economy-a technology review. Chemical Engineering Journal Advances, 8, 100172 (2021).

[13] L. Zhang, C. Jia, F. Bai, W. Wang, S. An, K. Zhao, ... & H. Sun. A comprehensive review of the promising clean energy carrier: Hydrogen production, transportation, storage, and utilization (HPTSU) technologies. Fuel, 355, 129455 (2024).

[14] M. Aravindan, V. S. Hariharan, T. Narahari, A. Kumar, K. Madhesh, P. Kumar, & R. bakaran. Fuelling the future: A review of non-renewable hydrogen production and storage techniques. Renewable and Sustainable Energy Reviews, 188, 113791 (2023).

[15] L. Vidas, & R. Castro. Recent developments on hydrogen production technologies: state-of-the-art review with a focus on green-electrolysis. Applied Sciences, 11(23), 11363 (2021).

[16] S. U. Batgi, & I. Dincer. A study on comparative environmental impact assessment of thermochemical cycles and steam methane reforming processes for hydrogen production processes. Computers & Chemical Engineering, 180, 108514 (2024).

[17] H. Ishaq, I. Dincer, & C. Crawford. A review on hydrogen production and utilization: Challenges and opportunities. International Journal of Hydrogen Energy, 47(62), 26238-26264 (2022).

[18] X. Xu,Q. Zhou, & D. Yu. The future of hydrogen energy: Bio-hydrogen production technology. International Journal of Hydrogen Energy, 47(79), 33677-33698 (2022).

[19] Younas, M., Shafique, S., Hafeez, A., Javed, F., & Rehman, F. (2022). An overview of hydrogen production: current status, potential, and challenges. Fuel, 316, 123317.

[20] L. Van Hoecke, L. Laffineur, R. Campe, P. Perreault, S.W. Verbruggen, & S. Lenaerts. Challenges in the use of hydrogen for maritime applications. Energy & Environmental Science, 14(2), 815-843 (2021).

[21] S. Alfei, B. Marengo, & G. Zuccari. Nanotechnology application in food packaging: A plethora of opportunities versus pending risks assessment and public concerns. Food Research International, 137, 109664 (2020).

[22] G. W. Meijer, L. Lähteenmäki, LR. H. Stadler, & J. Weiss. Issues surrounding consumer trust and acceptance of existing and emerging food processing technologies. Critical reviews in food science and nutrition, 61(1), 97-115 (2021).

[23] N. Norouzi. Future of hydrogen in energy transition and reform. Journal of Chemistry Letters, 2(2), 64-72 (2021).

[24] D. Guan, B. Wang, J. Zhang, R. Shi, K. L. L. Jiao, ... & M. Ni,. Hydrogen society: From present to future. Energy & Environmental Science, 16(11), 4926-4943 (2023).

[25] Q. Hassan, A. Z. Sameen, H. M., Salman, M., Jaszczur, & A. K. Al-Jiboory. Hydrogen energy future: Advancements in storage technologies and implications for sustainability. Journal of Energy Storage, 72, 108404 (2023).

[26] M. Usman, «Hydrogen storage methods: Review and current status, Renew.,» vol. 167, 2022.

[27] A. Koufi, Y. Ziat, H. Belkhanchi, & A. Bouzaid. DFT and BoltzTrap investigations on the thermal and structural characteristics of the perovskite MgCuH3 and MgCoH3. Computational Condensed Matter, e01010 (2025), https://doi.org/10.1016/j.cocom.2025.e01010.

[28] Y. Liu, W. Lv, J. Feng, J. Tian, P. Wang, L. Xu, ... & L. Yao. Emerging Thermochromic Perovskite Materials: Insights into Fundamentals, Recent Advances and Applications. Advanced Functional Materials, 2402234 (2024).

[29] Koufi, A., Ziat, Y., & Belkhanchi, H. (2024). Study of the Gravimetric, Electronic and Thermoelectric Properties of $XAlH_3$ (X= Be, Na, K) as hydrogen storage perovskite using DFT and the BoltzTrap Software Package. Solar Energy and Sustainable Development, 53-66.https://doi.org/10.51646/jsesd.v14iSI_MSMS2E.403.

[30] S. Bahhar, A. Tahiri, A. Jabar, M. Louzazni, M. Idiri, & H. Bioud. Computational assessment of MgXH3 (X= Al, Sc and Zr) hydrides materials for hydrogen storage applications. International Journal of Hydrogen Energy, 58, 259-267 (2024).

[31] S. Y. Lee, J. H. Lee, Y. H. Kim, J. W. Kim, K. J. Lee, & S. J. Park. Recent progress using solid-state materials for hydrogen storage: a short review. Processes, 10(2), 304 (2022).

[32] S. P. Filippov, & A. B. Yaroslavtsev. Hydrogen energy: Development prospects and

materials. Russian Chemical Reviews, 90(6), 627 (2021).

[33] C. Xia, H. Wang, J. K. Kim, & J. Wang. Rational design of metal oxide-based heterostructure for efficient photocatalytic and photoelectrochemical systems. Advanced Functional Materials, 31(12), 2008247 (2021).

[34] E. Mousset, & D. D. Dionysiou. Photoelectrochemical reactors for treatment of water and wastewater: a review. Environmental Chemistry Letters, 18(4), 1301-1318 (2020).

[35] A. Koufi, Y. Ziat, H. Belkhanchi, ... & F. Z. Baghli. A computational study of the structural and thermal conduct of MgCrH3 and MgFeH3 perovskite-type hydrides: FP-LAPW and BoltzTraP insight. E3S Web of Conferences (2024), (Vol. 582, p. 02003). https://doi.org/10.1051/e3sconf/202458202003

[36] M. Dolors Baro, S. Surinach, E. Rossinyol, A. Marini, A. Girella, C. Milanese, E. Pellicer et S. Garroni, «Hydrogen sorption performance of MgH2 doped with mesoporous nickeland cobalt-based oxides,» pp. 540-5410 2011.

[37] I. U. Haq, G. Rehman, H. A. Yakout, & I. Khan. Structural and optoelectronic properties of Ge-and Si-based inorganic two dimensional Ruddlesden Popper halide perovskites. Materials Today Communications, 33, 104368 (2022).

[38] A. Bouzaid, Y. Ziat, H. Belkhanchi, H. Hamdani, A. Koufi, M. Miri, ... & Z. Zarhri. Ab initio study of the structural, electronic, and optical properties of MgTiO3 perovskite materials doped with N and P. E3S Web of Conferences (2024), (Vol. 582, p. 02006). https://doi.org/10.1051/e3sconf/202458202006.

[39] K. Burke, R. Car, & R. Gebauer. Density functional theory of the electrical conductivity of molecular devices. Physical review letters, 94(14), 146803 (2005).

[40] M. Orio, D. A. Pantazis, F. & Neese. Density functional theory. Photosynthesis research, 102, 443-453 (2009), https://doi.org/10.1007/s11120-009-9404-8.

[41] N. Argaman, & G. Makov. Density functional theory: An introduction. American Journal of Physics, 68(1), 69-79 (2000), https://doi.org/10.1119/1.19375.

[42] P. Blaha, K. Schwarz, F. Tran, R. Laskowski, G. K. Madsen, & L. D. Marks, WIEN2k: An APW+ lo program for calculating the properties of solids. The Journal of chemical physics, 152(7) (2020). https://doi.org/10.1063/1.5143061.

[43] J. P. Perdew, k. Burke, M. Ernzerhof, Generalized gradient approximation made simple. Phys. Rev. Lett. 77(18), 3865 (1996). https://doi.org/10.1103/PhysRevLett.77.3865.

[44] M. Miri, Y. Ziat, H. Belkhanchi, & Y. A. El Kadi, The effect of pressure on the structural, optoelectronic and mechanical conduct of the XZnF3 (X= Na, K and Rb) perovskite: First-principles study. Mod. Phys. B, 2550096 (2024). https://doi.org/10.1142/S0217979225500961

[45] W. Khan. Computational screening of BeXH3 (X: Al, Ga, and In) for optoelectronics and hydrogen storage applications. Materials Science in Semiconductor Processing, 174, 108221 (2024).

[46] E. Ededet, H. Louis, U. G. Chukwu, T. O. Magu, A. E. Udo, S. A. Adalikwu, & A. S. Adeyinka. Ab Initio Study of the Effects of d-Block Metal (Mn, Re, Tc) Encapsulation on the Electronic, Phonon, Thermodynamic, and Gravimetric, Hydrogen Capacity of BaXH4 Hydride Perovskites. Electronic Materials, 53(1), 250-264 (2024).

[47] H. H. Raza, G. Murtaza, S. Razzaq, & A. Azam. Improving thermodynamic properties and desorption temperature in MgH2 by doping Be: DFT study. Molecular Simulation, 49(5), 497-508 (2023).

[48] N. Cargioli. Standard model physics and beyond in low energy neutrino scattering and parity violating electron interactions with nuclei (2024).

[49] H. Takabe. Physical of Warm Dense Matters. In The Physics of Laser Plasmas and Applications-Volume 2: Fluid Models and Atomic Physics of Plasmas (pp. 397-450). Cham: Springer International Publishing (2024).

[50] X. Diao. A Computational study of mixed metal oxides (Doctoral dissertation, UCL (University College London)) (2024).

[51] A. Siddique, A. Khalil, B. S. Almutairi, M. B. Tahir, M. Sagir, Z. Ullah, ... & M. Alzaid. Structures and hydrogen storage properties of AeVH3 (Ae= Be, Mg, Ca, Sr) perovskite hydrides by DFT calculations, International Journal of Hydrogen Energy, 48(63), 24401-24411 (2023).

[52] B. P. Tarasov, P. V. Fursikov, A. A. Volodin, M. S. Bocharnikov, Y. Y. Shimkus, A. M. Kashin, ... & M. V. Lototskyy. Metal hydride hydrogen storage and compression systems for energy storage technologies., International Journal of Hydrogen Energy, 46(25), 13647-13657 (2021).

[53] M. Yaseen, H. Ambreen, Remsha, Mehmood, I. Munawar, A. Nessrin, Kattan,Thamraa Alshahrani, S. Noreen, & A. Laref. "Investigation of optical and thermoelectric properties of PbTiO3 under pressure", Physica B: Condensed Matter, (2021).

[54] D. Chang-Hao, D. Zhi-Fu, D. Zhong-Ke, P. Hui & al. " XMoSiN (X=S, Se, Te): A novel 2D Janus semiconductor with ultra-high carrier mobility and excellent thermoelectric performance ", Europhysics Letters, (2023).

Solar Energy
And Sustainable Development
Refereed, biannual scientific journal issued by:
The Libyan Center for Solar Energy Research and Studies

Forecasting Energy Consumption on a Microgrid Using ARIMA-GRU Model

Lahoucine Oumiguil [1]*, Ali Nejmi [2].

[1,2]Laboratory of Automatics, Energy Conversion and Microelectronics (LACEM), Faculty of Sciences and Technics, Sultan Moulay Slimane University, Campus Mghilla, Beni Mellal, Morocco.

E-*mail:* [1]lahoucine.oumiguil@usms.ma ,[2]ali.nejmi@gmail.com .

SPECIAL ISSUE ON:

The 1St International Conference on Sciences and Techniques for Renewable Energy and the Environment.

(STR2E 2025)

May 6-8, 2025 at FST-Al Hoceima-Morocco.

KEYWORDS

ARIMA; GRU; Deep learning; Energy consumption; Microgrid.

ABSTRACT

Accurate forecasting of energy consumption is crucial for the efficient management and control of modern energy grids, particularly amid the escalating integration of renewable energy sources. This study proposes a hybrid approach that combines the Autoregressive Integrated Moving Average (ARIMA) and the Gated Recurrent Unit neural network (GRU) to predict energy consumption in a microgrid setting. The proposed hybrid ARIMA-GRU model integrates ARIMA's residuals with GRU's non-linear modeling capabilities, enabling enhanced prediction accuracy while capturing both linear and non-linear dependencies in microgrid energy data. The model's performance is evaluated using real-world energy consumption data, achieving an RMSE of 38.28 kWh, MAE of 31.24 kWh, and MAPE of 10.29%. These results highlight the model's effectiveness in improving energy forecasting and providing practical insights for better energy management in microgrids.

*Corresponding author.

DOI: https://doi.org/10.51646/jsesd.v14iSTR2E.791

This is an open access article under the CC BY-NC license (http://Attribution-NonCommercial 4.0 (CC BY-NC 4.0)).

التنبؤ باستهلاك الطاقة في الشبكة الكهربائية الصغيرة باستخدام نموذج ARIMA-GRU

الحسين اوميكيل، علي نجمي.

ملخص: يُعد التنبؤ الدقيق باستهلاك الطاقة أمرًا بالغ الأهمية لإدارة شبكات الطاقة الحديثة والتحكم فيها بكفاءة، لا سيما في ظل تصاعد تكامل مصادر الطاقة المتجددة. تقترح هذه الدراسة نهجًا هجينًا يجمع بين المتوسط المتحرك المتكامل الانحداري الذاتي الانحداري (ARIMA) والشبكة العصبية للوحدة المتجددة المسندة (GRU) للتنبؤ باستهلاك الطاقة في بيئة الشبكات الصغيرة. يدمج نموذج GRU-ARIMA الهجين المقترح بين المتبقي من المتوسط المتحرك الانحداري التلقائي المتكامل (ARIMA) وقدرات النمذجة غير الخطية لوحدة GRU. يتيح هذا النموذج دقة تنبؤ محسّنة مع التقاط الترابطات الخطية وغير الخطية في بيانات طاقة الشبكة المصغرة. تم تقييم أداء النموذج باستخدام بيانات استهلاك الطاقة في العالم الحقيقي، محققًا متوسط خطأ جذر متوسط المربع (RMSE) قدره 28. 38 كيلوواط ساعة، ومتوسط خطأ مطلق (MAE) قدره 24. 31 كيلوواط ساعة، ومتوسط خطأ النسبة المئوية المطلقة (MAPE) قدره 10.29 %. تسلط هذه النتائج الضوء على فعالية النموذج في تحسين التنبؤ بالطاقة وتوفير رؤى عملية لتحسين إدارة الطاقة في الشبكات الصغيرة.

الكلمات المفتاحية –الكلمات المفتاحية: ARIMA ؛ GRU؛ التعلم العميق؛ استهلاك الطاقة؛ الشبكة الكهربائية الصغيرة.

1. INTRODUCTION

The growing complexity of power systems, driven by factors such as the integration of renewable energy sources, the rise of electric vehicles, and the need for flexible distribution grids, has made accurate energy consumption forecasting more critical than ever before[1]. Recent advancements in machine learning and deep learning techniques have exhibited encouraging outcomes in enhancing the precision of energy forecasting models, with techniques like Long Short-Term Memory (LSTM) and Gated Recurrent Unit networks (GRU) demonstrating superior performance with traditional statistical approaches[2].

Traditional statistical methods such as Autoregressive Integrated Moving Average (ARIMA) have been widely used for time series forecasting due to their simplicity and effectiveness in modeling linear relationships[3]. ARIMA has demonstrated notable success in various applications, including energy demand prediction[4]. However, its inability to capture non-linear patterns and its reliance on stationary data limit its effectiveness for more complex energy datasets[5]. In contrast, machine learning approaches, particularly Support Vector Machines (SVM) and neural networks, have gained traction for their ability to model non-linear dynamics and adapt to diverse data patterns[6]. Among these, deep learning algorithms such as LSTM and GRU have shown superior performance in capturing temporal dependencies and handling sequence data[7], [8].

The integration of traditional statistical techniques and modern machine learning approaches has emerged as a promising solution for energy forecasting challenges. Hybrid models that combine statistical and deep learning techniques, such as ARIMA-GRU or ARIMA-LSTM, leverage the strengths of both methodologies[9,10]. This synergistic approach leverages ARIMA's capability to capture linear trends and temporal patterns, while simultaneously harnessing the non-linear modeling capacity of deep learning models[11]. This hybrid framework has been demonstrated to enhance the accuracy of energy forecasts[12], particularly for complex and volatile energy consumption datasets, making it a highly suitable technique for microgrid energy forecasting applications[13].

Recent studies have highlighted the potential of hybrid models in addressing the challenges of energy forecasting[14]. For example, ARIMA-LSTM models have demonstrated improved

performance over standalone models in predicting renewable energy outputs[15], while ARIMA-GRU hybrids have been noted for their computational efficiency and accuracy[16]. However, research specifically focused on using the ARIMA-GRU hybrid approach for energy consumption forecasting in microgrids remains limited, creating a gap that this study aims to address[17].
This paper proposes an ARIMA-GRU hybrid model for forecasting energy consumption in a microgrid. By combining ARIMA's ability to model linear trends with GRU's capacity to capture non-linear dependencies, the model aims to enhance prediction accuracy and reliability. The approach is validated using real-world energy consumption data and benchmarked against standalone models such as ARIMA, SVM, GRU, and LSTM, as well as other hybrid techniques like ARIMA-LSTM. The findings contribute to the growing knowledge on energy forecasting and provide practical insights for improving energy management in microgrids.

2. MATERIALS & METHODS

This study employs a hybrid ARIMA-GRU model to forecast energy consumption, leveraging the strengths of both linear statistical models and deep learning techniques. The ARIMA model is first applied to identify and predict the linear trends and temporal patterns in the time series data. The residuals, representing the nonlinear components not captured by ARIMA, are then modeled using a GRU neural network. The GRU model is trained on lagged sequences of the ARIMA residuals to learn complex temporal dependencies. Finally, The forecasts from the ARIMA and GRU models are integrated to produce the final prediction. This approach harnesses ARIMA's ability to model linear relationships and GRU's capacity to handle nonlinear patterns, providing a robust solution for energy consumption prediction. The model performance is evaluated using standard metrics, including Mean Absolute Error, Root Mean Squared Error, and Mean Absolute Percentage Error, which validate the reliability of the results. The methodology is illustrated in Figure 1 as a series of sequential phases. Table 1 encompasses the different abbreviations used in this paper.

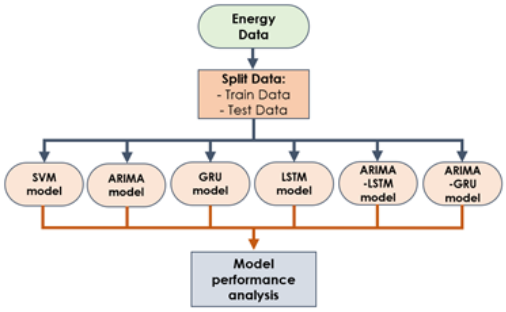

Figure 1. architecture of proposed method.

Table 1. Abbreviations meaning.

Abbreviations	Definition
ARIMA	Autoregressive Integrated Moving Average
GRU	Convolutional Neural Network
LSTM	Long-Short Term Memory
SVM	Support vector machine
RMSE	Root Mean Square Error
MAE	Mean Absolute Error
MAPE	Mean Absolute Percentage Error

2.1. Long-Short Term Memory (LSTM)

Long short-term memory is a type of recurrent neural network that is well-suited for modeling sequential data. LSTM models are capable of learning long-term dependencies in the data and effectively capturing the temporal dynamics of energy consumption[18]. The architecture of the LSTM is illustrated in Figure 2.

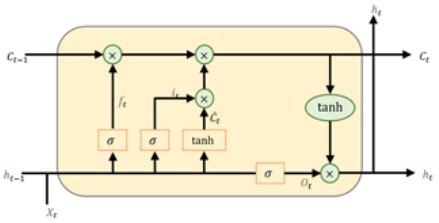

Figure 2. The architecture of LSTM.

The key components of an LSTM model are the memory cell, the forget gate, the input gate, and the output gate. The memory cell holds the state of the LSTM, which is updated at each time step based on the current input, the previous hidden state, and the previous cell state. The forget gate determines what information from the previous cell state should be retained, the input gate controls what new information from the current input and previous hidden state should be added to the cell state, and the output gate decides what parts of the cell state should be used to generate the current output. Equations (1, 2, 3, 4, 5, and 6) define the mathematical formulation of the LSTM model[19]:

$$i_t = \sigma(W_i x_t + U_i h_{t-1} + b_i) \quad (1)$$

$$f_t = \sigma(W_f x_t + U_f h_{t-1} + b_f) \quad (2)$$

$$o_t = \sigma(W_o x_t + U_o h_{t-1} + b_o) \quad (3)$$

$$\hat{C}_t = tanh(W_c x_t + U_c h_{t-1} + b_c) \quad (4)$$

$$C_t = f_t \odot C_{t-1} + i_t \odot \hat{C}_t \quad (5)$$

$$h_t = o_t \odot tanh(C_t) \quad (6)$$

In the equations above, i_t, f_t and o_t are the three gates, input, output and forget gates, respectively at the time t, The W_i, W_f and W_o: denotes the weight matrices from the input, forget and output gates to the input, respectively. The b_i, b_f and b_o are the bias of input, forget and output gate, respectively. The U_i, U_f and U_o denote the weight matrices from the input, forget and output gates to the hidden, respectively. σ is a logistic sigmoid function and ⊙ denotes the Hadamard product of two vectors. x_t is a vector that is located in the input layer of the LSTM. h_t is an output vector of the hidden layer and is located in the LSTM unit at the time, t. C_t denotes the current cell state and $\hat{C}_t$ denotes the new candidate value for the next cell state. h_{t-1} denotes the previous state and is determined by the forget gate, f_t, by how much is passed to the next state. C_{t-1} denotes the update of the old cell state to the new cell state C_t.

2.2. Gated Recurrent Unit (GRU)

The Gated Recurrent Unit represents a type of recurrent neural network architecture that is a

simplified version of the LSTM cell, as proposed by Chung et al[20]. The architecture of the GRU is depicted in Figure 3.

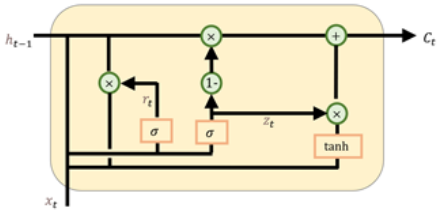

Figure 3. The architecture of GRU.

The GRU architecture includes two key gates that regulate the flow of information through the network. The reset gate determines the amount of past information to be retained, while the update gate controls the incorporation of new information into the cell state. The following equations (7, 8, 9, and 10) represent the formula of the GRU model[19]:

$$Z_t = \sigma(W_z \odot [h_{t-1}, z_t]) \qquad (7)$$

$$r_t = \sigma(W_r \odot [h_{t-1}, x_t]) \qquad (8)$$

$$\tilde{h}_t = tanh(W \odot [r_t \odot h_{t-1}, x_t] \qquad (9)$$

$$h_t = (1 - z_t) \odot h_{t-1} + z_t \odot \tilde{h}_t \qquad (10)$$

The equations in the Gated Recurrent Unit model involve several mathematical components. The sigmoid activation function is represented by σ, while W_r and W_z denote the weight coefficients for the reset gate and update gate, respectively. The hidden state at the previous time step *t-1* is given by h_{t-1}, and x_t represents the input at the current time t. The candidate hidden state at time t is denoted by $\tilde{h}_t$, and the tanh activation function is represented by tanh. The weight coefficients are denoted by W, the Hadamard product is represented by $\odot$, and ht is the hidden state at the current time t.

2.3. Autoregressive Integrated Moving Average (ARIMA)

The ARIMA model is a well-established time series forecasting technique commonly employed for predicting electrical load, which represents the amount of electrical energy demanded by consumers within a power system[21]. Accurate forecasting of electrical load is crucial for the efficient planning and operation of power systems. The ARIMA model integrates autoregressive and moving average components, enabling the capture of key temporal characteristics. The Autoregressive (AR) component leverages the dependence between an observed value and its past counterparts to generate predictions, which is particularly useful for forecasting upcoming energy consumption or potential demand peaks. The Integrated (I) component accounts for the necessary degree of differentiation required to achieve stationarity in the time series. Furthermore, the Moving Average (MA) component allows the model error to be defined as a linear combination of past error values, capturing the dependencies between observations and residual errors. The ARIMA (p,d,q) model, which utilizes the lag polynomial L is represented by the equation (11).

$$\left(1-\sum_{k-1}^{p}\varphi_k L^k\right)(1-L)^d=\theta\left(1-\sum_{j=1}^{a}\theta_j L^k\right)\varepsilon_t \qquad (11)$$

where the lag operator L^k represents past values in the series, φ_k denotes the parameters of the autoregressive (AR) component, and θ_j signifies the parameters of the moving average (MA) component, while ε_t represents the error terms. To determine the optimal parameters for the model, the Akaike Information Criterion (AIC) is commonly employed.

The Akaike Information Criterion (AIC) is a widely used metric for selecting the optimal parameters of an ARIMA model[21]. It balances model fit and complexity by maximizing the likelihood function while imposing a penalty for the number of estimated parameters. The mathematical expression for the AIC is as follows:

$$AIC=-2\log k+2m \qquad (12)$$

where the number of estimated model parameters is denoted by m, and k represents the maximized likelihood function for the model.

2.4. Support vector machine (SVM)

The Support Vector Machine (SVM) is a supervised machine learning algorithm widely used for classification and regression tasks. SVM works by finding the optimal hyperplane that separates data points of different classes with the maximum margin [22]. For linearly separable data, the algorithm constructs a hyperplane using support vectors, which are the closest data points to the hyperplane.

The decision boundary can be expressed as:

$$f(x)=sign(\omega.x+b) \qquad (13)$$

$$min\frac{1}{2}\|\omega\|^2 \qquad (14)$$

subject to the constraint:

$$y(\omega.x_i+b)\geq 1 \qquad (15)$$

where yi represents the class label of a data point xi .

2.5. Proposed ARIMA-GRU Model

The proposed approach combines the strengths of the ARIMA model and the GRU neural network to capture the linear and non-linear patterns in energy consumption data.

The ARIMA model is first used to fit the time series data and generate residuals, which represent the non-linear and seasonal components not captured by the linear ARIMA model.

The GRU network is then trained on the residuals to learn the remaining non-linear patterns. The final forecast is obtained by combining the ARIMA and GRU predictions, as shown in Figure 4. Table 2 resume all various layers and parameters of proposed approach, which were determined using grid search.

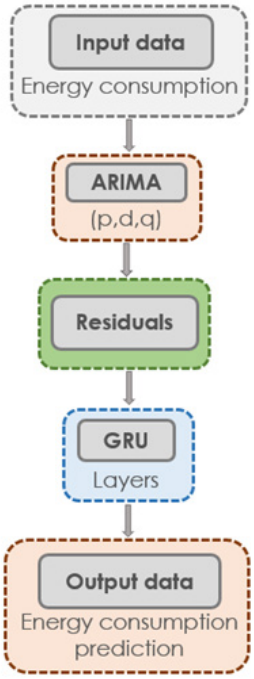

Figure 4. Proposed approach's architecture.

Table 2. Configuration of the various layers and parameters of ARIMA-GRU model.

Algorithm	Parameters	Values
ARIMA	P	12
	d	1
	q	21
GRU	GRU	50, activation='relu'
	GRU	50, activation='relu'
	Dense	1

2.6. Data description

The dataset used in this study was gathered from residential households within an energy community in Ireland as part of the StoreNet project[23]. It includes local weather parameters and detailed per-household power and energy measurements, encompassing active power consumption, photovoltaic generation, grid import and export, energy storage charging and discharging, as well as the state of charge of energy storage systems. The weather data is available at a 1-minute temporal resolution for the year 2020, while the energy consumption data has been aggregated to a daily resolution for forecasting daily energy consumption.

2.7. Evaluation metrics

The forecasting performance is evaluated using accuracy metrics including Mean Absolute Error (MAE), Root Mean Square Error (RMSE), and Mean Absolute Percentage Error (MAPE). These metrics quantitatively evaluate the discrepancy between the predicted and actual values, as defined below:

$$MAE = \frac{1}{N}\sum_{i=1}^{N}\left|(y_i - f_i)\right| \qquad (16)$$

$$RMSE = \sqrt{\frac{1}{N}\sum_{i=1}^{N}(y_i - f_i)^2} \qquad (17)$$

$$MAPE = \frac{1}{N}\sum_{i-1}^{N}\left|\frac{y_i - f_i}{y_i}\right| \times 100 \qquad (18)$$

where N represents the number of values and yi is the actual value, and fi is the forecasted value. MAE, RMSE, and MAPE are widely used in energy prediction due to their ability to capture prediction errors in various forms. RMSE is particularly sensitive to large errors, making it suitable for detecting peaks, while MAPE provides an intuitive percentage error that is easy to interpret. These metrics were chosen to reflect the challenges of energy data, including sudden peaks and seasonal variations[24]. The MAE is a commonly used statistical metric that calculates the average of the absolute differences between the predicted and actual values, offering insight into the model's performance. In contrast, the RMSE reflects the standard deviation of these differences, placing greater emphasis on larger errors due to its mathematical structure. Additionally, the MAPE metric provides a measure of prediction accuracy as a percentage by calculating the average of the absolute percentage differences between the forecasted and actual values. In general, a model with lower MAE, RMSE, MAPE values, indicate a more accurate predictive model [25].

3. RESULTS & DISCUSSION

Figure 5 provides a visual representation of the performance of different forecasting models, while Table 3 presents the numerical evaluation of their accuracy using RMSE, MAE, and MAPE." The results depicted in Figure 5 illustrate the comparative performance of the various models in predicting energy consumption. The standalone models, such as ARIMA and SVM, exhibited challenges in capturing the non-linear patterns in the data, leading to higher deviations from the actual trends. Conversely, the deep learning models, particularly the GRU, demonstrated a closer alignment with the observed data, outperforming the LSTM in tracking the rapid changes. The hybrid models, which combined the ARIMA and deep learning approaches, further improved the prediction accuracy by effectively integrating the strengths of linear and non-linear modeling. Notably, the ARIMA-GRU hybrid model provided the most accurate predictions, exhibiting minimal deviations and effectively capturing the variability in energy consumption, thus establishing it as the most robust approach for this forecasting task.

The comparisons shown in Table 3 reveal the performance of different models, as evaluated by RMSE, MAE, and MAPE. Among the standalone models, the ARIMA model exhibited the highest RMSE and MAE, along with a MAPE of 18.70%. This suggests that while the ARIMA approach is effective for modeling linear patterns, it struggled to capture the complex non-linear relationships inherent in the data. In contrast, the Support Vector Machine model demonstrated moderate performance, with an RMSE of 59.79kWh, MAE of 41.90kWh, and MAPE of 12.78%, but it was outperformed by the deep learning models.

The deep learning models, GRU and LSTM, displayed better adaptability to the complexities of the dataset. The GRU model achieved the lowest RMSE and MAE among the standalone models, along with a MAPE of 11.10%, outperforming the LSTM model, which reported an RMSE of 49.91kWh, MAE of 42.05kWh, and MAPE of 13.74%. This highlights the superior ability of the GRU model to capture long-term dependencies and temporal dynamics compared to the LSTM model in this context.

The hybrid models, which combine the ARIMA approach with deep learning architectures,

provided notable improvements. The ARIMA-LSTM model achieved an RMSE of 44.30kWh, MAE of 33.59kWh, and MAPE of 12.35%, surpassing its standalone counterpart. However, The ARIMA-GRU model demonstrated the most favorable overall performance, as reflected in the lowest recorded values for RMSE, MAE, and MAPE. These results emphasize the effectiveness of hybrid models in leveraging the strengths of both statistical and deep learning techniques to enhance prediction accuracy.

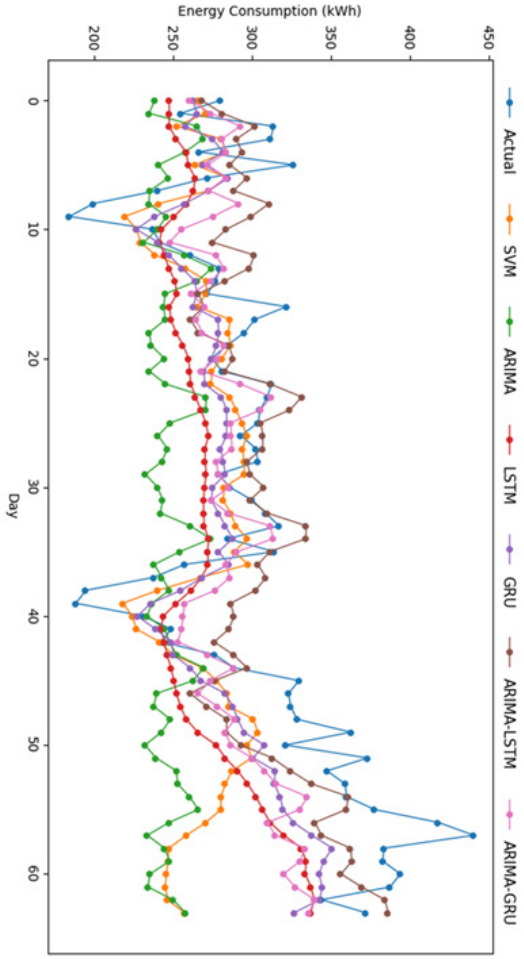

Figure 5. Daily energy consumption predictions.

Table 3. Comparison of the proposed model's performance with other models

Model	RMSE (kWh)	MAE (kWh)	MAPE (%)
SVM	59.79	41.90	12.78
ARIMA	76.25	60.68	18.70
GRU	43.50	32.10	11.10
LSTM	49.91	42.05	13.74
ARIMA-LSTM	44.30	33.59	12.35
ARIMA-GRU	38.28	31.24	10.29

Although the ARIMA-GRU model demonstrates overall superior performance, it struggles to capture sharp peaks in energy consumption accurately. This limitation may arise from the smoothing effects of both ARIMA and GRU during forecasting. Future enhancements could include incorporating external features such as real-time weather data or using attention

mechanisms to prioritize peak prediction.

In summary, the ARIMA-GRU hybrid model emerged as the most accurate for the forecasting task, demonstrating the potential of combining traditional time series models with advanced machine learning architectures to address complex forecasting challenges.

4. CONCLUSION

This study investigated the performance of various forecasting models, including standalone ARIMA, SVM, GRU, and LSTM, as well as hybrid ARIMA-LSTM and ARIMA-GRU, for predicting energy consumption. The results reveal that traditional time series models like ARIMA struggle to capture complex non-linear patterns, while deep learning models, particularly GRU, exhibit superior performance in tracking temporal dynamics and abrupt changes.

The hybrid models that integrate the strengths of statistical and deep learning methods have demonstrated superior performance compared to their individual counterparts. Notably, the ARIMA-GRU hybrid model emerges as the most accurate and robust approach, demonstrating the lowest RMSE, MAE, and MAPE.

These findings highlight the potential of integrating advanced machine learning architectures with traditional time series models to improve the precision and reliability of energy consumption forecasting. Future research should explore scalability across diverse datasets and environments. The integration of additional contextual variables, such as real-time weather and economic indicators, could further improve model accuracy. Additionally, optimizing computational efficiency without compromising accuracy remains a critical avenue for exploration.

REFERENCES

[1] N. M. Manousakis, P. S. Karagiannopoulos, G. J. Tsekouras, and F. D. Kanellos, "Integration of Renewable Energy and Electric Vehicles in Power Systems: A Review," Processes, vol. 11, no. 5, 2023, doi: 10.3390/pr11051544.

[2] M. Abumohsen, A. Y. Owda, and M. Owda, "Electrical Load Forecasting Using LSTM, GRU, and RNN Algorithms," Energies (Basel), vol. 16, no. 5, 2023, doi: 10.3390/en16052283.

[3] W. Liao, B. Bak-Jensen, J. R. Pillai, Z. Yang, and K. Liu, "Short-term power prediction for renewable energy using hybrid graph convolutional network and long short-term memory approach," Electric Power Systems Research, vol. 211, p. 108614, 2022, doi: https://doi.org/10.1016/j.epsr.2022.108614.

[4] B.-M. Hodge, A. Zeiler, D. Brooks, G. Blau, J. Pekny, and G. Reklatis, "Improved Wind Power Forecasting with ARIMA Models," in 21st European Symposium on Computer Aided Process Engineering, vol. 29, E. N. Pistikopoulos, M. C. Georgiadis, and A. C. Kokossis, Eds., in Computer Aided Chemical Engineering, vol. 29. , Elsevier, 2011, pp. 1789–1793. doi: https://doi.org/10.1016/B978-0-444-54298-4.50136-7.

[5] Y. E. Shao and Y.-S. Tsai, "Electricity Sales Forecasting Using Hybrid Autoregressive Integrated Moving Average and Soft Computing Approaches in the Absence of Explanatory Variables," Energies (Basel), vol. 11, no. 7, 2018, doi: 10.3390/en11071848.

[6] D. Koschwitz, J. Frisch, and C. van Treeck, "Data-driven heating and cooling load predictions for non-residential buildings based on support vector machine regression and NARX Recurrent Neural Network: A comparative study on district scale," Energy, vol. 165, pp. 134–142, 2018, doi: https://doi.org/10.1016/j.energy.2018.09.068.

[7] G. Lai, W.-C. Chang, Y. Yang, and H. Liu, "Modeling long-and short-term temporal patterns with deep neural networks," in The 41st international ACM SIGIR conference on research & development in information retrieval, 2018, pp. 95–104.

[8] Y. Hua, Z. Zhao, R. Li, X. Chen, Z. Liu, and H. Zhang, "Deep Learning with Long Short-Term Memory for Time Series Prediction," IEEE Communications Magazine, vol. 57, no. 6, pp. 114–119, 2019, doi: 10.1109/MCOM.2019.1800155.

[9] M. Dong and L. Grumbach, "A Hybrid Distribution Feeder Long-Term Load Forecasting Method Based on Sequence Prediction," IEEE Trans Smart Grid, vol. 11, no. 1, pp. 470–482, 2020, doi: 10.1109/TSG.2019.2924183.

[10] J. Lee and Y. Cho, "National-scale electricity peak load forecasting: Traditional, machine learning, or hybrid model?," Energy, vol. 239, p. 122366, 2022, doi: https://doi.org/10.1016/j.energy.2021.122366.

[11] H. Hewamalage, C. Bergmeir, and K. Bandara, "Recurrent Neural Networks for Time Series Forecasting: Current status and future directions," Int J Forecast, vol. 37, no. 1, pp. 388–427, 2021, doi: https://doi.org/10.1016/j.ijforecast.2020.06.008.

[12] H. Hamdoun, A. Sagheer, and H. Youness, "Energy time series forecasting-analytical and empirical assessment of conventional and machine learning models," Journal of Intelligent & Fuzzy Systems, vol. 40, pp. 12477–12502, 2021, doi: 10.3233/JIFS-201717.

[13] J. Wan, W. Hua, and B. Wang, "Compulsory Islanding Transition Strategy Based on Fuzzy Logic Control for a Renewable Microgrid System," Math Probl Eng, vol. 2021, no. 1, p. 9959222, 2021, doi: https://doi.org/10.1155/2021/9959222.

[14] X. Ma and D. Liu, "Comparative Study of Hybrid Models Based on a Series of Optimization Algorithms and Their Application in Energy System Forecasting," Energies (Basel), vol. 9, no. 8, 2016, doi: 10.3390/en9080640.

[15] Y. Wang, Y. Shen, S. Mao, G. Cao, and R. M. Nelms, "Adaptive Learning Hybrid Model for Solar Intensity Forecasting," IEEE Trans Industr Inform, vol. 14, no. 4, pp. 1635–1645, 2018, doi: 10.1109/TII.2017.2789289.

[16] M. Du, "Improving LSTM Neural Networks for Better Short-Term Wind Power Predictions," in 2019 IEEE 2nd International Conference on Renewable Energy and Power Engineering (REPE), 2019, pp. 105–109. doi: 10.1109/REPE48501.2019.9025143.

[17] S. Haben, S. Arora, G. Giasemidis, M. Voss, and D. Vukadinović Greetham, "Review of low voltage load forecasting: Methods, applications, and recommendations," Appl Energy, vol. 304, p. 117798, 2021, doi: https://doi.org/10.1016/j.apenergy.2021.117798.

[18] S. and O. S. Hoyer Michael and Eivazi, "Efficient LSTM Training with Eligibility Traces," in Artificial Neural Networks and Machine Learning – ICANN 2022, P. and J. C. and P. A. and A. M. Pimenidis Elias and Angelov, Ed., Cham: Springer Nature Switzerland, 2022, pp. 334–346.

[19] K. E. ArunKumar, D. V Kalaga, Ch. Mohan Sai Kumar, M. Kawaji, and T. M. Brenza, "Comparative analysis of Gated Recurrent Units (GRU), long Short-Term memory (LSTM) cells, autoregressive Integrated moving average (ARIMA), seasonal autoregressive Integrated moving average (SARIMA) for forecasting COVID-19 trends," Alexandria Engineering Journal, vol. 61, no. 10, pp. 7585–7603, 2022, doi: https://doi.org/10.1016/j.aej.2022.01.011.

[20] J. Chung, C. Gulcehre, K. Cho, and Y. Bengio, "Gated feedback recurrent neural networks," in International conference on machine learning, 2015, pp. 2067–2075.

[21] N. Guo, W. Chen, M. Wang, Z. Tian, and H. Jin, "Appling an Improved Method Based on ARIMA Model to Predict the Short-Term Electricity Consumption Transmitted by the Internet of Things (IoT)," Wirel Commun Mob Comput, vol. 2021, no. 1, p. 6610273, 2021, doi: https://doi.org/10.1155/2021/6610273.

[22] M. Awad and R. Khanna, "Support Vector Machines for Classification," in Efficient

Learning Machines, Berkeley, CA: Apress, 2015, pp. 39–66. doi: 10.1007/978-1-4302-5990-9_3.

[23] R. Trivedi, M. Bahloul, A. Saif, S. Patra, and S. Khadem, "Comprehensive Dataset on Electrical Load Profiles for Energy Community in Ireland," Sci Data, vol. 11, no. 1, p. 621, 2024, doi: 10.1038/s41597-024-03454-2.

[24] H. Yin, D. Jin, Y. H. Gu, C. J. Park, S. K. Han, and S. J. Yoo, "STL-ATTLSTM: Vegetable Price Forecasting Using STL and Attention Mechanism-Based LSTM," Agriculture, vol. 10, no. 12, 2020, doi: 10.3390/agriculture10120612.

[25] A. Youssfi, and Youssef El Y. Kadi, "A New Advanced Strategy for Controlling the Charging and Discharging of a Storage Unit in a Microgrid Using a Finite Control Set Predictive Model" Solar Energy and Sustainable Development Journal, 14(SI_MSMS2E), 38–52, 2024, https://doi.org/10.51646/jsesd.v14iSI_MSMS2E.404.

Solar Energy
And Sustainable Development
Refereed, biannual scientific journal issued by:
The Libyan Center for Solar Energy Research and Studies

Role Of Embedded Systems In Smart Energy Management: Challenges, Innovations, And Future Trends

Sachin Srivastava[1],G. Sai Satyanarayana[2], Abhay Dhasmana[3],

Vineet Rawat[4], Aditya Singh Rana[5], Yashwant Singh Bisht*[6].

[1,3,4,5]Department of Aerospace Engineering, Uttaranchal Institute of Technology, Uttaranchal University,Dehradun, Uttarakhand, India.
[2]Department of Aeronautical Engineering, MRCET, Hyderabad, Telangana, India.
[6]Department of Mechanical Engineering, Uttaranchal Institute of Technology, Uttaranchal University,Dehradun, 248007 Uttarakhand, India.

E-*mail:* [1] sachinrash2004@gmail.com ,[2]asathyasai.satti@gmail.com ,[3] sachinrash2004@gmail.com , [4]asathyasai.satti@gmail.com,[5]asathyasai.satti@gmail.com ,[6] yashwantb3@gmail.com .

SPECIAL ISSUE ON:

The 1st International Conference on Sciences and Techniques for Renewable Energy and the Environment.

(STR2E 2025)

May 6-8, 2025 at FST-Al Hoceima- Morocco.

KEYWORDS

Renewable Energy, Artificial Intelligence, Internet of Things, Machine Learning, Embedded System.

ABSTRACT

With smart grids, renewable power, and efficient energy management transforming the energy sector, embedded systems are the prime impetus for real-time monitoring, control, and optimization. Energy efficiency, scalability, reliability, cybersecurity, and cost are, however, areas of concern. Power consumption is reduced by 30–50% by optimized embedded controllers, and battery management systems extend EV life by 20–40%. Scalability is essential, with smart grids capable of handling 100,000 nodes. Reliability in rugged environments (-40°C to 85°C) is paramount, and 1.5 million attacks per year carry financial risks of over $10 billion. Cost factors ($50–500 per unit) limit deployment in developing countries.

This paper discusses embedded system architecture, application, and challenges in energy systems, namely smart grids, renewable integration, and EV infrastructure which is displayed in figure 1. It discusses AI-based edge computing and novel communication protocols to address limitations. Based on case studies, the research estimates embedded systems' contribution to energy efficiency and reliability and predicts future advancements, including hardware evolution, machine learning for predictive management, and IoT-based smart ecosystems, which will improve efficiency by 15–25% within the next decade.

*Corresponding author.

DOI: https://doi.org/10.51646/jsesd.v14iSTR2E.797

This is an open access article under the CC BY-NC license (http://Attribution-NonCommercial 4.0 (CC BY-NC 4.0)).

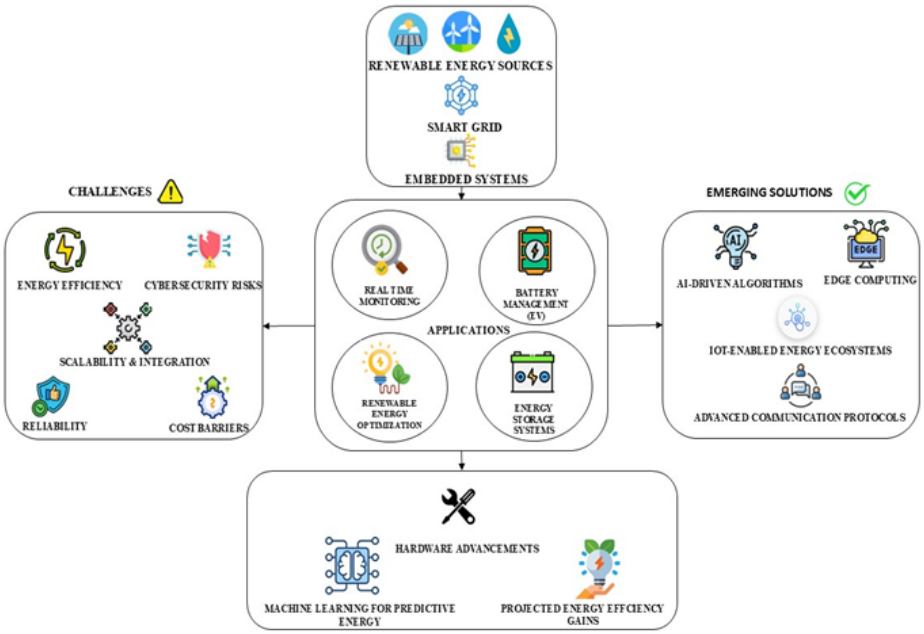

Figure 1. Graphical presentation of abstract.

دور الأنظمة المدمجة في إدارة الطاقة الذكية: التحديات والابتكارات والاتجاهات المستقبلية

اساشين سريفاستافا، جي. ساي ساتيانارايانا، أبهاي دهسمانا، فينيت راوات، أديتيا سينغ رانا، ياشوانت سينغ بيشت.

ملخص: مع اعتماد الشبكات الذكية، والطاقة المتجددة، والإدارة الفعّالة للطاقة في تحويل قطاع الطاقة، تُعد الأنظمة المدمجة الدافع الرئيسي للمراقبة والتحكم والتحسين في الوقت الفعلي. ومع ذلك، فإن الكفاءة في استهلاك الطاقة، وقابلية التوسع، والموثوقية، والأمن السيبراني، والتكلفة تُعد من أبرز مجالات القلق. تسهم وحدات التحكم المدمجة المحسّنة في تقليل استهلاك الطاقة بنسبة تتراوح بين 30–50 % ، بينما تُطيل أنظمة إدارة البطاريات عمر المركبات الكهربائية بنسبة 20–40 .
تُعد قابلية التوسع ضرورية، حيث يمكن للشبكات الذكية التعامل مع 100,000 عقدة. وتُعد الموثوقية في البيئات القاسية (من 40- درجة مئوية إلى 85 درجة مئوية) أمرًا بالغ الأهمية، خاصة مع تسجيل 1.5 مليون هجوم سنويًا تسبب مخاطر مالية تتجاوز 10 مليارات دولار. كما أن عامل التكلفة (من 50 إلى 500 دولار لكل وحدة) يُقيد النشر في الدول النامية.
تناقش هذه الورقة بنية الأنظمة المدمجة وتطبيقاتها وتحدياتها في أنظمة الطاقة، مثل الشبكات الذكية، ودمج مصادر الطاقة المتجددة، وبُنى المركبات الكهربائية، كما هو موضح في الشكل 1. وتتناول الورقة الحوسبة الطرفية المعتمدة على الذكاء الاصطناعي وبروتوكولات الاتصال الحديثة لمعالجة القيود الحالية. واستنادًا إلى دراسات الحالة، تُقدّر هذه الدراسة مساهمة الأنظمة المدمجة في كفاءة وموثوقية الطاقة، كما تتنبأ بالتطورات المستقبلية، بما في ذلك تطور الأجهزة، وتعلم الآلة للإدارة التنبؤية، والنظم البيئية الذكية القائمة على إنترنت الأشياء، والتي من المتوقع أن تحسّن الكفاءة بنسبة 15–25 % خلال العقد القادم.

الكلمات المفتاحية: الطاقة المتجددة، الذكاء الاصطناعي، إنترنت الأشياء، تعلم الآلة، النظام المدمج.

1. INTRODUCTION

The transition to renewable energy solutions has become a strategic priority worldwide due to growing environmental and economic challenges. It maximizes energy harvesting over the course of the day as the position and angle of the panels are changed to optimize them with

the quantity of sunlight. In case of wind turbines, it controls critical parameters such as rotor speed and blade pitch for maximum energy output if these are optimized according to the wind conditions [2]. They follow variables such as solar irradiance and wind speed with which they make predictions over their energy production and regulate performance at the system level. Output energy is stabilized with their immediate monitoring and adjustment on sources that are renewable, in response, enhancing performance under all aspects of environment [3]. These technologies also support the construction of a much more reliable energy-generating system that will not need to sit idle but rather, be proactive and self-fixing as things start falling into place. A modern smart grid is therefore made possible by what embedded systems bring in new ways in managing electricity alongside its transfer [4]. For the guarantee of stability, dependability, and efficiency of energy systems, smart grids use real data from the embedded system. These systems constantly collect and process data related to supply, demand, and the flow of energy in the grid. For instance, they ensure that power is supplied from areas where supply is surplus to the areas where there is heavy consumption so as not to waste much power and experience blackouts [5]. In addition, they enable integration of the grid with the diversified sources of energy, like wind farms, energy storage devices, and rooftop solar panels, thereby making the grid much more resilient and flexible, such that it can accommodate increased proportions of renewable energy without relying much on fossil fuel [6]. AI embedded system is being increasingly used in automotive sector which shows their increasing adoption, as shown in figure 2.

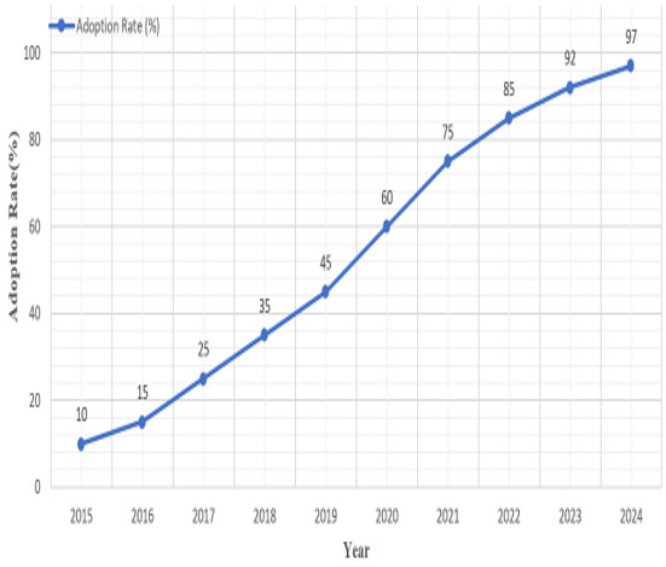

Figure 2. Growth of Embedded Systems in Energy (2015-2024) [7].

The embedded systems reduce energy consumption by creating smart meters and home automation systems. This embedded technology in smart meters helps customers to better monitor and control their consumption patterns in real time. The system thus analyzes the usage pattern and identifies areas where saving of energy and, hence, money is possible. For instance, the user can adjust his behavior to avoid peak periods when rates are expensive by knowing when peak consumption happens. Home automation allows the integration of embedded systems into the control of heating, cooling, and lighting appliances to enable intelligent control [8]. This technology optimizes energy usage and reduces waste and utility costs based on ownership, weather, and preferences. They also fight for the incorporation of sources that are environmentally friendly. For instance, rooftop solar panels should be incorporated into homes to help users in households be able to create and regulate their energy. This can be termed as innovation leading to a more sustainable source of energy since it means efficient and responsible use of the energy.

Integrating such technologies into the energy sector, however holds significant challenges despite their potential magnitude to change things [9]. Since these systems are expected to operate at low power during complex operations, their main concern is energy efficiency. When using renewable energy, there is often a variable availability of electricity, and it has to be as rugged as possible and efficient, when needed. The final significant issue is scalability; scaling up energy systems is essential once they have to service so many more linked devices plus increased needs [10]. For embedded systems to operate smoothly, they must scale appropriately with high-density deployments. Moreover, they should be reliable and, therefore, be capable of robust operation in all generally hostile environments-from remote solar farms to metropolitan cities. The third issue relates to cybersecurity. The stability and integrity of the energy infrastructure would depend critically on the capability of embedded systems to defend against cyber-attacks. Finally, because investment has to be made in order to achieve a balance between cost and performance, financial elements of developing and implementing embedded systems may be very challenging. It is quite very important to deal with all these challenges so as to unlock full potential for using embedded systems to enable an enhanced energy sector that will be sustainable and efficient [5]. Table 1. Shows different IOT based embedded systems, their application and their respective technical aspects.

Table 1. Summary of Case Studies on IoT-Enabled Embedded Systems in Energy Applications

Table 1. Summary of Case Studies on IoT-Enabled Embedded Systems in Energy Applications	Table 1. Summary of Case Studies on IoT-Enabled Embedded Systems in Energy Applications	Table 1. Summary of Case Studies on IoT-Enabled Embedded Systems in Energy Applications
Table 1. Summary of Case Studies on IoT-Enabled Embedded Systems in Energy Applications	Table 1. Summary of Case Studies on IoT-Enabled Embedded Systems in Energy Applications	Table 1. Summary of Case Studies on IoT-Enabled Embedded Systems in Energy Applications
Table 1. Summary of Case Studies on IoT-Enabled Embedded Systems in Energy Applications	Table 1. Summary of Case Studies on IoT-Enabled Embedded Systems in Energy Applications	Table 1. Summary of Case Studies on IoT-Enabled Embedded Systems in Energy Applications
Table 1. Summary of Case Studies on IoT-Enabled Embedded Systems in Energy Applications	Table 1. Summary of Case Studies on IoT-Enabled Embedded Systems in Energy Applications	Table 1. Summary of Case Studies on IoT-Enabled Embedded Systems in Energy Applications
Table 1. Summary of Case Studies on IoT-Enabled Embedded Systems in Energy Applications	Table 1. Summary of Case Studies on IoT-Enabled Embedded Systems in Energy Applications	Table 1. Summary of Case Studies on IoT-Enabled Embedded Systems in Energy Applications
Table 1. Summary of Case Studies on IoT-Enabled Embedded Systems in Energy Applications	Table 1. Summary of Case Studies on IoT-Enabled Embedded Systems in Energy Applications	Table 1. Summary of Case Studies on IoT-Enabled Embedded Systems in Energy Applications

2. EMBEDDED SYSTEMS IN ENERGY SYSTEMS

It opened a new era for the energy sector by enhancing its sustainability, reliability, and productivity. Software and hardware, specifically designed for some applications, are the characteristic features of embedded systems. Embedded systems have been highly indispensable to modern energy systems from the very beginning of time. This chapter deals with the structural elements of the embedded systems while describing their application in different situations with the aim of ensuring efficient application toward the existing problems of the energy industry [16-17].

2.1. Architecture of Embedded Systems

The performance and operation of most energy applications rely on the presence of embedded systems. The architecture of an embedded system is composed of various important parts that collaborate effectively to carry out particular functions [18]. Examples of these parts include controllers or processors, sensors and actuators, communication modules, and power management units as shown in figure 3.

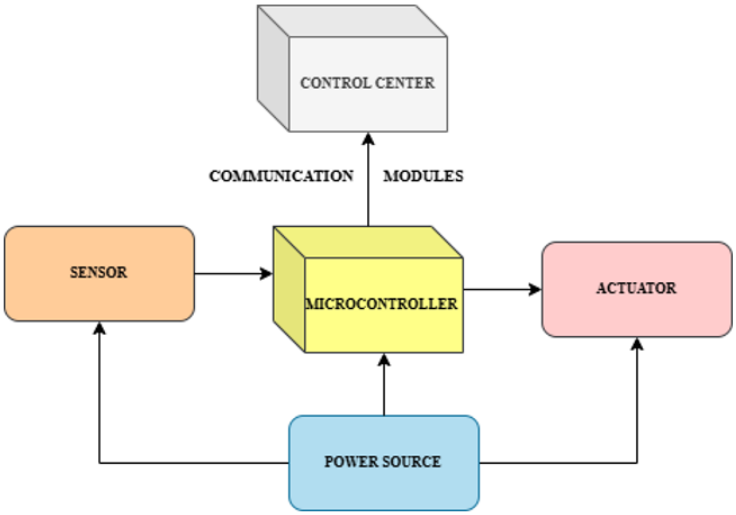

Figure 3. Architecture of an Embedded System.

The devices that carry out all the calculations in an embedded system are known as microcontrollers or microprocessors and are needed to execute the program commands that describe how the system operates. for this reason, microcontrollers are primarily used because they are relatively affordable and consume low power when compared with other devices, thus becoming the best fit for applications requiring low power consumption. A microprocessor has higher processing power, and is applied in programs that require extensive mathematical operations and real-time data manipulations [19]. Deciding which one to apply between the two, be it microcontroller or a microprocessor will mainly be based on which particular demand there might be for your energy application. In the embedded system, sensors and actuators are essential components that provide opportunities for data acquisition and control. The sensors obtain data from the system's physical environment, which includes temperature, pressure, voltage, and current and convert them into electrical signals that can be interpreted by the microcontroller or the CPU [20]. In return, the actuators carry out operations such as opening a valve, turning on a relay, or changing a solar panel's orientation using the information obtained from the analysis. Embedded systems can monitor and control energy systems, thus providing optimal performance and efficiency with smooth communication between sensors and actuators.

Microcontrollers and actuators play a critical part in what enables an embedded system to gather data as well as control operations, hence having sensors extract the data needed from the environment surrounding an embedded system-such information may include temperatures, pressures, voltage and current-converting that to electrical signal that the microprocessor could interpret. It is rather low consumption compared to other devices, and also rather inexpensive. So, this is fairly suitable for applications that just require minimal power consumption. The other hand, microprocessors can process more power and have applications that require complex mathematical calculations and real-time manipulation of data. Actuators, on the other hand, perform tasks in accordance with data from the analysis, such as opening a valve, turning on a

relay, or adjusting the angle of a solar panel. The ease of communication between sensors and actuators enables embedded systems to monitor and control the energy system, ensuring a proper performance and efficiency in it [21].

2.2. Applications in Energy Systems

Embedded systems are extensively utilized in numerous applications in the energy sector to handle problems pertaining to energy production, distribution, and consumption. A few pertinent and significant applications are covered in this chapter, such as BMSs, EV infrastructure, smart grids, and renewable energy resource management [22]. A significant advancement in contemporary energy utilities is represented by smart grids. The operation of the smart grid is based on, almost entirely, on embedded system designs that enable dynamic load balancing. Furthermore, it detects anomalies through fault detection and directs its energy distribution in optimization models. Embedded systems incorporated into sensors and communication modules with real-time information input include energy usage, its transference losses, or general efficiency of the given network [23]. This data is then optimized to ensure energy flow, reduce peak demand, and improve the reliability of the grid. Moreover, the integration of DERs and renewable energy sources is facilitated by the embedded systems, which improve the overall sustainability of the grid. Management of Renewable Energy: Since renewable energy sources, such as solar and wind power, fluctuate and vary, their replacement needs to be monitored immediately and then controlled to balance the difference. The control of renewable energy facilities requires embedded systems because the systems continuously monitor irradiance, wind speed, temperature, and power generation [24]. The data in question is utilized to modify the functioning of solar panels, wind turbines, and energy storage systems in order to optimize efficiency and guarantee consistent energy generation.

2.3. Battery Management Systems (BMS)

A battery management system (BMS) continuously monitors parameters such as voltage, current, temperature, and state of charge (SoC) in each battery cell; using these, a BMS determines charge and discharge cycles that can be carried out with that particular cell; a BMS can thus prevent conditions such as overcharging or deep discharge; it is possible to provide good thermal conditions; battery management systems are embedded systems that can monitor and control the behavior of a battery to ensure proper safe operation. Figure 4 represents the bock diagram of a typical battery management system.

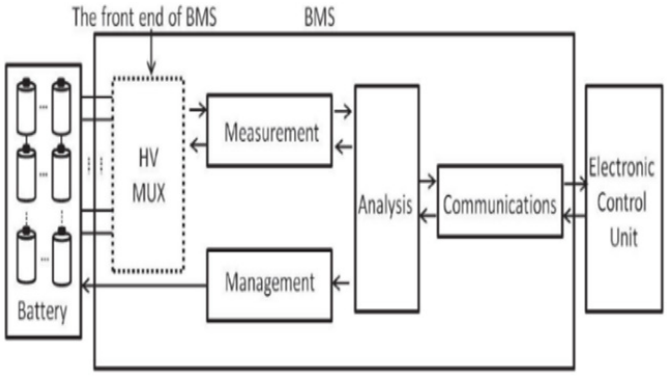

Figure 4. A block diagram of a typical battery management system [25].

A BMS in a renewable energy installation maximizes the use of energy storage systems by efficient storage and subsequent release of surplus energy generated in a solar panel or wind turbine [26]. For EVs, BMS enhances battery performance, prolongs battery life, and provides

safe operation that promotes dependability and efficiency of electric transportation. Electric Vehicle Infrastructure: As more EVs gain acceptance, they need a strong infrastructure for energy management and charging. Without embedded systems for features like real-time monitoring, load management, and grid communication, an EV charging station cannot function; the system monitors consumption, regulates the charging schedule, and distributes energy efficiently to many vehicles [27]. Further, the development of smart charging strategies based on demand response and V2G integration in embedded systems enables EVs to support grid stability and energy storage. Therefore, through the maximally deployment of embedded systems in charging infrastructures, adoption of electric vehicles and sustainable transportation options is supported.

3. CHALLENGES IN INCORPORATING EMBEDDED SYSTEMS IN ENERGY SYSTEMS

The integration of embedded systems within the energy sector provides immense benefits; however, severe challenges (as depicted in figure 5) must be addressed for smooth implementation and usage. The main challenges are the costs and complexity, environmental pressure, cybersecurity threats, issues concerning scalability and integration, and energy efficiency aspects. This section explains the detailed elaboration of the challenges, its implications, and strategies of mitigation.

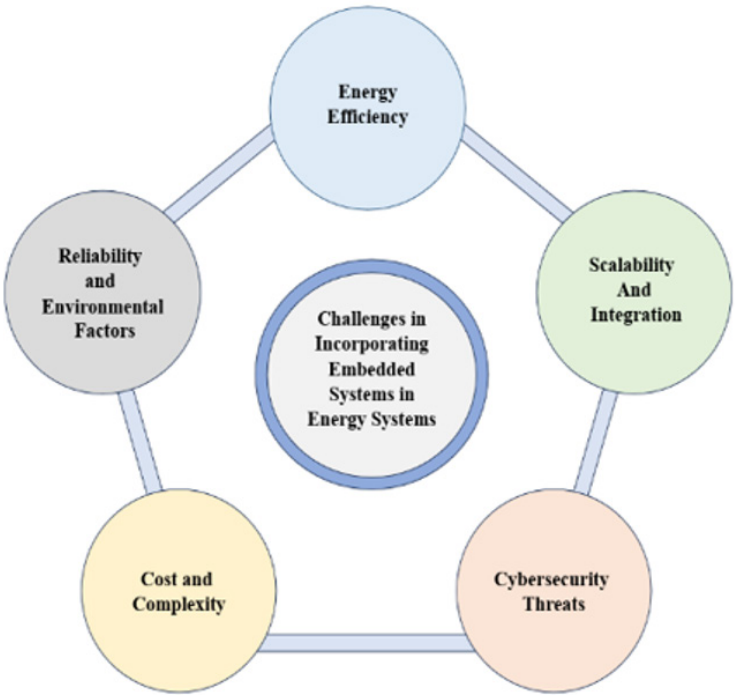

Figure 5. Challenges in Incorporating Embedded Systems in Energy Systems.

3.1. Energy Efficiency

Energy efficiency is one of the most important factors in the implementation of embedded systems in energy systems. To make these systems ensure sustainable and economical energy management, the systems should be low-power devices while still providing optimal performance.

3.1.1. Low-Power Operation

Most of the embedded systems have been deployed in power-constrained environments such as remote installations of renewable energy or battery-powered appliances. Hence, these systems have to be designed to consume very little power to maximize their lifespan and minimize maintenance. Dynamic voltage scaling, power gating, and energy harvesting are among the

techniques that are used to optimize the use of power [28]. However, the challenge in balancing low power consumption with high performance is quite a difficult issue, especially in applications that require real-time processing and data analysis. An important application of the embedded system in renewable energy and BMS is its use in monitoring and control energy production, storage, and distribution within installations, such as solar and wind farms. Efficient energy management is thus critical to achieve maximum usage of renewable resources and power supply stability. Similarly, BMS in electric vehicle and energy storage systems rely upon embedded systems to monitor the state of battery health, thereby optimizing charging cycles and preventing overcharging as well as deep discharge conditions [29]. Ensuring energy efficiency becomes critical for enhancing the entire efficiency and reliability of these renewable energy and storage solutions.

3.1.2. Trade-Offs and Optimization

There are natural trade-offs of designing an embedded system towards energy efficiency. In almost all cases, the means of lowering power consumption in an embedded system will likely mean the sacrifice of power in computing, memory storage, or communication bandwidths [30]. Therefore, engineers carefully optimize these trade-offs within the constraints of the actual application requirements. Advanced techniques in designing such systems range from ultra-low-power microcontrollers to low-power communication protocols and efficient algorithms for controlling power usage [31].

3.2. Scalability and Integration

Scalability and integration of the embedded systems are a huge challenge due to the different devices, communication protocols, and architectures used in modern energy systems. Modern energy systems integrate many types of devices, ranging from sensors, actuators, controllers, and communication modules. The capabilities and requirements vary in each device [32]. For the most part, most devices use various communication protocols like Wi-Fi, Zigbee, Bluetooth, or even proprietary protocols. Seamless communication and interoperability of heterogeneous devices is one of the greatest challenges. To integrate the embedded devices into the existing energy infrastructure, some compatibility issues with legacy devices need to be resolved along with ensuring data consistency and reliable communication across layers [33]. In order to bridge between several protocols and make communication seamless for data flow, middleware and gateways are built. It will then include the scalability of the integration for future expansion and extra devices. To ensure scalability and integration of such embedded systems, network management is of high priority. This relates to data traffic management, boosting bandwidth utilization, and reducing high communication latency. The performance and reliability of the system would thus inevitably deteriorate due to network congestion and data bottlenecks caused by additional devices attached [34]. In a meshed network environment with adaptive routing, the approach of cutting-edge strategies, such as load balancing is necessary to effectively establish scalable communication.

3.3. Reliability and Environmental Factors

One of the most fundamental requirements for the energy applications of embedded systems is reliability, especially if such systems operate in hostile environments. For example, areas where energy systems are installed in harsh locations usually have extreme temperatures, high humidity, dust, and vibrations. Outdoor installation of solar inverters and wind turbine controls has to be very reliable since it is exposed to the environment [35]. Similarly, the systems in offshore wind farms remote energy plants are susceptible to corrosion by saltwater and strong winds and other unfavorable conditions. Embedded systems under such harsh conditions require robust casings

and a strong hardware design so that it can work efficiently under such unfavorable conditions. Such a system calls for sealed enclosures, conformal coatings, and ruggedized components so as not to be affected by environmental damage [36]. In addition, advanced thermal management techniques such as fans, heat sinks, and phase-change materials ensure that the system operates within its optimal temperature range in order to avoid overheating. Redundancy and fault-tolerant characteristics make embedded systems more reliable. Redundant systems can continue to operate by serving as backup components for malfunctioning parts. Examples of fault-tolerant designs are watch-dog clocks, fail-safe devices that can recognize and recover from faults and algorithms for error detection and correction. All these are necessary to keep energy systems dependable and available [37].

3.4. Cybersecurity Threats

The integration of IoT-enabled embedded technologies into the energy infrastructure makes it vulnerable to significant risks of cybersecurity that need management to avoid any kind of disruption and ensure the integrity of the system. The connection and distributed design of an Internet of Things-enabled system make it intrinsically vulnerable. Exploiting weaknesses or vulnerabilities in software programs, hardware components, or communication protocols may allow an attacker to gain unauthorized access to modify data and interfere with operations [38]. Cyberattacks may have negative impacts such as equipment damage, power outages, and safety risks in energy systems. Cybersecurity threats therefore require multiple levels of robust security to be designed and built. One of the precautions against tampering and eavesdropping is data transmission encryption. The policies on access control should limit unauthorized access, and strict authentication processes should validate individuals' and devices' identities. There must be software updates and patches to counter identified vulnerabilities to increase system security. Sophisticated intrusion and response systems are required in the detection and mitigation of real-time cybersecurity threats. These will monitor suspicious network traffic that may have the potential to harm responses to potential threats by combining machine learning algorithms with anomaly detection techniques [39]. The other type of layered security technique is known as defense in depth, and this may be able to offer several layers of protection against cyber-attacks and hence improve the overall security of embedded systems in their applications related to energy.

3.5. Cost and Complexity

High costs and complexity in designing and implementing embedded systems for energy applications may be a limiting factor, especially in underdeveloped regions. With the use of embedded systems for energy applications, software development, hardware design, testing, and certification all incur high expenditures. The cost of its development is proportional to the more comprehensive design of the system in terms of performance and low power usage while still maintaining reliability and security [40]. The cost is also increased by the need for certain knowledge and abilities in embedded programming, electronics, and cybersecurity. Embedded systems demand a lot of investment apart from development, deployment, and maintenance costs. This will also involve the establishment cost of the devices, integrating them with the available infrastructure, and long-term maintenance support. Maintenance might be very costly because in remote or hard-to-reach areas, specialized equipment and personnel are required. Some of the biggest challenges for embedded systems include their costs, which may be far too high [41]. It would be challenging to implement such a system, especially for weak economy regions or smaller energy businesses with low budgets. Cost-effective methods include modular designs that can be updated step by step, open-source technologies, and government financing

and subsidies for the implementation of new technologies.

4. EMERGING SOLUTIONS IN EMBEDDED SYSTEMS FOR ENERGY APPLICATIONS

As the energy industry is transforming, embedded systems introduce innovative solutions to some of the long-standing issues that existed. Along with AI-based edge computing, new sophisticated communication protocols, hardware innovation, and IoT integration, this pathway will pave the way to much smarter, more reliable, and efficient energy systems. New solutions are explored in depth in this section along with their importance and the resultant impact on the energy sector.

4.1. AI-Driven Edge Computing

Innovation in the energy business is artificial intelligence, particularly when combined with edge computing. AI-based edge computing further enhances energy systems efficiency and dependability due to predictive energy management, including device-level problem detection [42]. By analyzing sensor and device data in real-time fashion, AI systems predict trends within consumption and detect inefficiencies. When edge embedded systems are able to analyze data locally, they can make immediate adjustments to the flows of energy, which would reduce the wastage and increase system performance. For example, AI-driven edge computing might allow smart grids to balance supply and demand in real-time and distribute energy based on consumption patterns. AI-driven edge computing also plays a major role in predictive maintenance and fault detection. Through continuous monitoring of energy systems' health and performance, AI algorithms will identify anomalies and potential failure patterns before they become critical issues. Thus, proactive maintenance leads to less downtime, cost on maintenance, and the prolonged lifetime of energy infrastructure [43]. For instance, artificial intelligence can analyze vibration data from a wind turbine to identify early signs of mechanical wear and schedule maintenance before it fails. Perhaps one of the most impressive benefits of using AI-driven edge computing is reduced latency and dependence on centralized systems. When data are processed in embedded systems, these embedded systems can now respond quickly and in real-time, minus the data being streamed into a central server. It also reduces delay and offers fast decisions-making that is critical with certain applications which involve instantaneous response, particularly applications related to grid balancing or fault detection [44]. In another case, decentralizing also helps to bring robustness to energy network distribution of computing workload, reducing single-point failures.

4.2. Advanced Communication Protocols

The integration of heterogeneous devices within energy systems would depend significantly on advanced communication protocols. Protocols like MQTT (Message Queuing Telemetry Transport) and Zigbee are among the key enablers of efficient and secure data transmission in embedded systems [45]. Figure 6 shows different communication protocols along with MQTT. QTT is a light publish/subscribe messaging protocol primarily for constrained devices and low-bandwidth, high-latency networks. It is best for applications where the efficiency of data transfer is critical such as in remote monitoring and control of energy systems. MQTT minimizes overhead as it uses a simple format for messages and reduces data transfer, thus conserving bandwidth and power. In energy systems, MQTT can use real-time information from sensors and devices delivered to control centers for prompt decisions and optimization [47].

With the communication of embedded systems, the major concern is security, particularly within the energy infrastructure. Zigbee offers low-power, wireless mesh networking protocol with strong features for security, including encryption and secure key exchange for data transmission.

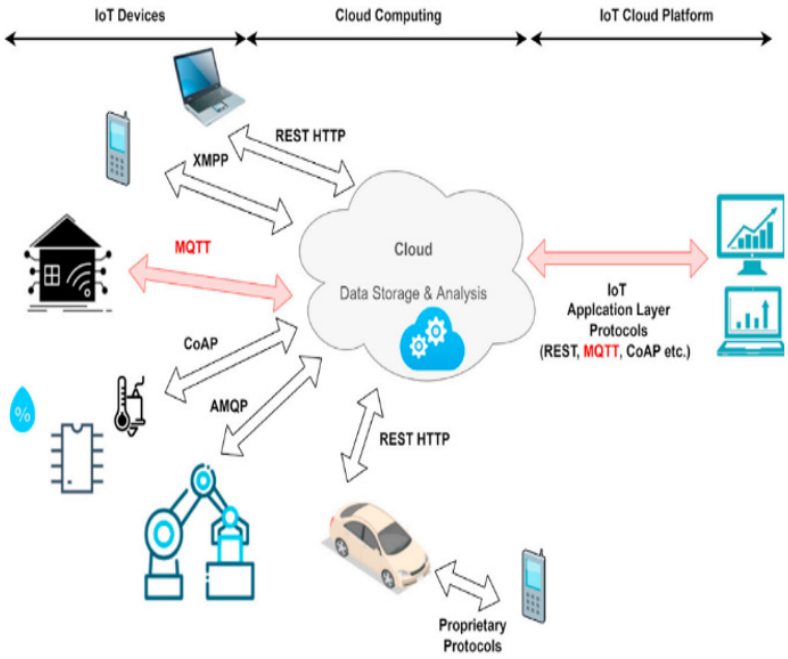

Figure 6. General IoT system architecture [46].

Zigbee's mesh network topology has improved network reliability and resiliency through multiple paths for data transmission, lowering the possibility of communication failure [48]. In smart grids and IoT-enabled energy systems, Zigbee can facilitate secure and reliable communication between devices, ensuring the integrity and confidentiality of data. It is important that advanced communication protocols should support seamless integration of heterogeneous devices in an energy system. Through standardized communication interfaces, advanced communication protocols allow disparate devices to communicate and hence act effectively. This cohesiveness is necessary to be achieved for the construction of intelligent energy ecosystems since these would contain various disparate parts, including sensors, actuators, controllers, and modules for communication, acting together in harmony. For instance, in a smart home energy management system, MQTT and Zigbee can enable the integration of smart meters, thermostats, and home appliances to enable coordinated energy use and optimization.

Case Study: A renewable energy company utilized high communication protocols to optimize the integration of its solar energy systems. Implementing MQTT for data transmission and Zigbee for secure communication allowed the company to make monitoring and control processes more efficient and reliable [49]. Using such protocols ensures easy exchange of data among solar panels, inverters, and energy storage systems, optimizing energy production while lowering the costs of running operations.

4.3. Hardware Advancements

Development of energy-efficient microcontrollers and sensors designed particularly for energy applications is one of the factors that leads to significant progress in the development of embedded systems. Such hardware innovations are crucial for developing high-performance, reliable, and sustainable energy systems. Energy-Efficient Microcontrollers are designed in such a way that energy efficiency forms the base of their design with low power modes, dynamic voltage scaling, and the integration of power management units into the designs [50]. These can provide the processing power to support real-time data gathering and control applications with very low power consumption. This is particularly critical in the energy sector for things

like smart meters and renewable energy systems because it extends the operating life of devices and reduces maintenance requirements. Sensors are an integral part of embedded systems because they provide the data for monitoring and control. Advanced sensors will, therefore, be a product of design that gives much sensitivity, accuracy, and energy efficiency. Advanced sensitivity and accuracy in temperature, pressure, and concentration measuring devices will be used. It is possible to precisely place solar panels for maximum energy gathering, for instance, by very sensitive photovoltaic devices with high accuracy in measuring sun irradiance. Similarly, improved temperature and pressure sensor equipment will reduce operating cost as well as energy losses within the HVAC system controlling mechanism. Hardware development is part of this process, which includes developing customized solutions for a given energy application. A good example in the case of a BMS could be dedicated microcontrollers featuring onboard battery monitoring and balancing for improved performance and reliability. High efficiency power converters and charge controllers are also crucial elements of the EV infrastructure with the purpose of regulating the energy flow and ensuring safe and effective charging [51].

4.4. IoT Integration

The Internet of Things has developed intelligent energy systems with improved data interchange and decision-making capabilities, transforming the energy sector. The embedded systems enabled by IoT have made energy management more effective and dependable by allowing the seamless integration of many components.

4.4.1. Intelligent Energy Ecosystems

The traditional energy systems now become intelligent ecosystems. These are connected, communicate with each other, and, generally speaking, are systems and pieces of equipment. These technologies let the data be shared in a real-time manner and make decisions in consonance, which further results in the improvement of overall performance and energy systems' efficiency. For example, to realize the dynamic load balancing and effective energy distribution, IoT-enabled devices in a smart grid may exchange information on production, consumption, and grid conditions. Such enormous volumes of data gathered from many sources may be aggregated, transmitted, and processed using the systems that are enabled by the Internet of Things. Through such means, data is useful for the understanding of the problems, the performance of systems, and the patterns that have to do with the use of energy. Data analytics and machine learning algorithms can help energy providers better understand their systems and make the right decisions to optimize energy management. Similarly, IoT sensors integrated into a building management system, for instance, can offer data on temperature, humidity, and occupancy, enabling effective control of the HVAC system [52].

IoT enables energy systems in terms of real-time visibility and control in the augmentation of decision-making capabilities. Real-time data acquired through IoT-enabled devices allow devices to readjust their operations for being efficient and optimal. As an example, IoT sensors on a renewable energy installation track the weather and shift panels or turbines for optimized utilization of solar or wind energy. The other IoT-enabled devices can be used for demand response techniques, which optimizes the stability of the grid by reducing costs by adjusting the usage of energy based on price signals and grid circumstances [53]. Smart energy networks greatly enhance the efficiency of any system as shown in figure 7.

Case Study: A utility business integrated the Internet of Things with an intelligent energy ecosystem for a smart grid. IoT-enabled sensors, smart meters, and communication devices have been installed in order to share real-time data and make synchronized decisions. The IoT-enabled system is designed to support optimized energy distribution, predictive maintenance,

and dynamic load balancing. It has reduced operation costs by a huge amount and improved the dependability of the grid.

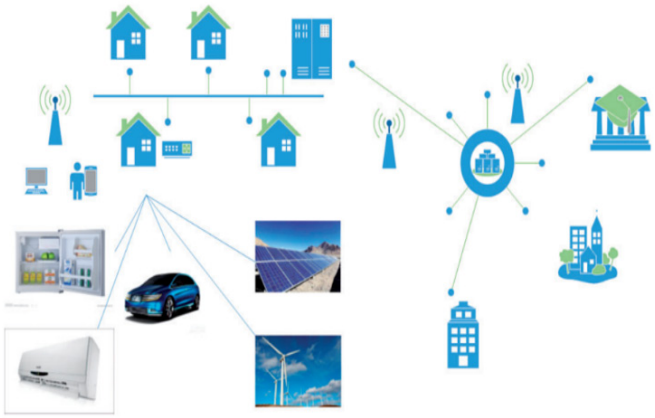

Figure 7. The structure of smart energy network [54].

5. CASE STUDIES AND DATA ANALYSIS

The above section describes a number of case studies demonstrating, in detail, applications and implications of IoT-based embedded systems in various energy applications, from which one can derive knowledge through the analysis of the benefits and drawbacks associated with such integration of the embedded system with smart grids, renewable energy installation, and charging infrastructure of electrical vehicles. This progress also brings along with it significant improvements in efficiency, reliability, and effective management of energy. Table 2 summarizes some of the key aspects of IoT-Enabled Embedded Systems in Energy Applications.

Table 2. Key Aspects of IoT-Enabled Embedded Systems in Energy Applications.

Aspect	Details	Case Study Examples
Technology Used	IoT-enabled embedded systems, AI algorithms, advanced sensors, and real-time communication.	Smart grids [55-56], Renewable monitoring [57-58], EV charging [59-60].
Key Parameters Monitored	Load balance, fault detection, energy consumption, irradiance, wind speed, and charging schedules.	Renewable energy systems [57-58], smart grids [55-56].
Challenges Overcome	Variability of renewable sources, grid overload during peak demand, and EV charging bottlenecks.	All case studies [55-60].

5.1. Case Study 1: Smart Grids in Urban Environments

Implementation: IoT-enabled embedded technologies have been integrated into the urban smart grid infrastructure of a utility provider. Reducing energy losses and raising the dependability of the grid are the main targets through improved fault detection and load balancing. The embedded systems are fitted with advanced sensors and communication modules that capture data on energy usage, proper functioning of the grid, and potential problems in real time. In essence, AI algorithms monitored data transmitted to a central control system to detect anomalies in order to optimize the usage of energy [55].

Outcomes: IoT-enabled embedded technologies reduced energy losses to a great extent. That helped improve the urban smart grid's efficiency generally by a significant margin. Dynamic load balancing made with the help of the data received in real time through the embedded systems helped allocate energy according to its requirements. The advanced capability to detect faults resulted in timely discovery and rectification, raising the dependability quotient and reducing the occurrence of as well as duration of the power outage. This case study shows the revolutionizing potential of embedded technologies provided by the Internet of Things in optimizing urban energy systems and addressing today's energy problems. The use of leading-edge sensors and communication technologies, the application of AI algorithms for data analysis, and a proactive approach to fault detection and maintenance are all factors that may be specifically responsible for the effective implementation. The utility company made the necessary decisions as it could rely on the real-time data for optimal distribution of energy with reduced losses. Customers were more satisfied and had more faith in the energy provider due to the quality of the service delivery of the grid in addition to higher dependability [56].

5.2. Case Study 2: Renewable Energy Monitoring

This article explores the implementation of embedded systems in the monitoring and control of real-time data within wind and solar farms. This application aimed to optimize the operations of renewable energy power plants for the generation of energy with greater efficiency. Embedded systems employed sensors that measure temperature, electricity, wind velocity, and irradiance. Localized microcontrollers did process these sensors' collected data locally before it is forwarded for further evaluation through a centralized monitoring system [57].

Outcomes: The energy-generating efficiency increased by 25% after installing the embedded systems in renewable energy installations. Real-time monitoring enabled the precise adjustment of the solar panels and wind turbines so that they would function with maximum efficiency. For instance, to ensure the acquisition of as much energy as possible, the solar panels were dynamically adjusted based on the levels of irradiance. Similarly, the wind speed was used in tuning the wind turbines in order to boost electricity production. Predictive maintenance is made easier as these installations can be monitored and managed real-time, with a result of reduced downtimes, thus extending the lifespan of renewable energy assets. From this case study, therefore, it has been demonstrated that greater efficiency is achieved with the integration of embedded systems with renewable energy management systems. The capability to get real-time data and control also allows the better usage of renewable resources, resulting in increased sustainability and security of energy. Therefore, the success of this implementation has further brought to light the importance of incorporating cutting-edge monitoring and control technologies in renewable energy projects for better efficiency and to mitigate variability and intermittency issues [58].

5.3. Case Study 3: Electric Vehicle Infrastructure

This is a case study of one municipality developing installed technology into their electrical vehicle charging to maintain their infrastructures. This was intended to enhance distribution, minimize the time consumed when recharging, and optimize the performance of the network. This installation at electric vehicle charging stations possesses sensor as well as communication modules. The sensors with these modules enable them to track how much energy is used or the times when they could be recharged. In order to enhance the energy distribution based on real-time data, these systems interacted with a central control system [59].

Results: Integration of the embedded technology within the EV charging infrastructure improved energy supply distribution. It also saved the charging time. Embedded systems better managed energy use as there was real-time monitoring of energy consumption. EV charging

also became faster and efficient. Moreover, effective scheduling of charging relieved grid peaks, thus mitigating some of the loads, thus preventing overloading in advance. Dynamic energy distribution management, which improved system-wide dependability and efficiency, was another added contribution. This case study shows how much potential the embedded systems have to elevate the effectiveness and dependability of the EV charging infrastructure. Efficient energy management became possible because of the features of the real-time monitoring and control of the embedded systems. Fast charging times and thus a positive user experience was thus achieved. Its success emphasizes how it is necessary to integrate advanced technologies in the EV infrastructure to increase electric vehicles and environmentally friendly transport modes [60].

6. FUTURE TRENDS AND INNOVATIONS

The energy sector holds much promise for transformation driven by on-going innovations within embedded systems. The upcoming trends and innovations in these areas would include significant developments in hardware, applications of machine learning-based predictive energy management, as well as enhanced IoT integration to realize intelligent energy ecosystems. This section goes through these trends and discusses their possible outcomes on energy systems in terms of efficiency, reliability, and sustainability.

6.1. Advancements in Hardware

One of the critical drivers for future innovations in embedded systems for energy applications is advances in hardware technologies. Low-power, high-performance microcontrollers and sensors are needed to improve the efficiency and functionality of embedded systems. High-Performance, Low-Power Microcontrollers Design for the next generation of microcontrollers should be balanced between low power consumption and excellent performance. The sophisticated power management strategies, dynamic voltage and frequency scaling, will be implemented to maximize energy efficiency without reducing the computational capacity. For applications such as remote renewable energy installations and battery-operated devices where energy resources are not easily accessible, this balance is crucial. These improvements are going to increase the longevity of microcontrollers and ensure that more environmentally friendly solutions for energy consumption will occur. Because they use leading-edge materials that maximize their efficiency and durability, these advances in materials science are likely to significantly raise the life spans and effectiveness of microcontrollers and sensors [61]. For instance, silicon carbide (SiC) and gallium nitride (GaN) will be used in power electronics to enhance thermal conductivity, thus reducing energy losses. Such materials are resistant to higher temperatures and hostile operating conditions, hence very relevant for energy applications where solutions with robustness and long durability are desired. In consequence, the related embedded systems, fitted with advanced materials, will thus be more suited to cope with demanding environments such as offshore wind farms and solar power plants.

Case study: One of the major semiconductor companies designed and developed a new generation of low-power microcontrollers on advanced materials targeted to applications related to energy. Those microcontrollers showed up to 40% power savings in comparison to state-of-the-art products at the time without sacrificing computation performance. Such microcontrollers, embedded into solar inverters, delivered significant enhancements in terms of energy efficiency and reliability. This illustrates the scope and potential effects of hardware improvement on the energy sector.

6.2. Machine Learning for Predictive Energy Management

The future for energy management is expected to have profound reliance on machine learning - with better demand forecasting as well as fault prediction capabilities becoming a reality. With ample data analysis, AI-driven algorithms can produce actionable insights; therefore, energy production and distribution as well as usage will be optimized. Accurate Demand Forecasting: Demand forecasting is one of the primary applications of machine learning in energy systems. The algorithms in ML can predict future energy demand with high accuracy by analyzing historical consumption data, weather patterns, and socio-economic factors. This enables energy providers to plan and allocate resources more effectively, reducing the risk of overproduction or shortages. The correct demand forecasting also enables the use of renewable energy sources. It provides better alignment between the energy supply and the variable renewable generation. Fault Prediction and Preventive Maintenance: Machine learning algorithms will predict potential faults in an energy system by analyzing sensors and monitoring equipment data. Identifying patterns and anomalies predicting component failure allows for appropriate preventive maintenance before issues escalate; thereby reducing downtime, minimizing cost in maintenance, and making it possible to extend the length of time energy infrastructure works. For example, an ML model could process data from the vibrations of wind turbines to indicate possible early signs of mechanical wear and therefore schedule maintenance accordingly.

The use of machine learning in energy systems helps better decision-making through the immediacy of insights and recommendations at any point in time. Algorithms, being driven by AI, can continue learning and adjusting according to incoming data; hence, increasing their precision and efficiency gradually over time. It enables a responsive and efficient use of energy management that maintains optimality in the performance of the system. For instance, ML algorithms might optimize the operation of an HVAC system in buildings according to occupancy patterns and even outside weather conditions, yielding the benefits of energy efficiency, as well as improving the comfort level [62].

Case study: An energy utility firm, on its wind farm, installed machine learning-based predictive maintenance of its wind turbine fleet. The ML-based models are able to precisely predict when faults might develop and therefore suggest the exact maintenance needed. This type of advance planning resulted in a reduction of 30% of downtime and increased energy output by 20%, which further shows how tremendous the role of machine learning is for the predictive management of energy resources.

6.3. IoT for Intelligent Energy Ecosystems

The integration of the Internet of Things into energy systems is creating intelligent energy ecosystems that allow for seamless energy management through enhanced data sharing and decision-making capabilities. Figure 8. Shows the basic architecture of model layer. There are two node types: edge and fog. Each facility (building, solar generation, etc.) can have its own local network. All the nodes and all local networks are related to the energy (smart grid) and cloud management layers.

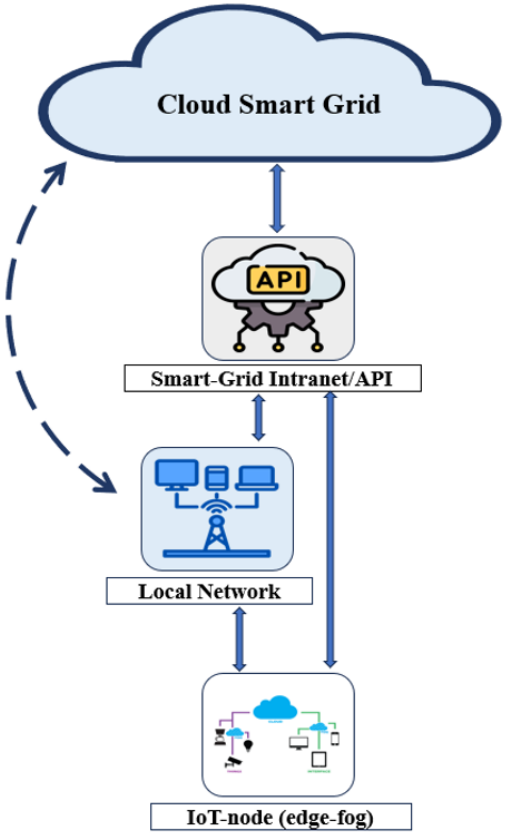

Figure 8. Model layer architecture with the main elements and their relationship.

6.3.1. Interconnected Systems

By the integration of IoT technology, interconnected energy systems can be formed where devices and components can directly communicate and collaborate in real time. This interconnectivity allows for increased efficiency and coordination in terms of energy management because data aggregation and analysis from multiple sources allow for optimization of flow of energy. For instance, in a smart grid system, IoT-enabled sensors and meters provide real-time information relating to energy consumption, production, and conditions on the grid, which enables dynamic balancing of loads and efficient use of energy [63].

6.3.2. Improved Data Sharing

IoT-based embedded systems can collect, transmit, and analyze massive amounts of data from different energy sources. Such information can help decision-makers get a better understanding of how the system is performing and, therefore, how much energy is being used in trend and where the problem is. Data analytics with all its sophisticated machine learning capabilities can be used to provide useful insights that may positively influence proactive energy management. For example, for exact control of HVAC systems while saving energy consumption, sensors incorporated with an IoT-based building management system can monitor temperature, humidity, and occupancy in a building [64].

6.3.3. Intelligent Decision Making

The integration of IoT in energy systems enables intelligent decision-making with real-time visibility and control. Based on the data, the IoT devices can make modifications automatically in real time, and it will ensure a state of optimal performance and efficiency. For instance, IoT sensors could track the weather around a renewable energy installation to maximize the output

of the installed wind turbines or solar panels. In addition, IoT-enabled systems can use demand response tactics for improving grid stability and saving money through dynamically modifying energy consumption in terms of price signals and grid circumstances [65].

6.3.4. Case Study

The smart city project helped create an intelligent energy environment. Through its energy network, it provided the necessary infrastructure for it to share information in real-time and be able to take coherent decisions as it introduced IoT-enabled sensors, smart meters, and communication devices in the entire set-up. The system accomplished dynamic load balancing, predictive maintenance, and more enhanced energy distribution, bringing greater reliability, reduced losses in energy and overall efficiency into the power grid [66].

7. CONCLUSION

The embedded systems revolution, which gives them the critical features of real-time monitoring, control, and optimization, is at the core of the new wave that will transform the energy industry. In highly specialized hardware and software, they combine to be used in different smart grid applications such as electricity vehicle infrastructure and renewable energy management. There is, therefore, a potential of transforming the sustainability, dependability, and efficiency of energy systems. One of the great advantages of an embedded system is that it can collect and evaluate data in real time. Such a system can continuously monitor energy production, consumption, and distribution by integrating sensors, actuators, microcontrollers, and modules for communication. Realtime monitoring allows for dynamic load balancing, fault detection, and predictive maintenance, thus providing assurance for the reliable and efficient operation of energy systems. In the case of a smart grid, for instance, it may give operators real-time information regarding how the grid is performing. Such knowledge helps the operator in optimizing energy flow and swiftly acting against any problems that may emerge. Despite all these benefits, there have been issues with the adoption of embedded systems in the energy sector. Since embedded systems are meant to operate as low-power devices while providing optimum performance, energy efficiency is an important challenge. Such embedded systems require sophisticated design methods and energy-efficient components in order to balance power consumption and processing capability. The interconnectedness of these embedded systems also increases their vulnerability to cyberattacks, hence raising cybersecurity threats with their deployment. This will ensure that data transmission is safe and that illegal access is prevented so that the integrity and dependability of the energy system are preserved.

Emerging technologies have made the embedded systems so widespread and standard in usage in the energy sector. For example, AI-empowered edge computing is one of the inventions that support predictive energy management and fault detection on the device level. As a result, AI algorithms are able to make immediate changes to the energy system on site and reduce latency without depending on centralized systems. This has ensured the optimized use of energy resources to enhance responsiveness and efficiency. Advanced communication protocols like MQTT and Zigbee, for example, have revolutionized data transfer within most embedded systems and, subsequently, enhanced data security and transmission efficiency. Protocols like these allow for heterogeneous devices with seamless integration capabilities to integrate real-time data sharing capabilities and coordinated decision-making across the entire network. It makes the ideal applications suitable for low bandwidth and resource-constrained devices. Zigbee improves reliability in a robustly secure mesh topology with communications between energy systems. Additionally, hardware innovations will make a difference with new-generation microcontrollers and sensors focused specifically on low-power designs that target the energy-related market.

Advanced materials like silicon carbide and gallium nitride also improve the durability and efficiency of these components, allowing them to be used better in extreme environmental conditions. These hardware innovations are a critical necessity for enhancing the performance and reliability of embedded systems for effective working in diverse energy environments. The second most important trend is IoT integration, which will transform the energy sector to create intelligent energy ecosystems. IoT-enabled embedded systems integrate different energy components seamlessly so that real-time data sharing becomes possible and allows for intelligent decision-making processes. In smart grids, in renewable energy installations, as well as in electric vehicle infrastructure, IoT integration enhances energy management efficiency and coordination while contributing to more sustainability and resilience. Real-world applications clearly portray the impact of embedded systems towards energy efficiency and reliability. Case studies of implementing IoT-enabled embedded systems in a smart grid led to vast energy losses reductions and significant enhancements in grid reliability. Embedded systems, thus, have shown that their introduction in renewable energy installations have enhanced the energy generation efficiency. In electric vehicle infrastructure, embedded systems improve energy distribution while reducing the time taken in charging the vehicle, creating a superior user experience to support widespread adoption of the electric vehicle. As technology further advances, embedded systems will be at the heart of developing intelligent, sustainable energy ecosystems. The advancements in low-power, high-performance hardware in combination with AI-driven algorithms and enhanced integration of the IoT will power further innovation in energy management. The energy sector will achieve much greater efficiency, reliability, and sustainability by unlocking all that is possible in terms of embedded systems through efforts at energy efficiency and cybersecurity while using emerging solutions. In fact, this transformation journey will be more sustainable and resilient for a much more environmentally friendly energy future.

Authors contribution: Sachin Srivastava:Conceptualization (equal); Formal analysis (equal); Methodology (equal); Resources (equal); Validation (equal); Visualization (equal); Writing - original draft (equal); Writing - review & editing (equal). G. Sai Satyanarayana: Conceptualization (equal); Methodology (equal); Visualization (equal); Writing - original draft (equal); Writing - review & editing (equal). Abhay Dhasmana: Conceptualization (equal); Methodology (equal); Visualization (equal); Writing - review & editing (equal). Vineet Rawat: Conceptualization (equal); Formal analysis (equal); Methodology (equal); Validation (equal); Writing - review & editing (equal). Aditya Singh Rana: Conceptualization (equal); Formal analysis (equal); Methodology (equal); Validation (equal); Writing - review & editing (equal). Yashwant Singh Bisht: Formal analysis (equal); Methodology (equal); Supervision (equal); Visualization (equal); Writing - review & editing (equal).

Funding: No Funding.

Data Availability Statement: Data available on demand.

Conflicts of Interest: No Conflicts of interest.

REFERENCES

[1].Mellit, A., Benghanem, M., Kalogirou, S., & Pavan, A. M. (2023). An embedded system for remote monitoring and fault diagnosis of photovoltaic arrays using machine learning and the internet of things. Renewable Energy, 208, 399-408. https://doi.org/10.1016/j.renene.2023.03.096

[2].Chehouri, A., Younes, R., Ilinca, A., & Perron, J. (2015). Review of performance optimization techniques applied to wind turbines. Applied Energy, 142, 361-388. https://doi.org/10.1016/j.apenergy.2014.12.043

[3].Omer, A. M. (2008). Energy, environment and sustainable development. Renewable and

sustainable energy reviews, 12(9), 2265-2300. https://doi.org/10.1016/j.rser.2007.05.001

[4].Bayindir, R., Colak, I., Fulli, G., & Demirtas, K. (2016). Smart grid technologies and applications. Renewable and sustainable energy reviews, 66, 499-516. https://doi.org/10.1016/j.rser.2016.08.002

[5].Omer, A. M. (2008). Focus on low carbon technologies: The positive solution. Renewable and Sustainable Energy Reviews, 12(9), 2331-2357. https://doi.org/10.1016/j.rser.2007.04.015

[6].Hassan, Q., Hsu, C. Y., Mounich, K., Algburi, S., Jaszczur, M., Telba, A. A., ... & Barakat, M. (2024). Enhancing smart grid integrated renewable distributed generation capacities: Implications for sustainable energy transformation. Sustainable Energy Technologies and Assessments, 66, 103793. https://doi.org/10.1016/j.seta.2024.103793

[7].Plantec, Q., Deval, M. A., Hooge, S., & Weil, B. (2023). Big data as an exploration trigger or problem-solving patch: Design and integration of AI-embedded systems in the automotive industry. Technovation, 124, 102763. https://doi.org/10.1016/j.technovation.2023.102763

[8].Taiwo, O., & Ezugwu, A. E. (2021). Internet of Things-Based Intelligent Smart Home Control System. Security and Communication Networks, 2021(1), 9928254. https://doi.org/10.1155/2021/9928254

[9].Andoni, M., Robu, V., Flynn, D., Abram, S., Geach, D., Jenkins, D., ... & Peacock, A. (2019). Blockchain technology in the energy sector: A systematic review of challenges and opportunities. Renewable and sustainable energy reviews, 100, 143-174. https://doi.org/10.1016/j.rser.2018.10.014

[10]. Jun, H. J., & Yang, H. S. (2021). Performance of the XMPP and the MQTT protocols on IEC 61850-based micro grid communication architecture. Energies, 14(16), 5024. https://doi.org/10.3390/en14165024

[11]. Bayindir, R., Colak, I., Fulli, G., & Demirtas, K. (2016). Smart grid technologies and applications. Renewable and sustainable energy reviews, 66, 499-516.

a. https://doi.org/10.1016/j.rser.2016.08.002

[12]. Ellabban, O., Abu-Rub, H., & Blaabjerg, F. (2014). Renewable energy resources: Current status, future prospects and their enabling technology. Renewable and sustainable energy reviews, 39, 748-764.

a. https://doi.org/10.1016/j.rser.2014.07.113

[13]. Das, H. S., Rahman, M. M., Li, S., & Tan, C. W. (2020). Electric vehicles standards, charging infrastructure, and impact on grid integration: A technological review. Renewable and Sustainable Energy Reviews, 120, 109618.

a. https://doi.org/10.1016/j.rser.2019.109618

[14]. Hemmati, R., & Saboori, H. (2016). Emergence of hybrid energy storage systems in renewable energy and transport applications–A review. Renewable and Sustainable Energy Reviews, 65, 11-23.

a. https://doi.org/10.1016/j.rser.2016.06.029

[15]. Kailas, A., Cecchi, V., & Mukherjee, A. (2012). A survey of communications and networking technologies for energy management in buildings and home automation. Journal of Computer Networks and Communications, 2012(1), 932181.

a. https://doi.org/10.1155/2012/932181

[16]. Koohi-Kamali, S., Tyagi, V. V., Rahim, N. A., Panwar, N. L., & Mokhlis, H. (2013). Emergence of energy storage technologies as the solution for reliable operation of smart power systems:

A review. Renewable and Sustainable Energy Reviews, 25, 135-165. https://doi.org/10.1016/j.rser.2013.03.056

[17]. Borgia, E. (2014). The Internet of Things vision: Key features, applications and open issues. Computer Communications, 54, 1-31. https://doi.org/10.1016/j.comcom.2014.09.008

[18]. Zha, X. F., & Sriram, R. D. (2005, January). Distributed Modeling and Framework for Collaborative Embedded System Design. In International Design Engineering Technical Conferences and Computers and Information in Engineering Conference (Vol. 47411, pp. 61-74). https://doi.org/10.1115/DETC2005-85608

[19]. Mutlu, O., Ghose, S., Gómez-Luna, J., & Ausavarungnirun, R. (2019). Processing data where it makes sense: Enabling in-memory computation. Microprocessors and Microsystems, 67, 28-41. https://doi.org/10.1016/j.micpro.2019.01.009

[20]. Benghanem, M. (2009). Measurement of meteorological data based on wireless data acquisition system monitoring. Applied energy, 86(12), 2651-2660. https://doi.org/10.1016/j.apenergy.2009.03.026

[21]. Jawad, H. M., Nordin, R., Gharghan, S. K., Jawad, A. M., & Ismail, M. (2017). Energy-efficient wireless sensor networks for precision agriculture: A review. Sensors, 17(8), 1781. https://doi.org/10.3390/s17081781

[22]. Rathor, S. K., & Saxena, D. (2020). Energy management system for smart grid: An overview and key issues. International Journal of Energy Research, 44(6), 4067-4109. https://doi.org/10.1002/er.4883

[23]. Arshad, J., Aziz, M., Al-Huqail, A. A., Zaman, M. H. U., Husnain, M., Rehman, A. U., & Shafiq, M. (2022). Implementation of a LoRaWAN based smart agriculture decision support system for optimum crop yield. Sustainability, 14(2), 827. https://doi.org/10.3390/su14020827

[24]. Rahman, M. M., Selvaraj, J., Rahim, N. A., & Hasanuzzaman, M. (2018). Global modern monitoring systems for PV based power generation: A review. Renewable and Sustainable Energy Reviews, 82, 4142-4158. https://doi.org/10.1016/j.rser.2017.10.111

[25]. Li, X., Xu, D., Zhu, H., Chen, Z., Yang, Z., Cheng, X., ... & Ng, W. T. (2017). A high voltage multiplexer with rail to rail output swing for battery management system applications. IEICE Electronics Express, 14(1), 20161144-20161144.

https://doi.org/10.1587/elex.13.20161144

[26]. Gabbar, H. A., Othman, A. M., & Abdussami, M. R. (2021). Review of battery management systems (BMS) development and industrial standards. Technologies, 9(2), 28. https://doi.org/10.3390/technologies9020028

[27]. Savari, G. F., Krishnasamy, V., Sathik, J., Ali, Z. M., & Aleem, S. H. A. (2020). Internet of Things based real-time electric vehicle load forecasting and charging station recommendation. ISA transactions, 97, 431-447. https://doi.org/10.1016/j.isatra.2019.08.011

[28]. Ma, K., Li, X., Liu, H., Sheng, X., Wang, Y., Swaminathan, K., ... & Narayanan, V. (2017). Dynamic power and energy management for energy harvesting nonvolatile processor systems. ACM Transactions on Embedded Computing Systems (TECS), 16(4), 1-23. https://doi.org/10.1145/3077575

[29]. Lipu, M. H., Ansari, S., Miah, M. S., Meraj, S. T., Hasan, K., Shihavuddin, A. S. M., ... & Hussain, A. (2022). Deep learning enabled state of charge, state of health and remaining useful life estimation for smart battery management system: Methods, implementations, issues and prospects. Journal of Energy Storage, 55, 105752. https://doi.org/10.1016/j.est.2022.105752

[30]. Venkatachalam, V., & Franz, M. (2005). Power reduction techniques for microprocessor

systems. ACM Computing Surveys (CSUR), 37(3), 195-237. https://doi.org/10.1145/1108956.1108957

[31]. Polonelli, T. (2021). Ultra-low power iot applications: from transducers to wireless protocols. 10.6092/unibo/amsdottorato/9604

[32]. Rahman, M. M., Selvaraj, J., Rahim, N. A., & Hasanuzzaman, M. (2018). Global modern monitoring systems for PV based power generation: A review. Renewable and Sustainable Energy Reviews, 82, 4142-4158. https://doi.org/10.1016/j.rser.2017.10.111

[33]. Ntafalias, A., Tsakanikas, S., Skarvelis-Kazakos, S., Papadopoulos, P., Skarmeta-Gómez, A. F., González-Vidal, A., ... & Vlachou, M. C. (2022). Design and Implementation of an Interoperable Architecture for Integrating Building Legacy Systems into Scalable Energy Management Systems. Smart Cities, 5(4), 1421-1440. https://doi.org/10.3390/smartcities5040073

[34]. Ancillotti, E., Bruno, R., & Conti, M. (2013). The role of communication systems in smart grids: Architectures, technical solutions and research challenges. Computer Communications, 36(17-18), 1665-1697. https://doi.org/10.1016/j.comcom.2013.09.004

[35]. Jaen-Cuellar, A. Y., Elvira-Ortiz, D. A., Osornio-Rios, R. A., & Antonino-Daviu, J. A. (2022). Advances in fault condition monitoring for solar photovoltaic and wind turbine energy generation: A review. Energies, 15(15), 5404. https://doi.org/10.3390/en15155404

[36]. Panahi, M., Hanson, A., Maddipatla, D., Masihi, S., Narakathu, B., Bazuin, B., ... & Atashbar, M. (2024). Condition monitoring system: a flexible hybrid electronics approach for sealed container applications. Journal of Surface Mount Technology, 37(2), 6-18. https://doi.org/10.37665/631d5y77

[37]. Ratasich, D., Khalid, F., Geissler, F., Grosu, R., Shafique, M., & Bartocci, E. (2019). A roadmap toward the resilient internet of things for cyber-physical systems. IEEE Access, 7, 13260-13283. https://doi.org/10.1109/ACCESS.2019.2891969

[38]. Aslan, Ö., Aktuğ, S. S., Ozkan-Okay, M., Yilmaz, A. A., & Akin, E. (2023). A comprehensive review of cyber security vulnerabilities, threats, attacks, and solutions. Electronics, 12(6), 1333. https://doi.org/10.3390/electronics12061333

[39]. Alzaabi, F. R., & Mehmood, A. (2024). A review of recent advances, challenges, and opportunities in malicious insider threat detection using machine learning methods. IEEE Access, 12, 30907-30927. https://doi.org/10.1109/ACCESS.2024.3369906

[40]. Faisal, M., Hannan, M. A., Ker, P. J., Hussain, A., Mansor, M. B., & Blaabjerg, F. (2018). Review of energy storage system technologies in microgrid applications: Issues and challenges. Ieee Access, 6, 35143-35164. 10.1109/ACCESS.2018.2841407

[41]. Gunasekaran, V., & Harmantzis, F. C. (2007). Emerging wireless technologies for developing countries. Technology in society, 29(1), 23-42. https://doi.org/10.1016/j.techsoc.2006.10.001

[42]. Tuli, S., Mirhakimi, F., Pallewatta, S., Zawad, S., Casale, G., Javadi, B., ... & Jennings, N. R. (2023). AI augmented Edge and Fog computing: Trends and challenges. Journal of Network and Computer Applications, 216, 103648. https://doi.org/10.1016/j.jnca.2023.103648

[43]. Afridi, Y. S., Ahmad, K., & Hassan, L. (2022). Artificial intelligence based prognostic maintenance of renewable energy systems: A review of techniques, challenges, and future research directions. International Journal of Energy Research, 46(15), 21619-21642. https://doi.org/10.1002/er.7100

[44]. Faheem, M., Shah, S. B. H., Butt, R. A., Raza, B., Anwar, M., Ashraf, M. W., ... & Gungor, V. C. (2018). Smart grid communication and information technologies in the perspective of Industry 4.0: Opportunities and challenges. Computer Science Review, 30, 1-30. https://doi.org/10.1016/j.cosrev.2018.08.001

[45]. Froiz-Míguez, I., Fernández-Caramés, T. M., Fraga-Lamas, P., & Castedo, L. (2018). Design, implementation and practical evaluation of an IoT home automation system for fog computing applications based on MQTT and ZigBee-WiFi sensor nodes. Sensors, 18(8), 2660. https://doi.org/10.2174/2210327913666221216152446

[46]. Bayılmış, C., Ebleme, M. A., Çavuşoğlu, Ü., Küçük, K., & Sevin, A. (2022). A survey on communication protocols and performance evaluations for Internet of Things. Digital Communications and Networks, 8(6), 1094-1104. https://doi.org/10.1016/j.dcan.2022.03.013

[47]. Jia, K., Xiao, J., Fan, S., & He, G. (2018). A mqtt/mqtt-sn-based user energy management system for automated residential demand response: Formal verification and cyber-physical performance evaluation. Applied Sciences, 8(7), 1035. https://doi.org/10.3390/app8071035

[48]. Apanaviciene, R., Vanagas, A., & Fokaides, P. A. (2020). Smart building integration into a smart city (SBISC): Development of a new evaluation framework. Energies, 13(9), 2190. https://doi.org/10.3390/en13092190

[49]. Froiz-Míguez, I., Fernández-Caramés, T. M., Fraga-Lamas, P., & Castedo, L. (2018). Design, implementation and practical evaluation of an IoT home automation system for fog computing applications based on MQTT and ZigBee-WiFi sensor nodes. Sensors, 18(8), 2660. https://doi.org/10.3390/s18082660

[50]. Newell, D., & Duffy, M. (2019). Review of power conversion and energy management for low-power, low-voltage energy harvesting powered wireless sensors. IEEE Transactions on Power Electronics, 34(10), 9794-9805. https://doi.org/10.1109/TPEL.2019.2894465

[51]. Das, H. S., Rahman, M. M., Li, S., & Tan, C. W. (2020). Electric vehicles standards, charging infrastructure, and impact on grid integration: A technological review. Renewable and Sustainable Energy Reviews, 120, 109618. https://doi.org/10.1016/j.rser.2019.109618

[52]. Ahmad, T., Madonski, R., Zhang, D., Huang, C., & Mujeeb, A. (2022). Data-driven probabilistic machine learning in sustainable smart energy/smart energy systems: Key developments, challenges, and future research opportunities in the context of smart grid paradigm. Renewable and Sustainable Energy Reviews, 160, 112128. https://doi.org/10.1016/j.rser.2022.112128

[53]. Sedhom, B. E., El-Saadawi, M. M., El Moursi, M. S., Hassan, M. A., & Eladl, A. A. (2021). IoT-based optimal demand side management and control scheme for smart microgrid. International Journal of Electrical Power & Energy Systems, 127, 106674. https://doi.org/10.1016/j.ijepes.2020.106674

[54]. Pan, F., Lin, G., Yang, Y., Zhang, S., Xiao, J., & Fan, S. (2019). Data-driven demand-side energy management approaches based on the smart energy network. Journal of Algorithms & Computational Technology, 13, 1748302619891611. https://doi.org/10.1177/1748302619891

[55]. Kayastha, N., Niyato, D., Hossain, E., & Han, Z. (2014). Smart grid sensor data collection, communication, and networking: a tutorial. Wireless communications and mobile computing, 14(11), 1055-1087. https://doi.org/10.1002/wcm.2258

[56]. Ahmad, T., Madonski, R., Zhang, D., Huang, C., & Mujeeb, A. (2022). Data-driven probabilistic machine learning in sustainable smart energy/smart energy systems: Key developments, challenges, and future research opportunities in the context of smart grid paradigm. Renewable and Sustainable Energy Reviews, 160, 112128. https://doi.org/10.1016/j.rser.2022.112128

[57]. Al Mamun, M. A., & Yuce, M. R. (2019). Sensors and systems for wearable environmental monitoring toward IoT-enabled applications: A review. IEEE Sensors Journal, 19(18), 7771-7788. https://doi.org/10.3390/su13158120

[58]. Ukoba, K., Olatunji, K. O., Adeoye, E., Jen, T. C., & Madyira, D. M. (2024). Optimizing renewable energy systems through artificial intelligence: Review and future prospects. Energy &

Environment, 0958305X241256293. https://doi.org/10.1177/0958305X241256293

[59]. Mahmud, K., Town, G. E., Morsalin, S., & Hossain, M. J. (2018). Integration of electric vehicles and management in the internet of energy. Renewable and Sustainable Energy Reviews, 82, 4179-4203. https://doi.org/10.1016/j.rser.2017.11.004

[60]. Lukasiewycz, M., Steinhorst, S., Andalam, S., Sagstetter, F., Waszecki, P., Chang, W., ... & Chakraborty, S. (2013, May). System architecture and software design for electric vehicles. In Proceedings of the 50th Annual Design Automation Conference (pp. 1-6) https://doi.org/10.1145/2463209.248885

[61]. Hassani, S., & Dackermann, U. (2023). A systematic review of advanced sensor technologies for non-destructive testing and structural health monitoring. Sensors, 23(4), 2204. https://doi.org/10.3390/s23042204

[62]. Civera, M., & Surace, C. (2022). Non-destructive techniques for the condition and structural health monitoring of wind turbines: A literature review of the last 20 years. Sensors, 22(4), 1627. https://doi.org/10.3390/s22041627

[63]. El-Afifi, M. I., Sedhom, B. E., Padmanaban, S., & Eladl, A. A. (2024). A review of IoT-enabled smart energy hub systems: Rising, applications, challenges, and future prospects. Renewable Energy Focus, 100634. https://doi.org/10.1016/j.ref.2024.100634

[64]. Kumar, T., Srinivasan, R., & Mani, M. (2022). An emergy-based approach to evaluate the effectiveness of integrating IoT-based sensing systems into smart buildings. Sustainable Energy Technologies and Assessments, 52, 102225. https://doi.org/10.1016/j.seta.2022.102225

[65]. Hafeez, G., Wadud, Z., Khan, I. U., Khan, I., Shafiq, Z., Usman, M., & Khan, M. U. A. (2020). Efficient energy management of IoT-enabled smart homes under price-based demand response program in smart grid. Sensors, 20(11), 3155. https://doi.org/10.3390/s20113155

[66]. Alhamrouni, I., Abdul Kahar, N. H., Salem, M., Swadi, M., Zahroui, Y., Kadhim, D. J., ... & Alhuyi Nazari, M. (2024). A comprehensive review on the role of artificial intelligence in power system stability, control, and protection: Insights and future directions. Applied Sciences, 14(14), 6214. https://doi.org/10.3390/app14146214

Solar Energy
And Sustainable Development
Refereed, biannual scientific journal issued by:
The Libyan Center for Solar Energy Research and Studies

DFT Approach for Improving the Electronic and Optical Properties of $KZnF_3$ Perovskite: Impact of Copper Doping

Noureddine Elmeskini[1]*, Younes Ziat[2], Hamza Belkhanchi[3], Ayoub Koufi[4].

[1,2,3,4]Engineering and Applied Physics Team, Superior School of Technology, Sultan Moulay Slimane University, Beni Mellal, Morocco.
[1,2,3,4]The Moroccan Association of Sciences and Techniques for Sustainable Development, Beni Mellal, Morocco.

E-*mail:* [1] noureddine.el-meskini@usms.ma ,[4]ayoub.koufi@usms.ma.

SPECIAL ISSUE ON:

The 1St International Conference on Sciences and Techniques for Renewable Energy and the Environment.
(STR2E 2025)
May 6-8, 2025 at FST-Al Hoceima- Morocco.

KEYWORDS

$KZnF_3$; Wien2k code;
Absorption coefficient;
Optical conductivity.

ABSTRACT

This study investigates the structural, electronic and optical properties of cubic perovskite $KZnF_3$, in its pure state and doped with copper (Cu) at a concentration of 12.5%, using the full-potential linearized augmented plane wave (FP-LAPW) method within the framework of density functional theory (DFT) which is implemented in the Wien2k code . Density-of-state (DOS) analysis reveals that doping significantly alters electronic properties, notably through the emergence of Cu-3d impurity states near the Fermi level, resulting in a shift towards the valence band and a decrease of the band gap to 2.72 eV. Optical properties were also analyzed through dielectric functions (real and imaginary parts), absorption coefficient, optical conductivity, refractive index and reflectivity. Cu doping enhances absorption in the visible spectrum, increases electron polarization and optimizes charge carrier mobility, boosting the material's performance in optoelectronic devices. These results highlight the key role of doping in engineering perovskite properties for advanced applications, including photovoltaic technologies, optical sensors and next-generation electronic systems.

*Corresponding author.

DOI: https://doi.org/10.51646/jsesd.v14iSTR2E.798

This is an open access article under the CC BY-NC license (http://Attribution-NonCommercial 4.0 (CC BY-NC 4.0)).

نهج DFT لتحسين الخصائص الإلكترونية والبصرية لبيروفسكايت $KZnF_3$: تأثير التنشيط بالنحاس

نور الدين المسكيني، يونس زيات، حمزة بلخنشي، أيوب كوفي.

ملخص: تتبحث هذه الدراسة في الخواص التركيبية والإلكترونية والبصرية للبيروفسكايت المكعب $KZnF_3$ في حالته النقية والمُطعّم بالنحاس (Cu) بتركي. 5. 12 %، باستخدام طريقة الموجة المستوية المعززة الخطية كاملة الإمكانات (FP-LAPW) في إطار نظرية الكثافة الوظيفية (DFT) التي يتم تنفيذها في كود Wien2k. ويكشف تحليل كثافة الحالة (DOS) أن التطعيم يغير الخصائص الإلكترونية بشكل كبير، لا سيما من خلال ظهور حالات شوائب النحاس ثلاثية الأبعاد بالقرب من مستوى فيرمي مما يؤدي إلى تحول نحو نطاق التكافؤ وانخفاض فجوة النطاق إلى2.72 للالكترون فولت. تم تحليل الخواص البصرية أيضًا من خلال الدوال العازلة (الأجزاء الحقيقية والتخيلية)، ومعامل الامتصاص، والتوصيل البصري، ومعامل الانكسار والانعكاسية. يعزز التطعيم بالنحاس الامتصاص في الطيف المرئي، ويزيد من استقطاب الإلكترون ويحسّن من حركة ناقل الشحنة، مما يعزز أداء المادة في الأجهزة الإلكترونية الضوئية. وتسلط هذه النتائج الضوء على الدور الرئيسي للتطعيم في هندسة خصائص البيروفسكايت للتطبيقات المتقدمة، بما في ذلك التقنيات الكهروضوئية وأجهزة الاستشعار البصرية والأنظمة الإلكترونية من الجيل التالي.

الكلمات المفتاحية: $KZnF_3$؛Wien2k؛معامل الامتصاص؛الموصلية الضوئية.

1. INTRODUCTION

The transition to renewable energy solutions has become a strategic priority worldwide due to growing environmental and economic challenges. Renewable energies, such as photovoltaics (PV), wind power and batteries, offer promising opportunities to meet ever-increasing energy demand, while minimizing environmental impacts [1, 2, 3, 4]. These technologies help reduce dependence on fossil fuels and promote sustainable development thanks to their economic, social, and ecological benefits. The identification and development of renewable, sustainable and economically competitive energy sources thus remain crucial to meeting the world's energy challenges. Among these solutions, solar energy stands out for its abundance, renewable nature and low environmental impact. Its conversion into chemical energy through processes such as artificial photosynthesis represents an innovative and indispensable approach to tackling the current energy and climate crises [5, 6, 7]. Inspired by natural mechanisms, this technology opens the way to revolutionary advances capable of transforming the world's energy system over the long term.

Indeed, these technological advances open up unprecedented prospects for transforming the global energy landscape and responding effectively to the current energy and climate crises. Among the materials emerging in this context, the ABX_3 family of cubic perovskites with a crystalline structure, and in particular the ABF3 fluorinated perovskite, stand out for their unique properties and exceptional potential for energy applications. These applications include fuel cells [8], photovoltaic systems [9], coating materials [10, 11, 12], spintronic applications [13], thermal [14], and renewable energy generation [15]. Several elements are used as A and B cations to arrange the atomic structure of fluoroperovskite ABF_3 compounds, with fluorine acting as the anion [16, 17]. Fluoroperovskite, a member of the large perovskite family, has drawn attention due to its distinct physical properties, which include high electron mobility [18], dielectric property [19, 20], magnetism [21], UV transparency, and piezoelectricity. Fluoroperovskite solids have attracted much interest in the semiconductor and lens industries [22, 23]. The absence of birefringence in the cubic perovskite materials makes them preferable candidates for lenses. The huge energy band gap that these compounds display is a noteworthy feature. These materials can be used to create glass materials that effectively transmit ultraviolet (UV) and vacuum ultraviolet (VUV) wavelengths due to their narrow absorption edges [24]. In their ideal configuration, the B

atoms occupy the centers of the octahedra formed by the X anions. These octahedra are organized in a simple cubic structure, but this crystal lattice conceals remarkable chemical and physical properties. For example, ABF3 fluoroperovskites (with A=K and B=Zn) adopt a cubic symmetry belonging to the space group $Pm\bar{3}m$ (221), where the A and B cations occupy the vertices and center of the unit cell respectively. At the same time, the F anions are positioned at the center of the faces [25, 26, 27, 28, 29]. Cubic fluoroperovskites, are characterized by their mechanical stability, elastic anisotropy, and electrical properties. These properties make these materials particularly suitable for applications in photovoltaic devices [30, 31, 32]. In addition, F anions, due to their high electronegativity, interact efficiently with A and B metal cations, giving fluoroperovskites a unique combination of structural, electrical, and thermoelectric properties. Their mechanical and thermal properties open up promising prospects in various industrial sectors, including the automotive and electronic gadget industries [33, 34, 35, 36]. Moreover, Yb3+ doped glass ceramics with $KZnF_3$ nanocrystals were fabricated successfully [37]. This structural flexibility, combined with the possibility of stabilizing fluoroperovskites by integrating organic or inorganic transition metals, makes them exciting materials for research and advanced technological applications [38, 39, 40, 41]. DFT offers a powerful framework for exploring in detail the fundamental properties of $KZnF_3$, such as electronic structure, band gap, interband transitions, and mechanical stability [42, 43]. Doping, particularly with transition metals such as copper (Cu), is an effective strategy for improving the properties of $KZnF_3$, by modifying the electronic and optical structure. This study analyzes the structural, electrical, and optical properties of the material $KZnF_3$ doped with a precise 12.5% concentration of Cu (Copper) using simulations based on density functional theory (DFT). This choice of concentration was carefully selected to optimize the interaction of the dopants with the host structure while minimizing crystal defects that could affect the overall stability of the material. DFT provides a rigorous theoretical framework for examining doping-induced modifications to the fundamental properties of $KZnF_3$, such as lattice parameters, electron density, and band structure. In particular, the aim is to assess how each type of dopant influences the band gap, essential for applications in optoelectronic devices. In addition, this approach makes it possible to investigate changes in optical properties. This research, combining advanced simulations and predictive analyses, will contribute to a broader understanding of the fundamental mechanisms involved in doping $KZnF_3$. They will also provide avenues for designing innovative materials with tuned properties, meeting the specific needs of renewable energy technologies and next-generation optoelectronic devices.

2. PACKAGE AND CALCULATION PROCESS

This study focuses on the structural, electronic and optical properties of cubic $KZnF_3$ perovskites, both in the pure state and doped with 12.5% copper (Cu). The calculations have been carried out using the full-potential linearized augmented plane wave (FP-LAPW) method, implemented in the WIEN2k code, to solve the Kohn-Sham equation within the framework of density functional theory (DFT) [44, 45, 46]., the generalized gradient correction (GGA) was employed for the exchange and correlation approximations [47]. $KZnF_3$ perovskites adopt a cubic structure characterized by the space group $Pm\bar{3}m$, typical of perovskite-structured compounds. This structure is confirmed by precisely measured crystal parameters $a_0 = b_0 = c_0 = 4.021$ Å [48], and $\alpha=\beta=\gamma=90^\circ$, in perfect agreement with available experimental data ($a_0 = b_0 = c_0 = 4.055$ Å [49]), Figure 1. To study the effect of doping, Cu atoms were introduced at a concentration of 12.5%, replacing Zn atoms at the specific Wyckoff positions, where the K atoms occupy the cube corner positions at the 1-a Wyckoff coordinates of (0, 0, 0), the metal Zn site is located at Wyckoff site 1-b (0.5, 0.5, 0.5) in positions centered on the crystal body, while the halogen atoms (F) occupy the face-centered positions at Wyckoff site 3-c (0, 0.5, 0.5), these configurations enable us to examine

in detail the changes induced by doping on the material's electronic and optical properties. The simulation parameters have been carefully chosen to ensure convergence of the calculations. A cut-off value Rmt* Kmax = 7, where Kmax is the maximum magnitude of the K vector, and Kmax represents the smallest atomic sphere radius of the unit cell. Convergence criteria were defined to an accuracy of 10^{-5} Ry for energy and 10^{-4}e for charge. With octahedral integration, a 1000 k-point mesh was used to sample the Brillouin zone intensively, ensuring high resolution of the calculated properties. In addition, the location of the central state charge was set to a value of -6 Ry, guaranteeing precise optimization of structures and electronic properties. Optimizing the crystal lattice volume was a crucial step before examining the electrical and optical characteristics to make sure the structure under study was in its condition of least energy stability. The Birch-Murnaghan equation of state, which is incorporated into the Wien2k code, was used to perform this optimization [36]:

$$E = E_0 + \frac{B_0}{B_0'}(V - V_0) - \frac{B_0 V_0}{B_0'(1 - B_0')}\left[\left(\frac{V}{V_0}\right)^{1-B_0'} - 1\right] \qquad (1)$$

Where B is the modulus of compressibility, B' the pressure derivative, E is taken as the minimum energy which is the ground state energy corresponding to the volume V_0 of the unit cell.

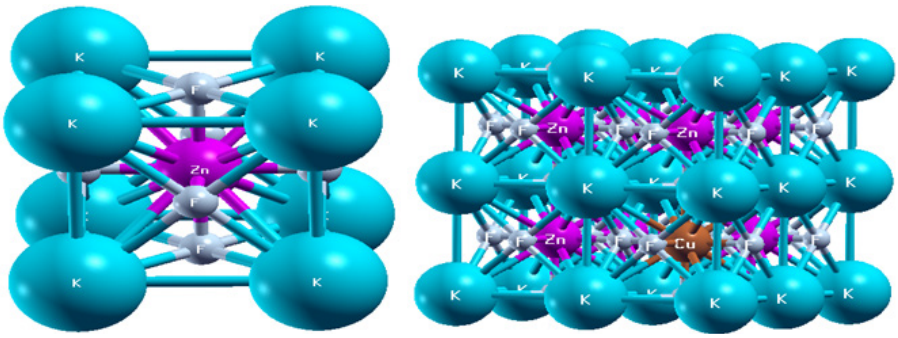

(a) (b)

Figure 1: a) The structure of the unit cell and, b) The structure of 2 × 2 × 2 Supercells of $KZnF_3$.

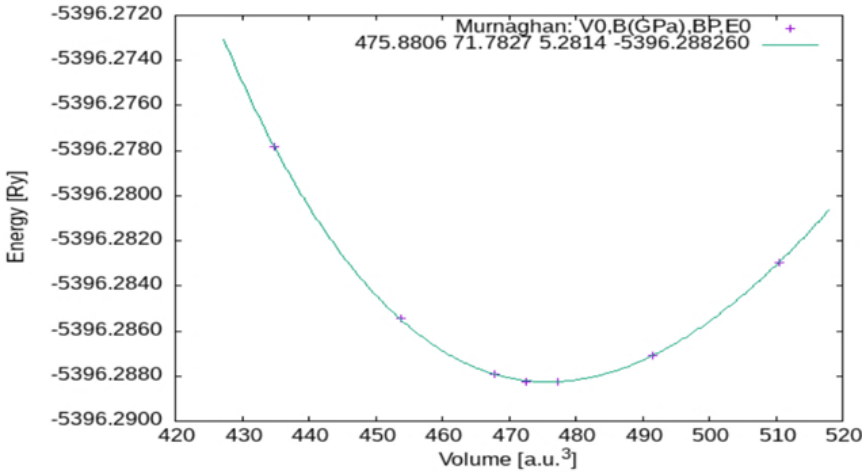

Figure 2: Variation of total energy versus volume curve of $KZnF_3$.

Figure 2 shows the volume optimization curve of total energy against the volume of $KZnF_3$-doped with 12.5% of Cu.

The optimized lattice parameters of pure $KZnF_3$ is $a_0 = b_0 = c_0 = 4.1314$ Å. The ground state derived from the optimization curve, based on the lattice parameter, is used to calculate the electronic and optical properties of the compounds self-consistently.
To model the effects of doping, a 2×2×2 supercell of pure $KZnF_3$ was constructed, in this model, some Zn sites were replaced by doping with Cu at a concentration of 12.5%. This approach enables accurate simulation of dopant-host interactions. Figure 1a illustrates the $KZnF_3$ unit cell, and Figure 1b shows the 2×2×2 supercell. This structure enables us to explore in detail the impact of doping on the crystal structure, electron density, and optical properties of the material. These results will contribute to a better understanding of the fundamental mechanisms and optimize the properties of perovskites for advanced applications in optoelectronic devices and energy technologies.

3. RESULTS AND DISCUSSION

3.1. Electronic properties

Calculations based on DFT were carried out to analyze the electronic properties of pure and doped $KZnF_3$. These calculations revealed the changes made to the electronic structure of $KZnF_3$ as a result of doping. Figure 3a and 3b show the energy band structures of the various compounds, in the energy range from -6 to 8 eV. The bandgap of the compounds are plotted along the high-symmetry path (W-L-Γ-X-W-K) in the Brillouin zone for a cubic structure, with the Fermi energy level (EF) aligned at zero. For pure $KZnF_3$ Figure 3a, an indirect band gap is observed between the L and Γ points. The bandgap width, calculated via the GGA approximation, is estimated at 3.91 eV. In doped $KZnF_3$ Figure 3b, produces subtle but significant changes in the band gap to 2.72 eV. The doped compounds exhibit similar electronic behavior, marked by electron transitions from the valence band (VB) to the conduction band (CB). Doping also induces the formation of new electronic energy levels within the band gap. These intermediate levels facilitate electronic transitions between the VB and CB, thereby improving the overall electronic properties of the material. More specifically, doped with Cu retain a direct band gap with electronic transitions in the Γ point of the Brillouin zone.

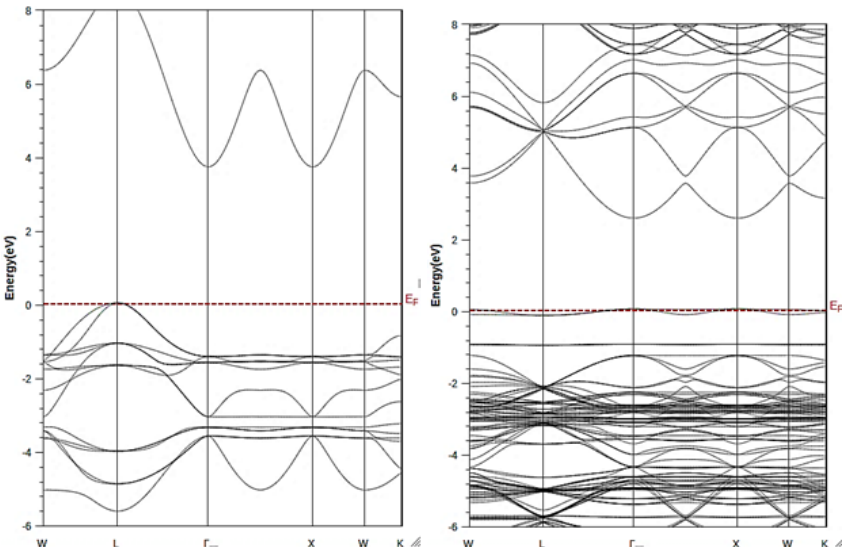

(a) (b)

Figure 3: The band structure of : a) pure $KZnF_3$; and b) doped $KZnF_3$ with Cu.

The density of states (DOS) analysis plays a crucial role in understanding the electronic properties

and chemical interactions of solid materials. In this study, the total (TDOS) and partial (PDOS) density of states of $KZnF_3$ perovskites Figure 4a and 4b, in the pure state and doped with Cu, has been examined to assess the impact of doping on their electronic properties. Calculations were performed after fully relaxing the crystal structures using the GGA potential, over an energy range from -6 eV to 7 eV, with the Fermi level fixed at 0 eV. For pure $KZnF_3$, the electronic contribution is mainly dominated by the hybridization of the K-4s and F-2p orbitals, reflecting a characteristic band structure. In doped structures, significant changes appear in the DOS, particularly at the bandgap level, with a measured reduction in band gap width to 2.72 eV. The Cu-3d doping also leads to a shift in the Fermi level towards the VB, indicating p-type semiconductor behavior. This phenomenon is attributed to an increase in hole carrier density, due to a greater concentration of F-2p states in the VB. The doped compounds also exhibit distinct electronic transitions between the VB and the CB, associated with significant hybridization between F-2p and Zn-3d electronic states in the VB, and relatively weaker hybridization in the CB.

Adding Cu atoms introduces Cu-3d impurity states that predominate in the VB, while F-2p states mainly influence the CB. This hybridization, combined with the modification of the band structure, reduces the energy gap between the VB and the CB, thus promoting a decrease in the band gap. In addition, the extra electronic states introduced by Cu near the CB create donor energy levels, facilitating electron movement.

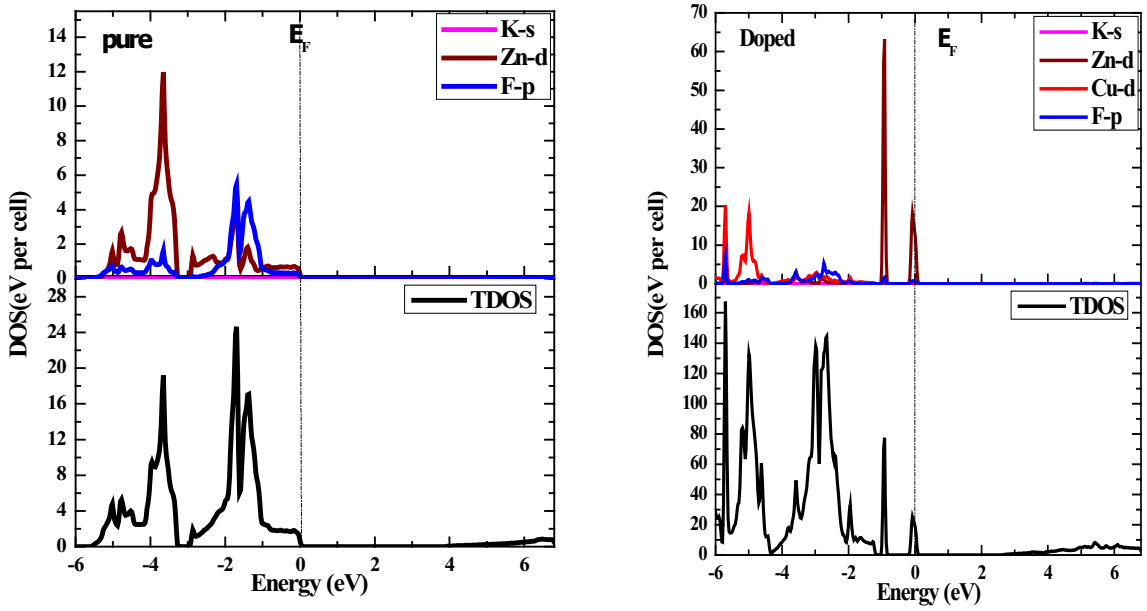

(a) (b)

Figure. 4: DOS of : a) pure; and b) doped $KZnF_3$.

This study demonstrates that Cu doping profoundly alters the electronic properties of $KZnF_3$. The decrease in the band gap, combined with the p-type behavior induced by the shift in the Fermi level, highlights the potential of this material for applications in electronic and optoelectronic devices requiring p-type conductivity. These results also open up prospects for tailoring the properties of $KZnF_3$ to the specific needs of applications ranging from semiconductors to metallic conductors, depending on the dopant used.

3.2. Optical properties

The optical properties of pure and doped $KZnF_3$ have been studied to assess the impact of dopants on its electronic structure. Various important optical parameters are presented in Figures 5 to 9.

Mathematical equations used to extract the dielectric functions (real part, $\varepsilon_1(\omega)$, and imaginary part, $\varepsilon_2(\omega)$, the absorption coefficient $\alpha(\omega)$, the optical conductivity $\sigma(\omega)$, the refractive index $n(\omega)$ and the reflectivity $R(\omega)$. The dielectric function $\varepsilon(\omega)$ was computed [50, 51]:

$$\varepsilon(\omega) = \varepsilon_1(\omega) + i\varepsilon_2(\omega) \qquad (2)$$

The dielectric function real part ($\varepsilon_1(\omega)$) is obtained through the Kramers-Kronig transformation [52, 53]:

$$\varepsilon_1(\omega) = 1 + \frac{2}{\pi} p\int \frac{\omega'\varepsilon_2(\omega')}{(\omega'^2 - \omega^2)} d\omega' \qquad (3)$$

The imaginary part ($\varepsilon_2(\omega)$) values are calculated using the following procedure [52, 54]:

$$\varepsilon_2(\omega) = \left(\frac{4\pi^2 e^2}{m^2\omega^2}\right)\sum_{i,j} \langle i|M|j\rangle^2 f_i(1-f_j)\delta(E_f - E_i - \omega) d^3k \qquad (4)$$

The element of the dipole matrix is denoted M, the electron mass is m, the elementary charge is e, and P represents the principal value of the integral in this context. The initial and final states are denoted by the indices i and j respectively. The energy of the electron in state i, with wave vector k, is denoted by E_i, and the Fermi-Dirac distribution function associated with state i is denoted by f_i.

The $\varepsilon_1(\omega)$ and $\varepsilon_2(\omega)$ components enable the determination of various optical properties, such as the absorption coefficient $\alpha(\omega)$, the optical conductivity $\sigma(\omega)$, the refractive index $n(\omega)$ and the reflectivity $R(\omega)$ using the following formula [55, 56, 57, 58]:

$$a(\omega) = \sqrt{2}\,\omega\left[\sqrt{\varepsilon_1(\omega)^2 + \varepsilon_2(\omega)^2} - \varepsilon_1(\omega)\right]^{1/2} \qquad (5)$$

$$\sigma(\omega) = \frac{\omega}{4\pi}\varepsilon_2(\omega) \qquad (6)$$

$$R(\omega) = \left|\frac{\sqrt{\epsilon(\omega)} - 1}{\sqrt{\epsilon(\omega)} + 1}\right|^2 \qquad (7)$$

$$n(\omega) = \frac{1}{\sqrt{2}}\left[\sqrt{\varepsilon_1^2(\omega) + \varepsilon_2^2(\omega)} + \varepsilon_1(\omega)\right]^{1/2} \qquad (8)$$

Figure 5a shows the variation of $\varepsilon_1(\omega)$ for pure and doped $KZnF_3$, in an energy range from 0 to 14 eV. This function describes the material's response to an electric field, in particular its ability to polarize and store electrical energy. The static dielectric constant $\varepsilon_1(0)$, which reflects polarization at low frequencies, shows a significant increase after doping. For pure $KZnF_3$, $\varepsilon_1(0)$ is 1.67, and when doped at a concentration of x = 12.5%, the values of $\varepsilon_1(0)$ increases to 6.73. This trend indicates that the introduction of dopants enhances the material's polarizability. The observed increase in $\varepsilon_1(0)$ can be attributed to the dopants' ability to induce additional dipoles, alter both ionic and electronic polarizability, and modify the local electronic structure, thereby amplifying the dielectric response of the material [59]. Figure 5b shows the $\varepsilon_2(\omega)$ for pure and doped $KZnF_3$, in an energy range from 0 to 14 eV. This parameter plays a key role in understanding the electronic absorption processes of materials. The analysis of the optical spectrum reveals several distinct peaks, resulting from inter-band transitions between the VB and CB. For pure $KZnF_3$, the spectrum reaches a notable energy peak at 5.45 eV in the ultraviolet, corresponding to electronic transitions involving K-4s, F-2p and Zn-3d orbitals in the VB, and F-2p orbitals in the CB. An increase in $\varepsilon_2(\omega)$ is observed with photon energy, peaking around 13 eV. After

Cu doping, the peaks in the spectrum undergo an energy shift to lower values, accompanied by changes in their intensity and position, including the appearance of peaks at 2 eV, associated with transitions characteristic of Cu-doped $KZnF_3$. Also, a maximum peak is observed at 0 eV, where this one is 6.5 eV. When comparing Figure 5b with Figure 4a, this value is due to the shifting of the Zn-3d state to 0 eV, where the system is being doped.

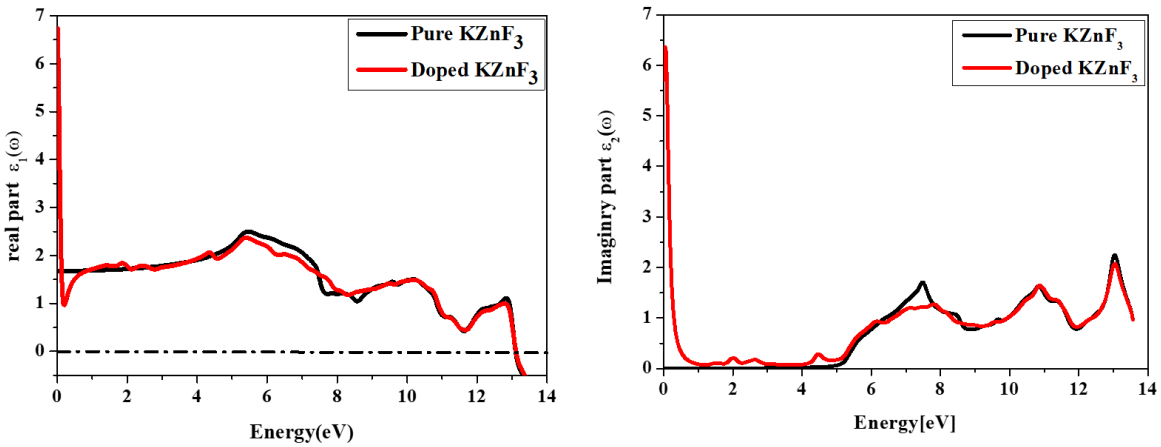

a) b)

Figure 5: Dielectric function of pure and doped $KZnF_3$: (a) Real part; and (b) Imaginary part.

Figure 6 illustrates σ(ω) for pure and doped $KZnF_3$ over an energy range of 0 to 14 eV, which represents the material's ability to transport electrons in response to an applied electromagnetic field [60]. Transparency in the 0–4.1 eV region is indicated by the absence of optical conductivity in pure $KZnF_3$, which can be attributed to the absence of light-absorbing electronic transitions.

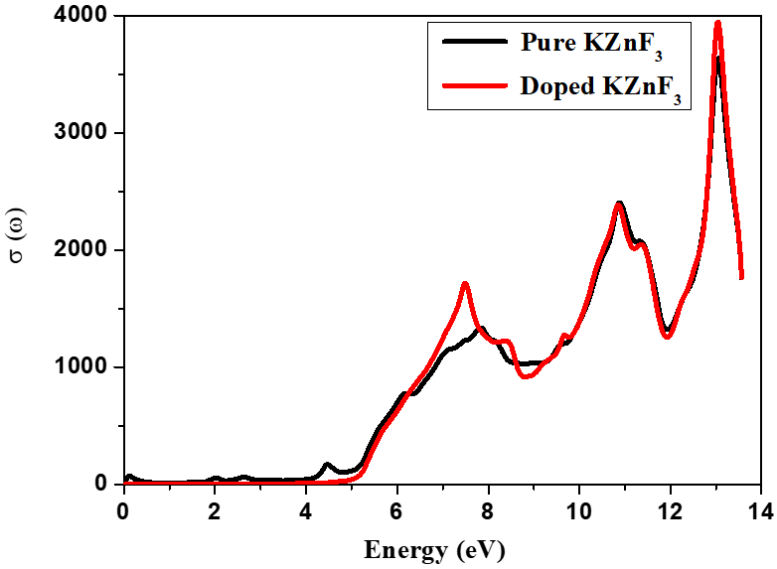

Figure 6: Optical conductivity as a function of energy of pure and doped $KZnF_3$.

Additionally, the optical conductivity of the pure $KZnF_3$ compound has a noteworthy value, increasing gradually from 4.9 eV to a maximum of roughly 13.02 eV. The conductivity maximum, as demonstrated by the previously mentioned peak, is 3614.18 $\Omega^{-1}.cm^{-1}$. The doped compound's maximum σ(ω) value is roughly 3930.88 $\Omega^{-1}.cm^{-1}$. The results show that doping changes the compound's electronic structure, which raises its reactivity at particular photon energy. Material qualities are tailored for certain applications, such as optoelectronics, even if doping reduces

maximum optical conductivity.

Figure 7 illustrates the absorption coefficient α(ω) of pure and Cu-doped KZnF3 in the energy range from 0 to 14 eV. Pure KZnF3 shows no optical absorption in the 0 to 4.5 eV range, but begins to absorb the light between 4.5 and 13.5 eV, with increasing intensity as a function of photon energy, and when doped with Cu, absorption peaks appear at 4.2 eV. This doping considerably enhances absorption properties in the visible, with coefficients reaching values as high as 10^4 cm^{-1}, and broadens absorption capacity, 12.5% Cu doping further optimizes these properties, demonstrating the material's potential for applications in photovoltaic cells and optoelectronic devices. The results indicate that the doping introduces additional electronic states favoring interband transitions, making the material capable of absorbing a greater proportion of the solar spectrum. This significant enhancement of absorption capabilities in the visible and ultraviolet range also suggests promising applications for photochemical reactions activated by visible light, reinforcing the interest of Cu-doped KZnF3 as a versatile material for advanced energy and optical technologies.

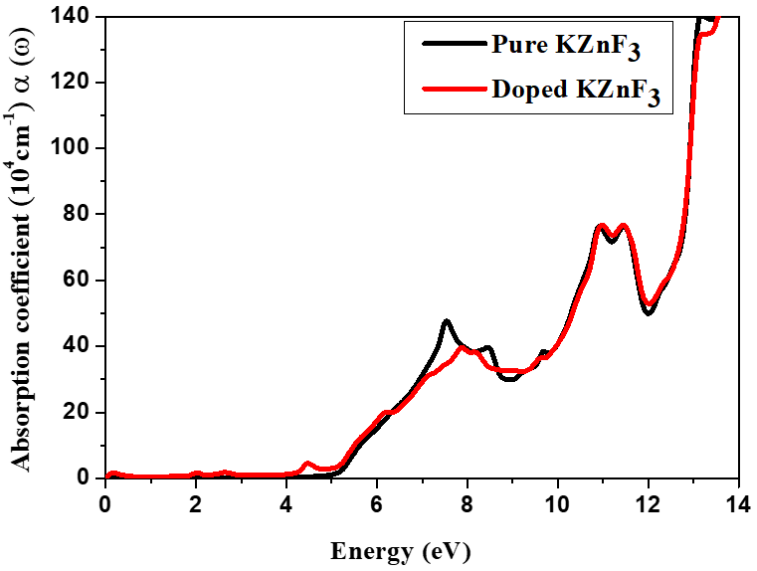

Figure 7: Absorption coefficient as a function of energy of pure and doped $KZnF_3$.

Figure 8 shows the evolution of the refractive index n(ω) of pure and Cu-doped Figure 8 shows the evolution of the refractive index n(ω) of pure and Cu-doped $KZnF_3$ over a given energy range. The results reveal that the static refractive index n(0) of $KZnF_3$, initially is of 1.25 in the pure state, increases significantly to reach a value of 2.78 after Cu doping. This reflects an enhanced interaction with light, indicating a notable improvement in the material's optical properties. Pure $KZnF_3$ exhibits its maximum refractive index at 5.9 eV, while Cu doping shifts these peaks towards 0.4 eV. By modifying the interaction between electronic bands, Cu doping transforms the optical properties of $KZnF_3$, this enhancement gives doped $KZnF_3$ greater potential for advanced optoelectronic applications. over a given energy range. The results reveal that the static refractive index n(0) of Figure 8 shows the evolution of the refractive index n(ω) of pure and Cu-doped $KZnF_3$ over a given energy range. The results reveal that the static refractive index n(0) of $KZnF_3$, initially is of 1.25 in the pure state, increases significantly to reach a value of 2.78 after Cu doping. This reflects an enhanced interaction with light, indicating a notable improvement in the material's optical properties. Pure $KZnF_3$ exhibits its maximum refractive index at 5.9 eV, while Cu doping shifts these peaks towards 0.4 eV. By modifying the interaction between electronic bands, Cu doping transforms the optical properties of $KZnF_3$, this enhancement gives doped $KZnF_3$ greater potential for advanced optoelectronic applications., initially is of 1.25 in the pure

state, increases significantly to reach a value of 2.78 after Cu doping. This reflects an enhanced interaction with light, indicating a notable improvement in the material's optical properties. Pure $KZnF_3$ exhibits its maximum refractive index at 5.9 eV, while Cu doping shifts these peaks towards 0.4 eV. By modifying the interaction between electronic bands, Cu doping transforms the optical properties of $KZnF_3$, this enhancement gives doped $KZnF_3$ greater potential for advanced optoelectronic applications.

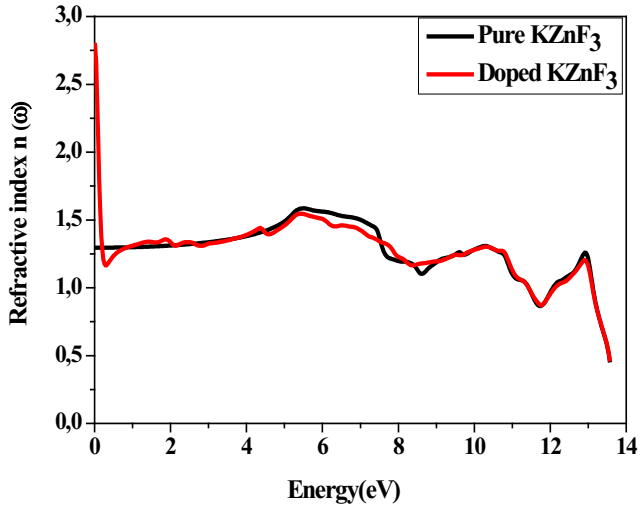

Figure 8: Refractive index as a function of energy of pure and doped $KZnF_3$.

The reflectivity R(ω), which describes the ability of a surface to reflect incident electromagnetic radiation, is analyzed from the results presented in Figure 9.

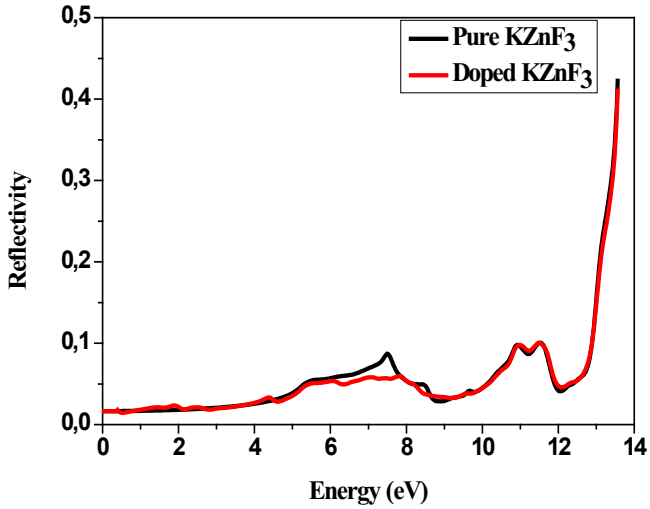

Figure 9: Reflectivity as a function of energy of pure and doped $KZnF_3$.

From the range of 0 to 4 eV, the reflectivity is lower, where this conduct is explained when comparing Figure 9 and the TDOS at the same range in Figure 4a, where no PDOS is observed. The results show that the reflectivity spectrum reaches its maximum values when the real ε1 (ω), shown in Figure 5a, becomes negative. This reflects a key property of metallic or semi-metallic materials, where negative values of ε1 (ω) mean total reflection of incident electromagnetic waves. This characteristic is essential for applications in optical devices such as selective mirrors

or optical filters. In addition, Cu doping modifies the position and intensity of reflectivity peaks, indicating a reorganization of $KZnF_3$'s electronic structure that optimizes its interactions with electromagnetic radiation. These adjustments enhance the material's potential for applications in advanced optical technologies, including the manufacture of anti-reflective coatings, high-performance mirrors and photovoltaic devices. Further analysis could also explore the effect of different levels of doping to refine optical properties and tailor the material to specific uses in a variety of fields.

4. CONCLUSION

This study combining analysis of the electronic, structural and optical properties of cubic perovskite $KZnF_3$, both in the pure and Cu-doped states, has demonstrated the notable impacts of doping on the fundamental characteristics of the material using the DFT, to address the electron–ion interaction. Density of states (DOS) analysis revealed that, in the pure state, electronic contributions are dominated by hybridized F-2p and K-4s orbitals. After Cu doping, Cu-3d impurity states emerged near the Fermi level, causing it to shift towards the VB, reflecting p-type semiconductor behavior. These modifications resulted in a 2.72 eV band gap decrease, facilitating a smooth electronic transition between the VB and CB. This hybridization between the F-2p, 3d-Zn and Cu-3d states, particularly pronounced in VB, also contributes to improved electronic and optical properties. In terms of optical properties, analysis of the dielectric functions ($\varepsilon_1(\omega)$ and $\varepsilon_2(\omega)$) revealed significant changes in the electronic response following doping. The real part, $\varepsilon_1(\omega)$, showed improved electronic polarization, while the imaginary part, $\varepsilon_2(\omega)$, revealed increased absorption in the visible spectrum. The absorption coefficient $\alpha(\omega)$ confirmed a better interaction with photons, essential for photovoltaic applications. In addition, the optical conductivity $\sigma(\omega)$ showed an increase in electron mobility, reinforcing the material's compatibility for optoelectronic devices. Refractive indices $n(\omega)$ and reflectivity $R(\omega)$ also showed optimized responses after doping, indicating increased potential for lightwave management in advanced technological applications. In summary, the simultaneous enhancement of the electronic and optical ($\varepsilon(\omega)$, $\alpha(\omega)$, $\sigma(\omega)$, $n(\omega)$, $R(\omega)$) properties of Cu-doped $KZnF_3$ demonstrates its potential for applications in photovoltaic devices, optical sensors and optoelectronic systems. These results illustrate the power of doping-based materials engineering to tailor perovskites to current and future technological needs.

Authors Contribution: Noureddine Elmeskini: Writing – original draft, visualization, validation, investigation, formal analysis, data curation, and conceptualization. Younes Ziat: Bibliography and references. Hamza Belkhanchi: Writing – original draft, and Ayoub Koufi: Visualization.

Funding: The authors are warmly grateful to the support of "The Moroccan Association of Sciences and Techniques for Sustainable Development (MASTSD), Beni Mellal, Morocco" and to its president, professor Charaf Laghlimi, for the valuable proposals.

Data Availability Statement: Not applicable.

Acknowledgments: A special thank you to Professor Hanane Reddad from Sultan Moulay Slimane University, Beni Mellal, Morocco, for her technical and scientific support, as well as her full collaboration and discussion during the different steps of the present investigation.

Conflicts of Interest: The authors declare that they have no conflict of interest.

REFERENCES

[1] G,Batra . Renewable energy economics: achieving harmony between environmental protection and economic goals. Social Science Chronicle, 2(2), 1-32 2023., https://doi.org/10.56106/

ssc.2023.009.

[2] L. P. S. S. Panagoda, R. A. H. T. Sandeepa, W. A. V. T. Perera,D. M. I. Sandunika, S. M. G. T. Siriwardhana, M. K. S. D. Alwis & S. H. S. Dilka. Advancements In Photovoltaic (Pv) Technology for Solar Energy Generation, Journal of Research Technology & Engineering, 4(30), 30-72. 2023.

[3] N. M. Manousakis,P. S. Karagiannopoulos,G. J. Tsekouras, & F. D. Kanellos. Integration of renewable energy and electric vehicles in power systems: a review. Processes, 11(5), 1544 2023., https://doi.org/10.3390/pr11051544.

[4] A. Koufi, Y. Ziat, H. Belkhanchi, & A. Bouzaid. DFT and BoltzTrap investigations on the thermal and structural characteristics of the perovskite MgCuH3 and MgCoH3. Computational Condensed Matter, e01010 2025., https://doi.org/10.1016/j.cocom.2025.e01010.

[5] Tu, Wenguang, Yong Zhou, and Zhigang Zou. "Photocatalytic conversion of CO2 into renewable hydrocarbon fuels: state-of-the-art accomplishment, challenges, and prospects." Advanced Materials 26.27 (2014): 4607-4626, https://doi.org/10.1002/adma.201400087.

[6] Chen, Xiaobo, et al. "Nanomaterials for renewable energy production and storage." Chemical Society Reviews 41.23 (2012): 7909-7937, https://doi.org/10.1039/C2CS35230C.

[7] Du, Shiwen, and Fuxiang Zhang. "General applications of density functional theory in photocatalysis." Chinese Journal of Catalysis 61 (2024): 1-36, https://doi.org/10.1016/S1872-2067(24)60006-9.

[8] M. H. Benkabou, M. Harmel, A. Haddou, A. Yakoubi, N. Baki, and R. Ahmed. "Structural , electronic , optical and thermodynamic investigations of NaXF3 (X = Ca and Sr): First-principles calculations.". Nanoscale, 56:131–144, 2018, https://doi.org/10.1016/j.cjph.2017.12.008.

[9] S. A. Shah, M. Husain, N. Rahman, M. Sohail, and R. Khan. "Insight into the struvtural, electronic, elastic, optical, and magnetic properties of cubic fluoroperovskites ABF3 (A = Tl , B = Nb , V) compounds: Probed by DFT.". Nanomaterials, 3, 2022, https://doi.org/10.3390/ma15165684.

[10] Z. Jin, Y. Wu, S. Li, Q. Wu, S. Chen, and Y. Chen. "Results in physics electronic structure , elastic , optical and thermodynamic properties of cubic perovskite NaBaF3 with pressure effects: First-principles calculations.". Results Phys., 22:103860, 2021, https://doi.org/10.1016/j.rinp.2021.103860.

[11] N. A.Bahmid, S. A. Siddiqui, H. D. Ariyanto, K. S.Sasmitaloka, N. B.Rathod,S. K. Wahono, ... & A. W. Indrianingsih,Cellulose-based coating for tropical fruits: method, characteristic and functionality. Food Reviews International, 40(4), 1069-1092. 2024. https://doi.org/10.1080/87559129.2023.2209800.

[12] S.Wang,Y. Wan,N. Song, Y. Liu, T. Xie, & B.Hoex.Automatically Generated Datasets: Present and Potential Self-Cleaning Coating Materials. Scientific Data, 11(1), 146 2024., https://doi.org/10.1038/s41597-024-02983-0.

[13] A. A. Pasha, H. Khan, M. Sohail, N. Rahman, R. Khan, and A. Ullah. "A computational first principle examination of the elastic, optical, structural and electronic properties of AlRF3 (R = N, P) fluoroperovskites compounds.". Molecules, 28, 2023, https://doi.org/10.3390/molecules28093876.

[14] A. Koufi, Y. Ziat, H. Belkhanchi, ... and F. Z. Baghli. A computational study of the structural and thermal conduct of MgCrH3 and MgFeH3 perovskite-type hydrides: FP-LAPW and BoltzTraP insight. E3S Web of Conferences (Vol., 582, p. 02003). 2024. EDP Sciences. https://doi.org/10.1051/e3sconf/202458202003.

[15] R. Ullah and A. H. Reshak. "Pressure-dependent elasto-mechanical stability and thermoelectric properties of MYbF3 (M = Rb , Cs) materials for renewable energy.". International

Journal of Energy Research, 45:1–13, 2021, https://doi.org/10.1002/er.6408.

[16] W. Ullah, R. Nasir, M. Husain, N. Rahman, and H. Ullah. "Revealing the remarkable structural, electronic, elastic, and optical properties of Zn-based fluoropervskite ZnXF3 (x = Sr, Ba) employing DFT. ". Indian J. Phys., 3, 2024, https://doi.org/10.1007/s12648-024-03146-y.

[17] N. Chouit, S. A. Korba, M. Slimani, H. Meradji, S. Ghemid, and R. Khenata. "First-principles study of the structural, electronic and thermal properties of CaLiF3. ". Phys. Scr., 88:139–153, 2013, 10.1088/0031-8949/88/03/035702.

[18] J. Zhang, Y. Chen, S. Chen, J. Hou, R. Song, and Z. F. Shi. "Electronic structure, mechanical, optical and thermodynamic properties of cubic perovskite InBeF3 with pressure effects: First-principles calculations.". Results Phys., 50:106590, 2023, https://doi.org/10.1016/j.rinp.2023.106590.

[19] M. R. Kabli, J. ur Rehman, M. Bilal Tahir, M. Usman, A. Mahmood Ali, and K. Shahzad. "Structural, electronics and optical properties of sodium based fluoroperovskites NaXF3 (X = Ca, Mg, Sr and Zn): First principles calculations.", Phys. Lett. Sect. A Gen. At. Solid State Phys., 412:127574, 2021. https://doi.org/10.1016/j.physleta.2021.127574.

[20] M. I.Abdulraheem, H., Li, L. Chen, A. Y. Moshood, W. Zhang, Y.Xiong, ... & Hu, J. Recent Advances in Dielectric Properties-Based Soil Water Content Measurements. Remote Sensing, 16(8), 1328. 2024., https://doi.org/10.3390/rs16081328.

[21] J. ur Rehman, M. Usman, M. B. Tahir, and A. Hussain. "First-principles calculations to investigate structural , electronic and optical properties of Na based fluoroperovskites NaXF3 (X = Sr, Zn). ". Solid State Commun., 334–335:114396, 2021., https://doi.org/10.1016/j.ssc.2021.114396.

[22] T. N. Ishimatsu, N. T. Erakubo, H. M. Izuseki, Y. K. Awazoe, and D. A. P. Awlak. "Band structures of perovskite-like fluorides for vacuumultraviolet-transparent lens materials.". Japanese Journal of Applied Physics, 41:10–13, 2002., DOI 10.1143/JJAP.41.L365.

[23] A.Jehan, M. Husain, N. Rahman,V. Tirth, N. Sfina,M. Elhadi, ... & S. N.Khan, Investigating the structural, elastic, and optoelectronic properties of LiXF3 (X= Cd, Hg) using the DFT approach for high-energy applications. Optical and, Quantum Electronics. 56(2) 169. 2024. https://doi.org/10.1007/s11082-023-05750-4.

[24] M. Usman, J. ur Rehman, and M. B. Tahir. "Screening of ABF3 fluoroperovskites by using first-principles calculations.". Solid State Commun., 369:1–6, 2023, https://doi.org/10.1016/j.ssc.2023.115198.

[25] H. M.Ghazi, & A. H. Reshak. First principle investigation of the structural, electronic, optical, and elastic properties of Ba-based fluoroperovskite (BaYF3; Y= Li, Na, K, and Rb) compounds. Journal of Theoretical and Applied Physic, 2024., 18(5), 1-13. 10.57647/j.jtap.2024.1805.58.

[26] D.Ceriotti, P. Marziani, F. M.Scesa, A.Collorà, C. L. Bianchi, L. Magagnin, & M.Sansotera. Mechanochemical synthesis of fluorinated perovskites KCuF 3 and KNiF 3. RSC Mechanochemistry, 1(5), 520-530. 2024., https://doi.org/10.1039/d4mr00037d.

[27] D. A.Ahmed, S.Bağcı, E.Karaca, & H. M.Tütüncü. Elastic properties of ABF3 (A: Ag, K and B: Mg, Zn) perovskites. In AIP Conference Proceedings (Vol. 2042, No. 1). AIP Publishing 2018., https://doi.org/10.1063/1.5078907.

[28] L.L.Boyer, P.J.Edwardson, Perovskite to antiperovskite in abf3 compounds. Ferroelectrics 104, 417–422 1990,, https://doi.org/10.1080/00150199008223849.

[29] M. Miri , Y. Ziat, H. Belkhanchi, A. Koufi, Y. A. El Kadi, Modulation des propriétés électroniques et optiques de la pérovskite InGeF3 sous pression : une approche computationnelle,

"The European Physical Journal B", 2025. https://link.springer.com/journal/10051

[30] M.Mubashir, Z. Bibi, M.Ali, M. Muzamil, U.Afzal, & M. D.Albaqami, First-principles prediction of antimony based XSbF3 (X= Be, Mg, Ca and Sr) fluoroperovskites: An insight into structural, optoelectronic and thermal properties. 2024., Physica B: Condensed Matter, 685, 415986. https://doi.org/10.1016/j.physb.2024.415986.

[31] S.u Zaman, I.Ghani, J.Riaz, A.Bibi, & M.Arif, DFT-based ab initio study of structural, electronic, optical and thermodynamics properties of Al based fluoroperovskite AlMF3 (M= Ca and Cd). Optical and Quantum Electronics, 56(7), 1205. 2024., https://doi.org/10.1007/s11082-024-07130-y.

[32] J.Khan, & M.Faisal, Exploring the Potential of Nitrogen-Based Anti-Perovskite Compounds for Solar Cells: A Theoretical Investigation of Their Structural and Optoelectronic Properties Using Density Functional Theory (Dft)., http://dx.doi.org/10.2139/ssrn.4888926.

[33] N.Rahman ; M.Husain; J.Yang; M. Sajjad ; G.Murtaza ; M.Ul Haq ; A.Habib ; Zulfiqar; A. Rauf ; A.Karim ; et al. First principle study of structural, electronic, optical and mechanical properties of cubic fluoro-perovskites: (CdXF3, X = Y, Bi)., Eur. Phys. J. Plus 136, 347. 2021. https://doi.org/10.1140/epjp/s13360-021-01177-6.

[34] L.Tian ; Z.Hu ; X.Liu ; Z. Liu ; P.Guo ; B.Xu ; Q.Xue ; H.-L.Yip ; F.Huang ; Y.Cao, Fluoro- and amino-functionalized conjugated polymers as electron transport materials for perovskite solar cells with improved efficiency and stability., ACS Appl. Mater. Interfaces 11, 5289–5297. 10.1021/acsami.8b19036 2019,.

[35] Turner, G. Global Renewable Energy Market Outlook 2013. Bloom. New Energy Financ. 2013, 26, 506. 7. Mahmoud, N.T.; Khalifeh, J.M.; Mousa, A.A. Effects of rare earth element Eu on structural, electronic, magnetic, and optical properties of fluoroperovskite, compounds SrLiF3: First principles calculations. Phys. B Condens. Matter 2019, 564, 37–44. https://doi.org/10.3390/ma15165684.

[36] M. Miri, Y. Ziat, H. Belkhanchi, and YA. El Kadi, The effect of pressure on the structural, optoelectronic and mechanical conduct of the XZnF3(X = Na, K and Rb) perovskite: First-principles study,, "International Journal of Modern Physics B", 2024, 2550096. https://doi.org/10.1142/S0217979225500961.

[37] X. Wang, W. Li, H. Zhao, S. Wang ... & P. Wang. Yb3+-Yb3+ cooperative upconversion in oxyfluoride glass and glass ceramics. Journal of Luminescence, 226, 117461. 2020., https://doi.org/10.1016/j.jlumin.2020.117461.

[38] A.Meziani , D.Heciri , & H. Belkhir. Structural, electronic, elastic and optical properties of fluoro-perovskite $KZnF_3$*. Physica B: Condensed Matter, 406(19), 3646-3652 2011., https://doi.org/10.1016/j.physb.2011.06.063.*

[39] N.Erum , & M. A.Iqbal. Ab initio study of structural, opto-electronic, elastic, and thermal properties of $KZnF_3$*. Canadian Journal of Physics, 99(7), 551-558 2021., https://doi.org/10.1139/cjp-2020-0303.*

[40] A.Ayub , H. M. N.Ullah , M.Rizwan , A. A.Zafar, Z.Usman , & U.Hira. Impact of Zn alloying on structural, mechanical anisotropy, acoustic speeds, electronic, optical, and photocatalytic response of KMgF3 perovskite material., Materials Science in Semiconductor Processing, 173, 108049. 2024. https://doi.org/10.1016/j.mssp.2023.108049.

[41] A. Mubarak, and S. Al-Omari,First-principles calculations of two cubic fluoropervskite compounds: RbFeF3 and RbNiF3., J. Magn. Magn. Mater. 2015, 382, 211–218. https://doi.

org/10.1016/j.jmmm.2015.01.073.

[42] M.Miri , Y.Ziat , H.Belkhanchi , Z.Zarhri , & Y. A.El Kadi. Structural and optoelectronic properties of LiYP (Y= Ca, Mg, and Zn) half-Heusler alloy under pressure: A DFT study. Physica B: Condensed Matter, 667, 415216 2023., https://doi.org/10.1016/j.physb.2023.415216.

[43] M.Miri ,Y. Ziat , H.Belkhanchi , & Y. A. El Kadi. Structural, elastic, and opto-electronic conduct of half Heusler Li (Ca, Mg, Zn) N alloys: Ab initio computation. Solid State Communications, 396, 115765 2025., https://doi.org/10.1016/j.ssc.2024.115765.

[44] Ziat, Y., Belkhanchi, H., & Zarhri, Z. (2025). DFT analysis of structural, electrical, and optical properties of S, Si, and F-Doped GeO2 Rutile: implications for UV-transparent conductors and photodetection. Solar Energy and Sustainable Development, 14(1), 74-89. https://doi.org/10.51646/jsesd.v14i1.232.

[45] Y.Ziat , H.Belkhanchi , Z.Zarhri , & S.Rzaoudi. Electronegativity effect of (Z=S, O, F and Cl) doping on the electrical, electron density and optoelectronic properties of half-Heusler LiMgP: DFT overview. Physica B: Condensed Matter, 646,, 414324. 2022. https://doi.org/10.1016/j.physb.2022.414324.

[46] P. Blaha, K. Schwarz, F. Tran, R. Laskowski, G.K. Madsen, & L. D. Marks. WIEN2k: An APW+ lo program for calculating the properties of solids. The Journal of chemical physics, 152(7). 2020, https://doi.org/10.1063/1.5143061.

[47] J. P.Perdew , K.Burke , & M.Ernzerhof. Generalized gradient approximation made simple. Physical review letters, 77(18), 3865.1996., https://doi.org/10.1103/PhysRevLett.77.3865.

[48] T. Seddik, & al. "Elastic, electronic and thermodynamic properties of fluoro-perovskite $KZnF_3$ *via first-principles calculations." Applied Physics A 106 2012: 645-653., https://doi.org/10.1007/s00339-011-6643-2.*

[49] K.Knox. Perovskite-like fluorides. I. Structures of KMnF3, KFeF3, KNiF3 and $KZnF_3$*. Crystal field effects in the series and in KCrF3 and KCuF3. Acta Crystallographica, 14(6), 583-585. 1961., https://doi.org/10.1107/S0365110X61001868.*

[50] Y Ziat, Z Zarhri, H Belkhanchi, O Ifguis, A D Cano, & C Lazrak . Effect of Be and P doping on the electron density, electrical and optoelectronic conduct of half-Heusler LiMgN within ab initio scheme. Physica Scripta, 97(10): 105802 2022;, 10.1088/1402-4896/ac8b40.

[51] A. Bouzaid, Y. Ziat, H. Belkhanchi, H, Hamdani, A. Koufi, M. Miri, ... & Z. Zarhri. Ab initio study of the structural, electronic, and optical properties of MgTiO3 perovskite materials doped with N and P. E3S Web of Conferences, (Vol. 582, p. 02006). EDP Sciences 2024. https://doi.org/10.1051/e3sconf/202458202006.

[52] Y. Ziat, Z. Zarhri, M. Hammi, H. Belkhanchi, & A. C. Bastos. Effect of (Na, Si, Al, K or Ca) doping on the electronic structure and optoelectronic properties of half-Heusler LiMgN alloy: Ab initio framework., Solid State Communications, 343, 114665, 2022. https://doi.org/10.1016/j.ssc.2022.114665.

[53] R Majumder, M M Hossain, & D Shen . First-principles study of structural, electronic, elastic, thermodynamic and optical properties of LuPdBi half-Heusler compound. Modern Physics Letters B, 33(30):1950378 2019;, https://doi.org/10.1142/S0217984919503780.

[54] A. Bouzaid, Y. Ziat, & H. Belkhanchi. Prediction the effect of (S, Se, Te) doped MgTiO3 on optoelectronic, catalytic, and pH conduct as promised candidate photovoltaic device: Ab initio framework., International Journal of Hydrogen Energy, 100, 20-32. 2025. https://doi.org/10.1016/j.ijhydene.2024.12.284.

[55] C. M. I.Okoye, "Theoretical study of the electronic structure, chemical bonding and optical properties of KNbO3 in the paraelectric cubic phase." Journal of Physics: Condensed Matter 15.35 : 5945 2003, 10.1088/0953-8984/15/35/304 .

[56] S Saha, T P Sinha, & A Mookerjee . Electronic structure, chemical bonding, and optical properties of paraelectric BaTiO 3. Physical Review B, 62(13): 8828 2000;, https://doi.org/10.1103/PhysRevB.62.8828.

[57] Delin, Anna, et al. "Optical properties of the group-IVB refractory metal compounds." Physical Review B 54.3 (1996): 1673, https://doi.org/10.1103/PhysRevB.54.1673.

[58] Y.Ziat, A.Abbassi, A.Slassi , M.Hammi , A. A. Raiss , O. E.Rhazouani , ... & A. E. Kenz. First-principles investigation of the electronic and optical properties of Al-doped FeS 2 pyrite for photovoltaic applications., Optical and Quantum Electronics, 48, 1-8. 2016. https://doi.org/10.1007/s11082-016-0781-x.

[59] M. Rizwan, A. Ayub, M. Shakil, Z. Usman, S. S. A. Gillani, H. B. Jin, & C. B. Cao. Putting DFT to trial: For the exploration to correlate structural, electronic and optical properties of M-doped (M= Group I, II, III, XII, XVI), lead free high piezoelectric c-BiAlO3. Materials Science and Engineering: B, 264, 114959 2021. https://doi.org/10.1016/j.mseb.2020.114959.

[60] Ilyas, Asif, & al. "Investigation of the structural, electronic, magnetic, and optical properties of $CsXO_3$ (X= Ge, Sn, Pb) perovskites: A first-principles calculations." Optik 244 : 167536 2021, https://doi.org/10.1016/j.ijleo.2021.167536.

Solar Energy
And Sustainable Development
Refereed, biannual scientific journal issued by:
The Libyan Center for Solar Energy Research and Studies

First-Principles Study of Ge-Doped $CH_3NH_3PbI_3$ Perovskite: Optical and Electronic Properties

Lhouceine Moulaoui[1*], Abdelhafid Najim[2], Abdelmounaim Laassouli[3], Omar Bajjou[4], Khalid Rahmani[5], Bouzid Manaut[6].

[1,6]LRPSI, Faculty of Polydisciplinary, Sultan Moulay Slimane University, Beni Mellal-Morocco.
[2,3,4]Laboratory of Engineering in Chemistry and Physics of Matter (LIPCM), Faculty of Sciences and Technics, Sultan Moulay Slimane University, Beni Mellal, Morocco.
[4]UNESCO UNISA Africa Chair in Nanosciences & Nanotechnology (U2ACN2), College of Graduate Studies, University of South Africa (UNISA), Pretoria, South Africa.
[5]PSES, ERC, Ecole Normale Supérieure, Mohammed V University in Rabat, Takkadoum Rabat-10000, Morocco.

E-*mail:* [1] moulaoui.h.fpbm@gmail.com .

SPECIAL ISSUE ON:

The 1St International Conference on Sciences and Techniques for Renewable Energy and the Environment.
(STR2E 2025)
May 6-8, 2025 at FST-Al Hoceima- Morocco.

KEYWORDS

$CH_3NH_3PbI_3$, Absorption coefficient, Bandgap energy, Density of states, Refractive index.

ABSTRACT

This study focuses on the examination of the optical and electronic properties of CH_3 NH_3 PbI_3 perovskite structures, with particular emphasis on the effect of germanium (Ge) doping on these properties. The aim of this study is to explore how doping CH_3NH_3 PbI_3 with Ge can affect its optoelectronic properties and thus optimize its efficiency in applications such as photovoltaic solar cells. We used the code CASTEP from the Materials Studio software to calculate the optical and electronic attributes of perovskite structures $CH_3NH_3PbI_3$, doping the lead (Pb) metal with three different percentages of germanium: 12.5%, 25%, and 37.5%. Pure $CH_3NH_3PbI_3$ perovskite has a bandgap energy (Eg) of 1.733 eV. The bandgap energies of the doped materials are 1.57 eV, 1.545 eV, and 1.503 eV, respectively. The pure $CH_3NH_3PbI_3$ structure has a maximum absorption coefficient of $8{,}11x10^{-4}$ cm^{-1} in the wavelength range of 400 nm to 800 nm. This calculation also studied the effects of Ge doping on the bandgap energy, absorption, total density of states, the real and imaginary components of the dielectric function, as well as the refractive index, the optical conductivity, and the loss function. The computed results align with the experimental findings and provide information on the possibility of modulating the optical properties and electronic of $CH_3NH_3PbI_3$ through Ge doping, doping $CH_3NH_3PbI_3$ with Ge enhances its optoelectronic properties, particularly its

*Corresponding author.

DOI: https://doi.org/10.51646/jsesd.v14iSTR2E.799

This is an open access article under the CC BY-NC license (http://Attribution-NonCommercial 4.0 (CC BY-NC 4.0)).

absorption in the visible range, optimizing its efficiency in photovoltaic solar cells. These improvements make Ge-doped $CH_3NH_3PbI_3$ promising for renewable energy applications, as well as in light-emitting diodes and laser devices.

دراسة من المبادئ الأولى للبيروفسكايت $CH_3\ NH_3\ PbI_3$ المطعَّم بالجرمانيوم: الخصائص البصرية والإلكترونية

الحسين مولاوي، عبد الحافظ نجيم، عبد المنعم العسولي ، عمر باجو، خالد الرحماني، بوزيد مانوط.

ملخص: تركز هذه الدراسة على فحص الخصائص البصرية والإلكترونية لهياكل البيروفسكايت $CH_3\ NH_3\ PbI_3$، مع التركيز بشكل خاص على تأثير تطعيمها بالجرمانيوم (Ge) على هذه الخصائص. تهدف هذه الدراسة إلى استكشاف كيفية تأثير تطعيم $CH_3\ NH_3\ PbI_3$ بالجرمانيوم على خصائصه البصرية والإلكترونية، مما يساعد في تحسين كفاءته في تطبيقات مثل الخلايا الشمسية الكهروضوئية. استخدمنا شفرة CASTEP من برنامج Materials Studio لحساب الخصائص البصرية والإلكترونية لهياكل البيروفسكايت $CH_3\ NH_3\ PbI_3$ ، حيث تم استبدال معدن الرصاص (Pb) بثلاث نسب مختلفة من الجرمانيوم 2.5 1 %، 25 %، و 37.5 % . يتمتع البيروفسكايت النقي $CH_3\ NH_3\ PbI_3$ بطاقة فجوة نطاق (Eg) قدرها 1.733 eV، في حين أن قيم فجوة النطاق للمواد المطعمة هي 1.57 eV، 1.545eV ، 1.503eV، على التوالي. تمتلك البنية النقية لـ $CH_3\ NH_3\ PbI_3$ معامل امتصاص أقصى يبلغ $8{,}11x10^{-4}\ cm^{-1}$ ضمن نطاق الطول الموجي بين 400 nm و 800nm. كما تناولت هذه الدراسة تأثيرات تطعيم الجرمانيوم على طاقة فجوة النطاق، الامتصاص، الكثافة الكلية لحالات الطاقة، المكونات الحقيقية والتخيلية للدالة العازلة، معامل الانكسار، التوصيلية البصرية، ودالة الفقد البصري. تتوافق النتائج المحسوبة مع النتائج التجريبية، مما يوفر معلومات حول إمكانية تعديل الخصائص البصرية والإلكترونية لـ $CH_3\ NH_3\ PbI_3$ من خلال تطعيمه بالجرمانيوم. يساهم تطعيم $CH_3\ NH_3\ PbI_3$ بالجرمانيوم في تحسين خصائصه البصرية والإلكترونية، خاصةً قدرته على الامتصاص في نطاق الضوء المرئي، مما يعزز كفاءته في الخلايا الشمسية الكهروضوئية. تجعل هذه التحسينات بيروفسكايت $CH_3\ NH_3\ PbI_3$ المطعم بالجرمانيوم مادة واعدة لتطبيقات الطاقة المتجددة، بالإضافة إلى استخدامه في الثنائيات الباعثة للضوء (LEDs) وأجهزة الليزر.

الكلمات المفتاحية: $CH_3NH_3PbI_3$؛ معامل الامتصاص، طاقة فجوة النطاق، كثافة حالات الطاقة، معامل الانكسار.

1. INTRODUCTION

Energy consumption is rising sharply due to the rapid growth of the global population and the expansion of industrial units [1]. This situation not only exacerbates the energy shortage but also worsens environmental pollution. Therefore, it has become imperative and it is crucial to discover new sources of sustainable and clean energy. In this context, solar energy possesses now emerged as one of the leading options [2-5].

Photovoltaic energy is a form of renewable energy that generates no pollution, utilizing solar cells to capture and convert light rays into electricity. Currently, innovative research is focusing on metal halide perovskites with a general formula of ABX_3 [6]. In this formula, A^+ refers to the organic ion $CH_3\ NH_3^+$ (MA^+), B^{2+}, corresponds to Pb^{2+}, where X^-denotes a halide ion such as I^-, Cl^-, or Br^-. These types of perovskites are known for their outstanding optical and electronic properties, which hold significant promise for solar technology applications. In the year 2009, Kojima and his team successfully used 3D perovskite $MAPbI_3$ in combination with a liquid electrolyte in solar cells, achieving a 3.8% efficiency More recently, in 2012, Other rese arch substituted the liquid electrolyte with a solid one, achieving an efficiency of 9% [7]. Our research is centered on a detailed analysis of characteristics of organometallic methylammonium lead triiodide perovskite $CH_3\ NH_3\ PbI_3$.

The use of perovskites in photovoltaic technology has seen significant advancements over the past decade, with recently certified power conversion efficiencies surpassing 25.2% [8]. However, all perovskites that have achieved such high efficiencies to date contain lead. As a result, there has been growing interest in lead-free perovskites made from alternative metals, such as germanium (Ge). Although germanium-based perovskites are still relatively underexplored, it is expected that interest in these materials will increase in the coming years, driven by their potential for a wide range of applications. Ge is an abundant metal, and when compared to lead, it offers lower toxicity and fewer environmental concerns [9]. However, additional research is still required to fully explore the broad potential applications of germanium-based perovskite cells.

Doping perovskite materials with Ge significantly boosts their performance in photovoltaic applications. It enables precise control over the band gap, enhancing light absorption and overall efficiency. Germanium-based perovskites also demonstrate greater stability, particularly against environmental challenges such as moisture and UV radiation, while offering lower toxicity compared to conventional lead-based perovskites, making them a more sustainable option. Furthermore, Ge doping helps reduce charge carrier recombination, improving charge transport and increasing power conversion efficiency. These advantages make germanium-doped perovskites a promising alternative for high-performance, environmentally friendly solar cells. In recent years, $MAPbI_3$ perovskite has become extensively utilized as an effective photovoltaic absorption layer, thanks to its considerable gains [10]. These include a high absorption, an optimal bandgap energy, notable photoelectric conversion efficiency [11]. Three distinct crystal structures are observed in $MAPbI_3$: $MAPbI_3$ has an orthorhombic phase with P221 space group at temperatures below 162.2 K, a tetragonal phase with the space group I4/mcm between 162 K and 327.4 K, and a cubic phase with the Pm3m space group at temperatures exceeding 327.4 K[12].

This study focused on analyzing the optoelectronic characteristics of pure $MAPbI_3$ and examined the impact of doping with Ge on these properties. Specifically, we introduced Ge atoms into the Pb sites at doping levels of 12.5%, 25%, and 37.5%.

2. COMPUTATIONAL PROCEDURES

Optical and elctronic characteristics attributes of $MAPbI_3$ were analyzed using Density Functional Theory (DFT). These properties were computed employing the Cambridge Sequential Total Energy Program (CASTEP) [13,14]. In the $MAPbI_3$ structure, to ensure precise calculations, ultrasoft pseudopotentials were utilized for representing the electrons of valence, using functional of Perdew-Burke-Ernzerhof (PBE) and the generalized gradient approximation (GGA) [15]. Electron-ion interactions were characterized through the OTFG ultrasoft pseudopotential [16,17]. Optimizing the geometry of the materials was essential for attaining stable configurations of the relaxed structures, necessitating stringent convergence criteria for both atomic positions and lattice parameters. A energy cut-off of 500 eV was used for calculations. The Brillouin zone was sampled using K points arranged in a 5×5×1. For the self-consistent field operations, the Pulay density mixing method was used, adopting a convergence criterion of $2x10^{-6}$ eV/atom [12]. The maximum allowable stress was 0.1 GPa. The valence shell configurations of the atoms considered are: H: 1s1, C: $2s^22p^2$, N: $2s^22p^3$, Ge: $4s^24p^2$, Pb: $6s^2$, and I: $5s^25p^5$. A 2×1×1 supercell of $MAPbI_3$ tetragonal was the focus of this study, with lattice dimensions of a = b = 8.851 Å, c = 12.642 Å and $\alpha = \beta = \gamma = 90°$ The lattice dimensions adopted in this study, namely a = b = 8.851 Å and c = 12.642 Å, were extracted from experimental studies [12] . These values have been validated and serve as the basis for our calculations and analyses. Figure 1 illustrates the tetragonal structure of $MAPbI_3$ and its germanium-doped variants, the bond lengths of the atoms in the $MAPbI_3$ perovskite are presented in the table 1 below. These values may vary slightly depending on the crystal phase and

experimental conditions.

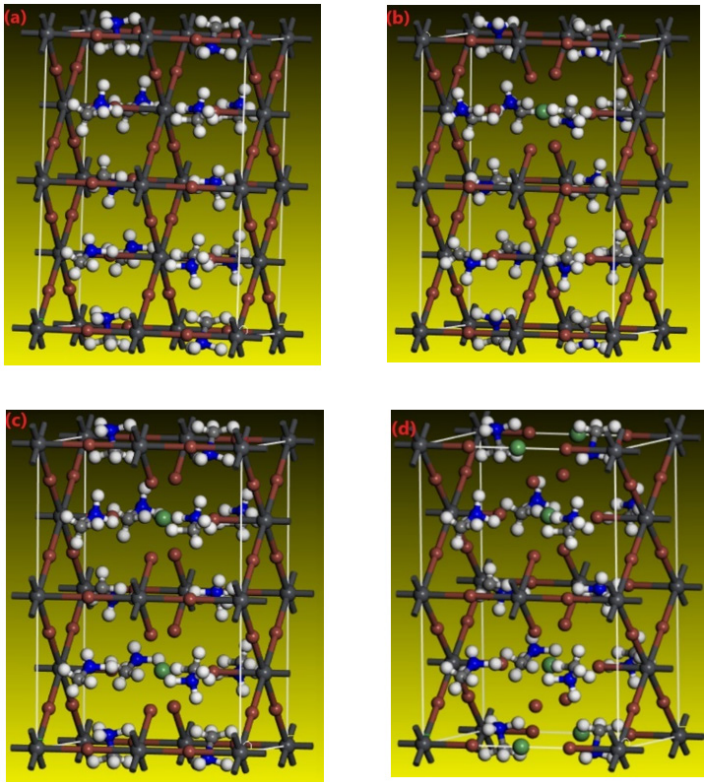

Fig.1.Tetragonal structures of $CH_3NH_3PbI_3$, showing (a) pure $MAPbI_3$, (b) $MAPb_{0.85}Ge_{0.125}PbI_3$, (c) $MAPb_{0.75}Ge_{0.25}PbI_3$, and (d) $MAPb_{0.625}Ge_{0.375}PbI_3$, with color codes: black (C), white (H), blue (N), bluish-gray (Pb), dark gray (I) and green (Ge).

Table 1 . Bond lengths of the atoms in the $MAPbI_3$.

Bands	Length (Å)
Pb-I	3.2
N–H	1.03
C–H	1.09
C–N	1.42

3. FINDINGS AND EVALUATION

3.1. Electronic structure

3.1.1. Band gap

A material's photoelectric properties and band structure are essential factors influencing the efficiency of photovoltaic conversion in solar cells. We calculated the bandgap energy for $CH_3NH_3PbI_3$, and its germanium-doped variants $MAPb_{1-x}Ge_xPbI_3$ with x values of 0.125, 0.25, and 0.375 along the high-symmetry directions as illustrated in Figure 2. The results show that $MAPbI_3$ functions as a semiconductor characterized by a direct bandgap, with an enegy of 1.733 eV. For the doped structures, the bandgap energies are 1.57 eV for x = 0.125, 1.545 eV for x = 0.25 and 1.503 eV for x = 0.375. These findings confirm that all these structures are made up of semiconductor materials. The conduction band's lowest energy point and the highest energy point of the valence band both take place at the G point in the Brillouin zone. These findings

suggest that varying the germanium doping concentration affects the bandgap of the $MAPbI_3$ perovskite. In summary, the decrease in the bandgap energy observed when doping germanium into $MAPbI_3$ results from perturbations in the crystal lattice structure and associated energy levels. These disturbances alter the electronic properties of the material, leading to a reduction in the bandgap width.

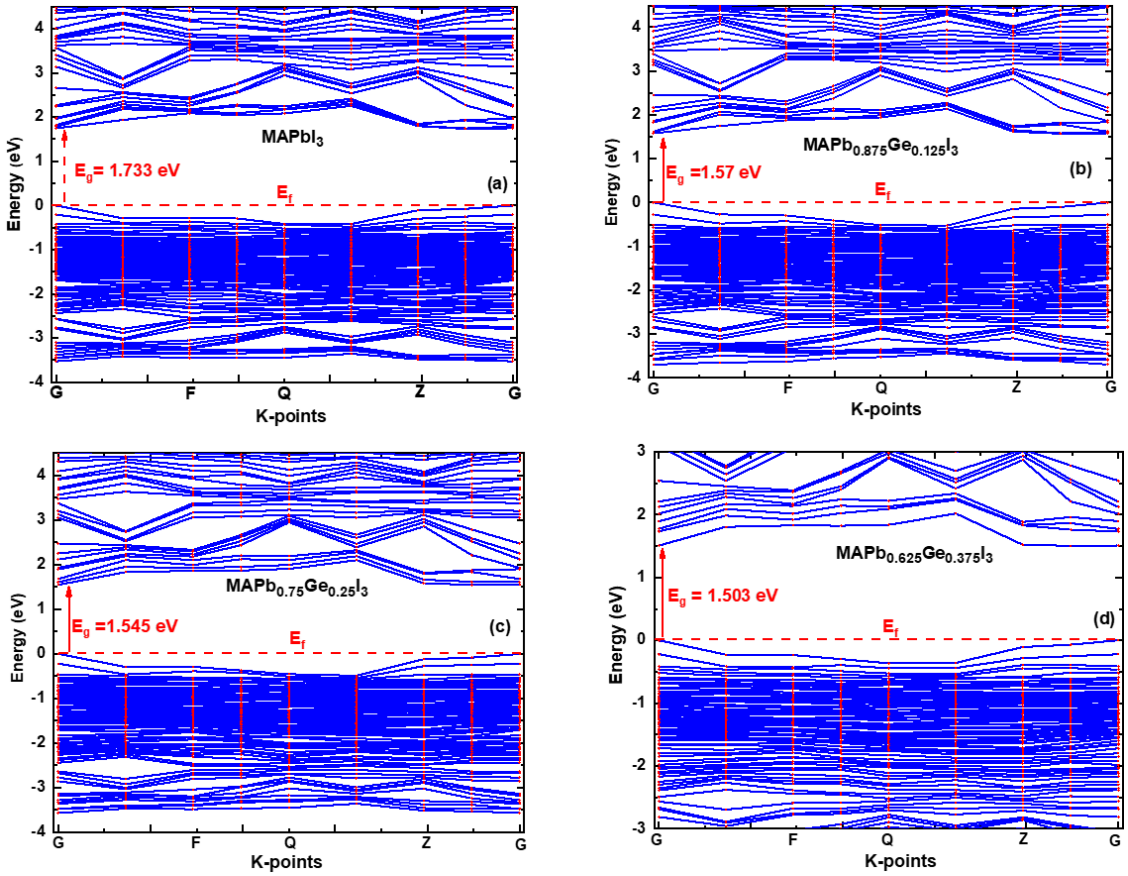

Fig. 2. Energy band of pure and doped $MAPbI_3$, (a) pure structure, (b) $MAPb_{0.85}Ge_{0.125}PbI_3$, structure, (c) $MAPb0.75\ Ge_{0.25}\ PbI_3$ structure (d) $MAPb_{0.625}\ Ge_{0.375}\ PbI_3$.

Doping the $MAPbI_3$ perovskite with Ge decreases the bandgap [18]. These results are consistent with other previously published findings. The table 1 below presents the bandgap obtained in our calculation along with those from other calculations using different approximations.

Table 2 : Comparison of the Bandgap (Eg) of $MAPbI_3$ using different approximations.

Apprimations	**Bandgap (Eg)**
GGA-PBE	1.733 eV [This work]
GGA-PBE	1.761 [18]
HSE06	1.97 eV [19]
Experimental	1,55 eV [20]

3.1.2. Density of states

The total density of states (TDOS) plays a crucial role in defining these characteristics, which shows how Kohn-Sham eigenvalues are distributed across various occupied and unoccupied orbitals. The bandgap energy is indicated by the contrast between states in the upper valence band (VB) and those in the lower conduction band (CB). Figure 3 displays the TDOS for both

undoped $MAPbI_3$ and $MAPb_{1-x}Ge_x PbI_3$. These calculations utilized the GGA-PBE method [21]. The TDOS profiles highlight the positions of distinct peaks and illustrate the contributions of specific electronic states linked to H, C, N, Pb, I, and Ge atoms. The interaction of these states forms the perovskite. The spectra of TDOS obtained show distinct regions for the VB and a separate region for the CB. In summary, doping lead with germanium in the $MAPbI_3$ perovskite modifies the TDOS by introducing new energy levels, reconfiguring electronic states, and adjusting the intensity of peaks [22]. These changes influence the distribution of electronic states in the material and can affect its optical and electronic properties.

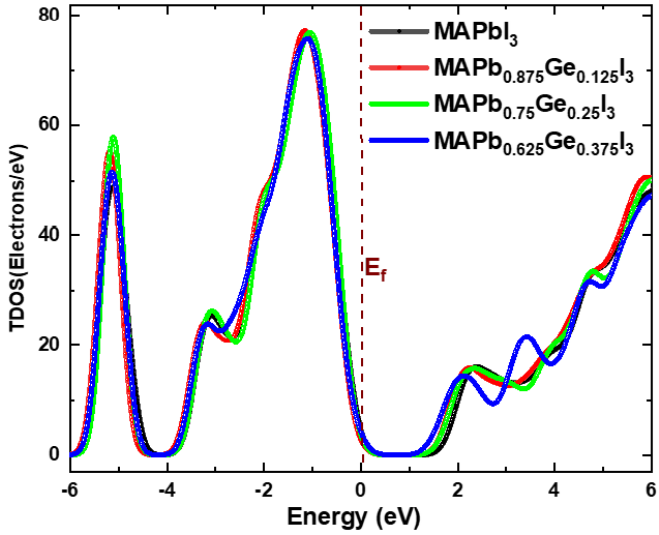

Fig. 3. TDOS for $MAPbI_3$ and $MAPb_{1-x}Ge_x PbI_3$ structures at doping ratios of x = 0.125 ; 0.25 and 0.375.

3.2. Optical characteristics

3.2.1. Absorption

The absorption is a critical parameter for assessing the performance of SC and other materials utilized in technologies associated with energy. This property indicates how effectively a material can absorb light at specific wavelengths, which directly impacts its efficiency in converting solar energy into usable power. Figure 4 displays the spectral absorption coefficients for both $MAPbI_3$ and $MAPb_{1-x}Ge_x PbI_3$. The data reveal an absorption peak within the 300 nm to 400 nm wavelength range. For the pure $MAPbI_3$ structure, this peak is situated around 350 nm, illustrating its wavelength-specific absorption characteristics, spanning both the UV and visible spectra. In the span of 300-400 nm, doping Pb with Ge in the perovskite leads to a lower level of absorption, while in the interval of 400 nm to 800 nm, doping increase the absorption coefficient, as shown in Fig.4. This variation can be attributed to several mechanisms. In the UV range 300-400 nm, germanium doping alters the perovskite's bandgap, introducing intermediate electronic states that may interfere with photon absorption in this energy range. These intermediate states can reduce the material's effectiveness in absorbing UV light. Conversely, in the visible range 400-800 nm, doping improves absorption by narrowing the bandgap, which better aligns the material's energy levels with photons in this range. Consequently, germaniun-doped perovskite exhibits enhanced absorption in the visible spectrum, which proves advantageous for photovoltaic and photonic technologies where visible light absorption is critical. Doping the $MAPbI_3$ perovskite with Ge enhances absorption in the visible range, these results are consistent with previously published studies [18].These doping-induced properties optimize the performance of solar cells by making more efficient use of incident light.

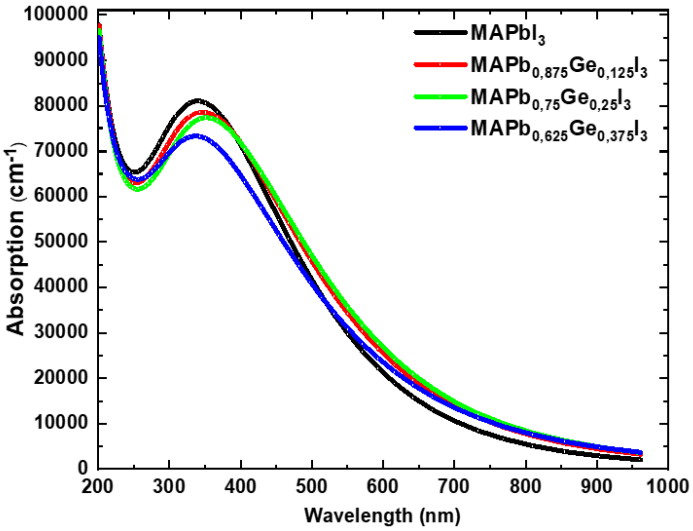

Fig. 4. Absorption of $MAPbI_3$ and $MAPb_{1-x}Ge_x$ PbI_3 materials (x = 0.125, 0.25, 0.375).

Dielectric function

The complex dielectric function provides insight into how light interacts as it propagates through a material. It distinguishes dispersion effects through its real part, $\varepsilon_1(\omega)$, and absorption effects through its imaginary part, $\varepsilon_2(\omega)$. The general expression for this relationship is given by [22].

$$\varepsilon(\omega) = \varepsilon_1(\omega) + i\varepsilon_2(\omega) \qquad (1)$$

In our investigation, we focus on measuring the dielectric function of $MAPbI_3$ and $MAPb_{1-x}Ge_x$ PbI_3 within the range of 200 to 1000 nm, as shown in Figure 5.

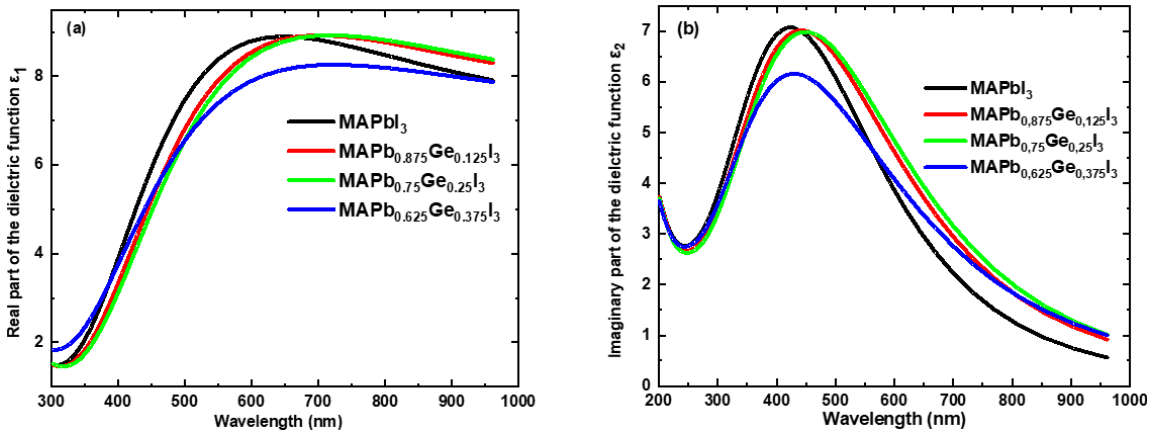

Fig. 5. Real component (a) and imaginary Component of dielectric function of $MAPbI_3$ and $MAPb_{1-x}$ Ge_x PbI_3 stucture (x = 0.125, 0.25, 0.375).

The real part $\varepsilon_1(\omega)$ exhibits two peaks for the pure MAPbI3 structure: the first at 209 nm and the second at 642 nm. In contrast, for the doped $MAPb_{1-x}Ge_x$ PbI_3 structures (with x = 0.125, 0.25, 0.375), each structure also shows two distinct peaks. The first peak is observed at 642 nm for all doped structures, while the second peaks appear at 670 nm, 700 nm, and 700 nm for the different germanium concentrations. The variation of $\varepsilon_1(\omega)$ with respect to λ indicates that $MAPbI_3$ and $MAPb_{1-x}Ge_x$ PbI_3 are dispersive media. After doping lead (Pb) with germanium (Ge) in the $MAPbI_3$ perovskite, I found that the imaginary part $\varepsilon_2(\omega)$ shows a single peak for both the pure $MAPbI_3$ structure and the doped $MAPb_{1-x}Ge_x$ PbI_3 structures (with x = 0.125, 0.25, 0.375). This

finding indicates that germanium doping enhances absorption in the visible range. The rise in $\varepsilon_2(\omega)$ suggests that germanium introduces new intermediate energy levels within the bandgap, which facilitates electronic transitions and improves the perovskite's ability to absorb visible light [23]. Consequently, doping with germanium optimizes absorption of light, offering benefits for optoelectronic applications like solar cells and photonic devices.

3.2.2. Refractive index

The complex refractive index, $n^*(\omega)$ is a parameter used to describe how light propagates through a material [24]. This index is typically expressed in a complex form to account for the material's dissipative properties. It can be represented as follows :

$$n^*(\omega) = n(\omega) + ik(\omega) \quad (2)$$

$$n(\omega) = \sqrt{\frac{\varepsilon_1(\omega)}{2} + \sqrt{\frac{(\varepsilon_1(\omega))^2 + (\varepsilon_2(\omega))^2}{2}}} \quad (3)$$

$$k(\omega) = \sqrt{\frac{\left(\varepsilon_1^2 + \varepsilon_2^2\right)^{\frac{1}{2}} - \varepsilon_1}{2}} \quad (4)$$

As the doping of Pb by Ge in $MAPbI_3$ perovskite increases, both the real $n(\omega)$ and imaginary $k(\omega)$ parts of $n^*(\omega)$ in the visible range rise due to alterations in the material's electronic structure, as illustrated in Figure 6. The introduction of Ge creates new energy levels and alters electronic interactions, leading to a higher density of states for electronic transitions. This results in increased polarization of the material, which raises the $n(\omega)$, while also enhancing absorption in the visible spectrum, thereby increasing the $k(\omega)$.

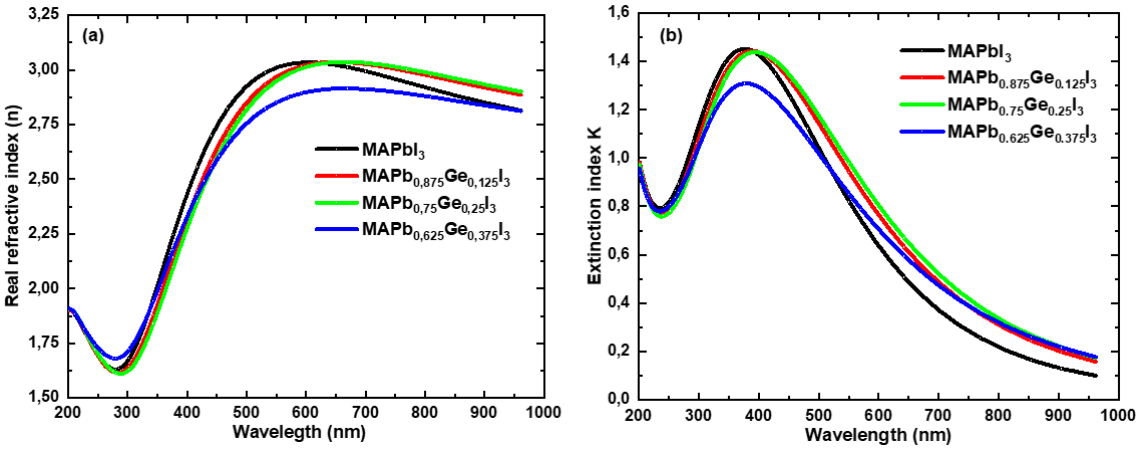

Fig. 6. Refractive index (a) and extinction index (b) of $MAPbI_3$ and its MAPb1-xGexI3 Structures.

3.2.3. Optical conductivity

Optical conductivity, denoted as σ, which is directly related to the $\varepsilon(\omega)$, characterizes the linear response of a material's charge carriers to an externally applied electromagnetic (EM) field. This optical conductivity is typically represented in the following form [25,26].

$$\sigma(\omega) = \sigma_1(\omega) + i\sigma_2(\omega) \quad (5)$$

$$\sigma_1(\omega) = 2nk\left(\frac{\omega}{4\pi}\right) \quad (6)$$

$$\sigma_2(\omega) = \left[1 - \left(n^2 - k^2\right)\right]\left(\frac{\omega}{4\pi}\right) \qquad (7)$$

Figure 7 shows the variation in optical conductivity for the materials $MAPbI_3$ and $MAPb_{1-x}Ge_xI_3$ within the range of 200 to 1000 nm. The MAPbI3 and $MAPb_{0.635}Ge_{0.375}I_3$ structures exhibit peaks with different intensities at 386 nm. In contrast, the $MAPb_{0.875}Ge_{0.125}I_3$ and $MAPb_{0.75}Ge_{0.25}I_3$ structures also display peaks with varying intensities at a wavelength of 406 nm. The peak value of real part of optical conductivity for the $MAPbI_3$ perovskite is 2.61 (1/fs). The σ_1 component of $MAPbI_3$ and doped structures reduces in the UV range and increases with the percentage of doping in the visible region, due to changes in light absorption by the material. The imaginary part, $\sigma_2(\omega)$, for $MAPbI_3$ and $MAPb_{1-x}Ge_xI_3$ exhibits negative values, with the minimum value reaching -2 (1/fs) at a wavelength of 500 nm.

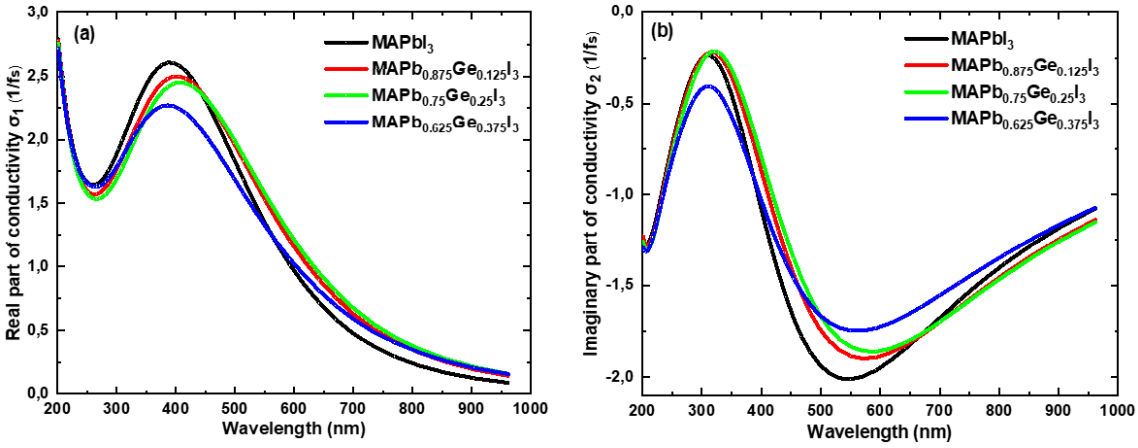

Fig.7. Real part (a) and the imaginary part (b) of the complex Optical conductivity, (b) imaginary part for the perovskite $MAPbI_3$ and its $MAPb_{1-x}Ge_xI_3$ as a function of wavelength.

3.2.4. Loss function

The optical loss function L(ω), determines the energy dissipated by incident photons as they propagate through a material. It can be expressed as [27-29].

$$L(\omega) = -Im\left(\frac{1}{\varepsilon(\omega)}\right) = \frac{\varepsilon_2(\omega)}{\varepsilon_1^2(\omega) + \varepsilon_2^2(\omega)} \qquad (8)$$

The variation of the function L(ω) for $MAPbI_3$ and $MAPb_{1-x}Ge_xI_3$ materials as a function of the incident wavelength as represented in Figure 8.

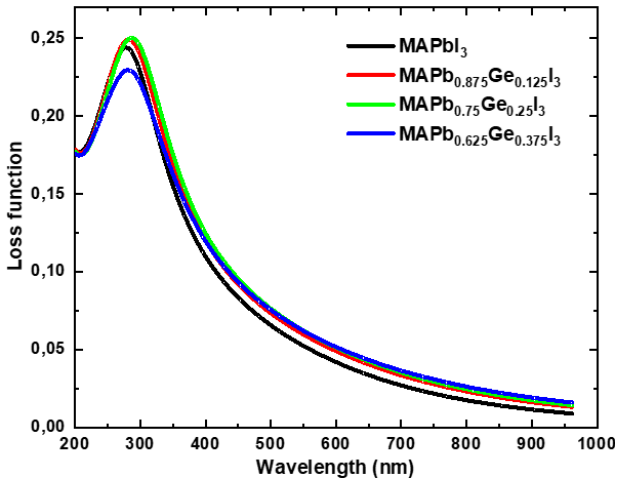

Fig. 8. Loss Function of $MAPb_{1-x}Ge_xI_3$ Structures (x = 0, 0.125, 0.25, 0.375) versus Wavelength.

The increase in Pb doping by Ge in $MAPbI_3$ perovskite results in a rise in the loss function L(ω) in the visible region of the spectrum. This effect is primarily due to the addition of novel energy states within the material's structure, which enhances the density of available electronic states for transitions. Additionally, changes in polarization and electronic interactions promote greater absorption of visible light. As a result, these combined factors lead to a significant increase in energy losses within the material.

4. CONCLUSION

We examined and analyzed in this research the electronic and optical features of $MAPbI_3$, as well as those of the $MAPb_{1-x}Ge_xI_3$ structure, where x denotes the germanium doping concentration. The investigation was conducted using first-principles calculations based on the DFT method. We employed the GGA+PBE approximation, as implemented in the CASTEP software. Doping $MAPbI_3$ with Ge at concentrations of 12.5%, 25%, and 37.5% led to a gradual reduction in bandgap energy and an an enhancement in the absorption coefficient within the visible spectrum. Additionally, Ge doping affected the overall TDOS, the components of $n^*(\omega)$, the $\varepsilon(\omega)$, $\sigma(\omega)$ and the L(ω). Doping $MAPbI_3$ with Ge enhances its optical and electronic properties by reducing the bandgap energy and improving absorption in the visible range, making it ideal for photovoltaic applications. These improvements open opportunities for its use in optoelectronic devices such as LEDs, as well as in laser systems and energy storage technologies.

Author Contributions: M. Lhouceine : Initial draft writing, software development, and investigation. A. Najim : Writing – original draft, Software, Investigation. A. Laassouli: Writing and Investigation. O. Bajjou: Supervision, Review and editing, Validation.K. Rahmani : Supervision, Review and editing. B. Manaut : Supervision, Review and validation.

Funding: No external funding was provided for this article.

Data availability Statement: Data will be made available upon inquiry.

Conflicts of Interest: The authors declare that they are not affiliated with any organization that has a direct or indirect financial interest in the subject matter discussed in this article.

Acknowledgments: The authors of this work would like to express their sincere gratitude to Sultan Moulay Slimane University and UNISA University.

REFERENCES

[1] S. Bilgen, "Structure and environmental impact of global energy consumption," Renewable and Sustainable Energy Reviews, vol. 38, pp. 890–902, Oct. 2014, doi: 10.1016/j.rser.2014.07.004.

[2] A. Shukla, V.K. Sharma, S.K. Gupta, A.S. Verma, "Computational determination of the physical-thermoelectric parameters of tin-based organomatallic halide perovskites (CH3NH3SnX3, X = Br and I): Emerging materials for optoelectronic devices". Materials Chemistry and Physics. 253, 123389 (2020). https://doi.org/10.1016/j.matchemphys.2020.123389

[3] A. Nicolas, J.-L. Barrat, J. Rottler, "Effects of inertia on the steady-shear rheology of disordered solids,". Phys. Rev. Lett. 116, 058303 (2016).

[4] L. Moulaoui, O. Bajjou, Y. Lachtioui, A. Najim, M. Archi, K. Rahmani, B. Manaut, "Modeling of Highly Efficient Lead Free MASnI3 Based Solar Cell with Graphene Oxide as Hole Transport Layer Using SCAPS 1D," . J. Electron. Mater. 52, 7541–7553 (2023). https://doi.org/10.1007/s11664-023-10684-4

[5] L. Moulaoui, A. Najim, A. Laassouli, M. Archi, A. Bakour, Y. Lachtioui, K. Rahmani, O. Bajjou, B. Manaut, "Theoretical investigations on the electronic and optical properties of Na-doped

CH3NH3PbI3 perovskite ''. E3S Web of Conferences.469, 00086 (2023). https://doi.org/10.1051/e3sconf/202346900086

[6] Bahadur, A. H. Ghahremani, S. Gupta, T. Druffel, M. K. Sunkara, K. Pal, ''Enhanced moisture stability of MAPbI3 perovskite solar cells through Barium doping". Solar Energy, 190, 396-404 (2019). https://doi.org/10.1016/j.solener.2019.08.033

[7] L. Qiu, S. He, J. Yang, F. Jin, J. Deng, H. Sun, X. Cheng, G. Guan, X. Sun, H. Zhaob, H. Peng, ''An all-solid-state fiber-type solar cell achieving 9.49% efficiency". J. Mater. Chem. A . 4, 10105 (2016). DOI: 10.1039/c6ta03263j

[8] J. Lu, S. Chen, H. Wang, L. Qiu, C. Wu, W. Qian, Z. Wang, K. Huang, J. Wu, H. Chen, and Y. Gao, "Replacing the electron-hole transport layer with doping: SCAPS simulation of lead-free germanium-based perovskite solar cells based on CsGeI3," Solar Energy Mater. Sol. Cells, vol. 271, p. 112883, Apr. 2024, doi: 10.1016/j.solmat.2024.112883.

[9] R. Chiara, M. Morana, and L. Malavasi, "Germanium-based halide perovskites: Materials, properties, and applications," ChemPlusChem, vol. 86, no. 8, pp. 879–888, 2021, doi: 10.1002/cplu.202100191.

[10] I. Diomandé, A. Bouich, A. A. Hyacinthe, B. M. Soucasse, and A. Boko, "Comparative Performance Analysis of MAPbI3 and FAPbI3 Perovskites: Study of Optoelectronic Properties and Stability," Modeling and Numerical Simulation of Material Science, vol. 13, no. 4, p. 134004, Oct. 2023, doi: 10.4236/mnsms.2023.134004.

[11] L. Moulaoui, O. Bajjou, A. Najim, K. Rahmani, A. Marouane, A. Laassouli, Y Lachtioui, B Manaut, ''Numerical Simulation of FAPbI3 perovskite based solar cells with graphene oxide as hole transport layer using SCAPS-1D", 2023 3rd International Conference on Innovative Research in Applied Science, Engineering and Technology (IRASET). https://doi.org/10.1109/IRASET57153.2023

[12] P. S.Whitfield, N. Herron, W. E.Guise, K. Page1, Y.Q. Cheng1, I. Milas and M. K. Crawford, ''Structures, Phase Transitions and Tricritical Behavior of the Hybrid Perovskite Methyl Ammonium Lead Iodide". Scientific Repots 6:35685 (2016). DOI: 10.1038/srep35685.

[13] K. Hossain, S. Khanom, F. Israt, M.K. Hossain, M.A. Hossain, F. Ahmed, First-principles study on structural, mechanical and optoelectronic properties of lead-free mixed Ge–Sn hybrid organic-inorganic perovskites. Solid State Communications. 320, 114024 (2020). https://doi.org/10.1016/j.ssc.2020.114024

[14] Y.Q. Huang, J. Su, Q.F. Li, D. Wang, L.H. Xu, Y. Bai, Structure, optical and electrical properties of $CH_3NH_3SnI_3$ single crystal. Physica B: Condensed Matter 563, 107–112 (2019). https://doi.org/10.1016/j.physb.2019.03.035.

[15] S.S. Bagade, M.M. Malik, P.K. Patel, The charm of entwining two major competitors CZTS and $CH_3NH_3SnI_3$ to feasibly explore photovoltaic world beyond Shockley–Queisser limit. Surfaces and Interfaces 46, 104020 (2024). https://doi.org/10.1016/j.surfin.2024.104020.

[16] K. Yan, B. Sun, T. Lu, X.D. Feng, Simulation of $MASnI_3$-based inverted perovskite solar cells with double hole transport layers and an electron transport layer. Optik 287, 171100 (2023). https://doi.org/10.1016/j.ijleo.2023.171100.

[17] J.H. Yoo, S.B. Kwon, J. Park, S.H. Choi, H.C. Yoo, B.K. Kang, Y.H. Song, S. Hong, D.H. Yoon, Potential usage of cesium manganese halide for multi-functional optoelectronic devices: Display & photodetector application. Chemical Engineering Journal 479, 147277 (2024). https://doi.org/10.1016/j.cej.2023.147277.

[18] J. Chang, G. Wang, Y. Huang, X. Luo, H. Chen, New insights into the electronic structures

and optical properties in the orthorhombic perovskite $MAPbI_3$: a mixture of Pb and Ge/Sn, New J. Chem. 41, 11413–11421 (2017). https://doi.org/10.1039/c7nj01442b.

[19] D. Liu, Q. Li, J. Hu, R. Sa, K. Wu, Photovoltaic Performance of Lead-Less Hybrid Perovskites from Theoretical Study. J. Phys. Chem. C 123, 12638–12646 (2019). https://doi.org/10.1021/acs.jpcc.9b02705.

[20] Y. Ogomi, A. Morita, S. Tsukamoto, T. Saitho, N. Fujikawa, Q. Shen, T. Toyoda, K. Yoshino, S.S. Pandey, T. Ma, S. Hayase, $CH_3NH_3Sn_xPb(1-_x)I_3$ Perovskite Solar Cells Covering up to 1060 nm. J. Phys. Chem. Lett. 5, 1004–1011 (2014). https://doi.org/10.1021/jz5002117.

[21] G. Niu, W. Li, J. Li, X. Liang, L. Wang, Enhancement of thermal stability for perovskite solar cells through cesium doping. RSC Advances 7, 17473–17479 (2017). https://doi.org/10.1039/C6RA28501E.

[22] H. Choi, J. Jeong, H.B. Kim, S. Kim, B. Walker, G.H. Kim, J.Y. Kim, Cesium-doped methylammonium lead iodide perovskite light absorber for hybrid solar cells. Nano Energy 7, 80–85 (2014). http://dx.doi.org/10.1016/j.nanoen.2014.04.017.

[23] S. Nations, T. Jia, S. Wang, Y. Duan, Electronic and optical properties of orthorhombic $(CH_3NH_3)BX_3$ (B = Sn, Pb; X = F, Cl, Br, I) perovskites: a first-principles investigation. RSC Adv. 11, 22264–22272 (2021). https://doi.org/10.1039/d1ra01586a.

[24] H. Arif, M.B. Tahir, M. Sagir, H. Alrobei, M. Alzaid, S. Ullah, M. Hussien, Effect of potassium on the structural, electronic, and optical properties of $CsSrF_3$ fluoro-perovskite: First-principles computation with GGA-PBE. Optik 259, 168741 (2022). https://doi.org/10.1016/j.ijleo.2022.168741.

[25] A. Taya, P. Rani, J. Thakur, M.K. Kashyap, First principles study of structural, electronic and optical properties of Cs-doped $CH_3NH_3PbI_3$ for photovoltaic applications. Vacuum 160, 440–444 (2019). https://doi.org/10.1016/j.vacuum.2018.12.008.

[26] L. Moulaoui, A. Najim, A. Laassouli, M. Archi, A. Bakour, Y. Lachtioui, K. Rahmani, O. Bajjou, B. Manaut, Theoretical investigations on the electronic and optical properties of Na-doped $CH_3NH_3PbI_3$ perovskite. E3S Web of Conferences 469, 00086 (2023). https://doi.org/10.1051/e3sconf/202346900086.

[27] A. Laassouli, O. Bajjou, Y. Lachtioui, A. Najim, L. Moulaoui, K. Rahmani, DFT investigation on the electronic and optical properties of Br-doped $CH_3NH_3SnI_3$ perovskite. 3rd International Conference on Innovative Research in Applied Science, Engineering and Technology (IRASET), Mohammedia, Morocco, May 18-19, June 21 (2023). https://doi.org/10.1109/IRASET57153.2023.10153066.

[28] A. Najim, O. Bajjou, L. Moulaoui, A. Laassouli, M. Archi, A. Bakour, Y. Lachtioui, K. Rahmani, Effects of lithium intercalation on the electronic and optical properties of graphene: Density Functional Theory (DFT) computing. 3rd International Conference on Innovative Research in Applied Science, Engineering and Technology (IRASET), Mohammedia, Morocco, May 18-19, June 21 (2023). https://doi.org/10.1109/IRASET57153.2023.10153044.

[29] A. Laassouli, L. Moulaoui, A. Najim, H. Errahoui, K. Rahmani, Y. Lachtioui, O. Bajjou, Phosphorus Doping Effects on the Optoelectronic Properties of $K_2AgAsBr_6$ Double Perovskites for Photovoltaic Applications. Solar Energy and Sustainable Development Journal, 14(SI_MSMS2E), 1–11 (2024). DOI:https://doi.org/10.51646/jsesd.v14iSI_MSMS2E.407.

Solar Energy
And Sustainable Development
Refereed, biannual scientific journal issued by:
The Libyan Center for Solar Energy Research and Studies

Industrial Rock Packed-Bed Heat Storage System: Thermal Behavior and Performance Assessment

Aicha Eddemani [1*], Omar Achahour [2], Hayat El Baamrani [3], Ahmed Aharoune [4], Lahcen Bouirden [5], Ahmed Ihlal [6].

[1,3,4,5]Thermodynamic and Energetics Laboratory, Faculty of Science, Ibn Zohr University, Agadir, Morocco.
[2,6]Materials and Renewable Energies Laboratory, Faculty of Science, Ibn Zohr University, Agadir, Morocco.

E-*mail:* [1] eddemani.aicha@gmail.com ,[2]omar.achahour@edu.uiz.ac.ma ,[3] hayatelbaamrani92@gmail.com , [4]aharoune@gmail.com ,[5] elahcen.bouirden@gmail.com ,[6]a.ihlal@uiz.ac.ma .

SPECIAL ISSUE ON:

The 1St International Conference on Sciences and Techniques for Renewable Energy and the Environment.
(STR2E 2025)
May 6-8, 2025 at FST-Al Hoceima-Morocco.

KEYWORDS

Rock-bed, storage material, thermal stratification, industrial packed-bed, computational fluid. dynamics (CFD) analysis.

ABSTRACT

The first industrial-scale packed-bed configuration for a Thermal Energy Storage (TES) using rocks, offering a thermal capacity of 100 MWhth, has been constructed for a Concentrated Solar Power (CSP) facility in Ait Baha, Morocco.

It employs environmentally friendly materials, using natural pebbles as the energy storage material and ambient air as the heat exchange fluid. The storage unit features an innovative design characterized by a truncated-cone form, is embedded in the ground, and operates at high temperatures ranging from 293K to 843K. To assess the thermal performance and behavior of the system, a verified Computational Fluid Dynamics (CFD) method is employed over thirty days of operation under real-world daily conditions. The results of the cyclic behavior show that the impact of thermal cycles is most pronounced in the initial cycles, while thermal stratification during both the energy storage and release phases is significantly enhanced through repeated operation. Furthermore, the system's performance improves over the thermal cycles, achieving an efficiency of 80% by the 30th cycle.

*Corresponding author.

DOI: https://doi.org/10.51646/jsesd.v14iSTR2E.800

This is an open access article under the CC BY-NC license (http://Attribution-NonCommercial 4.0 (CC BY-NC 4.0)).

نظام صناعي لتخزين الحرارة في الصخور بتقنية السرير المعبأ: سلوك حراري وتقييم الأداء

عائشة الدماني، عمر أشحور، حياة البعمراني، أحمد أهروان، لحسن بويردن، أحمد إهلال.

ملخص: تم إنشاء أول نظام على النطاق الصناعي لتخزين الطاقة الحرارية (TES) باستخدام الصخور، والذي يوفر سعة حرارية قدرها 100 ميغاواط ساعة حرارية، في مرفق الطاقة الشمسية المركزة (CSP) في أيت باها، المغرب. يعتمد النظام على مواد صديقة للبيئة، مثل الحصى الطبيعي كمادة للتخزين والهواء المحيط كسائل لتبادل الحرارة. يتميز التصميم بشكل مخروطي مقلوب، وهو مدفون في الأرض، ويعمل في درجات حرارة تتراوح من 293 كلفن إلى 843 كلفن. لتقييم الأداء الحراري وسلوك النظام، تم تطبيق طريقة ديناميكيات الموائع الحسابية (CFD) على مدار ثلاثين يومًا من التشغيل في ظل ظروف يومية واقعية. تظهر نتائج السلوك الدوري أن تأثير الدورات الحرارية يكون أكثر وضوحًا في الدورات الأولية، بينما يتم تعزيز التراصف الحراري بشكل كبير خلال مراحل تخزين وإطلاق الطاقة من خلال التشغيل المتكرر. علاوة على ذلك، يتحسن أداء النظام مع الدورات الحرارية، حيث يتم تحقيق كفاءة تبلغ 80 % بحلول الدورة الثلاثين.

الكلمات المفتاحية –السرير الحجري، مادة التخزين، التمايز الحراري، السرير المعبأ الصناعي، تحليل الديناميات الحركية الحسابية (CFD) .

1. INTRODUCTION

The need for energy is constantly growing due to accelerated industrialization, demographic expansion, and technological innovations [1]. Solar energy, being a clean, abundant, and renewable resource, offers considerable promise in addressing these growing energy challenges [2]. To decrease reliance on fossil fuels and significantly cutting greenhouse gas emissions, solar energy presents a viable option for meeting the world's expanding energy needs while mitigating negative environmental impacts [2]. Nevertheless, the fluctuating nature of solar energy, particularly during periods of low sunlight, presents a challenge in ensuring uninterrupted energy provision [3]. To address this limitation, the implementation of TES technologies in solar power facilities is critical for providing a consistent and reliable energy output [3, 4].

A packed-rock serves as an efficient and reliable solution for TES, positioning it as a highly appropriate choice for high-temperature TES uses in solar concentrators, particularly when air is employed as the HTF [5, 6]. These systems operate as thermocline TES systems, with rocks acting as the storage medium to capture surplus thermal energy during peak solar availability. This stored energy can be discharged during periods of low solar radiation [7]. Beyond its cost-effectiveness and favorable environmental impact thanks to the use of rocks and air, this system is also highly efficient, as it can function effectively at elevated temperatures, enhancing overall performance and scalability [7].

The thermal storage potential of rock-bed has been a central focus in numerous research studies [6, 8, 9]. Various categories of rocks have been evaluated to assess their suitability as heat storage materials, with an emphasis on their properties such as thermal capacity, conductivity, durability, and cost-effectiveness. Z. Liu et al. [10] assessed fifteen major rock types spanning igneous, sedimentary, and metamorphic classifications. Their investigation focused on examining primary thermophysical characteristics, including thermal diffusivity, heat conductivity, specific heat, and thermal expansion, as well as mechanical properties across a temperature span ranging from room temperature to 1000°C. E. Abddaim et al. [11] conducted a comparative study of four Moroccan magmatic rocks to evaluate their suitability as sustainable materials for TES. The rocks

were tested for their chemical, structural, mechanical, and thermophysical properties, with a particular focus on the impact of temperature variations and thermal cycling. The samples were subjected to five thermal cycles at 300 °C and 600 °C to evaluate changes in their structure and properties compared to the untreated samples. Parametric studies were conducted to examine the main factors influencing the performance of packed-bed heat storage configurations, including mass flow rate, fluid inlet temperature, charge-discharge cycles, and the heat absorption capability of the storage medium [3, 12, 13]. Recent reviews have highlighted the main characteristics and analytical methodologies used to examine the effectiveness of packed-bed TES systems [14-17]. These studies also summarize the major findings and outcomes from research conducted in this field. M. Tawalbeh et al. [18] have provided a detailed review of the three main energy storage methods for packed-bed systems, highlighting the recent advancements in storage materials for each approach: sensible energy, latent phase change, and thermochemical reactions. I. Calderón-Vásquez et al. [19] reviewed the heat transfer mechanisms in rock beds and examined various numerical modeling approaches. They highlighted that most existing studies focus primarily on single charge-discharge cycles, whereas a comprehensive understanding of repeated cycling operations is vital for the effective performance of these systems.
For small-scale packed-bed systems, numerous studies have been extensively documented in the literature [20-22]. However, there is a notable gap in research addressing large-scale packed bed systems, with only a few exceptions [23, 24]. This study investigates an industrial-scale packed-bed with a design capacity of 100 MWhth. The performance of the system is assessed through a time-dependent CFD simulation model, which has been effectively validated to ensure accurate and reliable simulations of its thermal dynamics and overall efficiency. Furthermore, the storage unit is assessed over 30 repeated thermal cycles, including charge, discharge, and rest phases, to investigate the influence of successive cycles on temperature layering in the packed-bed and its influence on the overall effectiveness and operational stability of the system over time.

2. METHODOLOGY

2.1. Ait Baha solar plant

The CSP plant constructed at the Ait Baha cement factory (Morocco), is designed to deliver a 3.9 MWth peak to the Organic-Rankine process for energy production. It consists of three parabolic trough collectors, each with a length of 211m (Figure 1). This thermosolar site features a packed-rock TES unit providing a capacity of 100MWth [24]. Its technology is developed by the Swiss company Airlight-Energy. The contribution of our laboratory in this project focuses on characterizing the thermal behavior and evaluating the TES unit's efficiency.

Figure 1 : Photograph of the Ait Baha CSP plant [24].

The rock used as storage material is Quartz-Sandstone. The storage unit is embedded in the ground (Figure 2) and is shaped like a truncated cone, designed to utilize lateral earth pressure for enhanced structural stability and to reduce the perpendicular stress on the walls caused by the heat-induced expansion of the rocks [25]. The lateral walls are composed of different layers

of concrete and insulating materials. The innermost layer, 0.03 m thick, is made of Ultra High Performance Concrete (UHPC), known for its outstanding mechanical strength, high thermal conductivity, and low porosity [25]. Surrounding the UHPC layer is low-density (LD) concrete, which provides structural support while maintaining low thermal conductivity. To minimize thermal losses, advanced insulation materials, including Foamglas® and Microtherm®, are integrated into the tank walls. The total thermal losses, including losses through the lateral walls, cover and bottom, remain below 3.5% of the input energy [26].

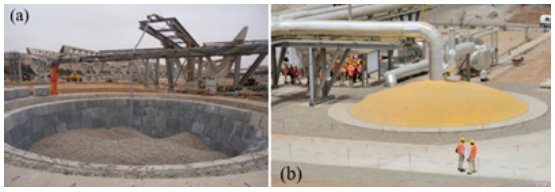

Figure 2: a) Tank filled with rocks, and b) complete system installation [24].

The system follows a daily cycle consisting of three phases: a 10h charging period, a 4h discharging phase with a high mass flow rate, and a 10h resting period to complete the cycle. The operating parameters are outlined in Table 1.

Table 1. Operating conditions of the storage unit of the Ait Baha solar power plant [24].

Parameters	
Charge inlet temperature, Tin-ch	843K
Discharge inlet temperature, Tin-disch	543K
Minimal temperature, Tmin	293K
Upper radius, Rupper	6 m
Lower radius, Rlower	5 m
Length, L	4 m
Equivalent sphere diameter, ds	0.03 m
Porosity, ε	0.35
Charging time, tcharge	10h
Discharging time, tdischarge	4h
Idle time, tidle	10h

In the charging stage, heated air is pumped into the vessel from its upper section at a temperature of 843 K and a mass flow rate of 1.716 kg/s. Conversely, during energy extraction, cold air enters the bed from the bottom at 543 K with a flow rate of 4.058 kg/s to retrieve the heat stored within the rocks.

2.2. Numerical Approach

This research employed the ANSYS-Fluent solver for numerical simulations, utilizing the finite volume method to resolve the fundamental equations governing fluid dynamics and thermal energy transfer. The storage system was modeled using a 2D-axisymmetric geometry for the computational domains. To ensure accuracy, a mesh sensitivity study was conducted to determine the optimal grid size. The computational domain was treated as a porous medium, where the rocks served as the solid component and air as the fluid component. The PISO algorithm was used for pressure-velocity correlation, and a second-order upwind scheme was implemented to solve the equations with enhanced precision. Figure 3 illustrates the numerical domain and the corresponding boundary conditions.

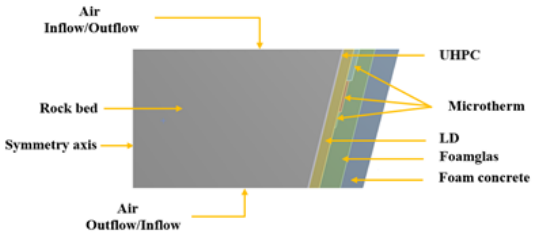

Figure 3: Overview of the numerical domain with the specified boundary conditions.

The accuracy of the numerical model was confirmed through a comparison with the experimental outcomes of A. Meier et al. [27]. The experiment involved a stainless steel cylinder, which contained rocks with an equivalent diameter of 0.02m as the thermal storage medium, through which air circulated as the HTF. The results showed a strong correlation between the experimental findings and the numerical simulations, as illustrated in Figure 4.

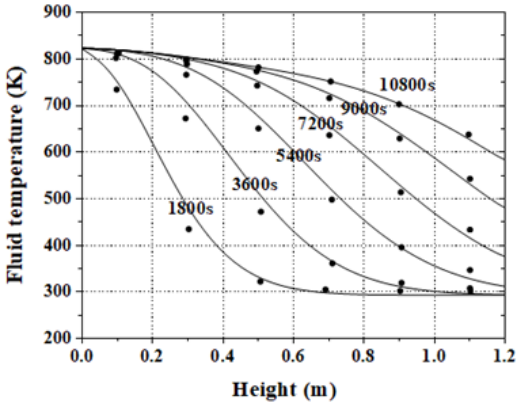

Figure 4: A comparison of the simulation predictions (line) with the experimental data (points) provided by A. Meier et al. [27].

The heat transfer model utilized in this study follows a two-phase approach adopts a two-phase approach, solving distinct energy equations for the fluid and solid phases. This method enables a more accurate representation of energy transfer between the two phases, capturing the distinct thermal behaviors of each. The fluid phase equation governs the thermal exchange within the working fluid, whereas the solid equation addresses heat conduction within the storage material. The energy conservation expressions for the air and rocks are given by Eqs. (1) and (2), respectively [28].

$$\frac{\partial}{\partial t}\left(\varepsilon\rho_f E_f\right)+\nabla\left(\vec{v}\left(\rho_f E_f+p\right)\right)=$$

$$\nabla\left[\varepsilon k_f\nabla T_f-\left(\sum_i h_i j_i\right)+\left(\overline{\overline{\tau}}\vec{v}\right)\right]+S_{heat}+h_v a\left(T_s-T_f\right) \qquad (1)$$

$$\frac{\partial}{\partial t}\left((1-\varepsilon)\rho_s E_s\right)=\nabla\left((1-\varepsilon)k_s\nabla T_s\right)+S_{heat}+h_v a\left(T_f-T_s\right) \qquad (2)$$

$\frac{\partial}{\partial t}\left(\varepsilon\rho_f E_f\right)$ and $\frac{\partial}{\partial t}\left((1-\varepsilon)\rho_s E_s\right)$ represent the rates of change of internal energy for the fluid and solid phases. ε denotes the porosity of the medium, ρ_f and ρ_s are the densities of the fluid and solid. E_f and E_s are the internal energy for the fluid and solid phases, respectively.

$\frac{\partial}{\partial t}\left((1-\varepsilon)\rho_s E_s\right)$ represents the term for convective transport of internal energy, where $\vec{v}$ is

velocity vector of the fluid, and P is the pressure of the fluid.

The terms $\nabla(\varepsilon k_f \nabla T_f)$ and $\nabla\left((1-\varepsilon)k_s \nabla T_s\right)$ represent the conductive heat flux within the fluid phase and solid phase, respectively, where k_f and k_s are the thermal conductivities of the fluid and solid, and T_f and T_s denote the temperatures of the fluid and solid.

$\nabla\left(\sum_i h_i j_i\right)$ represents the heat sources due to chemical reactions, where h_i is the enthalpy of the component, and J_i is the mass flux of the component.

$\nabla\left(\overline{\overline{\tau}}\,\vec{v}\right)$ is the viscous dissipation term, representing the conversion of mechanical energy into heat caused by fluid friction.

S_{heat} represents the external heat source term, which accounts for any thermal energy introduced into or extracted from the system.

$h_v a\left(T_f - T_s\right)$ represents the thermal interaction between the solid and fluid phases, where h_v is the heat transfer coefficient, and a is the area for heat exchange.

The numerical model is solved based on the following main assumptions: the fluid is assumed to be a perfect-gas flowing in a laminar regime, with no consideration for external heat sources, mass transfer, or chemical reactions. Additionally, the rocks are approximated as spherical to simplify the computational analysis.

The input energy during the charge represents the thermal energy provided by the HTF as it moves through the packed-bed. This energy depends on the mass flow rate of the air, temperature, and specific heat capacity, and can be mathematically expressed by Eq. (3) [29-30]:

$$E_{in} = \int_0^t \int_{T_f(0)}^{T_f(t)} \dot{m}_{ch} c_\rho \, dT_f(t) \, dt \qquad (3)$$

The energy stored throughout the storage height during the first cycle is calculated by the following equation (Eq. 4) [12]:

$$E_s = \int_0^L \rho_s c_s (1-\varepsilon)\left(T_s(y) - 293\right) dy \qquad (4)$$

Where c_s is the solid specific heat capacity, and A is the surface area.

Throughout successive cycles, the average energy stored in cycle (n) is calculated by considering the average solid temperature at the conclusion of the charge stage for cycle (n) and the temperature at the end of the idle period for cycle (n-1) (Eq. 5) [12].

$$E_{s(n)} = \rho_s c_s (1-\varepsilon) V_T \left(T_{s_end_ch(n)} - T_{s_end_idle(n-1)}\right) \qquad (5)$$

$T_{s_end_ch(n)}$ is the mean temperature of the solid at the conclusion of the charging period for cycle (n), and $T_{s_end_idle(n-1)}$ denotes the average temperature of the rocks at conclusion of the idle associated with cycle (n-1). The recovered energy E_r is defined as the heat absorbed by the air in the discharging stage (Eq. 6) [29].

$$E_r = \int_0^t \int_{T_f(0)}^{T_f(t)} \dot{m}_{disch} c_\rho dT_f(t) \, dt \qquad (6)$$

The efficiency of a thermal storage system is typically expressed as the ratio of the energy output during the discharging phase to the total energy input during the charge phase, which also accounts for the energy used in pumping during both the charging and discharging cycles.

This can be expressed mathematically as (Eq. 7) [29]:

$$\eta = \frac{E_r}{E_{in} + E_{\rho_ch} + E_{\rho_disch}} \qquad (7)$$

E_(p_ch) and E_(p_disch) are respectively the pumping energies during the charge and discharge processes. They are calculated using the following equation (Eq. 8) [29]:

$$E_\rho = \int_0^t \frac{\dot{m}}{\rho_f} \Delta P \, dt \qquad (8)$$

3. RESULTS

3.1. First thermal cycle

In the first phase of charging, the tank's initial temperature is set to 293 K. During this cycle, air heated by the solar concentrators is introduced into the tank at a temperature of 843 K, and a mass flow of 1.716 kg/s.

Figure (5) depicts the temperature variation within the fluid and solid phases after 3h and 10h of the initial charging process. It reveals that the thermal difference between the fluid and solid at the inlet is greater after 3h $(T_f(3h) - T_s(3h) = 135\,K)$ compared to the difference at the end of charging $(T_f(10h) - T_s(10h) = 43\,K)$. Nevertheless, the temperature of both phases remains identical across the tank. The observed results can be attributed to the heat transfer mechanisms governing the charging process. After 3h, a significant temperature difference is present, with the fluid being considerably hotter. However, as the charging process progresses, heat gradually transfers to the solid phase, reducing the temperature difference and promoting thermal equilibrium over time.

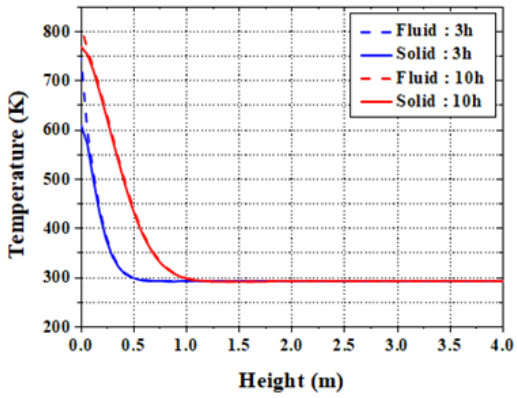

Figure 5: Temperature profiles of the solid and fluid at 3h and 10h during the initial charging.

To retrieve the stored heat during discharge, cold fluid is introduced at the bottom of the tank, having a mass flux of 4.058 kg/s and an initial temperature of 543 K. Figure (6) presents the thermal distributions in both the fluid and solid after 2h and at the completion of the first discharge process. During the first discharge, the fluid enters at a temperature higher than the one at the tank's bottom (543 K), resulting in the formation of three distinct zones within the bed: a thermocline zone located in the first quarter of the tank, followed by a thermal equilibrium zone at a temperature of 293K and a thermocline zone at the lower part of the tank.

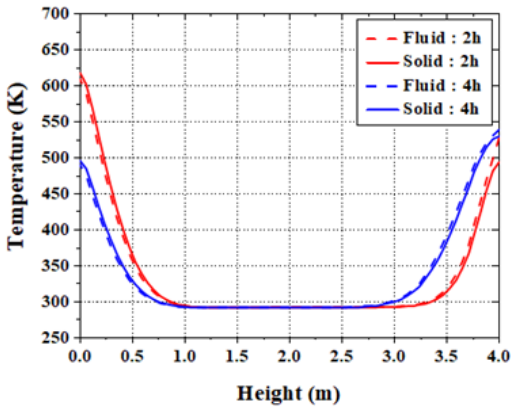

Figure 6: Temperature variations in the fluid and solid mediums after 2h and 4h of the first discharge process.

In the lower thermocline zone, the reservoir behaves as if it is experiencing the charging process because the fluid enters at a higher temperature than that obtained at the bottom. Consequently, the fluid heats the lower part of the reservoir, then a thermal equilibrium is established as it ascends, and effective discharge only occurs in the top quarter of the reservoir: the fluid temperature increases as it approaches the top of the reservoir. Therefore, in this zone, the solid temperature exceeds that of the fluid.

3.2. Cyclic operation

To characterize the storage system behavior during cyclic operation, thirty consecutive cycles are considered. Each thermal cycle consists of three phases: 10h of charging, 4h of discharging, and 10h of rest.

Figure 7 (a, b) shows respectively the temperature along the axis of the rocks medium during the first ten cycles and during the next twenty cycles. Figure (7, a) demonstrates the temperature profile during the initial charging cycle differs from the subsequent cycles; the temperature continuously decreases from the upper to the lower part of the tank during the initial charge time. However, for the second charging cycle, the temperature profile is affected by the first discharge process, which explains the appearance of two thermocline zones and a thermal equilibrium zone. Additionally, As the number of cycles increases, the two thermocline zones widen, while the thermal equilibrium zone contracts during the first three cycles.

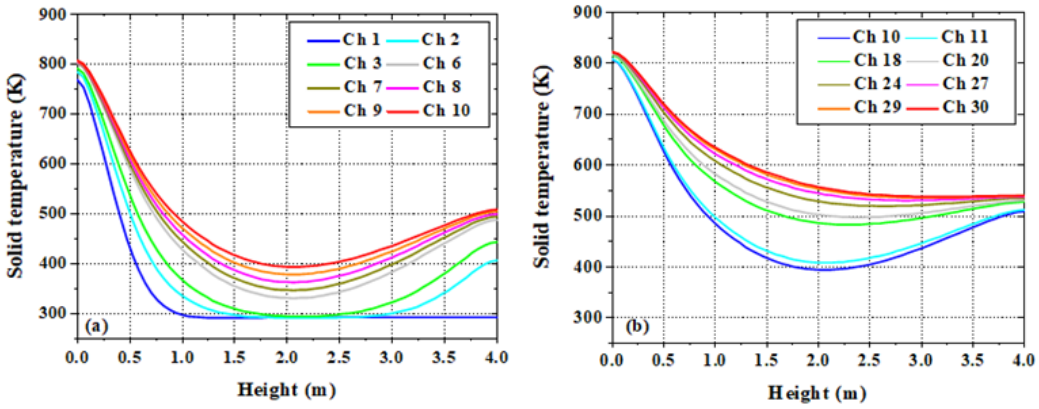

(a) (b)

Figure 7: Solid temperature distributions at the conclusion of the charging, a) for the first ten cycles, b) the subsequent twenty cycles.

Figure (7, b) illustrates the variation in solid temperature from the 10th to the 30th cycle. It can be

observed that, as the thermal cycles progress, the width of the upper thermocline zone increases at the expense of the second one, until they converge into a singular zone from the 27th cycle.
The evolution of the average solid temperature at the end of the charge period over thirty consecutive cycles is shown in Figure (8). It demonstrates that the average solid temperature grows exponentially with the progression of thermal cycles.

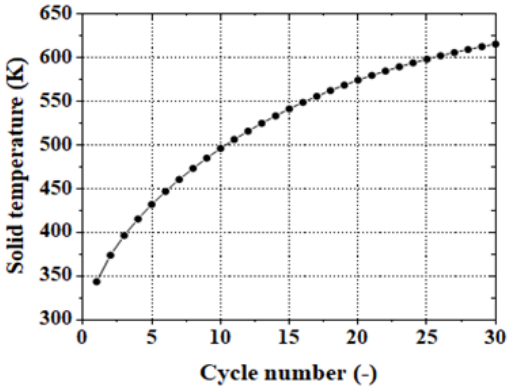

Figure 8: Evolution of the average solid temperature at the close of the charging process over thirty consecutive cycles.

The evolution of the fluid outlet temperature and the storage system's overall effectiveness throughout discharge over thirty consecutive cycles are shown in Figure (9). It indicates that the fluid outlet temperature during discharge rises significantly with the increasing cycle number, it varies between 617K in the 1st cycle and 782K in the 30th cycle. Furthermore, there is an improvement in the system efficiency as the number of cycles increases; the efficiency ranges from 3% in the 1st cycle and 80% in the 30th cycle (Figure 9).

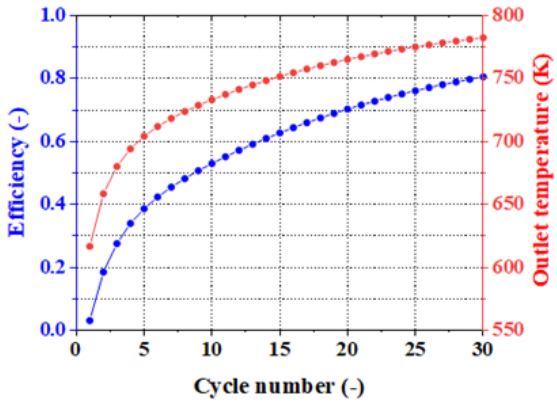

Figure 9: Progression of the outlet fluid temperature throughout discharge and the efficiency of the system over the thirty cycles.

4. CONCLUSIONS

This work presents a numerical investigation of the thermal dynamics within the energy storage system of the CSP plant in Ait Baha, Morocco. The two-phase model, which has been developed and successfully validated, is applied to analyze the storage system's response during the charge and discharge processes and to evaluate its performance. Depending on the operating conditions, numerical simulations are conducted over 30 thermal cycles, corresponding to 30 days of operation. The results of the cyclic behavior indicate that the influence of the thermal cycles is more noticeable in the initial cycles. It is found that the thermal stratification within the reservoir is enhanced with the progression of cycles. By the end of the discharge period, the fluid

outlet temperature increases from 617 K in the first cycle to 782 K in the 30th cycle. Moreover, as thermal cycles progress, the efficiency of the storage unit has been significantly improved, reaching 80% in the 30th cycle.

Authors' Contribution: Conceptualization: Aicha Eddemani, Ahmed Aharoune. Simulation and data analysis: Aicha Eddemani. Writing-Original Draft: Aicha Eddemani. Review and Editing: Omar Achahour, Hayat El Baamrani. Supervision: Ahmed Aharoune, Lahcen Bouirden. Project Coordination: Ahmed Ihlal.

Funding: This research was funded by IRESEN (Institut de Recherche en Énergie Solaire et Énergies Nouvelles, Morocco) as part of the INNOTHERM 1 project. Additional financial support was provided by the Moroccan Ministry of Higher Education and Research through the PPR/2015/31 and PPR/2015/56 projects.

Data Availability Statement: The data presented in this study are available on request from the corresponding author.

Conflicts of Interest: The authors declare no conflict of interest.

Acknowledgements: The authors express their sincere gratitude to all individuals and organizations that contributed to this work.

REFERENCES

[1] A. Z. A. Shaqsi, K. Sopian, and A. Al-Hinai, "Review of energy storage services, applications, limitations, and benefits," Energy Reports, vol. 6, pp. 288–306, Dec. 2020, doi: 10.1016/j.egyr.2020.07.028.

[2] S. Kakran, J. S. Rathore, A. Sidhu, and A. Kumar, "Solar Energy Advances and CO2 Emissions: A Comparative review of leading nations path to sustainable future," Journal of Cleaner Production, p. 143598, Oct. 2024, doi:10.1016/j.jclepro.2024.143598.

[3] A. Gil, M. Medrano, I. Martorell, A. Lázaro, P. Dolado, B. Zalba, and L.F. Cabeza, "State of the art on high temperature thermal energy storage for power generation. Part 1- Concepts, materials and modellization," Renewable and Sustainable Energy Reviews, vol. 14, no. 1, pp. 31–55, Jan. 2010, doi: 10.1016/j.rser.2009.07.035.

[4] T. Kousksou, P. Bruel, A. Jamil, T. E. Rhafiki, and Y. Zeraouli, "Energy storage: Applications and challenges," Solar Energy Materials and Solar Cells, vol. 120, pp. 59–80, Sep. 2013, doi: 10.1016/j.solmat.2013.08.015.

[5] V. Bhardwaj, S. C. Kaushik, and H. P. Garg, "Sensible thermal storage in rock beds for space conditioning: a state of the art study," International Journal of Ambient Energy, vol. 20, no. 4, pp. 211–219, 30 Mar. 2011, doi: 10.1080/01430750.1999.9675342.

[6] V. Dreißigacker, S. Zunft, Müller- H. Steinhagen, "A thermomechanical model of packed-bed storage and experimental validation". Applied Energy, vol. 111, pp. 1120–1125, 2013. doi: 10.1016/j.apenergy.2013.03.067.

[7] Z. Lai, L. Ding, H. Lyu, C. Hou, J. Chen, X. Guo, G. Han, and K. Zhang. "Experimental study on energy storage characteristics of sintered ore particle packed beds," Journal of Thermal Science, vol. 34, no. 1, pp. 242-253, Dec. 2024, doi: 10.1007/s11630-024-2079-9.

[8] N. B. Desai, M. E. Mondejar, and F. Haglind, "Techno-economic analysis of two-tank and packed-bed rock thermal energy storages for foil-based concentrating solar collector driven cogeneration plants," Renewable Energy, vol. 186, pp. 814–830, Mar. 2022, doi: 10.1016/j.renene.2022.01.043.

[9] Y. Jemmal, N. Zari, M. Asbik, and M. Maaroufi, "Experimental characterization and thermal performance comparison of six Moroccan rocks used as filler materials in a packed bed storage

system," Journal of Energy Storage, vol. 30, p. 101513, Aug. 2020, doi: 10.1016/j.est.2020.101513.

[10] Z. Liu, L. N. Y. Wong, and S.-C. Chang, "Experimental investigation of major rocks in Hong Kong as potential sensible thermal energy storage medium," Engineering Geology, vol. 343, p. 107763, Dec. 2024, doi: 10.1016/j.enggeo.2024.107763.

[11] E. Abddaim, S. Sakami, A. E. Hassnaoui, and L. Boukhattem, "Impact of temperature on chemical, thermo-physical, and mechanical properties of four rock materials for sensible thermal energy storage," Journal of Energy Storage, vol. 89, p. 111602, June 2024, doi: 10.1016/j.est.2024.111602.

[12] A. M. Rabi, J. Radulovic, and J. M. Buick, "Packed bed thermal energy storage system: Parametric study," Thermo, vol. 4, no. 3, pp. 295–314, Jul. 2024, doi: 10.3390/thermo4030016.

[13] P. Negi, Y. Singh, J. Dixit, M. Gwalwanshi, and R. Kanojia, "Experimental analysis based parametric study of packed bed heat regenerator with air as passing medium," Materials Today Proceedings, vol. 46, pp. 10488–10491, Feb. 2021, doi: 10.1016/j.matpr.2020.12.1193.

[14] G. F. Al-Sumaily, H. A. Dhahad, and M. C. Thompson, "Mixed convection phenomenon in packed beds: A comprehensive review," Thermal Science and Engineering Progress, vol. 32, p. 101242, July 2022, doi: 10.1016/j.tsep.2022.101242.

[15] W.C. Chen, Y.W. Fan, L.L. Zhang, B.C. Sun, Y. Luo, H.K. Zou, G.W. Chu, and J.F. Chen, "Computational fluid dynamic simulation of gas-liquid flow in rotating packed bed: A review," Chinese Journal of Chemical Engineering, vol. 41, pp. 85–108, Jan. 2021. doi: 10.1016/j.cjche.2021.09.024.

[16] A. Gautam and R. P. Saini, "A review on sensible heat based packed bed solar thermal energy storage system for low temperature applications," Solar Energy, vol. 207, pp. 937–956, Sept. 2020, doi: 10.1016/j.solener.2020.07.027.

[17] M. Díaz-Heras, J. F. Belmonte, and J. A. Almendros-Ibáñez, "Effective thermal conductivities in packed beds: Review of correlations and its influence on system performance," Applied Thermal Engineering, vol. 171, p. 115048, May 2020, doi: 10.1016/j.applthermaleng.2020.115048.

[18] M. Tawalbeh, H. A. Khan, A. Al-Othman, F. Almomani, and S. Ajith, "A comprehensive review on the recent advances in materials for thermal energy storage applications," International Journal of Thermofluids, vol. 18, p. 100326, May 2023, doi: 10.1016/j.ijft.2023.100326.

[19] I. Calderón-Vásquez, E. Cortés, J. García, V. Segovia, A. Caroca, C. Sarmiento, R. Barraza, and J. M. Cardemil, "Review on modeling approaches for packed-bed thermal storage systems," Renewable and Sustainable Energy Reviews, vol. 143, p. 110902, June 2021, doi: 10.1016/j.rser.2021.110902.

[20] M. M. Abera, V. R. Ancha, B. Amare, L. S. Sundar, K. V. V. C. Mouli, and S. Sangaraju, "Simulation and optimization of energy efficiency and total enthalpy analysis of sand based packed bed solar thermal energy storage," Frontiers in Heat and Mass Transfer, vol. 22, no. 4, pp. 1043–1070, Aug. 2024, doi: 10.32604/fhmt.2024.049525.

[21] R. Kothari, C. S. Hemmingsen, N. V. Voigt, A. La Seta, K. K. Nielsen, N. B. Desai, A. Vijayan, and F. Haglind, "Numerical and experimental analysis of instability in high temperature packed-bed rock thermal energy storage systems," Applied Energy, vol. 358, p. 122535, March 2024, doi: 10.1016/j.apenergy.2023.122535.

[22] H. Geng, Y. Wu, D. Ma, Y. Hao, D. Li, and H. Zhou, "Experimental study on the heat storage characteristics of rock bed heat storage system with different packing structure," Journal of Energy Storage, vol. 101, p. 113973, Nov. 2024, doi: 10.1016/j.est.2024.113973.

[23] G. Zanganeh, A. Pedretti, A. Haselbacher, and A. Steinfeld, "Design of packed bed thermal

energy storage systems for high-temperature industrial process heat," Applied Energy, vol. 137, pp. 812–822, Jan. 2015, doi: 10.1016/j.apenergy.2014.07.110.

[24] S. A. Zavattoni, G. Zanganeh, A. Pedretti, and M. C. Barbato, "Numerical analysis of the packed bed TES system integrated into the first parabolic trough CSP pilot-plant using air as heat transfer fluid," AIP Conference Proceedings, vol. 2033, p. 090027, Jan. 2018, doi: 10.1063/1.5067121.

[25] G. Zanganeh, A. Pedretti, S. Zavattoni, M. Barbato, and A. Steinfeld, "Packed-bed thermal storage for concentrated solar power – Pilot-scale demonstration and industrial-scale design," Solar Energy, vol. 86, no. 10, pp. 3084–3098, Aug. 2012, doi: 10.1016/j.solener.2012.07.019.

[26] G. Zanganeh, A. Pedretti, S. A. Zavattoni, M. C. Barbato, A. Haselbacher, and A. Steinfeld, "Design of a 100 MWhth packed-bed thermal energy storage," Energy Procedia, vol. 49, pp. 1071–1077, Jan. 2014, doi: 10.1016/j.egypro.2014.03.116.

[27] A. Meier, C. Winkler, and D. Wuillemin, "Experiment for modelling high temperature rock bed storage," Solar Energy Materials, vol. 24, no. 1–4, pp. 255–264, Dec. 1991, doi: 10.1016/0165-1633(91)90066-t.

[28] J. Ochmann, K. Rusin, S. Rulik, S. Waniczek, and L. Bartela, "Experimental and computational analysis of packed-bed thermal energy storage tank designed for adiabatic compressed air energy storage system," Applied Thermal Engineering, vol. 213, p. 118750, May 2022, doi: 10.1016/j.applthermaleng.2022.118750.

[29] M. Hänchen, S. Brückner, and A. Steinfeld, "High-temperature thermal storage using a packed bed of rocks – Heat transfer analysis and experimental validation," Applied Thermal Engineering, vol. 31, no. 10, pp. 1798–1806, July 2011, doi: 10.1016/j.applthermaleng.2010.10.034.

[30] A. Eddemani, H. El Baamrani, A. Aharoune, L. Bouirden and A. Ihlal, "Comparative Study of the Performance of Packed Beds Using Different Types of Thermal Storage Materials". Solar Energy and Sustainable Development Journal, 14 (SI_MSMS2E), 176–184, 2024, https://doi.org/10.51646/jsesd.v14iSI_MSMS2E.395.

Solar Energy
And Sustainable Development
Refereed, biannual scientific journal issued by:
The Libyan Center for Solar Energy Research and Studies

Comprehensive Analysis of Optoelectronic Properties and Photovoltaic Performance of Rb2CuAsZ6 (Z = Br and Cl) Double Perovskites Using DFT and SCAPS-1D Modelling.

Kamal Assiouan[1*], Hanan Ziani[2], Jamal EL Khamkhami[3], Abdelfattah Achahbar[4].

[1,2,3,4]1Artificial Intelligence and Computational Physics Laboratory, Faculty of Sciences, Abdelmalek Essaadi University, B. P. 2121 M'Hannech II, Tetouan, 93030, Morocco..

E-*mail:* [1]kamal.assiouan@etu.uae.ac.ma , [2]hanane.ziani@etu.uae.ac.ma , [3]jelkhamkhami@uae.ac.ma , [4]aachahbar@uae.ac.ma .

SPECIAL ISSUE ON:

The 1St International Conference on Sciences and Techniques for Renewable Energy and the Environment.
(STR2E 2025)
May 6-8, 2025 at FST-Al Hoceima-Morocco.

KEYWORDS

Density Functional Theory (DFT); Double Perovskites; Rb_2CuAsZ_6 (Z = Br, Cl); Optoelectronic properties; solar cells.

ABSTRACT

Rb_2CuAsZ_6 (Z = Br, Cl) double perovskites were studied for their optoelectronic and photovoltaic properties using a comprehensive density functional theory (DFT) analysis. Using the HSE06 functional for electronic band structure calculations, $Rb_2CuAsBr_6$ and $Rb_2CuAsCl_6$ exhibit indirect band gaps (Eg) of 0.64 eV and 1.09 eV, respectively. Moreover, the analysis of the optical properties revealed substantial absorption (α) around 105 in both the visible and near-infrared regions, highlighting their suitability for solar cell and optoelectronic applications. Moreover, we utilised the absorber layer $Rb_2CuAsCl_6$ to construct an n-i-p structure perovskite and modelled it Using the SCAPS-1d program, this calculation was performed with a thickness of 400 nm of $Rb_2CuAsCl_6$, yielding remarkable performance: an open-circuit voltage Voc of 0.81 V, a short-circuit current density (J_{sc}) of 38.33 mA/cm², a fill factor (FF) of 68.65%, and a power conversion efficiency (PCE) of 20.63%.

*Corresponding author.

DOI: https://doi.org/10.51646/jsesd.v14iSTR2E.802

This is an open access article under the CC BY-NC license (http://Attribution-NonCommercial 4.0 (CC BY-NC 4.0)).

تحليل شامل للخصائص البصرية الإلكترونية والأداء الكهروضوئي للبيروفسكايت المزدوج Rb_2CuAsZ_6 (Z = Br, Cl) باستخدام نمذجة DFT و SCAPS-1D

كمال أسوان ،حنان الزياني ، جمال الخمخامي، عبد الفتاح اشهبار.

ملخص: تمت دراسة الخصائص البصرية الإلكترونية والكهروضوئية للبيروفسكايت المزدوج Rb_2CuAsZ_6 (Z = Br, Cl) باستخدام نظرية الكثافة الوظيفية (DFT). كشفت حسابات تركيب النطاق الإلكتروني باستخدام الوظيفة HSE06 عن فجوات نطاق غير مباشرة تبلغ 0.64 إلكترون فولت لـ $Rb_2CuAsBr_6$ و 1.09 إلكترون فولت لـ $Rb_2CuAsCl_6$. أظهرت التحليلات البصرية امتصاصًا قويًا حوالي 105 في كل من مناطق الضوء المرئي والأشعة تحت الحمراء القريبة، مما يبرز ملاءمتها للتطبيقات البصرية الإلكترونية والخلايا الشمسية. تم تصميم ومحاكاة هيكل خلية شمسية بيروفسكايت n-i-p تتضمن $Rb_2CuAsCl_6$ كطبقة ماصة باستخدام برنامج SCAPS-1D، وقد تم إجراء هذه الحسابات بسماكة 400 نانومتر من $Rb_2CuAsCl_6$، مما أسفر عن أداء جيد: جهد دائرة مفتوحة (V_{oc}) يبلغ 0.81 فولت، وكثافة تيار دائرة قصيرة (J_{sc}) تبلغ 38.33 مللي أمبير/سم^2، وعامل تعبئة (FF) يبلغ 68.65 %، وكفاءة تحويل الطاقة (PCE) تبلغ 20.63 %.

الكلمات المفتاحية – كنظرية الكثافة الوظيفية (DFT)؛ البيروفسكايت المزدوج؛ Rb_2CuAsZ_6 (Z = Br, Cl)؛ الخصائص البصرية الإلكترونية؛ الخلايا الشمسية.

1. INTRODUCTION

The growing global energy demand, driven by technological and industrial advancements, has heightened the need for clean energy sources to mitigate environmental concerns associated with fossil fuels. Solar and thermoelectric energy have emerged as sustainable and cost-effective solutions[1,2]. As silicon solar cells near their theoretical efficiency limits, researchers are increasingly exploring alternative materials that exhibit superior photovoltaic properties[3].

Organic perovskites, introduced in 2009[4], have emerged as promising alternatives, demonstrating significant advancements in photovoltaic efficiency reaching 25.5% within a decade driven by their exceptional electronic and optical properties[5,6]. However, issues like environmental toxicity (Pb^{2+}) and stability challenges under moisture and heat prompted the development of lead-free double perovskites (LFDPs)[7].

First-principles calculations have enabled researchers to identify eleven materials with suitable bandgaps for photovoltaic absorption, including $Cs_2CuSbCl_6$ and $Rb_2CuSbCl_6$[8,9]. However, only a limited number of these materials, such as $Cs_2AgBiBr_6$[10], $Cs_2AgBiCl_6$[11], and $(CH_3NH_3)_2AgBiBr_6$ [12], have been successfully synthesized. Furthermore, simulations play a crucial role in understanding the properties and performance metrics of various materials, complementing experimental research [13–15]. Recent studies have investigated the Power Conversion Efficiency (PCE) of lead-free double perovskite (LFDP) solar cells using numerical simulations, such as SCAPS-1D[16]. Utsho et al. investigated the use of $Cs_2CuBiBr_6$ as the absorber layer and Cu-based thiogallate (CBTS) as the hole transport layer (HTL), examining the impact of varying electron transport layers (ETLs) including WS_2, C_{60}, PCBM, and TiO_2 on solar cell performance. The corresponding Power Conversion Efficiencies (PCEs) achieved were 19.70%, 18.69%, 19.52%, and 19.65%, respectively[17]. Additionally, a Cs2TiBr6 based double perovskite solar cell (PSC) was simulated using SCAPS-1D and Density Functional Theory (DFT) calculations, confirming a bandgap of 1.6 eV. The cell employed La-doped $BaSnO_3$ (LBSO) as the ETL and $CuSbS_2$ as the HTL. Optimization of the absorber thickness, defect density, and bandgap resulted in an impressive PCE of 29.13%[18]. Moreover, an analysis of the ITO/ETL/$Cs_2AgBiBr_6$/Cu_2O/Au structure, with $Cs_2AgBiBr_6$ as the absorber layer, Cu_2O as the HTL, and TiO_2 as the ETL, achieved a PCE of 18.83%, highlighting the potential of lead-free double perovskite solar cells[19].

This study aims to explore the potential of the double perovskites Rb_2CuAsZ_6 (Z = Br, Cl) for applications in optoelectronic and photovoltaic devices. The investigation will begin with a structural analysis, followed by an in-depth examination of the electronic properties crucial for optoelectronic functionality. Subsequently, the optical characteristics will be calculated up to 10 eV. Finally, the efficiency of $Rb_2CuAsCl_6$ as the absorber layer in a solar cell will be evaluated using SCAPS-1D software.

2. COMPUTATIONAL FRAMEWORKS

2.1. Computation of Rb_2CuAsZ_6 properties using DFT

The optical, electronic, and structural characteristics of the double perovskites Rb_2CuAsZ_6 (Z = Br, Cl) were investigated using density functional theory (DFT) calculations with the Quantum ESPRESSO package[20]. Broyden–Fletcher–Goldfarb–Shanno (BFGS) method was used to optimise the crystal formations[21,22]. The Perdew-Burke-Ernzerhof (PBE) functional was employed to describe the exchange-correlation interaction within the Generalized Gradient Approximation (GGA) framework[23,24]. The convergence criteria for structural optimization were set to 10^{-6} eV/atom for total energy and 10^{-4} eV/Å for the maximum force. An 8 × 8 × 8 Monkhorst-Pack k-point grid was employed for Brillouin zone sampling during the optimization process, ensuring accurate structural relaxation. The kinetic energy cutoff (Ecut) was set at 70 Ry. The calculations of electronic properties, the GGA-PBE was employed with a denser 12 × 12 × 12 k-point grid. To overcome the band gap underestimation inherent to this approximation, the HSE06 hybrid functional with norm-conserving pseudopotentials (NCPP) was used to estimate the band gap.Additionally, the dielectric function was obtained using PBE with norm-conserving pseudopotentials Within the Random-Phase Approximation (RPA) framework, calculations were performed using the Yambo code [25].

2.2. Simulation methodology

The one-dimensional Solar Cell Capacitance Simulator (SCAPS-1D) is a widely used open-source numerical simulation program for analysing solar cell performance. This study aimed to design a double perovskite solar cell and comprehensively evaluate its performance under the Air Mass 1.5 Global (AM1.5G) spectrum by numerically solving Poisson's equation alongside the electron and hole continuity equations[26], using SCAPS-1D version 3.3.11.
Poisson's equation:

$$-\frac{\partial}{\partial x}\left(-\varepsilon(x)\frac{\partial V}{\partial x}\right)=q\left[p(x)-n(x)+N_D^+(x)-N_A^-(x)+p_t(x)-n_t(x)\right] \qquad (1)$$

Continuity equation for electrons:

$$\frac{\partial n}{\partial x}=\frac{1}{q}\frac{\partial J_n}{\partial x}+G_n-R_n \qquad (2)$$

Continuity equation for holes:

$$\frac{\partial p}{\partial x}=\frac{1}{q}\frac{\partial J_p}{\partial x}+G_p-R_p \qquad (3)$$

The following symbols represent the respective physical quantities: q denotes the electronic charge, ε the dielectric permittivity, V the electric potential, p(x) the free hole concentration, n(x) the free electron concentration, $N_A^-(x)$ the concentration of ionized acceptors, $N_D^+(x)$ the

concentration of ionized donors, nt(x) the electron trap density, and pt(x) the hole trap density. Furthermore, the current densities, generation rates, and recombination rates for electrons and holes are represented by J_n, J_p, G_n, G_p, R_n, and R_p, respectively.

3. RESULTS AND DISCUSSION

3.1. Structural Properties

The lead-free double perovskite Rb_2CuAsZ_6 (Z = Br, Cl) crystallizes in a cubic unit cell within the $Fm\bar{3}m$ space group (no. 225), as illustrated in Figure 1.

The Wyckoff positions occupied by Rb, Cu, As, and Br/Cl atoms in the structure are 8c, 4b, 4a, and 24e, respectively. The structural optimisation determines the equilibrium volume at which the material attains its minimum total energy, corresponding to its most stable configuration, known as the ground state energy.

The calculated equilibrium volumes, total energies, and unit cell parameters for the double perovskite structures $Rb_2CuAsBr_6$ and $Rb_2CuAsCl_6$ are summarized in Table 1.

The increase in the ionic radii of the halogens from Cl to Br accounts for the decrease in the lattice constant as we move from $Rb_2CuAsBr_6$ to $Rb_2CuAsCl_6$. Furthermore, the stability of both compounds was evaluated by calculating the Goldschmidt tolerance factor (t_G) using the following formula[27]:

$$t_G = \frac{r_{Rb} + r_Z}{\sqrt{2}\left(\frac{r_{Cu} + r_{As}}{2} + r_Z\right)} \qquad (4)$$

along with the formation energy (E_f), which was calculated using the following expression[28]:

$$E_f^{Rb_2CuAsZ_6} = \left(E_{Rb_2CuAsZ_6} - \left[2E^{Rb} + E^{Cu} + E^{As} + 6E^{Z}\right]\right)/10 \qquad (5)$$

In this context, ERb_2CuAsZ_6 represents the total energy of Rb_2CuAsZ_6 (Z=Br, Cl). The terms E^{Rb}, E^{Cu}, E^{As}, E^{Z} correspond to the energies of isolated Rb, Cu, As and Z (Br, Cl) atoms, respectively, while r_{Rb}, r_{Cu}, r_{As}, and r_Z represents the atomic radii of the Br and Cl atoms.

The negative formation energies calculated for both perovskites, as presented in Table 1, demonstrate their thermodynamic stability. Additionally, the tolerance factor values, which fall within the required range for a cubic structure ($0.8 < t_G < 1.0$), further substantiate the stability of $Rb_2CuAsBr_6$ and $Rb_2CuAsCl_6$, as detailed in Table 1.

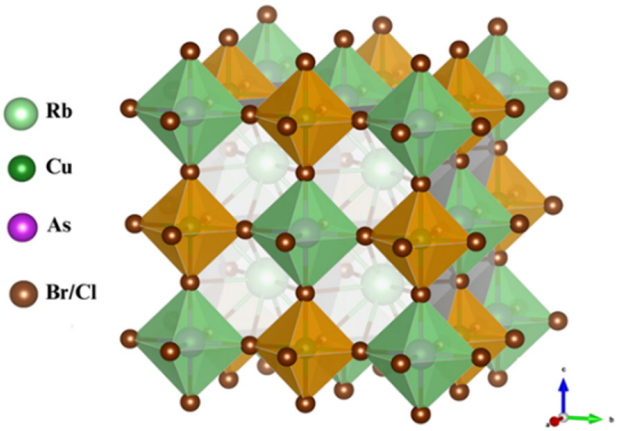

Figure1. FCC (Face-Centered Cubic) crystal structure of Rb_2CuAsZ_6 (Z = Br, Cl).

Table 1 Optimised Cell parameters and phase stability of Rb_2CuAsZ_6 (Z=Br, Cl).

Parameters	$Rb_2CuAsBr_6$	$Rb_2CuAsCl_6$
Lattice Constant (Å)	10.69	10.13
Volume at ground state-V_0 ($a.u^3$)	2072.97	1757.2
Ground State Energy-E_0 (Ry)	-3574.92	-1345.76
Tolerance Factor-t_G	0.98	1
Formation Energy-E_f(eV/atom)	-0.81	-1.17

3.2. Electronic properties

Understanding the electronic properties of a material, such as its energy band gap and density of states, is essential for predicting its performance in photovoltaic and optoelectronic applications. Based on the band structure calculated using the PBE-GGA method, as shown in Figure 2a and Figure 2b, the band gaps are determined to be 0.18 eV (L–X) for $Rb_2CuAsBr_6$ and 0.49 eV (L–X) for $Rb_2CuAsCl_6$, highlighting their semiconducting nature with a small indirect band gap. However, it is well known that the GGA-PBE approximation often underestimates the band gap of double perovskites[29]. Conversely, the use of the HSE06 functional enables the calculation of band gap values that more accurately align with experimental measurements. For $Rb_2CuAsBr_6$ and $Rb_2CuAsCl_6$, the band gaps are determined to be 0.64 eV and 1.09 eV, respectively, as shown in Figure 2c and Figure 2d. the smaller atomic radius of Cl is responsible for the increase in the band gap that results from replacing Br. The bandgap values of these lead-free double perovskites, which $Rb_2CuAsCl_6$ satisfies by falling within the ideal range from 0.9 to 1.6 eV for solar cell efficiency, are a key factor determining their suitability for photovoltaic applications[30].

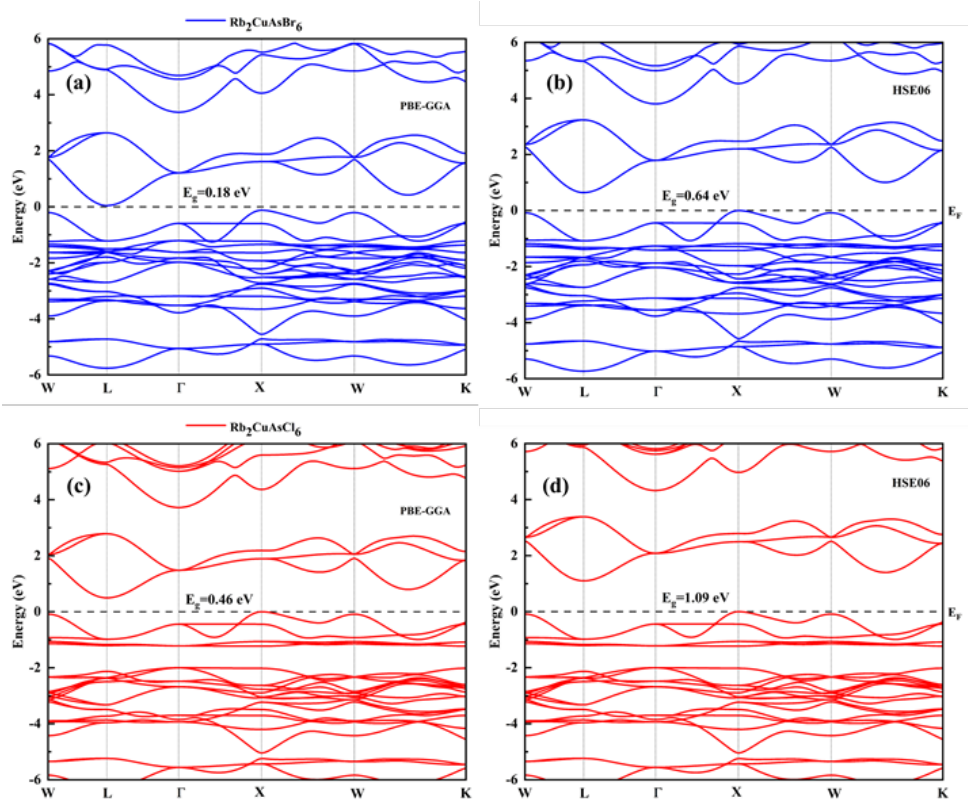

Figure 2. band structures calculated for (a, b) $Rb_2CuAsBr_6$ and (c, d) $Rb_2CuAsCl_6$ using PBE-GGA and HSE06.

A key factor in evaluating the performance of optoelectronic and photovoltaic materials is the effective mass of charge carriers. To assess the performance of these materials in such applications, it is crucial to determine the effective masses of both electrons and holes. Accordingly, using the method described in Equation (6)[31], we fitted a parabolic function near the valence band maximum (VBM) and conduction band minimum (CBM) at high symmetry points (L-X) to calculate the effective masses of electrons and holes.

$$m^* = \hbar^2 \left[\frac{\partial^2 E(k)}{\partial^2 k} \right]^{-1} \qquad (6)$$

Where E(k) represents the energy of the charge carrier as a function of its wave vector, and ħ is the reduced Planck's constant.

The effective masses calculated and presented in Table 2 demonstrate small values for both carrier species, thereby directly enhancing the material's ability to absorb phonons and generate electron pairs. These attributes are critical for the functionality of a variety of applications, including solar cells and optoelectronic devices like LEDs[32].

Table 2. Calculated Effective Mass (m*) and Band Gap (E_g) of Rb_2CuAsZ_6 (X = Br, Cl) Using PBE-GGA and HSE06 Approximations.

Perovskites	PBE (eV)	HSE06 (eV)	$(m_e^*)/m_e$	$(m_h^*)/m_e$	ε(0)
$Rb_2CuAsBr_6$	0.18	0.64	0.26	0.25	9.27
$Rb_2CuAsCl_6$	0.49	1.09	0.36	0.30	6.75

3.3. Optical properties

Calculating optical properties is crucial for advancements in optoelectronic and photovoltaic technology. This analysis is essential for understanding how materials interact with light, particularly their ability to absorb and emit it, which is governed by inter-band and intra-band transitions. In this context, only inter-band transitions are considered due to their significant impact, while intra-band transitions are disregarded due to their lower probabilities and minimal contribution to overall optical properties. This section presents a comprehensive examination of the optical characteristics across the photon energy spectrum from 0 to 10 eV, aiming to evaluate the potential of perovskite materials Rb_2CuAsZ_6 (Z = Br, Cl) for optoelectronic and photovoltaic applications.

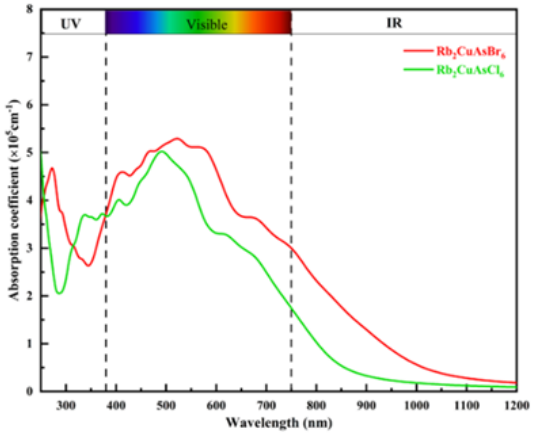

Figure 3. The absorption coefficients as function of wavelength of Rb_2CuAsZ_6 (X=Br, Cl) LFDPs.

Figure 3 displays the absorption coefficient of Rb_2CuAsZ_6 perovskites across a wavelength range from 250 nm to 1200 nm. The absorption edges, occurring around 380 nm for $Rb_2CuAsBr_6$ and 600 nm for $Rb_2CuAsCl_6$, align with their respective band gaps. Notably, $Rb_2CuAsBr_6$ exhibits higher absorption, peaking at 5.31×10^5 cm^{-1} around 525 nm, surpassing $Rb_2CuAsCl_6$, which peaks at 5.02×10^5 cm^{-1} around 490 nm within the visible energy range. Additionally, both perovskite materials also showed significant absorption in the NIR (near-infrared) spectrum. Additionally, the varying band gaps of these materials contribute to their versatility in practical applications. Specifically, $Rb_2CuAsCl_6$ is more suitable for solar cells due to its stability and absorption in the visible spectrum, whereas $Rb_2CuAsBr_6$ is better suited for infrared sensors.

The reflectivity analysis of Rb_2CuAsZ_6 (X=Br, Cl) perovskite, as depicted in Figure 4, reveals static reflection coefficients, with R (0) values of 12% and 17% respectively. Across a wavelength range of 250 nm to 1200 nm, the peak reflectivity remains approximately 40% within the visible spectrum. However, it starts at under 20% in the ultraviolet range, suggesting
that most photons either penetrate the material are absorbed by it.

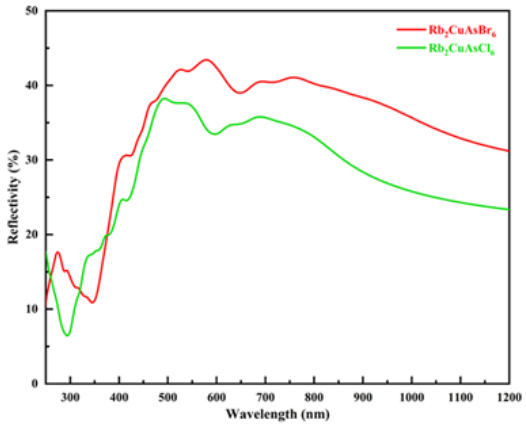

Figure 4. The calculated reflectivity as function of wavelength of Rb_2CuAsZ_6 (X=Br, Cl) LFDPs.

3.4. Efficiency of Perovskite Solar Cells Based on $Rb_2CuAsCl_6$ Absorber Layer

The simulation of photovoltaic (PV) systems, particularly through tools like SCAPS, is an excellent method for assessing the materials' effectiveness in solar cell applications. SCAPS is commonly used in research on thin-film solar cells. It allows researchers to model the thickness of multilayer systems and analyse how various design elements and material parameters influence the photovoltaic efficiency of these devices.

Figure 5 illustrates the perovskite solar cell (PSC) utilises an n-i-p architecture in the device modelling.

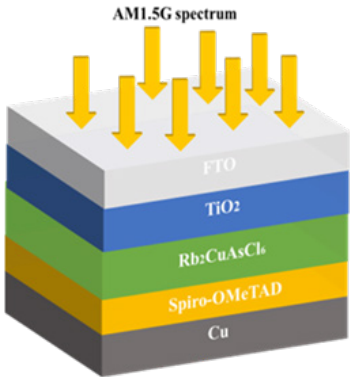

Figure 5. Schematic of the solar cell structure FTO/TiO_2/$Rb_2CuAsCl_6$/Spiro-OMeTAD/Cu.

A Spiro-OMeTAD (hole transport layer-HTL) combined with a titanium dioxide (TiO_2) electron transport layer-(ETL) is separated by the $Rb_2CuAsCl_6$ p-type absorber layer. Fluorine-doped tin oxide (FTO) serves as the front contact anode, while the cathode is composed of copper, which has a work function of 4.65 eV.

Table 3 presents the input parameters used in SCAPS-1D for each layer of the structure, including FTO, TiO_2, $Rb_2CuAsCl_6$, and Spiro-OMeTAD. The listed parameters include the effective density of states in the conduction and valence bands (N^c and Nv), defect density (N_t), band gap energy (E_g), electron affinity (χ), relative permittivity (ε_r), donor and shallow acceptor concentrations (N^d and N_a), electron and hole mobilities (μ_n and μ_p), and layer thicknesses. Furthermore, a uniform thermal velocity of 10^7 cm/s is assumed for both electrons and holes across all layers.

Table 3 The input parameters for SCAPS-1D using the $Rb_2CuAsCl_6$-based solar cell at 300 K.

Parameters	**FTO [33]**	**TiO_2 [34]**	**$Rb_2CuAsCl_6$**	**Spiro-OMeTAD [35]**
Thickness (μm)	0.5	0.1	0.4	0.02
E^g (eV)	3.5	3.2	1.09	2.8
χ (eV)	4.4	4	4.34	2.05
ε_r	9	9	6.75	3
NC ($1/cm^3$)	2×10^{18}	2×10^{18}	5.43×10^{18}	2.2×10^{18}
NV ($1/cm^3$)	1.8×10^{19}	1.8×10^{19}	4.13×10^{18}	1.8×10^{19}
μ_n (cm^2 V/s)	20	100	317	1×10^{-4}
μ_p (cm^2 V/s)	10	25	390	2×10^{-4}
N^D ($1/cm^3$)	10^{15}	10^{16}	10^{15}	0
N^A ($1/cm^3$)	0	0	10^{15}	10^{19}
N^t ($1/cm^3$)	10^{15}	10^{15}	10^{14}	10^{15}

In all our simulations, the temperature was controlled at 300 K, whereas the series (Rs) and shunt resistances (R_{sh}) were fixed at 1 Ω and 103 Ω, respectively, with an illumination intensity of 1000 W/m² under AM1.5G conditions.

Figure 6a displays the energy levels of the layers, whereas Figure 6b illustrates the band diagram of the FTO/TiO_2/$Rb_2CuAsCl_6$/Spiro-OMeTAD/Cu cell.

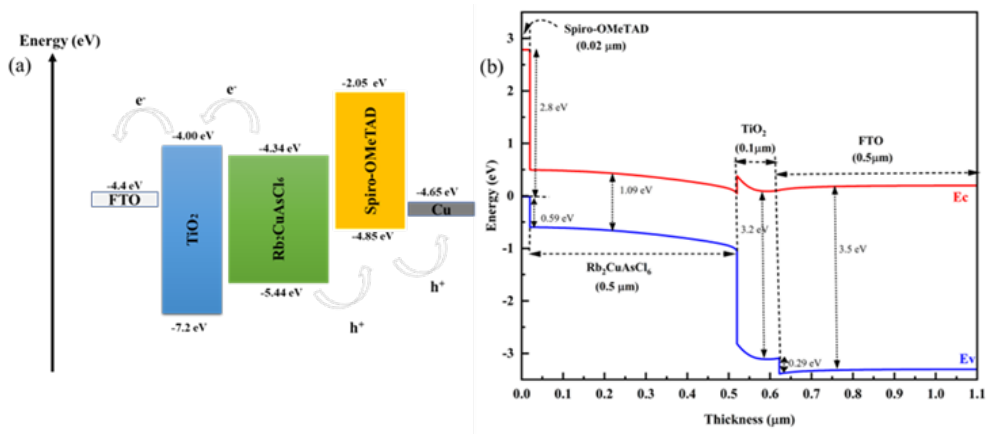

Figure 6. (a) band alignment (b) Diagram of the band energy determined by SCAPS simulation.

At the TiO_2/$Rb_2CuAsCl_6$ interface, the presence of a TiO_2 layer is associated with the formation of a built-in field and a notable VBO (Valence-Band Offset) of 2.9 eV. This configuration effectively impedes the movement of holes towards the TiO_2 layer. Conversely, the CBO (Conduction Band

Offset) of 0.52 eV at the TiO_2/$Rb_2CuAsCl_6$ interface is relatively low, facilitating efficient electron movement from $Rb_2CuAsCl_6$ to TiO_2 and subsequent collection by the FTO (fluorine doped tin oxide) electrode. Moreover, the substantial barrier at the $Rb_2CuAsCl_6$/HTL interface (Spiro-OMeTAD = 0.9 eV) and the intrinsic field at the $Rb_2CuAsCl_6$/hole transport layer interface, this can be ascribed to the organic HTL's higher least-occupied molecular orbital (LUMO) level, which facilitates efficient electron blocking. Holes can easily migrate to the electrode due to the small energy offset at the $Rb_2CuAsCl_6$/Spiro-OMeTAD interface, measured at 0.59 eV.

Figure 7a illustrates the variation in ETL (TiO_2) thickness within the range of 20 to 100 nm and examines its impact on PCE and FF. The results show that at thinner layers, particularly below 30 nm, both PCE and FF are reduced due to the increased prominence of defects. These defects create direct contact points between the perovskite and the cathode, leading to charge recombination. Furthermore, increasing the TiO_2 thickness mitigates recombination by providing more efficient charge transport pathways, thereby improving both PCE and FF. The performance stabilises at a thickness of approximately 100 nm.

Furthermore, the variation of PCE and FF as a function of HTL (Spiro-OMeTAD) thickness, as shown in Figure 7b, demonstrates that both parameters decrease linearly with increasing HTL thickness. This decline can be attributed to the introduction of bulk defects in thicker HTLs, which facilitate non-radiative recombination. Such recombination reduces the number of collected charge carriers, thereby adversely affecting both PCE and FF.

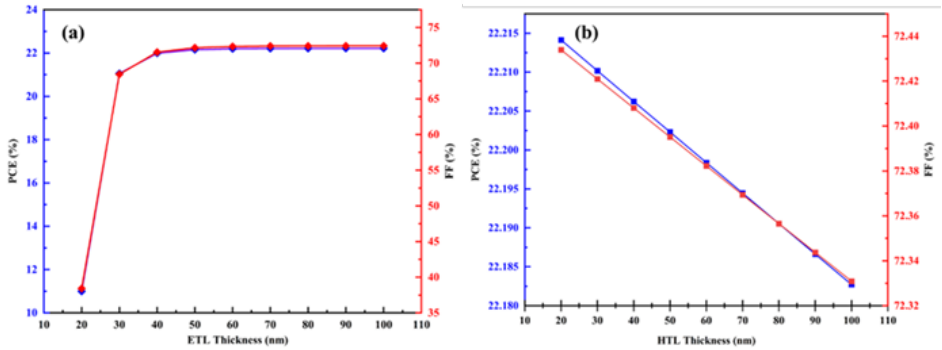

Figure 7. PCE and Fill Factor (FF) versus Thickness for (a) ETL Layer and (b) HTL Layer.

The PCE and FF of the absorber layer are optimized by varying its thickness from 300 nm to 1000 nm, as illustrated in Figure 8.

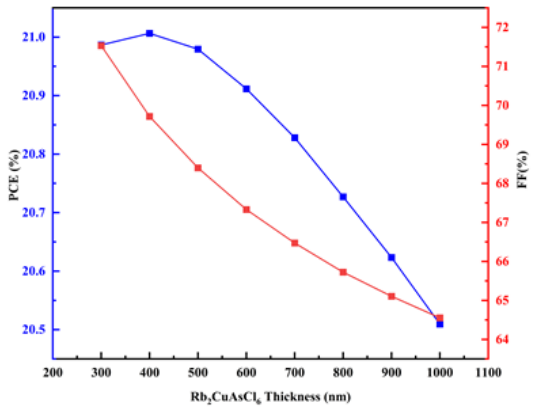

Figure 8. The effect of the absorber layer thickness on PCE and FF.

The PCE increased with thickness, reaching a maximum at 400 nm, with the highest efficiency recorded at 20.63%. However, beyond this optimal thickness, the PCE declined. Nevertheless, the

PCE decreased beyond this optimal thickness, as the perovskite thickness exceeded the carrier diffusion lengths for both electrons and holes, despite the enhanced generation of charge carriers, resulting in higher rates of recombination and, consequently, a decrease in efficiency. Moreover, the FF values fall dramatically with increasing $Rb_2CuAsCl_6$ layer thickness.

Numerous defect types, including vacancies, interstitials, Schottky, and Frenkel defects, can be observed in the perovskite layer. At high defect concentrations (N_t), the stability of perovskite solar cells (PSCs) is significantly reduced. In addition, high defect concentrations also affect carrier mobility by impeding the collection process, further reducing the fill factor and overall efficiency.

The effect of the absorber layer defect density on device performance was examined by modelling the system's efficiency across a range of absorber defect densities, from 10^{13} cm^{-3} to 10^{18} cm^{-3}. The power conversion efficiency (η) for each absorber defect density is shown in Figure 9, along with the J-V characteristics for each defect density. The results indicate a decrease in efficiency from 25.21% to 5.62% over this range.

The open-circuit voltage (V_{oc}) shows a clear decline, attributed to enhanced non-radiative recombination, which raises the saturation current (J_0) according to the formula[36]:

$$V_{oc} = \frac{nK_BT}{q} ln\left(\frac{J_{sc}}{J_0} + 1\right) \qquad (7)$$

where K_B is the Boltzmann constant, q is the elementary charge, J_{sc} is the short-circuit current density, J_0 is the saturation current density and n stands for the ideality factor.

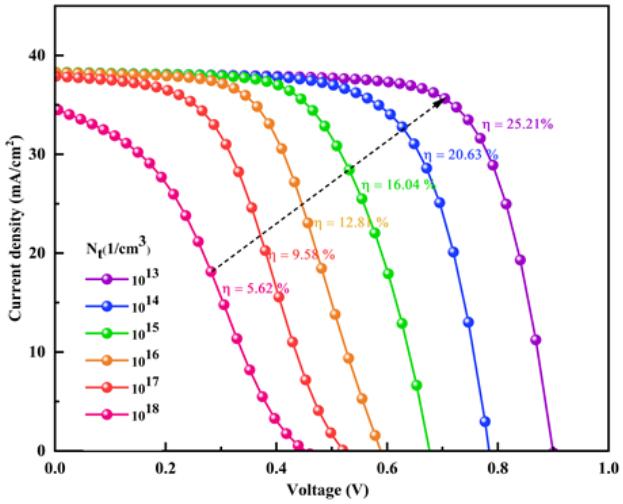

Figure 9. J-V characteristics for varying concentrations of absorber defects.

According to Table 4, $Rb_2CuAsCl_6$ exhibits a notable improvement in efficiency, characterized by higher $V_{oc,}$ J_{sc}, and fill factor (FF), compared to other lead-free double perovskites, such as $Cs_2CuBiBr_6$, Rb_2SnI_6, Cs_2BiAgI_6, and $Cs_2AgBiCl_6$-based solar cells. These further underscores its potential for future solar cell applications. Under an AM 1.5 solar spectrum, the maximum Shockley-Queisser efficiency limit for a single-junction solar cell is approximately 33% for a band gap of 1.4 eV. With a band gap of 1.09 eV, the efficiency of $Rb_2CuAsCl_6$-based solar cells in our study was 20.63%, corresponding to 62% of the theoretical limit.

Despite advancements, several challenges persist, including the occurrence of defects and contaminants during experimental fabrication. These defects serve as recombination centers in solar materials, thereby diminishing the efficiency of solar cells composed of this material.

Consequently, addressing these issues remains a key area of investigation within the scientific community.

Table 4. A comparative analysis of the single-junction solar cell results obtained in this work in relation to experimental and theoretical findings reported in previous research.

Device structure	Photovoltaic parameters				Type of research -Year	References
	V_{oc} (V)	J_{sc} (mA/cm^2)	FF (%)	η (%)		
ITO/Cu-NiO/$Cs_2AgBiBr_6$/C_{60}/BCP/Ag	1.01	3.19	69.2	2.23	Experimental-2018	[37]
ITO/SnO2/$Cs_2AgBiBr_6$/spiro-OMeTAD/Au	0.92	11.40	60.93	6.37	Experimental- 2022	[38]
ITO/ZnO/Cs_2BiAgI_6/CBTS/Au	1.08	23.76	83.78	21.59	Simulation-2022	[39]
ITO/WS_2/Rb_2SnI_6/CdTe/Ni	1.08	44.67	82.71	24.95	Simulation-2024	[40]
ITO/TiO_2/$Cs_2CuBiBr_6$/CBTS/Ni	0.71	35.62	77.52	19.65	Simulation- 2025	[41]
FTO/TiO_2/$Rb_2CuAsCl_6$/spiro-OMeTAD/Au	0.81	38.33	68.65	20.63	Simulation-2025	This work

4. CONCLUSION

The structural and optoelectronic characteristics of the lead-free double perovskites Rb_2CuAsZ_6 (Z = Br, Cl) were thoroughly analysed in this work. Formation energy calculations and the tolerance factor were used to assess structural stability. Using the HSE06 approach, indirect band gaps (Eg) of 0.64 eV and 1.09 eV were found for $Rb_2CuAsBr_6$ and $Rb_2CuAsCl_6$, respectively. Due to their high optical absorption coefficients (approximately 10^5 cm ^{1}), predominantly in the infrared-visible wavelength region, these materials exhibit significant potential as optoelectronic and photovoltaic materials.

Additionally, the use of a planar n-i-p PSC with an absorber layer composed of $Rb_2CuAsCl_6$ was proposed. By adjusting the absorber's defect density and the thicknesses of the hole transport layer (HTL), electron transport layer (ETL), and perovskite absorber layer, SCAPS-1D simulations were used to thoroughly analyse the performance of the PSC. The optimised device demonstrated a fill factor-(FF) of 68.65% and a power conversion efficiency-(PCE) of 20.63%.

Acknowledgment: The authors would like to acknowledge HPC-MARWAN for providing the cloud computing research facility, which is funded by the CNRST (National Centre for Scientific and Technical Research) in Rabat, Morocco. We also extend our appreciation to Professor Marc Burgelman of ghent university, Belgium, for kindly granting us access to the SCAPS-1d program.

REFERENCES

[1] T.D. Lee, A.U. Ebong, A review of thin film solar cell technologies and challenges, Renewable and Sustainable Energy Reviews 70 (2017) 1286–1297. https://doi.org/10.1016/j.rser.2016.12.028.

[2] G.M. Mustafa, A. Slam, S. Saba, N.A. Noor, M. Waqas Iqbal, A. Dahshan, Optoelectronic and thermoelectric characteristics of halide based double perovskites K2YAgX6 (X = Br, I) for energy storage applications, Polyhedron 229 (2023) 116184. https://doi.org/10.1016/j.poly.2022.116184.

[3] A. Augusto, J. Karas, P. Balaji, S.G. Bowden, R.R. King, Exploring the practical efficiency limit

of silicon solar cells using thin solar-grade substrates, J. Mater. Chem. A 8 (2020) 16599–16608. https://doi.org/10.1039/D0TA04575F.

[4] A. Kojima, K. Teshima, Y. Shirai, T. Miyasaka, Organometal Halide Perovskites as Visible-Light Sensitizers for Photovoltaic Cells, J. Am. Chem. Soc. 131 (2009) 6050–6051. https://doi.org/10.1021/ja809598r.

[5] H. Min, D.Y. Lee, J. Kim, G. Kim, K.S. Lee, J. Kim, M.J. Paik, Y.K. Kim, K.S. Kim, M.G. Kim, T.J. Shin, S. Il Seok, Perovskite solar cells with atomically coherent interlayers on SnO2 electrodes, Nature 598 (2021) 444–450. https://doi.org/10.1038/s41586-021-03964-8.

[6] M.A. Green, E.D. Dunlop, M. Yoshita, N. Kopidakis, K. Bothe, G. Siefer, X. Hao, Solar cell efficiency tables (Version 63), Progress in Photovoltaics 32 (2024) 3–13. https://doi.org/10.1002/pip.3750.

[7] B.P. Kore, M. Jamshidi, J.M. Gardner, The impact of moisture on the stability and degradation of perovskites in solar cells, Mater. Adv. 5 (2024) 2200–2217. https://doi.org/10.1039/D3MA00828B.

[8] A. Mera, G. Nazir, Q. Mahmood, N.A. Kattan, T. Alshahrani, A. Rehman, H. Sultana, M.A. Amin, H. Elhosiny Ali, The bandgap engineering of double perovskites Cs2CuSbX6 (X = Cl, Br, I) for solar cell and thermoelectric applications, Inorganic Chemistry Communications 148 (2023) 110303. https://doi.org/10.1016/j.inoche.2022.110303.

[9] Q. Mahmood, G.M. Mustafa, N.A. Kattan, T. Alshahrani, N. Sfina, A. Mera, Z. Hussain Shah, H.H. Somaily, S. Alharthi, M.A. Amin, Tunning of band gap of double perovskites halides Rb2CuSbX6 (X = Cl, Br, I) for solar cells and energy harvesting, Materials Science and Engineering: B 286 (2022) 116088. https://doi.org/10.1016/j.mseb.2022.116088.

[10] A.H. Slavney, T. Hu, A.M. Lindenberg, H.I. Karunadasa, A Bismuth-Halide Double Perovskite with Long Carrier Recombination Lifetime for Photovoltaic Applications, J. Am. Chem. Soc. 138 (2016) 2138–2141. https://doi.org/10.1021/jacs.5b13294.

[11] E.T. McClure, M.R. Ball, W. Windl, P.M. Woodward, Cs2 AgBiX6 (X = Br, Cl): New Visible Light Absorbing, Lead-Free Halide Perovskite Semiconductors, Chem. Mater. 28 (2016) 1348–1354. https://doi.org/10.1021/acs.chemmater.5b04231.

[12] Z. Deng, F. Wei, F. Brivio, Y. Wu, S. Sun, P.D. Bristowe, A.K. Cheetham, Synthesis and Characterization of the Rare-Earth Hybrid Double Perovskites: (CH3 NH3)2 KGdCl6 and (CH3 NH3)2 KYCl6, J. Phys. Chem. Lett. 8 (2017) 5015–5020. https://doi.org/10.1021/acs.jpclett.7b02322.

[13] T. Minemoto, M. Murata, Theoretical analysis on effect of band offsets in perovskite solar cells, Solar Energy Materials and Solar Cells 133 (2015) 8–14. https://doi.org/10.1016/j.solmat.2014.10.036.

[14] F. Liu, J. Zhu, J. Wei, Y. Li, M. Lv, S. Yang, B. Zhang, J. Yao, S. Dai, Numerical simulation: Toward the design of high-efficiency planar perovskite solar cells, Applied Physics Letters 104 (2014) 253508. https://doi.org/10.1063/1.4885367.

[15] H. Sabbah, Numerical Simulation of 30% Efficient Lead-Free Perovskite CsSnGeI3-Based Solar Cells, Materials 15 (2022) 3229. https://doi.org/10.3390/ma15093229.

[16] M. Burgelman, P. Nollet, S. Degrave, Modelling polycrystalline semiconductor solar cells, Thin Solid Films 361–362 (2000) 527–532. https://doi.org/10.1016/S0040-6090(99)00825-1.

[17] K.I. Ferdous Utsho, S.M.G. Mostafa, Md. Tarekuzzaman, M.S.M. Al-Saleem, N.I. Nahid, J.Y. Al-Humaidi, Md. Rasheduzzaman, M.M. Rahman, Md.Z. Hasan, Optimizing Cs2 CuBiBr6 double halide perovskite for solar applications: the role of electron transport layers in SCAPS-1D simulations, RSC Adv. 15 (2025) 2184–2204. https://doi.org/10.1039/D4RA08515A.

[18] K. Shivesh, I. Alam, A.K. Kushwaha, M. Kumar, S.V. Singh, Investigating the theoretical performance of Cs2TiBr6-based perovskite solar cell with La-doped BaSnO3 and CuSbS2 as the charge transport layers, Intl J of Energy Research 46 (2022) 6045–6064. https://doi.org/10.1002/er.7546.

[19] M. Mehrabian, M. Taleb-Abbasi, O. Akhavan, Effects of electron transport layer type on the performance of Pb-free Cs2AgBiBr6 double perovskites: a SCAPS-1D solar simulator–based study, Environ Sci Pollut Res 30 (2023) 118754–118763. https://doi.org/10.1007/s11356-023-30732-0.

[20] P. Giannozzi, S. Baroni, N. Bonini, M. Calandra, R. Car, C. Cavazzoni, D. Ceresoli, G.L. Chiarotti, M. Cococcioni, I. Dabo, A. Dal Corso, S. De Gironcoli, S. Fabris, G. Fratesi, R. Gebauer, U. Gerstmann, C. Gougoussis, A. Kokalj, M. Lazzeri, L. Martin-Samos, N. Marzari, F. Mauri, R. Mazzarello, S. Paolini, A. Pasquarello, L. Paulatto, C. Sbraccia, S. Scandolo, G. Sclauzero, A.P. Seitsonen, A. Smogunov, P. Umari, R.M. Wentzcovitch, QUANTUM ESPRESSO: a modular and open-source software project for quantum simulations of materials, J. Phys.: Condens. Matter 21 (2009) 395502. https://doi.org/10.1088/0953-8984/21/39/395502.

[21] D. Goldfarb, A family of variable-metric methods derived by variational means, Math. Comp. 24 (1970) 23–26. https://doi.org/10.1090/S0025-5718-1970-0258249-6.

[22] D.F. Shanno, Conditioning of quasi-Newton methods for function minimization, Math. Comp. 24 (1970) 647–656. https://doi.org/10.1090/S0025-5718-1970-0274029-X.

[23] J.P. Perdew, K. Burke, M. Ernzerhof, Generalized Gradient Approximation Made Simple, Phys. Rev. Lett. 77 (1996) 3865–3868. https://doi.org/10.1103/PhysRevLett.77.3865.

[24] J.P. Perdew, J.A. Chevary, S.H. Vosko, K.A. Jackson, M.R. Pederson, D.J. Singh, C. Fiolhais, Atoms, molecules, solids, and surfaces: Applications of the generalized gradient approximation for exchange and correlation, Phys. Rev. B 46 (1992) 6671–6687. https://doi.org/10.1103/PhysRevB.46.6671.

[25] A. Marini, C. Hogan, M. Grüning, D. Varsano, yambo: An ab initio tool for excited state calculations, Computer Physics Communications 180 (2009) 1392–1403. https://doi.org/10.1016/j.cpc.2009.02.003.

[26] H. El-assib, M. Alla, S. Tourougui, M. Alla, F. Elfatouaki, S.A. Dar, A. Chauhan, Naima, N. Chawki, N. Shrivastav, V. Manjunath, M. Rouchdi, B. Fares, High-performance optimization and analysis of $Cs_2CuSbCl_6$-Based lead-free double perovskite solar cells with theoretical efficiency exceeding 27 %, Renewable Energy 239 (2025) 122092. https://doi.org/10.1016/j.renene.2024.122092.

[27] V.M. Goldschmidt, Die Gesetze der Krystallochemie, Naturwissenschaften 14 (1926) 477–485. https://doi.org/10.1007/BF01507527.

[28] S.M. Alqahtani, A.Q. Alsayoud, F.H. Alharbi, Structures, band gaps, and formation energies of highly stable phases of inorganic ABX3 halides: A = Li, Na, K, Rb, Cs, Tl; B = Be, Mg, Ca, Ge, Sr, Sn, Pb; and X = F, Cl, Br, I, RSC Adv. 13 (2023) 9026–9032. https://doi.org/10.1039/D3RA00185G.

[29] W. Li, Z. Wang, X. Xiao, Z. Zhang, A. Janotti, S. Rajasekaran, B. Medasani, Predicting band gaps and band-edge positions of oxide perovskites using density functional theory and machine learning, Phys. Rev. B 106 (2022) 155156. https://doi.org/10.1103/PhysRevB.106.155156.

[30] Md.H. Miah, M.U. Khandaker, Md.B. Rahman, M. Nur-E-Alam, M.A. Islam, Band gap tuning of perovskite solar cells for enhancing the efficiency and stability: issues and prospects, RSC Adv. 14 (2024) 15876–15906. https://doi.org/10.1039/D4RA01640H.

[31] S. Zhao, K. Yamamoto, S. Iikubo, S. Hayase, T. Ma, First-principles study of electronic and optical properties of lead-free double perovskites Cs2NaBX6 (B = Sb, Bi; X = Cl, Br, I), Journal of Physics and Chemistry of Solids 117 (2018) 117–121. https://doi.org/10.1016/j.jpcs.2018.02.032.

[32] S. Ghosh, H. Shankar, P. Kar, Recent developments of lead-free halide double perovskites: a new superstar in the optoelectronic field, Mater. Adv. 3 (2022) 3742–3765. https://doi.org/10.1039/D2MA00071G.

[33] V. Deswal, S. Kaushik, R. Kundara, S. Baghel, Numerical simulation of highly efficient Cs2AgInBr6-based double perovskite solar cell using SCAPS 1-D, Materials Science and Engineering: B 299 (2024) 117041. https://doi.org/10.1016/j.mseb.2023.117041.

[34] G. Pindolia, S.M. Shinde, P.K. Jha, Optimization of an inorganic lead free RbGeI3 based perovskite solar cell by SCAPS-1D simulation, Solar Energy 236 (2022) 802–821. https://doi.org/10.1016/j.solener.2022.03.053.

[35] B.K. Ravidas, M.K. Roy, D.P. Samajdar, Investigation of photovoltaic performance of lead-free CsSnI3-based perovskite solar cell with different hole transport layers: First Principle Calculations and SCAPS-1D Analysis, Solar Energy 249 (2023) 163–173. https://doi.org/10.1016/j.solener.2022.11.025.

[36] A. Amjad, S. Qamar, C. Zhao, K. Fatima, M. Sultan, Z. Akhter, Numerical simulation of lead-free vacancy ordered Cs2 PtI6 based perovskite solar cell using SCAPS-1D, RSC Adv. 13 (2023) 23211–23222. https://doi.org/10.1039/D3RA04176J.

[37] W. Gao, C. Ran, J. Xi, B. Jiao, W. Zhang, M. Wu, X. Hou, Z. Wu, High-Quality Cs2 AgBiBr6 Double Perovskite Film for Lead-Free Inverted Planar Heterojunction Solar Cells with 2.2 % Efficiency, ChemPhysChem 19 (2018) 1696–1700. https://doi.org/10.1002/cphc.201800346.

[38] Z. Zhang, Q. Sun, Y. Lu, F. Lu, X. Mu, S.-H. Wei, M. Sui, Hydrogenated Cs2AgBiBr6 for significantly improved efficiency of lead-free inorganic double perovskite solar cell, Nat Commun 13 (2022) 3397. https://doi.org/10.1038/s41467-022-31016-w.

[39] M.K. Hossain, A.A. Arnab, R.C. Das, K.M. Hossain, M.H.K. Rubel, Md.F. Rahman, H. Bencherif, M.E. Emetere, M.K.A. Mohammed, R. Pandey, Combined DFT, SCAPS-1D, and wxAMPS frameworks for design optimization of efficient Cs2 BiAgI6 -based perovskite solar cells with different charge transport layers, RSC Adv. 12 (2022) 34850–34873. https://doi.org/10.1039/D2RA06734J.

[40] M.U. Alam, Md.K.I. Shifat, J.K. Modak, Md. Tarekuzzaman, Md.I. Haque, Md. Rasheduzzaman, M.A. Qader, R. Islam, Y. Arafat, Md.Z. Hasan, Improving the efficiency and performance of Rb2SnI6-based perovskite solar cells through comprehensive optimization: a numerical study, J Comput Electron 24 (2025) 41. https://doi.org/10.1007/s10825-024-02276-0.

[41] K.I. Ferdous Utsho, S.M.G. Mostafa, Md. Tarekuzzaman, M.S.M. Al-Saleem, N.I. Nahid, J.Y. Al-Humaidi, Md. Rasheduzzaman, M.M. Rahman, Md.Z. Hasan, Optimizing Cs2 CuBiBr6 double halide perovskite for solar applications: the role of electron transport layers in SCAPS-1D simulations, RSC Adv. 15 (2025) 2184–2204. https://doi.org/10.1039/D4RA08515A.

Solar Energy
And Sustainable Development
Refereed, biannual scientific journal issued by:
The Libyan Center for Solar Energy Research and Studies

Impact of Thermal Insulation on Vehicle Cabin Heat Loads and Energy Use

Hasnaa Oubnaki [1*], Charifa Haouraji [2], Ilham Mounir[3], Badia Mounir[4], Abdelmajid Farchi[5].

[1,2,5]IMMI Laboratory, Faculty of sciences and techniques, Hassan 1st University Settat, Morocco.
[3,4]LAPSSII Laboratory, Graduate School of Thechnology, Safi, Morocco.

E-*mail:* [1]h.oubnaki@uhp.ac.ma ,[2]haouraji.charifa@gmail.com ,[3]i.mounir@uca.ac.ma ,[4]b.mounir@uca.ac.ma , [5]abdelmajid.farchi1@gmail.com .

SPECIAL ISSUE ON:

The 1st International Conference on Sciences and Techniques for Renewable Enery and the Environment.

(STR2E 2025)

May 6-8, 2025 at FST-Al Hoceima-Morocco.

KEYWORDS

Automobile cabin; CFD; Energy; Thermal insulation; Optimization.

ABSTRACT

A car's passenger cabin's heating, ventilation, and air conditioning system is the biggest auxiliary charge, other than the primary traction charge. It may cause a vehicle with a motor to increase its energy consumption by up to 25%. The main factor contributing to the passenger compartment's excessive warmth is the car's exposure to maximum sun radiation. The goal of this study is to predict the thermal loads of the studied vehicle. Indeed, energy-saving measures such as using various types of insulating and storing materials have been implemented in this paper to predict their impact on the vehicle's interior thermal loads.

The inside fluid domain of a cabin was modeled and simulated using CATIA and FLUENT to investigate the temperature drop in the car's cabin based on their thermal characteristics. Computational Fluid Dynamics (CFD) simulations were used Using a vehicle cabin CFD model that was verified by climatic measurements, simulation information covering the full range of boundary conditions that affect thermal loads was methodically generated. The results strongly supported the CFD study, highlighting its effectiveness in analyzing the key parameters impacting the internal thermal loads. They reveal that aerogel polymers are distinguished by a significantly superior insulating capacity, reducing energy consumption by up to 40% compared to existing materials. These findings pave the way for adopting highly economical and well-optimized vehicles.

*Corresponding author.

DOI: https://doi.org/10.51646/jsesd.v14iSTR2E.803

This is an open access article under the CC BY-NC license (http://Attribution-NonCommercial 4.0 (CC BY-NC 4.0)).

أثر العزل الحراري على أحمال الحرارة في مقصورة المركبة واستهلاك الطاقة

حسناء أوبناكي , شريفة حوراجي , إلهام منير, بديعة منير, عبد المجيد الفارشي.

ملخص: يُعد نظام التدفئة والتهوية وتكييف الهواء في مقصورة ركاب السيارة أكبر شحنة مساعدة، بخلاف شحنة الجر الأساسية. وقد يتسبب ذلك في زيادة استهلاك السيارة ذات المحرك للطاقة بنسبة تصل إلى 25٪. والعامل الرئيسي الذي يساهم في ارتفاع درجة حرارة مقصورة الركاب هو تعرض السيارة لأقصى قدر من إشعاع الشمس. تهدف هذه الدراسة إلى التنبؤ بالأحمال الحرارية للمركبة المدروسة. في الواقع، تم تنفيذ تدابير توفير الطاقة مثل استخدام أنواع مختلفة من مواد العزل والتخزين في هذه الورقة للتنبؤ بتأثيرها على الأحمال الحرارية الداخلية للمركبة. تم نمذجة ومحاكاة المجال السائل الداخلي للمقصورة باستخدام CATIA وFLUENT للتحقيق في انخفاض درجة الحرارة في مقصورة السيارة بناءً على خصائصها الحرارية. تم استخدام عمليات محاكاة ديناميكا الموائع الحسابية (CFD) باستخدام نموذج ديناميكا الموائع الحسابية لمقصورة السيارة الذي تم التحقق منه من خلال القياسات المناخية، وتم توليد معلومات المحاكاة التي تغطي النطاق الكامل للظروف الحدودية التي تؤثر على الأحمال الحرارية بشكل منهجي. دعمت النتائج بقوة دراسة ديناميكا الموائع الحسابية، مسلطةً الضوء على فعاليتها في تحليل العوامل الرئيسية المؤثرة على الأحمال الحرارية الداخلية. وكشفت أنpolymer Aerogels تتميز بقدرة عزل فائقة، مما يقلل استهلاك الطاقة بنسبة تصل إلى 40 % مقارنةً بالمواد الحالية. تُمهد هذه النتائج الطريق لاعتماد مركبات اقتصادية للغاية ومُحسّنة.

الكلمات المفتاحية – كابينة السيارة؛ ديناميكا الموائع الحسابية؛ الطاقة؛ العزل الحراري؛ التحسين.

1. INTRODUCTION

Since almost all cars now have air conditioning, it has become a necessary element of contemporary automobiles [1]. During hot summer months, 5–15% of the energy needed for vehicle propulsion may be used for air cooling [2]. Drivers need warmth rather than cooling in colder climates. The range of the electric vehicle may be greatly reduced if direct electrical heating through resistive parts is powered by battery power [3]. For instance, cold weather can reduce an EV's range by up to 50% due to the energy required to heat both the cabin and the batteries [4].

In order to maximize the efficiency of the heating system in automobiles, it is critical to recognize that solar radiation and ambient temperature are important heat sources that impact passenger vehicles comfort [5]. Hence, controlling the flow of heat via the car's external surfaces is essential [6]. Indeed, the windows and interior wall surfaces allow solar radiation to enter the vehicle compartment both directly and indirectly. Due to this, the cabin air temperature increases [7].

Several investigations have examined how to anticipate the interior temperature of a car using models or experimental testing to improve thermal comfort [8]. Additionally, many studies address the characteristics of car surfaces, such as the kind of windows and walls, as well as the vehicle's overall design. A heating technique was developed by R. B. Farrington et al. [9] to quantify the energy of solar radiation that solar-reflective glazing rejects. Additionally, they took measurements of soak temperatures in several car models with various glass configurations. They also forecasted how improved glass will affect the vehicle's occupants' thermal comfort. C. Croitoru et al. [10] investigated comfort and thermal environment models for vehicles by combining thermal psychological models with cabin CFD simulations. However, they had to use manikins, which took a lot of time and money, because of computational limitations. J. W. Lee Lee et al. [11] investigated how temperature and airflow in an automobile cabin are affected by spectrum sun radiation. They discovered through CFD simulations that the spectrum distribution of light caused the temperature to rise by 3°C, emphasizing how crucial it is to take this effect into account for precise thermal conditions and airflow forecast. W. Huo et al. [12] investigated a car's cabin's thermal comfort using CFD, and assessed how the field synergy angle

affected heat distribution. They discovered that heat transmission performance is enhanced by a smaller synergy angle. H. Krishnaswamy et al. [13] investigate how vehicle structure affects air conditioning efficiency. They alter a small, low-cost Indian automobile by moving the air conditioner's outlet. I. Nastase et al. [14] investigate the thermal comfort of passengers in automobiles, with an emphasis on electric vehicles (EVs). They discuss current norms, ideas of thermal comfort, and the unique difficulties faced by EVs. They emphasize in their conclusion the necessity of modifying thermal comfort requirements to account for the particularities of EV cabins. Hariharan. C et al. [5] use CFD simulation to examine how a vehicle's HVAC system affects energy consumption. In order to lower cabin temperatures, they investigate the impact of window coverings and insulation. Based on HVAC settings, glazing characteristics, and climatic factors, A. Warey et al. [15] utilize CFD simulations to forecast thermal comfort in a car's cabin. Instead of depending on computationally costly simulations, they provide precise estimates of the Equivalent Homogeneous Temperature (EHT) and indicators like Predicted Mean Vote and Predicted Percentage of Dissatisfied. P. Bandi et al. [16] investigate how the temperature of a car cabin exposed to sunlight is affected by meteorological factors. They assess the driver position temperature and examine temperature cabin using CFD simulations.

Despite the large number of studies conducted on vehicle cabin thermal management, recent research still has a significant research lack, as the latest published study is that of Hariharan in 2022 [5], which lends our study a unique character and enhances its contribution to the corpus of current knowledge. As shown in figure 1, This study aims to determine the energy consumption for cabin temperature and examine the thermal performance of electric vehicle (EV) cabins. Evaluating the possible energy savings that could be attained by upgrading insulating materials is the goal. The findings of this study will aid in maximizing EV energy use, resulting in increased driving range and the sustainability of electric mobility as a whole. They will increase range, boost battery efficiency, and increase the sustainability of electric transportation in general.

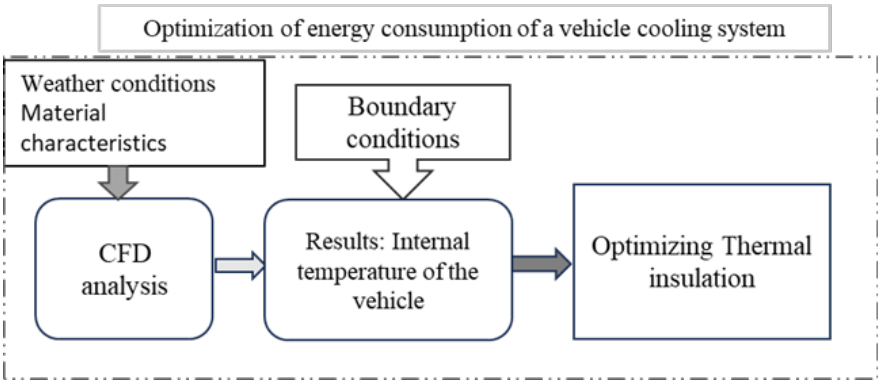

Figure 1. Overview of the temperature simulation method.

2. METHODOLOGY

2.1. Governing equations and boundary conditions

To study fluid behavior under different boundary conditions, including sun radiation, climate change, and ambient temperature, a CFD model of the fluid in the car cabin is constructed. Newton's second law and the conservation of mass, momentum, and energy equations are used to derive partial differential equations, and approximations are used to obtain numerical solutions. The Navier-Stokes equations, which are essential to CFD, explain the energy conservation of mass and momentum [17]:

Momentum Equation (1) (Conservation of Momentum):

$$\frac{\partial(pE)}{\partial t}+\nabla\cdot(\rho uu)=-\nabla\rho+\nabla\cdot\tau+f \quad (1)$$

where f stands for the external forces, p for the pressure, and τ for the stress tensor.
Continuity Equation (2) (Mass Conservation):

$$\frac{\partial\rho}{\partial t}+\nabla\cdot(\rho u)=0 \quad (2)$$

The velocity vector is represented by u, and the fluid's density is represented by ρ.

Energy Equation (3) (Conservation of Energy):

$$\frac{\partial(pE)}{\partial t}+\nabla\cdot(\rho Eu)=\nabla\cdot(k\nabla Tu)+\Phi \quad (3)$$

where viscous dissipation (Φ), thermal conductivity (E), temperature (T), and total energy (E). The CFD model receives time-dependent inputs from the models of solar radiation and ambient temperature. Two distinct thermal boundary conditions, convective and heat-flux were applied consistently throughout the analysis. The input parameters utilized in this study were selected in Morocco in order to ensure that the analysis represents relevant and realistic meteorological conditions [18]. The boundary conditions and surface material properties for the internal fluid flow were listed in Tables 1 and 2 [5].

Table 1. Vehicle Surface Boundary Conditions.

	Heat transfer coefficient ($W.m^{-2}.K^{-1}$)	**Internal Emissivity**	**Transmissivity**
Car wall	5	0.26	-
Glass	5	0.49	0.8

Table 2. Insulation material characteristics

Insulation Materials	**Thermal conductivity ($W.m^{-1}.K^{-1}$)**	**Density**	**Specific heat ($KJ.kg^{-1}K^{-1}$)(Kg/m^3)**
Polyurethane	0.19	1100	1.76
Thinsulate	0.030	240	1.3
Polymer Aerogels	0.040	300	1.2

2.2. Numerical methodology

An electric car's geometrical model was made for the analysis. The vehicle's pedals, storage spaces, nozzles, and other small components were left out. The vehicle's measurements (figure 2) are used to create the model in CATIA v5 software, which is then loaded.

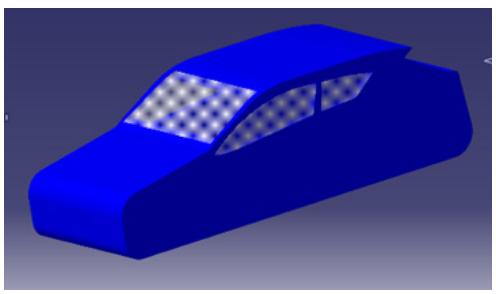

Figure 2. Car design in Catia v5.

The mesh test is also carried out. The spatial discretization method and convergence tolerances are examples of solver-specific parameters that have been chosen. These settings optimize calculation speeds while guaranteeing the simulations' correctness and stability.

Then the required simulations are run to look at the thermal loads in the passenger compartment. During mesh generation, the refining and sizing functions were used where necessary to provide a high-quality mesh and size ratio.

The analyzer used in this investigation has the following solver parameters: 3D; turbulent; incompressible; K-Epsilon turbulence model; solar heat addition modeled using the solar irradiation model. Below is an example of how to include a figure.

The CFD model uses wind speed, ambient temperature, and solar radiation as time-dependent inputs. It is necessary to specify the initial and boundary conditions in order to solve any computational fluid dynamics issue.

The mesh was created requiring several iterations for each of the transient simulation's 864-time steps (100 size) throughout a 24-hour period.

To validate the CFD simulations, the mesh quality was evaluated by checking skewness, aspect ratio and orthogonal quality parameters, in order to avoid numerical errors. Therefore, by reducing the residuals of the conservation equations, a convergence test was carried out. These tests verified that the mesh quality was at its best and that the outcomes were reliable.

2.3. Selection and Definition of the insulation materials studied and justification

This paragraph will discuss the criteria of insulating materials used in the automotive industry, highlighting their strengths and weaknesses. Table 2 provides a detailed overview of the thermal characteristics of these components, including parameters such as density, specific heat. and thermal conductivity, Polymer aerogel and Thinsulate are distinguished from Polyurethane by its extremely low thermal conductivity, providing optimum insulation and remarkable durability. On the other hand, although Thinsulate light weight, which results from its low density (240 Kg/m^3), is unquestionably advantageous, Polymer Aerogels stand out for having a little higher density (300 Kg/m^3), which guarantees stronger durability and long-lasting performance over time.

On the other hand, the use of this material insulant in vehicles has significant financial implications. The cost of aerogel families is estimated at between $\$40/m^2$ and $\$80/m^2$, while Thinsulate is generally more affordable. These initial investments can be offset by a significant reduction in energy consumption in the long term. In addition, aerogel and Thinsulate provide noticeably superior thermal performance than conventional insulation materials as rock wool or polyurethane foam (λ = 0.030-0.046 W.m-1.K-1) [5]. These materials offer extra advantages including durability and fire resistance together with more effective insulation that is thinner. The next section presents the results derived from the CFD study. These results highlight the efficacy of the suggested insulation materials by providing a thorough examination of their thermal performance.

3. RESULTS AND DISCUSSION

Figure 3 compares three insulating materials to illustrate how temperature changes inside a car cabin. Among these, polymers minimize temperature swings and have performant thermal insulation qualities and a remarkable ability to keep a steady internal temperature in spite of environmental fluctuations. It still has some vulnerability to heat peaks, though. In contrast, thinsulate stands out due to its thermal stability. Meanwhile, the third material shows the highest temperature fluctuations, highlighting its lower effectiveness compared to the other two materials.

The results indicate that the best insulation material tested in this study performed better than those reported by Hariharan [5].

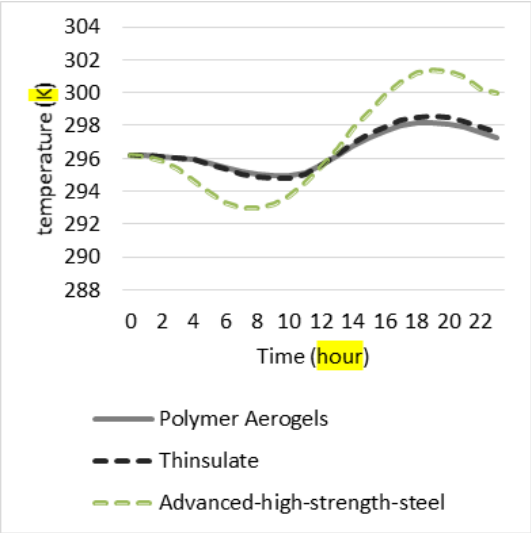

Figure 3. Temperature Variation Over Time for Different Insulation Materials.

The contrast between the highest temperatures attained in the car cabin for each type of insulation highlights the variations in their thermal performance. The highest temperature recorded for Polymer was 297.55 K, followed by Thinsulate at 298.006 K. These findings underscore the impact of insulation type on cabin temperature regulation and emphasize the importance of insulation selection for efficient thermal management in vehicles. These findings demonstrate how each kind of insulation impacts cabin thermal regulation and highlight the importance of insulation choices in vehicle thermal management.

Our primary goal is to maximize our car's energy usage, especially for the air conditioning system, which is one of the biggest energy users. Thus, our goal is to assess the chosen material's energy efficiency. In order to ascertain whether this insulation material actually lowers the vehicle's energy usage, we will use an electrical energy equation to model the air conditioning system:

$$E = P \cdot t \tag{4}$$

Where P is electric power and t is time.

Understanding the relationship between the air conditioner's electric power and coating is essential.

$$\mathrm{P} = \frac{Q}{COP} \tag{5}$$

Where:

Q: Thermal power required (in joules or watts if divided by time).

COP is the performance coefficient of the air conditioner.

Table 3. Energy Simulation Results (MJ).

Material	Energy (MJ)
Polyurethane	142.64
Polymers	78.73
Thinsulate	86.65

Based on Table 3, Polyurethane uses 142.64 MJ of energy when the air conditioner is turned

"ON". The compressor's electrical power usage drops to 78.73 MJ when Polymers are included in the simulation. In the same way, the third material lowers power usage to 86.65 MJ.

The findings demonstrate the substantial influence that insulating material selections have on air conditioning system energy usage and vehicle interior thermal management. When compared to polyurethane (301.52 K) and Thinsulate (298.006 K), the incorporation of Polymers allows for a significant decrease in energy consumption while preserving a lower interior temperature (297.55 K).

It is observed that the increase in indoor temperature coincides with the heat peaks of the day, as does the intensity of solar radiation. Thus, the indoor temperature curve is directly linked to fluctuations in outdoor temperature and the intensity of solar radiation. Similarly, the insulating materials have great importance.

4. CONCLUSION

This study emphasizes how important thermal insulation materials are for lowering the energy consumption of a car's heating, ventilation, and air conditioning (HVAC) system, which under some circumstances can account for up to 25% of the vehicle's overall energy consumption and is one of the biggest auxiliary energy demands.

Examining the thermal efficiency of several insulating materials helped to reduce the excessive heat accumulation in the passenger compartment, which was mostly caused by solar radiation. The car cabin's thermal loads were modeled and evaluated using CFD simulations with realistic boundary conditions.

The most efficient material, according to the results, is Aerogel Polymers, which achieved the lowest maximum cabin temperature of 297.55 K and drastically reduced energy usage to 78.73 MJ. On the other hand, polyurethane and Thinsulate used more energy and produced warmer cabin temperatures, indicating less effective performance.

These results highlight the possibility of enhancing energy efficiency and thermal comfort in automobiles using cutting-edge insulation materials like aerogel polymers. The usefulness of CFD simulation as a reliable method for assessing and forecasting the effects of different parameters on a vehicle's internal thermal loads is further demonstrated by this study. The knowledge acquired here serves as a basis for developing thermal management techniques in automobiles and for creating HVAC systems that use less energy. On the other hand, increasing energy efficiency by adding the suggested insulators also has a good environmental impact and indirectly lowers greenhouse gas emissions.

Although the findings of this paper make significant contributions to the field, they also highlight the need for a thorough investigation into material integration strategies in certain vehicle zones. This topic is a promising avenue for future research that would allow for a closer examination of the findings and the provision of practical answers to technical problems related to their implementation in current vehicle concepts.

In addition, future studies should examine how well these materials function in complicated geometries or unusual vehicle layouts.

Building on this, a study of the practical steps allowing their large-scale adoption in the automotive industry can be carried out. This includes the realization of real prototypes to evaluate their performance, the standardization of manufacturing processes to optimize costs.

Authors contribution: Hasnaa Oubnaki: Methodology, Software; Charifa Haouraji: Data. Ilham Mounir; Supervision, writing; Badia Mounir and Abdelmajid Farchi.: Validation, Writing-Reviewing and Editing.
Funding: No funding.
Data Availability Statement: Data is available upon reasonable request.
Conflicts of Interest: No conflict of interest.
Acknowledgements: The authors thank Abderahmane SAK for his support and contributions.

REFERENCES

[1] R. K. Shah, "Automotive Air-Conditioning Systems—Historical Developments, the State of Technology, and Future Trends," Heat Transf. Eng., vol. 30, no. 9, pp. 720–735, Aug. 2009, doi: 10.1080/01457630802678193.

[2] V. H. Johnson, "Fuel Used for Vehicle Air Conditioning: A State-by-State Thermal Comfort-Based Approach," presented at the Future Car Congress, Jun. 2002, pp. 2002-01–1957. doi: 10.4271/2002-01-1957.

[3] P. Lenzuni, P. Capone, D. Freda, and M. Del Gaudio, "Is driving in a hot vehicle safe?," Int. J. Hyperthermia, vol. 30, no. 4, pp. 250–257, Jun. 2014, doi: 10.3109/02656736.2014.922222.

[4] K. R. Kambly and T. H. Bradley, "Estimating the HVAC energy consumption of plug-in electric vehicles," J. Power Sources, vol. 259, pp. 117–124, Aug. 2014, doi: 10.1016/j.jpowsour.2014.02.033.

[5] Hariharan. C, Sanjana. S, Saravanan. S, S. Sundar. S, A. Prakash. S, and A. A. Raj. V, "CFD studies for energy conservation in the HVAC system of a hatchback model passenger car," Energy Sources Part Recovery Util. Environ. Eff., vol. 45, no. 2, pp. 4724–4741, Jun. 2023, doi: 10.1080/15567036.2019.1670757.

[6] Z.-K. Ding, Q.-M. Fu, J.-P. Chen, H.-J. Wu, Y. Lu, and F.-Y. Hu, "Energy-efficient control of thermal comfort in multi-zone residential HVAC via reinforcement learning," Connect. Sci., vol. 34, no. 1, pp. 2364–2394, Dec. 2022, doi: 10.1080/09540091.2022.2120598.

[7] F. Kader, M. A. Jinnah, and K.-B. Lee, "THE EFFECT OF SOLAR RADIATION ON AUTOMOBILE ENVIRONMENT THROUGH NATURAL CONVECTION AND MIXED CONVECTION," vol. 7, 2012, doi: 7(5):589-600.

[8] A. Alahmer, A. Mayyas, A. A. Mayyas, M. A. Omar, and D. Shan, "Vehicular thermal comfort models; a comprehensive review," Appl. Therm. Eng., vol. 31, no. 6–7, pp. 995–1002, May 2011, doi: 10.1016/j.applthermaleng.2010.12.004.

[9] R. B. Farrington, J. P. Rugh, and G. D. Barber, "Effect of Solar-Reflective Glazing on Fuel Economy, Tailpipe Emissions, and Thermal Comfort," presented at the International Body Engineering Conference & Exposition, Oct. 2000, pp. 2000-01–2694. doi: 10.4271/2000-01-2694.

[10] C. Croitoru, I. Nastase, F. Bode, A. Meslem, and A. Dogeanu, "Thermal comfort models for indoor spaces and vehicles—Current capabilities and future perspectives," Renew. Sustain. Energy Rev., vol. 44, pp. 304–318, Apr. 2015, doi: 10.1016/j.rser.2014.10.105.

[11] J. W. Lee, E. Y. Jang, S. H. Lee, H. S. Ryou, S. Choi, and Y. Kim, "Influence of the spectral solar radiation on the air flow and temperature distributions in a passenger compartment," Int. J. Therm. Sci., vol. 75, pp. 36–44, Jan. 2014, doi: 10.1016/j.ijthermalsci.2013.07.018.

[12] W. Huo, Y. Cheng, Y. Jia, and C. Guo, "Research on the thermal comfort of passenger compartment based on the PMV/PPD," Int. J. Therm. Sci., vol. 184, p. 107876, Feb. 2023, doi: 10.1016/j.ijthermalsci.2022.107876.

[13] H. Krishnaswamy, S. Muthukrishnan, S. Thanikodi, G. A. Arockiaraj, and V. Venkatraman, "Investigation of air conditioning temperature variation by modifying the structure of passenger car using computational fluid dynamics," Therm. Sci., vol. 24, no. 1 Part B, pp. 495–498, 2020, doi: 10.2298/TSCI190409397K.

[14] I. Nastase, P. Danca, F. Bode, C. Croitoru, L. Fechete, M. Sandu, & C. I. Coşoiu, "A regard on the thermal comfort theories from the standpoint of Electric Vehicle design — Review and perspectives," Energy Rep., vol. 8, pp. 10501–10517, Nov. 2022, doi: 10.1016/j.egyr.2022.08.186.

[15] A. Warey, S. Kaushik, B. Khalighi, M. Cruse, and G. Venkatesan, "Data-driven prediction of vehicle cabin thermal comfort: using machine learning and high-fidelity simulation results," Int. J. Heat Mass Transf., vol. 148, p. 119083, Feb. 2020, doi: 10.1016/j.ijheatmasstransfer.2019.119083.

[16] P. Bandi, N. P. Manelil, M. P. Maiya, S. Tiwari, and T. Arunvel, "CFD driven prediction of mean radiant temperature inside an automobile cabin using machine learning," Therm. Sci. Eng. Prog., vol. 37, p. 101619, Jan. 2023, doi: 10.1016/j.tsep.2022.101619.

[17] A. A. G. Maia, D. F. Cavalca, J. T. Tomita, F. P. Costa, and C. Bringhenti, "Evaluation of an effective and robust implicit time-integration numerical scheme for Navier-Stokes equations in a CFD solver for compressible flows," Appl. Math. Comput., vol. 413, p. 126612, Jan. 2022, doi: 10.1016/j.amc.2021.126612.

[18] Tadili (R.) and M. n. Bargach, "Une méthode d'estimation du rayonnement solaire global reçu par une surface inclinée : Application aux sites marocains," La Météorologie, vol. 8, no. 50, p. 46, 2005, doi: 10.4267/2042/34823.

Solar Energy
And Sustainable Development
Refereed, biannual scientific journal issued by:
The Libyan Center for Solar Energy Research and Studies

Robust Control for DFIG-Based WECS with ANN-Based MPPT

Achraf El Ouali [1*], Yassine Lakhal [2], Mohamed Benchagra[3], Hamid Chojaa[4], Mohamed Vall Ould Mohamed[5].

[1,2,3]Team of engineering and applied physics Higher school of Technology of Beni Mellal, Morocco.
[4]Higher School of Technology, Sidi Mohamed Ben Abdellah University, Fez 30000, Morocco.
[5]Department of Computer Engineering and Networks, College of Computer and Information Sciences, Jouf University, Sakaka 75471, Saudi Arabia.
[1,2]The Moroccan Association of Sciences and Techniques for Sustainable Development (MASTSD), Beni Mellal, Morocco.

E-*mail:* [1]elouali.hraf@gmail.com ,[2]lakhal.yassine.doc@gmail.com ,[3]m.benchagra@gmail.com , [4]hamid.chojaa@usmba.ac.ma , [5]medvall@ju.edu.sa .

SPECIAL ISSUE ON:

The 1St International Conference on Sciences and Techniques for Renewable Energy and the Environment.
(STR2E 2025)
May 6-8, 2025 at FST-Al Hoceima-Morocco.

KEYWORDS

Artificial Neural Network, Maximum Power Point Tracking, Integral Sliding Mode Control.

ABSTRACT

Mitigating nonlinearities and parameter fluctuations in high-rated wind energy systems is crucial for efficient energy conversion and grid integration. This paper presents a robust Integral Sliding Mode Control (ISMC) strategy for monitoring active and reactive power in a DFIG-based wind turbine. An artificial neural network based MPPT algorithm enhances speed control and addresses power fluctuations. The proposed ISMC ensures an optimal dynamic response to wind variations. Its performance is compared using a PI controller in Field-Oriented Control (FOC_PI) in MATLAB/Simulink on a wind system of 1.5 MW and tested under real-wind conditions. Simulation results confirm that ISMC outperforms FOC_PI in reference tracking, accuracy, dynamic behavior, and current distortion reduction.

*Corresponding author.

DOI: https://doi.org/10.51646/jsesd.v14iSTR2E.894

This is an open access article under the CC BY-NC license (http://Attribution-NonCommercial 4.0 (CC BY-NC 4.0)).

التحكم المتين في أنظمة تحويل طاقة الرياح القائمة على المولد الحثي مزدوج التغذية مع تعقب نقطة القدرة القصوى المعتمد على الشبكات العصبية الاصطناعية

أشرف الوالي, ياسين لكحل, محمد بنشكرة, حميد شوجاع, محمد فال ولد محمد.

ملخص: يُعدّ التخفيف من اللاخطيات وتغيرات المعلمات في أنظمة طاقة الرياح ذات القدرة العالية أمرًا بالغ الأهمية لتحقيق تحويل فعال للطاقة والتكامل مع الشبكة. يقدم هذا البحث استراتيجية تحكم قوية تعتمد على التحكم بالانزلاق التكاملي (ISMC) لمراقبة القدرة الفعالة وغير الفعالة في توربينات الرياح المعتمدة على المولد غير المتزامن ذو التغذية المزدوجة (DFIG). يعزز خوارزمية التتبع الأقصى لنقطة القدرة (MPPT) القائمة على الشبكات العصبية الاصطناعية من التحكم في السرعة ويعالج تقلبات القدرة. يضمن التحكم بالانزلاق التكاملي (ISMC) استجابة ديناميكية مثلى لتغيرات الرياح. يتم مقارنة أدائه باستخدام متحكم PI في التحكم الموجه للحقل (FOC-PI-) في بيئة Matlab/Simulink على نظام رياح بقدرة 1.5 ميجاواط، وتم اختباره في ظروف رياح حقيقية. تؤكد نتائج المحاكاة أن ISMC يتفوق على FOC-PI في تتبع الإشارة المرجعية، والدقة، والسلوك الديناميكي، وتقليل تشوه التيار.

الكلمات المفتاحية – الشبكات العصبية الاصطناعية، تعقب نقطة القدرة القصوى، التحكم بالانزلاق المتكامل.

1. INTRODUCTION

The increasing global demand for electricity, the depletion of fossil fuel resources, and the escalating impacts of global warming have intensified the search for sustainable and renewable energy solutions such as wind and solar power [1,2,3].

Among these, Wind Energy Conversion Systems (WECS) have gained significant attention due to their ability to provide clean and efficient energy. However, the nonlinear and fluctuating nature of wind speed presents a major challenge in maximizing energy extraction, necessitating the implementation of advanced control strategies [4,5,6]. To enhance energy capture, this study proposes an intelligent neural network-based Maximum Power Point Tracking (MPPT) control method especially designed to optimize power extraction under varying wind conditions. Unlike conventional MPPT techniques, which may struggle with dynamic wind variations, the proposed method leverages artificial intelligence to improve response time, robustness, and overall efficiency [7,8,9].

Doubly-Fed Induction Generators (DFIGs) are widely employed in WECS due to their robustness, durability, and ability to independently control active and reactive power, even under variable wind speeds [10,11].

However, achieving optimal performance requires efficient control strategies to regulate stator-generated power while ensuring a unity power factor. Among nonlinear control techniques, Sliding Mode Control (SMC) has proven to be a powerful approach for enhancing system performance [12]. Despite its advantages, traditional SMC suffers from chattering, a major drawback caused by discontinuous control action. To address this issue, this work introduces an Integral Sliding Mode Control (ISMC) strategy, which significantly reduces chattering while maintaining high dynamic performance and robustness. The main contributions of this paper are summarized as follows:

- The development of an intelligent MPPT strategy based on neural networks, applied on a wind turbine model described in figure1 ensuring optimal power extraction from wind energy.
- The implementation of an enhanced ISMC approach for DFIG-based WECS, effectively mitigating chattering effects and improving system stability.
- A comparative analysis between traditional SMC and the proposed ISMC, demonstrating the

advantages of the improved control methodology through numerical simulations.

This paper is structured as follows: Section 2 presents the dynamic modeling of the wind energy conversion system; Section 3 describes the configuration of the control strategies; Section 4 discusses the simulation results, providing a comparative analysis of the different control approaches; and, finally, Section 5 sums up the research findings and highlights future research prospects.

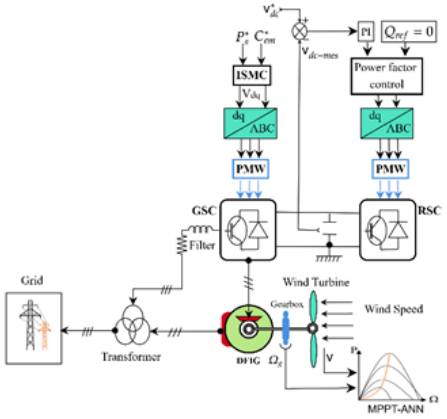

Figure 1. Diagrammatic Representation of the Studied System.

2. TURBINE MODEL

The wind turbine is characterized by the following expressions [2]:

$$P_t = \frac{1}{2}\rho\pi R^2 V^3 C_P(\lambda,\beta) \qquad (1)$$

In this work, the variations of Cp (λ,β) are modeled by the following equation.

$$\begin{cases} Cp(\lambda,\beta) = 0.5\left(\frac{116}{\lambda i} - 0.4\beta - 5\right)exp\left(\frac{-21}{\lambda i}\right) \\ \qquad\qquad +0.0068\,\lambda \\ \frac{1}{\lambda i} = \frac{1}{\lambda + 0.08\beta} - \frac{0.035}{\beta^3 + 1} \qquad ; \qquad \lambda = \frac{\Omega_t R}{V} \end{cases} \qquad (2)$$

2.1. MPPT WITH SPEED CONTROL

Maximizing WECS output power and performance requires MPPT. Additionally, a speed controller regulates rotor speed by imposing the necessary electromagnetic torque. The MPPT method generates the reference torque, to maintain the angular speed near its setpoint. Figure 2 illustrates the MPPT strategy.

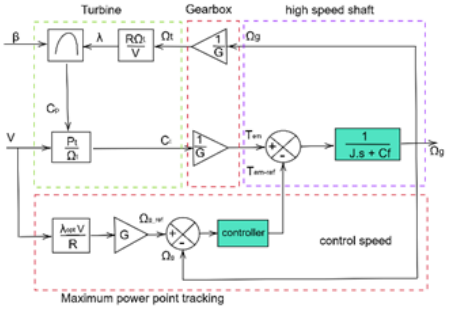

Figure 2. Integration of MPPT methodology.

2.2. ARTIFICIAL NEURAL NETWORKS (ANN)

The ANN model is inspired by the human brain, with interconnected neurons representing the nervous system. Each connection has a weight, similar to synapses. The study (detailed in Figure 3) uses a static Multi-Layer Perceptron (MLP) network, composed of input, hidden, and output layers arranged in a feed-forward style. The input layer processes sensor data, while hidden neurons are placed between the input and output layers.

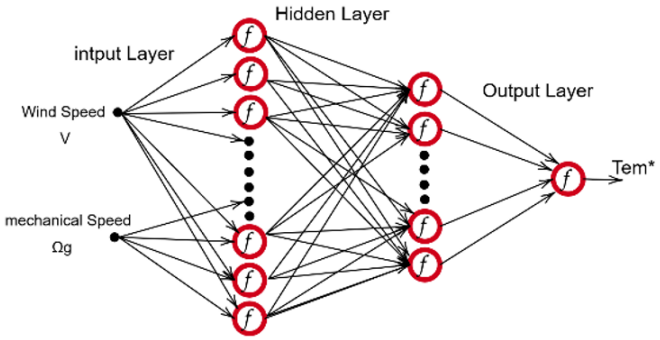

Figure 3. ANN Internal architecture.

3. DFIG MODEL

With respect to the dq Park reference frame, the DFIG's dynamic equations including the voltage equations, the flux equations, and the active and reactive powers' equations are defined by the equations (3) and (4), respectively, as follows [2,6]:

$$\begin{cases} V_{sd} = R_s i_{sd} + \dfrac{d}{dt}\phi_{sd} - \omega_s \phi_{sq} \\ V_{sq} = R_s i_{sq} + \dfrac{d}{dt}\phi_{sq} + \omega_s \phi_{sd} \\ V_{rd} = R_r i_{rd} + \dfrac{d}{dt}\phi_{rd} - (\omega_s - \omega_r)\phi_{rq} \\ V_{rq} = R_r i_{rq} + \dfrac{d}{dt}\phi_{rq} + (\omega_s - \omega_r)\phi_{rd} \end{cases} \quad (3)$$

$$\begin{cases} P_s = \dfrac{3}{2} Re\left\{\vec{V}_s \times \vec{I}_s^*\right\} = \dfrac{3}{2}\left(V_{sd} i_{sd} + V_{sq} i_{sq}\right) \\ Q_s = \dfrac{3}{2} Im\left\{\vec{V}_s \times \vec{I}_s^*\right\} = \dfrac{3}{2}\left(V_{sq} i_{sd} - V_{sd} i_{sq}\right) \end{cases} \quad (4)$$

4. SUGGESTED ISMC TECHNIQUE

Sliding Mode Control is a robust strategy known for its high efficiency and reliability in both transient and steady states, especially against system nonlinearities and disturbances [13,14]. It uses a discontinuous signal to drive the system to the sliding surface. However, the chattering phenomenon limits its use. This research develops an Integral Sliding Mode regulation technique to reduce chattering and regulate powers of DFIG [15].
The state representation of the DFIG is given by the equations:

$$\dot{X} = \mathrm{f}(x,t) + \mathrm{g}(x,t)u \tag{5}$$

$$f(x,t) = \begin{bmatrix} -\dfrac{R_r}{(\sigma L_r)^2}\left(\sigma L_r i_{rd} + \dfrac{MV_{sq}}{\omega_s L_S}\right) + \dfrac{R_r M \psi_{sd}}{L_S(\sigma L_r)^2} \\ +\dfrac{\omega_r}{\sigma L_r}\left(\sigma L_r i_{rq} + \dfrac{M}{\omega_s L_s} V_{sd}\right) \\ -\dfrac{R_r}{(\sigma L_r)^2}\left(\sigma L_r i_{rq} + \dfrac{MV_{sd}}{\omega_s L_s}\right) \\ +\dfrac{R_r M \psi_{sq}}{L_s(\sigma L_r)^2} + \dfrac{\omega_r}{\sigma L_r}\left(\sigma L_r i_{rd} + \dfrac{M}{\omega_s L_s} V_{sq}\right) \end{bmatrix} \tag{6}$$

$$g(x,t) = \begin{bmatrix} \dfrac{1}{\sigma L_r} & 0 \\ 0 & \dfrac{1}{\sigma L_r} \end{bmatrix} \tag{7}$$

Where : $X = \begin{bmatrix} i_{rd} & i_{rq} \end{bmatrix}$

$$\begin{cases} S_d = e_d(t) + \alpha_d e_I(t) \\ S_q = e_q(t) + \alpha_q e_I(t) \end{cases} \tag{8}$$

$$\begin{cases} \dot{S}_d = \dot{e}_d(t) + \alpha_d \dot{e}_I(t) = 0 \\ \dot{S}_q = \dot{e}_q(t) + \alpha_q \dot{e}_I(t) = 0 \end{cases} \tag{9}$$

$$\begin{cases} \dot{i}_{rd} - \dot{i}_{rd-ref} + \alpha_d \dot{e}_I(t) = 0 \\ \dot{i}_{rq} - \dot{i}_{rq-ref} + \alpha_q \dot{e}_I(t) = 0 \end{cases} \tag{10}$$

$$\begin{bmatrix} U_{rd} \\ U_{rq} \end{bmatrix} = g^{-1} \begin{bmatrix} \dot{i}_{rd-ref} - f_1 - \alpha_d sign(e_d(t)) \\ \dot{i}_{rq-ref} - f_2 - \alpha_q sign(e_q(t)) \end{bmatrix} \tag{11}$$

$$V = \frac{1}{2} S_{dq}^T S_{dq} \tag{12}$$

The derivative of (12) yields:

$$\dot{V} = \frac{S_d}{\sigma L_r}\left(\dot{i}_{rd-ref} - f_1 - \alpha_d sign(e_d(t))\right)$$

$$+\frac{S_q}{\sigma L_r}\left(\dot{i}_{rq-ref} - f_2 - \alpha_q sign(e_q(t))\right)$$

$$+\frac{S_q}{\sigma L_r}\gamma_q - \frac{S_q}{\sigma L_r}\alpha_q sign\left(e_q(t)\right) \qquad (13)$$

$$+\frac{S_q}{\sigma L_r}\gamma_q - \frac{S_q}{\sigma L_r}\alpha_q sign\left(e_q(t)\right) \qquad (13)$$

5. RESULTS AND DISCUSSIONS

The simulation evaluation of this sub-section employs a 1.5 MW DFIG model-based wind turbine. Figure 4 shows the simulated wind speed profile, which ranges from 7 to 9 m/s. Figures 5 and 6 show real-time variations of the power coefficient and TSR. At a 0° angle β, the power coefficient reaches its optimal value of 0.477, corresponding to the optimal TSR of λopt =8.14. Figure 7 shows that the ANN-MPPT controller keeps the DFIG's rotor speed close to the critical synchronous speed, following real-time data with no overshoot, demonstrating efficient and effective control under hyper- and hypo-synchronous conditions.

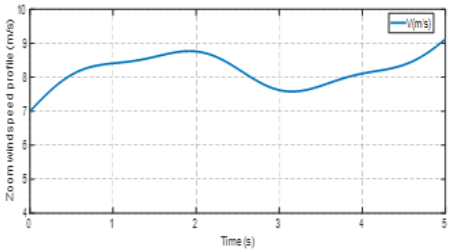

Figure 4. Wind speed

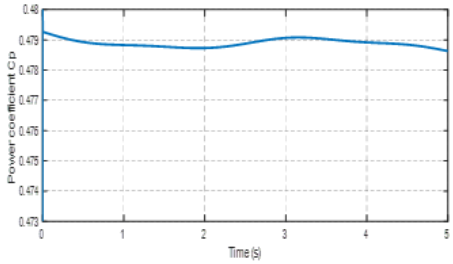

Figure 5. Coefficient Cp

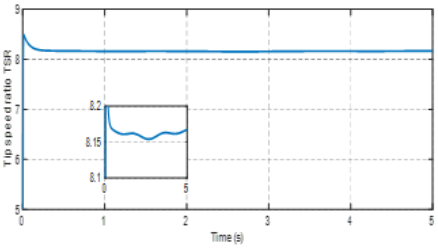

Figure 6. TSR

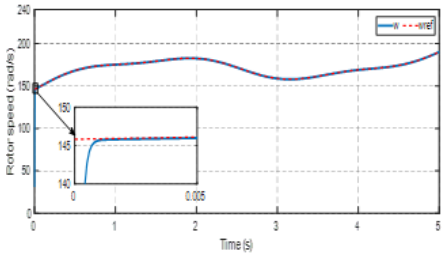

Figure 7. Rotor speed

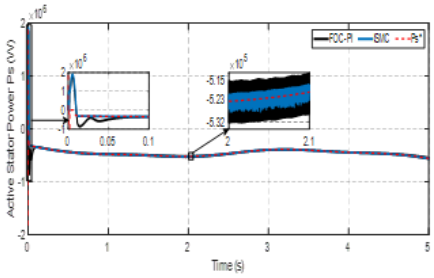

(a)

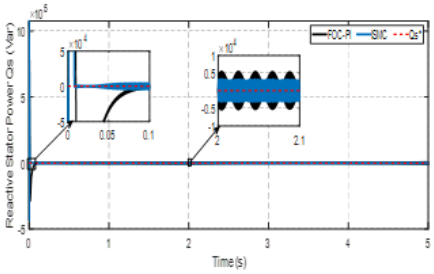

(b)

Figure 8. Stators Powers: (a) Ps, (b) Qs

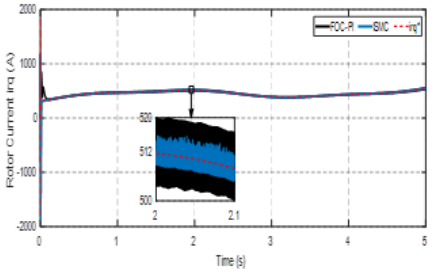

(a)

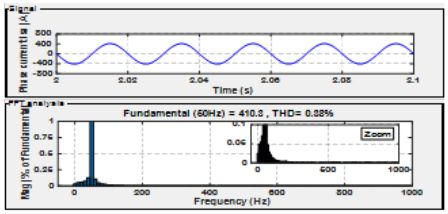

(a)

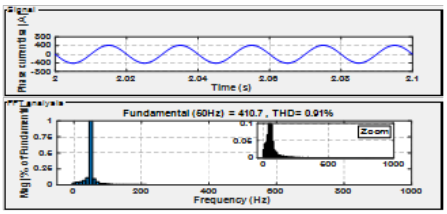

(b)

Figure 10. THD: (a) FOC_PI and (b) ISMC.

Figures 10(a) and 10(b) display the THD spectral analysis of the stator current for the 'a' phase, comparing the FOC_PI and ISMC controllers. Using FFT for frequency domain analysis, the FOC_PI shows a THD of 0.91%, while the ISMC significantly reduces it to 0.38%, demonstrating that the ISMC effectively minimizes current harmonics.

Table 1. Evaluation of FOC_PI vs adaptive ISMC.

Performance	FOC used PI	ISMC
Response time (s)	0.403	0.294
THD i_sa (%)	0.91	0.38
Rise time (s)	0.268	0.196
Set point tracking	Good	Very Good

Table 1 compares the ISMC and FOC_PI in terms of static error, response time, THD of Isa current, and set-point tracking, showing significant improvements with the ISMC, including reduced harmonics, minimal static errors, faster response, and better set-point accuracy. This makes it suitable for the field of wind turbines [16].

6. CONCLUSION

This study introduces the DFIG and turbine model. It implements an MPPT strategy with an ANN-based speed controller, which efficiently tracks peak power. ISMC and FOC_PI controllers are applied to regulate the DFIG's power flow components, with simulation results showing that ISMC outperforms FOC_PI in accuracy, reduced current distortion, improved dynamics, and better reference tracking. Using FFT for frequency domain analysis, the FOC_PI shows a THD of 0.91%, while the ISMC significantly reduces it to 0.38%, demonstrating that the ISMC effectively minimizes current harmonics. This makes it suitable for analyzing dynamic instabilities in wind energy generation.

Authors contribution: Achraf El Ouali : Conceptualization, Data collection, Writing – original draft. Yassine Lakhal : Supervision Writing – review & editing. Mohamed Benchagra : Formal analysis, Writing – review & editing. Hamid Chojaa : Formal analysis, Conceptualization, Writing – original draft, Methodology, Supervision. Mohamed Vall O. Mohamed : review & editing.
Funding: The authors are warmly grateful to the support of "The Moroccan Association of Sciences and Techniques for Sustainable Development (MASTSD), Beni Mellal, Morocco.
Data Availability Statement: The data that support the findings of this study are available from the corresponding au-thor upon reasonable request.
Conflicts of Interest: The authors declare no conflicts of interest.
Acknowledgements: The authors would like to thank the organizers of the 1st International Conference on Sciences and Techniques for Renewable Energy and the Environment, held from May 6th to 8th, 2025, at the Faculty of Sciences and Techniques, Al Hoceima, Morocco, for their valuable support and insightful discussions during this research.

REFERENCES

[1] H. Chojaa, A. Derouich, O. Zamzoum, A. Watil, M. Taoussi, A. Y. Abdelaziz, Z. M. Salem Elbarbary, and M. A. Mossa, "Robust Control of DFIG-Based WECS Integrating an Energy Storage System With Intelligent MPPT Under a Real Wind Profile," IEEE Access, vol. 11, pp. 90065–90083, 2023, doi: 10.1109/ACCESS.2023.3306722.

[2] Y. Sahri, S. Tamalouzt, F. Hamoudi, S. Lalouni, and M. Bajaj, "New intelligent direct power control of DFIG-based wind conversion system by using machine learning under variations of all operating and compensation modes," Energy Reports, vol. 7, pp. 6394–6412, 2021, doi: 10.1016/j.egyr.2021.09.042.

[3] Y. Lakhal, M. Haiek, F. Z. Baghli, Y. Ait El Kadi, M. Benchagra, and D. Sarsri, "Smart flow control of an airfoil with trailing edge flap for wind turbines using a fuzzy logic strategy," International Journal on Energy Conversion (IRECON), vol. 12, no. 5, p. 195, 2024, doi: 10.15866/irecon.v12i5.25100.

[4] I. Sami, S. Ullah, Z. Ali, N. Ullah, and J.-S. Ro, "A Super Twisting Fractional Order Terminal Sliding Mode Control for DFIG-Based Wind Energy Conversion System," Energies, vol. 13, no. 9, 2020, doi: 10.3390/en13092158.

[5] Y. Djeriri, A. Meroufel, and A. Massoum, "Artificial neural network based direct torque control of doubly fed induction generator," International Journal of Electrical Power & Energy Systems, vol. 49, pp. 234–242, 2013, doi: 10.1016/j.ijepes.2012.12.019.

[6] J. Bhukya, "Enhancing power system stability in wind-integrated networks through coordinated fuzzy logic control of PSS and POD for sustainable energy futures," International Journal of Ambient Energy, vol. 45, no. 1, 2024, doi: 10.1080/01430750.2024.2391096.

[7] M. Fdaili, A. Essadki, and T. Nasser, "Comparative analysis between robust SMC & conventional PI controllers used in WECS based on DFIG," International Journal of Renewable Energy Research (IJRER), vol. 7, no. 4, pp. 1795–1803, 2017, doi: 10.20508/ijrer.v7i4.6441.g7267.

[8] S. Karthikeyan, C. Ramakrishnan, "A hybrid fuzzy logic-based MPPT algorithm for PMSG-based variable speed wind energy conversion system on a smart grid," Energy Storage and Saving, Volume 3, Issue 4, Pages 295-304, 2024, doi : 10.1016/j.enss.2024.08.001.

[9] A. El Ouali, Y. Lakhal, M. Benchagra, H. Chojaa, and S. Samagassi, "Evaluating the impact of drivetrain vibrations on MPPT control performance in horizontal axis wind turbines," E3S Web of Conferences, vol. 582, p. 03001, 2024, doi: 10.1051/e3sconf/202458203001.

[10] A. Zanelli, J. Kullick, H. Eldeeb, G. Frison, C. Hackl, and M. Diehl, "Continuous Control Set Nonlinear Model Predictive Control of Reluctance Synchronous Machines," arXiv preprint arXiv:1910.10681, 2019.

[11] G. Han, L. Zhang, D. Wang, and X. Zhao, "Speed synchronization control of dual-SRM drive with ISMC-based cross coupling control strategy," IEEE Transactions on Transportation Electrification, vol. 9, no. 2, pp. 2524–2534, 2023, doi: 10.1109/TTE.2022.3208230.

[12] R. Subramaniam and Y. H. Joo, "Passivity-based fuzzy ISMC for wind energy conversion systems with PMSG," IEEE Transactions on Systems, Man, and Cybernetics: Systems, vol. 51, no. 4, pp. 2212–2220, 2021, doi: 10.1109/TSMC.2019.2930743.

[13] S. Rajendran, D. Jena, M. Diaz, J. Rodriguez, " Design of modified complementary terminal sliding mode controller for wind turbine at region II using a two-mass model, " Results in Engineering, Volume 24, 103026, ISSN 2590-1230, 2024, doi: 10.1016/j.rineng.2024.103026.

[14] L. Xiong, P. Li, M. Ma, Z. Wang, and J. Wang, "Output power quality enhancement of PMSG with fractional order sliding mode control," International Journal of Electrical Power & Energy Systems, vol. 115, p. 105402, 2020, doi: 10.1016/j.ijepes.2019.105402.

[15] S. Hassan, B. Abdelmajid, Z. Mourad, S. Aicha, and B. Abdennaceur, "PSO-Backstepping controller of a grid connected DFIG based wind turbine," International Journal of Electrical and Computer Engineering, vol. 10, no. 1, pp. 856–867, 2020, doi: 10.11591/ijece.v10i1.pp856-867.

Solar Energy
And Sustainable Development
Refereed, biannual scientific journal issued by:
The Libyan Center for Solar Energy Research and Studies

Analysis of the Thermal Response of a Floor Heating System Incorporating a Phase Change Material

Afaf Charraou[1*], Mohamed Errebii[2], Amina Mourid[3], Rachid Saadani[4], Miloud Rahmoune[5], Mustapha El Alami[6].

[1,3,4,5]Laboratory of Advanced Materials Studies and Applications, FS-EST, Moulay Ismail University, Meknes, Morocco.
[2,6]Advanced Materials and Thermal Physics Laboratory (LPMAT), FS Ain Chock, Hassan II University of Casablanca, Morocco.

E-*mail:* [1]afaf.charraou@gmail.com ,[2]errebii.mohammed@gmail.com ,[3]mouridamina@gmail.com , [4]rachidsaadani@gmail.com , [5]rahmoune@umi.ac.ma , [6]elalamimus@gmail.com .

SPECIAL ISSUE ON:

The 1St International Conference on Sciences and Techniques for Renewable Energy and the Environment.
(STR2E 2025)
May 6-8, 2025 at FST-Al Hoceima-Morocco.

KEYWORDS

Floor heating system; Latent storage; Phase Change Materials (PCM); Parametric analysis, Energy storage.

ABSTRACT

The rapid urbanization and the increasing demand for indoor comfort have resulted in a rise in energy consumption and a negative impact on the environment within the building sector. A promising approach to improving energy efficiency is the integration of phase change materials (PCM) into underfloor heating systems. This study aims to assess the impact of PCM integration on the thermal and energy performance of a hydronic floor heating system. To achieve this objective, a two-dimensional numerical model was developed using COMSOL Multiphysics software. The finite element method, combined with the effective heat capacity approach, was employed to accurately simulate the thermal behavior of the system.

The influence of several parameters, such as PCM type, thickness, and position within the floor structure, was analyzed to optimize system performance. The results reveal that integrating a 3 cm thick salt hydrate-based PCM, with a water supply temperature of 40 °C, significantly improves the thermal inertia of the floor. This configuration ensures a comfortable temperature (~27 °C) even after the heating system is turned off, with a time lag of 17 hours compared to a floor heating system without PCM. These findings highlight the potential of PCM in underfloor heating systems, offering an effective solution to reduce energy consumption in buildings while maintaining optimal thermal comfort.

*Corresponding author.

DOI: https://doi.org/10.51646/jsesd.v14iSTR2E.895

This is an open access article under the CC BY-NC license (http://Attribution-NonCommercial 4.0 (CC BY-NC 4.0)).

تحليل الأداء الحراري لنظام التدفئة الأرضية المدمج بمادة متغيرة الطور

عفاف شراو، محمد الزبيعي، أمينة موريد، رشيد السعداني، ميلود رحمون، مصطفى العلمي.

ملخص: أدى التحضر السريع وزيادة الطلب على الراحة الداخلية إلى ارتفاع استهلاك الطاقة وتأثير سلبي على البيئة في قطاع البناء. وتعدّ إحدى المقاربات الواعدة لتحسين كفاءة الطاقة دمج المواد متغيرة الطور في أنظمة التدفئة الأرضية. تهدف هذه الدراسة إلى تقييم تأثير دمج هذه المواد على الأداء الحراري والطاقي لنظام التدفئة الأرضية المائية. ولتحقيق هذا الهدف، تم تطوير نموذج عددي ثنائي الأبعاد باستخدام برنامج كومسول متعدد الفيزياء وقد تم اعتماد طريقة العناصر المحدودة جنبًا إلى جنب مع نهج السعة الحرارية الفعالة لمحاكاة السلوك الحراري للنظام بدقة. تم تحليل تأثير عدة عوامل، مثل نوع المادة متغيرة الطور وسمكها وموقعها داخل هيكل الأرضية، من أجل تحسين أداء النظام. أظهرت النتائج أن دمج مادة متغيرة الطور قائمة على هيدرات الملح بسماكة 3 سنتيمترات ومع درجة حرارة تغذية المياه عند 40 درجة مئوية يُحسن بشكل كبير القصور الذاتي الحراري للأرضية. يضمن هذا التكوين الحفاظ على درجة حرارة مريحة تقارب 27 درجة مئوية حتى بعد إيقاف تشغيل نظام التدفئة، مع تأخير زمني يصل إلى 17 ساعة مقارنةً بنظام تدفئة أرضية بدون مادة متغيرة الطور. تؤكد هذه النتائج الإمكانيات الكبيرة لاستخدام المواد متغيرة الطور في أنظمة التدفئة الأرضية، حيث توفر حلاً فعالًا لتقليل استهلاك الطاقة في المباني مع ضمان راحة حرارية مثالية.

الكلمات المفتاحية – نظام التدفئة الأرضية؛ التخزين الكامن؛ مواد متغيرة الطور؛ التحليل البارامتري؛ تخزين الطاقة.

1. INTRODUCTION

The building sector accounts for approximately 40% of global energy consumption [1]. One of the most effective passive methods to enhance the thermal performance of buildings and reduce their energy consumption is the integration of phase change materials (PCMs) into structural elements such as walls, roofs, floors, and ceilings [2]. Incorporating PCMs specifically into underfloor heating systems represents a significant technological, as it allows for efficient thermal energy storage and improves indoor thermal comfort [3]. This strategy uses the PCM's ability to capture, store, and release heat during phase changes, which reduces energy consumption and stabilizes internal temperatures.

Numerous studies have examined this technology, highlighting its potential to store and release heat more efficiently, particularly during periods of energy shortages [4]. For instance, S. Lu et al [5] integrated a composite PCM consisting of capric acid and hexadecyl alcohol into a floor heating system, resulting in a 5.87% reduction in energy usage. According to H. Ju et al [6], adding PCM to a standard heating floor lowers overall running costs by 13.8%, boosts load flexibility by 18.1%, and enhances indoor temperature stability by 8.6%. In this experimental study, B.Y. Yun et al [7] integrated macro-encapsulated PCMs into a radiant floor heating system to analyze their effects on thermal comfort and energy savings. The results showed that n-docosane achieved the greatest power reduction, while n-eicosane demonstrated the highest efficiency in terms of energy consumption and maintaining the floor's comfort temperature. W. Cheng et al [8] introduced PCM panels, known as HCE-SSMCP, composed of (solid paraffin + liquid paraffin) / high-density polyethylene / expanded graphite into a test room with a floor heating system in a house during winter. The findings demonstrated that enhancing the thermal conductivity of the PCM within a certain range could significantly improve the energy efficiency of the heating system. In the other hand, the feasibility of incorporating PCM into the heating floor is the subject of multiple research streams that focus on experimental and numerical analysis. K. Huang et al [9] conducted a study on a new PCM floor consisting of two layers of heating tubes and a macro-encapsulated PCM layer. They experimentally and numerically analyzed the heat storage and release processes. The results revealed that the new floor with PCM is capable of releasing 37677.6 kJ of heat over 16 hours during the pumping period in an 11 m^2 room, representing 47.7% of the energy supplied by

the solar-heated water. The dynamic thermal performance of a floor heating system using phase change material for thermal storage has been investigated experimentally and numerically by Q. Zhang et al [10]. According to the findings, PCM with a phase change temperature of 313 K was suggested because it could reduce the indoor temperature fluctuation range by 2.2 K, and boost the thermal energy storage rate by 12%. In addition, the radiant floor heating condenser's heat transfer performance using composite phase change material was investigated experimentally and numerically by T. Jiang et al [11].

Using numerical and experimental research, B. Larwa et al [12] investigated the effects of wet and dry sand, as well as the positioning of PCM containers above and below the pipes, in a radiant floor system with macro-encapsulated PCM. The study found that the advantageous effects of wet sand were further enhanced when PCM capsules were placed beneath the pipes. Moreover, the thermal behavior of floor heating systems incorporating PCMs has been extensively studied through numerical simulations by various researchers. M. T. Plytaria et al [13] investigated the efficiency of a heating system incorporating PCM.

They demonstrated that using a Bio PCM (Q29/M91) with a melting point of 29 °C, placed beneath the tube, optimizes the system's performance. This configuration reduced the auxiliary heating load by 65%, increased indoor temperature by 0.8 °C, and minimized both energy consumption and overall costs. Furthermore, B. González and M. M. Prieto [14] developed 2D models to analyze the performance of radiant floor heating systems integrated with PCM. Their findings revealed that the incorporation of PCM significantly increased thermal energy storage (TES) by over 155%, while heat transfer decreased by roughly 18%, resulting in a more consistent indoor temperature and reduced energy consumption.

In a recent work, Z. Kang et al [15] used Fluent software to numerically create a two-dimensional model of a heated floor that included the PCM layer.

CFD simulations were used to examine the temperature distributions and heat charging and discharging behaviors of three low-temperature PCMs. Furthermore, Q. Yu et al [16] studied the behavior of a floor heating system incorporating two distinct layers of PCM. A coupled numerical heat transfer model was developed to examine the heat charging and release processes.

The findings reveal that the thermal energy storage floor heating system prevents overheating while reducing energy consumption by more than 19% during the thermal charging process.

The numerical analysis of the thermal behavior of a floor heating system incorporating two distinct types of PCM to evaluate their heat storage capacity at the ground level during the intermittent period and under certain conditions remains relatively unexplored in the literature, particularly with the use of COMSOL software. Existing studies exhibit certain limitations, highlighting the need for a more in-depth investigation.

In this context, our work provides an original contribution by addressing these gaps and offering a detailed evaluation of the system's thermal performance under various scenarios. More specifically, we analyzed the impact of PCM placement and quantity variations on the thermal efficiency of the floor heating system to optimize its energy performance.

2. METHODOLOGY AND APPROACH

2.1. Presentation of the physical model

In the present study, an innovative heated floor model was developed by integrating a PCM layer to enhance energy and thermal performance, as well as to improve thermal comfort. The floor structure, illustrated in figure 1, comprises a base layer of limestone and heavy concrete with respective thicknesses of 300 mm and 100 mm. Directly above, a 50 mm thermal insulation layer is installed to minimize downward heat losses.

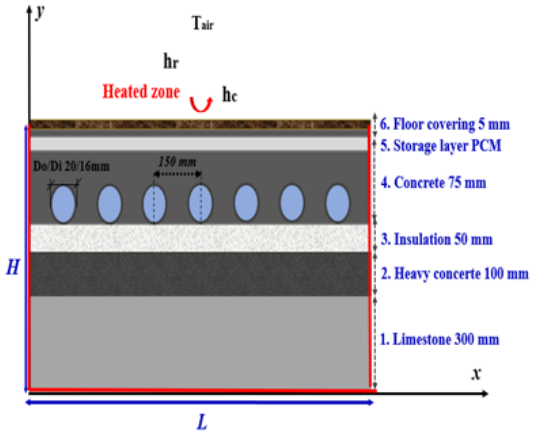

Figure 1. Structure of floor heating system with PCM, 2D View (X, Y) [17].

A network of heating pipes, arranged in a spiral configuration, is placed above the insulation layer to ensure the uniform circulation of hot water. The pipes are encapsulated within a 75 mm thick concrete screed, which serves to distribute heat evenly and provide structural stability. Above the screed, a 5 mm PCM layer is positioned to retain thermal energy as latent heat during periods of excess heat and release it when the temperature decreases, enabling passive temperature regulation. As a final step, A finishing layer made of tiles is applied at the surface, offering a durable and visually appealing finish while facilitating effective heat transfer.

2.2. Numerical model description

The numerical modeling of thermal interactions within the underfloor heating system with and without PCM was carried out using the COMSOL Multiphysics software [18]. This software allows for the simulation of heat transfer processes, as well as the charging and discharging of the PCM layer integrated into the structure of the underfloor heating system. Indeed, the phase change phenomenon was modeled using the effective heat capacity approach [19]. This method effectively replicates the thermal behavior of the PCM during phase transitions, guaranteeing the accuracy and dependability of the simulation outcomes. By adopting this method, the 2D model offers a precise and in-depth analysis of the thermal behavior of the system. It allows for an accurate representation of heat transfer dynamics while significantly reducing computational complexity.

The heat transfer occurs primarily through conduction, successively passing through the wall of the hot water pipes, the concrete layer, the PCM layer, and the finishing layer. Moreover, the finishing layer transfers heat to the ambient air through convection and radiation, ensuring an optimal distribution of heat in the environment. To streamline the calculations, the following assumptions were adopted:

1. The heat transfer through the insulation layer is assumed to be negligible.
2. Heat transfer within solid materials (concrete, finishing layer, etc.) is considered two-dimensional.
3. The PCM's thermophysical characteristics won't alter during the phase transition process.
4. Due to the liquid's high viscosity and moderate velocity, natural convection within the PCM layer is insignificant.

The governing equations used to precisely describe heat transfer across the layers of a heated floor system with PCM are as follows:

-The thermal conduction equation in solid materials (pipe walls, mortar, finishing layer, etc.) is governed by Fourier's equation (1) [20]:

$$\left(\rho c_{\mathrm{p}}\right)_{\mathrm{s}} \frac{\partial T_{\mathrm{s}}}{\partial t}=k_{\mathrm{s}} \nabla^{2} T_{\mathrm{s}} \qquad (1)$$

Where:
$(\rho c_p)_s$ represents the volumetric heat capacity of the solid material (product of density ρ and specific heat capacity c_p.
$(\partial T_s)/\partial t$ is the transient term that describes the rate of temperature change over time.
$k_s \nabla^2 T_s$ represents the heat conduction term, where k_s is the thermal conductivity of the solid material, and $\nabla^2 T_s$ is the Laplacian of temperature, describing the spatial distribution of heat within the solid.
To model the thermal behavior of PCM, which includes phase transitions (melting/ solidification), an effective heat capacity method is used. This approach adjusts the specific heat capacity to represent the latent heat in the thermal conduction equation (2) [19]:

$$\left(\rho c_{\mathrm{p}}\right)_{\mathrm{eff}} \frac{\partial \mathrm{T}}{\partial t}=\left(k_{\mathrm{eff}} \nabla^{2} \mathrm{T}\right) \qquad (2)$$

Where $C_{p_{eff}}$ is calculated using equation (3) [20]:

$$C_{eff}\left(T\right)=\left\{\begin{array}{c} C_{p,s}\ ,if\quad T<T_m-\delta T \\ \dfrac{C_{p,s}+C_{p,l}}{2}+\dfrac{L}{2\delta T}\ ,if\ T=T_m \\ C_{p,l}\ ,\qquad if\quad T>T_m+\delta T \end{array}\right\} \qquad (3)$$

Where: (L) is the latent heat of fusion of the PCM (J/kg), (T_m) the average melting temperature (K) and (δT) the temperature range over which the phase change occurs. In addition, the liquid fraction of a PCM represents the proportion of the material that has transitioned from the solid state to the liquid state at a given moment, depending on the temperature or the applied thermal energy. This fraction β is calculated using equation (4) that links the PCM's temperature to its melting temperature [20].

$$\beta=\left\{\begin{array}{l} \beta_S=0\ if\ T<T_m-\dfrac{\Delta T}{2}\left(solid\ phase\right) \\ \beta_m=\left[0,1\right]\ ,if\ \ T=T_m\ \left(mixed\ phase\right) \\ \beta_l=1 if\ T>T_m+\dfrac{\Delta T}{2}\left(liquid\ phase\right) \end{array}\right\} \qquad (4)$$

The following are the initial and boundary conditions:
1. The initial temperature of the heating system with PCM is set at 20°C (t=0).
2. The upper surface of the floor interacts with the indoor environment, exchanging heat through both convection and radiation. with a radiation emissivity factor of 0.9.
3. The lateral boundaries of the heated floor are considered adiabatic.
4. The insulation layer beneath the piping is defined as an adiabatic boundary to minimize heat losses downward.

2.3. Validation

The 2D numerical model of the heated floor, developed using COMSOL software, was validated by

comparison with the experimental results obtained by Larwa et al [12]. The analysis of the relative error in the surface temperature of the floor shows a minimal discrepancy of approximately 2.33% between the numerical and experimental data, exhibiting a high level of consistency between the numerical model and the findings reported in the literature.

3. RESULTS AND DISCUSSIONS

3.1. Types of PCM

In this investigation, two types of PCMs were tested under an inlet temperature of 40 °C to assess their performance in terms of thermal storage capacity and thermal regulation.
The studied PCMs have distinct melting temperatures and thermal capacities, which allows for comparing their efficiency in the context of a floor heating system.
The thermo-physical properties of each PCM are detailed in the following Table 1.

Table 1. Thermo-physical properties for the different PCM [12 , 21].

Type of PCM	Salt hydrates	Organic alkanes
	S27	N-octadecane
Density (Kg/m^3)	1530	722
Thermal conductivity (W/m. K)	0.54	0.192
Melting temperature Tm (°C)	27	29.95
Latent heat of fusion (kJ/Kg)	185	186.5
Specific heat capacity (kJ/Kg. K)	2.200	2.153

Figure 2 shows the evolution of the floor surface temperature (°C) as time progresses (h) for three scenarios: without PCM, with salt hydrate as an inorganic PCM, and with N-octadecane as an organic PCM.

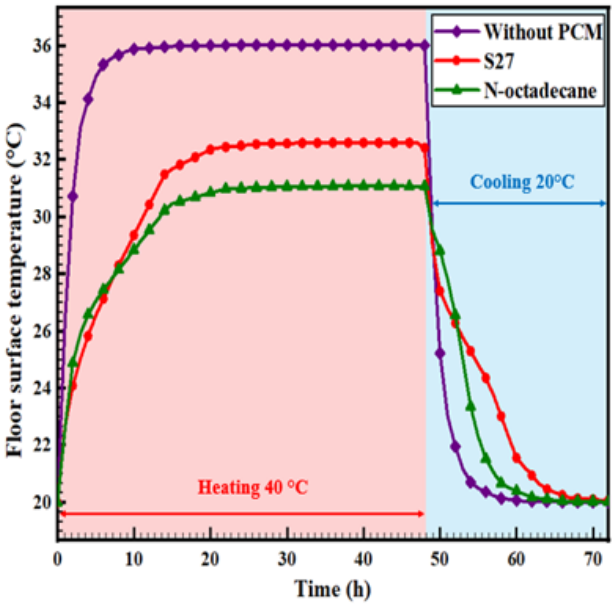

Figure 2. Evolution of floor surface temperature of heating system with and without PCM (salt hydrates and N-octadecane).

It can observe that the heated floor system without PCM shows no ability to store thermal energy, resulting in significant fluctuations and a rapid decrease in temperature.

In contrast, the temperature of the floor heating, incorporating a layer of hydrated salt with a thickness of 1 cm, gradually increases to stabilize around 32 °C during an extended heating period. This thermal behavior exceeds that of N-octadecane, whose temperature stabilizes between 28 °C and 30 °C. After the heating is stopped, the salt hydrate stands out for its superior ability to release heat, maintaining high temperatures for a longer duration compared to the reference case. On the other hand, n-octadecane releases heat over a narrower temperature range, stabilizing around t= 3h before rapidly decreasing to reach thermal equilibrium.
These results highlight that the choice of salt hydrates as PCM is particularly advantageous due to their specific thermal properties, including high thermal conductivity, significant specific heat capacity, substantial latent heat of fusion, and superior thermal storage capacity.
This ensures effective thermal storage within the comfort temperature range for an extended period.

3.2. Impact of thickness

Figure 3 shows the effect of the thickness of the salt hydrate-based PCM layer embedded in the soil on the surface temperature of the floor heating, comparing different PCM thicknesses of 1 cm, 2 cm, and 3 cm with the reference case (without PCM).

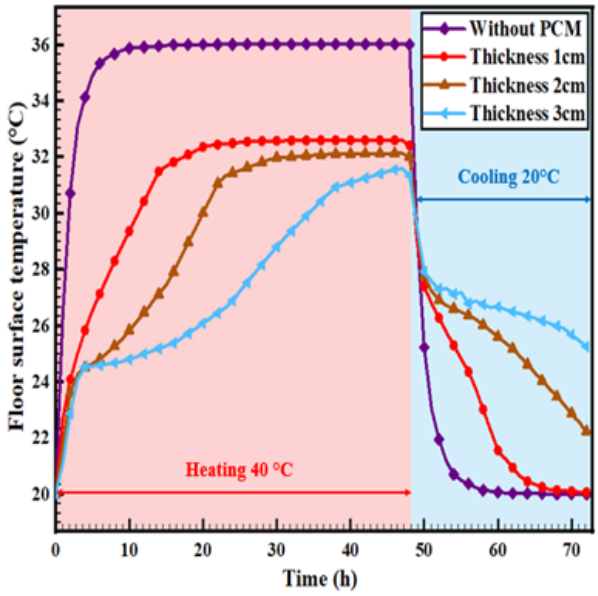

Figure 3. Evolution of floor surface temperature for difference thickness of PCM (salt hydrate)

During the heating period, the increase in the thickness of the PCM layer based on salt hydrate slightly slows the initial temperature rise compared to the reference case, due to the greater mass of PCM, which introduces higher thermal inertia.
After the heating is stopped, it is evident that heat dissipation with a 3 cm thick layer is very gradual, reducing thermal fluctuations and ensuring prolonged heat release for 17 hours. This layer maintains a temperature of 27 °C, with a divergence of 6.98 °C, 6.85 °C, and 1.18 °C when compared with the floor heating without PCM and the 1 cm and 2 cm layers, respectively.

3.3. Impact of position

Figure 4 illustrates the various possible positions of a 3 cm PCM layer within the coating layer.

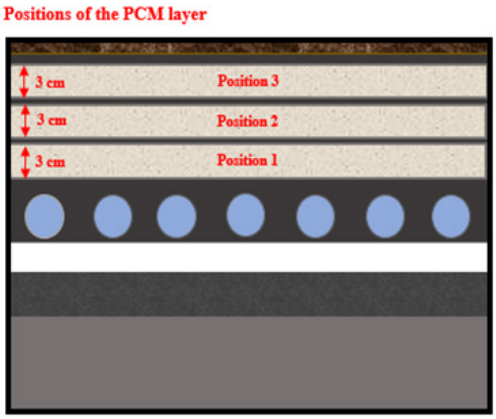

Figure 4. Positions of PCM salt hydrate with a thickness of 3 cm (2D view).

Figure 5 demonstrates the effect of varying the position of the salt hydrate PCM layer on the floor surface temperature, highlighting the differences compared with the reference case without PCM.

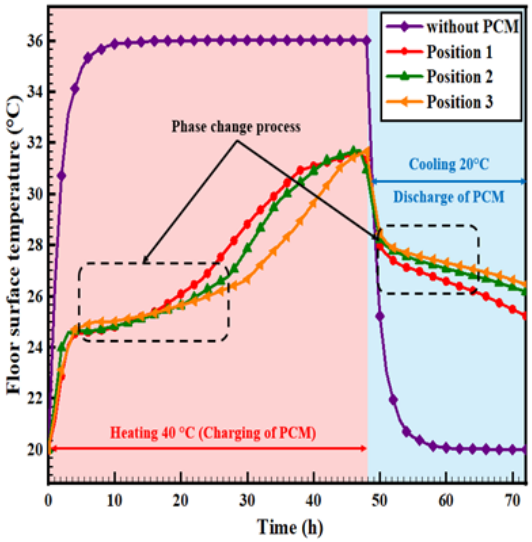

Figure 5. Different positions of PCM salt hydrate with a thickness of 3 cm

The incorporation of a 3 cm thick salt hydrate-based PCM layer significantly improves the thermal performance of the floor heating. Placing the PCM closer to the floor surface (below the finishing layer, i.e., position 3) guarantees more gradual heat dissipation, while ensuring a gradual decrease in floor temperature over a long discharge period. This is suitable for ensuring optimal thermal comfort above 28 °C.

In contrast, positioning it closer to the heat source (position 1) provides faster heating during the heating period. Therefore, placing the PCM at position 3 guarantees temperature stability for a long time, with a 7 °C difference compared to the reference case.

O. Babaharra et al [21] also tested the two types of PCM proposed in this study under different conditions. Their results indicate that using a hydrated salt-based PCM allows the floor temperature to reach approximately 26.4 °C, with a phase shift of 5.5 hours compared to the reference case. However, in our study, further performance improvements are achieved when the supply water temperature is increased while increasing the thickness of the MCP layer from 1 to 3 cm, placed close to the floor surface, which extends the heat release duration to 17 hours while keeping the floor temperature stabilized at (~27 °C). In comparison, our model provides a significant

improvement, increasing the heat release duration by 67.64% compared to the previous study. The choice of hydrated salt in this study offers several advantages, including a higher thermal storage capacity compared to organic PCMs, as well as high energy density and thermal conductivity. Despite the challenges related to its degradation over time, this type of PCM remains an ecological, non-toxic, and more cost-effective solution than its organic counterparts [22,23]. In this context, the use of hydrated salts represents a promising alternative to enhance energy efficiency and reduce heating costs in the long term.
Thanks to its thermal properties, it is particularly suitable for this type of heating application.

4. CONCLUSION

This study highlights the thermal effectiveness of heated floors incorporating phase change materials, testing two types of PCM (organic: N-octadecane; inorganic: salt hydrate) along with the reference case without PCM, as well as the impact of the thickness and positioning of the salt hydrate. The results demonstrate that both types of PCM enhance thermal regulation compared to the case without PCM. However, the salt hydrate, due to its specific thermal properties, proved to be more effective than N-octadecane, maintaining higher surface temperatures for an extended duration. Furthermore, increasing the thickness of the salt hydrate to 3 cm was found to be optimal, allowing surface temperatures to remain within the comfort zone (~27 °C) for more than 17 hours after the heating was turned off. Regarding positioning, the salt hydrate placed near the surface (under the finishing layer, position 3) provided a more gradual heat dissipation, extending the duration of thermal comfort compared to other positions.

Authors contribution: Afaf Charraou: conceptualization, methodology, data curation, writing original draft, formal analysis, visualization, supervision, writing review and editing. Mohamed Errebii: investigation, conceptualization, methodology, supervision, and editing.
Amina Mourid: conceptualization, data curation, supervision.
Rachid Saadani: conceptualization, data curation, supervision.
Miloud Rahmoune: conceptualization, data curation, supervision.
Mustapha El Alami: supervision and conceptualization.
Funding: The authors have not disclosed any funding.
Data Availability Statement: Not applicable.
Conflicts of Interest: The authors declare that they have no known conflicts of interest.

REFERENCES

[1] P. Nejat, F. Jomehzadeh, M. M. Taheri, M. Gohari, and M. Z. Abd. Majid, « A global review of energy consumption, CO2 emissions and policy in the residential sector (with an overview of the top ten CO 2 emitting countries) », Renewable and Sustainable Energy Reviews, vol. 43, p. 843-862, mars 2015, doi: 10.1016/j.rser.2014.11.066.

[2] P. Jaffar Abass and S. Muthulingam, « Comprehensive assessment of PCM integrated roof for passive building design: A study in energo-economics », Energy and Buildings, vol. 317, p. 114387, août 2024, doi: 10.1016/j.enbuild.2024.114387.

[3] K. Jiao, L. Lu, L. Zhao, and G. Wang, « Towards Passive Building Thermal Regulation: A State-of-the-Art Review on Recent Progress of PCM-Integrated Building Envelopes », Sustainability, vol. 16, no 15, p. 6482, juill. 2024, doi: 10.3390/su16156482.

[4] P. Devaux and M. M. Farid, « Benefits of PCM underfloor heating with PCM wallboards for space heating in winter », Applied Energy, vol. 191, p. 593-602, avr. 2017, doi: 10.1016/j.apenergy.2017.01.060.

[5] S. Lu, Y. Zhao, K. Fang, Y. Li, and P. Sun, « Establishment and experimental verification of TRNSYS model for PCM floor coupled with solar water heating system », Energy and Buildings, vol. 140, p. 245-260, avr. 2017, doi: 10.1016/j.enbuild.2017.02.018.

[6] H. Ju, X. Li, C. Chang, W. Zhou, G. Wang, and C. Tong, « Heating performance of PCM radiant floor coupled with horizontal ground source heat pump for single-family house in cold zones », Renewable Energy, vol. 235, p. 121306, nov. 2024, doi: 10.1016/j.renene.2024.121306.

[7] B. Y. Yun, S. Yang, H. M. Cho, S. J. Chang, and S. Kim, « Design and analysis of phase change material based floor heating system for thermal energy storage », Environmental Research, vol. 173, p. 480-488, juin 2019, doi: 10.1016/j.envres.2019.03.049.

[8] W. Cheng, B. Xie, R. Zhang, Z. Xu, and Y. Xia, « Effect of thermal conductivities of shape stabilized PCM on under-floor heating system », Applied Energy, vol. 144, p. 10-18, avr. 2015, doi: 10.1016/j.apenergy.2015.01.055.

[9] K. Huang, G. Feng, and J. Zhang, « Experimental and numerical study on phase change material floor in solar water heating system with a new design », Solar Energy, vol. 105, p. 126-138, juill. 2014, doi: 10.1016/j.solener.2014.03.009.

[10] Q. Zhang, Z. Yang, and G. Wang, « Numerical and experimental investigation on dynamic thermal performance of floor heating system with phase change material for thermal storage », Indoor and Built Environment, vol. 30, no 5, p. 621-634, juin 2021, doi: 10.1177/1420326X19900535.

[11] T. Jiang, C. Zheng, S. You, H. Zhang, Z. Wu, Y. Wang, and S. Wei « Experimental and numerical study on the heat transfer performance of the radiant floor heating condenser with composite phase change material », Applied Thermal Engineering, vol. 213, p. 118749, août 2022, doi: 10.1016/j.applthermaleng.2022.118749.

[12] B. Larwa, S. Cesari, and M. Bottarelli, « Study on thermal performance of a PCM enhanced hydronic radiant floor heating system », Energy, vol. 225, p. 120245, juin 2021, doi: 10.1016/j.energy.2021.120245.

[13] M. T. Plytaria, C. Tzivanidis, E. Bellos, and K. A. Antonopoulos, « Parametric analysis and optimization of an underfloor solar assisted heating system with phase change materials », Thermal Science and Engineering Progress, vol. 10, p. 59-72, mai 2019, doi: 10.1016/j.tsep.2019.01.010.

[14] B. González and M. M. Prieto, « Radiant heating floors with PCM bands for thermal energy storage: A numerical analysis », International Journal of Thermal Sciences, vol. 162, p. 106803, avr. 2021, doi: 10.1016/j.ijthermalsci.2020.106803.

[15] Z. Kang, R. Tan, Q. Yao, J. Zhang, S. Zhang, and Y. Wei, « Numerical simulation of energy storage radiant floor heating systems with phase change materials having different thermophysical properties », Construction and Building Materials, vol. 463, p. 140010, févr. 2025, doi: 10.1016/j.conbuildmat.2025.140010.

[16] Q. Yu, B. Sun, C. Li, F. Yan, and Y. Li, « Analysis of heat charging and release processes in cascade phase change materials energy storage floor heating systems: Performance evaluation », Journal of Energy Storage, vol. 78, p. 110020, févr. 2024, doi: 10.1016/j.est.2023.110020.

[17] A. Charraou, S. Oubenmoh, A. Mourid, R. Saadani, M. Rahmoune, and M. El Alami, « Experimental assessment and 3D numerical simulation of the thermal performance of a direct solar floor heating system installed in a bathroom in Casablanca city, Morocco: parametric, economic, and environmental analysis », J Build Rehabil, vol. 9, no 1, p. 78, juin 2024, doi: 10.1007/s41024-024-00408-4.

[18] R. W. Pryor, Multiphysics Modeling Using COMSOL: A First Principles Approach. Jones & Bartlett Publishers, 2009. ISBN: 978-0-7637-9233-6.

[19] S. A. Prakash, C. Hariharan, R. Arivazhagan, R. Sheeja, V. A. A. Raj, and R. Velraj, « Review on numerical algorithms for melting and solidification studies and their implementation in general purpose computational fluid dynamic software », Journal of Energy Storage, vol. 36, p. 102341, avr. 2021, doi: 10.1016/j.est.2021.102341.

[20] S. Lu, J. Gao, H. Tong, S. Yin, X. Tang, and X. Jiang, « Model establishment and operation optimization of the casing PCM radiant floor heating system », Energy, vol. 193, p. 116814, févr. 2020, doi: 10.1016/j.energy.2019.116814.

[21] O. Babaharra, K. Choukairy, S. Hamdaoui, K. Khallaki, and S. Hayani Mounir, « Thermal behavior evaluation of a radiant floor heating system incorporates a microencapsulated phase change material », Construction and Building Materials, vol. 330, p. 127293, mai 2022, doi: 10.1016/j.conbuildmat.2022.127293.

[22] H. Nazir, M. Batool, F.J. Bolivar Osorio, M. Isaza-Ruiz, Z. Xu, K. Vignarooban, P. Phelan, Inamuddin and A.M K.a.n.n.a.n, « Recent developments in phase change materials for energy storage applications: A review », International Journal of Heat and Mass Transfer, vol. 129, p. 491-523, févr. 2019, doi: 10.1016/j.ijheatmasstransfer.2018.09.126.

[23] Ashish Kumar Shrivastava, T Ravi Kiran, and Anil Singh Yadav, 'Enhancement of Productivity and Economic Analysis of Tubular Solar Still with Acrylic Cover Material', jsesd, vol. 14, no. 1, pp. 131–140, Feb. 2025, doi: 10.51646/jsesd.v14i1.359.

Symbol	Designation	Unity
k_{eff}	The effective thermal conductivity	W/(m·K)
$C_{p,s}$	The specific heat capacity of the solid phase	J/(kg·K)
$C_{p,l}$	The specific heat capacity of the liquid phase	J/(kg·K)
h_r	Heat transfer coefficient for radiation	W/(m²·K)
h_c	Heat transfer coefficient for convection	W/(m²·K)
T_{air}	Air temperature	°C

Solar Energy
And Sustainable Development
Refereed, biannual scientific journal issued by:
The Libyan Center for Solar Energy Research and Studies

Optoelectronic Properties of Doped $CaTiO_3$ (C, N, Si and P): A DFT Study for Photovoltaic Applications

Abdellah Bouzaid[1]*, Younes Ziat[2], Hamza Belkhanchi[3], Ayoub Koufi[4], Mohammed Miri[5], Hmad Fatihi[6], Charaf Laghlimi[7].

[1,2,3,4,5]Engineering and Applied Physics Team (EAPT), Superior School of Technology, Sultan Moulay Slimane University, Beni Mellal, Morocco.
[1,2,3,4,5,7]The Moroccan Association of Sciences and Techniques for Sustainable Development (MASTSD), Beni Mellal, Morocco.
[6]Laboratory of Research in Physics and Engineering Sciences, Sultan Moulay Slimane University, Polydisciplinary Faculty, Beni Mellal, 23000, Morocco.
[7]ERCI2A, FSTH, Abdelmalek Essaadi University, Tetouan, Morocco.

E-*mail:* [1]abdellah.bouzaid97@gmail.com .

SPECIAL ISSUE ON:

The 1St International Conference on Sciences and Techniques for Renewable Energy and the Environment.
(STR2E 2025)
May 6-8, 2025 at FST-Al Hoceima-Morocco.

KEYWORDS

$CaTiO_3$; Ca_4 Ti_4 O_{10} Y_2; DFT; Bulk modulus derivative; Band structure; electronic structure, optical properties.

ABSTRACT

This study uses density functional theory (DFT) with generalized gradient approximation (GGA) and modified Becke-Johnson potential (mBJ) to analyze the structural, electronic, and optical properties of Ca_4 Ti_4 $O_{(12-z_i)}$ Y_{zi} perovskite materials, where z_i indicates the number of dopant atoms at the oxygen (O) site. In this research, Y represents the elements C, N, Si, and P, which are substituted at oxygen sites with a doping concentration of x = 16%. Firstly, the structural optimization results reveal negative formation energies for both pure and doped $CaTiO_3$, confirming the stability.

Moreover, doping with Y significantly reduces the bandgap energy compared to undoped $CaTiO_3$ (2.766 eV). Specifically, the band gaps for Ca_4 Ti_4 O_{10} Y_2 materials (Y = C, N, Si, and P) are reduced to 0.87, 1.63, 0, and 0.6 eV respectively. In addition, doping with C and N retains the nature of the indirect band gap, with electronic transitions between the Γ and L points of the Brillouin zone, whereas doping with P results in a direct band gap. Additionally, doping with Si reduces the band gap to zero, resulting in metallic behavior. Furthermore, the Fermi level (EF) shifts towards the valence band (VB), indicating p-type semiconductor behavior for the doped systems, except Ca_4 Ti_4 O10 Si_2, which exhibits metallic behavior. Finally, analysis of the optical properties shows that doping increases the static dielectric constant, $\varepsilon_1(0)$, with specific values

*Corresponding author.

DOI: https://doi.org/10.51646/jsesd.v14iSTR2E.982

This is an open access article under the CC BY-NC license (http://Attribution-NonCommercial 4.0 (CC BY-NC 4.0)).

for each dopant 7.1 for $Ca_4 Ti_4 O_{10} C_2$, 6.72 for $Ca_4 Ti_4 O_{10} N_2$, 36.63 for $Ca_4 Ti_4 O_{10} Si_2$, and 23.69 for $Ca_4 Ti_4 O_{10} P_2$. Notably, doping $CaTiO_3$ with 16% of Y reduces the bandgap, improving optical absorption and conductivity in the visible range, making $Ca_4 Ti_4 O_{10} Y_2$ (Y= C, N, Si, and P) a promising material for photovoltaic cells and optoelectronic applications.

الخصائص الضوئية والإلكترونية لمركب $CaTiO_3$ المطعم (C، N، Si وP): دراسة باستخدام نظرية الوظيفة الكثيفة (DFT) للتطبيقات الكهروضوئية

عبد الله بوزايد، يونس زيات، حمزة بلخنشي، أيوب كوفي، محمد ميري، احمد فاتحي، شراف لغليمي.

ملخص: تستخدم هذه الدراسة نظرية الوظيفة الكثيفة (DFT) مع تقريب التدرج المعمم (GGA) وجهد بيك-جونسون المعدل (mBJ) لتحليل الخصائص التركيبية والإلكترونية والبصرية لمواد البيروفسكايت $Ca_4 Ti_4 O_{(12-z_i)} Y_{zi}$، حيث يشير z_i إلى عدد ذرات المنشطات في موقع الأكسجين (O). في هذا البحث، تمثل Y العناصر C و N وSi و P، التي تحل محل الأكسجين بتركيز تطعيم $x = 16\%$. أولًا، تكشف نتائج تحسين البنية عن طاقات تكوين سالبة لكل من $CaTiO_3$ النقي والمطعم، مما يؤكد استقرارهما. علاوة على ذلك، يقلل التطعيم بـ Y بشكل كبير من طاقة فجوة النطاق مقارنةً بـ $CaTiO_3$ غير المطعم (2.766 إلكترون فولت). على وجه التحديد، تنخفض فجوات النطاق لمواد $Ca_4 Ti_4 O_{10} Y_2$ حيث (Y = C, N, Si, P) إلى 0.87 و 1.63 و 0 و 0.6 إلكترون فولت على التوالي. بالإضافة إلى ذلك، يحافظ التطعيم بـ C و N على طبيعة فجوة النطاق غير المباشرة، حيث تحدث الانتقالات الإلكترونية بين نقاط Γ و L في منطقة بريلوان، بينما يؤدي التطعيم بـ P إلى فجوة نطاق مباشرة. كما يقلل التطعيم بـ Si فجوة النطاق إلى الصفر، مما يؤدي إلى سلوك معدني. علاوة على ذلك، يتحول مستوى فيرمي (EF) نحو نطاق التكافؤ (VB)، مما يشير إلى سلوك أشباه الموصلات من النوع p للأنظمة المطعمة، باستثناء $Ca_4 Ti_4 O_{10} Si_2$، الذي يظهر سلوكًا معدنيًا. أخيرًا، يُظهر تحليل الخصائص البصرية أن التطعيم يزيد من ثابت العزل الساكن، $\varepsilon_1(0)$، مع قيم محددة لكل مطعِّم: 7.1 لـ $Ca_4 Ti_4 O_{10} C_2$، و 6.72 لـ $Ca_4 Ti_4 O_{10} N_2$، و 36.63 لـ $Ca_4 Ti_4 O_{10} Si_2$، و 23.69 لـ $Ca_4 Ti_4 O_{10} P_2$. ومن الجدير بالذكر أن تطعيم $CaTiO_3$ بنسبة 16 % من Y يقلل من فجوة النطاق، مما يحسن امتصاص الضوء والتوصيلية في المجال المرئي، مما يجعل $Ca_4 Ti_4 O_{10} Y_2$ مادة واعدة للخلايا الكهروضوئية وتطبيقات البصريات الإلكترونية.

الكلمات المفتاحية – $CaTiO_3$؛ $Ca_4 Ti_4 O_{10} Y_2$؛ DFT؛ مشتق معامل الكتلة؛ هيكل النطاق؛ البنية الإلكترونية والخصائص البصرية.

1. INTRODUCTION

The development of renewable energy solutions has become a major strategic issue on a global scale, given the current environmental and economic challenges. Renewable energy sources such as photovoltaics (PV), wind power and batteries offer promising prospects for meeting growing energy demand while limiting environmental impacts [1, 2, 3, 4]. These technologies not only help to reduce dependence on fossil fuels, but also promote sustainable development thanks to their economic, social and environmental benefits [5]. Identifying and harnessing renewable, sustainable and economically competitive energy sources is therefore a key priority in meeting the world's energy challenges [6].

Among the solutions being considered, solar energy occupies a central position due to its abundance, renewable nature and environmental friendliness. Its conversion into chemical energy via artificial photosynthesis represents an innovative and essential way of responding to the current energy and climate crises [6, 7, 8]. This process, inspired by nature, paves the way for revolutionary technologies capable of transforming the world's energy landscape over the long term. In this context, perovskite oxides, following the general formula ABO_3, stand out as cutting-edge materials. Their stable crystal structure, formed by the coordination of large (site A) and small (site B) cations with oxygen, gives them unique properties [9]. These versatile

materials have demonstrated their effectiveness in a wide range of technological applications, from photovoltaic devices and sensors to catalysts and energy storage systems [10, 11, 12, 13]. Their advantages include remarkable thermal stability, virtually unlimited lifetime, rapid charge cycles and excellent cost-effectiveness, positioning them as ideal candidates for meeting future energy needs [14]. In addition, perovskite-based ceramics have recently gained in popularity thanks to their structural adaptability, ease of synthesis and low cost. These materials offer an exceptional combination of properties, including high mechanical strength, low thermal expansion, modularity of physico-chemical properties, non-toxicity and high melting point [15]. These characteristics make ceramics particularly attractive solutions for demanding applications, reinforcing their potential in the energy transition. In this context, $CaTiO_3$ perovskite is attracting growing interest due to its remarkable photocatalytic properties, including its effectiveness in degrading organic pollutants and reducing carbon dioxide emissions through environmentally friendly methods [16, 17, 18]. In addition to its semiconducting properties, $CaTiO_3$ exhibits exceptional dielectric behavior, with a relative permittivity of up to 186 and a band gap of 3 to 4 eV, making it a particularly promising material for optoelectronic devices [19]. However, despite these assets, the photocatalytic performance of pure $CaTiO_3$ remains limited for hydrogen evolution due to its wide band gap of 3.5 eV, restricting its absorption to the ultraviolet region, which represents only around 5% of the solar spectrum [16, 20]. To overcome this limitation, advanced studies have explored strategies such as doping and nano structuring, aimed at improving its efficiency in photovoltaic and photocatalytic applications. The properties of $CaTiO_3$ are strongly influenced by a variety of factors, including crystalline defects at the A or B cation sites, particle size and morphology, and exposed surface area [21]. $ATiO_3$-type perovskite oxides (where A represents Ca, Ba, or Sr) are thus emerging as competitive materials for the next generation of solar cells and optoelectronic devices. These materials crystallize in tetragonal or cubic structures, where the A cations occupy the corners of the unit cell, the Ti cation is in the center, and the O anions are located at the edges of the cube [10, 22, 23]. Recent work also highlights the positive effect of doping on the performance of $CaTiO_3$. Attou et al. have, for example, used DFT to investigate the effects of boron (B) doping as a replacement for oxygen sites. Their results show that this doping reduces the bandgap, improves visible light absorption, and optimizes optical and transport properties, particularly in the energy range from 2 to 4 eV [24]. In addition, (La-S) doping with a ratio of 0.25 demonstrated a notable improvement in photocatalytic hydrolysis, thanks to a narrower bandgap, improved carrier mobility and enhanced absorption of visible light [17]. Other studies have revealed that Sr doping alters the electronic band structure of $CaTiO_3$. This doping initially increases the band gap, but at higher concentrations it decreases, paving the way for fine-tuning of optical and electronic properties [25]. This study focuses on analyzing the structural, electrical, and optical properties of the material $CaTiO_3$ doped with a precise 16% concentration of various doping elements, including carbon (C), nitrogen (N), silicon (Si), and phosphorus (P), using simulations based on density functional theory (DFT). This choice of concentration was carefully selected to optimize the interaction of the dopants with the host structure while minimizing crystal defects that could affect the overall stability of the material. The use of DFT provides a rigorous theoretical framework for examining doping-induced modifications to the fundamental properties of $CaTiO_3$, such as lattice parameters, electron density, and band structure. In particular, the aim is to assess how each type of dopant influences the band gap, which is essential for applications in photocatalysis and optoelectronic devices. In addition, this approach makes it possible to investigate changes in optical response, such as absorption and extinction coefficients, as well as electrical properties such as charge carrier mobility and conductivity. This research, combining advanced simulations and predictive analyses, will contribute to a broader understanding of the fundamental mechanisms involved in doping $CaTiO_3$. They will also provide avenues for designing innovative materials with tuned

properties, meeting the specific needs of renewable energy technologies and next-generation optoelectronic devices.

2. COMPUTATIONAL METHOD

This study explored the structural, electronic, and optical properties of cubic $CaTiO_3$ perovskites, both in their pure state and doped with elements C, N, Si, and P, at a specific concentration of 16%. The research relies on the full-potential linearized augmented plane wave (FP-LAPW) method, integrated into the WIEN2k code, to solve the Kohn-Sham equation within the framework of DFT [26, 27]. To ensure greater accuracy, the GGA approximation was combined with the mBJ approximation, known to provide bandgap estimates consistent with experimental results [28, 29]. $CaTiO_3$ perovskites adopt a cubic structure characterized by the space group $Pm\bar{3}m$ (no. 221). In this configuration, the Ca and Ti cations occupy positions (0, 0, 0) and (1/2, 1/2, 1/2) respectively within the unit cell, while the oxygen anions are located at positions (0, 1/2, 1/2), (1/2, 0, 1/2) and (1/2, 1/2, 0), thus forming tetrahedra and octahedra around the cations. Simulation parameters include a cut-off value Rmt* Kmax = 7, where Kmax is the maximum magnitude of the K vector, and Kmax represents the smallest radius of the atomic sphere of the unit cell and Rmt Muffin-Tin Radii (see Table 1).

Table 1: Muffin-Tin Radii (RMT) for pure and doped $Ca_4Ti_4O_{10}Y_2$ (Y= C, N, Si, and P) perovskites.

Element	Ca	Ti	O	C	N	Si	P
RMT (a.u.)	2.5	1.92	1.74	1.64	1.69	1.74	1.74

These parameters guarantee the convergence of the basis set used for the calculations. The convergence criteria have been defined with a tolerance of 10-5 Ry for energy and 10-4 e for charge. For optimization, a k-mesh of 10×10×10 was used for Brillouin zone sampling, and the central state charge localization was established with a value of -6 Rydberg. To model the effects of doping, a 2×2×1 supercell of pure $CaTiO_3$ was constructed, comprising 4 Ca atoms, 4 Ti atoms, and 12 oxygen atoms. In this model, some oxygen sites were replaced by doping elements (C, N, Si, and P) at a concentration of 16%. This approach enables accurate simulation of dopant-host interactions. Figure 1(a) illustrates the $CaTiO_3$ unit cell, composed of one Ca atom, one Ti atom, and three oxygen atoms.

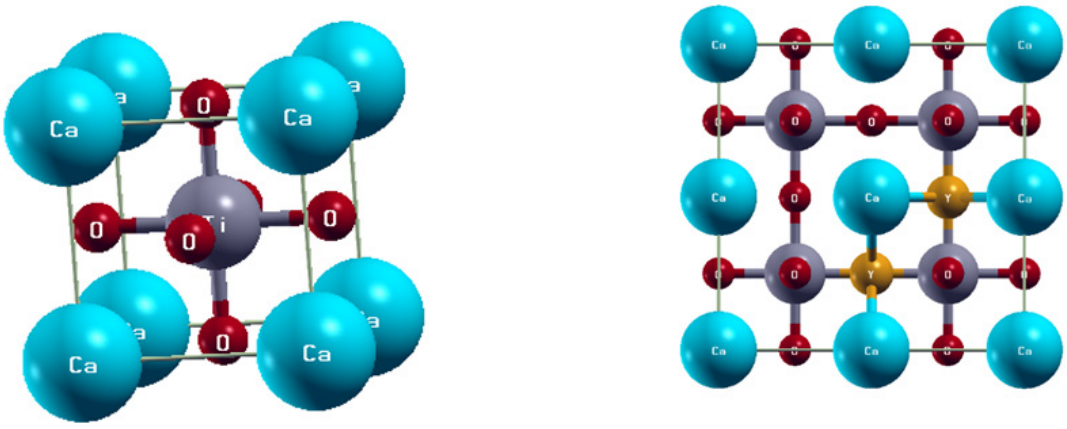

a) b)

Figure 1: Crystal Structure of $CaTiO_3$: (a) unit cell and (b) 2*2*1 supercell.

Figure 1(b) shows the 2×2×1 supercell, consisting of 4-unit cells arranged in a 2×2 grid along axes a and b, while axis c axis remains unchanged, reproducing a doping concentration of 16%.

In this arrangement, Ca cations occupy the central positions of the octahedra, with each Ti cation surrounded by six tilted oxygen anions. This structure enables us to explore in detail the impact of doping on the crystal structure, electron density, and optical properties of the material. These results will contribute to a better understanding of the fundamental mechanisms and optimize the properties of perovskites for advanced applications in optoelectronic devices and energy technologies.

3. RESULTS AND DISCUSSIONS

3.1. Properties Structural and formation energy:

The Birch-Murnaghan equation of state is used to optimize the volume and determine the equilibrium lattice parameters, considering the pressure derivative of the bulk modulus [30]:

$$E_{tot} = E_0 + \frac{9V_0B}{16}\left\{\left[\left(\frac{V_0}{V}\right)^{2/3} - 1\right]^2 B' + \left[\left(\frac{V_0}{V}\right)^{2/3} - 1\right]\left[6 - 4\left(\frac{V_0}{V}\right)^{2/3}\right]\right\} \quad (1)$$

Where E denotes the total energy of the material, E_0 is the ground state energy at zero pressure, V represents the volume, V_0 is the equilibrium volume, B is the bulk modulus, and B' is the pressure derivative of the bulk modulus [31].

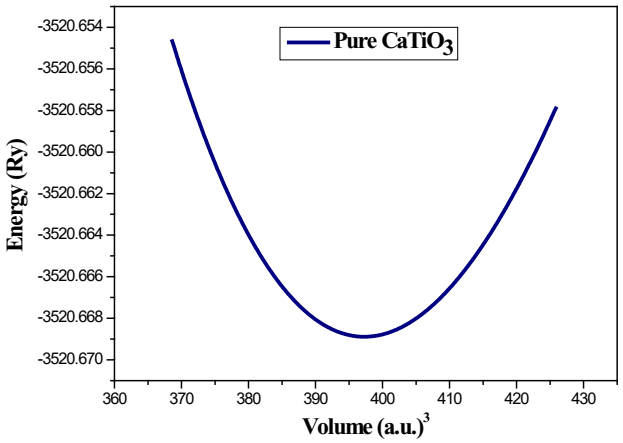

Figure 2: Total energy variation of $CaTiO_3$ as a function of volume.

Table 2: Properties of pure $CaTiO_3$ compounds, such as bulk modulus, lattice constant, and bulk modulus derivatives.

Parameter	Our work	other study
Lattice constant (Å)	3.8901	3.899 [17] 3.856 [9]
Bulk modulus (GPa)	177.4884	200.598 [9]
Bulk modulus derivative	4.2350	5.046 [9]
Volume (a.u)3	397.2763	386.846 [9]

Figure 2 shows the volume optimization curve of total energy against the volume of pure $CaTiO_3$. The optimized lattice parameters of pure $CaTiO_3$ $a_0 = b_0 = c_0 = 3.89$ Å were consistent with both experimental findings ($a_0 = 3.8967$ [32] and 3.90 Å [33]) and theoretical data ($a_0 = 3.899$ [17], and 3.856 Å [9]). Table 2 presents the relaxed lattice constants, bulk modulus, bulk modulus derivative, volume, and ground-state energy of the pure $CaTiO_3$ compound in its optimized

structure. The ground state derived from the optimization curve, based on the lattice parameter, is used to calculate the electronic and optical properties of the compounds self-consistently.
A negative formation energy reflects the thermodynamic stability of the compound compared to its constituent elements [34, 35, 36]. In this study, the formation energy was calculated to assess the thermodynamic stability of the material. The negative formation energy value for $CaTiO_3$, which is -3.33 eV/atom, clearly indicates its thermodynamic stability. The computation of defect formation energy allows inferring the experimental growth potential of a material. A lower formation energy makes the doping structure easier and more stable [37, 38]. The following formula is used to determine the defect production energy of the doped materials [39, 40, 41]:

$$\Delta E_f = (E_{Y-doped} - E_{undoped}) + z_i(\mu_o - \mu_Y) \qquad (2)$$

Where $E_{Y\text{-}doped}$ and $E_{undoped}$ are the total energies of the supercell with and without the dopant, μ_O and μ_Y (Y = C, N, Si, P) are the chemical potentials of oxygen and the dopants, z_i is the number of dopant atoms. Table 3 shows that doping reduces the Formation energy, improving the material's thermodynamic stability.

Table 3: Formation energy of pure $CaTiO_3$ and doped$Ca_4Ti_4O_{10}Y_2$ (Y= C, N, Si, and P).

Compounds	$CaTiO_3$	$Ca_4Ti_4O_{10}C_2$	$Ca_4Ti_4O_{10}N_2$	$Ca_4Ti_4O_{10}Si_2$	$Ca_4Ti_4O_{10}P_2$
Ef(eV/atom)	-3.33	-34.2856492	-41.9969731	-38.9171817	-33.9392253

3.2. Electronic properties:

Calculations based on DFT were carried out to analyze the electronic properties of pure $CaTiO_3$ and doped$Ca_4Ti_4O_{10}Y_2$(Y= C, N, Si, and P). These calculations revealed the changes made to the electronic structure of $CaTiO_3$ as a result of doping. Figure 3 (a, b, c, d, and e) shows the energy band structures of the various compounds, in the energy range from -5 to 8 eV. The bandgap diagrams of the compounds are plotted along the high-symmetry path (W-L-Γ-X-W-K) in the Brillouin zone for a cubic structure, with the Fermi energy level (E_f) aligned at zero.
For pure $CaTiO_3$ (Figure 3 (a)), an indirect bandgap is observed between the L and Γ points. The bandgap width, calculated via the GGA approximation, is estimated at 2.003 eV. However, the use of the mBJ potential improves this estimate to 2.766 eV, reducing the discrepancy with the experimental value measured at 3.46 eV [42]. This refinement corrects the underestimation typical of standard GGA calculations and validates the increased accuracy offered by the mBJ potential. Furthermore, the general characteristics of the band structure and shift trends remain consistent with previous studies [9, 40]. In$Ca_4Ti_4O_{10}Y_2$ (Y= C, N, Si, and P) produces subtle but significant changes in the bandgap. In general, doping with elements having a lower electronegativity than oxygen increases the valence band maximum (VB) while stabilizing the conduction band minimum (CBM) [40] . This interaction results in a slight narrowing of the band gap. Doped compounds exhibit similar electronic behavior, marked by electron transitions from the valence band (VB) to the conduction band (CB). Doping also induces the formation of new electronic energy levels within the band gap. These intermediate levels facilitate electronic transitions between the VB and CB, thereby improving the overall electronic properties of the material. More specifically, compounds doping with Y (C, N) result in the valence band maxima (VBM) and conduction band minima (CBM) being located at L and Γ points, respectively, indicating indirect band gap energy. In contrast, doping with P results in both the VBM and CBM being situated at the high-symmetry point Γ, indicating a direct band gap. In contrast, doping with silicon results in a complete overlap between the VB and the CB, effectively reducing the band gap to zero. As a consequence, the materials studied exhibit conductive properties.

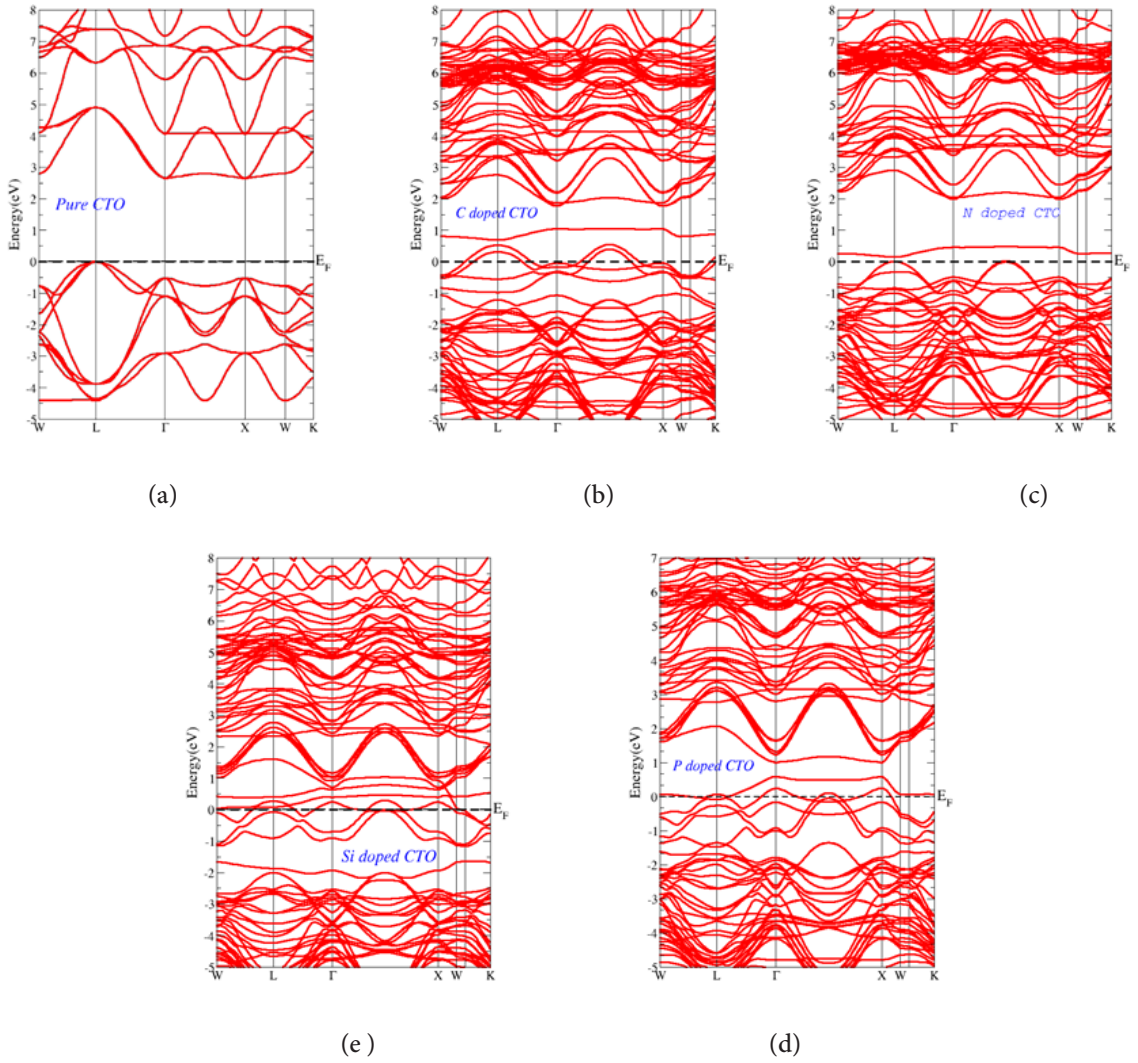

Figure 3: Band structure of (a) $CaTiO_3$, (b) $Ca_4Ti_4O_{10}C_2$, (c) $Ca_4Ti_4O_{10}N_2$, (d)$Ca_4Ti_4O_{10}Si_2$, and (e) $Ca_4Ti_4O_{10}P_2$.

Density of states (DOS) analysis provides crucial information on the electronic properties and chemical interactions of solid materials. In this study, the total DOS (TDOS) of pure $CaTiO_3$ and doped $Ca_4Ti_4O_{10}Y_2$ (Y= C, N, Si, and P) has been examined to assess the impact of doping on its electronic properties. The calculations, carried out after full relaxation of the crystal structures using the GGA+mBJ potential, cover an energy range from -6 eV to 7 eV, with the Fermi level fixed at 0 eV. For pure $CaTiO_3$, the electronic contribution is dominated by the hybridized O-2p, Ca-4s, and Ti-3d orbitals. The O-2p orbitals, located close to the Fermi level, play a decisive role by contributing a significant number of electrons. The lowest unoccupied band is dominated by Ti-3d orbitals, reflecting the intrinsic electronic nature of the material (Figure 4(a)). In doped structures, significant changes are observed in the DOS (Figures 4(b, c, d and e)), particularly at the bandgap level. Measured bandgap widths are 0.87 eV for $Ca_4Ti_4O_{10}C_2$ 1.63 eV for $Ca_4Ti_4O_{10}N_2$, 0 eV for $Ca_4Ti_4O_{10}Si_2$ and 0.6 eV for $Ca_4Ti_4O_{10}P_2$.

Furthermore, these results reveal a significant bandgap decrease in all doped compounds. In particular, Si doping reduces the band gap to zero, giving the material a metallic behavior. However, the movement of the Fermi level toward the VB in doped materials signifies p-type SC behavior. This reflects an increase in the concentration of hole carriers, which could improve performance in applications requiring p-type conductivity, such as electronic and optoelectronic devices. In

conclusion, this study demonstrates that doping $Ca_4Ti_4O_{10}Y_2$ (Y= C, N, Si, and P) substantially modifies its electronic properties. These results highlight the potential of this material to be tuned for specific applications, ranging from semiconductors to metallic conductors, depending on the dopant used.

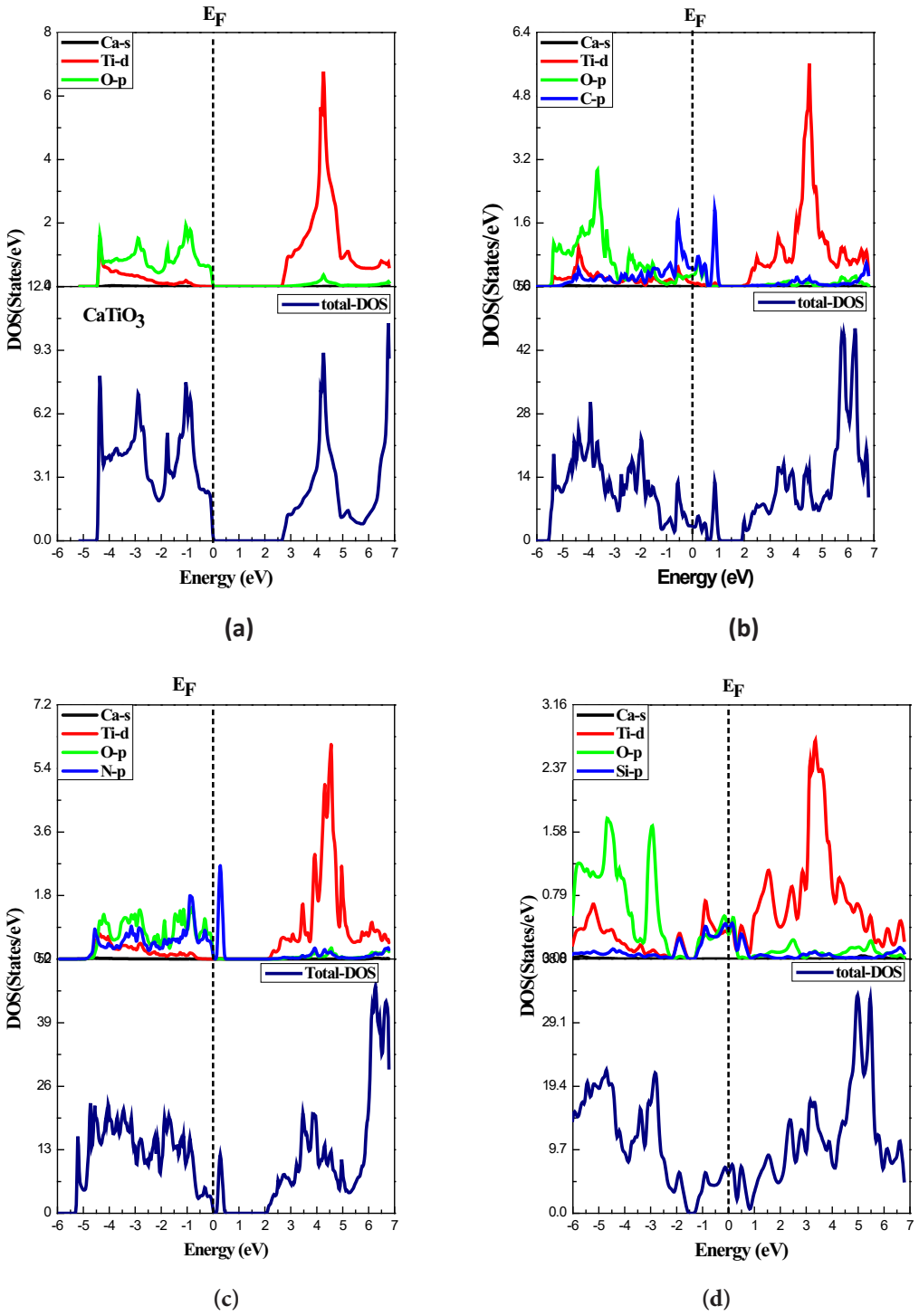

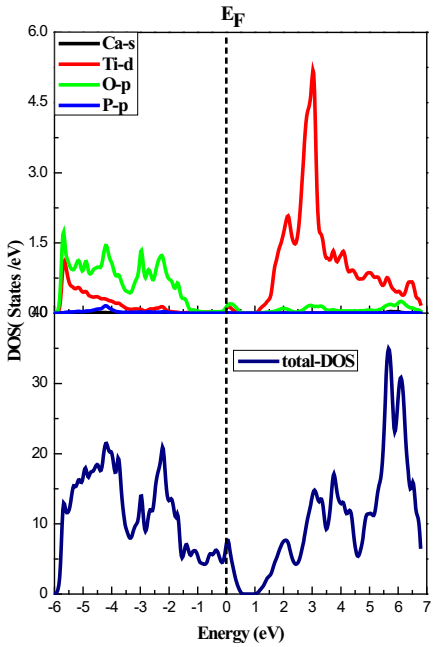

(e)

Figure 4: TDOS and PDOS for (a) $CaTiO_3$, (b)$Ca_4Ti_4O_{10}C_2$, (c) $Ca_4Ti_4O_{10}N_2$, (d)$Ca_4Ti_4O_{10}Si_2$, and (e)$Ca_4Ti_4O_{10}P_2$.

3.3. Optical properties

The optical properties of pure $CaTiO_3$ and doped$Ca_4Ti_4O_{10}Y_2$ (Y= C, N, Si, and P) have been studied to assess the impact of dopants on their electronic structure. These properties include dielectric functions (real part, $\varepsilon_1(\omega)$, and imaginary part, $\varepsilon_2(\omega)$), absorption coefficient, $\alpha(\omega)$, and optical conductivity, $\sigma(\omega)$.

The dielectric function $\varepsilon(\omega)$ was computed [43, 44, 45]:

$$\varepsilon(\omega) = \varepsilon_1(\omega) + i\varepsilon_2(\omega) \qquad (3)$$

The dielectric function real part ($\varepsilon 1(\omega)$) is obtained through the Kramers-Kronig transformation [46, 47]:

$$\varepsilon_1(\omega) = 1 + \frac{2}{\pi} P \int \frac{\omega' \varepsilon_2(\omega')}{\left(\omega'^2 - \omega_{12}\right)} d\omega' \qquad (4)$$

The imaginary part ($\varepsilon_2(\omega)$) values are calculated using the following procedure [48, 49, 50]:

$$\varepsilon_2(\omega) = \left(\frac{4\pi^2 e^2}{m^2 \omega^2}\right) \sum_{i.j} i \left|M\right| j^2 f_i \left(1 - f_j\right) \delta\left(E_f - E_i - \omega\right) d^3K \qquad (5)$$

The element of the dipole matrix is denoted M, the electron mass is m, the elementary charge is e, and P represents the principal value of the integral in this context. The initial and final states are denoted by the indices i and j respectively. The energy of the electron in state i, with wave vector k, is denoted by E_i, and the Fermi-Dirac distribution function associated with state i is denoted by f_i.

The $\varepsilon_1(\omega)$ and $\varepsilon_2(\omega)$ components enable the determination of various optical properties, such as the absorption coefficient $\alpha(\omega)$, using the following formula [48, 51, 52]:

$$\alpha(\omega)=\sqrt{2}\,\omega\left[\sqrt{\varepsilon_1(\omega)^2+\varepsilon_2(\omega)^2}-\varepsilon_1(\omega)\right]^{1/2} \quad (6)$$

The optical conductivity is calculated using the relationship that follows [48, 53]:

$$\sigma(\omega)=\frac{\omega}{4\pi}\varepsilon_2(\omega) \quad (7)$$

- **Dielectric function**

Figure 5(a) shows the variation of $\varepsilon_1(\omega)$ for pure and doped $CaTiO_3$, in an energy range from 0 to 14 eV. This function describes the material's response to an electric field, in particular its ability to polarize and store electrical energy. The static dielectric constant, $\varepsilon_1(0)$, which reflects polarization at low frequencies, shows a significant increase after doping. For pure $CaTiO_3$, $\varepsilon_1(0)$ is 4.25. However, when doped at a concentration of x = 16%, the values of $\varepsilon_1(0)$ increase to 7.1 for$Ca_4Ti_4O_{10}C_2$, 6.72 for $Ca_4Ti_4O_{10}N_2$, 36.63 for $Ca_4Ti_4O_{10}Si_2$, and 23.69 for $Ca_4Ti_4O_{10}P_2$. This trend indicates that the introduction of dopants enhances the material's polarizability. The observed increase in $\varepsilon_1(0)$ can be attributed to the dopants' ability to induce additional dipoles, alter both ionic and electronic polarizability, and modify the local electronic structure, thereby amplifying the dielectric response of the material [54]. At low energy, all dopants increase the material's polarizing strength, thereby decreasing its overall polarization. The arrangement of dopants by polarizing strength follows this order: Si > P > C > N > pure $CaTiO_3$. This indicates that Si is the most effective dopant for enhancing the material's dielectric response, as it has the greatest impact on polarization. In the high-energy range of 8 to 13 eV, the dielectric function becomes negative for both the pure and Y-doped materials, indicating that reflection is the dominant mechanism in this region [54]. Furthermore, the $\varepsilon_1(\omega)$ of the dielectric function's negative values indicate that the electromagnetic wave is dampened, and zero values suggest that longitudinally polarized waves may exist [55].

The $\varepsilon_2(\omega)$, is a key parameter for understanding electronic absorption processes in materials. Figure 5(b) illustrates $\varepsilon_2(\omega)$ for pure and doped $CaTiO_3$ in an energy range from 0 to 14 eV. The optical spectrum highlights several distinct peaks, associated with interband transitions between valence and conduction bands. Pure $CaTiO_3$, the absorption threshold is identified at around 2.766 eV, corresponding to electronic transitions involving the Ca-s, O-2p, and Ti-3d orbitals of the VB, and the Ti-3d and O-2p orbitals of the CB. An increase in $\varepsilon_2(\omega)$ is observed with photon energy, culminating in a notable peak around 4.88 eV. The latter is attributed to marked transitions between the Ti-3d and O-2p orbitals, which play a decisive role in the optical properties of $CaTiO_3$. Moreover, the presence of peaks within the visible spectrum indicates enhanced light absorption in this range, making $CaTiO_3$ a promising material for applications in optoelectronics [56]. Farther, Si- and P-doped structures show low-energy absorption thresholds (P_1, P_2) between 0 and 0.5 eV, indicating in-band transitions from occupied states near the valence band to Si-p and P-p acceptor states just below the E_f. These transitions suggest that electronic excitations from the valence band happen at lower energies, which enhances electrical conductivity by increasing hole concentration compared to the pure structure. The$Ca_4Ti_4O_{10}Y_2$(Y= C, N, Si, and P) notably alters its optical properties, shifting the absorption peaks to lower energies at approximately 2.60, 1.84, 2.27, and 3.20 eV, respectively. These peaks, associated with the $\varepsilon_2(\omega)$, indicate the material's electronic absorption and enhance its visibility within the spectrum. Furthermore, $Ca_4Ti_4O_{10}Y_2$ (Y= C, N, Si, and P) improves absorption in the visible range, making these compounds ideal for technological applications, especially in photovoltaics and optoelectronics [56].

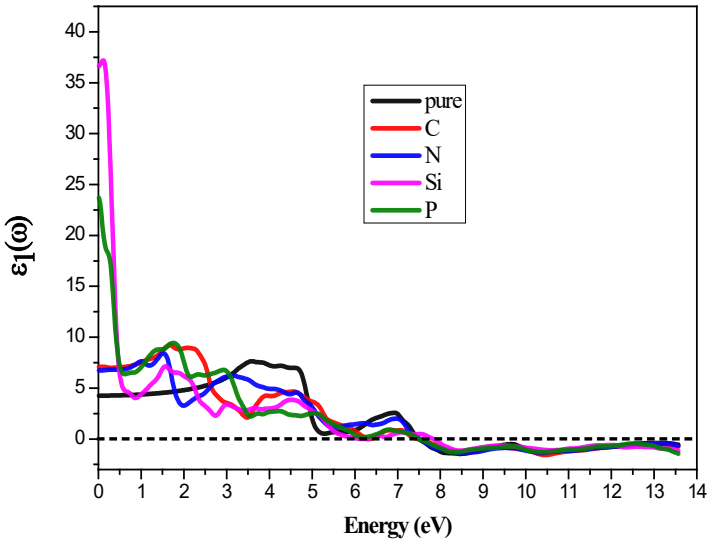

(a)

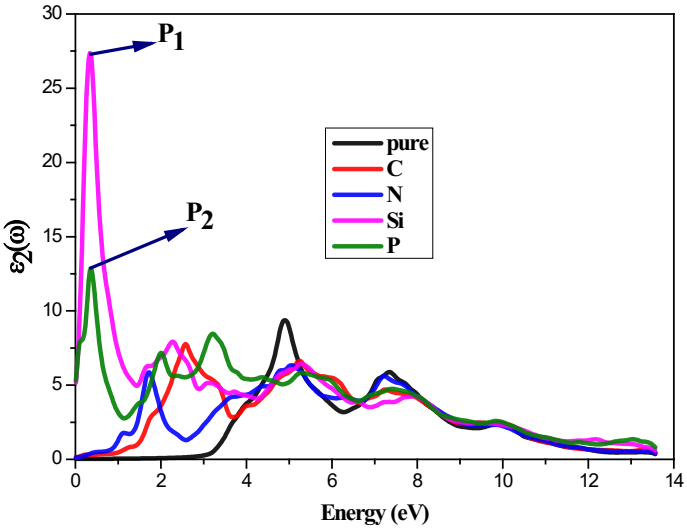

(b)

Figure 5: Dielectric function of pure $CaTiO_3$ and doped $Ca_4Ti_4O_{10}Y_2$ (Y= C, N, Si, and P): (a) Real part, (b) Imaginary part.

- **Absorption coefficient**

To maximize the efficiency of photovoltaic systems and fully exploit the solar spectrum, it is crucial to incorporate materials with strong absorption properties in the visible range (400-800 nm) [56, 57]. Optical absorption occurs when the energy of incident photons (E = hν) exceeds the energy of the band gap, allowing the excitation of electrons from the VB to the CB, thus generating a photovoltaic effect [57].

Figure 6 illustrates the absorption coefficient α(ω) of pure and doped $CaTiO_3$ in an energy range from 0 to 14 eV. It clearly appears that doping with chalcogen elements significantly enhances absorption in the visible range, with absorption coefficients reaching values as high as 104 cm^{-1}. This enhancement of absorption in the visible is attributed to the bandgap narrowing observed in

$Ca_4Ti_4O_{10}Y_2$ (Y= C, N, Si, and P). Notably, when the material is doped with 16% of Y and elements such as C, N, Si, and P, its absorption properties in this spectral range are significantly enhanced, demonstrating its potential as a promising material for photovoltaic cells and optoelectronic devices.

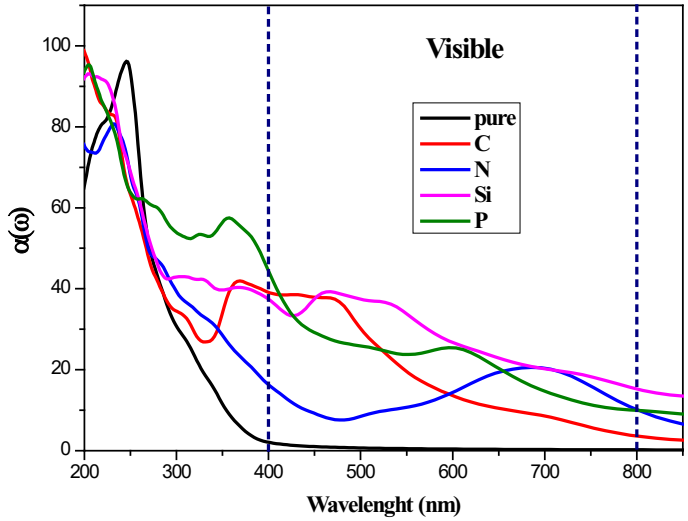

Figure 6: Absorption coefficient for pure $CaTiO_3$ and doped $Ca_4Ti_4O_{10}$ Y_2 (Y= C, N, Si, and P).

- **Optical conductivity**

Figure 7 illustrates σ(ω) for pure $CaTiO_3$ and doped $Ca_4Ti_4O_{10}Y_2$(Y= C, N, Si, and P) over an energy range of 0 to 14 eV, which represents the material's ability to transport electrons in response to an applied electromagnetic field [58]. For pure $CaTiO_3$, the σ(ω) curve reveals a threshold energy of 2.76 eV, marking the band edge associated with electronic transitions from O-2p to Ti-3d states near the VBM. This threshold indicates that indirect transitions primarily occur along the (Γ-L) directions in the Brillouin zone, reflecting electron movements through the crystal structure. The substituting Y dopants (Y= C, N, Si, and P) greatly enhance optical conductivity over a broad energy range, indicating better semiconducting properties and increased charge carrier mobility.

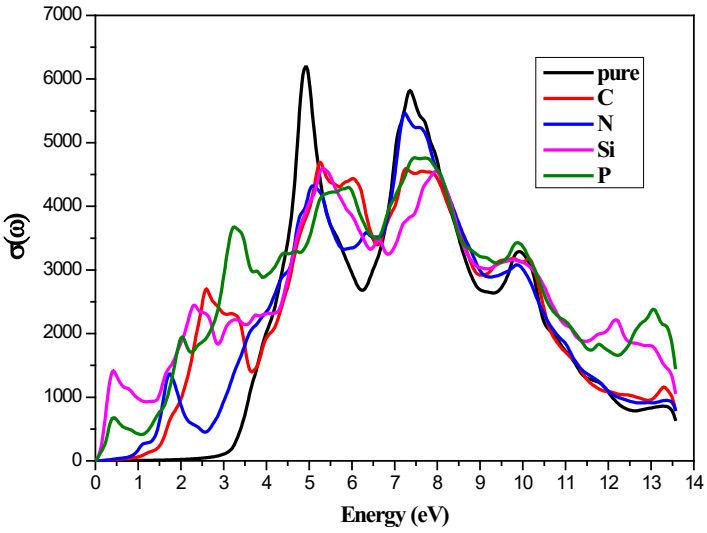

Figure 7: Optical conductivity for pure $CaTiO_3$ and doped $Ca_4Ti_4O_{10}Y_2$ (Y= C, N, Si, and P).

Distinct peaks in the σ(ω) curves for the doped compounds highlight enhanced excitation, demonstrating the effectiveness of substitutional doping in improving conductivity. Additionally, some peaks are observed in the visible range for $MgTiO_3$ doped with Y (C, N, Si, P), which may clarify the close relationship between the α(ω) and σ(ω). Further, the presence of peaks in the visible range indicates improved light absorption, which is beneficial for photocatalytic and optoelectronic applications. The maximum conductivity values for C, N, Si, and P doping are 4651.01, 5423.62, 4656.04, and 4748.27 Ω^{-1} cm^{-1}, respectively. This enhancement is due to the introduction of new electronic states from the dopants, which improve photon absorption, excitation capacity, and electron mobility, thereby optimizing the material's semiconducting performance. In conclusion, the analysis of σ(ω) shows that doping Ca_4 Ti_4 $O_{10}Y_2$(Y= C, N, Si, and P) is promising for advanced applications like photovoltaic and optoelectronic devices, where enhanced optical conductivity and tunable light absorption are essential for optimal performance.

4. CONCLUSION

This study explores in detail the structural, electronic and optical properties of the perovskite compound $CaTiO_3$, both in its pure form and doped with halogen elements such as C, N, Si and P. Using ab initio calculations based on the FP-LAPW approach within the framework of DFT via the Wien2k code and the GGA-mBJ approximation, we have demonstrated that pure $CaTiO_3$ has an indirect band gap of 2.766 eV, which indicates its semiconductor properties. Further, compounds doped with Y (C, N) exhibit an indirect band gap, whereas doping with P results in a direct band gap. Additionally, doping with Si reduces the band gap to zero. DOS reveals that the introduction of Y shifts the EF towards the VB, which is typical of p-type SC and reduces the bandgap width. The results also show that bandgap values decrease with increasing dopant concentrations: 0.87 eV for $Ca_4Ti_4O_{10}C_2$, 1.63 eV for$Ca_4Ti_4O_{10}N_2$, 0 eV for $Ca_4Ti_4O_{10}Si_2$ and 0.6 eV for $Ca_4Ti_4O_{10}P_2$. Concerning optical properties, doping influences optical conductivity σ(Ω), with maximum values of 4651.01, 5423.62, 4656.04, and 4748.27 Ω^{-1} cm^{-1} respectively for the elements C, N, Si, and P. These results indicate a significant improvement in the optical properties of the material. Notably, $Ca_4Ti_4O_{10}Y_2$ (Y= C, N, Si, and P) leads to a decrease in the bandgap, promoting absorption in the visible range and increasing optical conductivity. These improvements position Y-doped $CaTiO_3$ as a promising material for applications in photovoltaic cells and optoelectronic devices. In summary, this study highlights the crucial impact of doping on the electronic and optical properties of $CaTiO_3$, offering interesting prospects for using this material in renewable energy conversion technologies and next-generation optoelectronic devices.

Authors contribution: Abdellah Bouzaid: Writing – original draft, Visualization, Validation, Investigation, Formal analysis, Data curation, Conceptualization. Younes Ziat: Supervision. Hamza Belkhanchi: Visualization, Validation, Investigation, Formal analysis. Ayoub Koufi: Visualization. Mohammed Miri: Visualization. Hmad Fatihi: Visualization. Charaf Laghlimi: Visualization and validation. The author also reviewed and edited the manuscript for final approval.

Funding: The authors are warmly grateful to the support of "The Moroccan Association of Sciences and Techniques for Sustainable Development (MASTSD), Beni Mellal, Morocco".

Data Availability Statement: Not applicable.

Conflicts of Interest: The authors declare that they have no conflict of interest.

Acknowledgements: A deep thanks to Ms Saloua Rzaoudi, Miss Khadija Ziat and Miss Amina Ziat for their support. A special thank you to Professor Hanane Reddad from Sultan Moulay Slimane University, Beni Mellal, Morocco, for her technical and scientific support, as well as her full collaboration and discussion during the different steps of the present investigation.

REFERENCES

[1] A. Koufi, Y. Ziat, H. Belkhanchi, M. Miri, N. Lakouari, & F. Z. Baghli. A computational study of the structural and thermal conduct of MgCrH3 and MgFeH3 perovskite-type hydrides: FP-LAPW and BoltzTraP insight., E3S Web of Conferences (Vol. 582, p. 02003), 2024. https://doi.org/10.1051/e3sconf/202458202003

[2] A. Raihan, J. Rahman, T. Tanchangtya, M. Ridwan, & S. Islam. An overview of the recent development and prospects of renewable energy in Italy. Renewable and Sustainable Energy, 2(2), 0008 (2024).

[3] D. Gayen, R. Chatterjee, & S. Roy. A review on environmental impacts of renewable energy for sustainable development. International Journal of Environmental Science and Technology, 21(5), 5285-5310 (2024).

[4] U. M. Adanma, & E. O. Ogunbiyi. Assessing the economic and environmental impacts of renewable energy adoption across different global regions. Engineering Science & Technology Journal, 5(5), 1767-1793 (2024).

[5] C. Acar, I. Dincer, & G. F. Naterer. Review of photocatalytic water-splitting methods for sustainable hydrogen production. International Journal of Energy Research, 40(11), 1449-1473 (2016).

[6] S. Du, & F. Zhang. General applications of density functional theory in photocatalysis. Chinese Journal of Catalysis, 61, 1-36 (2024).

[7] W. Tu, Y. Zhou, & Z. Zou. Photocatalytic conversion of CO2 into renewable hydrocarbon fuels: state-of-the-art accomplishment, challenges, and prospects. Advanced Materials, 26(27), 4607-4626 (2014).

[8] X. Chen, C. Li, M. Grätzel, R. Kostecki, & S. S. Mao. Nanomaterials for renewable energy production and storage. Chemical Society Reviews, 41(23), 7909-7937 (2012).

[9] A. A. Adewale, A. Chik, T. Adam, O. K. Yusuff, S. A. Ayinde, & Y. K. Sanusi. First principles calculations of structural, electronic, mechanical and thermoelectric properties of cubic ATiO3 (A= Be, Mg, Ca, Sr and Ba) perovskite oxide., Computational Condensed Matter, 28, e00562 (2021).

[10] S. Dahbi, N. Tahiri, O. El Bounagui, & H. Ez-Zahraouy. Electronic, optical, and thermoelectric properties of perovskite BaTiO3 compound under the effect of compressive strain. Chemical Physics, 544, 111105 (2021).

[11] N. Tahiri, S. Dahbi, I. Dani, O. El Bounagui, & H. Ez-Zahraouy. Magnetocaloric and thermoelectric properties of the perovskite LaMnO3 material: a DFT study and Monte Carlo technique. Phase Transitions, 94(11), 826-834 (2021).

[12] S. Feng, P. Zhang, Y. Zhang, J. Cao, Y. Zheng, J. Wang, L Shi, J Pan, & C. Li. Self-cleaning transparent photovoltaic device in perovskite SrTiO3 quantum dot modified CuGaO2/Zn2SnO4 nanoarrays pn junction via surface plasma modification., Applied Physics Letters, 125(9) (2024).

[13] A. Koufi, Y. Ziat & H. Belkhanchi. Study of the Gravimetric, Electronic and Thermoelectric Properties of XAlH3 (X = Be, Na, K) as hydrogen storage perovskite using DFT and the BoltzTrap Software Package. Solar Energy and Sustainable Development, 53–66 (2024). https://doi.org/10.51646/jsesd.v14iSI_MSMS2E.403.

[14] H. S. Magar, A. M. Mansour, & A. B. A. Hammad. Advancing energy storage and supercapacitor applications through the development of Li+-doped MgTiO3 perovskite nano-ceramics. Scientific Reports, 14(1), 1849 (2024).

[15] T. A. Otitoju, P. U. Okoye, G. Chen, Y. Li, M. O. Okoye, & S. Li. Advanced ceramic

components: Materials, fabrication, and applications. Journal of industrial and engineering chemistry, 85, 34-65 (2020).

[16] M. Passi, & B. Pal. A review on CaTiO3 photocatalyst: Activity enhancement methods and photocatalytic applications. Powder Technology, 388, 274-304 (2021).

[17] Q. Zhang, Y. Wang, Y. Jia, W. Yan, Q. Li, J. Zhou, & K. Wu. Engineering the Electronic Structure towards Visible Lights Photocatalysis of CaTiO3 Perovskites by Cation (La/Ce)-Anion (N/S) Co-Doping: A First-Principles Study., Molecules, 28(20), 7134 (2023).

[18] D. K. Bhat, H. Bantawal, P. I. Uma, S. P. Kumar & U. S. Shenoy. Designing sustainable porous graphene-CaTiO3 nanocomposite for environmental remediation. Sustainable Chemistry for the Environment, 5, 100071 (2024).

[19] A. Krause, W. M. Weber, D. Pohl, B. Rellinghaus, A. Kersch & T. Mikolajick. Investigation of band gap and permittivity of the perovskite CaTiO3 in ultrathin layers. Journal of Physics D: Applied Physics, 48(41), 415304 (2015).

[20] X. J. Huang, Y. A. N. Xin, H. Y. Wu, F. A. N. G. Ying, Y. H. Min, W. S. Li, S. Y. Wang & Z. J.Wu. Preparation of Zr-doped CaTiO3 with enhanced charge separation efficiency and photocatalytic activity., Transactions of Nonferrous Metals Society of China, 26(2), 464-471 (2016).

[21] M. Rizwan, Z. Usman, M. Shakil, S. S. A. Gillani, S. Azeem, H. B. Jin, C. B. Cao, R. F. Mehmood, G. Nabi & M. A. Asghar. Electronic and optical behaviour of lanthanum doped CaTiO3 perovskite. Materials Research Express, 7(1), 015920 (2020).

[22] I. Grinberg, D. V. West, M. Torres, G. Gou, D. M. Stein, L. Wu, G. Chen, E. M. Gallo, A. R. Akbashev, P. K. Davies, J. E. Spanier & A. M. Rappe. Perovskite oxides for visible-light-absorbing ferroelectric and photovoltaic materials. Nature,, 503(7477), 509-512 (2013).

[23] H. Liu, J. Cheng, H. Dong, J. Feng, B. Pang, Z. Tian, S. Ma, F. Xia, C. Zhang & L. Dong. Screening stable and metastable ABO3 perovskites using machine learning and the materials project. Computational Materials Science, 177, 109614 (2020).

[24] L. Attou, A. Al-Shami, J. Boujemaâ, O. Mounkachi, & H. Ez-Zahraouy. Predicting the structural, optoelectronic, dynamical stability and transport properties of Boron-doped CaTiO3: DFT based study. Physica Scripta, 97(11), 115808 (2022).

[25] S. Chahar, K. K. Mishra, & R. Sharma. Analysing the suitability of CaTiO3/Ca1–xSrxTiO3/SrTiO3 perovskite for fabrication of optoelectronic devices using QuantumATK tool: a study for electronic and optical properties., Physica Scripta, 99(3), 035963 (2024).

[26] P. Blaha, K. Schwarz, G. K. Madsen, D. Kvasnicka & J. Luitz. wien2k. An augmented plane wave+ local orbitals program for calculating crystal properties, 60(1) (2001).

[27] M. Miri, Y. Ziat, H. Belkhanchi, & Y. A. El Kadi. Structural, elastic, and opto-electronic conduct of half Heusler Li (Ca, Mg, Zn) N alloys: Ab initio computation. Solid State Communications, 396, 115765 (2025). https://doi.org/10.1016/j.ssc.2024.115765

[28] D. Koller, F. Tran, & P. Blaha. Improving the modified Becke-Johnson exchange potential. Physical Review B—Condensed Matter and Materials Physics, 85(15), 155109 (2012).

[29] V. K. Solet, & S. K. Pandey. Assessing the performance of Mg $ _ {2} $ Si and Ca $ _ {2} $ Si from DFT and SLME calculations for solar cell applications. arXiv preprint arXiv:2401.05296 (2024).

[30] F. D. Murnaghan. The compressibility of media under extreme pressures. Proceedings of the National Academy of Sciences, 30(9), 244-247 (1944).

[31] P. H. Mott, J. R. Dorgan & C. M. Roland. The bulk modulus and Poisson's ratio of "incompressible" materials. Journal of Sound and Vibration, 312(4-5), 572-575 (2008).

[32] R. Ali, & M. Yashima. Space group and crystal structure of the perovskite CaTiO3 from 296 to 1720 K. Journal of Solid State Chemistry, 178(9), 2867-2872 (2005).

[33] B. J. Kennedy, C. J. Howard, & B. C. Chakoumakos. Phase transitions in perovskite at elevated temperatures-a powder neutron diffraction study. Journal of Physics: Condensed Matter, 11(6), 1479 (1999).

[34] Q. Mahmood, M. Yaseen, B. U. Haq, A. Laref, & A. Nazir. The study of mechanical and thermoelectric behavior of MgXO3 (X= Si, Ge, Sn) for energy applications by DFT. Chemical Physics, 524, 106-112 (2019).

[35] H. Fatihi, M. Agouri, H. Ouhenou, H. Benaali, A. Zaghrane, A. Abbassi, M. El Idrissi, S. Taj & B. Manaut. Enhancing Solar Cell Efficiency: A Comparative Study of Lead-Free Double Halide Perovskites $$ Rb_ {2} CuAsBr_ {6} $$ and, $$ Rb_ {2} TlAsBr_ {6} $$ using DFT and SLME Methods. Journal of Inorganic and Organometallic Polymers and Materials, 1-14 (2024).

[36] A. Bouzaid, Y. Ziat, H. Belkhanchi, H. Hamdani, A. Koufi, M. Miri, C. Laghlimi, Z. Zarhri. Ab initio study of the structural, electronic, and optical properties of MgTiO3 perovskite materials doped with N and P. E3S Web of Conferences, (Vol. 582, p. 02006), (2024) https://doi.org/10.1051/e3sconf/202458202006

[37] X. Zhou, J. Shi, & C. Li. Effect of metal doping on electronic structure and visible light absorption of SrTiO3 and NaTaO3 (Metal= Mn, Fe, and Co). The Journal of Physical Chemistry C, 115(16), 8305-8311. 2011..

[38] H. Bentour, M. Boujnah, M. Houmad, M. El Yadari, A. Benyoussef, & A. El Kenz. DFT study of Se and Te doped SrTiO 3 for enhanced visible-light driven phtocatalytic hydrogen production. Optical and Quantum Electronics, 53, 1-13. 2021..

[39] D. E. Vanpoucke, P. Bultinck, S. Cottenier, V. Van Speybroeck, & I. Van Driessche. Aliovalent doping of CeO_2: DFT study of oxidation state and vacancy effects. (2014).

[40] Q. Zhang, Y. Wang, Y. Jia, W. Yan, Q. Li, J. Zhou, & K. Wu. Engineering the Electronic Structure towards Visible Lights Photocatalysis of CaTiO3 Perovskites by Cation (La/Ce)-Anion (N/S) Co-Doping: A First-Principles Study., Molecules, 28(20), 7134 (2023).

[41] A. Bouzaid, Y. Ziat, H. Belkhanchi. Prediction the effect of (S, Se, Te) doped MgTiO3 on optoelectronic, catalytic, and pH conduct as promised candidate photovoltaic device: Ab initio framework. International Journal of Hydrogen Energy,, 100, 20-32 (2025) https://doi.org/10.1016/j.ijhydene.2024.12.284

[42] U. Balachandran, B. Odekirk, & N. G. Eror. Electrical conductivity in calcium titanate. Journal of Solid State Chemistry, 41(2), 185-194. 1982..

[43] Y. Ziat, H. Belkhanchi & Z. Zarhri. DFT Analysis of Structural, Electrical, and Optical Properties of S, Si, and F-Doped GeO2 Rutile: Implications for UV-Transparent Conductors and Photodetection. Solar Energy and Sustainable Development , 14(1), 74–89 (2025). https://doi.org/10.51646/jsesd.v14i1.232.

[44] R. Majumder, M. M. Hossain, & D. Shen. First-principles study of structural, electronic, elastic, thermodynamic and optical properties of LuPdBi half-Heusler compound. Modern Physics Letters B, 33(30), 1950378 (2019).

[45] Y. Ziat, Z. Zarhri, H. Belkhanchi, O. Ifguis, A. D. Cano. Effect of Be and P doping on the electron density, electrical and optoelectronic conduct of half-Heusler LiMgN within ab initio scheme. Physica Scripta, 97(10), 105802 (2022). https://iopscience.iop.org/article/10.1088/1402-4896/

ac8b40/meta

[46] L. De, R. Kronig. On the theory of dispersion of x-rays. Journal of the Optical Society of America, 12(6), 547-557 (1926).

[47] J. S. Toll. Causality and the dispersion relation: logical foundations. Physical review, 104(6), 1760 (1956).

[48] C. M. Okoye. Theoretical study of the electronic structure, chemical bonding and optical properties of KNbO3 in the paraelectric cubic phase. Journal of Physics: Condensed Matter, 15(35), 5945 (2003).

[49] C. Ambrosch-Draxl, & R. Abt. The calculation of optical properties within WIEN97. ICTP Lecture Notes. (1998).

[50] M. Kumar, R. P. Singh, & A. Kumar. Opto-electronic properties of HfO2: a first principle-based spin-polarized calculations. Optik, 226, 165937 (2021).

[51] S. Saha, T. P. Sinha, & A. Mookerjee. Electronic structure, chemical bonding, and optical properties of paraelectric BaTiO 3. Physical Review B, 62(13), 8828 (2000).

[52] M. Miri, Y. Ziat, H. Belkhanchi, Z. Zarhri, Y. A. El Kadi. Structural and optoelectronic properties of LiYP (Y= Ca, Mg, and Zn) half-Heusler alloy under pressure: A DFT study. Physica B: Condensed Matter, 667, 415216 (2023). https://doi.org/10.1016/j.physb.2023.415216

[53] A. Delin, O. Eriksson, R. Ahuja, B. Johansson, M. S. S. Brooks, T. Gasche, S. Auluck & J. M. Wills. Optical properties of the group-IVB refractory metal compounds. Physical Review B, 54(3), 1673 (1996).

[54] M. Rizwan, A. Ayub, M. Shakil, Z. Usman, S. S. A. Gillani, H. B. Jin, & C. B. Cao. Putting DFT to trial: For the exploration to correlate structural, electronic and optical properties of M-doped (M= Group I, II, III, XII, XVI), lead free high piezoelectric c-BiAlO3. Materials Science and Engineering: B, 264, 114959 (2021).

[55] E. Zahedi, M. Hojamberdiev, & M. F. Bekheet. Electronic, optical and photocatalytic properties of three-layer perovskite Dion–Jacobson phase CsBa 2 M 3 O 10 (M= Ta, Nb): a DFT study., Rsc Advances, 5(108), 88725-88735 (2015).

[56] S. Dahbi, N. Tahiri, O. El Bounagui, & H. Ez-Zahraouy. The new eco-friendly lead-free zirconate perovskites doped with chalcogens for solar cells: Ab initio calculations. Optical Materials, 109, 110442 (2020).

[57] B. Mouhib, S. Dahbi, A. Douayar, N. Tahiri, O. El Bounagui, & H. Ez-Zahraouy. Theoretical investigations of electronic structure and optical properties of S, Se or Te doped perovskite ATiO3 (A= Ca, Ba, and Sr) materials for eco-friendly, solar cells. Micro and Nanostructures, 163, 107124 (2022).

[58] A. Ilyas, S. A. Khan, K. Liaqat, & T. Usman. Investigation of the structural, electronic, magnetic, and optical properties of CsXO3 (X= Ge, Sn, Pb) perovskites: A first-principles calculations. Optik, 244, 167536., (2021).

Solar Energy
And Sustainable Development
Refereed, biannual scientific journal issued by:
The Libyan Center for Solar Energy Research and Studies

Improving PEM Water Electrolysis Efficiency with ANN-Based Control to Handle Rapid Photovoltaic Power Fluctuations

Abdellah El Idrissi[1*], Belkasem Imodane[2], Hamid Hamdani[3], M'hand Oubella[4], Mohamed Benydir[5], Mohamed Ajaamoum[6].

[1,2,4,5,6]Laboratory of Engineering Sciences and Energy Management (LASIME), Ibn Zohr University, National School of Applied Sciences, Agadir, Morocco.
[3]Engineering and Applied Physics Team (EAPT), Higher School of Technology, Sultan Moulay Slimane University, Beni Mellal, Morocco.

E-*mail:* [1] abdellah.elidrissi@edu.uiz.ac.ma ,[2] b.imodane@uiz.ac.ma ,[3] h.hamdani@usms.ma , [4] m.oubella@uiz.ac.ma , [5] mohamed.benydir@edu.uiz.ac.ma , [6] m.ajaamoum@uiz.ac.ma.

SPECIAL ISSUE ON:

The 1St International Conference on Sciences and Techniques for Renewable Energy and the Environment.
(STR2E 2025)
May 6-8, 2025 at FST-Al Hoceima-Morocco.

KEYWORDS

Hydrogen production, Renewable energy, PEM electrolyzer, DC-DC Converter, Artificial Neural Network.

ABSTRACT

This research presents an innovative method for enhancing hydrogen production through proton exchange membrane (PEM) water electrolysis, powered by photovoltaic (PV) energy. The system is based on the Perturbation and Observation (P & O) method of Maximum Power Point Tracking (MPPT) with a boost converter to maximize energy capture, and a buck converter to stabilize DC voltage, ensuring compatibility with the proton exchange membrane electrolyzer. An artificial neural network (ANN)-based controller manages the buck converter, effectively minimizing the effects of solar irradiation fluctuations on electrolyzer performance.

By using the adaptive learning capabilities of the ANN, the proposed approach increases the efficiency of hydrogen production under varying solar energy levels. Simulation results indicate that the ANN controller outperforms the conventional PI controller, reducing the mean absolute percentage error (MAPE) from 1.22 % to 0.95 %, decreasing overshoot from 12.84 % to 3.19 %, and achieving a faster settling time of 0.022 s compared to 0.023 s. This study advances renewable hydrogen production technologies, demonstrating that ANN-based control improves dynamic performance and contributes to the development of smarter, more resilient energy systems.

*Corresponding author.

DOI: https://doi.org/10.51646/jsesd.v14iSTR2E.985

This is an open access article under the CC BY-NC license (http://Attribution-NonCommercial 4.0 (CC BY-NC 4.0)).

تحسين كفاءة التحليل الكهربائي للماء بتقنية الغشاء البروتوني (PEM) عبر التحكم القائم على الشبكات العصبية الاصطناعية لمواجهة التقلبات السريعة في الطاقة الكهربائية المولدة من الألواح الشمسية

عبد الله الإدريسي، بلقاسم اموضان، حميد حمداني، محند أوبلا، محمد بنيدير ، محمد اجعموم.

ملخص: يقدم هذا البحث طريقة مبتكرة لتحسين إنتاج الهيدروجين من خلال التحليل الكهربائي للماء باستخدام غشاء تبادل البروتون، مدعومًا بالطاقة الكهروضوئية. يستفيد النظام من طريقة التشويش القابلة والمرنة لتتبع نقطة القدرة القصوى مع محول تعزيز لزيادة التقاط الطاقة إلى أقصى حد، ومحول باك لتثبيت جهد التيار المستمر، مما يضمن التوافق مع المحلل الكهربائي بغشاء تبادل البروتون. يدير نظام تحكم قائم على الشبكة العصبية الاصطناعية محول باك، مما يقلل بشكل فعال من آثار تقلبات الإشعاع الشمسي على أداء المحلل الكهربائي.

من خلال الاستفادة من القدرة التعلمية التكيفية لنظام التحكم القائم على الشبكة العصبية الاصطناعية، يزيد النهج المقترح من كفاءة إنتاج الهيدروجين في ظل مستويات طاقة شمسية متفاوتة. تشير نتائج المحاكاة إلى أن وحدة تحكم النظام القائم على الشبكة العصبية الاصطناعية تتفوق على وحدة التحكم التناسبي التكاملي التقليدية، مما يوفر أوقات استجابة أسرع ويعزز كفاءة النظام. تعمل هذه الدراسة على تطوير تقنيات إنتاج الهيدروجين المتجددة، مما يدعم تطوير أنظمة طاقة أكثر ذكاءً ومرونة.

الكلمات المفتاحية – إنتاج الهيدروجين، الطاقة المتجددة، المحلل الكهربائي، محول التيار المستمر، الشبكة العصبية الاصطناعية.

1. INTRODUCTION

The global transition to renewable energies is changing how we produce and use energy. As countries aim to reduce greenhouse gas emissions, they are increasingly turning to cleaner energy solutions. Hydrogen has become a promising energy source due to its clean-burning nature and high energy content, particularly valuable in industries and transportation sectors where direct electrification is challenging [1], [2]. However, for hydrogen to be truly sustainable, its production must also be efficient and environmentally friendly. One effective method for producing hydrogen is through Proton Exchange Membrane (PEM) water electrolysis powered by sources of renewable energy such as solar energy. Laghlimi et al. (2024) explores the historical evolution and modern techniques of green hydrogen production through water electrolysis, highlighting its role in sustainable energy. It emphasizes environmentally friendly methods for addressing the challenges of climate change [3]. Solar photovoltaic (PV) systems, which take advantage of the sun's energy, are widely used due to their reliability and availability [4]. Nevertheless, the integration of PV systems with PEM electrolyzers poses significant challenges, as solar energy varies throughout the day, causing fluctuations in the power generated [5]. These fluctuations can have an impact on the performance of PEM electrolyzers, which require a stable power supply to produce hydrogen efficiently[6]. Consequently, solving these problems requires advanced systems to efficiently manage and control the flow of energy [7]. Various techniques have been applied to meet the challenges of integrating photovoltaic systems with PEM electrolyzers [8]. Traditional control methods, such as proportional-integral (PI) and proportional-integral-derivative (PID) controllers, are widely utilized because they are straightforward and simple to implement [9]. These methods can effectively control voltage and current under stable, predictable conditions. However, their performance decreases when confronted with highly variable solar irradiation or rapid environmental changes, as they suffer from a lack of adaptability and may encounter non-linear system behavior [10]. Advanced control strategies such as fuzzy logic and model predictive control (MPC) have also been investigated for their ability to handle non-linearity and variability [11], but these approaches often require significant computational resources and may be less effective at adapting to dynamic conditions over time [12]. In contrast, artificial neural networks (ANNs) are a promising alternative, offering significant advantages in complex, dynamic systems [13]. ANNs can model non-linear relationships, learn from data and adapt to changing input

conditions, making them particularly well suited to renewable energy applications [14]. Unlike traditional methods, ANNs do not depend on predefined system models, enabling them to deal more effectively with variability and unpredictability. This study exploits the adaptive and learning capabilities of ANNs to improve the stability and performance of the integrated PV-PEM system, addressing the limitations of conventional techniques [15]. This research proposes an artificial neural network (ANN)-based control approach to improve the efficiency and stability of proton exchange membrane (PEM) water electrolysis when powered by a photovoltaic (PV) system under variable sunlight conditions. The inherent intermittency of solar energy leads to voltage and current fluctuations that can have a negative impact on electrolyzer performance, reducing hydrogen production efficiency and increasing stress on system components. To mitigate these issues, the proposed system incorporates maximum power point tracking (MPPT) using the Perturb and Observe (P and O) algorithm, which continuously adjusts the operating point of the photovoltaic array to extract the maximum available power [16]. A boost converter raises the photovoltaic voltage to an appropriate level for efficient energy conversion, while a buck converter precisely regulates the voltage supplied to the electrolyzer, ensuring optimal operating conditions for hydrogen production [17], [18]. At the heart of the proposed approach is an ANN-based control system that dynamically adapts to rapid changes in solar irradiance and temperature, enabling more efficient and stable power regulation compared to traditional proportional-integral (PI) control. Unlike fixed-parameter controllers, the ANN is trained to recognize complex patterns in power fluctuations and adjust control signals accordingly, improving voltage stability and reducing energy losses [19].The performance of the ANN-based controller is rigorously evaluated by comparing it with conventional PI control in terms of hydrogen production efficiency, voltage stability and overall system reliability.

The results of this study demonstrate that the ANN-based control approach significantly improves electrolyzer efficiency and durability, ensuring constant hydrogen production even under fluctuating solar energy conditions. This research contributes to the development of intelligent control strategies for electrolysis systems powered by renewable energies, paving the way for more sustainable, resilient and efficient hydrogen production technologies.

2. SYSTEM DESCRIPTION AND DESIGN

2.1. The Electrical Equivalent Representation of the PEM Electrolyzer

Our system consists of a photovoltaic hydrogen production setup that includes a solar panel, a boost converter for MPPT, and a buck converter to step down the voltage to 7.5V. This configuration powers a 400W PEM electrolyzer for efficient hydrogen generation, as shown in Figure 1.

The design parameters for the PEM electrolyzer, solar panel, boost converter, and buck converter are outlined in the following subsections.

The electrical equivalent model of the PEM electrolyzer is an essential tool for testing and validating the performance of control techniques and power topologies. It provides a robust method for simulating electrolyzer behavior without the need for physical hardware implementation, thus mitigating risks such as damage caused by voltage overshoot and current ripple.

Various electrical models of PEM electrolyzers have been proposed in the literature. Some studies, such as references [20], [21], represent the electrolyzer as a simple resistor. Others, including references [22], [23], model it using an equivalent electrical circuit made up of a resistor (R_{elz}) and a reversible voltage (E_{elz}) connected in series. This approach captures the electrolyzer's static electrical characteristics, such as its voltage, current, and power-current relationships.

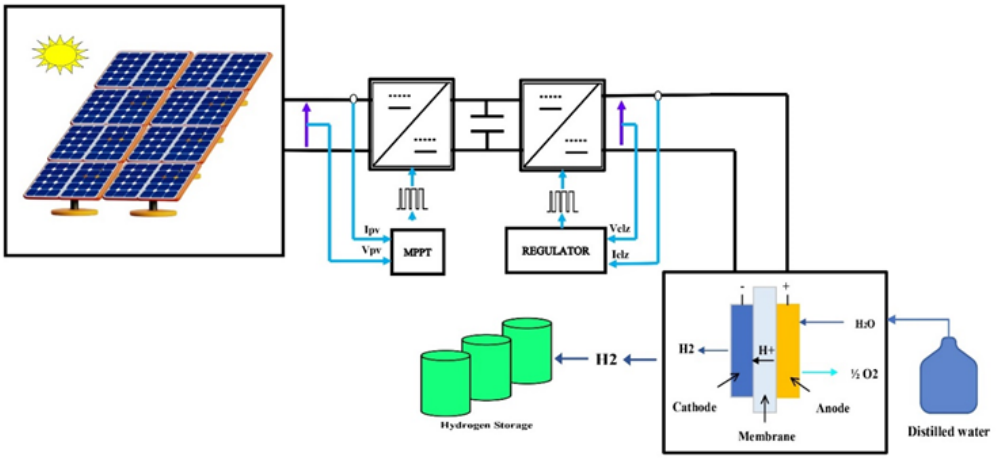

Figure 1 Schematic Representation of the Discussed System.

In this study, the PEM electrolyzer is represented as a series combination of a resistor and a reversible DC voltage. This model provides an accurate representation of the electrolyzer's operating range and behavior, expressed in the following mathematical equation (1.1):

$$V_{elz} = R_{elz} I_{elz} + E_{elz} = 0.0625 I_{elz} + 4.375 \qquad (1.1)$$

The electrical behavior in the range of 3A to 50A can be approximated through linear interpolation to determine the coefficients of this equation (1.1) [24]. The experimental data, sourced from [24] demonstrates a nearly linear relationship between voltage and current, as depicted in Fig. 2. This observation lends credence to the idea that the system can be modeled using resistances and a reversible voltage.

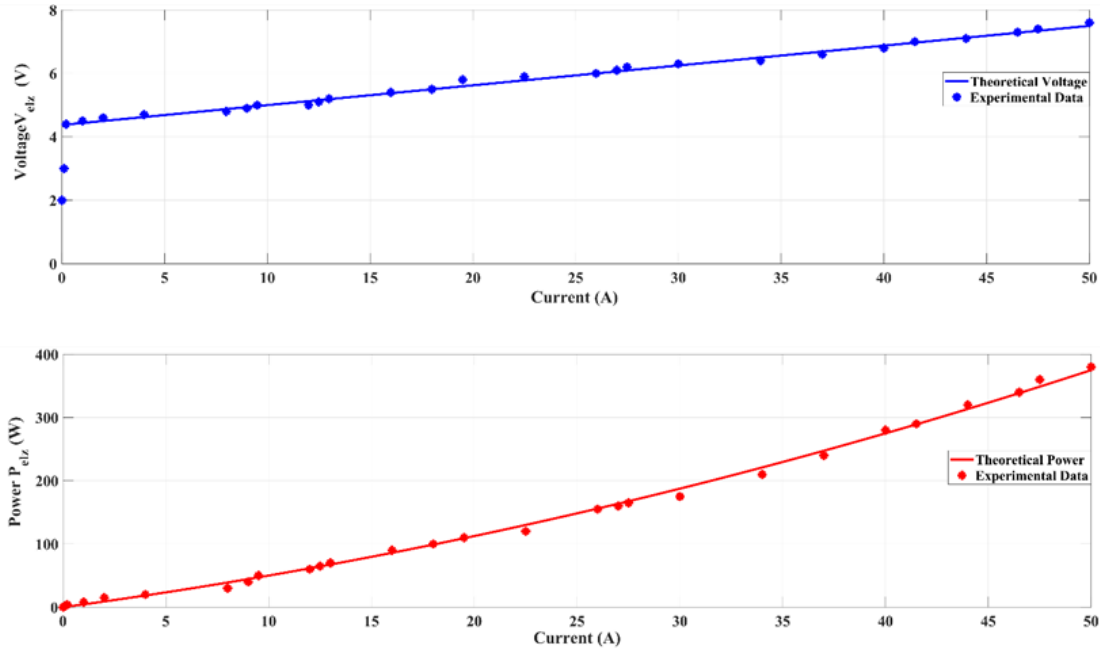

Figure 2 Static characteristics of the selected PEM electrolyzer cells.

The method for determining the hydrogen production rate (N_{H_2}) in moles per second, is presented in equation (1.2), where n is the number of electrons involved, I is the electric current in amperes, and F is Faraday's constant (96485 C/mol)}.

$$N_{H_2} = \frac{nI}{2F} \quad (\text{moles}/\text{s}) \qquad (1.2)$$

The hydrogen produced can be transformed from moles per second to liters per minute using the following equation (1.3):

$$N_{H_2} = 0.00696nI \quad (L/min) \tag{1.3}$$

Table 1 PEM Electrolyzer Specifications.

Specification	**Result**	
Rated Electrolyzer Power	400	Watts
Stack Operating Electrolyzer Voltage	2.2--8	Volts
Stack Electrolyzer Current	0 -- 50	Amperes
Output Pressure.	0.1--10.5	bar
Hydrogen Flow Rate at Standard Temperature and Pressure	1	Litre/min
Cell Numbers	3	-

2.2. Solar Photovoltaic Array

Solar photovoltaic units are arranged in parallel and series to increase power output and form solar photovoltaic arrays. The solar panel discussed in this article consists of two panels connected in series and four panels connected in parallel. Together, these panels have a total maximum power capacity of 965.6 W, as shown in Figure 2. The specifications of the solar modules are provided in Table 2.

Table 2 Solar panel parameters for Waaree Energies WU-120.

Parameters	Value
$\mathbf{I}_{mp}$	7.1 A
$\mathbf{V}_{mp}$	17 V
$\mathbf{P}_{max,e}$	120.7 W
$\mathbf{I}_{sc}$	8 A
$\mathbf{V}_{oc}$	21 V
PV solar irradiation (G)	1000 W/m²
PV operation temperature (T)	25 °C

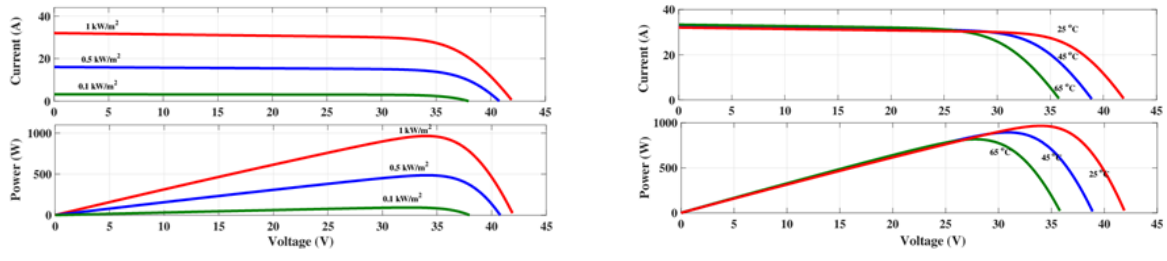

(a) **(b)**

Figure 3 Voltage-current and voltage-power characteristics of a photovoltaic panel (Waare Energies WU-120, 2 series modules, 4 parallel strings) (a) for different irradiance levels (G) at T = 25°C; (b) for different temperatures with $G = 1000\ W/m^2$

2.3. Boost Converter

A boost converter, as shown in Figure 4, is employed for MPPT operation. Its input is the peak voltage of the solar panel, with the MPP voltage fixed at 34V. The output of the boost converter is represented by the DC link voltage (V_{mppt}), which is set at 50V. The duty cycle D_{pv} , inductance

L_{pv} , and capacitor *Cpv* of the boost converter are determined using the following equations (1.4):

$$D_{pv} = \frac{V_{mppt} - V_{pv}}{V_{mppt}} \tag{1.4}$$

$$L_{pv} = \frac{V_{pv} D_{pv}}{f_{s_{pv}} \Delta I_{pv}} \tag{1.5}$$

$$C_{pv} = \frac{I_{pv}}{f_{s_{pv}} \Delta V_{pv}} \tag{1.6}$$

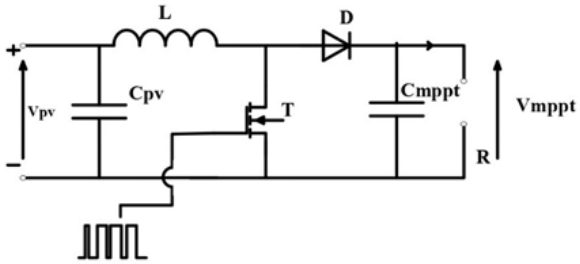

Figure 4. Electrical schematic of the DC-DC Boost converter.

Table 3 MPPT boost parameters [25].

Parameters	**Values**
Boost Input Voltage (V_{pv})	42V
Boost Output Voltage (V_{mppt})	50V
Inductor (L_{pv})	0.5 mH
Input capacitor (C_{pv})	1000µF
Output capacitor (C_{mppt})	1600µF
Switching Frequency (f_{spv})	10 kHz

2.4. Buck Converter

Electrolyzers typically require a low DC voltage for water electrolysis, which is why a DC/DC buck converter, as shown in Figure 5, is often used. These converters not only reduce the voltage but also perform voltage conditioning, owing to the non-linear voltage characteristics of the electrolyzer stack. The parameters of the buck converter are calculated as follows:

$$D_{elz} = \frac{V_{elz}}{V_{mppt}} \tag{1.7}$$

$$L_{elz} = \frac{V_{elz}(1 - D_{elz})}{f_{s_{elz}} \Delta I_{elz}} \tag{1.8}$$

$$C_{elz} = \frac{V_{elz}(1 - D_{elz})}{8 L_{elz} f_{s_{elz}}^2 \Delta V_{elz}} \tag{1.9}$$

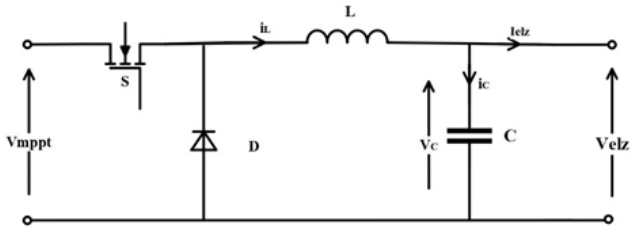

Figure 5. Electrical schematic of the DC-DC Buck converter.

Table 4 Specification of the Buck converter [25].

Parameters	Values
Buck Input Voltage (V_mppt)	50V
Buck Output Voltage (V_elz)	7.5V
Inductor (L_elz)	1.5 mH
Capacitor (C_elz)	100µF
Switching Frequency (f_sel)	10 kHz

3. CONTROL STRATEGIES

The electrical control strategy for the selected system uses two controllers: perturbation and observation (P&O) for maximum power point tracking (MPPT) and a proportional-integral (PI) controller. We replace the PI controller with an artificial neural network (ANN)-based control to compare their performance. Each controller is adapted to specific functions, working together to optimize system performance, ensure stability, and improve reliability.

3.1. MPPT Controller

The MPPT controller regulates the boost converter to maximize power extraction from the solar panel. The perturbation and observation (P&O) technique, shown in Figure 6, is employed as the MPPT algorithm due to its simplicity and broad practical use [26]

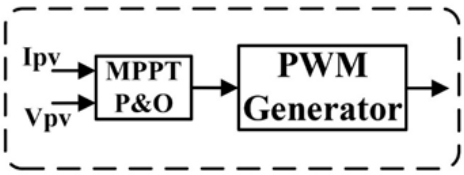

Figure 6. System Electrical Control Strategy using MPPT (P and O).

3.2. PI Controller

A proportional-integral (PI) controller Figure 7 is implemented to regulate the buck converter, ensuring that the output voltage supplied to the electrolyser remains stable. The PI controller evaluates the difference between the reference voltage and the actual voltage, generating the control signal for pulse-width modulation (PWM) to adjust the buck converter's duty cycle.

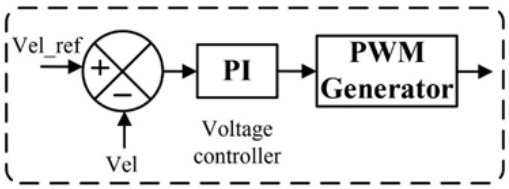

Figure 7. System Electrical Control Strategy using PI Controller.

3.3. ANN-based Controller

For our model Figure 8, we use 64 hidden neurons and the Levenberg-Marquardt learning algorithm. The data collected to train the ANN model includes the error between the desired value (7.5 V) and the actual output voltage, as well as the error variation , which indicates the variation in the error signal between successive time steps. In addition, the previous control output D is used as an input that reflects the control signal generated by the PI controller during the previous time step. The output of the model is the current output of the PI controller, which serves as a duty cycle sent to the PWM generator to convert it into a PWM signal for the power converter.

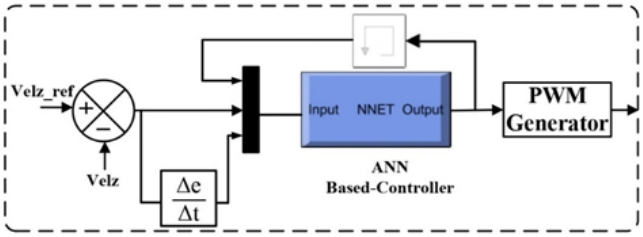

Figure 8. System Electrical Control Strategy using ANN Based-Controller.

4. RESULTS AND DISCUSSION

The dynamic performance of the system under varying atmospheric conditions is illustrated by data recorded in our laboratory. These results reflect the system's behavior under fluctuating solar irradiation and temperature conditions. Solar irradiance varies from 400 W/m² to 1000 W/m², while the temperature of the photovoltaic panel fluctuates between 42°C and 62°C, as shown in Figure 9(a) and Figure 9(b), respectively. These variations have a direct impact on PV system parameters such as PV voltage (V_{pv}) and power (p_{pv}), illustrated in Figure 9(c) and Figure 9(d) respectively. The irradiance curve Figure 9(b) first shows a steady increase, which is followed by a sharp decrease near the mid-point, corresponding to a temporary drop in solar irradiance. This reduction in irradiance is reflected in the PV voltage profile Figure 9(c). Power output (p_{pv}) Figure 9(d) also follows a similar pattern, fluctuating with irradiation and temperature changes, as well as with other system parameters.

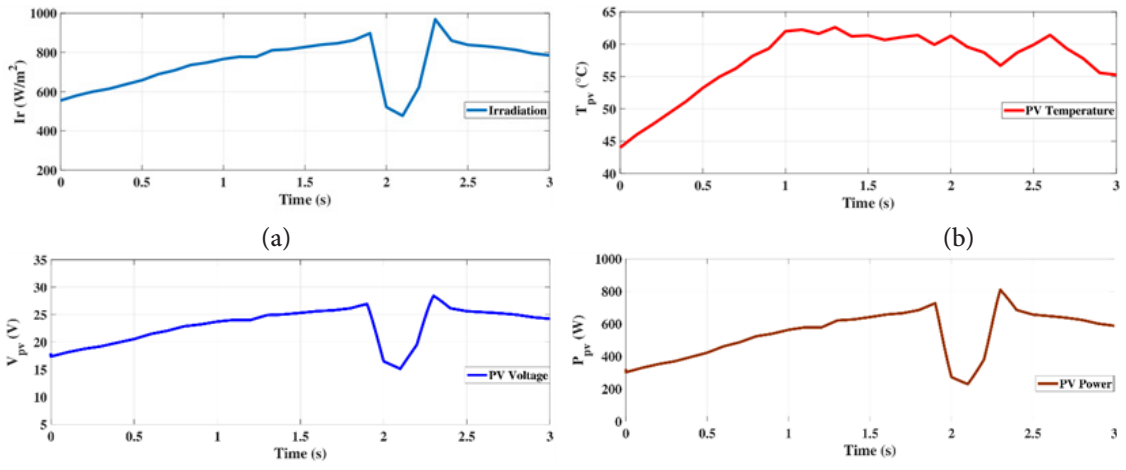

Figure 9. Dynamic performance of the system with varying solar irradiation and Temperature, where Solar irradiance, (b) Temperature of the photovoltaic panel, (c) PV voltage (V_{pv}) and (d) Power output (p_{pv}).

The Figure 10 shows how a photovoltaic (PV) system behaves under MPPT control. In Figure 10(a), the PV voltage (V_{pv}) and the MPPT voltage (V_{PPT}) are stable after an initial transient, but

a dip is visible around 2 seconds before the system recovers. Figure 10(b) focuses on the current response, where both the PV current (I_{PV}) and MPPT current (I_{MPPT}) experience a spike during the same disturbance. Figure 10(c) provides a closer look at the power response during steady-state and disturbance periods. Overall, the figure highlights how the system manages initial transients, maintains steady-state operation, and effectively responds to external disturbances.

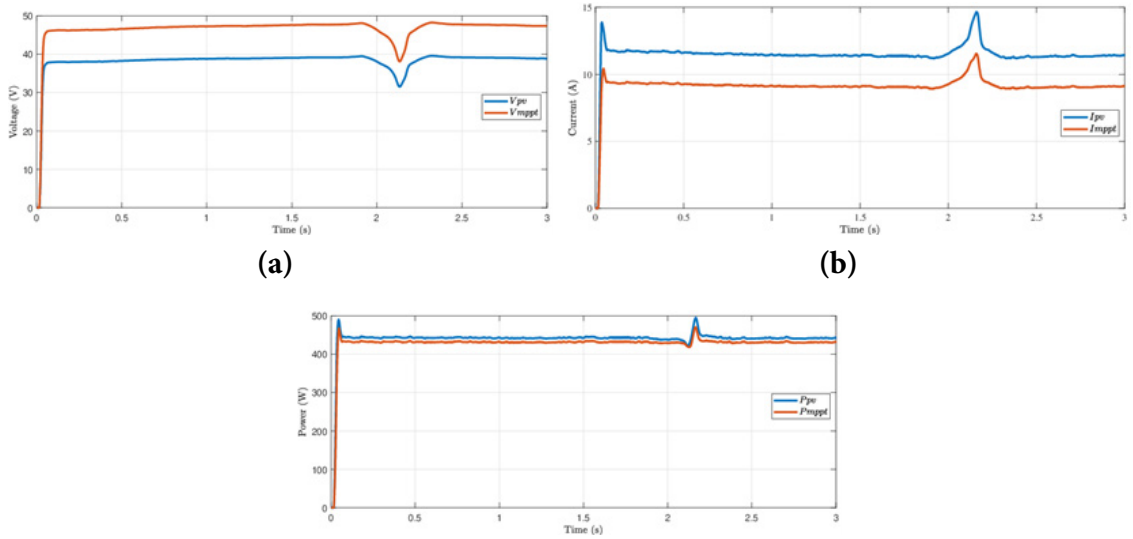

(a) **(b)**

(c)

Figure 10. Dynamic Response of a Photovoltaic System Under MPPT Control where (a) the PV voltage (V_{pv}) and the MPPT voltage (M_{PPT}), (b) the PV current (I_{pv}) & MPPT current (I_{mppt}) and (b) the PV Power (P_{pv}).

This Figure 11 compares the performance of a Proportional-Integral (PI) controller and an Artificial Neural Network (ANN) controller in regulating an electrolyzer system.

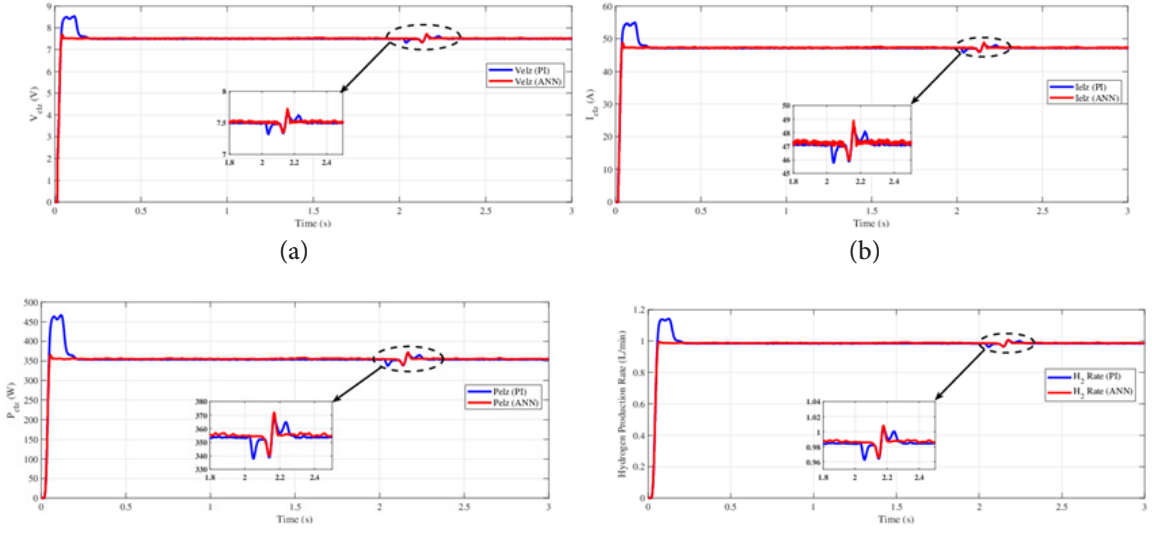

(a) (b)

(c) (d)

Figure 11. Dynamic performance of the system with varying solar irradiation (a) the voltage response (V_{elz}), (b) The current response (I_{elz}) (c) the power output (P_{elz}) and (d) the hydrogen production rate (Rate) all under PI and ANN control.

Figure 11(a) shows the voltage response(V_{elz}), where the ANN controller achieves faster stabilization and smoother behavior after a disturbance at around 2 seconds, while the PI controller shows more pronounced oscillations. In Figure 11(b), the current response (I_{elz}) is

displayed, with the ANN controller providing a more stable and consistent response, effectively suppressing fluctuations during the disturbance. Figure 11(c) focuses on the power output (P_{elz}), where the ANN controller demonstrates quicker recovery and steadier performance under transient and steady-state conditions compared to the PI controller.
Finally, Figure 11(d) presents the hydrogen production rate (H_2 Rate), highlighting the ANN controller's ability to maintain a more stable and reliable output, even during disturbances. Overall, the result shows that the ANN controller outperforms the PI controller, delivering faster responses, better stability, and improved efficiency under varying operating conditions.
The results Table 5 demonstrate that the ANN controller outperforms the PI controller on several performance parameters. The ANN has a minimum overshoot of 3.1%, significantly lower than the PI's 12.84%, indicating a more controlled and consistent response close to the target value. In terms of settling time, the PI controller has a settling time of 0.023 s, while the ANN stabilizes at 0.022 s. In addition, the PI controller's mean absolute percentage error MAPE is 1.22%, while the ANN achieves a lower MAPE of 0.95%, indicating improved tracking accuracy. Overall, these parameters suggest that the ANN controller performs better than the PI controller in terms of tracking accuracy. In addition, the average flow rates for hydrogen production are 0.98 L/min for the PI controller and 0.99 L/min for the ANN controller, indicating that the ANN performs better in terms of hydrogen production efficiency.

Table 5 Dynamic Performance of Controllers.

Controller	MAPE (%)	Settling Time (S)	Overshoot (%)
PI	1.22	0.023	12.84
ANN	0.95	0.022	3.19

5. CONCLUSIONS

In this study, we investigated a system integrating a PEM water electrolyzer and a photovoltaic panel to address the challenges of hydrogen production under fluctuating solar energy conditions. The system uses a boost converter with a perturbation and observation P&O algorithm for MPPT and a buck converter to stabilize the voltage supplied to the electrolyzer. Initially, the buck converter was controlled using a PI strategy, but to address the limitations caused by the system's non-linearity, we proposed the use of an ANN controller. The results indicated that the ANN controller outperformed the PI controller in terms of stability and overall system performance. The ANN achieved 3.19% less overshoot} than the PI's 12.84 %, 0.022 s faster stabilization than the PI's 0.023 s, and 0.95% less mean absolute percentage error (MAPE) than the PI's 1.22%. In addition, hydrogen production rates were higher with the ANN (0.99 L/min vs. 0.98 L/min for the PI). Future work could explore advanced ANN techniques, such as deep learning and reinforcement learning, to improve system accuracy and adaptability, even in the presence of different disturbances. In addition, the integration of improved converters and MPPT strategies can maximize energy extraction and system efficiency, contributing to the sustainability of the electrolyzer and the advancement of sustainable green hydrogen production.

Authors contribution: Abdellah EL IDRISSI / developed the concept and aims of the study; Belkasem Imodane/prepared and compared the literature; Mohamed Benydir/prepared and compared the literature; Hamid Hamdani/ reviewed and checked the structure of the manuscript; M'hand Oubella/ reviewed and checked the structure of the manuscript; Mohamed Ajaamoum/ reviewed and checked the structure of the manuscript.
All authors contributed to the final manuscript.

All authors have read and approved the manuscript.

Funding: The article is supported by the The Moroccan Association of Sciences and Techniques for Sustainable Development (MASTSD), Beni Mellal, Morocco.

Data Availability Statement: The data supporting the findings of this study are available upon reasonable request from the corresponding author.

Conflicts of Interest: The authors declare that there is no conflict of interest regarding the publication of this paper.

Acknowledgements: Authors may acknowledge any person, institution, or department that supported any part of the study.

REFERENCES

[1] Q. Hassan, S. Algburi, A. Z. Sameen, H. M. Salman, and M. Jaszczur, "Green hydrogen: A pathway to a sustainable energy future," Int J Hydrogen Energy, vol. 50, pp. 310–333, 2024, doi: https://doi.org/10.1016/j.ijhydene.2023.08.321.

[2] B. Reda, A. A. Elzamar, S. AlFazzani, and S. M. Ezzat, "Green hydrogen as a source of renewable energy: a step towards sustainability, an overview," Environ Dev Sustain, May 2024, doi: 10.1007/s10668-024-04892-z.

[3] C. Laghlimi, A. Moutcine, Y. Ziat, H. Belkhanchi, A. Koufi, and S. Bouyassan, "Hydrogen, Chronology and Electrochemical Production," JSESD, pp. 22–37, Dec. 2024, doi: https://doi.org/10.51646/jsesd.v14iSI_MSMS2E.405.

[4] D. Mazumdar, C. Sain, P. K. Biswas, P. Sanjeevikumar, and B. Khan, "Overview of solar photovoltaic MPPT methods: a state of the art on conventional and artificial intelligence control techniques," International Transactions on Electrical Energy Systems, vol. 2024, no. 1, p. 8363342, 2024, Accessed: Apr. 03, 2025. [Online]. Available: https://doi.org/10.1155/2024/8363342

[5] Y. Astriani, W. Tushar, and M. Nadarajah, "Optimal planning of renewable energy park for green hydrogen production using detailed cost and efficiency curves of PEM electrolyzer," Int J Hydrogen Energy, vol. 79, pp. 1331–1346, 2024, Accessed: Apr. 03, 2025. [Online]. Available: https://doi.org/10.1016/j.ijhydene.2024.07.107

[6] C. Yan, Y. Zou, Z. Wu, and A. Maleki, "Effect of various design configurations and operating conditions for optimization of a wind/solar/hydrogen/fuel cell hybrid microgrid system by a bio-inspired algorithm," Int J Hydrogen Energy, vol. 60, pp. 378–391, 2024, Accessed: Apr. 03, 2025. [Online]. Available: https://doi.org/10.1016/j.ijhydene.2024.02.004

[7] F. S. Al-Ismail, "A critical review on DC microgrids voltage control and power management," IEEE Access, 2024, doi: 10.1109/ACCESS.2024.3369609.

[8] V. A. M. Lopez, H. Ziar, J. W. Haverkort, M. Zeman, and O. Isabella, "Dynamic operation of water electrolyzers: A review for applications in photovoltaic systems integration," Renewable and Sustainable Energy Reviews, vol. 182, p. 113407, 2023, Accessed: Apr. 03, 2025. [Online]. Available: https://doi.org/10.1016/j.rser.2023.113407

[9] Z. Han, X. Yao, S. Yuan, H. Dong, S. Ma, and Y. Dong, "Research on control strategy of photovoltaic hydrogen generation system based on Fuzzy PI control," Energy Reports, vol. 9, pp. 4187–4194, 2023, doi: https://doi.org/10.1016/j.egyr.2023.02.079.

[10] M. Khalid, "Smart grids and renewable energy systems: Perspectives and grid integration challenges," Energy Strategy Reviews, vol. 51, p. 101299, 2024, Accessed: Apr. 03, 2025. [Online]. Available: https://doi.org/10.1016/j.esr.2024.101299

[11] Z. Wei, P. W. Tien, J. Calautit, J. Darkwa, M. Worall, and R. Boukhanouf, "Investigation

of a model predictive control (MPC) strategy for seasonal thermochemical energy storage systems in district heating networks," Appl Energy, vol. 376, p. 124164, 2024, Accessed: Apr. 03, 2025. [Online]. Available: https://doi.org/10.1016/j.apenergy.2024.124164

[12] L. Wang et al., "An integrated deep learning model for intelligent recognition of long-distance natural gas pipeline features," Reliab Eng Syst Saf, vol. 255, p. 110664, 2025, Accessed: Apr. 03, 2025. [Online]. Available: https://doi.org/10.1016/j.ress.2024.110664

[13] S. A. Kalogirou, "Applications of artificial neural networks in energy systems," Energy Convers Manag, vol. 40, no. 10, pp. 1073–1087, 1999, doi: https://doi.org/10.1016/S0196-8904(99)00012-6.

[14] L. Nolting, T. Spiegel, M. Reich, M. Adam, and A. Praktiknjo, "Can energy system modeling benefit from artificial neural networks? Application of two-stage metamodels to reduce computation of security of supply assessments," Comput Ind Eng, vol. 142, p. 106334, 2020, doi: https://doi.org/10.1016/j.cie.2020.106334.

[15] M. Abdelkareem et al., "Progress of artificial neural networks applications in hydrogen production," Chemical Engineering Research and Design, vol. 182, Mar. 2022, doi: 10.1016/j.cherd.2022.03.030.

[16] L. Zou, Q. Shen, G. Yang, S. Li, and N. Huang, "Improved hydrogen production efficiency of a Photovoltaic-Electrolysis system with P&O Algorithm: A case study," Chem Phys Lett, vol. 832, p. 140891, 2023, doi: https://doi.org/10.1016/j.cplett.2023.140891.

[17] A. Hassan, O. Abdel-Rahim, M. Bajaj, and I. Zaitsev, "Power electronics for green hydrogen generation with focus on methods, topologies, and comparative analysis," Sci Rep, vol. 14, no. 1, p. 24767, 2024, Accessed: Apr. 03, 2025. [Online]. Available: https://doi.org/10.1038/s41598-024-76191-6

[18] M. A. Hossain, M. R. Islam, M. A. Hossain, and M. J. Hossain, "Control strategy review for hydrogen-renewable energy power system," J Energy Storage, vol. 72, p. 108170, 2023, Accessed: Apr. 03, 2025. [Online]. Available: https://doi.org/10.1016/j.est.2023.108170

[19] S. Adiche et al., "Advanced control strategy for AC microgrids: a hybrid ANN-based adaptive PI controller with droop control and virtual impedance technique," Sci Rep, vol. 14, no. 1, p. 31057, 2024, Accessed: Apr. 03, 2025. [Online]. Available: https://doi.org/10.1038/s41598-024-82193-1

[20] M. E. Şahin, H. İ. Okumuş, and M. T. Aydemir, "Implementation of an electrolysis system with DC/DC synchronous buck converter," Int J Hydrogen Energy, vol. 39, no. 13, pp. 6802–6812, 2014, doi: https://doi.org/10.1016/j.ijhydene.2014.02.084.

[21] B. Yodwong, D. Guilbert, W. Kaewmanee, and M. Phattanasak, "Energy Efficiency Based Control Strategy of a Three-Level Interleaved DC-DC Buck Converter Supplying a Proton Exchange Membrane Electrolyzer," Electronics (Basel), vol. 8, no. 9, 2019, doi: 10.3390/electronics8090933.

[22] M. Albarghot and L. Rolland, "Comparison of experimental results with simulation of a PEM Electrolyzer powered by a horizontal wind turbine," in 2017 International Conference of Electrical and Electronic Technologies for Automotive, 2017, pp. 1–6. doi: 10.23919/EETA.2017.7993232.

[23] S. M. Muyeen, R. Takahashi, and J. Tamura, "Electrolyzer switching strategy for hydrogen generation from variable speed wind generator," Electric Power Systems Research, vol. 81, no. 5, pp. 1171–1179, 2011, doi: https://doi.org/10.1016/j.epsr.2011.01.005.

[24] F. Alonge, S. M. Collura, F. D'Ippolito, D. Guilbert, M. Luna, and G. Vitale, "Design of a robust controller for DC/DC converter–electrolyzer systems supplied by μWECSs subject to highly fluctuating wind speed," Control Eng Pract, vol. 98, p. 104383, 2020, doi: https://doi.org/10.1016/j.conengprac.2020.104383.

[25] R. K. Kumar and P. Samuel, "Designing a hydrogen generation system through PEM water electrolysis with the capability to adjust fast fluctuations in photovoltaic power," Int J Hydrogen Energy, vol. 82, pp. 1–10, 2024, Accessed: Apr. 03, 2025. [Online]. Available: https://doi.org/10.1016/j.ijhydene.2024.07.376

[26] S. D. Al-Majidi, M. F. Abbod, and H. S. Al-Raweshidy, "A novel maximum power point tracking technique based on fuzzy logic for photovoltaic systems," Int J Hydrogen Energy, vol. 43, no. 31, pp. 14158–14171, 2018, Accessed: Apr. 03, 2025. [Online]. Available: https://doi.org/10.1016/j.ijhydene.2018.06.002

List of Abbreviations:

Abbreviation	Meaning
ANN	Artificial Neural Network
DC	Direct Current
MAPE	Mean Absolute Percentage Error
MPPT	Maximum Power Point Tracking
P&O	Perturbation and Observation (MPPT algorithm)
PEM	Proton Exchange Membrane
PI	Proportional-Integral (Control)
PV	Photovoltaic

Nomenclature:

Symbol	Meaning
H_2	Hydrogen Gas
I_{elz}	Electrolyzer Current (A)
I_{mppt}	Maximum Power Point Tracking Current (A)
I_r	Irradiance (W/m²)
I_{pv}	Photovoltaic Current (A)
N_{h2}	Hydrogen Production Rate (moles/s or L/min)
P_{elz}	Electrolyzer Power (W)
P_{mppt}	Maximum Power Point Tracking Power (W)
P_{pv}	Photovoltaic Power (W)
T_{pv}	Photovoltaic Temperature (°C)
V_{elz}	Electrolyzer Voltage (V)
V_{mppt}	Maximum Power Point Tracking Voltage (V)
V_{pv}	Photovoltaic Voltage (V)

Solar Energy
And Sustainable Development
Refereed, biannual scientific journal issued by:
The Libyan Center for Solar Energy Research and Studies

Optimization of Adobe and Sawdust-Based Bricks for Improved Energy Efficiency in Construction

Mohammed Benfars[1*], Abdelmounaim Alioui[2], Youness Azalam[3], Mourad Kaddiri[4], Mustapha Mabrouki[5].

[1,2,3,4,5]Laboratory of Industrial and Surface Engineering Sultan Moulay Slimane FST, Mghila, B.P. 592, Beni Mellal, Morocco.
[2]EFP, Mghila, B.P. 592, Beni Mellal, Morocco.

E-*mail:* [1] mohammed.fars@usms.ma .

SPECIAL ISSUE ON:

The 1St International Conference on Sciences and Techniques for Renewable Energy and the Environment.
(STR2E 2025)
May 6-8, 2025 at FST-Al Hoceima-Morocco.

KEYWORDS

Adobe bricks, Sawdust, Thermal performance, Energy efficiency, Sustainable construction.

ABSTRACT

The exploration of bio-based materials for sustainable construction practices, particularly through the use of locally sourced resources like sawdust, is the focus of this study, which evaluates the thermal performance of adobe bricks reinforced with 2% sawdust in small, medium, and large sizes, ranging from 0.3 to 2 cm. The bricks were manufactured using local materials, and the physicochemical properties of the clay were initially analyzed and characterized. The laboratory examined the bricks' thermophysical characteristics, such as their density, thermal conductivity, and heat capacity.

The TRNSYS program was used to conduct annual thermal simulations based on representative meteorological data for a typical building in the semi-arid Moroccan city of Beni Mellal. The results indicate that the energy savings achieved in terms of both heating and cooling were comparable across all configurations of sawdust-reinforced adobe bricks. When compared to a reference concrete building, the heating energy demand was reduced by 59.14% for clay without sawdust, 72.61% for clay with small sawdust, 71.25% for clay with medium sawdust, and 69.88% for clay with large sawdust. Similarly, the cooling energy demand reductions were 45.71%, 58.82%, 57.68%, and 56.62%, respectively, for clay without sawdust, and with small, medium, and large sawdust. These findings suggest that the incorporation of sawdust, regardless of particle size, leads to similar energy savings, offering flexibility in utilizing locally available sawdust from Beni Mellal to optimize energy performance. This research highlights the importance of local clay-based materials and the use of sawdust as a natural reinforcement, to optimize the energy efficiency of buildings. It also offers new perspectives for their integration into sustainable construction practices, contributing to global sustainable development goals.

*Corresponding author.

DOI: https://doi.org/10.51646/jsesd.v14iSTR2E.983

This is an open access article under the CC BY-NC license (http://Attribution-NonCommercial 4.0 (CC BY-NC 4.0)).

التحسين الأمثل للطوب اللبن والطوب القائم على نشارة الخشب لتحسين كفاءة الطاقة في البناء

محمد بنفارس، عبد المنعم عليوي، يونس أزلام، مراد قديري، مصطفى مبروكي .

ملخص: تركز هذه الدراسة على استكشاف المواد الحيوية لممارسات البناء المستدام، لا سيما من خلال استخدام الموارد المحلية مثل نشارة الخشب، حيث تقوم هذه الدراسة بتقييم الأداء الحراري للطوب اللبن المدعم بنسبة 2 % من نشارة الخشب بأحجام صغيرة ومتوسطة وكبيرة تتراوح بين 0.3 و2 سم. تم تصنيع الطوب باستخدام مواد محلية، وتم تحليل وتوصيف الخصائص الفيزيائية و الكيميائية للطين في البداية. فحص المختبر الخصائص الفيزيائية الحرارية للطوب مثل الكثافة والتوصيل الحراري والسعة الحرارية. استُخدم برنامج TRNSYS لإجراء محاكاة حرارية سنوية بناءً على بيانات الأرصاد الجوية التمثيلية لمبنى نموذجي في مدينة بني ملال المغربية شبه القاحلة. تشير النتائج إلى أن وفورات الطاقة المحققة من حيث التدفئة والتبريد كانت قابلة للمقارنة في جميع تشكيلات الطوب اللبن المدعم بنشارة الخشب. عند مقارنته بمبنى خرساني مرجعي، انخفض الطلب على طاقة التدفئة بنسبة 59.14 % للطين بدون نشارة الخشب، و72.61 % للطين مع نشارة الخشب الصغيرة، و71.25 % للطين مع نشارة الخشب المتوسطة، و69.88 % للطين مع نشارة الخشب الكبيرة.

وبالمثل، بلغت نسبة الانخفاض في الطلب على طاقة التبريد 45.71 % و58.82 % و57.68 % و56.62 % على التوالي للطين بدون نشارة الخشب ومع نشارة الخشب الصغيرة والمتوسطة والكبيرة. تشير هذه النتائج إلى أن دمج نشارة الخشب، بغض النظر عن حجم الجسيمات، يؤدي إلى توفير مماثل في الطاقة، مما يوفر مرونة في استخدام نشارة الخشب المتوفرة محليًا من بني ملال لتحسين أداء الطاقة. يسلط هذا البحث الضوء على أهمية المواد المحلية القائمة على الطين واستخدام نشارة الخشب كتعزيز طبيعي لتحسين كفاءة الطاقة في المباني. كما يقدم وجهات نظر جديدة لدمجها في ممارسات البناء المستدام، مما يساهم في تحقيق أهداف التنمية المستدامة العالمية.

الكلمات المفتاحية – الطوب اللبن، نشارة الخشب، الأداء الحراري، كفاءة الطاقة، البناء المستدام.

1. INTRODUCTION

Currently, energy consumption is one of the major challenges on an international scale[1]. Indeed, one major factor in the world's energy consumption and CO_2 emissions is the construction industry, contributing to more than 30% of global CO_2 emissions and more than 36% of the world's total energy demand [2]. The construction sector in Morocco mostly uses traditional materials, including fired bricks, whose manufacture has a big influence on the environment. This manufacturing process requires firing temperatures exceeding 1000°C, leading to energy consumption ranging from 0.54 to 3.14 MJ/kg and CO_2 emissions between 70 and 282 g/Kg [3]. Furthermore, these materials generate substantial amounts of waste during construction and demolition phases, estimated at approximately 14×10^6 t/year in Morocco [4]. This situation highlights the urgent need for a transition towards more sustainable construction practices, where the pursuit of materials that are both thermally efficient and environmentally friendly becomes an essential priority [5]. In this context, the exploration of bio-based construction materials, combining local resources with technical innovations, has become essential to meet the energy needs of buildings while minimizing their environmental footprint. Among these materials, unfired earth bricks stand out as a particularly promising alternative. They offer numerous advantages, including accessibility, low environmental impact, recyclability, and the ability to regulate humidity while enhancing the thermal comfort of buildings. [3], [6]. Moreover, their manufacturing process requires significantly lower energy consumption[3]. However, the thermal performance can be further optimized through the addition of reinforcement natural additives. In this regard, recent research has focused on integrating filler and reinforcement materials to enhance the properties of construction materials [7]. In line with this approach, the present study investigates the thermal effects of incorporating sawdust waste into traditional clay bricks. In addition to improving thermal insulation, this integration promotes the recycling of wood waste as a sustainable building material, reducing landfill disposal and enhancing its valorization. Furthermore, this strategy aligns with Morocco's 2030 Circular Economy Strategy

[8], which aims to minimize environmental impact and encourage sustainable resource management. All of this while adopting an eco-friendly manufacturing process that eliminates high firing temperatures, promoting the production of low-cost, low-energy building structures with significant energy savings.

Numerous studies have highlighted the benefits of incorporating additives into building materials. For instance, M. Giroudon et al. [9] investigated the addition of lavender and barley straw fibers to adobe and found that both types of fibers' thermal conductivity decreased as the fiber quantity increased. M. Bouchefra et al. [10] also examined the impact of doum fibers on the characteristics of earth bricks, They found that the thermal conductivity of compressed earth bricks decreased with an increase in the percentage of doum fibers. Furthermore, M. Babé et al. [11] discovered that the thermal conductivity of adobe bricks decreased as the quantity of neem fibers increased. Building on existing research that highlights the benefits of reinforcing earth bricks with natural additives, this study investigates the impact of sawdust waste of varying particle sizes on the thermophysical properties of materials. It further assesses their thermal and energy performance to demonstrate their potential in reducing energy consumption in semi-arid regions. By focusing on these aspects, this work contributes to the development of sustainable, high-performance building materials suited for energy-efficient construction. The adobe bricks were made by hand utilizing a traditional technique that is common in southern Morocco. To this end, soil samples were collected from the Beni Mellal region, and sawdust fibers of varying sizes (small, medium, and large, with lengths ranging from 0.3 to 2 cm) were incorporated into the formulations. This research extends the work of M, Azalam et al. [12], which focused on the mechanical properties of these adobe bricks, While the earlier research addressed their structural behavior, the present study complements it by exploring the thermal performance and energy efficiency of the same material, providing a more comprehensive understanding of its potential for sustainable construction.

2. MATERIALS AND METHODOLOGY

2.1. Clay

The preparation of adobe bricks in this study relied on clay soil sourced from the Ouled Mbarek village in the north-central region of Morocco. The choice of this material was motivated by its abundant availability in the area, its natural suitability for construction, and its homogeneous composition, which ensures reliable performance in adobe applications.

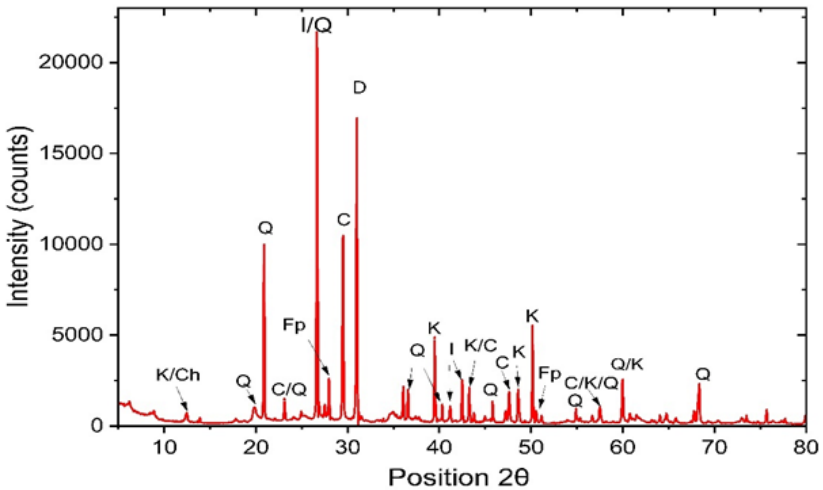

Figure 1: Pattern of X-ray diffraction for the clay sample[38].

To assess the clay's potential for use in adobe brick production, a detailed characterization was performed.

The Atterberg limits and key physical properties of the soil are outlined in Table 1, providing essential insights into its plasticity and workability. Mineralogical analysis was carried out using X-ray diffraction (XRD), with the results depicted in Figure 1, while the chemical composition, critical for understanding its thermal and mechanical behavior, is detailed in Table 2.

This comprehensive analysis not only establishes the suitability of the local clay for construction but also highlights its role as a sustainable and reproducible material for energy-efficient building practices. By leveraging locally available resources, this approach contributes to reducing the environmental footprint of construction while ensuring high-quality material performance.

Table 1: The chemical analysis of the clay sample[12].

Composition	**Value (%)**	**Characteristics**	**Value (%)**
Clay	41.5	Limit of liquidity	30
Sand	27	Limit of Plasticity	16
Gravel	8	Index of Plasticity	14
Silt	23.5	content of water	2.0

Table 2: Soil Composition Analysis[12].

Elements	SiO_2	Al_2O_3	CaO	Fe_2O_3	MgO	K_2O
unfired clay	67.37	12.43	7.18	7	4.13	1.89

2.2. Sawdust

The sawdust was obtained from woodworking wastes in the area in an attempt to lower production costs and encourage the recycling of regional garbage. After collection, a sorting process was carried out to classify the sawdust particles into three categories—short, medium, and long—as indicated in Figure 2.

X-ray diffraction (XRD)[13] analysis revealed that cellulose is the primary chemical component of the sawdust, providing the material with advantageous thermal properties due to its low thermal conductivity. Additionally, scanning electron microscopy (SEM) images highlighted a characteristic porous structure. This porosity plays a crucial role in reducing the bulk density of the bricks, directly influencing their ability to limit heat transfer.

Incorporating sawdust into the adobe bricks significantly enhances their thermal performance by acting as a natural insulator. The pores present in the sawdust trap air pockets, creating an effective thermal barrier that reduces the overall thermal conductivity of the bricks.

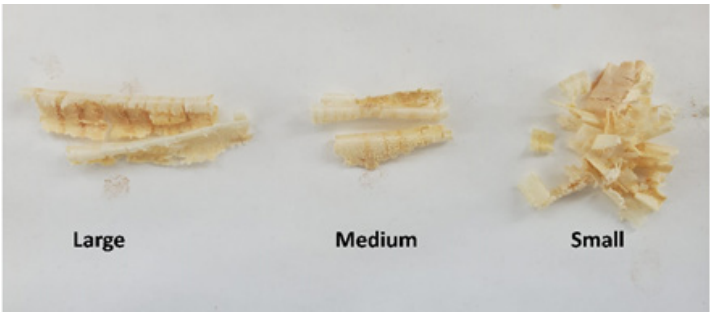

Figure 2: Small, medium, and large sawdust particle sizes

2.3. Preparation of Adobe Bricks

The fabrication process of adobe bricks, as illustrated in Figure 3, involves the following main steps:

A. Soil Preparation

The process began with the treatment of soil, the primary raw material. Large aggregates and organic waste (plants, tree leaves) were meticulously eliminated, either manually or through sieving with a hand sieve of suitable mesh size. Following purification, water was progressively added to the soil that had been sieved while being constantly mixed until a uniform paste was achieved. To improve the cohesion and durability of the mixture, the paste was allowed to rest for 72 hours. This resting period facilitated better hydration and integration of the soil particles, improving the adobe bricks' durability and strength[14].

B. Preparation and Integration of Sawdust Fibers

Sawdust, employed as reinforcement, were divided into three groups according to their length:

- **Short fibers (S)**: 0.2–0.6 cm
- **Medium fibers (M)**: 0.6–1.5 cm
- **Long fibers (L)**: 1.5–3.0 cm

A fixed sawdust content of 2% by weight was incorporated into the adobe formulations to optimize thermal performance while ensuring mechanical integrity. This concentration was chosen based on prior studies by M. Azalam et al.[12], which demonstrated that adobe bricks with 2% sawdust exhibited satisfactory mechanical properties. By maintaining a consistent sawdust dosage, the study specifically focused on the impact of fiber size on the thermophysical properties of the material, minimizing variability from concentration differences.

The decision to vary the sawdust size was guided by the findings of M. Limami et al.[15], who observed that thermal conductivity decreases as sawdust size decreases. This relationship was confirmed through experimental measurements using a heat flow meter, in accordance with ASTM D7896-19 standards.

C. Molding

The prepared mixture was molded into standard parallelepiped forms with dimensions of 18 × 10 × 5 cm. To ensure a consistent density and reduce internal flaws, air gaps were removed by manual compaction. The surfaces of the bricks were hand-smoothed to achieve a uniform finish, enhancing their appearance and reducing.

Figure 3: Process of Adobe Brick Preparation[39][40][12]

2.4. Thermal Properties Analysis

After the drying phase, the thermal properties of the sawdust-reinforced adobe brick samples were characterized, concentrating on heat capacity and thermal conductivity. A heat flow meter (HFM Lambda 446) was used to measure these characteristics[16]. The HFM Lambda 446, adhering to ASTM C518 and ISO 8301 standards, is equipped with highly calibrated heat flux sensors, offering a precision of ±1% to ±2%.

Each sample was positioned between two heating plates with a Peltier temperature control system, allowing for a regulated temperature gradient. Highly calibrated heat flow sensors were used to continually monitor the heat flux through the samples.

The system's motorized plate movement and thermocouple sensors (type K) enabled precise monitoring of the heat flow through the samples. After thermal equilibrium was achieved, the sawdust fiber-reinforced adobe bricks' heat capacity and thermal conductivity were calculated with thermal conductivity values ranging from 0.001 to 2 W/(m.K) depending on the sample configuration. These measurements were essential for calculating thermal diffusivity, which was derived using the following equation (1)[17], based on the sample's density, thermal conductivity, and heat capacity.

$$a = \frac{\lambda}{\rho . C_p} \qquad (1)$$

Where a,λ,ρ and C_p represent the thermal diffusivity, thermal conductivity, density of the sample and heat capacity, respectively.

2.5. Building and Material Properties Overview

A single-story, single-family home with 74 m² of floor space overall and an internal ceiling height of 3 m is the subject of the analysis. It is divided into four separate thermal zones. Figure 4 illustrates the building's geometry, highlighting its functional divisions.

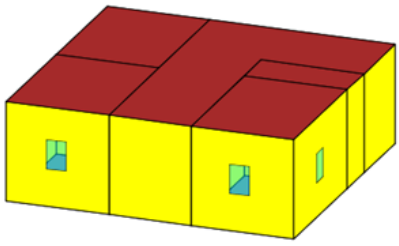

Figure 4: Illustration of the building within the energy simulation model.

Table 3 presents the key thermophysical properties of the building materials, including density, specific heat capacity, and thermal conductivity, to provide a comprehensive understanding of their thermal performance.

To assess and compare the energy efficiency of traditional adobe constructions against conventional cement-based structures, simulations were performed on five distinct building envelope configurations, as specified in Table 3.

The goal of these simulations was in order to quantify the impact of clay walls on the building's heating and cooling energy requirements, providing critical insights into the potential benefits of eco-friendly construction materials.

Table 3: The proposed building envelope's thermal properties.

Exterior wall layers		Thickness (cm)	Density (Kg/m3)	Thermal conductivity (W/m K)	Thermal capacity (kJ/kg K)	U-value [W/ m2 K]
Reference building	Concrete masonry [18]	20	2076	1.1	0.1	2.84
	Concrete [19]	16	2240	1.7	0.88	3.78
	Cement mortar [20]	2	1800	0.93	1.05	5.22
Clay (0%)		45	1996.67	0.57	0.774	1.04
Clay-Small Sawdust (2%)		45	1877.78	0.331	0.842	0.65
Clay-Medium Sawdust (2%)		45	1865.56	0.348	0.815	0.68
Clay-Large Sawdust (2%)		45	1 800.00	0.364	0.792	0.71

2.6. Energy Transfer Simulation in Buildings: Mathematical and Physical Modeling

This research utilizes the TRNSYS simulation tool to assess the energy performance of a building under realistic conditions. The building's geometric foundation was carefully developed using the SketchUp platform, ensuring an accurate digital representation of its physical structure. This model was subsequently integrated into the TRNSYS Type 56 module (TRNBuild), where detailed specifications related to the building's physical properties, materials, and thermal performance were defined to support precise energy simulations.

Heat transfer in buildings occurs through three primary mechanisms:

A. The transfer of heat through conduction:

The approach utilizing the conductive transfer function, derived from the principles established by Stephenson and Mitalas[21], is employed to analyze the thermal behavior of the building's walls. This method offers an efficient way to model heat conduction through the building envelope, facilitating precise assessment of thermal energy transfer.

The temporal correlations between surface temperatures and heat fluxes are expressed by equations (2) and (3). The time step is indicated by the variable k, where the current hour is denoted by k = 0 and the previous hour by k = -1. The parameters that control these temporal interactions are determined by the a, b, c, and d coefficients.

Accordingly, the surface heat conduction for any wall can be expressed as follows[22]:

$$\dot{q}_{so} = \Sigma_{k=0}^{n_a} a^k T_{s,o}^k - \Sigma_{k=0}^{n_b} b^k T_{s,i}^k - \Sigma_{k=1}^{n_d} \mathrm{d}^k \dot{q}_{s,o}^k \qquad (2)$$

$$\dot{q}_{si} = \Sigma_{k=0}^{n_b} b^k T_{s,o}^k - \Sigma_{k=0}^{n_c} c^k T_{s,i}^k - \Sigma_{k=1}^{n_d} \mathrm{d}^k \dot{q}_{s,i}^k \qquad (3)$$

The terms $\dot{q}_{so}$ and $\dot{q}_{si}$ depict the flow of heat into and out of the wall, respectively. Both the inside and exterior temperatures of the wall are shown by $T_{(s,o)}$ and $T_{(s,i)}$, as illustrated in Fig. 5.

B. The transfer of heat through Convection:

The equations (4,5) depict the heat flows that are transferred by convection at the outside and interior surfaces of the wall[23]:

$$\dot{q}_{c,s,o} = h_{outside}\left(T_{a,s} - T_{s,o}\right) \qquad (4)$$

$$\dot{q}_{c,s,i} = h_{inside}\left(T_i - T_{s,i}\right) \qquad (5)$$

The external and interior surfaces' convective coefficients of heat transfer are denoted by h_inside and h_outside respectively. Meanwhile, Ta,s symbolizes the external thermal zone's ambient air temperature, while Ti indicates the indoor temperature within the thermal zone.

C. The transfer of heat through Radiation:

The flux of radiative heat can be calculated using the following formula[24]:

$$\dot{q}_{r,s,o} = \sigma \varepsilon_{s,o} \left(T_{s,o}^4 - T_{fsky}^4 \right) \qquad (6)$$

where:
$\sigma_{theo}r$=(5.6696±0.0025)×$10^{(-8)}$ $Wm^{(-2)}$ $K^{(-4)}$: The constant known as Stefan-Boltzmann[25].
$\varepsilon_{(s,o)}$: The exterior wall surface's emissivity for long-wave radiation.
T_{fsky}: The apparent sky temperature concerning exchange of longwave radiation.

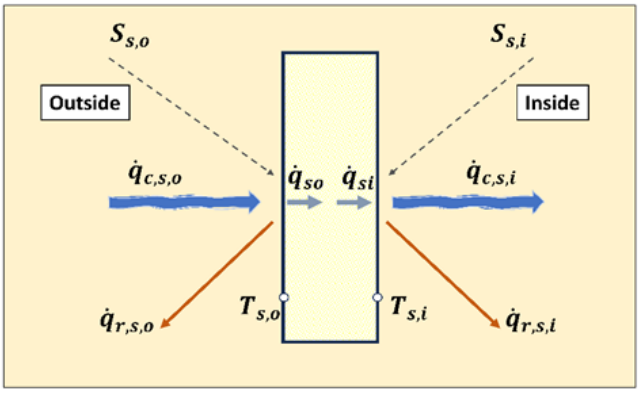

Figure 5: Fluxes of heat and temperatures close to the wall[41]

3. RESULTS AND DISCUSSION

3.1. Thermal Properties Analysis

The thermal characterization of adobe bricks containing varying types of sawdust highlights substantial changes in their thermophysical properties based on the inclusion and particle size (small, medium, large) of the sawdust. These variations are systematically analyzed in terms of density (ρ), thermal conductivity (λ), and specific heat capacity (Cp) as follows:

3.1.1. Density (ρ)

The incorporation of sawdust significantly reduces the density of the adobe bricks regardless of the particle size. The control sample, composed exclusively of clay (0% sawdust), exhibits an average density of 1996.67 kg/m³, while bricks with sawdust range from 1800.00 kg/m³ (large sawdust) to 1877.78 kg/m³ (small sawdust), This fact is confirmed by the research done by M. Limami et al.[15], which investigated the effect of varying sawdust sizes on bulk density. The results showed a reduction in bulk density for bricks incorporating larger-sized additives. This reduction in density, reaching up to 9.83%, is explained by sawdust's lower bulk density than clay. The substitution of a denser clay fraction with a lighter sawdust fraction effectively decreases the overall mass of the bricks.

3.1.2. Thermal Conductivity (λ)

When sawdust is added, thermal conductivity decreases, Comparable studies have verified that the inclusion of fibers results in a decrease in heat conductivity [26], [27], [28]. Compared to the control brick (λ = 0.57 W/m·K), bricks incorporating 2% sawdust show reduced conductivity levels between 0.331 W/m·K (small sawdust) to 0.364 W/m·K (large sawdust). This reduction of up to 41.93% aligns with the increased porosity introduced by the sawdust, which traps air and reduces the material's capacity to conduct heat. Smaller sawdust particles appear to enhance thermal insulation more effectively than larger particles, indicating that granulometry plays a critical role in optimizing thermal performance.

3.1.3. Specific Heat Capacity (Cp)

The inclusion of sawdust moderately increases the adobe bricks' specific heat capacity, with values rising from 0.774 kJ/kg·K for pure clay bricks to a maximum of 0.842 kJ/kg·K for bricks containing small-sized sawdust. This improvement is attributed to the presence of pores within the matrix of the adobe bricks. Studies by M. Ouedraogo et al. have shown that the increase in porosity, resulting from the incorporation of fonio straw into adobe, contributes to a significant reduction in thermal conductivity[29], thereby limiting heat transfer through the material[30]. As a result, the thermal resistance increases due to the reduced efficiency of energy and heat transfer [31].However, the improvement in specific heat capacity slightly decreases with larger particle sizes, possibly due to uneven thermal distribution within the brick matrix.

3.2. Clay-sawdust thermal behavior

Figure 6 illustrates the internal temperature variations over the coldest seven days of the winter period for different adobe envelope configurations. The results reveal that all four configurations utilizing earthen materials outperform the reference envelope in terms of thermal comfort, even under rigorous outdoor conditions characterized by minimum temperatures reaching as low as 0.25°C.

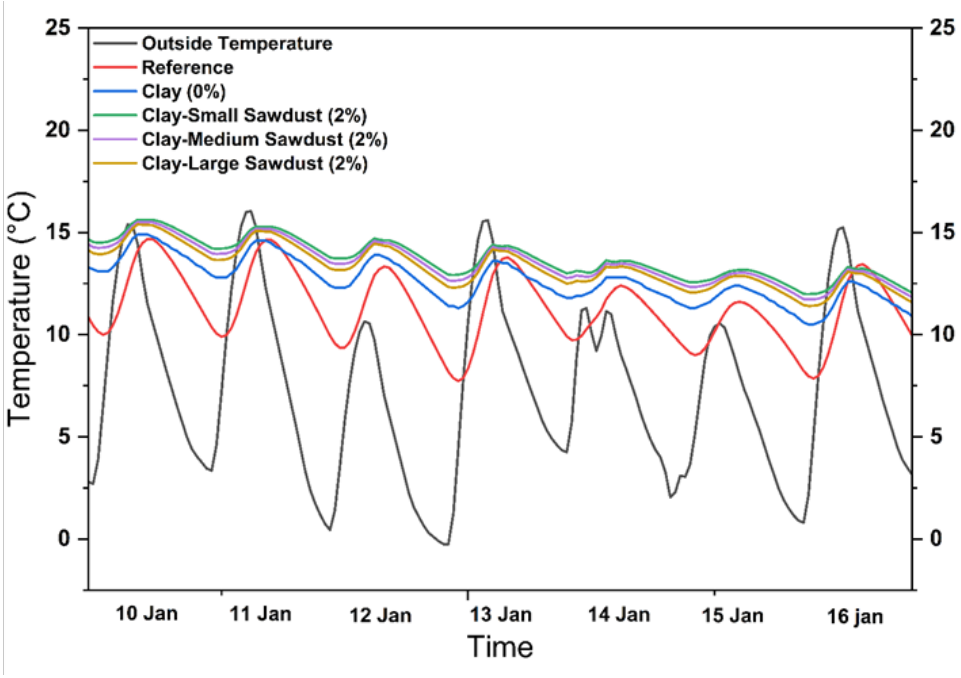

Figure 6: Temperature variations during the coldest seven days of 2024 for the reference building made of concrete and adobe clay bricks with sawdust additives of varying sizes.

Specifically, when the external temperature drops to 0.25°C, the internal temperature for the reference envelope is 8.63°C, while it rises to 11.60°C, 13.08°C, 12.81°C, and 12.50°C For configurations based on pure clay material, clay combined with small sawdust particles, clay with medium-sized sawdust particles, and clay with large sawdust particles, respectively.

These findings demonstrate that the incorporation of organic particles, such as sawdust, into earthen wall compositions significantly enhances their thermal insulation capacity. Sawdust acts as a porous material, increasing the thermal resistance of the envelope and thereby reducing heat losses to the exterior. This aligns with previous studies demonstrating that clay-based walls enriched with organic additives, such as peanut shells, provide superior insulation in winter compared to pure clay constructions[32]. Moreover, the particle size of the sawdust appears

to influence thermal performance: smaller particles maximize efficiency by improving the homogeneity of the mixture and enhancing the internal structure of the material, thus facilitating more effective heat retention.

In comparison, the envelope made of pure clay offers a notable improvement over the reference envelope but is less effective than configurations incorporating sawdust particles. This observation underscores the critical role of material composition and physical properties in governing thermal regulation.

Furthermore, the reduced temperature gradient between the interior and exterior in the earthen configurations demonstrates enhanced thermal stability—a key criterion for occupant comfort. These results are particularly significant in cold climates, where extreme fluctuations in outdoor temperatures can considerably impact the energy demands of buildings.

Figure 7 illustrates the variations in indoor temperature over the seven hottest days of the summer period for different envelope configurations. The results reveal that adobe buildings, whether or not enriched with sawdust, offer noticeably better thermal comfort than the concrete envelope used as a reference, even under extreme climatic conditions characterized by outdoor temperatures exceeding 46°C.

More specifically, when the outdoor temperature reaches 46°C, the internal temperature for the reference concrete envelope is 38.57°C, reflecting its limited capacity to regulate thermal fluctuations. In contrast, adobe envelopes exhibit lower internal temperatures: 37.10°C for the pure earth envelope, 36.12°C for the envelope enriched with small sawdust particles, 36.28°C for the medium-sized sawdust-particle envelope, and 36.52°C for the large-sized sawdust-particle envelope.

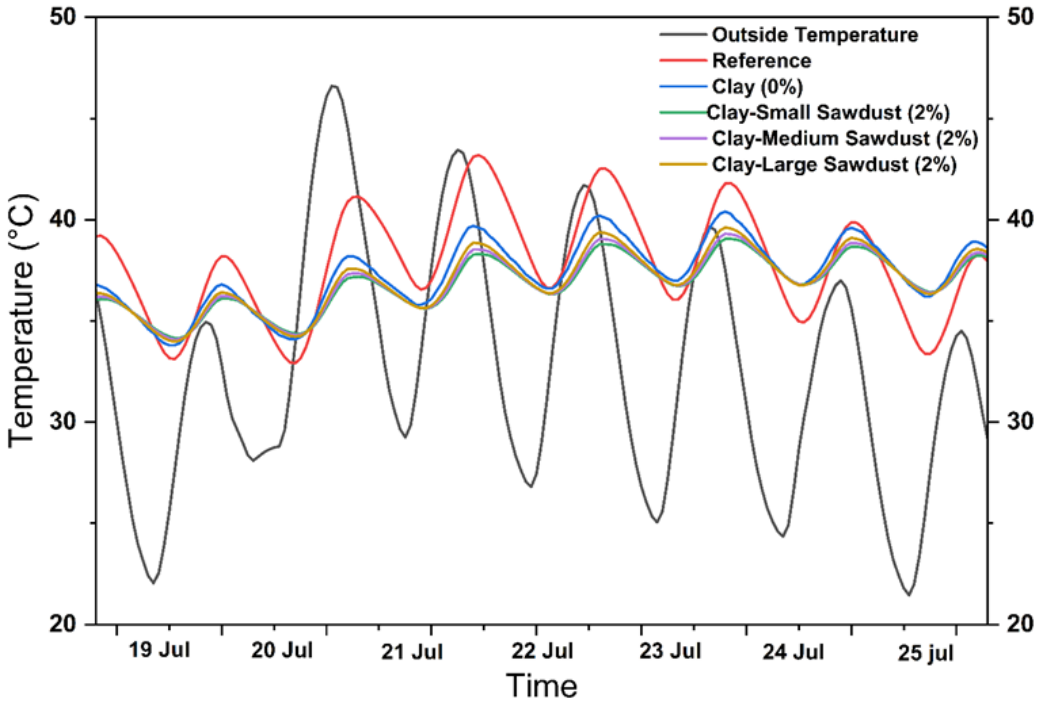

Figure 7: Temperature variations during the hottest seven days of 2024 for the reference building made of concrete and adobe clay bricks with sawdust additives of varying sizes.

These results highlight the superior thermal performance of earth-based materials over concrete. The ability of adobe to mitigate thermal fluctuations is attributed to its intrinsic properties, for example, its high thermal mass and low thermal conductivity, which enable it to limit heat gains and maintain a more stable indoor environment. The addition of sawdust, particularly small

particles, further enhances these thermal performance characteristics.

In comparison, while concrete is commonly used in modern construction, it exhibits notable limitations in thermal regulation under extreme climatic conditions. These results highlight how crucial it is to bring back traditional materials, such as sawdust-enriched adobe, into contemporary building practices to increase buildings' energy efficiency.

Furthermore, these findings support the rising demand for using natural, local building materials in hot climates. The integration of sawdust, an abundant industrial by-product, not only improves the thermal properties of adobe but also contributes to waste valorization, promoting sustainable construction practices.

Figures 8 and 9 illustrate the setups under study's heating and cooling needs, respectively. When comparing the energy performance of the several building configurations under study to a reference concrete building, the analysis of these results shows that the use of adobe bricks formed from clay and sawdust significantly reduces the energy demands for heating and cooling. The indoor air temperature set-points were maintained at 20 °C for heating and 26 °C for cooling. These values comply with the indoor thermal comfort conditions outlined in the Moroccan standard NM ISO 7730[33]. Under these conditions, the results indicate a substantial reduction in energy[33], the results indicate a substantial reduction in energy consumption.

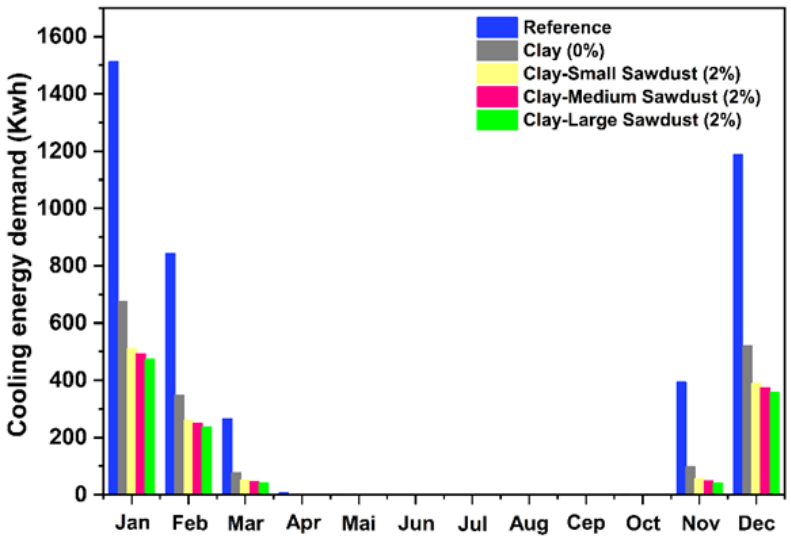

Figure 8: Monthly evolution of the heating needs in 2024 for the reference building made of concrete and adobe clay bricks with sawdust additives of varying sizes.

The simulation results indicate that the concrete building uses 4215.43 kWh of heating energy annually. By contrast, configurations using adobe bricks reduce this demand to 1722.42 kWh for pure clay (a reduction of 59.14%), 1154.60 kWh for clay mixed with fine sawdust (a reduction of 72.61%), 1211.92 kWh for clay with medium sawdust (a reduction of 71.25%), and 1269.68 kWh for clay with large sawdust (a reduction of 69.88%). The fine sawdust configuration stands out, likely due to a more homogeneous distribution of particles, optimizing thermal insulation.

In terms of cooling, the concrete building displays a high annual energy consumption of 9289.94 kWh. The use of adobe bricks reduces this consumption to 5042.08 kWh for pure clay (a reduction of 45.71%), 3824.79 kWh for clay with fine sawdust (a reduction of 58.82%), 3930.73 kWh for clay with medium sawdust (a reduction of 57.68%), and 4029.08 kWh for clay with large sawdust (a reduction of 56.62%). These findings show that because of their thermal inertia, adobe bricks can reduce indoor temperature variations. The integration of sawdust enhances this thermal inertia by limiting incoming heat flux, thereby reducing thermal loads and cooling requirements, with

fine sawdust-enriched bricks showing the highest efficiency.

These findings demonstrate that the use of adobe bricks, particularly those enriched with sawdust particles, significantly improves the energy efficiency of buildings. This optimization results in reduced energy needs for both heating and cooling, while simultaneously providing superior thermal comfort for occupants. Previous studies on energy simulations of building materials have reported similar findings, showing that integrating wool can substantially lower thermal loads compared to conventional clay buildings [34]. Further research has reinforced these findings by exploring the integration of various bioclimatic additives into building materials, such as vegetable matter [35], industrial waste [36], and Typha Australis [37] among others.

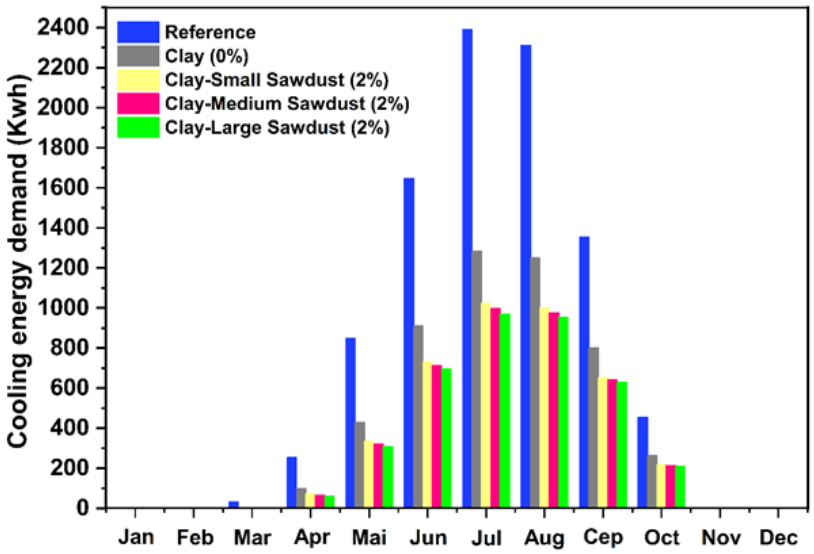

Figure 9: Monthly evolution of the cooling needs in 2024 for the reference building made of concrete and adobe clay bricks with sawdust additives of varying sizes.

4. GENERAL CONCLUSION

This study provides compelling evidence of the superior thermal efficiency of sawdust-enriched adobe compared to traditional concrete, while critically evaluating its performance as a sustainable building material in hot climates. Thermal simulations demonstrate that adobe, whether pure or enriched with sawdust, significantly enhances indoor comfort in both summer and winter. During summer, when external temperatures exceed 46°C, pure adobe maintains indoor temperatures around 37.10°C, whereas sawdust-enriched adobe achieves lower temperatures, ranging from 36.12°C to 36.52°C—up to 2.45°C cooler than concrete, which reaches 38.57°C. Similarly, in winter, when external temperatures drop to 0.25°C, pure adobe maintains an indoor temperature of 11.60°C, while sawdust-enriched adobe ranges from 12.50°C to 13.08°C, compared to just 8.63°C for concrete. These findings underscore the significant thermal efficiency of sawdust-enriched adobe in regulating indoor temperatures, reinforcing its potential as a viable alternative to conventional construction materials.

The results of this study further demonstrate a significant reduction in energy demand for both heating and cooling when sawdust-enriched adobe is utilized. For heating, the configuration with pure clay adobe results in a reduction of 59.14% in energy consumption compared to concrete. When sawdust is incorporated, the reduction ranges from 69.88% to 72.61%, indicating a notable improvement in energy efficiency. In terms of cooling, pure adobe leads to a 45.71% reduction in energy demand, while sawdust-enriched adobe configurations achieve reductions between 56.62% and 58.82%. These findings underscore the positive impact of sawdust incorporation,

regardless of particle size, in contributing to significant energy savings. In addition to its thermal and energy benefits, sawdust-enriched adobe presents economic and environmental advantages. With low production costs and reliance on locally available raw materials, it offers a cost-effective and ecologically responsible alternative to traditional construction materials. However, for its large-scale implementation, clear guidelines on sourcing, processing, and standardization must be developed. Regulatory frameworks should also define technical specifications to ensure its long-term durability, thermal efficiency, and structural integrity.

To facilitate its widespread adoption, collaboration between local governments, construction professionals, and policymakers is crucial. Establishing national and international standards for bio-based adobe formulations will strengthen confidence in its application, encouraging its integration into mainstream construction practices. Additionally, future research should explore its compatibility with other sustainable materials to further enhance the environmental performance of buildings.

Overall, this study contributes to the advancement of sustainable construction by demonstrating the viability of sawdust-enriched adobe as a low-energy, high-performance building material. With appropriate regulatory support and continued research, this innovative material holds great promise for promoting energy-efficient and climate-responsive architecture, particularly in regions with extreme temperatures.

Authors contribution: All authors have contributed to this work (conceptualization, methodology, data curation…).

Funding: The authors have not disclosed any funding.

Data Availability Statement: Not applicable.

Conflicts of Interest: The authors declare no conflicts of interest.

Acknowledgements: This work was supported by the industrial and surface engineering laboratory of the Faculty of Science and Technology of Béni Mellal, Morocco.

REFERENCES

[1] I. Bouchefra, F. Z. EL Bichri, H. Chehouani, and B. Benhamou, "Mechanical and thermophysical properties of compressed earth brick rienforced by raw and treated doum fibers," Constr Build Mater, vol. 318, p. 126031, Feb. 2022, doi: 10.1016/J.CONBUILDMAT.2021.126031.

[2] M. Benfars, A. Alioui, Y. Azalam, M. Kaddiri, and M. Mabrouki, "Impact of Ecological Thermal Roof Insulation on the Energy Efficiency of Conventional Buildings in a Semi-Arid Climate," Solar Energy and Sustainable Development Journal, pp. 78–88, Dec. 2024, doi: 10.51646/jsesd.v14iSI_MSMS2E.401.

[3] Y. Chihab, N. Laaroussi, and M. Garoum, "Thermal performance and energy efficiency of the composite clay and hemp fibers," Journal of Building Engineering, vol. 73, Aug. 2023, doi: 10.1016/j.jobe.2023.106810.

[4] S. Raefat, M. Garoum, N. Laaroussi, and Y. Chihab, "A simple laboratory flash apparatus for thermal diffusivity measurement: Modeling and application for composite material based on clay and straw," Case Studies in Construction Materials, vol. 15, Dec. 2021, doi: 10.1016/j.cscm.2021.e00657.

[5] F. Z. El Wardi, S. Ladouy, A. Atbir, and A. Khabbazi, "Study of the thermal and mechanical properties of local clay materials activated with quicklime, Sefrou (Morocco)," Mater Today Proc, vol. 58, pp. 1423–1430, Jan. 2022, doi: 10.1016/j.matpr.2022.02.348.

[6] P. Melià, G. Ruggieri, S. Sabbadini, and G. Dotelli, "Environmental impacts of natural and conventional building materials: A case study on earth plasters," J Clean Prod, vol. 80, pp. 179–

186, Oct. 2014, doi: 10.1016/j.jclepro.2014.05.073.

[7] H. Limami, I. Manssouri, O. Noureddine, S. Erba, H. Sahbi, and A. Khaldoun, "Effect of reinforced recycled sawdust-fibers additive on the performance of ecological compressed earth bricks," Journal of Building Engineering, vol. 68, p. 106140, Jun. 2023, doi: 10.1016/J.JOBE.2023.106140.

[8] "STRATÉGIE NATIONALE DE DÉVELOPPEMENT DURABLE (SNDD) 2016-2030 Résumé Exécutif Royaume du Maroc".

[9] M. Giroudon, A. Laborel-Préneron, J. E. Aubert, and C. Magniont, "Comparison of barley and lavender straws as bioaggregates in earth bricks," Constr Build Mater, vol. 202, pp. 254–265, Mar. 2019, doi: 10.1016/j.conbuildmat.2018.12.126.

[10] I. Bouchefra, F. Z. EL Bichri, H. Chehouani, and B. Benhamou, "Mechanical and thermophysical properties of compressed earth brick rienforced by raw and treated doum fibers," Constr Build Mater, vol. 318, Feb. 2022, doi: 10.1016/j.conbuildmat.2021.126031.

[11] C. Babé, D. K. Kidmo, A. Tom, R. R. N. Mvondo, B. Kola, and N. Djongyang, "Effect of neem (Azadirachta Indica) fibers on mechanical, thermal and durability properties of adobe bricks," Energy Reports, vol. 7, pp. 686–698, Nov. 2021, doi: 10.1016/J.EGYR.2021.07.085.

[12] Y. Azalam, M. Benfars, A. Alioui, M. Mabrouki, and E. M. Bendada, "Improving Adobe's Mechanical Properties through Sawdust Reinforcement: A Comparative Study of the effect of varying Sawdust Dimensions," in E3S Web of Conferences, EDP Sciences, Oct. 2024. doi: 10.1051/e3sconf/202458202005.

[13] M. Charai, H. Sghiouri, A. Mezrhab, M. Karkri, K. Elhammouti, and H. Nasri, "Thermal performance and characterization of a sawdust-clay composite material," in Procedia Manufacturing, Elsevier B.V., 2020, pp. 690–697. doi: 10.1016/j.promfg.2020.03.098.

[14] A. Alioui, S. Idrissi Kaitouni, Y. Azalam, N. Al armouzi, E. M. Bendada, and M. Mabrouki, "Effect of straw fibers addition on hygrothermal and mechanical properties of carbon-free adobe bricks: From material to building scale in a semi-arid climate," Build Environ, vol. 255, p. 111380, May 2024, doi: 10.1016/J.BUILDENV.2024.111380.

[15] H. Limami, I. Manssouri, O. Noureddine, S. Erba, H. Sahbi, and A. Khaldoun, "Effect of reinforced recycled sawdust-fibers additive on the performance of ecological compressed earth bricks," Journal of Building Engineering, vol. 68, p. 106140, Jun. 2023, doi: 10.1016/J.JOBE.2023.106140.

[16] "HFM 446 Lambda Series-Heat Flow Meter for Testing Insulation Materials".

[17] K. Pawlik, A. Kucharczyk, and M. Podpora, "Method of determining thermal diffusivity on the basis of measurements of linear displacements," Measurement, vol. 211, p. 112624, Apr. 2023, doi: 10.1016/J.MEASUREMENT.2023.112624.

[18] P. K. S. Rathore, N. K. Gupta, D. Yadav, S. K. Shukla, and S. Kaul, "Thermal performance of the building envelope integrated with phase change material for thermal energy storage: an updated review.," Sustain Cities Soc, vol. 79, p. 103690, Apr. 2022, doi: 10.1016/J.SCS.2022.103690.

[19] Y. Chihab, L. Essaleh, R. Bouferra, and A. Bouchehma, "Numerical study for energy performance optimization of hollow concrete blocks for roofing in a hot climate of Morocco," Energy Conversion and Management: X, vol. 12, p. 100113, Dec. 2021, doi: 10.1016/J.ECMX.2021.100113.

[20] Y. Zhang, G. Sang, P. Li, M. Du, T. Guo, X. Cui and W. Han, "Study on the influence of thermo-physical parameters of phase change material panel on the indoor thermal environment of passive solar buildings in Tibet," J Energy Storage, vol. 52, p. 105019, Aug. 2022, doi: 10.1016/J.EST.2022.105019.

[21] S. D. G., "Calculation of heat conduction transfer functions for multi-layer slabs," ASHRAE Trans, vol. 77, no. 2, pp. 117–126, 1971, Accessed: Mar. 25, 2025. [Online]. Available: https://cir.nii.ac.jp/crid/1573387449612155904

[22] S. Hamdaoui, M. Mahdaoui, A. Allouhi, R. El Alaiji, T. Kousksou, and A. El Bouardi, "Energy demand and environmental impact of various construction scenarios of an office building in Morocco," J Clean Prod, vol. 188, pp. 113–124, Jul. 2018, doi: 10.1016/J.JCLEPRO.2018.03.298.

[23] H. Kaddouri, A. Abidouche, M. S. H. Alaoui, I. Driouch, S. Hamdaoui, and A. A. Msaad, "Study of the Energy, Economic, Environmental, and Thermal Comfort Impact of the Integration of Hemp Concrete and Hemp Plaster in a Residential Building Envelope in Morocco," Journal of Advanced Research in Numerical Heat Transfer, vol. 23, no. 1, pp. 1–27, Aug. 2024, doi: 10.37934/arnht.23.1.127.

[24] S. Hamdaoui, M. Mahdaoui, A. Allouhi, R. El Alaiji, T. Kousksou, and A. El Bouardi, "Energy demand and environmental impact of various construction scenarios of an office building in Morocco," J Clean Prod, vol. 188, pp. 113–124, Jul. 2018, doi: 10.1016/J.JCLEPRO.2018.03.298.

[25] W. R. Blevin and W. J. Brown, "A Precise Measurement of the Stefan-Boltzmann Constant," Metrologia, vol. 7, no. 1, p. 15, Jan. 1971, doi: 10.1088/0026-1394/7/1/003.

[26] K. Al Rim, A. Ledhem, O. Douzane, R. M. Dheilly, and M. Queneudec, "Influence of the proportion of wood on the thermal and mechanical performances of clay-cement-wood composites," Cem Concr Compos, vol. 21, no. 4, pp. 269–276, Aug. 1999, doi: 10.1016/S0958-9465(99)00008-6.

[27] T. Ashour, H. Wieland, H. Georg, F. J. Bockisch, and W. Wu, "The influence of natural reinforcement fibres on insulation values of earth plaster for straw bale buildings," Mater Des, vol. 31, no. 10, pp. 4676–4685, Dec. 2010, doi: 10.1016/J.MATDES.2010.05.026.

[28] A. Laborel-Préneron, J. E. Aubert, C. Magniont, C. Tribout, and A. Bertron, "Plant aggregates and fibers in earth construction materials: A review," Constr Build Mater, vol. 111, pp. 719–734, May 2016, doi: 10.1016/J.CONBUILDMAT.2016.02.119.

[29] M. Ouedraogo, K. Dao, Y. Millogo, J. Aubert, A. Messan, M. Seynou, L.

Zerbo, M. Gomina, "Physical, thermal and mechanical properties of adobes stabilized with fonio (Digitaria exilis) straw," Journal of Building Engineering, vol. 23, pp. 250–258, May 2019, doi: 10.1016/J.JOBE.2019.02.005.

[30] Y. Gao and X. Meng, "A comprehensive review of integrating phase change materials in building bricks: Methods, performance and applications," J Energy Storage, vol. 62, p. 106913, Jun. 2023, doi: 10.1016/J.EST.2023.106913.

[31] J. H. She, Y. Beppu, J. F. Yang, D. D. Jayaseelan, and T. Ohji, "Effects of Porosity on Thermal Shock Resistance of Silicon Nitride Ceramics," pp. 247–252, Mar. 2008, doi: 10.1002/9780470294758.CH28.

[32] M. Lamrani, A. Lkouen, N. Laaroussi, and M. Ouakarrouch, "Thermal Behaviour Assessment of a New Local Clay-Based Building Material and Peanut Shell Waste: Experimental and Numerical Approaches," Civil Engineering and Architecture, vol. 11, no. 6, pp. 3451–3470, 2023, doi: 10.13189/cea.2023.110616.

[33] H. Oukmi, B. Chegari, O. Mouhat, M. Rougui, M. EL Ganaoui, and M. Cherkaoui, "Improving the efficiency of the trombe wall by integrating multi-fold glazing and sustainable materials: Ifrane, Morocco as a case study," Journal of Building Engineering, vol. 89, p. 109310, Jul. 2024, doi: 10.1016/J.JOBE.2024.109310.

[34] S. Mounir, A. Khabbazi, A. Khaldoun, Y. Maaloufa, and Y. El Hamdouni, "Thermal inertia

and thermal properties of the composite material clay–wool," Sustain Cities Soc, vol. 19, pp. 191–199, Dec. 2015, doi: 10.1016/J.SCS.2015.07.018.

[35] R. Saiah, B. Perrin, and L. Rigal, "Improvement of thermal properties of fired clays by introduction of vegetable matter," J Build Phys, vol. 34, no. 2, pp. 124–142, Oct. 2010, doi: 10.1177/1744259109360059.

[36] M. L. Mary, C. Peter, K. Mohan, S. Greens, and S. George, "Energy efficient production of clay bricks using industrial waste," Heliyon, vol. 4, no. 10, p. e00891, Oct. 2018, doi: 10.1016/J.HELIYON.2018.E00891.

[37] Y. Dieye, V. Sambou, M. Faye, A. Thiam, M. Adj, and D. Azilinon, "Thermo-mechanical characterization of a building material based on Typha Australis," Journal of Building Engineering, vol. 9, pp. 142–146, Jan. 2017, doi: 10.1016/J.JOBE.2016.12.007.

[38] A. Alioui, Y. Azalam, M. Benfars, E. M. Bendada, and M. Mabrouki, "Comparative analysis of energy performance between clay-based and conventional building materials: A case study in Moroccan semi-arid climate," in E3S Web of Conferences, EDP Sciences, Oct. 2024. doi: 10.1051/e3sconf/202458201005.

[39] A. Alioui, S. Idrissi Kaitouni, Y. Azalam, N. Al armouzi, E. M. Bendada, and M. Mabrouki, "Effect of straw fibers addition on hygrothermal and mechanical properties of carbon-free adobe bricks: From material to building scale in a semi-arid climate," Build Environ, vol. 255, p. 111380, May 2024, doi: 10.1016/J.BUILDENV.2024.111380.

[40] Y. Azalam, A. Alioui, N. Al Armouzi, M. Benfars, M. Mabrouki, and E. M. Bendada, "Physical and mechanical properties of adobe bricks reinforced by natural additives, a case study of alfalfa fibers," EUREKA: Physics and Engineering, vol. 2024-July, no. 4, pp. 144–159, Jul. 2024, doi: 10.21303/2461-4262.2024.003426.

[41] H. Kaddouri, A. Abidouche, M. S. H. Alaoui, I. Driouch, S. Hamdaoui, and A. A. Msaad, "Study of the Energy, Economic, Environmental, and Thermal Comfort Impact of the Integration of Hemp Concrete and Hemp Plaster in a Residential Building Envelope in Morocco," Journal of Advanced Research in Numerical Heat Transfer, vol. 23, no. 1, pp. 1–27, Aug. 2024, doi: 10.37934/ARNHT.23.1.127.

Solar Energy
And Sustainable Development
Refereed, biannual scientific journal issued by:
The Libyan Center for Solar Energy Research and Studies

Theoretical Insights into a High-Performance Optical Absorption in GaSeS/InSeS 2D van der Waals Heterostructure for Photovoltaic Applications

Hanan Ziani[1*], Kamal Assiouan[2], Fatima Zohra Ben Abdelouahab[3], El Hassan El Harouny[4], Mustapha El Hadri[5], Farid Ben Abdelouahab[6].

[1,2,3,4,5,6]Artificial Intelligence and Computational Physics Laboratory, Faculty of Sciences, Abdelmalek Essaadi university, Tetouan, Morocco.

E-*mail:* [1] hanane.ziani@etu.uae.ac.ma ,[2] kamal.assiouan@etu.uae.ac.ma , [3] fatimazohra.benabdelouahab@etu.uae.ac.ma , [4] elharounye@gmail.com , [5] elhadri.mustafa@gmail.com , [6] fbenabdelouahab@uae.ac.ma.

SPECIAL ISSUE ON:

The 1St International Conference on Sciences and Techniques for Renewable Energy and the Environment.
(STR2E 2025)
May 6-8, 2025 at FST-Al Hoceima-Morocco.

KEYWORDS

Density Functional Theory (DFT), Electronic structure, optical analysis, GaSeS/InSeS heterostructure, Photovoltaic devices.

ABSTRACT

Advances in heterostructure design are transforming electronic and optoelectronic technologies, with particular focus on Janus monolayer-based heterojunctions. These heterojunctions, arising from the broken symmetry of 2D materials, offer new possibilities for ultra-thin, high-performance vertical p-n heterojunction solar cells. In this study, we examine the electronic structure and optical properties of a 2D GaSeS/InSeS heterostructure, formed through van der Waals interactions, based on first-principles calculations using density functional theory (DFT). The heterostructure consists of Janus group III chalcogenide GaSeS and InSeS monolayers (MLs).

The electronic properties show that both the AA and AB stacking configurations exhibit indirect semiconductor band gaps, with values of 1.3207 eV and 1.3452 eV using the PBE (Perdew-Burke-Ernzerhof) functional, and 2.0997 eV and 2.1242 eV using the Heyd-Scuseria-Ernzerhof (HSE06) hybrid functional, respectively.

Both configurations also display the characteristic features of type-II heterojunctions, which promote efficient separation of photogenerated electrons and holes. Charge density analysis reveals a transfer of charge from GaSeS to InSeS. Furthermore, optical analysis shows that both stacking configurations (AA and AB) exhibit similar absorbance spectra, primarily in the UV range, with peak absorption around 11.6×10^5 cm^{-1}. Within the visible spectrum, the maximum absorption rate for both configurations is 2.8×10^5 cm^{-1}. The 2D GaSeS/InSeS heterostructure holds great

*Corresponding author.

DOI: https://doi.org/10.51646/jsesd.v14iSTR2E.986

This is an open access article under the CC BY-NC license (http://Attribution-NonCommercial 4.0 (CC BY-NC 4.0)).

potential as a high-performance material for future photovoltaic devices, with promising applications in both photovoltaic cells and optoelectronic systems.

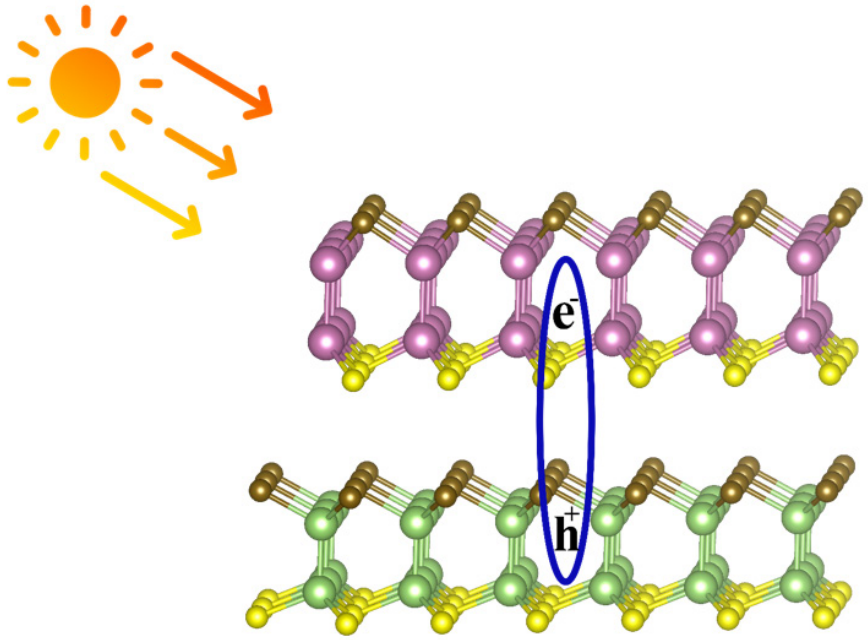

Graphical abstract.

رؤى نظرية حول الامتصاص البصري عالي الأداء في البنية المتغايرة GaSeS/InSeS 2D van der Waals للتطبيقات الكهروضوئية

حنان الزياني، كمال أسوان ، فاطمة الزهراء بن عبد الوهاب ، حسن الهاروني ، مصطفى الحضري ، فريد بن عبد الوهاب.

ملخص: تُحدث التطورات في تصميم الهياكل غير المتجانسة تحولاتٍ جذرية في التقنيات الإلكترونية والبصرية، مع التركيز بشكل خاص على الوصلات غير المتجانسة القائمة على طبقة جانوس أحادية. تُتيح هذه الوصلات غير المتجانسة، الناتجة عن اختلال تماثل المواد ثنائية الأبعاد، إمكانياتٍ جديدةً لخلايا شمسية عمودية فائقة الرقة وعالية الأداء ذات وصلات غير متجانسة p-n.

في هذه الدراسة، ندرس البنية الإلكترونية والخصائص البصرية لهيكل غير متجانس ثنائي الأبعاد من InSeS/GaSeS، مُشكّل من خلال تفاعلات فان دير فالس، استنادًا إلى حسابات المبادئ الأولية باستخدام نظرية الكثافة الوظيفية (DFT). يتكون الهيكل غير المتجانس من كالكوجينيد المجموعة الثالثة من جانوس بين طبقات أحادية (MLs) من GaSeS و InSeS. تُظهر الخصائص الإلكترونية أن تكويني التراص AA و AB يُظهران فجوات نطاق أشباه الموصلات غير المباشرة، بقيم 1.3207 إلكترون فولت و1.3452 إلكترون فولت باستخدام دالة (PBE) بيرديو-بيرك-إرنزرهو، و2.0997 إلكترون فولت و2.1242 إلكترون فولت باستخدام دالة هايد-سكوسيريا-إرنزرهوف الهجينة (HSE06)، على التوالي. كما يُظهر كلا التكوينين السمات المميزة للوصلات غير المتجانسة من النوع الثاني، والتي تُعزز الفصل الفعال للإلكترونات والفجوات المولدة ضوئيًا. يكشف تحليل كثافة الشحنة عن انتقال الشحنة من GaSeS إلى InSeS.

علاوة على ذلك، يُظهر التحليل البصري أن كلا تكويني التراص AA و AB يُظهران أطياف امتصاص متشابهة، في نطاق الأشعة فوق البنفسجية بشكل أساسي، مع ذروة امتصاص حوالي 11.6×10^5 سم$^{-1}$. في الطيف المرئي، يبلغ أقصى معدل امتصاص لكلا التكوينين $2.8 \times 11.6 \times 10^5$ سم$^{-1}$. تتمتع البنية غير المتجانسة ثنائية الأبعاد InSeS/GaSeS بإمكانيات هائلة كمواد عالية الأداء لأجهزة الطاقة الكهروضوئية المستقبلية، مع تطبيقات واعدة في كل من الخلايا الكهروضوئية والأنظمة البصرية الإلكترونية.

الكلمات المفتاحية – نظرية الكثافة الوظيفية DFT، البنية الإلكترونية، التحليل البصري، البنية غير المتجانسة لـ GaSeS/InSeS، الأجهزة الكهروضوئية.

1. INTRODUCTION

Graphite exfoliation into 2D graphene sheets has provided the scientific community with a remarkable material due to its mechanical and electronic characteristics [1].

For that, graphene is one of the most extensively researched materials among a much larger family of layered materials that can be isolated into 2D sheets, such as hexagonal boron nitride (h-BN) [2-4], transition metal dichalcogenides (TMDs) [5-8], blue or black phosphorus [9,10], and 2D Janus materials [11].

These 2D materials have drawn significant attention from the scientific community as progress in their fabrication through exfoliation or direct growth has advanced. Consequently, they exhibit multiple distinctive properties, including extremely thin dimensions, adjustable energy gaps, and exceptional mechanical attributes [12].

Nevertheless, specific imperfections in these substances, like the null energy gaps of graphene [13] and the readily corroded black phosphorus [14], Poor charge transport in TMDs leads to extended reaction durations and diminished signal-to-noise proportions [15], have restricted their possible utilizations.

To address these challenges, diverse approaches have been devised, including molecular adsorption [16-18], electrostatic field application [19-22], strain manipulation [23,24], doping [25], the formation of van der Waals heterostructures (vdWHs) [26,27], to modify the physical characteristics of 2D materials. One of the most effective strategies to address these challenges is the construction of heterostructures, which not only preserves the outstanding properties of the individual materials but also introduces new physical phenomena. This approach has proven to be both highly efficient and experimentally viable [28,29].

2D Stacked material are featured by weak van der Waals (vdW) forces between sheets, which ease the parameter alignment constraints for epitaxy and allow the production of complex vdW heterostructures [30]. This also enables new growth platforms that are difficult to achieve with conventional 3D materials. paving the way for numerous new applications, particularly such as solar photovoltaics [31,32], photodetection [33], catalytic processes [34], thermoelectric systems [35], and tunneling-based field-effect transistors [36].

For instance, many 2D van der Waals heterostructures (vdWHs) have attracted considerable interest due to their outstanding properties. For example, the $MoSe_2/PtS_2$ 2D vdW heterostructure has demonstrated exceptional optical and electronic characteristics [37,38]. Similarly, heterostructures such as graphene/phosphorene [39,40], graphene/MoS_2 [41,42], and phosphorene/MoS_2 [42,43] have gained significant attention in both theoretical and experimental studies. These structures not only retain the intrinsic properties of their individual monolayers but also offer novel or enhanced optoelectronic functionalities while remaining experimentally viable.

Recently, Janus materials have attracted considerable interest because of their unique geometry and properties [44-46]. Theoretical analyses show that monolayer MoSSe is a semiconductor with a direct band gap of 1.72 eV [45], ideal for optical absorption, and it has been successfully created by sulfurizing a $MoSe_2$ monolayer [44]. This demonstrates its potential in optoelectronic applications, especially in charge transfer and separation [46].

In a similar manner, Janus group-III monochalcogenide monolayers, represented as M_2XY (M = Ga, In; X/Y = S, Se, Te), display excellent energetic and dynamic stability [47] and also demonstrate promising optoelectronic characteristics [47,48].

For instance, In_2SeTe, In_2STe, Ga_2SeTe, and Ga_2STe have shown potential for photocatalysis [49] and can be modified by biaxial strain to engineer the optoelectronic properties of the Ga_2SSe Janus monolayer [50]. However, their relatively low photocatalytic efficiency [47] significantly limits their practical applications. Hence, improving the optoelectronic performance of group-

III monochalcogenide Janus monolayers is crucial. For example, vdW heterostructures such as In_2SeTe/Ga_2STe [51] exhibit strong optical absorption and a direct bandgap, positioning them as promising candidates for advanced solar cells. Herein, we investigate the architecture and optoelectronic characteristics of a vertical heterostructure with two stacking models, AA and AB, between GaSeS and InSeS monolayers, using first-principles simulations. The computed results indicate that both models exhibit type II band alignment. Our analysis of the optoelectronic properties of the lateral heterostructure composed of group-III monochalcogenide Janus monolayers offers valuable insights for the development and implementation of optoelectronic devices.

2. METHODOLOGY

In this present work, electronic and optical absorption calculations for GaSeS/InSeS van der Waals heterostructures were conducted through the use of density functional theory (DFT) within the Quantum ESPRESSO package [52].

The PAW (projector-augmented wave) approach [53] was utilized to include the influence of exchange-correlation contributions, alongside the PBE (Perdew-Burke-Ernzerhof) functional based on the generalized gradient approximation (GGA) [54].

The electronic and optical characteristics are carried out with a kinetic energy cutoff of 70 Ry. The Heyd-Scuseria-Ernzerhof (HSE06) hybrid functional [55] was applied to refine the electronic band structure calculations. A Gaussian broadening of 0.05 eV are utilized, and the convergence criterion for the self-consistent process are set at a total energy difference of 5×10^{-6} eV between consecutive iterations. A $12 \times 12 \times 1$ k-point grid is generated using the Monkhorst-Pack scheme to sample the first Brillouin zone [56].

To avoid interference between neighboring layers, a vacuum space of 26 Å are introduced over the axis of z. A $12\times 12 \times 1$ k-point grid is utilized to achieve static self-consistency and perform Projected density of states (PDOS) calculations along with optical property analysis.

The optical properties, including the real Re ($\varepsilon(\omega)$) and imaginary Im ($\varepsilon(\omega)$) components of the dielectric function, absorption coefficient $\alpha(\omega)$, and reflectivity, were calculated using the random phase approximation (RPA) implemented in the YAMBO code [57].

The absorption coefficient is given by Equation 1 [58]:

$$\alpha(\omega) = \frac{2\omega}{c}\left(\frac{\sqrt{\varepsilon_1^2 + \varepsilon_2^2} - \varepsilon_1}{2}\right)^{\frac{1}{2}} \qquad (1)$$

where $\varepsilon_1(\omega)$ and $\varepsilon_2(\omega)$ represent the real and imaginary parts of the complex dielectric function, respectively. XCrySDen [59] software was used to visualize the charge density variation and the optimized structures.

3. RESULTS AND ANALYSIS

3.1. Properties related to structure and stability

Before assembling the GaSeS/InSeS heterostructure, we initially examine the structural properties of the individual GaSeS and InSeS monolayers, as summarized in Table 1. Earlier investigations [47,49] have indicated that both monolayers exhibit exceptional stability, as confirmed by the absence of imaginary phonon modes. The geometric structure of GaSeS and InSeS monolayers is derived from their pristine counterparts, GaSe and InSe, which have been both theoretically studied and experimentally synthesized. These materials have been confirmed as suitable candidates for device applications due to their high absorption in the UV-visible range, significant carrier mobility, and wide band gap [47,60-62].

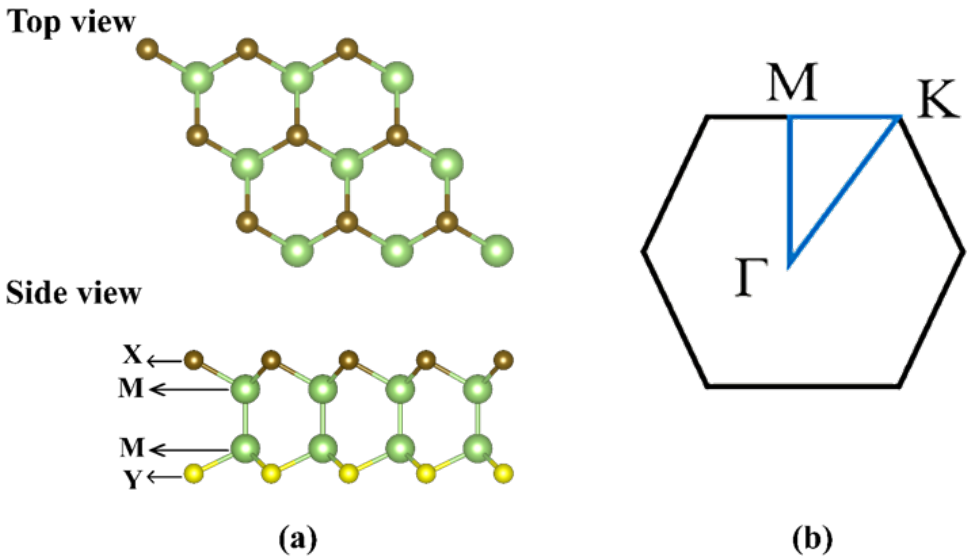

Figure 1. (a) Displays the top and side views of the 2D Janus material and (b) illustrates the Brillouin zone graph of the hexagonal structure.

Both monolayers crystallize in a hexagonal lattice with the symmetry group P3M1, and their respective Brillouin zones include high-symmetry points labeled as (Γ-M-K-Γ) (see Figure1). The optimized structural parameters, illustrated in Figure 2 (a) and (b), reveal that the equilibrium lattice constants are 3.71 Å for GaSeS and 3.89 Å for InSeS (see Table 1).

Furthermore, the band gap energies, calculated using both PBE and HSE approximations, are found to be 2.03 eV (3.07 eV) for GaSeS and 1.548 eV (2.40 eV) for InSeS, respectively, as presented in Table 1. These findings align closely with previously documented results [47,48]. Based on these results, InSeS can be considered a promising donor material for solar cell applications. The optimal band gap energy for solar cells is approximately 1.5 eV, as it falls within the primary energy range of the solar radiation. [63]

Next, we optimized the geometric structure and optoelectronic properties of the GaSeS/InSeS heterostructure, as depicted in Figure 2 (c) and (d).

Two distinct stacking configurations, AA and AB, are illustrated in these figures, showing both top and side views. The heterostructure was constructed by combining the unit cells of GaSeS and InSeS monolayers (MLs), resulting in a supercell comprising eight atoms.

To assess the lattice mismatch within the heterostructure, we employed Equation (2) [64]:

$$\delta = \left(a_{InSeS} - a_{GaSeS}\right) / a_{InSeS} \qquad (2)$$

where a_{InSeS} and a_{GaSeS} represent the refined lattice parameters of the InSeS and GaSeS monolayers, respectively.

Our calculations revealed a lattice mismatch of approximately 4.6%. Experimentally, this value remains below 5%, indicating favorable conditions for the fabrication of van der Waals (vdW) heterostructures [65].

As shown in Figure 2(c), the interlayer distance for the AA-stacked configuration is determined by the S–Se interaction, measuring 2.24 Å.

In contrast, for the AB-stacked configuration, the interlayer distance corresponds to the Se–In interaction, measuring 2.98 Å (see Figure2).

The optimized lattice constants were calculated as 3.86 Å for the AA configuration and 3.87 Å for the AB configuration. (see Table 1)

To evaluate the energetic stability of the GaSeS/InSeS heterostructure, we computed the interlayer binding energy using Equation (3) [66]:

$$E_b = E_{GaSeS/InSeS} - \left(E_{GaSeS} + E_{InSeS}\right) \quad (3)$$

where $E_{GaSeS/InSeS}$, E_{GaSeS}, and E_{InSeS} correspond to the total energies of the GaSeS/InSeS heterostructure, the GaSeS monolayer, and the InSeS monolayer, respectively.

A binding energy of –0.31 eV was obtained for both AA and AB configurations as shown in Table 1, confirming the thermodynamic stability of the heterostructure.

These binding energy values are comparable to previous results for WSSe-WS_2 (-0.350 eV), WSSe-WSe_2 (-0.492 eV) [67], BP/MoS_2 (-1.23 eV) [68], and Janus group-III chalcogenides (-31.68 eV) [69]. This highlights their role in enhancing the stability of vertical heterostructures, ensuring epitaxial quality and improved physical properties.

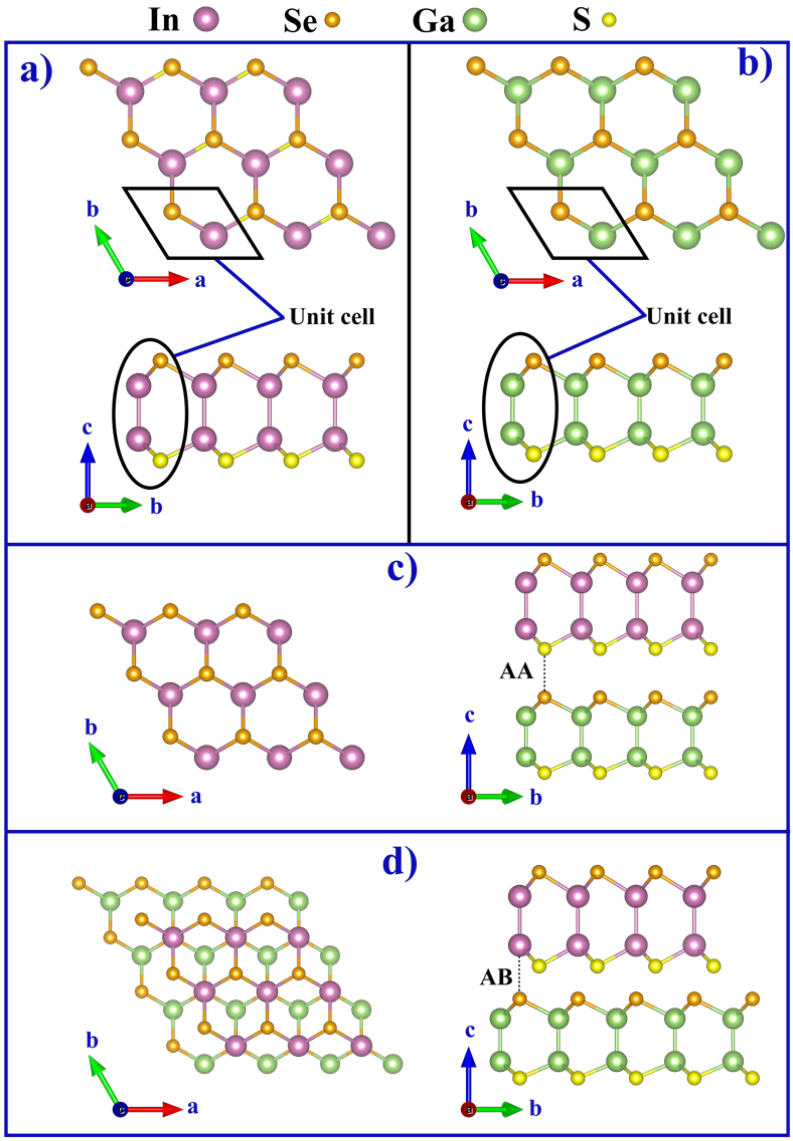

Figure 2. Schematic representation of the optimized structure, showing the top and side views of (a) InSeS and (b) GaSeS monolayers, as well as the GaSeS/InSeS heterostructures in (c) AA-stacking and (d) AB-stacking configurations.

Table 1. Computed lattice constants (in Å), binding energy (eV), electronic bandgap Eg (PBE and HSE (in eV) and interlayer distance Dinter for heterostructure (in Å).

system	a	E_b	E_g^{PBE}	E_g^{HSE}	D_{inter}	Ref.
GaSeS	3.71 3.73 3.72	-	2.03	3.07 2.91 2.97	-	This work [47] [49]
InSeS	3.89 4.01 4.00	-	1.54	2.40 2.28 2.34	-	This work [47] [49]
GaSeS/InSeS AA-stacking	3.86	- 0.31	1.32	2.09	2.24	This work
GaSeS/InSeS AB-stacking	3.87	- 0.31	1.36	2.12	2.98	This work
Al_2OS/Ga_2SSe	3.7	-22.8 meV/Å2	-	2.34	-	[73]
$In_2SeS/g\text{-}C_3N_4$	-	-2.21	-	2.03	3	[76]

3.2. Electronic properties

The electronic band structure plays a crucial role in defining the characteristics of materials for photovoltaic solar cell applications. Figures 3 and 4 illustrate the energy bands alongside the projected density of states (PDOS) for the GaSeS and InSeS monolayers, as well as for the GaSeS/InSeS van der Waals heterostructure (vdWH) for two AA and AB stacking.

Figure 3 (a, c) presents the band structures of the GaSeS and InSeS monolayers obtained using the HSE approximation. Table 1 summarizes the calculated energy band gaps for both PBE and HSE approximations, showing that GaSeS has an indirect band gap of 2.03 eV with the PBE method and 3.07 eV with the HSE06 approach. Similarly, the InSeS monolayer exhibits an indirect band gap of 1.54 eV (PBE) and 2.4 eV (HSE06), both positioned between the conduction and valence bands. In both cases, the indirect band gap is located between the Γ point in the conduction band and between the Γ and M points in the valence band.

The obtained band gap value for the GaSeS monolayer aligns closely with previous literature, which reports a value of 2.04 eV [49,69]. However, the calculated band gap for the InSeS monolayer is higher than that reported in earlier studies [49] However, it remains comparable to the experimental values for the original InSe and GaSe monolayers [70,71].

The electronic band structure of the GaSeS/InSeS van der Waals heterostructure were analyzed for two stacking configurations (AA and AB) using the HSE hybrid functional and PBE functional, as depicted in Figure 4 (a, c). Table 1 presents the calculated energy bandgap values obtained using both PBE and HSE approximations.

The results indicate that both stacking configurations exhibit an indirect bandgap, with the conduction band minimum (CBM) located at the Γ point and the valence band maximum (VBM) along the Γ-M path, without any significant alteration of energy levels. A detailed examination of Figure 4 (a, c) reveals that the band structures of the AA and AB configurations exhibit negligible differences, with energy bandgaps of 2.09 eV and 2.12 eV, respectively with HSE approch as similar findings regarding favorable stacking positions have been reported in previous studies on GaS/GaSe [72] and $WSSe/WSe_2$ [67] heterostructures. The obtained bandgap values for GaSeS/InSeS are comparable to those reported in other works, being lower than those of Al_2OS/Ga_2SSe (2.34 eV) [73] and GaN/SiS (2.45 eV) [74] but higher than those of BP/Ga_2SSe (0.85 eV) [75], In_2SeTe/Ga_2STe (1.91 eV) [51] and $In_2SeS/g\text{-}C_3N_4$ (2.03 eV) [76].

The bandgaps calculated using the PBE approach are 1.32 eV and 1.36 eV for the AA and AB configurations, respectively, as shown in Table 1. When compared to the optimal bandgap range for a single-junction solar cell according to Shockley-Queisser theory (1.1–1.6 eV) [77], the reduced bandgap suggests improved charge carrier separation and transfer, enhancing the

material's potential for photovoltaic applications.

Furthermore, the GaSeS/InSeS heterostructure exhibits a type-II band alignment, with a valence band offset (VBO) of 0.79 eV and a conduction band offset (CBO) of 0.29 eV between the GaSeS and InSeS layers. The relatively low CBO indicates a high open-circuit voltage, which is advantageous for photovoltaic applications, as previously reported for GeAs/GaSe [78]. This band alignment is further confirmed by the projected density of states (PDOS) analysis, reinforcing the potential of GaSeS/InSeS as a promising candidate for solar cell applications.

The projected density of states (PDOS) provides insight into the contributions of atomic orbitals and their relation to the Fermi level. Figures 3 and 4 (b and d) illustrate the PDOS for GaSeS, InSeS monolayers (MLs), and GaSeS/InSeS van der Waals heterostructures (vdWHs) in AA and AB stacking configurations, respectively. In the figures, negative values represent the valence bands, while positive values indicate the conduction bands, with zero corresponding to the Fermi level [79]. The PDOS, ranging from −5 eV to 5 eV, reveals the movement of electrons from the valence to the conduction bands, as well as on the hybridization of atomic orbitals in the materials. The computed PDOS, obtained using the PBE functional, supports the band gap values derived from previous analyses. For the GaSeS and InSeS MLs, the CBM and VBM are primarily influenced by p orbitals. Specifically, the contributions to the CBM mainly originate from Ga-p and In-p orbitals, while the VBM is primarily driven by S-p and Se-p orbitals (see Figure 3 b and d). As depicted in Figure 4 (b and d), the PDOS profiles for AA and AB stacking exhibit similar trends, with slight variations in valence state intensity. The valence band is strongly influenced by the S-p and Se-p orbitals, with values ranging from 2.78 to 2.52 states/eV, while the conduction band is governed by In-p and Ga-p orbitals at 1.88 and 1.42 states/eV, respectively.

Overall, the energy band gaps extracted from the PDOS for both stacking configurations are in good agreement with those obtained from their corresponding band structures.

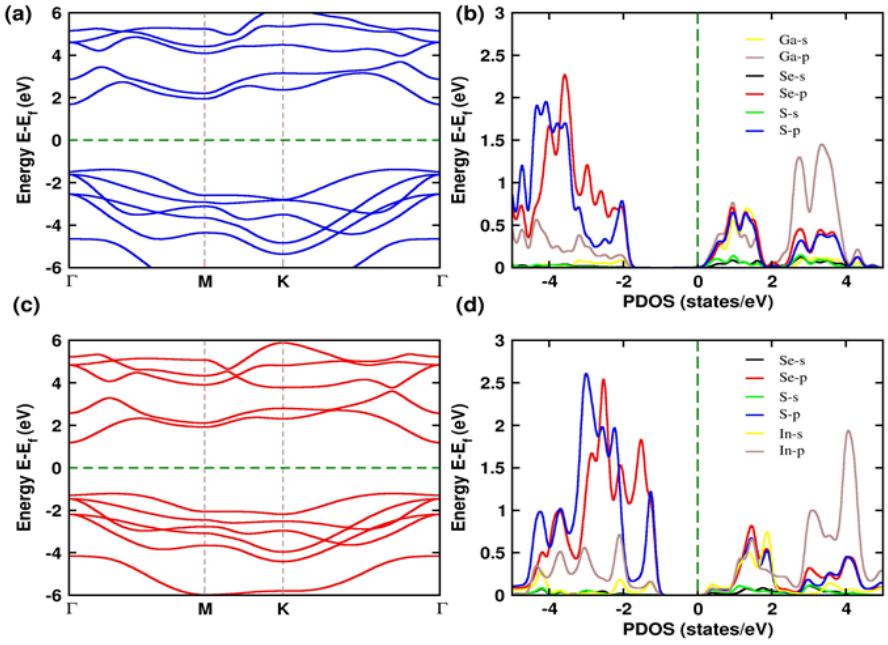

Figure 3. (a) and (c) depict the band structure calculated using the HSE functional, while (b) and (d) show the projected band structure obtained with the PBE functional for GaSeS and InSeS monolayers.

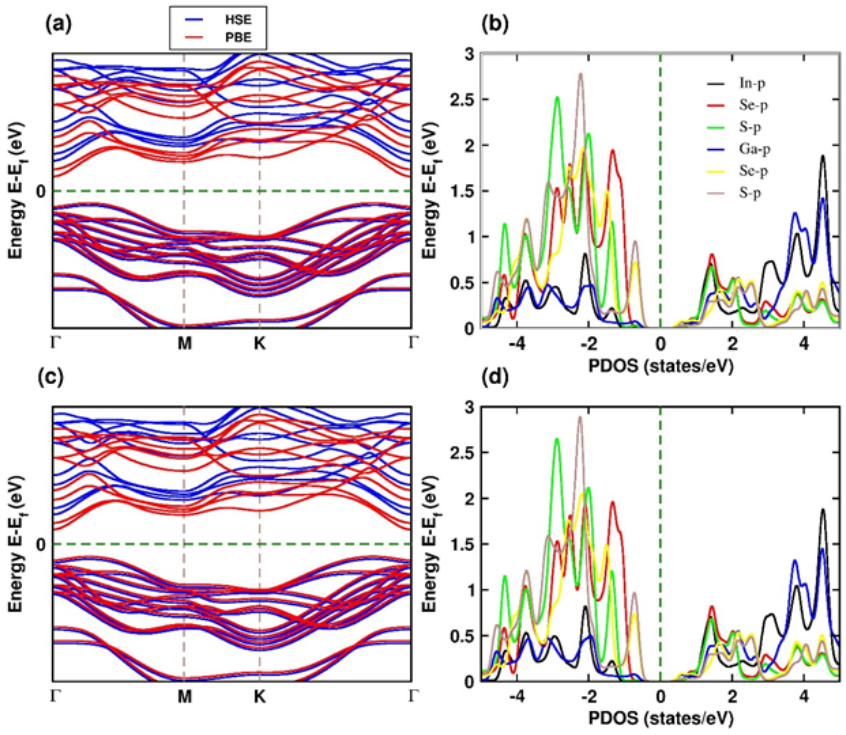

Figure 4. The band structure calculated using the (HSE &PBE) functional and the projected band structure obtained with the PBE functional for AA-stacking in (a) and (b), and AB-stacking in (c) and (d).

To analyze the movement of charge between GaSeS and InSeS monolayers in the vdWs stacked heterostructure, we evaluated the averaged z-direction planar electrostatic potential for both, AA and AB stacking (see Figure 5). Our observations indicate that, in both configurations, the InSeS-ML has a stronger energy than the GaSeS-ML, leading to a greater accumulation of electrons on the GaSeS monolayer. As given in Figure 5, the potential difference over the GaSeS/InSeS heterostructure is ΔV = 2.03 eV for the AA stacking and ΔV = 2.00 eV for the AB stacking as depicted in Figure 5 (a) and (b), respectively. This potential difference creates a built-in electric field that encourages the movement of electrons from the GaSeS monolayer to the InSeS monolayer, as well as the transfer of holes from the InSeS-ML to the GaSeS-ML.

In general, a strong built-in electric field can effectively suppress the recombination of photogenerated electron-hole pairs [79]. Compared to previous studies, the potential drop in GaSeS/InSeS is greater than that observed in Al_2OS/Ga_2SSe [73] and black-P/blue-P [80], which enhances carrier separation. Furthermore, to enhance our understanding of the electron movement at the boundary of the GaSeS/InSeS system, we analyzed the variation in charge density within the van der Waals (vdW) heterostructure. This difference is defined by the equation (4) [81]:

$$\Delta\rho = \rho\left(GaSeS\ /\ InSeS\right) - \rho\left(GaSeS\right) - \rho\left(InSeS\right) \qquad (4)$$

where ρ(GaSeS/InSeS), ρ(GaSeS), and ρ(InSeS) indicate the charge density of the heterostructure, the Janus GaSeS, and the InSeS monolayers.

Figure 6 (a) and (b) illustrate the charge density distributions for AA and AB stacking, respectively. The yellow region corresponds to an area of electron accumulation, while the cyan region corresponds to an area of electron depletion. At the interface region, charges redistribute: they accumulate near the GaSeS monolayer and deplete near the InSeS monolayer.

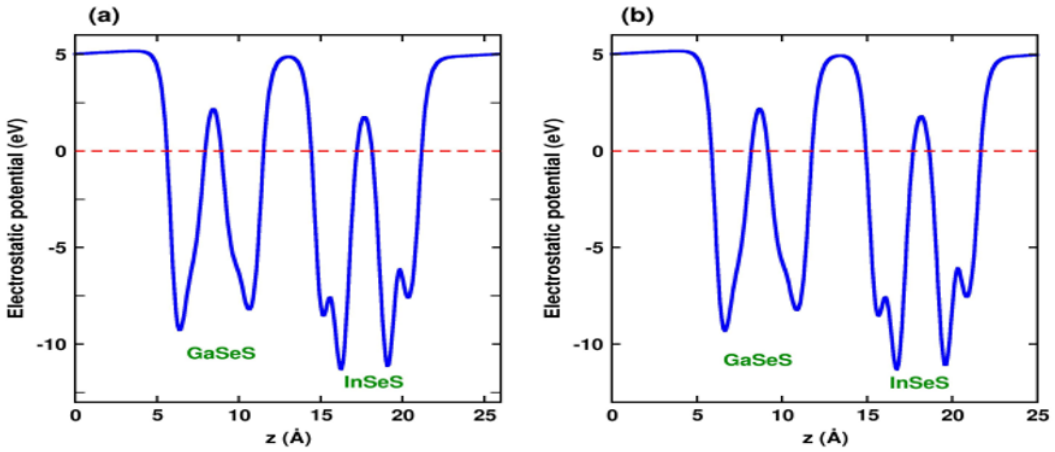

Figure 5. Electrostatic potential energy for a) AA-stacking and (b) AB-stacking of GaSeS/InSeS heterostructure.

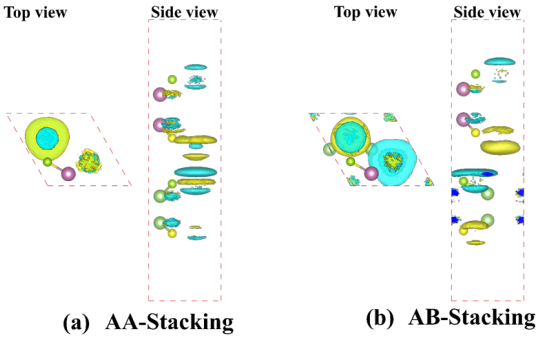

Figure 6. Visualization of the differential charge density with top and side views for (a) AA-stacking and (b) AB-stacking of the GaSeS/InSeS heterostructure.

3.3. Optical properties

A photovoltaic material should efficiently absorb sunlight and convert this energy into electron-hole pairs. Therefore, calculating its optical properties is crucial for assessing its light absorption efficiency [82].

To achieve this, we perform a detailed examination of the real (ε_1) and imaginary (ε_2) components of the dielectric response function, $\varepsilon(\omega)$, for the GaSeS/InSeS heterostructure in both AA and AB stacking configurations, as described by Equation 5 [58]:

$$\varepsilon(\omega) = \varepsilon_1(\omega) + i\varepsilon_2(\omega) \qquad (5)$$

According to Figure 7(a), the imaginary part of the dielectric response function (ε_2) reaches its highest peak at 4.14 eV, with a maximum value of 10.57 for the two-stack configuration of the GaSeS/InSeS heterostructure. Additionally, InSeS exhibits a secondary peak at 4.42 eV with a magnitude of 6.21, while GaSeS shows a lower-intensity peak at 4.42 eV with a value of 1.64.

As depicted in the inset of Figure 7(b), variations in ε_1, the real component of the dielectric response function, are analyzed for GaSeS and InSeS monolayers as well as the GaSeS/InSeS heterostructure. For both AA and AB stacking configurations of the heterostructure, the static dielectric constant $\varepsilon_1(0)$ is determined to be 4.5, indicating an enhancement compared to the individual monolayers. Moreover, distinct peaks appear in the $\varepsilon_1(\omega)$ spectrum across the visible and ultraviolet regions of the electromagnetic spectrum, corresponding to various interband transitions from the valence band maximum (VBM) to the conduction band minimum (CBM).

In addition, Figure 8 (a) illustrates the optical absorption of GaSeS and InSeS monolayers, as well as the GaSeS/InSeS heterostructure. The figure reveals that the first absorption edge, observed around 2 eV, closely matches the predicted band gaps of 2.09 eV for the AA stacking and 2.12

eV for the AB stacking. Notably, there is a strong agreement between the optical absorption coefficient and the imaginary component of the dielectric response function within the considered range. The incorporation of GaSeS and InSeS into the heterostructure significantly alters the absorption peaks, especially in the regions around 4 and 7 eV. These results clearly show that GaSeS/InSeS van der Waals heterostructures are more efficient at absorbing UV light compared to the individual monolayers.

While the maximum absorption peak value in the visible spectrum reaches 2.8×10^5 cm^{-1}, the absorption is primarily influenced by the presence of InSeS rather than GaSeS in the ultraviolet region, where the absorption peak reaches a maximum value of 11.6×10^5 cm^{-1}. These findings are consistent with those reported in the literature [48, 51, 62, 78]. The optical absorption of the vdW heterostructure remains relatively stable across different layer configurations, with only minor fluctuations [83].

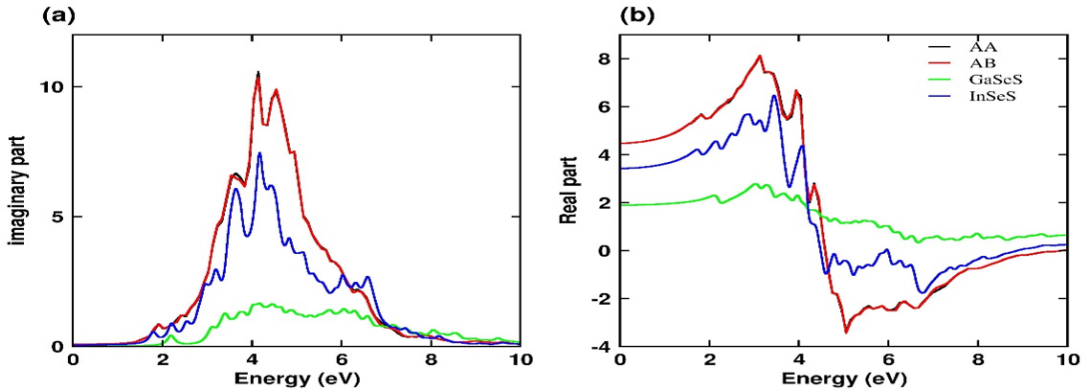

Figure 7. Imaginary ε_2 (ω) and the real ε_1(ω) components of the dielectric response function for AA-stacking and AB-stacking and Mls.

Moreover, the reflectivity coefficient R(λ) for the GaSeS/InSeS heterostructure is twice that of the individual monolayers (see Figure 8(b)), indicating that the GaSeS/InSeS vdW heterostructures hold significant potential for efficient solar cells and ultra-thin optoelectronic systems.

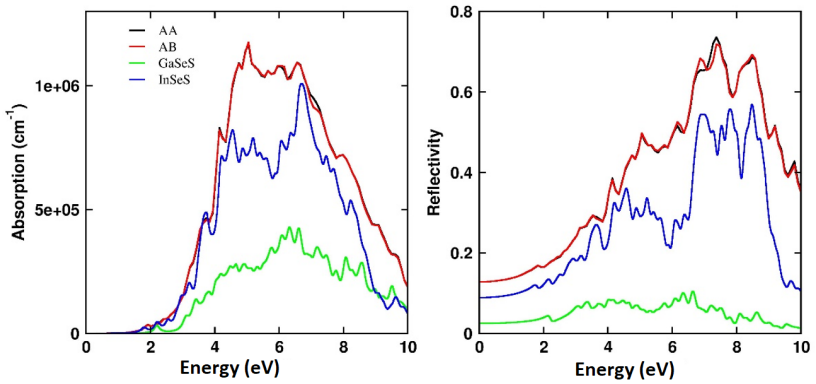

(a) (b)

Figure 8. The optical absorption and reflectivity factors for both AA and AB stacking configurations, along with the monolayer structures (MLs).

4. CONCLUSION

This study provides a comprehensive evaluation of the structural, optical, and electronic properties of the GaSeS/InSeS heterostructure, examining two stacking configurations through first-principles calculations. The results show that both stacking configurations are indirect

semiconductor band gaps, with values of 2.09 eV for AA and 2.12 eV for AB, using the HSE approximation. The heterostructure exhibits a Type-II band alignment, suggesting significant spatial separation of photogenerated carriers, which indicates its potential for use in photovoltaic device fabrication. Furthermore, substantial built-in electric fields were observed at the GaSeS/InSeS interfaces, which are expected to enhance the lifetime of photo-generated carriers. Notably, the GaSeS/InSeS heterostructure demonstrates exceptionally strong optical absorption in the visible and ultraviolet spectra, reaching up to 10^5 cm^{-1}. These results highlight the GaSeS/InSeS heterostructure as a promising candidate for solar cell applications. Our findings also offer valuable insights for guiding future experimental investigations.

Authors contribution: Ziani Hanan: Writing - Review & Editing, Conceptualization, Methodology, Software, Validation, Investigation, Writing - Original Draft, Visualization. Assiouan Kamal: Writing - Review & Editing, Formal analysis, Validation. Fatima Zohra Ben Abdelouahab: Writing, Formal analysis, Validation, Review & Editing. El Harouny El Hassan: Software, Formal analysis, Validation, Visualization. El Hadri Mustapha: Supervision, Formal analysis, Investigation, Validation. Ben Abdelouahab Farid: Writing - Review & Editing, Validation, Visualization.

Funding: The authors sincerely appreciate the support of "The Moroccan Association of Sciences and Techniques for Sustainable Development (MASTSD), Beni Mellal, Morocco," and extend their gratitude to its president, Professor Charaf Laghlimi, for his valuable contributions.

Data Availability Statement: Data is available on the request.

Conflicts of Interest: No conflict of interest.

Acknowledgements: The authors express their gratitude to CNRST (National Center for Scientific and Technical Research) in Rabat, Morocco, for providing access to its computational cloud resource - HPC-MARWAN.

REFERENCES

[1] C. Dean, A. F. Young, L. Wang, I. Meric, G. H. Lee, K. Watanabe, T. Taniguchi, P. Kim, K. L. Shepard, and J. Hone, "Graphene-based heterostructures," Solid State Commun., vol. 152, no. 15, pp. 1275–1282, Aug. 2012. doi: 10.1016/j.ssc.2012.04.021.

[2] J. Mawwa, S. U. D. Shamim, S. Khanom, M. K. Hossain, and F. Ahmed, "In-plane graphene/boron nitride heterostructures and their potential application as toxic gas sensors," RSC Advances, vol. 11, no. 52, pp. 32810–32823, Dec. 2021. doi: 10.1039/D1RA06304A.

[3] L. Song, L. Ci, H. Lu, P. B. Sorokin, C. Jin, J. Ni, A. G. Kvashnin, J. Lou, B. I. Yakobson, and P. M. Ajayan, "Large-scale growth and characterization of atomic hexagonal boron nitride layers," Nano Letters, vol. 10, no. 8, pp. 3209–3215, Aug. 2010. doi: 10.1021/nl1022139.

[4] L. Ci, L. Song, C. Jin, D. Jariwala, D. Wu, Y. Li, A. Srivastava, Z. F. Wang, K. Storr, L. Balicas, F. Liu, and P. M. Ajayan, "Atomic layers of hybridized boron nitride and graphene domains," Nature Materials, vol. 9, no. 5, pp. 430–435, May 2010. doi: 10.1038/nmat2711.

[5] A. Schleife, C. Rödl, F. Fuchs, J. Furthmüller, and F. Bechstedt, "Strain influence on valence-band ordering and excitons in ZnO: An ab initio study," Applied Physics Letters, vol. 91, no. 24, Dec. 2007. doi: 10.1063/1.2825277.

[6] S. Wang, M. S. Ukhtary, and R. Saito, "Strain effect on circularly polarized electroluminescence in transition metal dichalcogenides," Physical Review Research, vol. 2, no. 3, Sep. 2020. doi: 10.1103/PhysRevResearch.2.033340.

[7] M. Z. Bellus, M. Li, S. D. Lane, F. Ceballos, Q. Cui, X. C. Zeng, and H. Zhao, "Type-I van der Waals heterostructure formed by MoS_2 and ReS_2 monolayers," Nanoscale Horizons, vol. 2, no. 1,

pp. 31–36, Jan. 2017. doi: 10.1039/C6NH00144K.

[8] N. Huo, Y. Yang, and J. Li, "Optoelectronics based on 2D TMDs and heterostructures," Journal of Semiconductors, vol. 38, no. 3, p. 031002, Mar. 2017. doi: 10.1088/1674-4926/38/3/031002.

[9] X. Li, X. Wu, Z. Zhu, G. Li, and C. Mi, "On the elasticity and piezoelectricity of black (blue) phosphorus/ZnO van der Waals heterostructures," Computational Materials Science, vol. 169, p. 109134, Sep. 2019. doi: 10.1016/j.commatsci.2019.109134.

[10] T. Sahdane, S. Mtougui, F. Goumrhar, N. Mamouni, E. Salmani, H. Ez-Zahraouy, and O. Mounkachi, "Magnetic phase transitions of phosphorene-like nano-structure: Monte Carlo study," Philosophical Magazine, vol. 101, no. 16, pp. 1836–1848, Jun. 2021. doi: 10.1080/14786435.2021.1936260.

[11] J. Seeyangnok, M. U. Hassan, U. Pinsook, and G. J. Ackland, "Superconductivity and electron self-energy in tungsten-sulfur-hydride monolayer," 2D Materials, vol. 11, no. 2, p. 025020, Mar. 2024. doi: 10.1088/2053-1583/ad2523.

[12] N. Thakur, P. Kumar, S. Kumar, A. K. Singh, H. Sharma, N. Thakur, and P. Sharma, "A review of two-dimensional inorganic materials: Types, properties, and their optoelectronic applications," Progress in Solid State Chemistry, p. 100443, Feb. 2024. doi: 10.1016/j.progsolidstchem.2024.100443.

[13] M. Li, L. Wang, N. Yu, X. Sun, T. Hou, and Y. Li, "Structural stability and band gap tunability of single-side hydrogenated graphene from first-principles calculations," Journal of Materials Chemistry C, vol. 3, no. 15, pp. 3645–3649, Apr. 2015. doi: 10.1039/C5TC00209E.

[14] J. M. Hamm and O. Hess, "Two two-dimensional materials are better than one," Science, vol. 340, no. 6138, pp. 1298–1299, Jun. 2013. doi: 10.1126/science.1239501.

[15] K. Kaasbjerg, T. Low, and A. P. Jauho, "Electron and hole transport in disordered monolayer MoS_2: Atomic vacancy induced short-range and Coulomb disorder scattering," Physical Review B, vol. 100, no. 11, p. 115409, Sep. 2019. doi: 10.1103/PhysRevB.100.115409.

[16] K. Yang, Z. Cui, E. Li, Y. Shen, L. Zhang, D. Ma, Y. Liu, L. Yang, Z. Wu, W. Zhou, and S. Zhang, "Modulation of the magnetic, electronic, and optical behaviors of WS_2 after metals adsorption: A first-principles study," Chemical Physics, vol. 571, p. 111903, 2023, doi: 10.1016/j.chemphys.2023.111903.

[17] C. H. Hung, Y. C. Jiang, S. Y. Lei, R. Gao, X. W. Tao, N. Wan, and H. Yu, "Small gas adsorption on 2D material SnSe: A first-principles study," Journal of Physics D: Applied Physics, vol. 56, no. 39, p. 395302, 2023, doi: 10.1088/1361-6463/ace195.

[18] A. S. Alsaman, H. Maher, M. Ghazy, E. S. Ali, A. A. Askalany, and B. B. Saha, "2D materials for adsorption desalination applications: A state of the art," Thermal Science and Engineering Progress, vol. 49, p. 102455, 2024, doi: 10.1016/j.tsep.2024.102455.

[19] K. Rahimi, "Electric-field-and strain-induced adjustability of vdW heterostructure of g-ZnO/2H-TiS_2 for optoelectronic applications," Materials Letters, vol. 282, p. 128680, Jan. 2021. doi: 10.1016/j.matlet.2020.128680.

[20] Y. Cheng, L. Li, L. Li, Y. Zhang, L. Wang, L. Wang, and Y. Gao, "Linear regulation of electrical characteristics of InSe/Antimonene heterojunction via external electric field and strain," Surfaces and Interfaces, vol. 23, p. 101014, Jun. 2021. doi: 10.1016/j.surfin.2021.101014.

[21] X. P. Wang, X. B. Li, N. K. Chen, J. H. Zhao, Q. D. Chen, and H. B. Sun, "Electric field analyses on monolayer semiconductors: The example of InSe," Physical Chemistry Chemical Physics, vol. 20, no. 10, pp. 6945–6950, Mar. 2018. doi: 10.1039/C7CP07270H.

[22] Z. Yang and J. Ni, "Modulation of electronic properties of hexagonal boron nitride bilayers by

an electric field: A first principles study," Journal of Applied Physics, vol. 107, no. 10, May 2010. doi: 10.1063/1.3373571.

[23] C. Shi, Q. Song, H. Wang, S. Ma, C. Wang, X. Zhang, and Q. Chen, "Molecular hinges stabilize formamidinium-based perovskite solar cells with compressive strain," Advanced Functional Materials, vol. 32, no. 28, p. 2201193, Jul. 2022. doi: 10.1002/adfm.202201193.

[24] Y. Hu, S. Zhang, S. Sun, M. Xie, B. Cai, and H. Zeng, "GeSe monolayer semiconductor with tunable direct band gap and small carrier effective mass," Applied Physics Letters, vol. 107, no. 12, Sep. 2015. doi: 10.1063/1.4931459.

[25] G. Guo, Y. Shi, Y. Zhang, Y. Deng, F. Du, Z. Xie, and Y. Mao, "First-principles study on the electronic and magnetic properties of P edge-doped armchair germanium selenide nanoribbon," Computational Materials Science, vol. 172, p. 109348, Jan. 2020. doi: 10.1016/j.commatsci.2019.109348.

[26] X. Liu and M. C. Hersam, "Interface characterization and control of 2D materials and heterostructures," Advanced Materials, vol. 30, no. 39, p. 1801586, 2018, doi: 10.1002/adma.201801586.

[27] R. Long and O. V. Prezhdo, "Quantum coherence facilitates efficient charge separation at a MoS_2/$MoSe_2$ van der Waals junction," Nano Letters, vol. 16, no. 3, pp. 1996–2003, Mar. 2016. doi: 10.1021/acs.nanolett.5b05264.

[28] M. Luo, Y. E. Xu, and Y. X. Song, "Tunable electronic properties of MoS_2/ReS_2 van der Waals heterostructure from first-principles study," Optik, vol. 144, pp. 334–339, Sep. 2017. doi: 10.1016/j.ijleo.2017.06.100.

[29] K. Zhang, C. Ding, Y. She, Z. Wu, C. Zhao, B. Pan, and Q. Fan, "$CuFe_2O_4$/MoS_2 mixed-dimensional heterostructures with improved gas sensing response," Nanoscale Research Letters, vol. 15, p. 7, Jan. 2020. doi: 10.1186/s11671-020-3268-4.

[30] Y. Gong, J. Lin, X. Wang, G. Shi, S. Lei, Z. Lin, and P. M. Ajayan, "Vertical and in-plane heterostructures from WS_2/MoS_2 monolayers," Nature Materials, vol. 13, no. 12, pp. 1135–1142, Dec. 2014, doi: 10.1038/NMAT4091.

[31] M. J. Molaei, M. Younas, and M. Rezakazemi, "Van der Waals heterostructures in ultrathin 2D solar cells: State-of-the-art review," Materials Science and Engineering: B, vol. 285, p. 115936, 2022, doi: 10.1016/j.mseb.2022.115936.

[32] P. Wang, X. Li, Z. Xu, Z. Wu, S. Zhang, W. Xu, and S. Lin, "Tunable graphene/indium phosphide heterostructure solar cells," Nano Energy, vol. 13, pp. 509–517, 2015, doi: 10.1016/j.nanoen.2015.03.023.

[33] F. Yan, C. Hu, Z. Wang, H. Lin, and K. Wang, "Perspectives on photodetectors based on selenides and their van der Waals heterojunctions," Applied Physics Letters, vol. 118, no. 19, 2021, doi: 10.1063/5.0045941.

[34] S. Wang, C. Ren, H. Tian, J. Yu, and M. Sun, "MoS_2/ZnO van der Waals heterostructure as a high-efficiency water splitting photocatalyst: A first-principles study," Physical Chemistry Chemical Physics, vol. 20, no. 19, pp. 13394–13399, 2018, doi: 10.1039/C8CP00808F.

[35] R. D'Souza and S. Mukherjee, "Thermoelectric transport in graphene/h-BN/graphene heterostructures: A computational study," Physica E: Low-dimensional Systems and Nanostructures, vol. 81, pp. 96–101, 2016, doi: 10.1016/j.physe.2016.03.006.

[36] L. Britnell, R. V. Gorbachev, R. Jalil, B. D. Belle, F. Schedin, A. Mishchenko, and L. A. Ponomarenko, "Field-effect tunneling transistor based on vertical graphene heterostructures,"

Science, vol. 335, no. 6071, pp. 947–950, 2012, doi: 10.1126/science.1218461.

[37] A. O. M. Almayyali, B. B. Kadhim, and H. R. Jappor, "Stacking impact on the optical and electronic properties of two-dimensional $MoSe_2/PtS_2$ heterostructures formed by PtS_2 and $MoSe_2$ monolayers," Chemical Physics, vol. 532, p. 110679, 2020, doi: 10.1016/j.chemphys.2020.110679.

[38] A. O. M. Almayyali, B. B. Kadhim, and H. R. Jappor, "RETRACTED: Tunable electronic and optical properties of 2D PtS_2/MoS_2 van der Waals heterostructure," Physica E: Low-dimensional Systems and Nanostructures, vol. 113, p. 113866, 2020, doi: 10.1016/j.physe.2019.113866.

[39] X. Tian, L. Liu, Y. Du, J. Gu, J. B. Xu, and B. I. Yakobson, "Variable electronic properties of lateral phosphorene–graphene heterostructures," Physical Chemistry Chemical Physics, vol. 17, no. 47, pp. 31685–31692, 2015, doi: 10.1039/C5CP05443E.

[40] Y. Cai, G. Zhang, and Y. W. Zhang, "Electronic properties of phosphorene/graphene and phosphorene/hexagonal boron nitride heterostructures," The Journal of Physical Chemistry C, vol. 119, no. 24, pp. 13929–13936, 2015, doi: 10.1021/acs.jpcc.5b02634.

[41] M. T. Hossain and M. A. Rahman, "A first principle study of the structural, electronic, and temperature-dependent thermodynamic properties of graphene/MoS_2 heterostructure," Journal of Molecular Modeling, vol. 26, no. 1, pp. 1–8, 2020, doi: 10.1007/s00894-020-4306-y.

[42] W. Hu and J. Yang, "Two-dimensional van der Waals heterojunctions for functional materials and devices," Journal of Materials Chemistry C, vol. 5, no. 47, pp. 12289–12297, 2017, doi: 10.1039/C7TC04697A.

[43] P. Vishnoi, K. Pramoda, U. Gupta, M. Chhetri, R. G. Balakrishna, and C. N. R. Rao, "Covalently linked heterostructures of phosphorene with $MoS_2/MoSe_2$ and their remarkable hydrogen evolution reaction activity," ACS Applied Materials & Interfaces, vol. 11, no. 31, pp. 27780–27787, 2019, doi: 10.1021/acsami.9b06910.

[44] A. Y. Lu, H. Zhu, J. Xiao, C. P. Chuu, Y. Han, M. H. Chiu, and L. J. Li, "Janus monolayers of transition metal dichalcogenides," Nature Nanotechnology, vol. 12, no. 8, pp. 744–749, 2017, doi: 10.1038/nnano.2017.100.

[45] M. Palsgaard, T. Gunst, T. Markussen, K. S. Thygesen, and M. Brandbyge, "Stacked Janus device concepts: abrupt pn-junctions and cross-plane channels," Nano Letters, vol. 18, no. 11, pp. 7275–7281, 2018, doi: 10.1021/acs.nanolett.8b03474.

[46] A. C. Riis-Jensen, T. Deilmann, T. Olsen, and K. S. Thygesen, "Classifying the electronic and optical properties of Janus monolayers," ACS Nano, vol. 13, no. 11, pp. 13354–13364, 2019, doi: 10.1021/acsnano.9b06698.

[47] Y. Bai, Q. Zhang, N. Xu, K. Deng, and E. Kan, "The Janus structures of group-III chalcogenide monolayers as promising photocatalysts for water splitting," Applied Surface Science, vol. 478, pp. 522–531, 2019, doi: 10.1016/j.apsusc.2019.02.004.

[48] H. D. Bui, H. R. Jappor, and N. N. Hieu, "Tunable optical and electronic properties of Janus monolayers Ga_2SSe, Ga_2STe, and Ga_2SeTe as promising candidates for ultraviolet photodetectors applications," Superlattices and Microstructures, vol. 125, pp. 1–7, 2019, doi: 10.1016/j.spmi.2018.10.020.

[49] A. Huang, W. Shi, and Z. Wang, "Optical properties and photocatalytic applications of two-dimensional Janus group-III monochalcogenides," The Journal of Physical Chemistry C, vol. 123, no. 18, pp. 11388–11396, 2019, doi: 10.1021/acs.jpcc.8b12450.

[50] H. R. Jappor, M. M. Obeid, T. V. Vu, D. M. Hoat, H. D. Bui, N. N. Hieu, and R. Khenata, "RETRACTED: engineering the optical and electronic properties of Janus monolayer Ga_2SSe by biaxial strain," Superlattices and Microstructures, vol. 125, p. 105031, 2019, doi: 10.1016/j.

spmi.2019.05.031.

[51] G. Guo, G. Zhang, H. Wu, Y. Zhang, and Z. Xie, "Insights on the optoelectronic properties in two-dimensional Janus lateral In_2SeTe/Ga_2STe heterostructure," Thin Solid Films, vol. 718, p. 138479, 2021, doi: 10.1016/j.tsf.2020.138479.

[52] P. Giannozzi, S. Baroni, N. Bonini, M. Calandra, R. Car, C. Cavazzoni, A. D. Corso, S. Giannozzi, M. de Gironcoli, F. (Giannozzi), A. Kokalj, and R. M. Wentzcovitch, "QUANTUM ESPRESSO: a modular and open-source software project for quantum simulations of materials," Journal of Physics: Condensed Matter, vol. 21, no. 39, p. 395502, 2009, doi: 10.1088/0953-8984/21/39/395502.

[53] P. E. Blöchl, "Projector augmented-wave method," Physical Review B, vol. 50, no. 24, p. 17953, 1994, doi: 10.1103/PhysRevB.50.17953.

[54] J. P. Perdew, K. Burke, and M. Ernzerhof, "Generalized gradient approximation made simple," Physical Review Letters, vol. 77, no. 18, p. 3865, 1996, doi: 10.1103/PhysRevLett.77.3865.

[55] J. Heyd, G. E. Scuseria, and M. Ernzerhof, "Hybrid functionals based on a screened Coulomb potential," The Journal of Chemical Physics, vol. 118, no. 18, pp. 8207–8215, 2003, doi: 10.1063/1.1564060.

[56] H. J. Monkhorst and J. D. Pack, "Special points for Brillouin-zone integrations," Physical Review B, vol. 13, no. 12, p. 5188, 1976, doi: 10.1103/PhysRevB.13.5188.

[57] A. Marini, C. Hogan, M. Grüning, and D. Varsano, "Yambo: an ab initio tool for excited state calculations," Computer Physics Communications, vol. 180, no. 8, pp. 1392–1403, 2009, doi: 10.1016/j.cpc.2009.02.003.

[58] M. Ait Tamerd, M. Zanouni, A. Nid-bahami, M. Diani, and A. Marjaoui, "Strain effects on the structural, electronic, optical and thermoelectric properties of Si_2SeS monolayer with puckered honeycomb structure: A first-principles study," International Journal of Quantum Chemistry, vol. 122, no. 13, p. e26906, 2022, doi: 10.1002/qua.26906.

[59] A. Kokalj, "XCrySDen—a new program for displaying crystalline structures and electron densities," Journal of Molecular Graphics and Modelling, vol. 17, no. 3-4, pp. 176–179, 1999, doi: 10.1016/S1093-3263(99)00028-5.

[60] Y. Guo, S. Zhou, Y. Bai, and J. Zhao, "Enhanced piezoelectric effect in Janus group-III chalcogenide monolayers," Applied Physics Letters, vol. 110, no. 16, 2017, doi: 10.1063/1.4981877.

[61] P. Hu, L. Wang, M. Yoon, J. Zhang, W. Feng, X. Wang, and K. Xiao, "Highly responsive ultrathin GaS nanosheet photodetectors on rigid and flexible substrates," Nano Letters, vol. 13, no. 4, pp. 1649–1654, 2013, doi: 10.1021/nl400107k.

[62] G. W. Mudd, S. A. Svatek, L. Hague, O. Makarovsky, Z. R. Kudrynskyi, C. J. Mellor, and A. Patanè, "High broad-band photoresponsivity of mechanically formed InSe–graphene van der Waals heterostructures," Advanced Materials (Deerfield Beach, Fla.), vol. 27, no. 25, p. 3760, 2015, doi: 10.1002/adma.201500889.

[63] Z. Hussein, A. Laref, H. R. Alqahtani, E. A. Alghamdi, M. E. A. Monir, N. A. Noor, and H. A. Yakout, "Optoelectronic properties of solar cell materials based on copper-zinc-tin-sulfide Cu2ZnSn(SxTe1-x)4 alloys for photovoltaic device applications," Solar Energy, vol. 225, pp. 851–862, 2021, doi: 10.1016/j.solener.2021.07.019.

[64] Z. Hui, X. Tang, R. Wei, L. Hu, J. Yang, H. Luo, X. Zhang, Y. Yang, and Y. Sun, "Facile chemical solution deposition of nanocrystalline CrN thin films with low magnetoresistance," RSC Advances, vol. 4, no. 24, pp. 12568–12571, 2014, doi: 10.1039/C4RA00263F.

[65] B. T. Beshir, K. O. Obodo, and G. A. Asres, "Janus transition metal dichalcogenides in

combination with MoS2 for high-efficiency photovoltaic applications: A DFT study," RSC Advances, vol. 12, no. 22, pp. 13749–13755, 2022, doi: 10.1039/D2RA00775D.

[66] B. J. Wang, X. H. Li, R. Zhao, X. L. Cai, W. Y. Yu, W. B. Li, and S. H. Ke, "Electronic structures and enhanced photocatalytic properties of blue phosphorene/BSe van der Waals heterostructures," Journal of Materials Chemistry A, vol. 6, no. 19, pp. 8923–8929, 2018.

[67] T. A. Alrebdi and B. Amin, "Van der Waals heterostructure of Janus transition metal dichalcogenides monolayers (WSSe-WX2 (X = S, Se))," Chemical Physics, vol. 549, p. 111252, 2021, doi: 10.1016/j.chemphys.2021.111252.

[68] R. González-Reyes, J. D. Correa, F. M. Nava-Maldonado, K. A. Rodríguez-Magdaleno, M. E. Mora-Ramos, and J. C. Martínez-Orozco, "Black Phosphorene/MoS2 van der Waals heterostructure: Electronic and optical properties," Physica B: Condensed Matter, vol. 673, p. 415489, 2024, doi: 10.1016/j.physb.2023.415489.

[69] Y. Zhao, Q. Tan, H. Li, Z. Li, Y. Wang, and L. Ma, "Tunable electronic and photoelectric properties of Janus group-III chalcogenide monolayers and based heterostructures," Scientific Reports, vol. 14, no. 1, p. 10698, 2024, doi: 10.1038/s41598-024-61373-z.

[70] S. V. Eremeev, M. Papagno, I. Grimaldi, O. De Luca, L. Ferrari, A. K. Kundu, G. Autès, L. Moreschini, A. Crepaldi, M. Battiato, O. V. Yazyev, F. Parmigiani, and D. Pacilè, "Insight into the electronic structure of semiconducting ε-GaSe and ε-InSe," Physical Review Materials, vol. 4, no. 8, p. 084603, Aug. 2020, doi: 10.1103/PhysRevMaterials.4.084603.

[71] J. Zhou, J. Shi, Q. Zeng, Y. Chen, L. Niu, F. Liu, Y. Wang, D. Huang, Y. Cai, H. Lin, S. T. Pantelides, and Z. Liu, "InSe monolayer: synthesis, structure and ultra-high second-harmonic generation," 2D Materials, vol. 5, no. 2, p. 025019, Mar. 2018, doi: 10.1088/2053-1583/aab390.

[72] H. R. Jappor and M. A. Habeeb, "Tunable electronic and optical properties of GaS/GaSe van der Waals heterostructure," Current Applied Physics, vol. 18, no. 6, pp. 673–680, June 2018, doi: 10.1016/j.cap.2018.03.019.

[73] F. Opoku, A. Aniagyei, O. Akoto, E. E. Kwaansa-Ansah, N. K. Asare-Donkor, and A. A. Adimado, "Investigation of 2D Janus Al_2OS/Ga_2SSe van der Waals heterojunction as next-generation thermoelectric and photocatalytic devices," Next Materials, vol. 1, no. 4, p. 100042, Dec. 2023, doi: 10.1016/j.nxmate.2023.100042.

[74] S. S. Ullah, M. Farooq, H. U. Din, Q. Alam, M. Idrees, M. Bilal, and B. Amin, "First principles study of electronic and optical properties and photocatalytic performance of GaN–SiS van der Waals heterostructure," RSC Advances, vol. 11, no. 52, pp. 32996–33003, Sept. 2021, doi: 10.1039/D1RA06011B.

[75] H. T. Do, T. V. Vu, A. A. Lavrentyev, N. Q. Cuong, P. V. Cuong, and H. D. Tong, "Electronic structure and interface contact of two-dimensional van der Waals boron phosphide/Ga_2SSe heterostructures," RSC Advances, vol. 12, no. 30, pp. 19115–19121, Aug. 2022, doi: 10.1039/D2RA02748H.

[76] C. He, F. S. Han, J. H. Zhang, and W. X. Zhang, "The In_2SeS/gC_3N_4 heterostructure: A new two-dimensional material for photocatalytic water splitting," Journal of Materials Chemistry C, vol. 8, no. 20, pp. 6923–6930, May 2020, doi: 10.1039/D0TC00852D.

[77] S. Rühle, "Tabulated values of the Shockley–Queisser limit for single-junction solar cells," Solar Energy, vol. 130, pp. 139–147, 2016, doi: 10.1016/j.solener.2016.02.015.

[78] M. H. Dalsaniya, T. K. Gajaria, N. N. Som, P. K. Jha, P. Śpiewak, and K. J. Kurzydłowski, "Type-II GeAs/GaSe heterostructure as suitable candidate for solar power conversion efficiency," Solar Energy, vol. 223, pp. 87–99, May 2021, doi: 10.1016/j.solener.2021.05.034.

[79] X. H. Li, B. J. Wang, H. Li, X. F. Yang, R. Q. Zhao, X. T. Jia, and S. H. Ke, "Two-dimensional layered Janus-In_2SeTe/C_2N van der Waals heterostructures for photocatalysis and photovoltaics: first-principles calculations," New Journal of Chemistry, vol. 44, no. 37, pp. 16092–16100, Oct. 2020, doi: 10.1039/D0NJ03296D.

[80] T. Z. Wen, Y. H. Yang, and J. L. Li, "A novel Black-P/Blue-P heterostructure for the photovoltaic applications," Chemical Physics Letters, vol. 812, p. 140242, Jan. 2023, doi: 10.1016/j.cplett.2022.140242.

[81] Y. Ding, S. Fang, H. Zhou, J. Qi, J. Fan, R. Zhang, Y. Wang, J. Liu, X. Chen, L. Sun, and H. Tang, "High-performance type II WSOx/WS_2-based heterojunction photodetectors," Applied Surface Science, vol. 683, p. 161848, 2025, doi: 10.1016/j.apsusc.2024.161848.

[82] Z. Guan, C. S. Lian, S. Hu, S. Ni, J. Li, and W. Duan, "Tunable structural, electronic, and optical properties of layered two-dimensional C_2N and MoS_2 van der Waals heterostructure as photovoltaic material," The Journal of Physical Chemistry C, vol. 121, no. 6, pp. 3654–3660, 2017, doi: 10.1021/acs.jpcc.6b12681.

[83] Y. Xu, D. Li, Q. Zeng, H. Sun, and P. Li, "Type-II 2D AgBr/SiH van der Waals heterostructures with tunable band edge positions and enhanced optical absorption coefficients for photocatalytic water splitting," RSC Advances, vol. 13, no. 40, pp. 27676–27685, 2023, doi: 10.1039/D3RA05079C.

Solar Energy
and Sustainable Development
Refereed, biannual scientific journal issued by
The Libyan Center for Solar Energy Research and Studies

Geometry-Dependent Thermal Transport in Porous Silicon: A Computational Study of Pore Geometry and Porosity Effects

Othman Soubai[1]*, Younes Abouelhanoune[1], and Mohammed Taibi[1]

[1]LSA, EMAO, ENSAH Al-Hoceima, Abdelmalek Essaadi University, 93000 Tetouan, Morocco.

E-*mail*: [1*]soubai.othman@etu.uae.ac.ma

SPECIAL ISSUE ON.
The 1St International Conference on Sciences and Techniques for Renewable Energy and the Environment.
(STR2E 2025)
May 6-8, 2025 at FST-Al Hoceima-Morocco.

KEYWORDS

Boltzmann transport equation; Thermal transport; Porous Silicon; Thermal management; Semiconductor

ABSTRACT

This study investigates how pore geometry and porosity modulate the thermal conductivity and heat transfer characteristics of porous silicon. Leveraging OpenBTE—an open-source computational tool based on the Boltzmann Transport Equation (BTE)—the research analyzes three distinct pore geometries (circular, rectangular, and hexagonal) with porosity ranging from 5% to 45% in order to quantify their impact on phonon-mediated thermal transport. The results shown a clear dependence of thermal conductivity on pore shape and porosity. Rectangular pores showed the highest thermal conductivity, ranging from 64.4 W/(m·K) at 5% porosity to 26.7 W/(m·K) at 45%. Circular pores yielded intermediate thermal conductivity values, varying from 56.8 W/(m·K) at 5% to 9.5 W/(m·K) at 45%. Hexagonal pores show the lowest thermal conductivity, ranging from 54.6 W/(m·K) to 7.2 W/(m·K). These insights demonstrate the critical role of pore architecture in tailoring heat dissipation pathways, providing actionable guidelines for engineering optimized pore networks. Experimental results advance the understanding of structure-property relationships in porous materials, enabling precise control over thermal performance for applications in thermoelectric, microelectronics, and energy-efficient systems.

*Corresponding author.

DOI: https://doi.org/10.51646/jsesd.v14iSTR2E.1180

This is an open access article under the CC BY-NC license (http://Attribution-NonCommercial 4.0 (CC BY-NC 4.0)).

النقل الحراري المعتمد على الهندسة في السيليكون المسامي: دراسة حسابية لتأثير هندسة المسام والمسامية

عثمان السبيعي، يونس أبو الحنون، محمد الطيبي

ملخص: تستعرض هذه الدراسة كيفية تأثير هندسة المسام والمسامية على التوصيل الحراري وخصائص نقل الحرارة في السيليكون المسامي، باستخدام أداة "أوبن بي تي إي"، وهي أداة حسابية مفتوحة المصدر تعتمد على معادلة بولتزمان للنقل. قمنا بدراسة ثلاث أشكال هندسية للمسام (دائرية، مستطيلة وسداسية) مع نسب مسامية من 5% إلى 45% لدراسة تأثيرها على النقل الحراري الذي يتم بواسطة الفونونات. أظهرت النتائج علاقة واضحة بين التوصيل الحراري وشكل المسام ونسبة المسامية، إذ سجلت المسام ذات الشكل المستطيل أعلى قيم للتوصيل الحراري التي تتراوح من 64.4 واط/(متر•كلفن) عند نسبة 5% من المسامية إلى 26.7 واط/(متر•كلفن) عند نسبة 45% من المسامية. بينما أعطت للمسام الدائرية قيما متوسطة للتوصيل الحراري، تتراوح من 56.8 واط/(متر•كلفن) عند نسبة 5% من المسامية إلى 9.5 واط/(متر•كلفن) عند نسبة 45% من المسامية. أما بالنسبة للمسام السداسية فقد حققت أدنى قيم للتوصيل الحراري، حيث تراوحت بين 54.6 واط/(متر•كلفن) عند نسبة 5% من المسامية إلى 7.2 واط/(متر•كلفن) عند نسبة 45% من المسامية.

الكلمات المفتاحية: النقل الحراري، السيليكون المسامي، إدارة الحرارة، معادلة بولتزمان للنقل

1. INTRODUCTION

The study of thermal transport properties is essential in many fields of science and engineering and play a critical role in the performance and reliability of microscale and nanoscale devices. With the continued miniaturization of materials and the emergence of novel porous materials such as porous silicon, material systems and devices are entering a nanometer scale, classical macroscopic methods of heat transfer are challenged by size effects and the increased significance of phonon-boundary scattering. which necessitates a thorough understanding of thermal transport at the microscopic level. For micro- or mesoporous media, such as porous silicon, a classical theory based on equivalent macroscopic medium can hardly provide a reliable prediction of the heat transfer coefficient. At the nanoscale, the interplay between intrinsic phonon–phonon interactions and additional scattering mechanisms introduced by porosity requests a refined theoretical framework. This is particularly important for porous silicon, where the high surface area and unique pore geometries, the porosity modifies the material thermal properties, reducing its thermal conductivity by tuning the phonon mean-free path as supported by both experimental and computational studies [1]. Previously reported measurements of the thermal conductivity of Si are primarily carried out as a function of doping density. It is also well established that the thermal conductivity of porous silicon can be significantly reduced in the porous state due to multiple phonon scatterings by the pores [2, 3].

Porous silicon stands out as a multifunctional material not only for its superior heat transfer characteristics but also due to its seamless integration with established manufacturing and device assembly protocols. Its alignment with conventional semiconductor fabrication techniques, combined with its adaptability for use in electronic and photonic systems, positions it as a highly suitable substrate for engineering thermally

optimized [4]. By exclusively studying the distinct pore geometries, we aim to uncover the fundamental mechanisms that govern heat flow, phonon scattering, and thermal conductivity in porous structures [5].

However, while previous measurements have largely emphasized the effects of doping on thermal conductivity, less attention has been paid to how the tortuous pore surfaces and specific geometric configurations of p-Si membranes affects heat transport. This gap in the literature calls for a more detailed computational study that examines pore geometry-dependent heat transport.

A several of studies have shown that increased porosity in porous silicon results in a reduction in thermal conductivity due to enhanced phonon scattering [5, 6]. For example, experimental investigations and computational analyses demonstrated that the thermal behavior of porous silicon can be significantly modified by altering pore size and distribution [5]. Some works have indicated that different pore shapes can alter heat conduction pathways and there by affect the overall thermal performance [7, 8]. These studies suggest that pore geometry plays a critical role in determining thermal performance, but a systematic comparative analysis remains lacking.

The tunable nature of porous silicon—achieved through engineered porosity—has solidified its role in advanced thermal regulation. Customizable pore dimensions, geometries, and spatial arrangements permit fine-grained control overheat dissipation profiles, addressing challenges in sectors such as aerospace, renewable energy infrastructure, and high-density microelectronics [9-12].

Isolating individual pore geometries (e.g., circular, hexagonal, rectangular) provides insights into optimizing composite pore networks for targeted thermal performance. These findings directly inform the design of efficient heat sinks, passive cooling architectures, and precision devices reliant on stable thermal environments [10-12]. Consequently, this systematic investigation of pore driven thermal behavior establishes foundational insights for fabricating next-generation porous silicon membranes, engineered to address escalating demands in thermal management across cutting-edge technologies [13].

By addressing these issues, our study not only confirms the experimentally observed trend of reduced thermal conductivity in porous silicon but also provides new insights into the role of pore geometry. The results have significant implications for the design of thermoelectric materials and microelectronic devices, where controlled thermal management is crucial. Our work contributes to the growing body of research aimed at optimizing the thermal properties of nano porous materials by tuning their structural parameters.

2. METHODOLOGY

2.1. Mathematical Model Theory

In nonmagnetic semiconductor crystals, such as silicon, thermal transport is predominantly facilitated by lattice vibrations, with phonons representing the quantized units of these vibrational modes. In contrast to metals, where electrons play a significant role in heat conduction, the contribution of electrons to thermal conductivity in semiconductors is minimal or negligible at room temperature [14].

The Boltzmann transport equation (BTE) is often used in the modeling of the heat conduction

where the Fourier law breaks down because this law assumes that heat transport is purely diffusive meaning energy carriers (phonon in our case) undergo many collisions as they travel in the materials, this law work well for macroscale system. But when system size is comparable or smaller (our case L=50 nm) than the mean free path (100-300 nm at room temperature in Silicon (Si)). In this case we are in regime where phonons can traverse significant portions of the structure without collisions (ballistic regime), and the presence of pore in our system complicate more the thermal transport. This place our system in the quasi-ballistic transport regime that mean we see a mixture of transport behaviors because our system isn't purely ballistic. Some phonons will still experience collisions with other phonons before reaching a boundary, especially in the regions farther from the pore and in the regions immediately adjacent to the pore, you'll observe largely ballistic transport. Here, phonons travel in straight lines until they encounter either the pore boundary or the system edges.

The Boltzmann Transport Equation (BTE) effectively models both equilibrium and non-equilibrium thermal processes [15]. This framework approximates phonons as discrete particles, neglecting their wave-like characteristics. BTE spans modeling scales from macroscopic continuum regimes to nanoscale systems, as it accounts for both ballistic phonon transport (wave-like propagation without scattering) and diffusive scattering-dominated behavior. This versatility makes BTE particularly suitable for simulating devices or structures that are too small for traditional continuum-based approaches (e.g., Fourier's law) yet too large for fully atomistic simulations like molecular dynamics or quantum mechanical methods [16].

The steady-state, linearized Boltzmann Transport Equation (BTE) under the temperature formulation describes how phonons, the primary heat carriers in non-metallic solids, propagate and scatter within the material. The general form of the BTE for phonon transport can be expressed as:

$$-C_\mu \mathbf{v}_\mu \cdot \nabla \Delta T_\mu(\mathbf{r}) = \sum_\vartheta W_{\mu\vartheta} \Delta T_\vartheta(\mathbf{r}) \quad (1)$$

Where C_μ represents the specific heat capacity of phonon mode μ, $\mathbf{v}_\mu$ is the phonon group velocity, $\nabla \Delta T_\mu(\mathbf{r})$ is the spatial gradient of the temperature deviation for mode μ, and $W_{\mu\vartheta}$ is the scattering matrix element describing the transition rate between phonon modes μ and ϑ.

A commonly used simplification to the phonon Boltzmann transport equation is the relaxation time approximation (RTA), which suppose that phonon repopulation can be neglected. When we use this approximation, the scattering operator is treated as diagonal, meaning that phonon scattering events are supposed to return the system to local equilibrium without any consideration about inter-mode transitions. This approximation is particularly valid for many relevant materials, including silicon, where phonon-phonon scattering dominates the thermal transport [17]. Within the RTA approximation, Equation (1) reduces to:

$$-\mathbf{v}_\mu \cdot \nabla \Delta T_\mu(\mathbf{r}) = \frac{\Delta T_\mu(\mathbf{r}) - \Delta T(\mathbf{r})}{\tau_\mu} \quad (2)$$

Where, τ_μ is the relaxation time for phonon mode μ, is the average time between scattering events. $\Delta T(\mathbf{r})$ is the local temperature deviation from equilibrium, and $\Delta T_\mu(\mathbf{r})$ is the temperature deviation specific to phonon mode μ.

2.1.1. Analytical Study

The solution to Equation (2) under the RTA provides a mathematical approach for calculating the temperature deviation $\Delta T_\mu(\mathbf{r})$ and the resulting heat flux $\mathbf{q}$. This approach enables the calculation of thermal conductivity in porous Silicon by considering the effects of phonon scattering and relaxation times approximation.

The results can be used to analyze the effect of pore geometry and porosity on thermal properties, offering perception for optimizing material design for thermal management applications.

Step 1: Rearrange Equation (2) to isolate $\Delta T_\mu(\mathbf{r})$:

$$\Delta T_\mu(\mathbf{r}) - \Delta T(\mathbf{r}) = -\tau_\mu \mathbf{v}_\mu \cdot \nabla \Delta T_\mu(\mathbf{r}) \tag{3}$$

This can be rewritten as:

$$\Delta T_\mu(\mathbf{r}) = \Delta T(\mathbf{r}) - \tau_\mu \mathbf{v}_\mu \cdot \nabla \Delta T_\mu(\mathbf{r}) \tag{4}$$

For simplicity, assume a linear temperature gradient $\nabla \Delta T(\mathbf{r}) = \mathbf{G}$, where $\mathbf{G}$ is a constant vector representing the applied temperature gradient. This hypothesis is valid for small deviations from equilibrium and is frequently used in thermal transport analysis.

Under this assumption, the temperature deviation $\Delta T(\mathbf{r})$ can be expressed as:

$$\Delta T(\mathbf{r}) = \mathbf{G} \cdot \mathbf{r} \tag{5}$$

Step 2: To solve for $\Delta T_\mu(\mathbf{r})$, we substitute $\Delta T(\mathbf{r}) = \mathbf{G} \cdot \mathbf{r}$ into Equation (4):

$$\Delta T_\mu(\mathbf{r}) = \mathbf{G} \cdot \mathbf{r} - \tau_\mu \mathbf{v}\mu \cdot \nabla \Delta T_\mu(\mathbf{r}) \tag{6}$$

Assuming that $\Delta T_\mu(\mathbf{r})$ has a similar linear form:

$$\Delta T_\mu(\mathbf{r}) = \mathbf{G}_\mu \cdot \mathbf{r} \tag{7}$$

Where $\mathbf{G}_\mu$ is the effective temperature gradient for phonon mode μ. Substituting this into the equation gives:

$$\mathbf{G}_\mu \cdot \mathbf{r} = \mathbf{G} \cdot \mathbf{r} - \tau_\mu \mathbf{v}\mu \cdot \mathbf{G}_\mu \tag{8}$$

Step 3: Since this must hold for all $\mathbf{r}$, we can equate the coefficients of $\mathbf{r}$:

$$\mathbf{G}_\mu = \mathbf{G} - \tau_\mu \left(\mathbf{v}_\mu \cdot \mathbf{G}_\mu\right) \tag{9}$$

This can be written in matrix form as:

$$\left(\mathbf{I} + \tau_\mu \mathbf{v}\mu \otimes \mathbf{v}_\mu\right)\mathbf{G}_\mu = \mathbf{G} \tag{10}$$

Where $\mathbf{I}$ is the identity matrix and $\otimes$ denotes the outer product. Solving for $\mathbf{G}_\mu$:

$$\mathbf{G}_\mu = \left(\mathbf{I} + \tau_\mu \mathbf{v}\mu \otimes \mathbf{v}_\mu\right)^{-1}\mathbf{G} \tag{11}$$

To compute the Heat Flux, the heat flux $\mathbf{q}$ is given by the sum of contributions from all phonon modes:

$$\mathbf{q} = \sum_\mu C_\mu \mathbf{v}\mu \Delta T_\mu(\mathbf{r}) \tag{12}$$

Where C_μ is the specific heat capacity of phonon mode μ. Substituting $\Delta T_\mu(\mathbf{r}) = \mathbf{G}_\mu \cdot \mathbf{r}$:

$$\mathbf{q} = \sum_\mu C_\mu \mathbf{v}_\mu \left(\mathbf{G}_\mu \cdot \mathbf{r}\right) \tag{13}$$

Using the expression for $\mathbf{G}_\mu$:

$$\mathbf{q} = \sum_\mu C_\mu \mathbf{v}_\mu \left[\left(\mathbf{I} + \tau_\mu \mathbf{v}\mu \otimes \mathbf{v}\mu\right)^{-1}\mathbf{G}\right] \cdot \mathbf{r} \tag{14}$$

Step 4: Relate to Thermal Conductivity

The thermal conductivity tensor $\mathbf{K}$ relates the heat flux $\mathbf{q}$ to the temperature gradient

$$\mathbf{q} = -\mathbf{K}\mathbf{G} \tag{15}$$

By comparing this with the expression for $\mathbf{q}$, we can extract the thermal conductivity tensor:

$$\mathbf{K} = -\sum_\mu C_\mu \mathbf{v}\mu \otimes \left(\mathbf{I} + \tau_\mu \mathbf{v}\mu \otimes \mathbf{v}_\mu\right)^{-1} \tag{16}$$

2.2. Numerical Approach

To solve the phonon Boltzmann Transport Equation (BTE). Even after using the relaxation time approximation, is a difficult task due to the high dimensionality of this partial differential equation (PDE), a numerical approach is necessary due to the complexity of the governing equations and the need to account for multiple phonon modes, scattering mechanisms, and geometric effects. Numerous computational approaches have been developed to address this challenge, broadly categorized into stochastic techniques (e.g., Monte Carlo simulations) and deterministic discretization strategies (e.g., finite-volume or spectral methods) [18, 19]. However, conventional Monte Carlo methods exhibit limitations due to statistical uncertainties and reduced computational efficiency at low Knudsen numbers (Kn), where strict constraints on time-step resolution and spatial meshing hinder performance [20, 21]. On the deterministic side, methods such as the discrete ordinate method (DOM) approximate angular space by dividing it into discrete solid angles to resolve non-equilibrium phonon distributions. Despite their utility, DOM-based approaches and similar frameworks often suffer from slow convergence rates in diffusive transport regimes and demand significant memory allocation for high-resolution simulations [22]. By

introducing OpenBTE, a first-principles multidimensional phonon Boltzmann transport equation (BTE). Solver can handle with space-dependent heat transport deterministically. And calculate the temperature and heat flux, and the mode-resolve effective thermal conductivity. OpenBTE employs the anisotropic Mean Free Path Boltzmann Transport Equation (aMFP-BTE) [21] a method to optimize computational efficiency. By interpolating phonon pseudo-temperatures onto vectorial mean free path (MFP) space, this approach reduces the computational cost while preserving accuracy and the upwind finite-volume discretization of Eq. 2.

The discretization of aMFP-BTE model in real and momentum space yields the following iterative linear system [4]

$$A_{ml}\Delta T_{ml}^{(n)} = \sum_{m'l'} S_{ml}^{m'l'}\Delta T_{m'l'}^{(n-1)} + P_{ml} \tag{17}$$

Where A_{ml} is the stiffness matrix for a given MFP and direction, $S_{ml}^{m'l'}$ is associated to the lattice temperature and adiabatic boundary conditions, and P_{ml} represents the perturbation due to the applied temperature gradient. Once Eq 4 converges, the effective thermal conductivity is computed as

$$k_{eff} = \frac{k_{bal}}{2} + \sum_{ml} K_{ml}^{T} \cdot \Delta T_{ml} \tag{18}$$

Where k_{bal} is the ballistic thermal conductivity, K_{ml} is associated to thermal flux. The first guess to Eq. 4 is given by the standard heat conduction equation. OpenBTE solves this system iteratively, leveraging LU factorization for the stiffness matrix and parallel computation via MPI4Py for efficient runtime.

3. THERMAL TRANSPORT IN POROUS SILICON

Thermal transport in porous silicon is a complex phenomenon that need computational tools to model the interplay between phonon scattering mechanisms and material geometry. The numerical simulations utilized the OpenBTE framework, a Boltzmann transport equation solver, which incorporated first-principles-derived material properties for porous silicon. Prior studies [24-26] have documented the development and experimental validation of the OpenBTE framework. The numerical framework accounted for four distinct phonon scattering mechanisms: (1) three-phonon interactions, (2) mass impurity scattering (elastic), (3) grain boundary scattering, and (4) pore-induced scattering. Physical pore obstacles were explicitly represented in the simulation domain, while the first three mechanisms were addressed through the single relaxation time approximation. Matthiessen's rule was applied to combine scattering rates from these three processes. The 2nd and 3rd order interatomic force constants (IFCs) for crystalline silicon were sourced from the AlmaBTE repository, calculated via density functional theory within the virtual crystal approximation. For three-phonon scattering processes, AlmaBTE computed the full scattering matrices from third order IFCs, enabling the solution of the linearized Boltzmann transport equation for phonons [27].

The Figure 1 present the mode resolved phonon properties of silicon at room temperature, heat capacity C_μ , scattering times τ_μ , group velocity v_μ and frequencies ω_μ are required for calculating thermal properties of porous silicon via OpenBTE code because they are the input data for Boltzmann transport equation solver (OpenBTE).

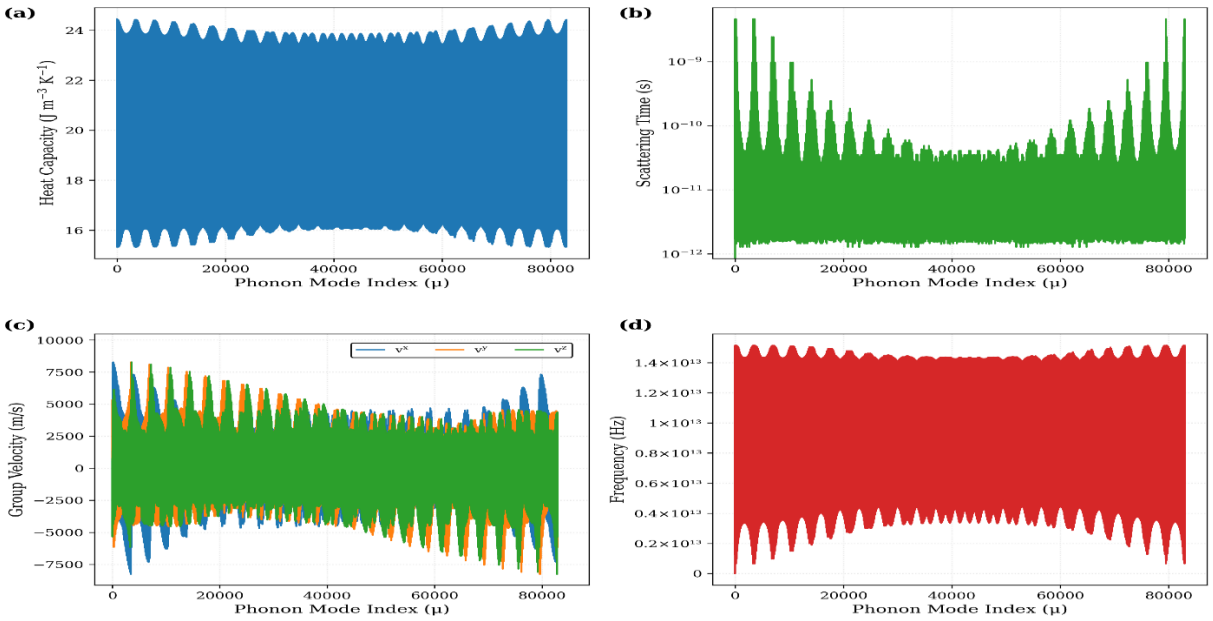

Figure 1: Mode-resolved phonon properties of Si at room temperature using AlmaBTE code [28].
(a) Heat Capacity, (b) Scattering Time, (c) Group Velocity Components, and (d) Frequency Distribution as Functions of Phonon Mode.

The heat capacity presented in figure 2-a is calculated through

$$C_\mu = \frac{k_B}{N_q\, V}\left[\frac{\eta_\mu}{\sinh\left(\eta_\mu\right)}\right]^2, \qquad \eta_\mu = \frac{\hbar\omega_\mu}{2k_B T} \tag{19}$$

And the bulk thermal conductivity tensor is calculated via:

$$k^{\alpha\beta} = \sum_\mu C_\mu \tau_\mu v_\mu^\alpha v_\mu^\beta \tag{20}$$

Where C_μ heat capacity, τ_μ scattering times, v_μ group velocity, ω_μ frequencies and k_B is the Boltzmann constant.

Table 1: Properties for bulk Silicon at room temperature computed using AlmaBTE [28]

Properties	Value
Heat capacity [$Jm^{-3}K^{-1}$]	[24.4476, 24.4476, 24.4476, ..., 15.3429, 15.3429, 15.3338]
Scattering time[s]	[0.00000e+00, 0.00000e+00, 0.00000e+00, ..., 2.60888e-12, 2.52698e-12, 2.34337e-12]
Group velocity[ms^{-1}]	[[0. , 0. , 0.], [0. , 0. , 0.], [0. , 0. , 0.], ..., [141.015, 141.015, 141.015], [263.584, 263.584, 263.584], [120.304, 120.304, 120.304]]
Frequency [s^{-1}]	[0.00000000e+00, 0.00000000e+00, 0.00000000e+00, ..., 1.51217409e+13, 1.51217409e+13, 1.51317995e+13]
Thermal conductivity tensor [$Wm^{-1}K^{-1}$]	[[156.14520455, 0.42324272, 0.42324272], [0.42324272, 156.14520455, 0.42324272], [0.42324272, 0.42324272, 156.14520455]]

3.1. Heat Flux Analysis

Our simulations using a code python to investigate the thermal properties of 2D porous square silicon plate with dimensions of L=50 nm, using tree different pore geometries to see how pore geometry affect heat flux and thermal conductivity.

We use periodic boundary conditions along both axes (x, y), with a temperature difference of 1K applied along the x-direction to drive the thermal transport and because we interest on thermal conductivity along x. Diffuse boundary conditions were applied along all internal pore surfaces to accurately model phonon boundary scattering effects.

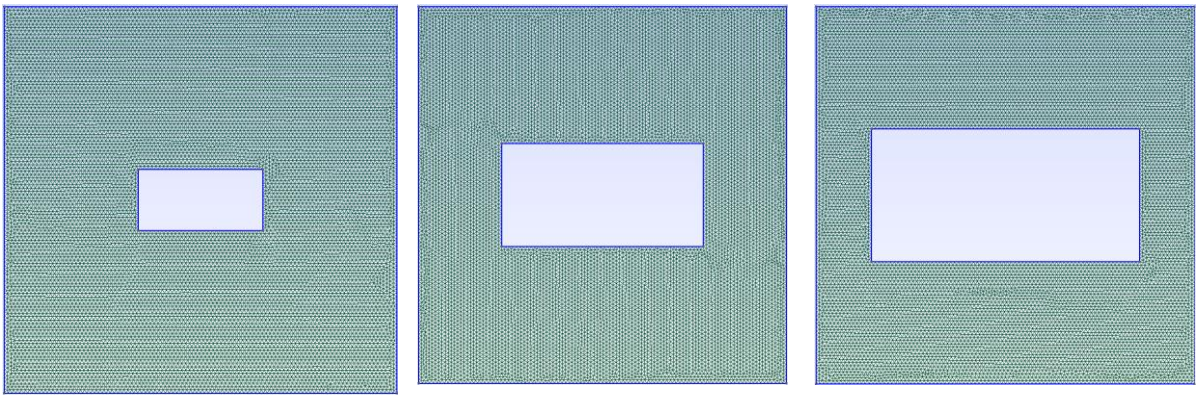

(a) 5% Porosity (b) 15% Porosity (c) 25% Porosity

Figure 2: Mesh Geometry Representations for Rectangular Pore Case using GMSH Code [29].

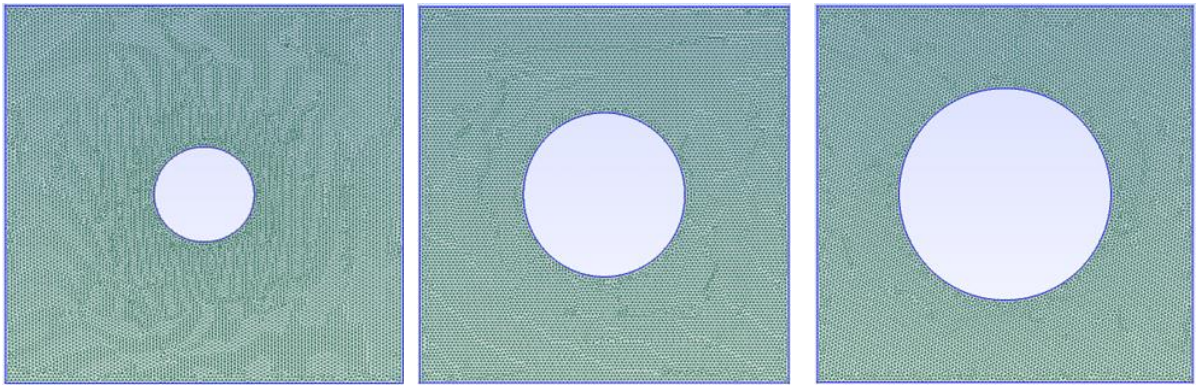

(a) 5% Porosity (b) 15% Porosity (c) 25% Porosity

Figure 3: Mesh geometry representations for circular pore case using GMSH code [29].

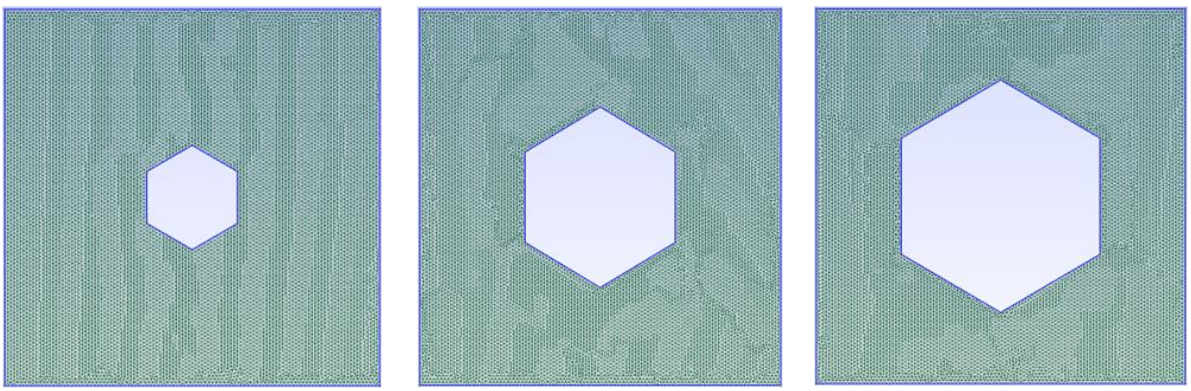

(a) 5% Porosity (b) 15% Porosity (c) 25% Porosity

Figure 4: Mesh geometry representations for hexagonal pore case using GMSH [29].

The system was designed inf Figure 2, 3 and 4 (a, b and c) with a fixed porosity of (5% et 15% 25%) to allow direct comparison between different pore configurations and porosity.

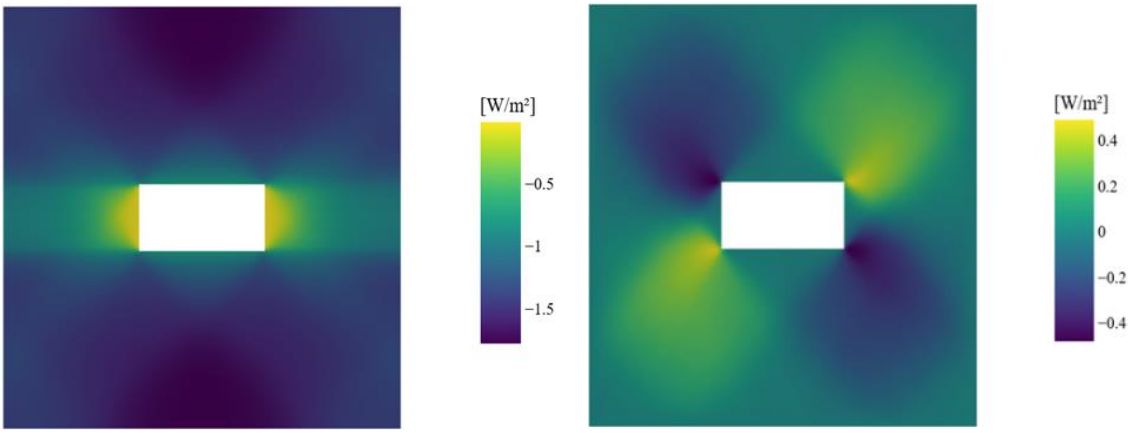

(a) Heat Flux in x-direction (b) Heat Flux in y-direction

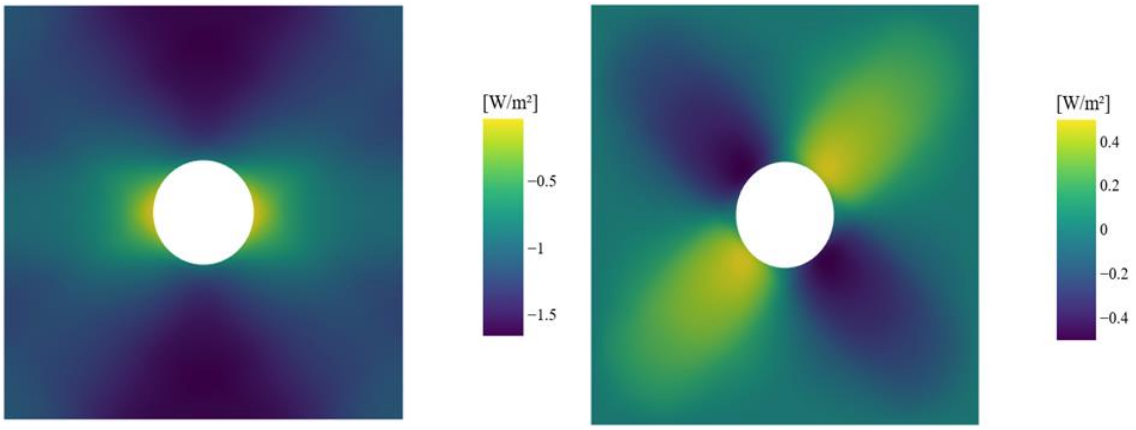

(c) Heat Flux in x-direction (d) Heat Flux in y-direction

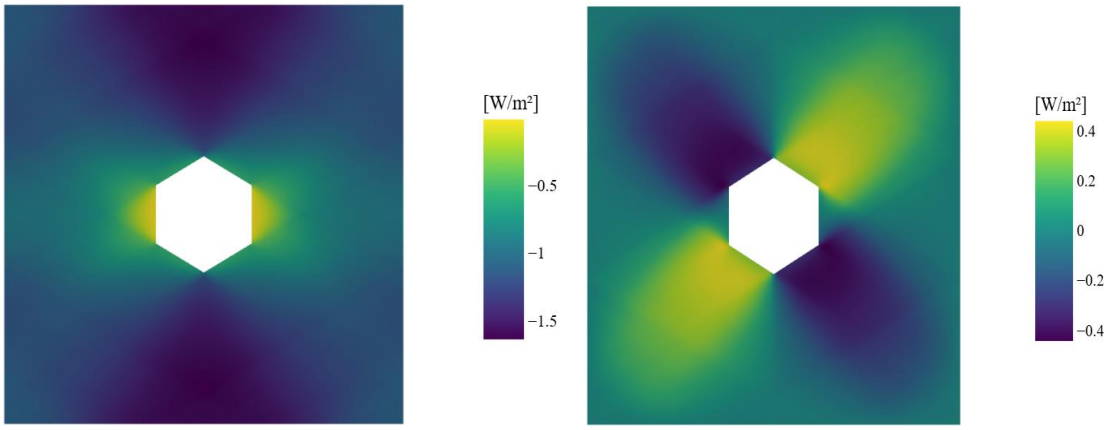

(e) Heat Flux in x-direction (f) Heat Flux in y-direction

Figure 5: Comparative heat flux distributions for different pore geometries at 5% of the porosity.

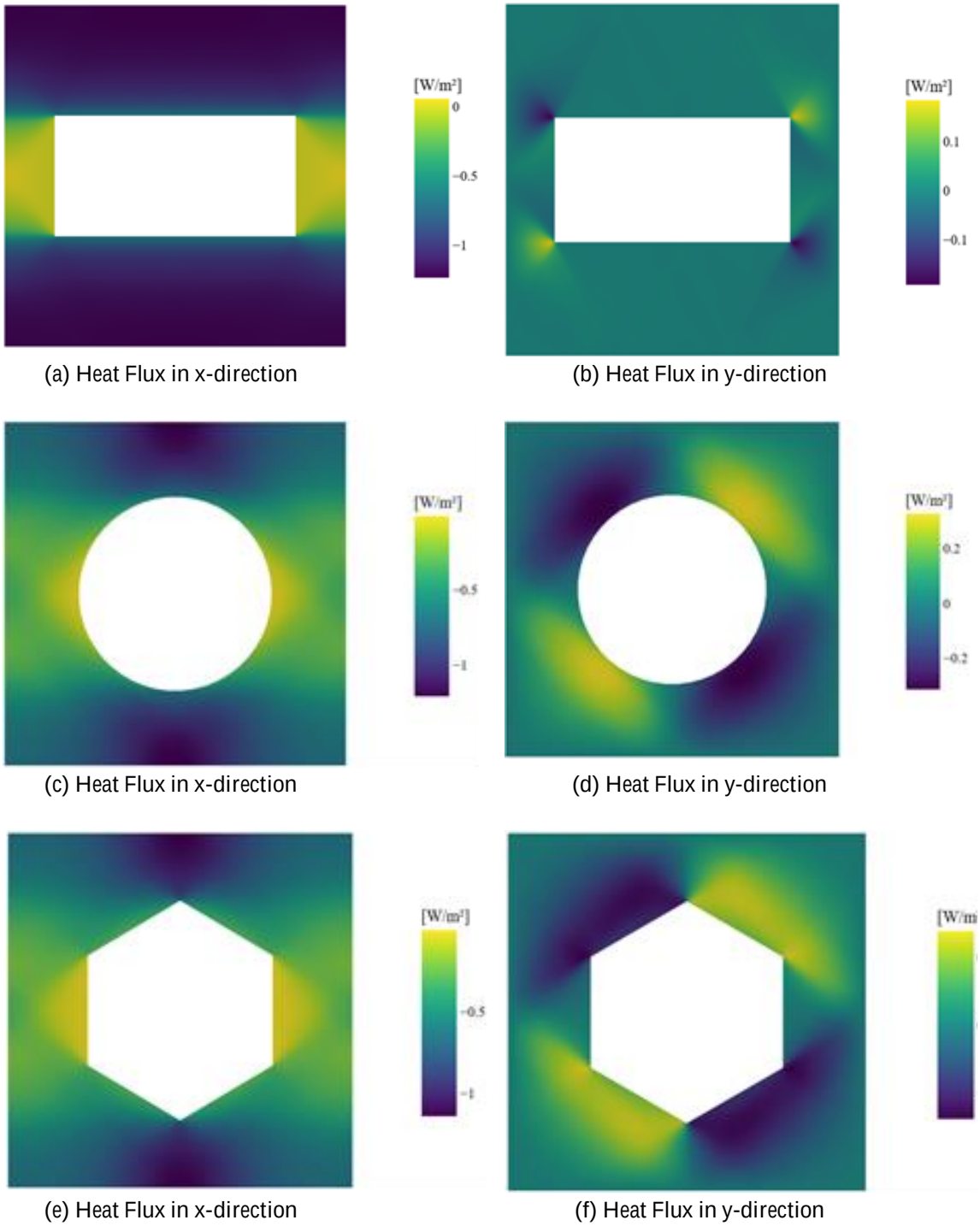

(a) Heat Flux in x-direction (b) Heat Flux in y-direction

(c) Heat Flux in x-direction (d) Heat Flux in y-direction

(e) Heat Flux in x-direction (f) Heat Flux in y-direction

Figure 6: Heat flux in x-direction and in y-direction for porosity 25%

3.1.1. X-Directional Heat Flux Behavior

The x-directional heat flux patterns in subfigures (a, c, e) in Figures (5, 6) reveals how different pore geometries affect thermal transport pathways. The rectangular pore shows concentrated heat flux regions at its vertical edges, with sharp transitions between high and low flux areas but with extended regions of concentrated flux along its longer vertical edges, indicating an enhanced channeling effect due to the increased aspect ratio. The circular pore

demonstrates the most gradual thermal transition profile, with smooth flux distribution around its perimeter, avoiding sharp local concentrations. The hexagonal pore presents an intermediate case, where its angled surfaces create more distributed flux patterns compared to the rectangular and square configurations, yet still maintain some directional preference in heat transport.

3.1.2. Y-Directional Heat Flux Distribution

The analysis of y-directional heat flux patterns in subfigures (b, d, f) in Figures (3-5) reveals a characteristic quadrupolar distribution around all pore shapes, manifested as alternating positive and negative flux regions. This pattern is most symmetrically distributed in the circular pore case, while the rectangular pore shows elongated flux regions corresponding to its extended geometry. The hexagonal geometry displays intermediate patterns and creating more uniform distributions around its six vertices compared to the four corners of the square pore. The rectangular geometry's elongated shape creates an asymmetric quadrupolar pattern, suggesting enhanced vertical heat transport barriers along its longer dimension.

3.2. Thermal Conductivity Analysis

The figure 6 presents a comprehensive comparison of thermal conductivity behavior across three distinct pore geometries (rectangular, circular, and hexagonal), examined over a porosity range of 5% to 45%. The bulk thermal conductivity of silicon, indicated by the dashed line at approximately 154.59 W/(m.K), serves as a reference point for understanding the impact of porosity introduction.

All pore geometries exhibit a consistent trend of decreasing thermal conductivity with increasing porosity, following an approximately linear relationship. This behavior indicates that the volume fraction of void space plays a dominant role in determining thermal transport properties, regardless of pore shape. However, the rate of decrease varies slightly among different geometries, with rectangular pores showing the most gradual decline and hexagonal pores demonstrating the steepest reduction.

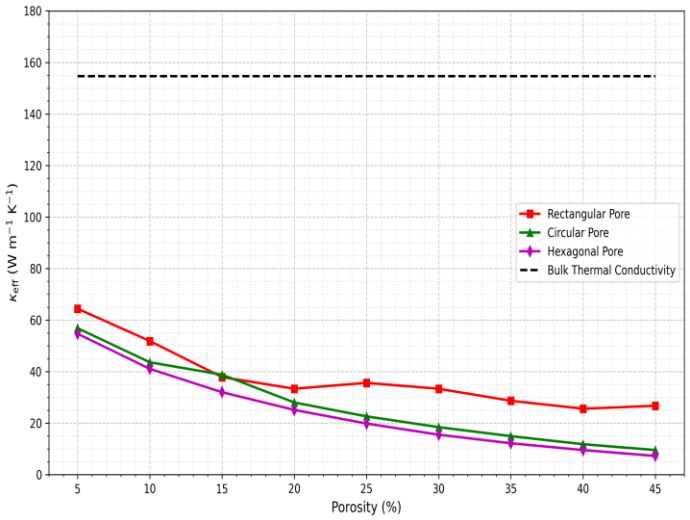

Figure 7: Thermal conductivity of different pore shapes for different porosity

The results demonstrate a clear hierarchy in thermal conductivity values among different pore shapes. The rectangular pore geometry consistently maintains the highest thermal conductivity across all porosity levels, ranging from approximately 64.4 W/(m·K) at 5% porosity to 26.7 W/(m.K) at 45% porosity. This performance preserves the continuous pathways for heat conduction in one primary direction.

The circular pore is the second highest thermal conductivity values, showing a variation between 56.8 W/(m.K) to 9.5 W/(m.K) over the porosity range. This behavior aligns with our heat flux analysis, where circular pores demonstrated uniform heat distribution patterns with minimal local disruptions.

The hexagonal pores show slightly lower thermal conductivity compared to circular pores, with values variations between 54.6 W/(m.K) to 7.2 W/(m.K). This reduction is assigned to the hexagonal geometry that increase phonon scattering.

3.3. Validation and Comparison with Analytical Model

The bulk thermal conductivity of silicon was calculated using the AlmaBTE code, yielding a value of 154.59 W/(m.K). This result shows a very good agreement with experimental data; Chen et al. (2023) reported ~140.2 ± 14.4 W/(m.K) using Raman thermometry [30].

To validate our simulation, we compare the Fourier solver results for circular pore geometry with the analytical model provided by the Eucken–Maxwell model because this analytical model is only applicable for circular pore geometries. The effective thermal conductivity normalized to the bulk value is given by:

$$\frac{k_{eff}}{k_{bulk}} = \frac{1-\emptyset}{1+\emptyset} \tag{21}$$

Where ∅ is the porosity and k_{bulk} is the bulk thermal conductivity.

The following table summarizes the comparison for the circular pore case.

Table 2: Comparison of Fourier Effective Thermal Conductivity

Porosity	Eucken–Maxwell model (W/(m·K))	Fourier solver (W/(m·K))
5%	~139.60	139.8570
15%	~114.18	114.2449
25%	~92.75	92.68315
35%	~74.41	74.14977
45%	~58.69	57.78650

The excellent agreement between the Fourier effective conductivity and the Eucken–Maxwell predictions confirms that the Fourier solver is correctly implemented. But the full solution of the Boltzmann transport equation (BTE) which incorporates non-diffusive effects such as enhanced phonon boundary scattering and ballistic transport that are not captured by Fourier's law. As a result, the effective thermal conductivities obtained from the full BTE

solution are significantly lower.

3.4. Thermal Conductivity Convergence Analysis

3.4.1. Rectangular Pore Case

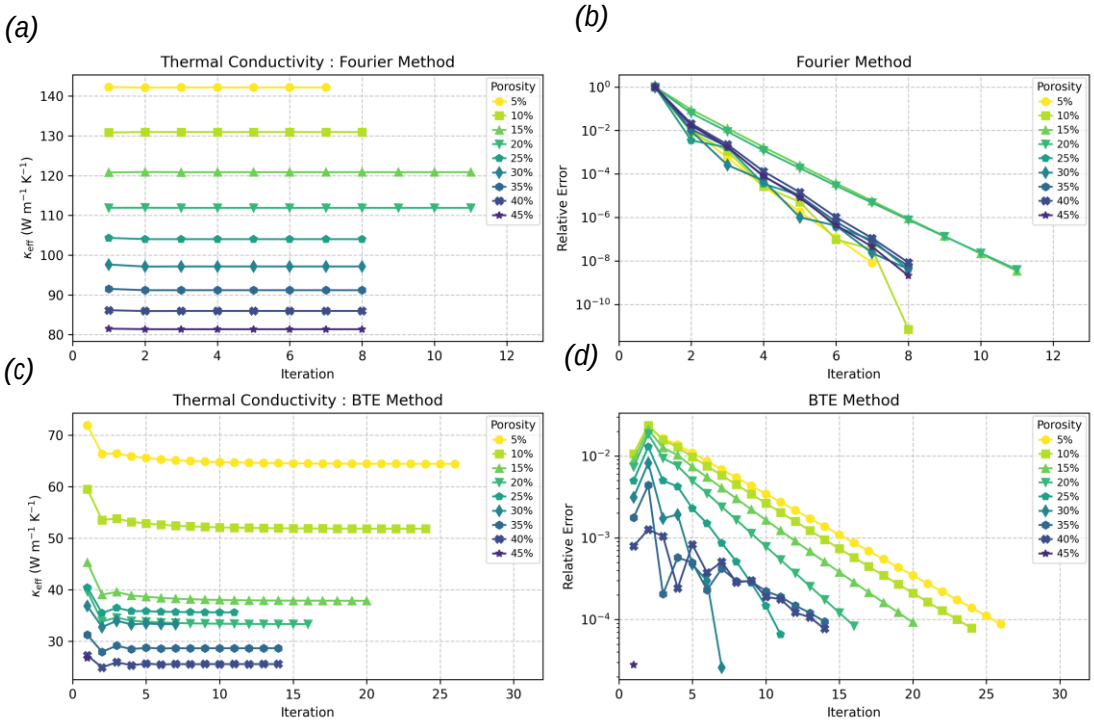

Figure 8: Thermal Conductivity Convergence Analysis for Rectangular Pore at Different Porosities. (a) Convergence of Thermal Conductivity using Fourier, (b) Relative Error in Fourier, (c) Convergence using BTE Method, and (d) Relative Error in BTE Method.

3.4.2. Circular Pore Case

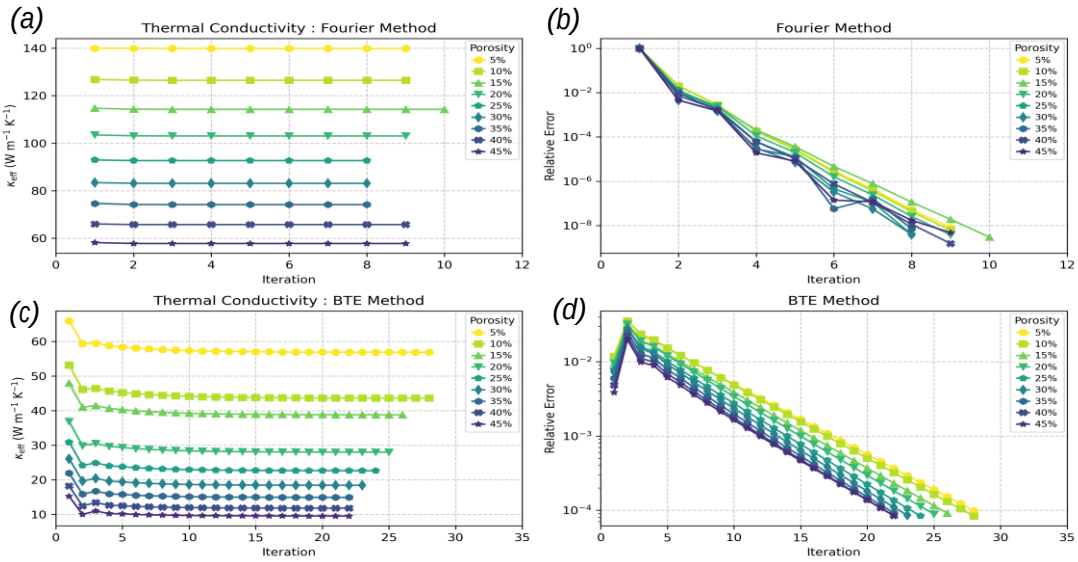

Figure 9: Thermal Conductivity Convergence Analysis for Circular Pore at Different Porosities.

(a) Convergence of Thermal Conductivity using Fourier Method, (b) Relative Error in Fourier Method, (c) Convergence of Thermal Conductivity using BTE Method, and (d) Relative Error in BTE Method.

3.4.3. Hexagonal Pore Case

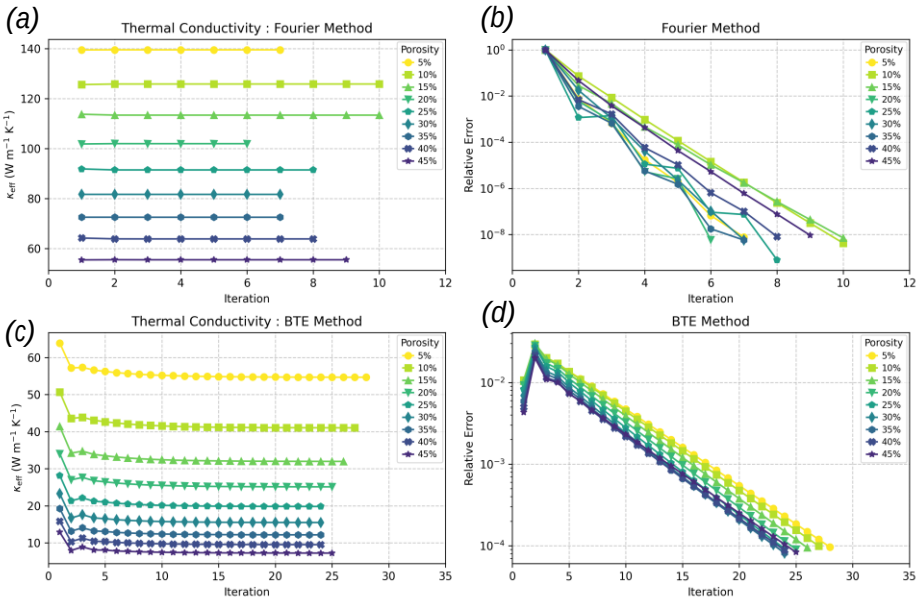

Figure 10: Thermal Conductivity Convergence Analysis for Hexagonal Pore at Different Porosities. (a) Convergence of Thermal Conductivity using Fourier Method, (b) Relative Error in Fourier Method, (c) Convergence of Thermal Conductivity using BTE Method, and (d) Relative Error in BTE

This Results demonstrate that Fourier method converge very quickly take approximately 6 to 10 iterations for all geometry and different porosity making it efficient as an initial guess to solve the problem. The initial error spike in the BTE method indicate the degree of discrepancy between the Fourier method and BTE method and this discrepancy increases as porosity decreases indicate how nanoscale effect become increasingly dominate at lower porosity where the structural dimensions are larger. But the BTE method need more iterations to converge approximately in general take 20 to 25 iterations to converge and, we see that in general low porosity take more iterations to converge but in Fourier we notice that iterations to converge independent to the porosity.

In the BTE method we see also a distinct sensitivity to porosity between 5% to 20% compared to convergence pattern between 25% to 45%. The coupling approach using in OpenBTE Fourier method with BTE show a good computational strategy because the initial Fourier method solutions speed up the convergence of the BTE method by offering a reasonable starting point.

4. CONCLUSIONS

The pore geometry plays a major role in shaping local heat flux distributions in porous Silicon. Circular pores are suitable for applications that requiring a uniform heat distribution, but rectangular pores are suitable for applications that need the directional heat transport pathways. hexagonal pores offer intermediate solutions where hexagonal pores give a more

uniform angular distribution of heat flow.

The study focuses on two aspects of heat transport in porous silicon. First, heat flow patterns are highly sensitive to pore geometry, with circular pores enabling uniform heat distribution and rectangular pores facilitating directional heat flow along their major axes. And second, thermal conductivity with rectangular pores is ideal for scenarios demanding higher thermal conductivity with reduced bulk properties, while hexagonal pores excel in thermal isolation applications where minimal heat conduction is desired. The boundary effects at the Silicon-pore interface vary significantly with geometry. Circular pores promote smooth phonon scattering, while sharp-cornered geometry (hexagonal) induce distinct scattering behaviors that influence thermal resistance.

These results provide a valuable knowledge for optimizing porous silicon structures for specific thermal management applications because the significant reduction in effective thermal conductivity suggests that pore geometry and distribution need to be carefully considered in multi-pore design in porous Silicon, and the complex heat flow patterns observed around the individual pore show that pore-to-pore interactions play an essential role for determining the thermal performance of the porous Silicon. The consistent ordering of thermal conductivity values across all porosity levels suggests that pore geometry and porosity selection can be used to target specific thermal conductivity ranges.

Authors contribution: Othman Soubai: carried out the numerical simulations and contributed to the analysis and validation of the model. Younes Abouelhanoune: Conceptualization of the study, the development of the mathematical model, and the interpretation of the results. Mohammed Taibi: participated in the theoretical framework, literature review, and manuscript drafting. All authors have made an intellectual contribution to the work.

Funding: The authors have not disclosed any funding.

Data Availability Statement: All data are available in the manuscript.

Conflicts of Interest: There are no conflicts to declare.

Acknowledgement: This research was supported through computational resources of HPC-MARWAN provided by the National Center for Scientific and Technical Research (CNRST), Rabat, Morocco. hpc.marwan.ma

REFERENCES

[1] J. Chen and X. Zhang, "Pore-size dependence of the heat conduction in porous silicon and phonon spectral energy density analysis," Physics Letters A, vol. 384, no. 21, p. 126503, 2020. doi: 10.1016/j.physleta.2020.126503

[2] Y. Belaroussi, "High performance porous silicon substrate for the integration of millimeter-wave passive devices," Przegląd Elektrotechniczny, July 2024. doi: 10.15199/48.2024.07.48

[3] E. Amin-Chalhoub et al., "Thermal conductivity measurement of porous silicon by the pulsed-photothermal method," J. Phys. D: Appl. Phys., vol. 44, no. 35, p. 355401, Aug. 2011, doi: 10.1088/0022-3727/44/35/355401.

[4] G. Romano, "Openbte: a solver for ab-initio phonon transport in multidimensional

structures," arXiv preprint arXiv:2106.02764, 2021. https://doi.org/10.48550/arXiv.2106.02764

[5] S. A. Hosseini, S. Khanniche, P. A. Greaney, and G. Romano, "Universal effective medium theory to predict the thermal conductivity in nanostructured materials," International Journal of Heat and Mass Transfer, vol. 183, p. 122040, 2022. https://doi.org/10.3390/thermo4010004

[6] M. Isaiev, N. Kyrychenko, V. Kuryliuk, and D. Lacroix, "Features of phonon scattering by a spherical pore: Molecular dynamics insight," Applied Physics Letters, vol. 124, no. 14, p. 142202, 2024.

[7] Z. Deng, X. Liu, Y. Huang, C. Zhang, and Y. Chen, "Heat Conduction in Porous Media Characterized by Fractal Geometry," Energies, vol. 10, p. 1230, 2017. https://doi.org/10.3390/en10081230

[8] A. Pavlenko, "Heat and Mass Transfer in Porous Materials," Materials, vol. 16, p. 5591, 2023. https://doi.org/10.3390/ma16165591

[9] A. Jain, Y.-J. Yu, and A. J. H. McGaughey, "Phonon transport in periodic silicon nanoporous films with feature sizes greater than 100 nm," Physical Review B, vol. 87, p. 195301, 2013. https://doi.org/10.1103/PhysRevB.87.195301

[10] W. Xing, Y. Xu, C. Song, and T. Deng, "Recent Advances in Thermal Interface Materials for Thermal Management of High-Power Electronics," Nanomaterials, vol. 12, p. 3365, 2022. https://doi.org/10.3390/nano12193365

[11] M. Kashiwagi, Y. Sudo, T. Shiga, and J. Shiomi, "Modeling Heat Conduction in Nanoporous Silicon with Geometry Distributions," Physical Review Applied, 2018. DOI: https://doi.org/10.1103/PhysRevApplied.10.044018

[12] U. Ijaz, M. Siyar, and C. Park, "The power of pores: review on porous thermoelectric materials," RSC Sustainability, vol. 2, no. 4, pp. 852-870, 2024. doi: 10.1039/D3SU00451A

[13] A. S. Fedorov and A. S. Teplinskaia, "Thermal Properties of Porous Silicon Nanomaterials," Materials, vol. 15, no. 23, p. 8678, Dec. 2022. https://doi.org/10.3390/ma15238678

[14] J. M. Ziman, Electrons and Phonons: The Theory of Transport Phenomena in Solids, Oxford University Press, 2001. https://doi.org/10.1093/acprof:oso/9780198507796.001.0001

[15] J.-P. M. Péraud, C. D. Landon, and N. G. Hadjiconstantinou, "Monte carlo methods for solving the boltzmann transport equation," Annual Review of Heat Transfer, vol. 17, pp. 205–265, 2014. doi: 10.1615/AnnualRevHeatTransfer.2014007381

[16] W. Cheng, A. Alkurdi, and P.-O. Chapuis, "Coupling Mesoscopic Boltzmann Transport Equation and Macroscopic Heat Diffusion Equation for Multiscale Phonon Heat Conduction," Nanoscale and Microscale Thermophysical Engineering, vol. 24, no. 3-4, pp. 150-167, 2020. doi: 10.1080/15567265.2020.1836095

[17] Z. Wang, J. E. Alaniz, W. Jang, J. E. Garay, and C. Dames, "Thermal Conductivity of Nanocrystalline Silicon: Importance of Grain Size and Frequency-Dependent Mean Free Paths," Nano Letters, vol. 11, no. 6, pp. 2206-2213, Jun. 2011. doi: 10.1021/nl1045395

[18] S. Mazumder and A. Majumdar, "Monte Carlo study of phonon transport in solid thin films including dispersion and polarization," Journal of Heat Transfer, vol. 123, pp. 749-759, 2001. https://doi.org/10.1115/1.1377018

[19] Q. Hao, G. Chen, and M.-S. Jeng, "Frequency-dependent Monte Carlo simulations of phonon transport in two-dimensional porous silicon with aligned pores," Journal of Applied Physics, vol. 106, p. 114321, 2009. https://doi.org/10.1063/1.3266169

[20] C. Ni and J. Y. Murthy, "Parallel computation of the phonon Boltzmann transport

equation," Numerical Heat Transfer, Part B, vol. 55, pp. 435-456, 2009. DOI:10.1080/10407780902864771

[21] S. V. J. Narumanchi, J. Y. Murthy, and C. H. Amon, "Comparison of Different Phonon Transport Models for Predicting Heat Conduction in Silicon-on-Insulator Transistors," Journal of Heat Transfer, vol. 127, no. 7, pp. 713-723, Jul. 2005. doi: 10.1115/1.1924571

[22] D. Lacroix, K. Joulain, and D. Lemonnier, "Monte Carlo transient phonon transport in silicon and germanium at nanoscales," Physical Review B, vol. 72, p. 064305, 2005. https://doi.org/10.1103/PhysRevB.72.064305

[23] A. Mittal and S. Mazumder, "Monte Carlo Study of Phonon Heat Conduction in Silicon Thin Films Including Contributions of Optical Phonons," Journal of Heat Transfer, vol. 132, p. 052402, 2010. https://doi.org/10.1115/1.4000447

[24] G. Romano, "Efficient calculations of the mode-resolved ab-initio thermal conductivity in nanostructures," arXiv preprint arXiv:2002.08940, 2020. DOI: 10.48550/arXiv.2105.08181

[25] R. A. Duncan et al., "Thermal transport in nanoporous holey silicon membranes investigated with optically induced transient thermal gratings," Journal of Applied Physics, vol. 128, p. 235106, 2020. https://doi.org/10.1063/1.5141804

[26] W. Park et al., "Phonon conduction in silicon nanobeam labyrinths," Scientific Reports, vol. 7, p. 6233, 2017. https://doi.org/10.1038/s41598-017-06479-3

[27] W. Li, J. Carrete, N. A. Katcho, and N. Mingo, "ShengBTE: A solver of the Boltzmann transport equation for phonons," Computer Physics Communications, vol. 185, pp. 1747–1758, 2014. https://doi.org/10.1016/j.cpc.2014.02.015

[28] J. Carrete et al., "almaBTE: A solver of the space–time dependent Boltzmann transport equation for phonons in structured materials," Computer Physics Communications, vol. 220, pp. 351–362, 2017. https://doi.org/10.1016/j.cpc.2017.06.023

[29] C. Geuzaine and J.-F. Remacle, "Gmsh: a three-dimensional finite element mesh generator with built-in pre- and post-processing facilities," International Journal for Numerical Methods in Engineering, vol. 79, no. 11, pp. 1309-1331, 2009. https://doi.org/10.1002/nme.2579

[30] R. An, J. Zhao, J. Yang, S. Zhai, L. Dai, Q. Wang, J. Li, W. Hu, G. Sun, Y. Fan, S. Wu, and G. Niu, "Accurate and wide-range measurement of thermal conductivity of semiconductor materials by laser-excited Raman spectroscopy," Journal of Applied Physics, vol. 134, no. 1, p. 015103, Jul. 2023. doi: 10.1063/5.0152963

Solar Energy
and Sustainable Development
Refereed, biannual scientific journal issued by
The Libyan Center for Solar Energy Research and Studies

Parametric study of the impact of insulation and wall thickness in straw-reinforced adobe structures on energy performance in a Moroccan desert climate: A case study of Errachidia

Abdelmounaim Alioui[1*], Youness Azalam[2], Mohammed Benfars[3], El Maati Bendada[4], Mustapha Mabrouki[5].

[1,2,3,4,5]Laboratory of Industrial and Surface Engineering Sultan Moulay Slimane FST, Mghila, B.P. 592, Beni Mellal, Morocco.

E-*mail :* [1]abdelmounaim.aliouifpb@usms.ac.ma

SPECIAL ISSUE ON.

The 1St International Conference on Sciences and Techniques for Renewable Energy and the Environment. (STR2E 2025)
May 6-8, 2025 at FST-Al Hoceima-Morocco.

KEYWORDS

Straw-reinforced adobe structures; Thermal comfort; Insulation; Building energy performance; Desert climate

ABSTRACT

In hot and arid desert climates, the thermal performance of passive buildings is strongly influenced by external climatic factors such as solar radiation, air temperature, humidity, and wind speed. However, these challenges can be mitigated through a judicious selection of construction materials and the optimization of their properties to ensure occupant thermal comfort. This study aims to identify the optimal combinations of insulation and wall thickness in straw-reinforced adobe structures to enhance the energy performance of buildings in a Moroccan desert context, specifically in the city of Errachidia.

To achieve this aim, the study employs a validated energy model to investigate two key parameters: (1) the addition of natural fiber insulation (0.10 m) and (2) the variation of wall thickness (0.3 m to 0.5 m).

The thermal simulation results indicate that adding 0.10 m of insulation significantly enhances thermal performance compared to non-insulated walls. Without insulation, wall thicknesses ranging from 0.4 m to 0.5 m reduce thermal fluctuations by 2°C. However, with insulation, a 0.3 m thick wall achieves a reduction of 3.7°C in summer indoor temperature peaks and maintains winter indoor temperatures as high as 12.1°C, even under extreme outdoor conditions. The integration of eco-friendly insulation panels also leads to a 23.18% reduction in cooling energy demand and a 40% decrease in heating needs compared to uninsulated walls.

*Corresponding author.

DOI: https://doi.org/10.51646/jsesd.v14iSTR2E.1060

This is an open access article under the CC BY-NC license (http://Attribution-NonCommercial 4.0 (CC BY-NC 4.0)).

These findings underscore the importance of designing walls specifically tailored to the climatic conditions of desert regions, especially those near the city of Errachidia to optimize energy efficiency, lower ecological footprints, and promote sustainable architectural practices.

دراسة بارومتريه لتأثير العزل وسماكة الجدران في الهياكل المبنية من الطوب اللبن المدعوم بالقش على أداء الطاقة في المناخ الصحراوي في المغرب: دراسة حالة من مدينة الرشيدية

عبد المنعم عليوي، يونس أزالم، محمد بنفارس، المعطي بن دادة، مصطفى مبروكي

ملخص: في المناخات الصحراوية الحارة والقاحلة، يتأثر الأداء الحراري للمباني السلبية بشدة بالعوامل المناخية الخارجية مثل الإشعاع الشمسي ودرجة حرارة الهواء والرطوبة وسرعة الرياح. ومع ذلك، يمكن التخفيف من حدة هذه التحديات من خلال الاختيار الحكيم لمواد البناء وتحسين خصائصها لضمان الراحة الحرارية للساكن. تهدف هذه الدراسة إلى تحديد التوليفات المثلى للعزل وسماكة الجدران في الهياكل المبنية من الطوب اللبن المدعوم بالقش لتعزيز أداء الطاقة في المباني في سياق صحراوي مغربي، وتحديداً في مدينة الرشيدية. ولتحقيق هذا الهدف، توظف الدراسة نموذجًا للطاقة تم التحقق من صحته للتحقق من متغيرين رئيسيين: (1) إضافة عازل من الألياف الطبيعية (0.10 م) و (2) تباين سماكة الجدار (0.3 م إلى 0.5 م). تشير نتائج المحاكاة الحرارية إلى أن إضافة 0.10 م من العزل يعزز الأداء الحراري بشكل كبير مقارنة بالجدران غير المعزولة. بدون العزل، تقلل سماكة الجدران التي تتراوح من 0.4 متر إلى 0.5 متر من التقلبات الحرارية بمقدار درجتين مئويتين. ومع ذلك، مع العزل، يحقق الجدار بسماكة 0.3 متر انخفاضًا قدره 3.7 درجة مئوية في ذروة درجات الحرارة الداخلية في الصيف ويحافظ على درجات حرارة داخلية في الشتاء تصل إلى 12.1 درجة مئوية، حتى في ظل الظروف الخارجية القاسية. يؤدي دمج الألواح العازلة الصديقة للبيئة أيضًا إلى انخفاض الطلب على طاقة التبريد بنسبة 23.18٪ وانخفاض احتياجات التدفئة بنسبة 40٪ مقارنة بالجدران غير المعزولة. تؤكد هذه النتائج على أهمية تصميم جدران مصممة خصيصًا للظروف المناخية للمناطق الصحراوية، خاصة تلك القريبة من مدينة الرشيدية لتحسين كفاءة الطاقة وخفض الآثار البيئية وتعزيز الممارسات المعمارية المستدامة.

الكلمات المفتاحية: الطوب اللبن المدعوم بالقش؛ الراحة الحرارية؛ العزل؛ أداء الطاقة في المباني؛ المناخ الصحراوي

The graphical abstract:

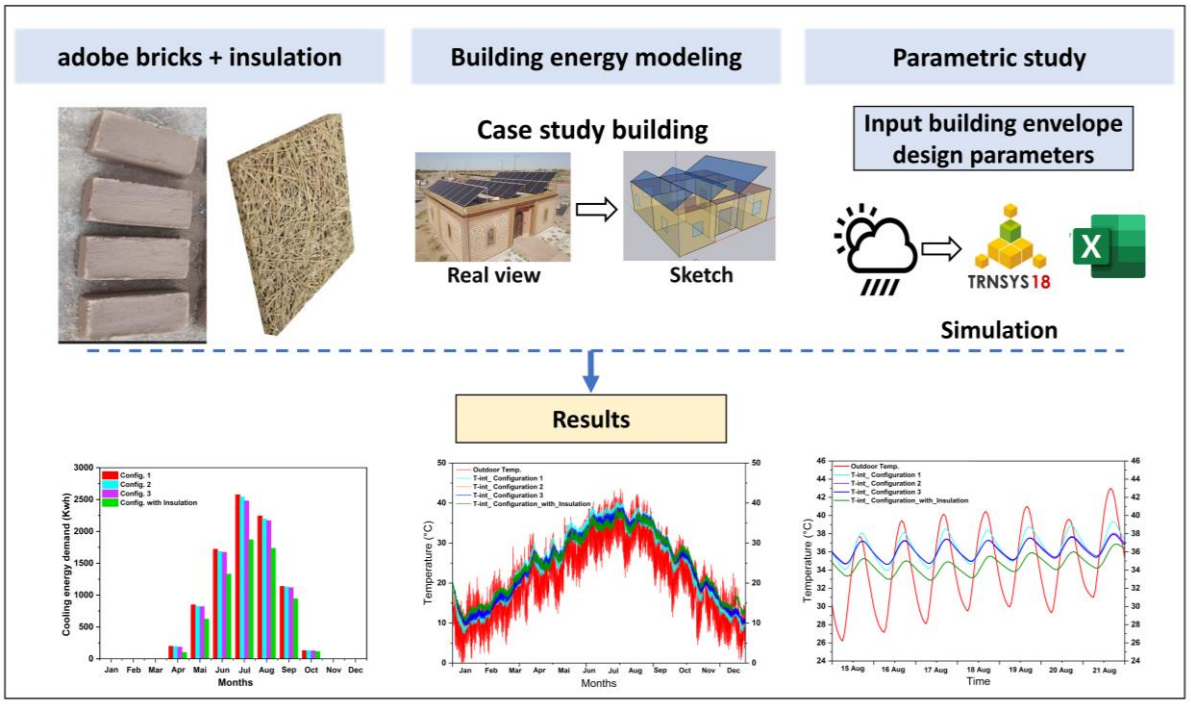

1. INTRODUCTION

Today, Africa's population is experiencing rapid demographic growth, coupled with a high rate of construction, which increases the demand for decent housing that provides satisfactory thermal comfort conditions for residents [1]. In hot regions, the need for cooling is particularly significant to adapt to current heat conditions, making thermal regulation a key aspect of housing design. This challenge is further amplified by the fact that nearly one-third of global energy is consumed by the building sector, which also accounts for 40% of all CO_2 emissions, highlighting the urgent need for sustainable and energy-efficient construction solutions [2-4] . Moreover, heating, ventilation, and air conditioning (HVAC) systems alone account for half of the total energy consumption in residential buildings, highlighting the urgent need for energy-efficient solutions [5, 6]. To reduce heating and cooling demands, recent and efficient traditional construction techniques, such as earthen buildings, can be employed. This involves adapting the building envelope by adding ecological insulation or enhancing earthen building materials with natural fibers [4]. Clay is one of the oldest and most widely used building materials, valued for its exceptional hygrothermal properties, natural abundance, and outstanding ecological benefits, particularly in conserving non-renewable resources [7].

Adobe bricks are traditionally composed of a mixture of sand, clay, and water. The bricks are formed by molding the clay-water mixture into desired shapes and allowing them to dry naturally in open air. To enhance their properties, extensive research has been conducted on incorporating natural additives into adobe bricks and evaluating their impact on thermal, mechanical, and durability characteristics. Notable additives studied include straw [7,8], alfalfa fibers [9], Alfa fibers [10], sawdust [11, 12], palm fibers [13], fonio straw [14], dry grass fibers [15]. These natural reinforcements aim to improve the bricks' performance, making them more suitable for modern sustainable construction.

In addition to enhancing the properties of adobe bricks, the integration of environmentally friendly thermal insulation materials into building walls has become a key strategy for improving energy efficiency and indoor comfort. For instance, the integration of thermal insulation in concrete walls has been shown to significantly reduce heat conduction across the envelope, thereby enhancing indoor thermal stability and lowering energy consumption [16]. Thermal insulation plays a vital role in reducing heat transfer, which is particularly critical in climates with extreme temperatures, such as hot desert regions. Research has shown that natural insulation materials, including bio-composites and fibers such as date palm fibers [17], hemp fibers [18], coconut fibers, cellulose fibers [19], and Sugarcane Bagasse [20], can significantly reduce temperature fluctuations and enhance the thermal stability of buildings. For example, a study evaluated recycled insulation panels made of cork, rice husk, and coffee chaff, achieving a thermal conductivity as low as 0.08 W/m.K and a Global Warming Potential of only 2.6 kg CO_2 eq/m², highlighting their strong environmental and thermal performance [21]. Another study assessed the effect of insulation and thermal mass on the thermal performance of a stabilized compressed earth block wall in a hot, dry tropical climate. The results indicated that a wall thickness of 0.14 m, with insulation, provided the best thermal efficiency, reducing the external temperature range by 22% [22].

In that scope, this paper aims to explore and propose construction solutions tailored to warm climates by optimizing the properties of building materials to enhance the thermal performance

of buildings. The study focuses on combining earth-stabilized bricks reinforced with straw and ecological thermal insulation panels applied to walls to improve energy efficiency. A detailed parametric analysis, conducted through simulations using TRNSYS software, investigates the impact of adding thermal insulation to earth walls. The originality of this research lies in the use of locally sourced materials, such as clay bricks reinforced with straw, which not only contribute to reducing indoor overheating but also minimize the ecological footprint of the construction process. In this context, the straw fibers incorporated in the adobe mix were collected from the Beni Mellal region in central Morocco, underlining the importance of valorizing renewable, regionally available resources. Overall, this study contributes to the advancement of sustainable and eco-friendly architecture that meets thermal comfort requirements while limiting the exploitation of natural resources.

2. MATERIALS AND METHODS

2.1. Materials

2.1.1. Clay Bricks

The main raw material used in this study is natural clay extracted from the Beni Mellal region in north-central Morocco. It was employed during the summer season to produce adobe bricks reinforced with 2% straw by weight, as shown in Figure 1. The addition of straw enhances both the thermal insulation and mechanical performance of the bricks. To evaluate the workability and plasticity of the clay, the Atterberg limits were determined. These limits help assess the suitability of the clay for construction purposes. The corresponding values are presented in Table 1. Furthermore, Figure 2 presents the X-ray diffraction (XRD) analysis of the studied clay, revealing a range of minerals including quartz (Q), illite (I), kaolinite (K), calcite (C), dolomite (D), feldspar (Fp), and chlorite (Ck), with quartz identified as the predominant phase. The high presence of silicon dioxide (SiO_2) indicates that the clay is suitable for construction [7], as SiO_2 is associated with enhanced mechanical strength, reduced water absorption, and improved thermal insulation properties—key characteristics for building materials [23]. In addition, this is further supported by the chemical composition of the clay shown in Figure 3. The significant presence of aluminum oxide (Al_2O_3) confirms the clayey nature of the soil [24]. Moreover, the elevated concentrations of calcium oxide (CaO) and potassium oxide (K_2O) suggest that the clay belongs to the kaolinite and illite mineral types [25].

Figure 1. Sample clay brick

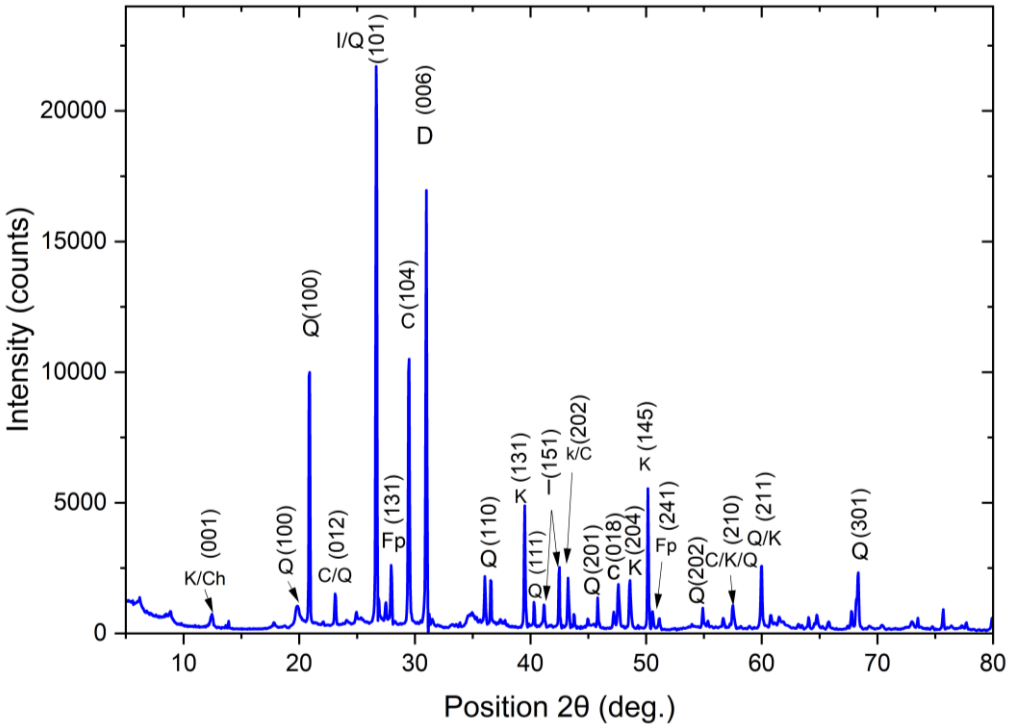

Figure 2. XRD pattern of the studied clay. Indexes: Q – quartz, C – calcite, K – kaolinite, I – illite, D – dolomite, Fp – feldspat, Ch – Chlorite [7].

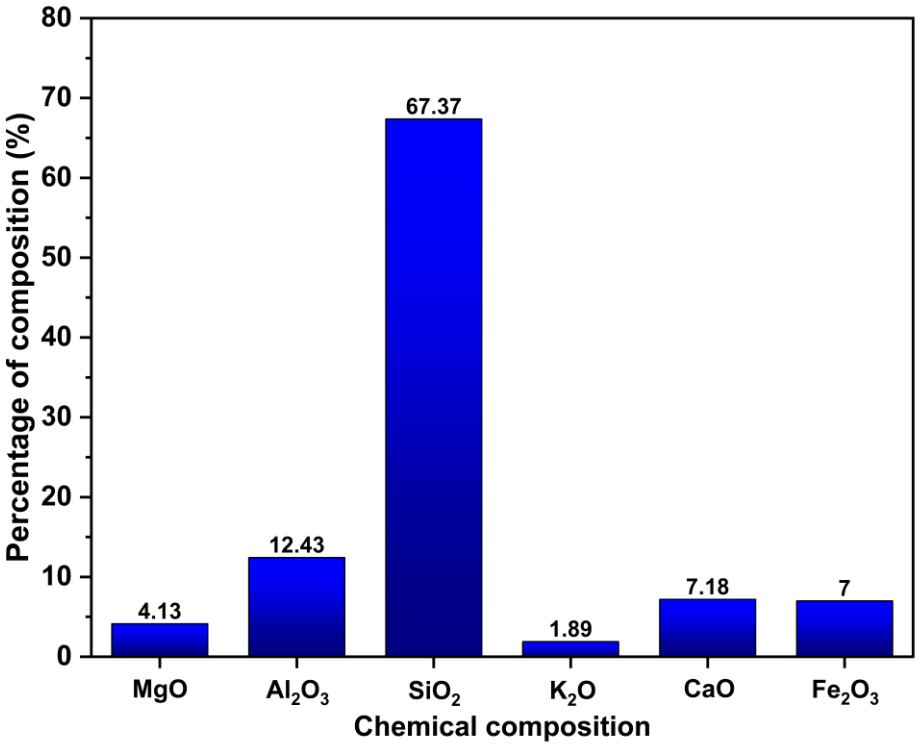

Figure 3. The chemical composition of the studied clay [7].

Table 1. The Atterberg limits of the soil [9].

Atterberg limits	Value
Plasticity limit (%)	16
Liquidity limit (%)	30
Plasticity index	14

2.1.2. Preparation of bricks samples

The adobe brick depicted in Figure 1 was fabricated using a traditional technique widely employed in southern Morocco. First, natural soil was mixed with water at 19% of the soil's dry mass. The mixture was then cured for 72 hours to ensure uniform moisture distribution. Subsequently, varying proportions of straw fibers were thoroughly incorporated into the hydrated clay matrix to form adobe bricks. The samples were then air-dried for four weeks under ambient conditions to achieve complete drying.

Once dried, the bricks' thermal properties were analyzed using an HFM Lambda 446 thermal flow meter. This instrument applies Fourier's law to determine thermal conductivity, as expressed in Equation (1) [26]:

$$\dot{Q} = \lambda \times A \times \frac{\Delta T}{\Delta x} \quad (1)$$

The equation (1) represents heat flow (Q, in Watts) measured by a heat flow meter, where:

λ: thermal conductivity of the material (W/m.K)
A: cross-sectional area (m²)
ΔT: temperature difference (K) across the sample
Δx: thickness of the sample (m).

2.1.3. Thermal Insulation

The thermal insulation material employed in this study is a bio-composite made from cardboard and date palm fibers. These natural fibers were chosen for their durability, local availability, and superior thermal insulation properties, as noted by Bennallel et al. [17]. The bio-composites were transformed into eco-friendly panels and integrated between adobe walls to assess their effectiveness in reducing thermal fluctuations and improving energy efficiency.

2.2. Methodology

The methodology of this study consists in a comprehensive parametric analysis of adobe walls reinforced with straw, supplemented by ecological thermal insulation panels, to evaluate their thermal performance in hot desert climates. The thermal behavior of the reinforced adobe walls is examined in three configurations, as shown in Table 2, first by varying their thickness between 0.4 m, 0.45 m and 0.5 m. Then, Thermal insulation panels are placed between two adobe walls to determine the optimal balance between material efficiency and thermal stability. Simulations are performed using TRNSYS software to evaluate the impact of different insulation thicknesses on energy efficiency and indoor thermal comfort. These simulations allow the analysis of key parameters such as surface temperature fluctuations, indoor temperature stability and energy demand for heating and cooling. The results are then used to identify optimal wall and insulation configurations, minimizing thermal variations, improving interior comfort and reducing energy consumption. To clarify this methodology, a flowchart is presented in Figure 4, which outlines the key steps of the research process. The first part shows the design and modeling steps of the reference building, including the creation of the architectural model and its thermal simulation in TRNSYS 18, followed by validation according to the RTCM. The second part illustrates the comparative analysis of thermal performance between traditional adobe walls and insulated walls. The diagram shows the different configurations tested and the parameters

measured, including indoor temperatures and energy requirements. This approach has identified the most efficient insulation thickness, suitable for designing and building energy-efficient buildings adapted to hot desert climates while promoting environmentally friendly architecture.

Table 2. The wall configurations of the study.

Wall configurations	Materials	Thickness
Configuration 1	Reinforced adobe brick	0.40 m
Configuration 2	Reinforced adobe brick	0.45 m
Configuration 3	Reinforced adobe brick	0.50 m
Configuration with insulation	Reinforced adobe brick+ insulation+ Reinforced adobe brick	(0.15 + 0.1 + 0.15) m

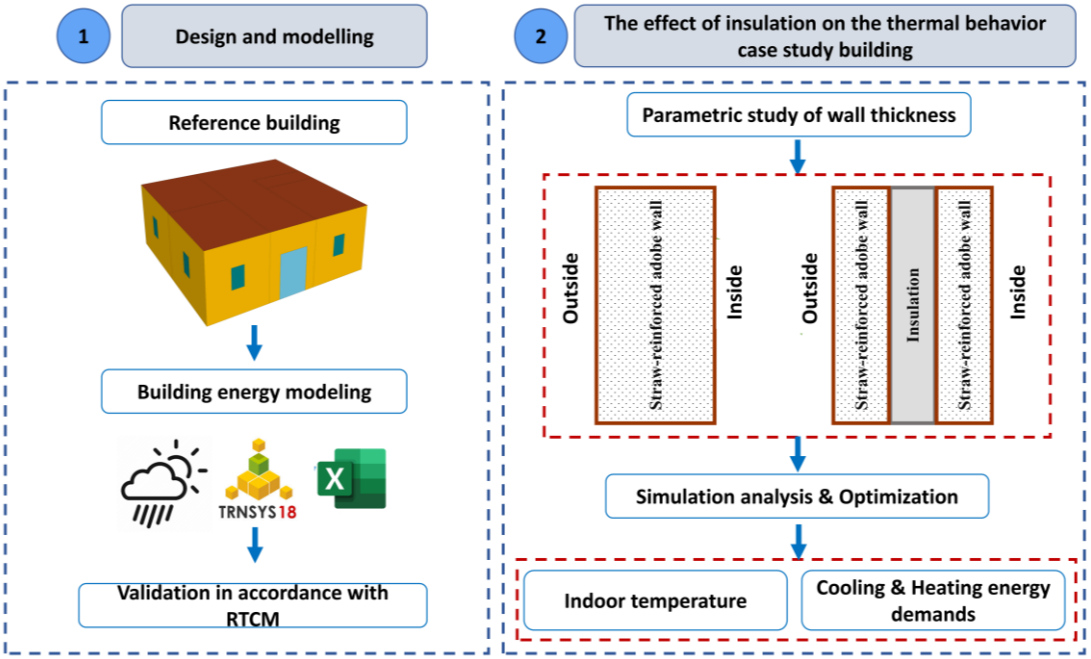

Figure 4. Flow chart of the study.

2.2.1. Description of the building and materials

The studied structure is a single-story building covering a total area of 74 m² with an internal height of 3 meters. The building is segmented into four distinct thermal zones, as illustrated in the sketch provided in Figure 5.

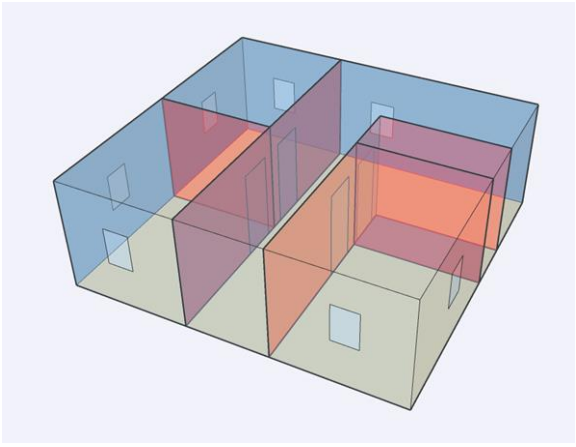

Figure 5. The sketch of case study building

This architectural sketch was created using SketchUp software and subsequently integrated into the TRNSYS simulation environment to define the thermal model. Each zone represents a specific usage area (e.g., living room, kitchen, bedroom, and rooms), which allows for more accurate simulation of internal thermal behavior and energy consumption. To ensure a comprehensive analysis, the thermophysical characteristics of the construction materials, such as thermal conductivity, density, and specific heat capacity, are detailed in Table 3.

Table 3. Thermophysical Properties of Wall-Building Materials

Materials	Density (Kg/m3)	Thermal conductivity (W/ m K)	Thermal (kJ/kg K)	capacity
Clay-straw (2%)	1703	0.40	0.75	
Insulation panel	265.7	0.081	1.411	

2.2.2. Climatic Conditions

The study area, Er-Rachidia, situated on the edge of the Moroccan Sahara Desert, experiences a hot desert climate. Summer is extremely hot, with temperatures often exceeding 43°C, while winter is relatively cool, with nighttime temperatures frequently dropping to around -1°C. The annual temperature profile of Er-Rachidia, depicted in Figure 6, highlights the pronounced seasonal variations and the thermal challenges characteristic of this harsh environment.

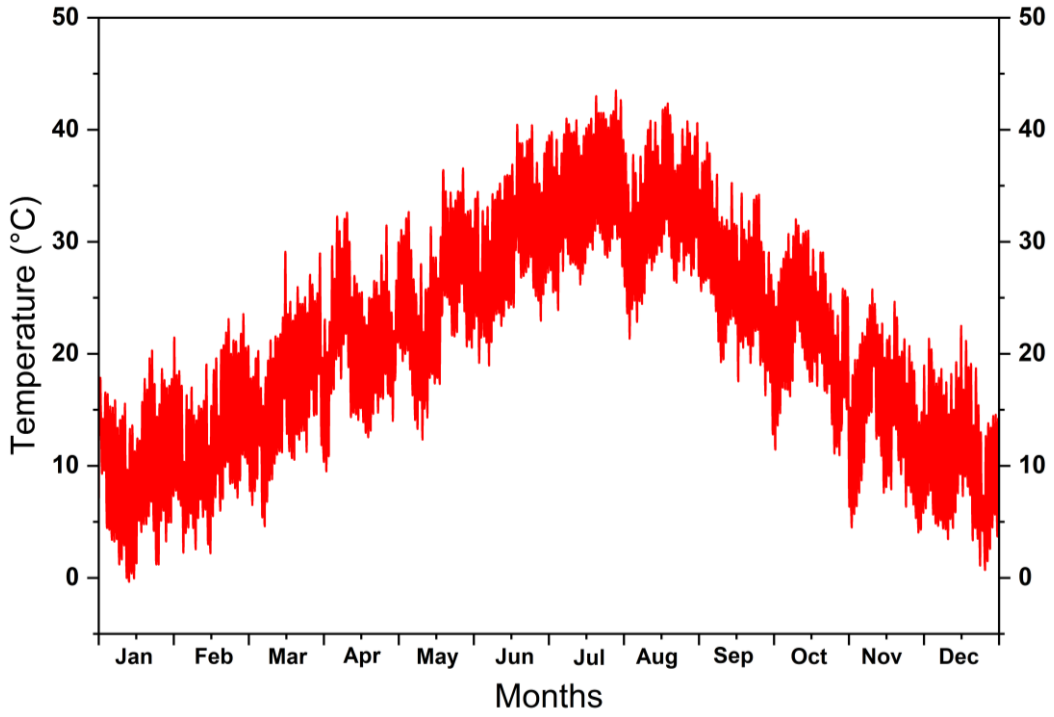

Figure 6. Outdoor air temperature of Er-rachidia city in 2024, showing extremes ranging from -1 °C (winter) to 43 °C.

3. RESULTS AND DISCUSSION

3.1. Annual Indoor air Temperature

The results of the dynamic thermal simulation for the four envelope configurations are

presented in Figure 7. These findings clearly demonstrate that the insulated configuration significantly enhances indoor thermal comfort compared to the reference configuration (Configuration 1), even under the extreme climatic conditions typical of the study area, characterized by intense summer heat and cold winter temperatures.

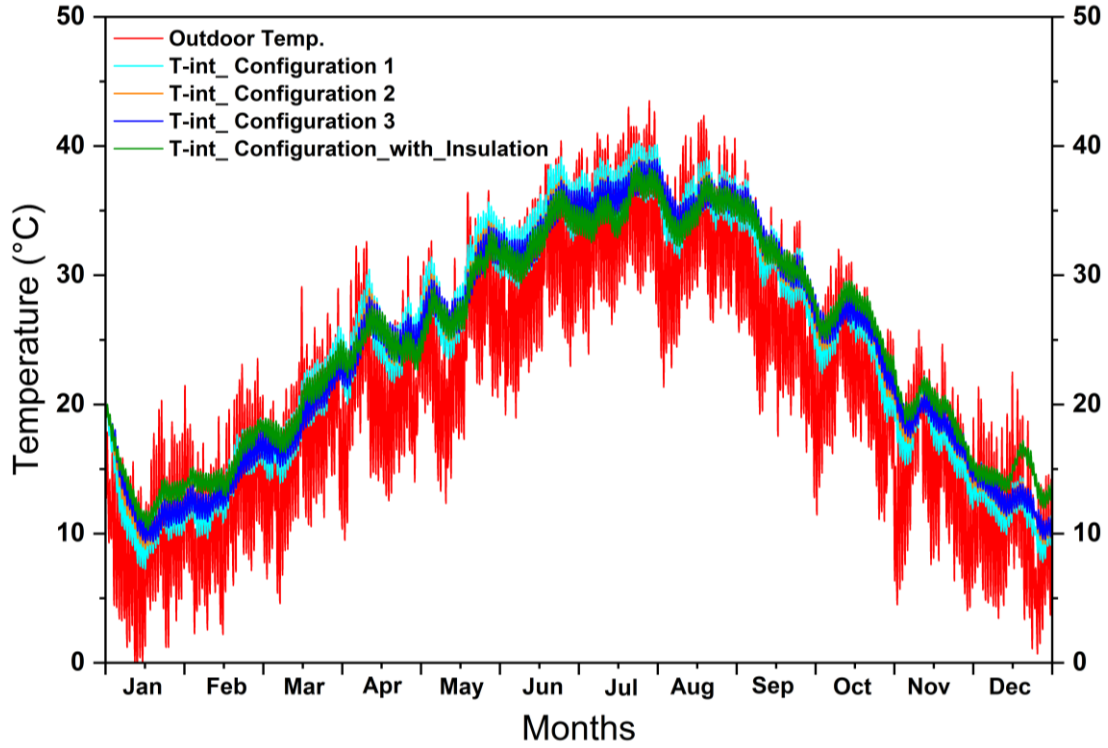

Figure 7. Annual variation in indoor and outdoor temperatures in 2024.

3.2. Summer and winter indoor temperature

During the winter period (Figure 8), the insulated configuration consistently outperforms the other configurations by maintaining higher indoor temperatures, despite outdoor temperatures dropping as low as -1°C. The minimum indoor temperatures recorded for the four configurations are 7.2°C, 8.7°C, 9.2°C, and 12.1°C, respectively, highlighting the superior thermal retention capacity of the insulated configuration. Similarly, during the summer period (Figure 9), when outdoor temperatures often exceed 43°C, the insulated configuration demonstrates a significant reduction in maximum indoor temperatures. The maximum indoor temperatures for the four configurations are recorded at 40.3°C, 39.1°C, 38.3°C, and 36.6°C, respectively. These results underscore the critical role of insulation in minimizing heat ingress and improving indoor thermal comfort during hotter periods.

Moreover, the analysis reveals that integrating locally sourced ecological insulation materials significantly enhances thermal regulation. The reduction in indoor temperature fluctuations observed in insulated adobe buildings, compared to those constructed with adobe alone, highlights improved thermal stability. This performance underscores the effectiveness of insulation in optimizing energy efficiency and thermal comfort for traditional adobe constructions in extreme climatic conditions.

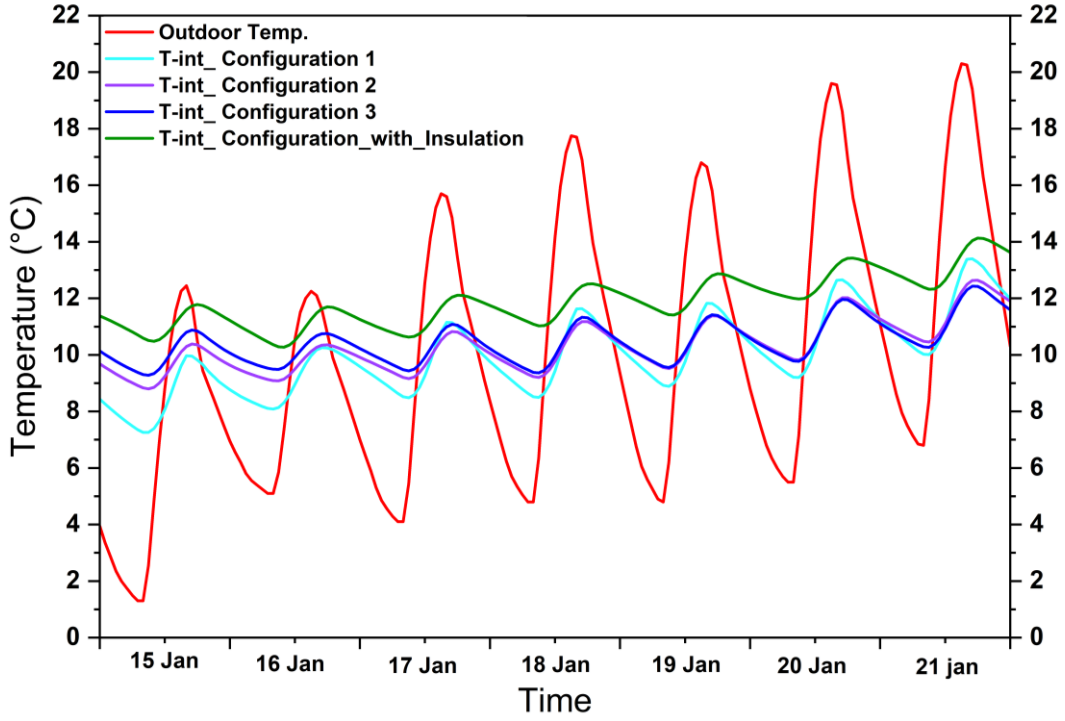

Figure 8. Indoor air temperature during the winter from January 15 to 21, 2024, under extreme outdoor conditions ranging from -1 °C to 22.5 °C.

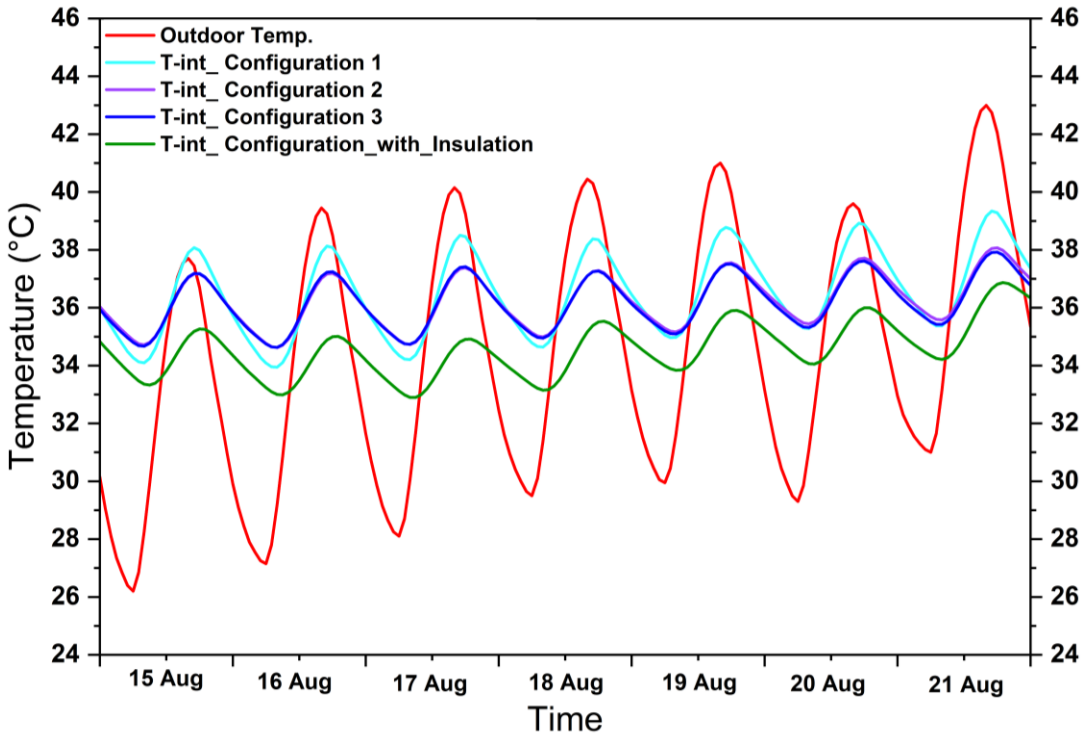

Figure 9. Indoor air temperature during the winter from August 15 to 21, 2024, under extreme outdoor conditions ranging from 26.2 °C to 43 °C.

3.3.Effect of Insulation on energy requirements

Figures 10 and 11 present the annual and monthly energy requirements for cooling and heating, respectively, across the various wall configurations studied. A detailed analysis of the results reveals that integrating 0.1 m thick thermal insulation panels between two layers of adobe

significantly lowers energy demand, particularly for cooling. The insulated configuration decreases cooling requirements from 8,855 to 6,802.3 kWh, representing a 23.18% improvement compared to the initial configuration (Configuration 1). Similarly, heating requirements drop from 7,265 to 4,359.38 kWh, marking a 40.00% reduction.

These findings emphasize the effectiveness of insulation panels in enhancing the thermal performance of walls, especially in hot, dry climates. In contrast, walls without insulation (Configurations 1, 2, and 3) exhibit lower performance, with only modest reductions achieved through increased wall thickness. Thus, incorporating ecological insulation between two layers of adobe proves to be an optimal solution for improving energy efficiency and thermal comfort in traditional buildings.

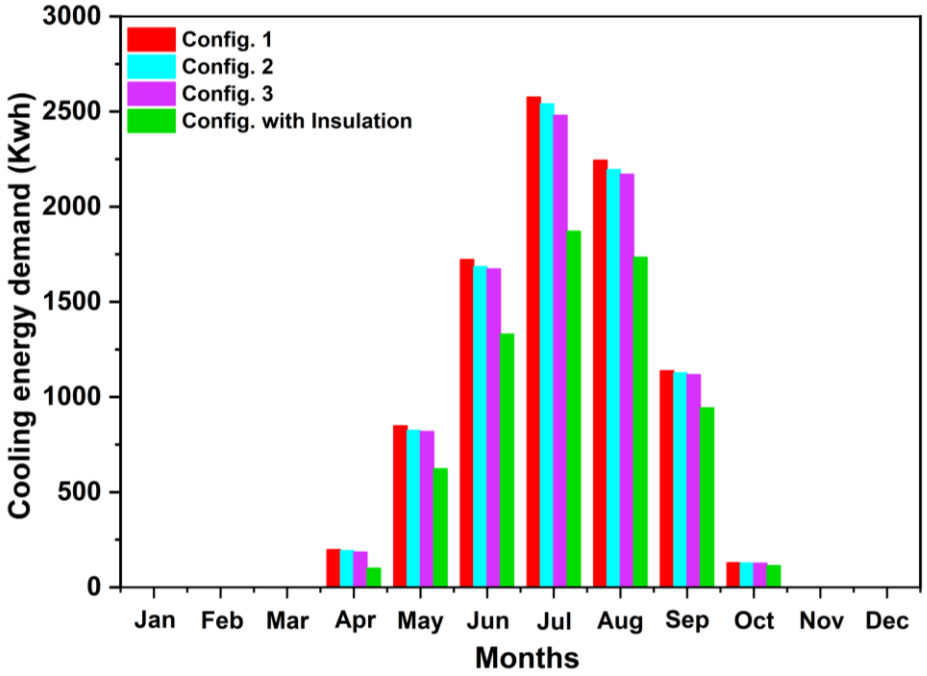

Figure 10. Energy requirements for cooling in 2024 for the city of Errachidia.

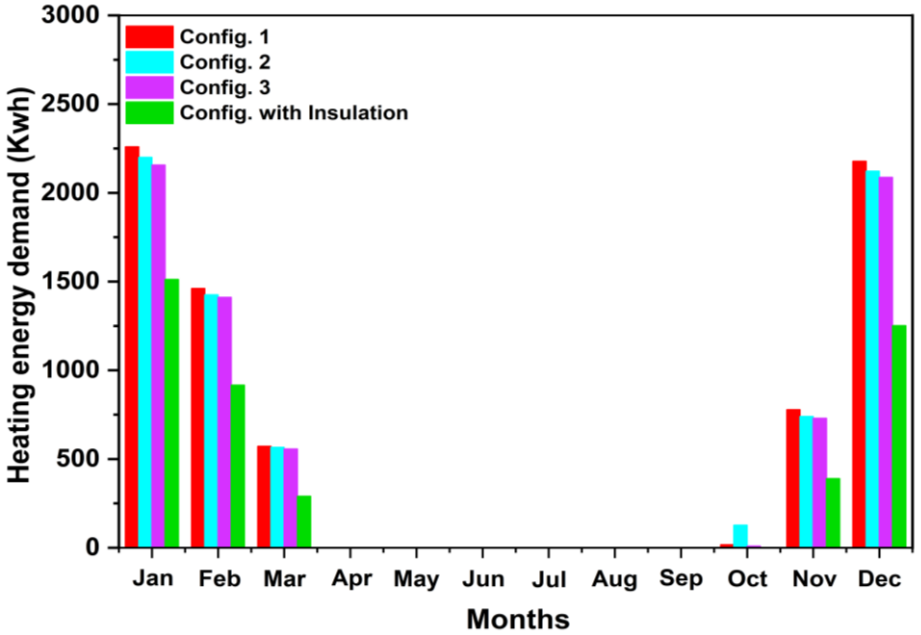

Figure 11. Energy requirements for heating in 2024 for the city of Errachidia.

4. CONCLUSION

This study highlights the advantages of integrating eco-friendly insulation panels with traditional adobe walls to enhance thermal performance and energy efficiency in hot desert climates. The simulations demonstrate that adding 0.1 meters of insulation between adobe layers significantly improves indoor thermal comfort, reducing summer indoor temperature peaks by up to 3.7°C and maintaining winter temperatures at levels as high as 12.1°C, even under extreme outdoor conditions. The energy demand analysis further confirms the effectiveness of this approach, with cooling requirements reduced by 23.18% and heating needs by 40% compared to non-insulated configurations. These findings underscore the superior thermal regulation provided by insulated adobe walls, particularly in climates with significant temperature fluctuations.

Moreover, the use of locally sourced materials, such as adobe and bio-composite insulation made from date palm fiber and cardboard, supports sustainable construction practices. This method not only enhances building performance but also minimizes environmental impact, aligning with the principles of environmentally responsible architecture.

However, this study is limited to the thermal performance of insulated adobe walls in single-story buildings under a hot desert climate. Future research should extend its scope to multi-story buildings and assess performance under real-time climatic variations. This could involve integrating adaptive insulation strategies that respond dynamically to seasonal changes, thereby improving the general applicability of these solutions. Additionally, the combination of bio-based insulation with phase change materials (PCMs) could be explored to further enhance thermal inertia and energy efficiency. Finally, a life cycle assessment (LCA) and a cost-benefit analysis should be conducted to evaluate the long-term environmental and economic impact of these solutions, ensuring their scalability for widespread adoption in sustainable construction.

In summary, this study offers valuable insights into optimizing traditional construction techniques with modern, sustainable solutions. It provides practical guidelines for designing energy-efficient, climate-resilient structures suitable for desert regions.

Author Contributions: Abdelmounaim Alioui: Writing – original draft, Data curation, Methodology, Conceptualization; Youness Azalam: Data curation, Software, Methodology, Conceptualization, Mohammed Benfars: Writing – original draft Software, Methodology; El Maati Bendada: Project administration, Supervision; Mustapha Mabrouki: Project administration, Supervision, Writing – review & editing.

Funding source: The authors have not disclosed any funding.

Data Availability Statement: Not applicable.

Conflicts of Interest: The authors declare no conflicts of interest.

Acknowledgements: This work was supported by the industrial and surface engineering laboratory of the Faculty of Science and Technology of Béni Mellal, Morocco.

REFERENCES

[1] *X. Li, L. C. Stringer, and M. Dallimer, "The Impacts of Urbanisation and Climate Change on the Urban Thermal Environment in Africa," Climate 2022, Vol. 10, Page 164, vol. 10, no. 11, p. 164, Oct. 2022, doi: 10.3390/CLI10110164.*

[2] *Y. Han, J. Li, X. Lou, C. Fan, and Z. Geng, "Energy saving of buildings for reducing*

carbon dioxide emissions using novel dendrite net integrated adaptive mean square gradient," Appl. Energy, vol. 309, p. 118409, Mar. 2022, doi: 10.1016/J.APENERGY.2021.118409.

[3] *A. Alioui, Y. Azalam, M. Benfars, E. M. Bendada, and M. Mabrouki, "Comparative analysis of energy performance between clay-based and conventional building materials: A case study in Moroccan semi-arid climate," E3S Web of Conferences, vol. 582, p. 01005, Oct. 2024, doi: 10.1051/E3SCONF/202458201005.*

[4] *N. Es-sakali et al., "Energy efficiency and hygrothermal performance of hemp clay walls for Moroccan residential buildings: An integrated lab-scale, in-situ and simulation-based assessment," Appl. Energy, vol. 352, p. 121967, Dec. 2023, doi: 10.1016/J.APENERGY.2023.121967.*

[5] *J. W. Lee, H. J. Jung, J. Y. Park, J. B. Lee, and Y. Yoon, "Optimization of building window system in Asian regions by analyzing solar heat gain and daylighting elements," Renew. Energy, vol. 50, pp. 522–531, Feb. 2013, doi: 10.1016/J.RENENE.2012.07.029.*

[6] *A. Alioui, S. Idrissi Kaitouni, M. Benfars, Y. Azalam, E. M. Bendada, and M. Mabrouki, "Effects of alfalfa fibers on the thermophysical properties of carbon-free adobe bricks to improve the energy efficiency of buildings in hot and semi-arid climates: an innovative approach to sustainable construction," Journal of Building Pathology and Rehabilitation 2026 11:2, vol. 11, no. 2, pp. 132-, Mar. 2026, doi: 10.1007/s41024-026-00808-8.*

[7] *A. Alioui, S. Idrissi Kaitouni, Y. Azalam, N. Al armouzi, E. M. Bendada, and M. Mabrouki, "Effect of straw fibers addition on hygrothermal and mechanical properties of carbon-free adobe bricks: From material to building scale in a semi-arid climate," Build. Environ., vol. 255, p. 111380, May 2024, doi: 10.1016/J.BUILDENV.2024.111380.*

[8] *A. Laborel-Préneron, C. Magniont, and J. E. Aubert, "Hygrothermal properties of unfired earth bricks: Effect of barley straw, hemp shiv and corn cob addition," Energy Build., vol. 178, pp. 265–278, Nov. 2018, doi: 10.1016/J.ENBUILD.2018.08.021.*

[9] *Y. Azalam, A. Alioui, N. Al Armouzi, M. Benfars, M. Mabrouki, and E. M. Bendada, "Physical and mechanical properties of adobe bricks reinforced by natural additives, a case study of alfalfa fibers," EUREKA: Physics and Engineering, vol. 2024-July, no. 4, pp. 144–159, Jul. 2024, doi: 10.21303/2461-4262.2024.003426.*

[10] *S. Ajouguim et al., "Effect of Alfa fibers on the mechanical and thermal properties of compacted earth bricks," Mater. Today Proc., vol. 37, pp. 4049–4057, Jan. 2021, doi: 10.1016/J.MATPR.2020.07.539.*

[11] *Y. Azalam, M. Benfars, A. Alioui, M. Mabrouki, and E. M. Bendada, "Improving Adobe's Mechanical Properties through Sawdust Reinforcement: A Comparative Study of the effect of varying Sawdust Dimensions," E3S Web of Conferences, vol. 582, p. 02005, Oct. 2024, doi: 10.1051/E3SCONF/202458202005.*

[12] *A. Alioui et al., "Prediction and optimization of the thermomechanical performance of carbon-free Adobe bricks reinforced with straw and sawdust using machine learning," Sci. Afr., vol. 31, p. e03167, Mar. 2026, doi: 10.1016/J.SCIAF.2025.E03167.*

[13] *A. Eslami, H. Mohammadi, and H. Mirabi Banadaki, "Palm fiber as a natural reinforcement for improving the properties of traditional adobe bricks," Constr. Build. Mater., vol. 325, p. 126808, Mar. 2022, doi: 10.1016/J.CONBUILDMAT.2022.126808.*

[14] *M. Ouedraogo et al., "Physical, thermal and mechanical properties of adobes stabilized with fonio (Digitaria exilis) straw," Journal of Building Engineering, vol.*

23, pp. 250–258, May 2019, doi: 10.1016/J.JOBE.2019.02.005.

[15] *H. Limami et al., "Thermophysical and Mechanical Assessment of Unfired Clay Bricks with Dry Grass Fibrous Filler," Int. J. Thermophys., vol. 43, no. 8, pp. 1–15, Aug. 2022, doi: 10.1007/S10765-022-03043-8/METRICS.*

[16] *M. S. Al-Homoud, "Performance characteristics and practical applications of common building thermal insulation materials," Build. Environ., vol. 40, no. 3, pp. 353–366, Mar. 2005, doi: 10.1016/J.BUILDENV.2004.05.013.*

[17] *A. Benallel, A. Tilioua, and M. Garoum, "Development of thermal insulation panels bio-composite containing cardboard and date palm fibers," J. Clean. Prod., vol. 434, p. 139995, Jan. 2024, doi: 10.1016/J.JCLEPRO.2023.139995.*

[18] *H. R. Kymäläinen and A. M. Sjöberg, "Flax and hemp fibres as raw materials for thermal insulations," Build. Environ., vol. 43, no. 7, pp. 1261–1269, Jul. 2008, doi: 10.1016/J.BUILDENV.2007.03.006.*

[19] *P. Brzyski, P. Kosiński, A. Skoratko, and W. Motacki, "Thermal properties of cellulose fiber as insulation material in a loose state," AIP Conf. Proc., vol. 2133, no. 1, Jul. 2019, doi: 10.1063/1.5120136/766766.*

[20] *F. Abedom, S. Sakthivel, D. Asfaw, B. Melese, E. Solomon, and S. S. Kumar, "Development of Natural Fiber Hybrid Composites Using Sugarcane Bagasse and Bamboo Charcoal for Automotive Thermal Insulation Materials," Advances in Materials Science and Engineering, vol. 2021, no. 1, p. 2508840, Jan. 2021, doi: 10.1155/2021/2508840.*

[21] *P. Ricciardi, E. Belloni, F. Merli, and C. Buratti, "Sustainable Panels Made with Industrial and Agricultural Waste: Thermal and Environmental Critical Analysis of the Experimental Results," Applied Sciences 2021, Vol. 11, Page 494, vol. 11, no. 2, p. 494, Jan. 2021, doi: 10.3390/APP11020494.*

[22] *I. Neya, D. Yamegueu, Y. Coulibaly, A. Messan, and A. L. S. N. Ouedraogo, "Impact of insulation and wall thickness in compressed earth buildings in hot and dry tropical regions," Journal of Building Engineering, vol. 33, p. 101612, Jan. 2021, doi: 10.1016/J.JOBE.2020.101612.*

[23] *F. Changizi and A. Haddad, "Strength properties of soft clay treated with mixture of nano-SiO2 and recycled polyester fiber," Journal of Rock Mechanics and Geotechnical Engineering, vol. 7, no. 4, pp. 367–378, Aug. 2015, doi: 10.1016/J.JRMGE.2015.03.013.*

[24] *H. Limami, I. Manssouri, K. Cherkaoui, and A. Khaldoun, "Study of the suitability of unfired clay bricks with polymeric HDPE & PET wastes additives as a construction material," Journal of Building Engineering, vol. 27, p. 100956, Jan. 2020, doi: 10.1016/J.JOBE.2019.100956.*

[25] *A. Elgamouz, N. Tijani, I. Shehadi, K. Hasan, and M. Al-Farooq Kawam, "Characterization of the firing behaviour of an illite-kaolinite clay mineral and its potential use as membrane support," Heliyon, vol. 5, no. 8, Aug. 2019, doi: 10.1016/j.heliyon.2019.e02281.*

[26] *J. Meseguer, I. Pérez-Grande, and A. Sanz-Andrés, "Conductive heat transfer," Spacecraft Thermal Control, pp. 59–71, Jan. 2012, doi: 10.1533/9780857096081.59.*

Solar Energy
and Sustainable Development
Refereed, biannual scientific journal issued by
The Libyan Center for Solar Energy Research and Studies

DFT Analysis of Structural, Elastic and Optoelectronic Enhancements in $LiGeCl_3$ Under Pressure for Photovoltaic Applications

Mohammed Miri [1*], Younes Ziat [2], Hamza Belkhanchi [3], Abdellah Bouzaid [4], Youssef Jouad [5], Youssef Ait El Kadi [6]

[1, 2, 3, 4, 5] Engineering and Applied Physics Laboratory (EAPL), Superior School of Technology, Sultan Moulay Slimane University, Beni Mellal, Morocco

[1, 2, 3, 4, 5] The Moroccan Association of Sciences and Techniques for Sustainable Development (MASTSD), Beni Mellal, Morocco

[6] Engineering Sciences and Energy Management Laboratory, Higher School of Technology, Ibn Zohr University, Agadir, Morocco

E-*mail:* [1]miri.estbm@gmail.com

SPECIAL ISSUE ON.

The 1St International Conference on Sciences and Techniques for Renewable Energy and the Environment. (STR2E 2025) May 6-8, 2025 at FST-Al Hoceima-Morocco.

KEYWORDS

Absorption; Optical properties; semiconductor; perovskite.

ABSTRACT

This study focuses on the crystalline lithium-based perovskite material, $LiGeCl_3$, with a view to improving its structural, elastic, electronic and optical properties by exploiting the effect of hydrostatic pressure. Combining density of states (DOS and PDOS) analysis with DFT and GGA approximation results, it is shown that the application of pressure reduces the lattice parameter, enhancing self-cohesion and stabilising the atomic structure. At ambient pressure, $LiGeCl_3$ exhibits semiconducting properties with a direct band gap, dominated by the p-orbitals of Cl atoms in the valence band and Ge in the conduction band. Under increasing pressure (0 to 6 GPa), the band gap is progressively reduced until it disappears at 6 GPa, leading to an electronic transition from a semiconducting to a metallic state.

This transition results from the compression of the crystal lattice, which intensifies orbital interactions and causes the valence and conduction bands to overlap. In addition, pressure significantly enhances the optoelectronic properties of $LiGeCl_3$, including absorption in the visible spectrum, spectral reflectivity and refractive index, making the material more suitable for photovoltaic applications. These results highlight the potential of $LiGeCl_3$ in engineering advanced materials for semiconductor and optoelectronic devices, while demonstrating the crucial role of hydrostatic pressure as a tool for modulating material properties.

*Corresponding author.

DOI: https://doi.org/10.51646/jsesd.v14iSTR2E.1181

This is an open access article under the CC BY-NC license (http://Attribution-NonCommercial 4.0 (CC BY-NC 4.0)).

تحليل DFT للتحسينات الهيكلية والمرنة والبصرية الإلكترونية في $LiGeCl_3$ تحت الضغط لتطبيقات الطاقة الكهروضوئية

محمد ميري، يونس زيات، حمزة بلخنشي، عبد الله بوزايد، يوسف جواد، يوسف ايت القاضي

ملخص: تركز هذه الدراسة على مادة بيروفسكايت الليثيوم البلورية القائمة على الليثيوم، $LiGeCl_3$، بهدف تحسين خصائصها الهيكلية والمرنة والإلكترونية والبصرية من خلال استغلال تأثير الضغط الهيدروستاتيكي. من خلال الجمع بين تحليل كثافة الحالات (DOS وPDOS) مع نتائج تحليل DFT وتقريب GGA، يظهر أن تطبيق الضغط يقلل من معامل الشبكة، مما يعزز التماسك الذاتي ويثبت البنية الذرية. عند الضغط المحيط، يُظهر $LiGeCl_3$ خصائص شبه موصلة مع فجوة نطاق مباشرة، تهيمن عليها المدارات p لذرات Cl في نطاق التكافؤ وGe في نطاق التوصيل. تحت ضغط متزايد (من 0 إلى 6 جيجا باسكال)، تتقلص فجوة النطاق تدريجيًا حتى تختفي عند 6 جيجا باسكال، مما يؤدي إلى انتقال إلكتروني من حالة شبه موصلة إلى حالة معدنية. وينتج هذا الانتقال من انضغاط الشبكة البلورية التي تكثف التفاعلات المدارية وتتسبب في تداخل نطاقات التكافؤ والتوصيل. وبالإضافة إلى ذلك، يعزز الضغط بشكل كبير من الخصائص الإلكترونية الضوئية لـ $LiGeCl_3$، بما في ذلك الامتصاص في الطيف المرئي والانعكاسية الطيفية ومعامل الانكسار، ما يجعل المادة أكثر ملاءمة للتطبيقات الكهروضوئية. وتسلط هذه النتائج الضوء على إمكانات $LiGeCl_3$ في هندسة المواد المتقدمة لأشباه الموصلات والأجهزة الإلكترونية الضوئية، مع إظهار الدور الحاسم للضغط الهيدروستاتيكي كأداة لتعديل خصائص المواد.

الكلمات المفتاحية: الامتصاص؛ الخواص البصرية؛ أشباه الموصلات؛ البيروفسكايت.

1. INTRODUCTION

Today's environmental challenges, such as dependence on unsustainable energy sources and their negative impact on the environment, call for innovative, ecosystem-friendly solutions [1]. Energy transition has become a global priority, with growing interest in the development and adoption of renewable energies, notably photovoltaics and wind power. These technologies offer a unique opportunity to produce clean energy while significantly reducing greenhouse gas emissions, by harnessing abundant natural resources such as solar cells and wind [2, 3, 4].

In this context, solar cells occupy a central position as key solutions for sustainable energy [5]. They have been the focus of intensive research aimed at fully exploiting their potential for converting solar energy into electricity. This work has focused on analyzing the intrinsic properties of photovoltaic materials, in particular their photonic and photoluminescent characteristics, which play a crucial role in improving their efficiency and durability [6]. This in-depth exploration has also uncovered other remarkable properties of the materials used, including their ability to be integrated into advanced devices such as lasers, radiation detectors or thermoelectric systems [7, 8, 9].

Among these materials, perovskites have attracted particular interest thanks to their unique chemical structure and great versatility [10, 11, 12]. Their ABX_3 structure (where "A" and "B" are metal cations and "X" is an anion, often a halogen) gives these materials exceptional properties for photovoltaic applications [13]. For example, studies on $CsXCl_3$ perovskites (X = Sn, Pb) have demonstrated a clear relationship between their lattice parameter and their band gap, establishing a direct link between their crystal structure and their electronic properties [14]. These results underline the importance of theoretical modeling in understanding the fundamental behavior of materials.

With this in mind, density functional theory (DFT) has established itself as an essential tool for analyzing the properties of materials, particularly in the field of perovskites [15, 16].

Beyond the study of intrinsic characteristics, the application of hydrostatic pressure has been identified as a promising lever for tuning and optimizing electronic, optical and mechanical properties. Work on $AGeF_3$ compounds (A = K, Rb) has revealed that pressure can significantly enhance atomic interactions, thereby modifying elastic constants, band gap and other key properties [10, 17, 18, 19]. These results demonstrate that by manipulating external conditions, such as pressure, materials can be optimized to meet the requirements of advanced technological applications [20, 21, 22].

During this time, the $LiGeCl_3$ production is a study and comparison with other theoretical analytical elements and experiments. It does not work because there is no experimental solution available regarding the crystalline structure and the proprietary electronics of $LiGeCl_3$. This signifies the limit of the original approximation and simulation numbers to improve these properties. In the absence of experimental research, we have discovered that the first exploration theory of $LiGeCl_3$ will be visible to future experimental investigations that reveal these results [23, 24]. $LiGeCl_3$ differs from other metal halides in its more gradual and controlled phase transitions under pressure, allowing for finer modulation of optoelectronic properties. Unlike the halide perovskites $CsPbCl_3$ and $RbGeCl_3$, which undergo more abrupt and less stable transitions [25, 26, 27, 28], $LiGeCl_3$ offers greater flexibility and reliability, opening the way for applications in high-pressure environments requiring optimal optical and electronic stability. $LiGeCl_3$ offers precise and stable control of its electronic and optical properties under pressure, unlike more unstable perovskites. Its gradual phase transitions give it better adaptability to extreme environments, ensuring increased durability and reliability for high-pressure applications.

In this context, this study focuses on $LiGeCl_3$ perovskite, a particularly promising material for photovoltaic and optoelectronic technologies [29]. Using density functional theory, we analyze its optoelectronic, mechanical and elastic properties, taking into account the effect of pressure. The application of pressure leads to significant changes in crystal structure, lattice parameters and chemical bonding, resulting in notable improvements in material performance. By exploring these aspects, this research contributes to an in-depth understanding of the relationships between lattice parameters, band gap and mechanical stability under pressure. This knowledge paves the way for optimizing perovskites for next-generation energy and technology applications, responding to the growing need for sustainability and efficiency in renewable energies.

2. CALCULATION METHOD

To study the characteristics of the $LiGeCl_3$ material, density functional theory (DFT) was used, based on the WIEN2k code, known for its precision in modeling crystalline materials [30, 16, 11, 12]. This method is based on linearized full potential augmented waves (FP-LAPW), enabling detailed analysis of electronic, structural and optical properties. To describe exchange and correlation interactions, the generalized gradient approximation (GGA), based on the Perdew-Burke-Ernzerhof (GGA-PBE) formalism, has been applied [31, 32], this approach enables better modeling of electronic interactions by taking into account spatial variations in electron densities, thus improving the accuracy of predictions and making this methodology particularly suitable for the study of crystalline systems such as $LiGeCl_3$. To guarantee adequate

accuracy, the parameter RMTKmax, which corresponds to the product between the radius of the Muffin-Tin sphere and the maximum wave vector, was set to an optimum value after convergence tests. The radii of the Muffin-Tin spheres were adjusted for each atom, taking into account the dimensions of the crystal lattice. A dense k-point grid, based on the Monkhorst-Pack method, was used to sample the Brillouin zone with optimized density, guaranteeing reliable results for total energies and electronic properties. The static calculations for the $LiGeCl_3$ material were performed with a dense mesh of 1000 k-points and energy convergence limit of 10^{-5} Ry to ensure accuracy. The relation $RMT.K_{max} = 7$ was used to optimize the calculation basis and balance accuracy and efficiency. The atomic sphere radii (RMT) for Li, Ge, and Cl atoms are 2.50, 2.50 and 2.32, respectively.

The effect of hydrostatic pressure was simulated by applying uniform stresses to the optimized crystal cell. Calculations were carried out for pressures ranging from 0 GPa to 6 GPa, with regular increments, and at each step, a complete optimization of the geometry enabled the total energy to be minimized and the lattice parameters to be readjusted according to the applied stresses. This approach made it possible to explore variations in electronic, optical and mechanical properties under pressure.

Electronic properties were studied through electronic band structures and densities of states, enabling the evolution of the band gap with pressure to be monitored. Optical properties, such as absorption coefficient, refractive index and complex dielectric function, were calculated taking into account state-dependent electronic transitions. Elastic constants were also determined by applying small strains to the optimized lattice parameters, enabling mechanical stability to be assessed and material stiffness variations to be analyzed under stress.

Thanks to this methodology, it has been possible to provide a comprehensive analysis of the fundamental properties of $LiGeCl_3$, highlighting its optoelectronic and mechanical behavior under various pressure conditions. These results are essential for optimizing the performance of this material in advanced technological applications, notably in photovoltaic and optoelectronic devices.

3. RESULTS AND DISCUSSION

3.1. Structural Properties

The cubic structure of $LiGeCl_3$ belongs to the class of single-halide inorganic perovskites, renowned for their unique crystallographic arrangement and remarkable properties. As illustrated in Figure 1, the crystal structure of $LiGeCl_3$ consists of a unit cell containing five distinct atoms. The geometric configuration and precise arrangement of these atoms play a decisive role in the material's optoelectronic and mechanical properties.

Inorganic perovskites based on metal halides, such as $LiGeCl_3$, are particularly valued for their high symmetry and structural stability. These features make them ideal for theoretical research using advanced computational methods such as density functional theory (DFT), as well as for practical applications in fields such as photovoltaic and optoelectronic devices. The simplicity of the cubic structure provides a solid basis for modeling and predicting material performance under a variety of conditions. In this cubic structure, which belongs to space

group 221 (Pm3m), the Li cation is located in (0, 0, 0), the metal cation Ge in (0.5, 0.5, 0.5), and the Cl anions are arranged in (0.5, 0, 0.5), (0.5, 0.5, 0) and (0, 0.5, 0.5) according to Wyckoff coordinates [33]. The unit cell characterized by lattice parameter of $LiGeCl_3$ is a0= 5.21 Å, these values corresponding to the theoretical values in which a0= 5.19 Å [34]. This perfectly symmetrical and balanced arrangement is essential for maintaining the material's structural and electronic properties.

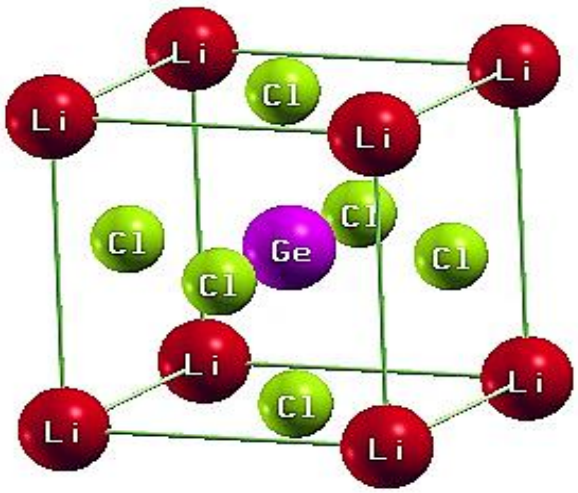

Figure 1: Structure crystalline of $LiGeCl_3$

Detailed understanding of this atomic structure provides a valuable basis for exploring the relationships between structure and material properties, such as mechanical stability, elastic constants and electronic transitions. These fundamental characteristics confirm $LiGeCl_3$'s potential as a key material for many modern technological applications, particularly in the fields of energy and advanced electronics.

To optimize the material's stability and strength, the size of the unit cells was carefully adjusted while taking into account the total energy of the system. This approach has enabled us to determine the optimum structural parameters for stable crystal formation and low energy. The lattice parameter, which determines the dimensions of the unit cell, plays a crucial role in determining the overall properties of the material.

Precise total energy calculations were carried out by systematically varying the size of each unit cell. These variations were used to plot a characteristic energy-volume curve, describing the energy behavior of the crystal as a function of lattice compression or expansion. To analyze these data, the Birch-Murnaghan equation of state was used [35].

$$E = E_0 + \frac{B_0}{B_0'}(V - V_0) - \frac{B_0 V_0}{B_0'(1-B_0')}\left[\left(\frac{V}{V_0}\right)^{1-B_0'} - 1\right] \quad (1)$$

This equation offers a robust theoretical framework for modeling the relationship between energy, volume and pressure in crystalline solids, and is particularly well suited to describing behavior under high pressure or extreme conditions, providing valuable information on the structural stability of materials.

By minimizing the total energy E while optimizing the volume V of the unit cell, the

optimal values of two critical parameters, the mass modulus B and its derivative B′ at zero pressure, have been determined (see Figure 2). These two parameters provide essential information on the mechanical response of the material and are crucial for designing strong, stable structures.

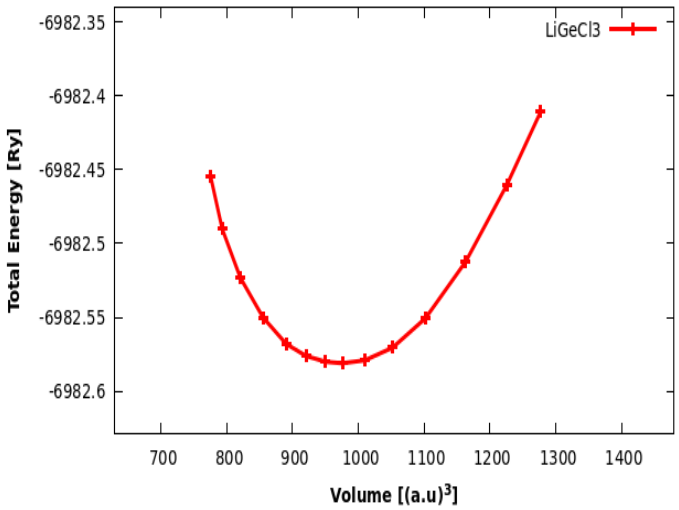

Figure 2 : Variation of total energy as a function of volume for $LiGeCl_3$

The mass modulus B, which measures the material's resistance to compression, is particularly important for applications requiring strength and durability. A high value of B indicates high stiffness. The derivative B′, representing the variation of B under pressure, provides additional information on the material's thermoplastic and elastic properties, such as ductility and crystalline rigidity [36]. Simultaneous optimization of B and B′ improves the overall strength of the material and its ability to resist deformation under stress.

Table 1 summarizes the optimized parameters E, V, B, and B′, providing an overview of the structural performance of $LiGeCl_3$. These results also enable relevant comparisons between different materials and crystal configurations, contributing to a better understanding of structure-property relationships.

Table1: Lattice parameters and gap energy as a function of pressure of $LiGeCl_3$

Lattice Parameter a_0 (Å)		E (Ry)	V (a.u)^3	B (GPa)	(B')
Optimized	Other				
5.21	5.19 [34]	970.77	6982.58	28.97	4.71

The dependence of the cubic lattice constant on pressure was determined using the relationship established by according to the following formulae [37]:

$$P(V) = \frac{B_0}{B_0'}\left[\left(\frac{V_0}{V}\right)^{B_0'} - 1\right] \quad (2)$$

$$a_0 = (V(P))^{1/3} \quad (3)$$

Moreover, the results are summarized in Table 2.

Table 2: Lattice parameter and gap energy versus pressure.

Pressure (GPa)	Parameter a_0 (Å)	Energy Gap Eg (eV)
0	5.21	0.72
2	5.11	0.34
4	5.03	0.12
6	4.97	0.00

Hydrostatic pressure has a significant influence on the structural and electronic properties of materials such as $LiGeCl_3$. As pressure increases from 0 to 6 GPa, there is a steady decrease in the lattice parameters and cell volume, which results in a reduction of interatomic distances. This closer atomic proximity strengthens chemical bonds and enhances the repulsive forces between atoms, leading to greater rigidity and hardness in the crystal structure. These structural changes contribute to an improved mechanical response and increased resistance to crystalline compression under high pressure.

The influence of pressure on the electronic properties of $LiGeCl_3$ is equally notable. At zero pressure, the material exhibits a direct band gap of 0.72 eV, making it suitable for electronic and optoelectronic applications. However, with increasing pressure, the band gap undergoes significant changes. Initially, the band gap widens, reflecting the saturation of compression effects on electronic transitions, as observed in Table 2. Conversely, Table 2 illustrates that under the influence of PBE-GGA functions, the band gap decreases with increasing pressure, a behavior attributed to structural effects. The reduction in lattice constants narrows the atomic distances, intensifies electron-ion interactions, and increases the overlap of atomic orbitals. This leads to a decreased energy separation between the valence and conduction bands, thereby reducing the band gap.

These findings underscore the dual effects of hydrostatic pressure on both structural and electronic properties. While it enhances the material's strength and hardness by intensifying interatomic interactions, it simultaneously modifies electronic transitions, affecting its band gap characteristics. Such insights are crucial for applications requiring materials with stable structural and electronic properties under high-pressure conditions.

3.2. Elastic properties:

The elastic constants of solids represent fundamental parameters that make it possible to describe the mechanical behavior of materials. These constants characterize in particular the way in which a solid reacts to mechanical deformations under the influence of external stresses. In the case of crystals with a cubic structure, such as the studied sample $LiGeCl_3$, there are three independent elastic constants denoted C_{ij}, represented by C_{11} , C_{12} , and C_{44} [38]. These parameters play a fundamental role in assessing the mechanical stability of solids as well as the internal forces acting between their atoms. In addition, they make it possible to establish an accurate relationship between the mechanical properties (such as hardness) and the dynamic properties (such as the propagation of sound waves) of crystals [39]. In order to validate the mechanical stability of materials, the elastic coefficients must satisfy the stability criteria defined by Born [40]:

$$C_{11}+2C_{12} > 0,\ C_{11}-C_{12}>0,\ C_{11}> 0 \text{ and } C_{11}>B > C_{12} \quad (4)$$

The analysis of Table 3 clearly reveals a crystalline stability of $LiGeCl_3$, since the three parameters C_{11}, C_{12} and C_{44} respect the criteria of the limits previously defined. This confirms that the material studied is mechanically stable.

Table 3: Elastic constants of $LiGeCl_3$

Pressure	C_{11}	C_{12}	C_{44}	C_p
0 GPa	46.07	10.68	8.52	2.16
2 GPa	57.44	13.96	9.81	4.15
4 GPa	69.32	16.73	10.54	6.19
6 GPa	78.98	19.20	11.44	7.76

At 0 GPa, the elastic constants and mechanical properties of the material are in good agreement with previous theoretical analyses, thus confirming the validity of the results obtained [34, 23]. When the material is subjected to increasing pressures, ranging from 0 to 6 GPa, a progressive and significant increase in mechanical parameters is observed. This trend indicates a notable improvement in the strength and ductility of the material under compression. When examining the specific elastic constants, it is noted that the constants C_{11} and C_{12} increase at a faster rate than C_{44}. This difference is attributed to the fact that C_{11} ,and C_{12} are mainly influenced by the strengthening of atomic bonds in the longitudinal direction and between crystal planes. Under pressure, these bonds become stiffer, resulting in higher values of these constants. In contrast, C_{44}, which reflects the resistance of the material to shear deformation, shows a more moderate increase. This trend indicates that the flexibility related to shape deformations is less affected by pressure compared to longitudinal and transverse stresses. These disparities in the behavior of elastic constants highlight a complex interplay between the effects of pressure, the overall strength of the material, and its ability to deform without fracture. More specifically, pressure contributes to increasing the material hardness while adjusting its ductility properties, providing a balance between stiffness and flexibility [41]. This correlation is particularly important for applications where robust mechanical properties are required in high-stress environments.

The Cauchy pressure ($C_p=C_{12}-C_{44}$) is a key parameter for assessing the brittleness and ductility of materials, with a positive value indicating ductility and a negative value signaling brittleness [42]. For the perovskite $LiGeCl_3$, Cp remains positive at all pressures studied and increases with pressure, highlighting a progressive improvement in the ductility of the material with increasing pressure. The three moduli — bulk modulus (B), shear modulus (G), and elastic modulus (E) — are essential for evaluating elastic interactions within materials. These parameters help distinguish between ductile materials, which can absorb large amounts of energy before rupture, and brittle materials, which fail abruptly under stress without significant deformation. Such distinctions are critical for understanding how materials behave under mechanical stress, including their capacity to withstand collisions or resist catastrophic failure. These parameters offer a specific classification, adapting to diverse applications: ductile materials for use tolerant of deformations, such as structures, and fragile materials for stable and controlled environments [43]. This analysis provides a comprehensive framework for the design and selection of materials, as well as for industrial applications and technological advancements, in line with Hill's approximations [44, 45, 46].

$$B = \frac{C_{11} + 2C_{12}}{3} \quad (5)$$

$$G = \frac{G_V + G_R}{2} \quad (6)$$

$$E = \frac{9BG}{3B+G} \quad (7)$$

$$\nu = \frac{(3B-2G)}{3(2B+G)} \quad (8)$$

Or

$$G_V = \frac{C_{11} - 2C_{12} + 3C_{44}}{5} \quad (9)$$

$$G_R = \frac{5(C_{11} - C_{12})C_{44}}{4C_{44} + 3(C_{11} - C_{12})} \quad (10)$$

Table 4 shows the significant impact of pressure on the material's elasticity and mechanical strength parameters. As pressure increases, mechanical properties change significantly, reflecting an overall improvement in material performance. The incompressibility modulus (B), which measures the material's resistance to volumetric compression, increases from 22.47 GPa to 39.12 GPa, indicating improved resistance at higher pressures. At the same time, the shear modulus (G), which reflects the material's rigidity to shear-type deformation, increases from 11.47 GPa to 17.00 GPa, reflecting increased rigidity. Furthermore, the modulus of elasticity (E), an indicator of the material's overall capacity for reversible deformation, increased from 29.40 GPa to 44.54 GPa, underlining a significant improvement in its elastic properties.

Based on the moduli B, G and E, two ratios can be determined: Pugh (B/G) [47], and Poisson's ratio (ν), both considered as criteria that describe the proposed mechanical behavior of crystals. B/G and v are identified the brittleness and toughness of materials according to their critical values 1.75, and 0.26 [48], respectively. Whereas brittleness is indicated by a low value, ductility is linked to a high B/G ratio. Roughly 1.75 is the crucial number that divides materials into ductile and brittle categories; that is, (brittle < 1.75 < ductile) [49]. In addition, when Poisson's ratio is greater than 0.26, the material is ductile, and a larger value corresponds to a higher ductility [48]. Analysis of the B/G ratio, which rises from 1.96 to 2.30 at a pressure of 6 GPa, reveals a marked tendency for the material to become more ductile under pressure. This trend is corroborated by the increase in Poisson's ratio (ν), which rises from 0.261 to 0.293. This increase indicates a better ability of the material to resist volumetric deformation, confirming a more ductile behavior as pressure increases.

These results show that the application of pressure simultaneously improves the material's stiffness and ductility, offering an optimum balance between these two properties, essential for applications requiring both mechanical strength and the ability to absorb deformation.

Table 4: The parameters of elastic

Pressure	B	G	E	B/G	v
0	22.47	11.47	29.40	1.96	0.261
2	28.45	13.57	35.12	2.09	0.275

4	34.26	15.35	40.06	2.22	0.286
6	39.12	17.00	44.54	2.30	0.293

3.3. Electronic Properties

The analysis of electronic structures is a fundamental tool for understanding the intrinsic properties of materials, in particular for examining the distribution of energy bands and their evolution under different external factors [50]. This study provides crucial information on the relative position of the top of the valence band (VB), the bottom of the conduction band (CB), and the precise location of the Fermi level. These data not only allow us to characterize the electronic states of a material, but also to differentiate between insulators, semiconductors and conductors according to their band structure. Furthermore, the detailed interpretation of electronic band structures provides information on conduction mechanisms, electron-lattice interaction, and the tailoring of materials' physical properties to technological applications, such as semiconductor devices, sensors, or optoelectronic systems.

In the case of the perovskite $LiGeCl_3$, the electronic band structure was studied under increasing hydrostatic pressures ranging from 0 to 6 GPa, as illustrated in Figure 3. At 0 GPa, the electronic structure at the R symmetry point in the Brillouin zone shows an energy gap of 0.72 eV between CB and VB, confirming that $LiGeCl_3$ is a direct band gap semiconductor. The valence band is well-defined and high, while the conduction band is relatively low, reinforcing its semiconducting behavior at ambient pressure (Figure 3(a)).

With increasing pressure, significant changes in band structure are observed. At 2 GPa and 4 GPa (Figure 3 (a and b)), the CB minimum shifts to lower energies, while the VB maximum remains localized at the R-point. This evolution, while reducing the value of the energy gap to 0.34 eV at 2 GPa and 0.12 eV at 4 GPa, demonstrates that $LiGeCl_3$ retains its direct band gap semiconducting character. However, beyond 4 GPa, the band gap progressively decreases until it becomes 0 ev at 6 GPa, at which point a major electronic transition is observed: the material changes from a semiconducting to a metallic state. This transformation is directly linked to the compression of the crystal lattice and the intensification of interactions between atoms.

Compression under high pressure tightens inter-atomic distances, enhancing interactions between neighboring atomic orbitals. This causes the conduction and valence bands to overlap, removing the energy barrier necessary for electron excitation. As a result, electrons become free to circulate in the crystal, transforming the material's electronic properties from semiconductor to metallic conductor, this phenomenon highlights the crucial impact of pressure on the modulation of electronic properties [51].

Pressure is also emerging as a powerful tool for fine-tuning the optical and electronic properties of crystalline materials. It allows controlled modification of key parameters such as band gap width, density of states and charge carrier mobility. This approach paves the way for the exploration of new states of matter, where phase transitions, changes in crystallographic symmetry, or even novel electronic behaviors can be observed under high pressure. From a practical perspective, the use of pressure in high-performance semiconductor engineering represents a bridge between fundamental research and technological applications.

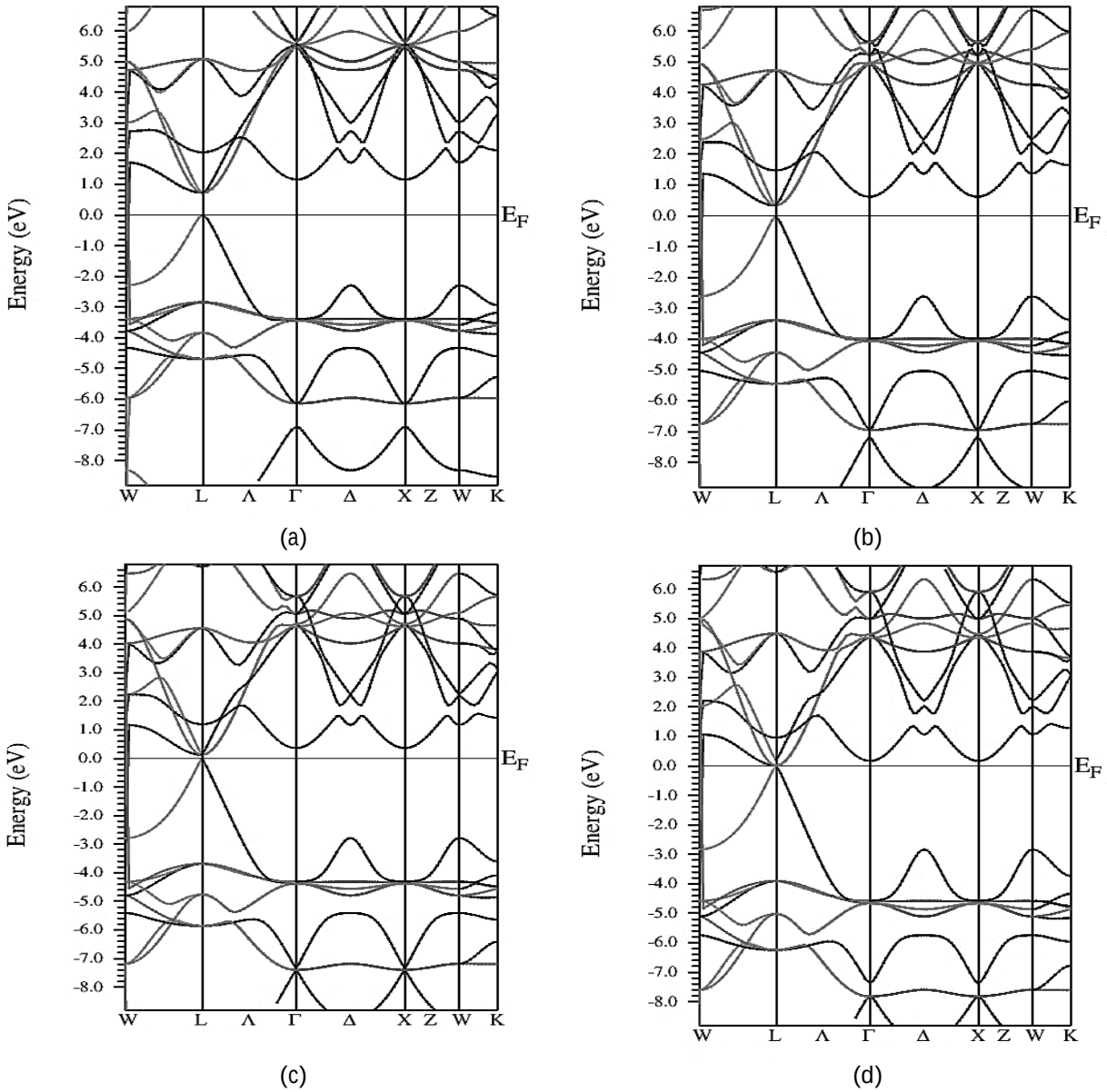

Figure 3 : Band structure at (a) 0, (b) 2, (c) 4 and (d) 6GPa

Figures 4 and 5 illustrate the densities of electronic states (DOS) and projected densities of states (PDOS) for $LiGeCl_3$ perovskite, highlighting the distribution of electronic states within the crystal lattice. These analyses identify the contribution of atoms and orbitals to specific energy levels, offering a detailed understanding of the electronic interactions and fundamental mechanisms of the material. While total density of states (TDOS) gives an overview of the electronic structure, PDOS attributes these contributions to specific atoms such as lithium (Li), germanium (Ge) and chlorine (Cl), and their respective orbitals (s, p and d). This differentiation is crucial to deciphering the atomic and orbital electronic interactions that underlie the fundamental properties of the material.

At zero pressure, the electronic structure of $LiGeCl_3$ reveals a dominance of the p-orbitals of chlorine (Cl) atoms in the valence band (VB), while the conduction band (CB) is mainly influenced by the p-orbitals of germanium (Ge) and to a lesser extent by the s-orbitals of lithium (Li). The main orbital peaks are located as follows: Li s-orbitals at around 3 eV (CB),

Ge p-orbitals at 2.8 eV and 4.5 eV (CB), and Cl p-orbitals at -3.5 eV and -4.5 eV (VB). These observations underline the central role of Ge in the electronic transition properties, as well as the importance of Cl in chemical bonding and balanced electronic interactions within the material. The Fermi level (EF), located just above the peak of the valence band, confirms that $LiGeCl_3$ has a semiconducting nature with a direct band gap. Under pressure, significant changes are observed in the electronic structure. With increasing pressure up to 6 GPa, the p-orbitals of Ge and Cl in the CB approach the Fermi level, reflecting enhanced electronic interaction due to crystal lattice compression. At the same time, the p-orbitals of Cl atoms in the VB shift to lower energies, from -3.5 eV and -4.5 eV to -4 eV and -6.1 eV respectively. These energy shifts reflect an electronic transfer that progressively reduces the band gap width and modifies the material's electronic properties.

Above a critical pressure of 4 GPa, the reduction of interatomic distances intensifies orbital interactions, leading to a significant shift of electronic levels, particularly the p orbitals of Ge and Cl, toward the Fermi level. As pressure increases, the overlap between atomic orbitals becomes more pronounced, increasing the density of states near the Fermi level and facilitating electron transitions to the conduction band. At 6 GPa, this culminates in a semiconductor-to-metal transition, where the band gap completely closes, and the material exhibits metallic conductivity [51]. This behavior, characteristic of materials undergoing significant crystalline compression, results from the enhanced overlap of electronic bands, allowing electrons to flow more freely and transforming $LiGeCl_3$ into a conductive metal.

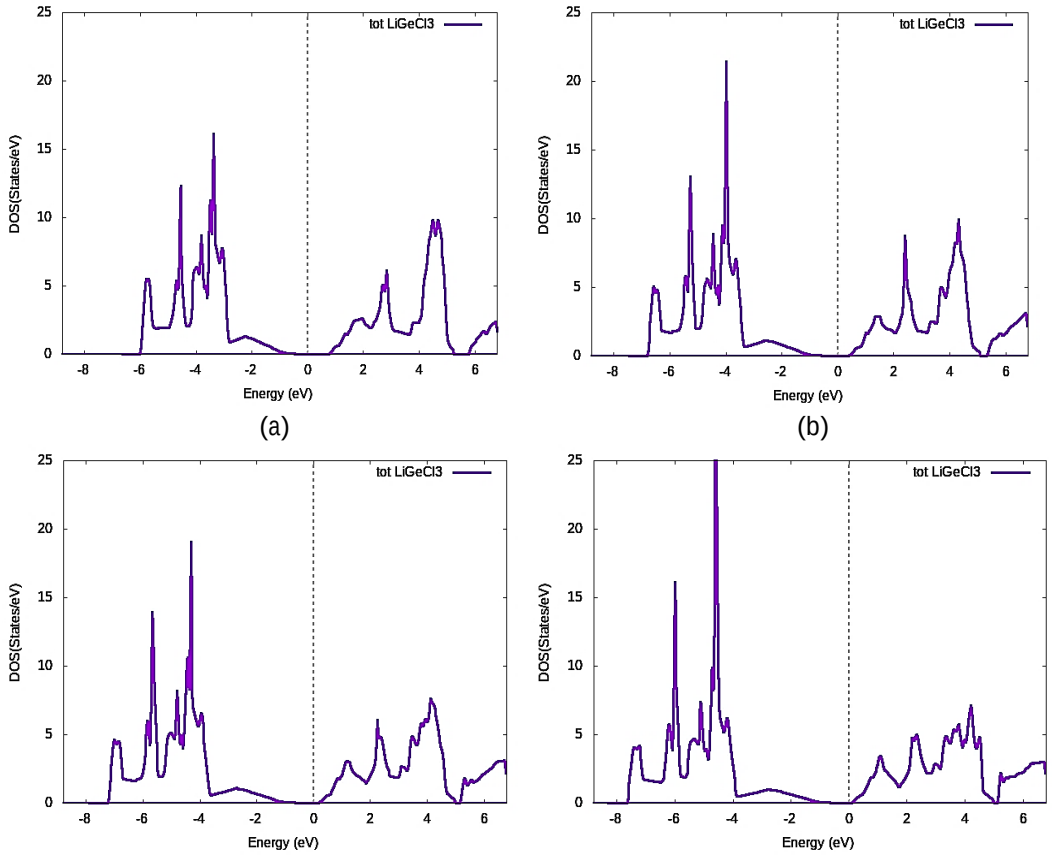

Figure 4: DOS for $LiGeCl_3$ at (a) 0, (b) 2, (c) 4 and (d) 6GPa.

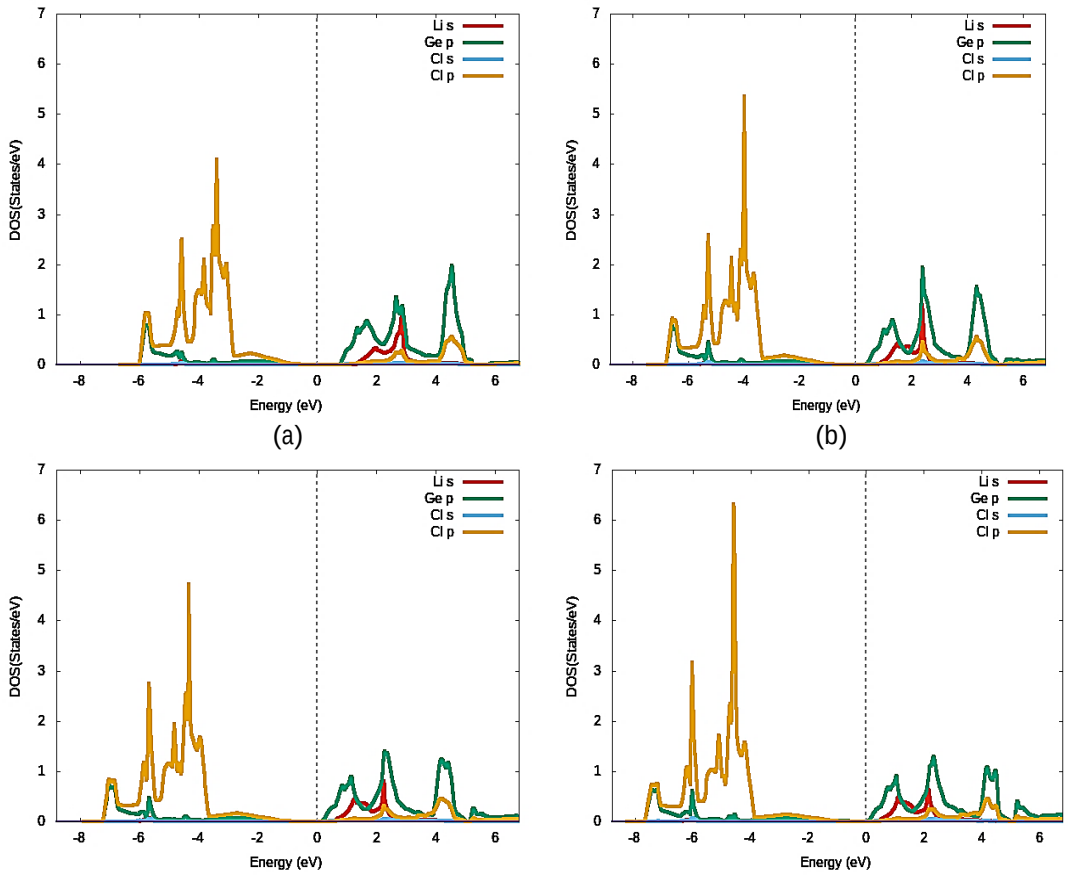

Figure 5: PDOS for $LiGeCl_3$ at (a) 0, (b) 2, (c) 4 and (d) 6GPa.

This pressure-induced phase transition illustrates the crucial role of hydrostatic pressure as a parameter for tuning the electronic and optical properties of materials. The application of pressure not only makes it possible to explore phase transitions and changes in crystallographic symmetry, but also to design materials with controlled electronic properties for advanced applications, notably in semiconductors, optoelectronic devices and pressure-sensitive systems. These results reinforce our understanding of electronic transition phenomena in condensed matter, and pave the way for potential applications in high-performance materials engineering.

3.4. Optical properties

The band gap values of the materials studied, located in the UV and visible ranges, confirm their promising potential for advanced optoelectronic applications. In particular, these materials offer interesting prospects for improving the performance of photovoltaic cells and solar panels, technologies at the heart of renewable energy solutions. The effect of hydrostatic pressure has proved to be a simple and effective method for modulating the electronic structures of materials and, consequently, optimizing their optical properties. In this context, we have examined $LiGeCl_3$ materials under the influence of induced pressure ranging from 0 to 6 GPa. Structural and electronic changes due to this pressure have a significant impact on several key optical properties such as absorption coefficient (α), optical conductivity (σ), reflectance (R) and refractive index (n). These results provide valuable information for the selection and development of new optoelectronic materials. [52, 11].

$$\alpha(\omega) = \sqrt{2}\omega\left[\sqrt{\varepsilon_1^2(\omega) + \varepsilon_2^2(\omega)} - \varepsilon_1(\omega)\right]^{\frac{1}{2}} \quad (11)$$

$$\sigma(\omega) = \frac{\omega}{4\pi}\varepsilon_2(\omega) \quad (12)$$

$$n(\omega) = \frac{1}{\sqrt{2}}\left[\sqrt{\varepsilon_1^2(\omega) + \varepsilon_2^2(\omega)} + \varepsilon_1(\omega)\right]^{\frac{1}{2}} \quad (13)$$

$$R(\omega) = \left|\frac{\sqrt{\epsilon(\omega)} - 1}{\sqrt{\epsilon(\omega)} + 1}\right|^2 \quad (14)$$

In addition, the evolution of optical conductivity and refractive index under pressure testifies to improved light-matter interactions, opening up prospects for applications in advanced photonic systems and integrated optoelectronic devices. These results also underline the importance of materials engineering under stress to tailor optical properties to specific application needs. The data obtained from this study provide valuable information for the design and development of new optoelectronic materials. In particular, the ability of these materials to respond to external pressures while modifying their optical properties represents a significant advance in research into multifunctional materials for next-generation technologies. These results encourage future investigations into the combined effects of pressure and chemical composition in the quest for even higher-performance materials.

The absorption coefficient α(ω) represents a fundamental quantity that quantifies the attenuation of light intensity per unit distance traveled in a material, and is directly related to electronic transitions between energy bands. Detailed analysis of absorption spectra provides essential information on the electronic and optical properties of the material, including its ability to interact with light in different spectral ranges [53]. Absorption spectra calculated for $LiGeCl_3$ under different hydrostatic pressures, shown in Figure 6, reveal significant trends. At ambient pressure (0 GPa), the material remains transparent to photons with energies below around 1.0 eV, corresponding to the band gap width. When the pressure is increased to 2 GPa, 4 GPa and 6 GPa, the absorption thresholds are reduced to 0.8 eV, 0.7 eV and 0.5 eV respectively, indicating a progressive narrowing of the band gap under the effect of pressure. This behavior reflects an increase in the overlap of electronic orbitals and an increased density of states near the Fermi level, favoring electronic transitions at lower energies. Beyond the absorption thresholds, α(ω) values increase progressively with photon energy, reaching maximum peaks of around $138*10^4.cm^{-1}$, $149*10^4.cm^{-1}$, $157*10^4.cm^{-1}$ and $165*10^4.cm^{-1}$ respectively for 0 GPa, 2 GPa, 4 GPa and 6 GPa, around 4 eV. These peaks indicate intense electronic transitions, mainly between valence bands dominated by the p-orbitals of chlorine atoms and conduction bands influenced by the p-orbitals of germanium and s-orbitals of lithium. After these maxima, a decrease in the absorption coefficient is observed, followed by a gradual increase to around 12 eV. This complex optical response is attributed to the diversity of electronic transitions available at high energies, involving electronic states located further away from the fundamental bands. A notable feature of these spectra is the overall shift of absorption peaks towards lower energies as pressure increases, a phenomenon consistent with

the narrowing of the band gap. This shift highlights the effect of hydrostatic pressure on the electronic structure of $LiGeCl_3$, resulting in a significant enhancement of light absorption, particularly in the visible and ultraviolet ranges. Thus, pressure induction appears to be an effective tool for optimizing the optical properties of $LiGeCl_3$, increasing its absorption efficiency in spectral ranges relevant to optoelectronic applications, such as photovoltaic cells and photodetectors. These results confirm the potential of this material in the development of advanced devices, where enhanced absorption in the visible and UV ranges is crucial to maximizing performance.

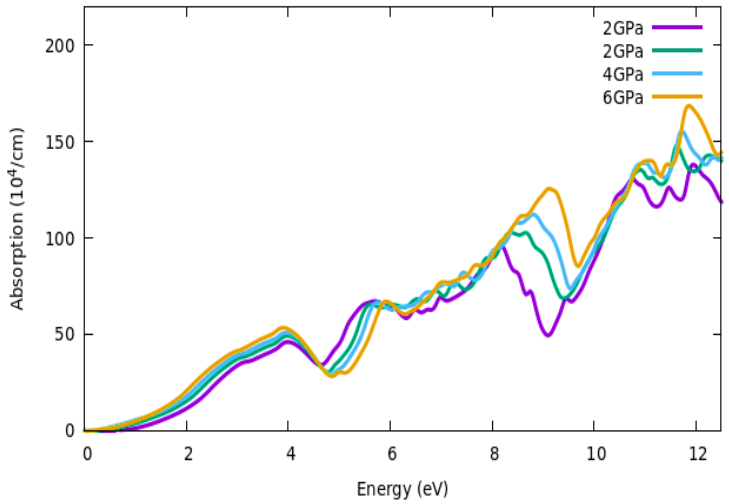

Figure 6: Absorption coefficient versus energy at 0, 2, 4 and 6 GPa for $LiGeCl_3$.

Figure 7 shows the optical conductivity ($\sigma(\omega)$) of $LiGeCl_3$, which reflects the material's ability to carry electric currents upon interaction with an electromagnetic field. Optical conductivity is directly related to interband electronic transitions and is a crucial indicator of the material's optoelectronic properties. In the energy range from 0 to 4 eV, optical conductivity increases steadily. This can be attributed to electronic transitions in the valence bands close to the Fermi level. This region is less influenced by pressure, suggesting that structural modifications due to hydrostatic compression do not significantly affect these low-energy transitions. However, when the photon energy exceeds 4 eV, the optical conductivity shows well-defined peaks that vary significantly in amplitude and position under the effect of pressure. These peaks, mainly located between 4 and 8 eV, are highly sensitive to increasing pressure. At 6 GPa, peak amplitudes are considerably higher than those observed at ambient pressure, indicating a redistribution of electronic states and an increased density of states available for high-energy interband transitions. This increase in the density of electronic states under pressure can be explained by the increased overlap of electronic orbitals in the compressed crystal lattice, leading to enhanced electronic transitions. Above 8 eV, optical conductivity reaches a saturation point, where it remains high but shows more subtle variations. This may indicate that the majority of electronic transitions accessible at high energies are saturated. In particular, the effect of pressure becomes more pronounced in this high energy range, especially at 6 GPa, where a significant increase in optical conductivity is observed. This increase is indicative of the improved optical and electronic behavior induced

by compression. Analysis of low energies (below 6 eV) reveals that the effect of pressure on optical conductivity remains limited. This suggests that the dominant electronic transitions in this range originate from bands relatively unaffected by pressure-induced structural changes. However, at high energies (above 6 eV), pressure-induced changes become significant, indicating a reorganization of the electronic structure and an increase in the density of available high-energy states. In conclusion, hydrostatic pressure proves to be an effective lever for modifying the electronic structure of $LiGeCl_3$, thereby increasing its optical conductivity, particularly in the high energy ranges. This behavior highlights a potential application in optoelectronic devices, where increased conductivity under pressure can be exploited as a performance factor. Enhanced electronic and optical properties under pressure could also open up interesting prospects for applications in extreme environments or devices requiring fast, efficient response at high energies.

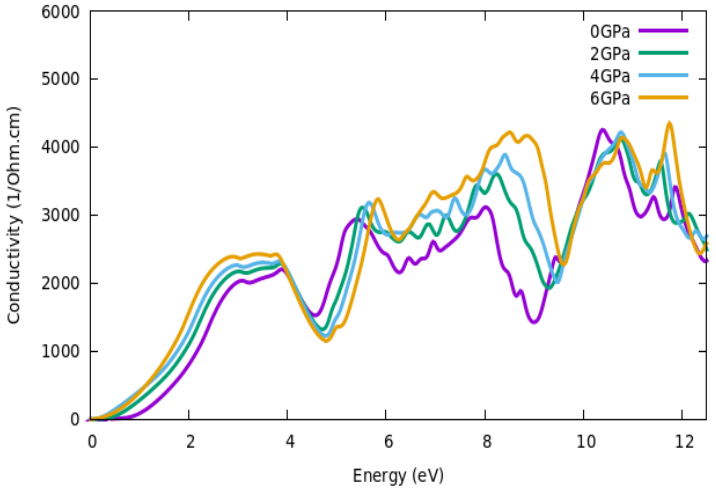

Figure 7: Conductivity versus energy at 0, 2, 4 and 6 GPa for $LiGeCl_3$.

Figure 8 shows the reflectance spectra (R(ω)) of $LiGeCl_3$ subjected to different hydrostatic pressures, highlighting the effect of compression on the optical properties of the material. Reflectance is a key property for characterizing interactions between incident light and the surface of a crystalline material, offering valuable information on optical reflection and absorption processes at the surface [54, 53]. At R(0), reflectance values increase with pressure, rising from 0.165 at 0 GPa to 0.252 at 6 GPa. This increase indicates an improvement in the material's ability to reflect low-energy light, which can be attributed to the change in electron density near the surface under compression. This trend could also reflect an increase in the actual refractive index, often correlated with a densified electronic structure under pressure. Examining the spectra for increasing energies, reflectance increases progressively until around 2.5 eV, where it reaches a maximum. This behavior may be associated with electronic transitions in the lower energy bands, which strongly influence the interaction of incident light with the material's surface and bulk states. At this stage, pressure seems to play a key role in modifying the electronic structure and, consequently, the optical reflection properties. Above 2.5 eV, the spectra show a rapid decline in reflectance up to around 4.5 eV. This decline can be explained by an increase in optical absorption, where more of the incident energy is absorbed by the material, reducing the reflected fraction. This region corresponds to more energetic

electronic transitions, where the photonic interaction penetrates further into the volume of the material, reducing surface reflection. After this drop, reflectance rises again for energies above 4.5 eV. This second rise could be attributed to high-energy interband electronic transitions, where excited electrons interact strongly with incident light, resulting in increased reflection. This increase could also result from a plasmonic effect linked to the increased electron density under pressure. Pressure analysis reveals that reflectance spectra are particularly sensitive to variations in hydrostatic pressure, with a noticeable increase in reflectance values across all the energy ranges studied. This suggests that pressure acts as an effective tool for tuning the optical properties of $LiGeCl_3$, increasing its reflectance, particularly at low frequencies and in certain high energy ranges.

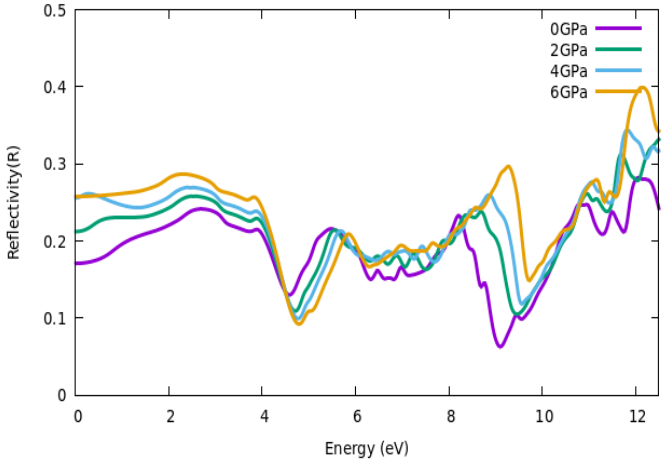

Figure 8: Reflectivity versus energy at 0, 2, 4 and 6GPa for $LiGeCl_3$.

Figure 9 shows spectral variations in refractive index n(ω) of $LiGeCl_3$ under different pressures, offering a detailed insight into how the material interacts with light through its transparency properties. The refractive index is an essential parameter for assessing the propagation speed of light in a material, and provides crucial information on light scattering and diffusion, enabling a better understanding of light-matter interaction mechanisms. Between 0 and 2.5 eV, values of n(ω) are significantly higher under a pressure of 6 GPa, with respective values of 3.21, 3.20, 2.70 and 2.40 at 6 GPa, 4 GPa, 2 GPa and 0 GPa. This increase in refractive index with pressure indicates a densification of the electronic structure under the effect of compression, resulting in a slowing of light propagation in the material. The higher refractive index at higher pressure reflects a pressure-induced increase in electron-induced polarization, which may suggest a better interaction between light and electronic states in this energy range. This decreasing trend in n(ω) with pressure is probably explained by the effect of compression on electronic orbitals. More precisely, increasing pressure causes the crystal lattice to contract, thus modifying electron dynamics and affecting the optical properties of the material, notably its refractive index. High values at 6 GPa may be linked to a greater density of electronic states, facilitating stronger interaction between photons and the material. Above 2.5 eV, the refractive index n(ω) decreases progressively with increasing energy, from relatively high values to a minimum value of around 0.75 at 12 eV. This phenomenon is typical of materials where absorption begins to dominate at higher energies, and the refractive index adjusts accordingly to reflect this transition. The continued decrease in refractive index after

2.5 eV could also be linked to the delocalization of electrons into more energetic states, reducing the material's ability to effectively polarize incident light. This reduction in the 1.5 to 4.3 eV range probably indicates a transition from regimes where light is more strongly scattered to regimes where interactions with excited electrons become less significant.

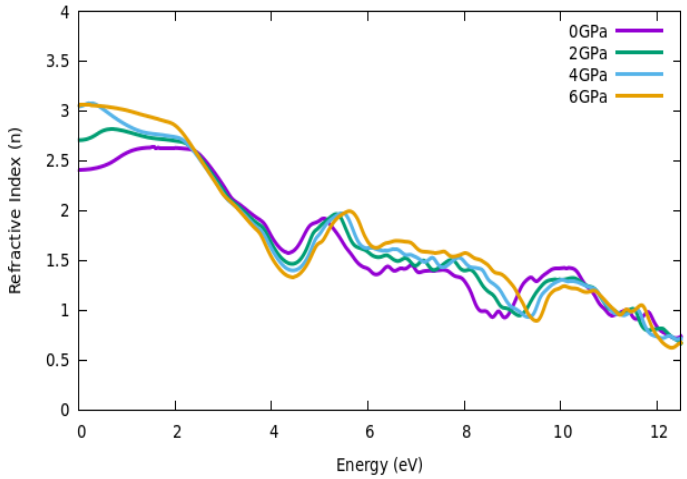

Figure 9: Reflective index versus energy at 0, 2, 4 and 6 GPa for $LiGeCl_3$.

4. CONCLUSION:

The DFT method, implemented in the Wien2k code, has been employed to analyse the physical and optical properties of $LiGeCl_3$ compounds. The results obtained for the equilibrium structure are consistent with previous theoretical studies, confirming the validity of the calculations. The optimization curve was used to evaluate the parameters required to ensure the stability of the systems. Calculations using the GGA reveal that the elastic constants (Cij) of $LiGeCl_3$ meet the criteria for mechanical stability, while the progressive increase in pressure contributes to a reduction in the lattice parameter, leading to a narrowing of the electronic band gap. Analysis of the electronic structures of $LiGeCl_3$ under pressure reveals a notable transition from semiconductor to metal. At ambient pressure (0 GPa), $LiGeCl_3$ has a direct band gap of 0.72 eV, which gradually decreases under pressure (0.34 eV at 2 GPa, 0.12 eV at 4 GPa) before disappearing at 6 GPa, where the material becomes metallic. This transformation, due to the compression of the crystalline lattice and the overlapping of bands, demonstrates the crucial impact of pressure on electronic properties, opening up prospects for the engineering of advanced optoelectronic materials. The study also examined in detail the optical properties of the material under different pressures (from 0 to 6 GPa), focusing on their effects on the electronic structure and optical characteristics of $LiGeCl_3$, including absorption, optical conductivity, reflectance and refractive index. The material's absorption improves in the visible and UV ranges under pressure, with a shift in absorption thresholds towards lower energies and an increase in the absorption coefficient to 6 GPa. These results highlight the increased potential of $LiGeCl_3$ for photovoltaic devices and other optoelectronic applications. Optical conductivity shows a redistribution of electronic states under pressure, with notable changes in conductivity peaks, particularly at high pressures. This indicates a densification of the electronic states, reinforcing the material's conductive properties, particularly at high pressure and high energy. The study revealed a progressive increase in Reflectivity with energy,

modified by pressure. At 6 GPa, the refractive index is significantly higher in the 0-2.5 eV range, indicating better interaction of the material with light. This development is consistent with the compression of the crystal lattice and the increase in electron density. In conclusion, this work shows that hydrostatic pressure is a key parameter for optimizing the electronic and optical properties of $LiGeCl_3$. Under pressure, the material exhibits improved optical characteristics, particularly in the visible and UV ranges, making it particularly promising for modern applications such as photovoltaic cells and light-based optoelectronic devices. The optimization of $LiGeCl_3$ through pressure thus opens up new prospects for the engineering of advanced materials in energy harvesting and other optoelectronic technologies. However, the synthesis and shaping of $LiGeCl_3$ under pressure pose challenges related to its structural stability, with dangers of irreversible structural changes. The challenge of producing uniform materials on a large scale also persists due to the difficulty in ensuring the reproducibility and purity of samples. To integrate $LiGeCl_3$ into operational systems, it is crucial that it is compatible with existing technologies (LEDs, solar panels, sensors), which implies carrying out studies on its deposition and encapsulation. In addition, it is necessary to examine the durability and reliability of the material when subjected to prolonged pressure to prevent any deterioration in its performance.

Author Contributions: Mohammed Miri: Writing – original draft, Visualization, Validation, Investigation, Formal analysis, Data curation, Conceptualization. Younes Ziat: Supervision. Hamza Belkhanchi: Visualization, Validation, Investigation, Formal analysis. Abdellah Bouzaid: Visualization. Youssef Jouad: Visualization. Youssef Ait El Kadi: Visualization. The author also reviewed and edited the manuscript for final approval.

Funding: The authors are warmly grateful to the support of "The Moroccan Association of Sciences and Techniques for Sustainable Development (MASTSD), Beni Mellal, Morocco".

Data Availability Statement: Not applicable.

Acknowledgments: A special thank you to Professor Hanane Reddad from Sultan Moulay Slimane University, Beni Mellal, Morocco, for her technical and scientific support, as well as her full collaboration and discussion during the different steps of the present investigation.

Conflicts of Interest: The authors declare that they have no conflict of interest.

REFERENCE

[1] *D. Shiwen, and F. Zhang. "General applications of density functional theory in photocatalysis." Chinese Journal of Catalysis 61 (2024): 1-36.*

[2] *V. Nitsenko, A. Mardani, J. Streimikis, I. Shkrabak, I. Klopov, O. Novomlynets, & O. Podolska. Crite-ria for evaluation of efficiency of energy transformation based on renewable energy sources. Montenegrin Jour-nal of Economics, 14(4), (2018), 237-247.*

[3] *H. Belkhanchi, Y. Ziat, M. Hammi, C. Laghlimi, A. Moutcine, A. Benyounes, & F. Kzaiber. Nitrogen doped carbon nanotubes grafted TiO2 rutile nanofilms: Promising material for dye sensitized solar cell application. Optik, 229, 166234. (2021), https://doi.org/10.1016/j.ijleo.2020.166234.*

[4] H. Belkhanchi, Y. Ziat, M. Hammi, C. Laghlimi, A. Moutcine, A. Benyounes, & F. Kzaiber. Synthesis of N-CNT/TiO2 composites thin films: surface analysis and optoelectronic properties. E3S Web of Conferences (Vol. 183, p. 05002) (2020), EDP Sciences. https://doi.org/10.1051/e3sconf/202018305002.

[5] F. Yang, Y. Pan, & J. Zhu. Enhanced catalytic activity of noble metal@ borophene/WS2 heterojunction for hydrogen evolution reaction. Applied Surface Science, 680, 161321 (2025).

[6] A. Waqdim, M. Agouri, A. Abbassi, B. Elhadadi, Z. Zidane, S. Taj, M. El Idrissi, Theoretical investigation of the physical properties of cubic perovskite oxides SrXO3 (X= Sc, Ge, Si). Mater. Sci. Semicond. Process. 158, 107340 (2023)., https://doi.org/10.1016/j.mssp.2023.107340.

[7] F.Zhang, Y. Mao, T.J. Park, S.S. Wong, Green synthesis and property characterization of single-crystalline perovskite fluoride nanorods, Adv. Funct.Mater. 18 (1) (2008) 103112..

[8] S. Collavini, S.F. Volker, J.L. Delgado, Angew. Chem. Int. Ed. 54 (2015) 9757–9759..

[9] H. Mu, F. Hu, R. Wang, J. Jia and S. Xiao, J. Lumin. , 2020, 226, 117493..

[10] X. Z. Deng, Q. Q. Zhao, Y. Q. Zhao, & M. Q. Cai. Theoretical study on photoelectric properties of lead-free mixed inorganic perovskite RbGe1-xSnxI3. Current Applied Physics, 19(3), 279-284 (2019).

[11] A. Bouzaid, Y. Ziat, H. Belkhanchi, H. Hamdani, A. Koufi, M. Miri, ... & Z. Zarhri. Ab initio study of the structural, electronic, and optical properties of MgTiO3 perovskite materials doped with N and P. E3S Web of Conferences. (2024), (Vol. 582, p. 02006). EDP Sciences.

[12] A. Koufi, Y. Ziat, H. Belkhanchi, M. Miri, N. Lakouari ... & F. Z. Baghli. A computational study of the structural and thermal conduct of MgCrH3 and MgFeH3 perovskite-type hydrides: FP-LAPW and BoltzTraP insight. (2024), E3S Web of Conferences (Vol. 582, p. 02003). EDP Sciences. https://doi.org/10.1051/e3sconf/202458202003.

[13] A. S. Bhalla, R. Guo, & R. Roy. The perovskite structure—a review of its role in ceramic science and technology. Materials research innovations, 4(1), 3-26 (2000).

[14] Y. Wang, J. Lv, P. Gao, & Y. Ma. Crystal structure prediction via efficient sampling of the potential energy surface. Accounts of Chemical Research, 55(15), 2068-2076. (2022).

[15] S. Karlheinz. "DFT calculations of solids with LAPW and WIEN2k." Journal of Solid State Chemistry 176.2 (2003): 319-328.

[16] A. Bouzaid, Y. Ziat, & H. Belkhanchi. Prediction the effect of (S, Se, Te) doped MgTiO3 on optoelectronic, catalytic, and pH conduct as promised candidate photovoltaic device: Ab initio framework. International Journal of Hydrogen Energy, (2025), 100, 20-32. https://doi.org/10.1016/j.ijhydene.2024.12.284.

[17] S. Bouhmaidi, R. K. Pingak, A. Azouaoui, A. Harbi, M. Moutaabbid, & L. Setti. Ab initio study of structural, elastic, electronic, optical and thermoelectric properties of cubic Ge-based fluoroperovskites AGeF3 (A= K, Rb and Fr) (2023), Solid State Communications, 369, 115206.

[18] M. S. Alam, M. Saiduzzaman, A. Biswas, T. Ahmed, A. Sultana, & K. M. Hossain. Tuning band gap and enhancing optical functions of AGeF3 (A= K, Rb) under pressure for improved optoelectronic applications. Scientific Reports, 12(1), 8663 (2022).

[19] M. Houari, B. Bouadjemi, S. Haid, M. Matougui, T. Lantri, Z. Aziz, ... & B. Bouhafs. Semiconductor behavior of halide perovskites AGeX 3 (A= K, Rb and Cs; X= F, Cl and

Br): first-principles calculations. Indian Journal of Physics, 94, (2020), 455-467.

[20] M. A. Sarker, M. Muntasir, M. A. Momin, M. Solayman, & M. R. Islam. Pressure-Induced Structural, Electronic, and Optical Properties of Lead-Free NaGeX3 (X= F, Cl, Br, and I) Perovskites: First-Principles Calculation. Advanced Theory (2024), and Simulations, 7(7), 2400112..

[21] J. K. Rony, M. N. Hasan, M. N. Rifat, M. Saiduzzaman, & M. Islam. Pressure-induced DFT evaluation of MSnI3 (M= K, Rb) perovskites for electronic phase transition and enhanced optoelectronic utilization. Computational and Theoretical Chemistry, (2024), 1233, 114512..

[22] M. D. Ratul Hasan, I. A. Apon, I. Ahmed Ovi, & F. T. Zahra. Impact of applied pressure on tin-based cubic halide perovskite ASnX3 (A= Li, Na and X= Cl, Br, and I) in reference to their optoelectronic applications. International Journal (2024), of Energy Research, 2024(1), 8213804.

[23] S. Pooja, P. Ranjan, and T. Chakraborty. "DFT and TD-DFT studies of perovskite materials LiAX3 (A= Ge, Sn; X= F, Cl, Br, I) in reference to their solar cell applications." Materials Today Sustainability 26 (2024): 100791.

[24] N. A. Abdulkareem, B. M. Ilyas, S. A. & Sami. A first principle investigation of the non-synthesized cubic perovskite LiGeX3 (X= I, Br, and Cl). Materials Science in Semiconductor Processing, 131, 105858 (2021).

[25] K. Gesi, K. Ozawa, & S. Hirotsu. Effect of hydrostatic pressure on the structural phase transitions in CsPbCl3 and CsPbBr3. Journal of the Physical Society of Japan, 38(2), 463-466 (1975).

[26] L. Zhang, L. Wang, K. Wang, & B. Zou. Pressure-induced structural evolution and optical properties of metal-halide perovskite CsPbCl3. The Journal of Physical Chemistry C, 122(27), 15220-15225 (2018).

[27] Y. Huang, Z. Li. K. Hu, & X. Shao. First principles investigation on pressure induced phase transition and photocatalytic properties in RbPbCl3. Computational Materials Science, 143, 403-410 (2018).

[28] I. M. Alsalamah, A. Shaari, N. A. Alsaif, S. A. Yamusa, G. Lakshminarayana, & N. Rekik. Exploring the structural properties and the optoelectronic features of RbPbX3 (X= Cl, F) perovskite crystals for solar cells solicitations: (2023)., Showcasing the DFT predictions. Chemical Physics, 573, 111978.

[29] M. R. Hasan, I. A Apon, M. M. Islam, J. Y. Al-Humaidi, & M. R. Islam. First principles calculations to investigate structural, mechanical, electronic, optical and magnetic properties of LiGeX3 (X= Cl, Br, and I) perovskite under (2025),, pressure effect. Materials Science and Engineering: B, 313, 117936..

[30] P. Blaha, K. Schwarz, F. Tran,R. Laskowski,G.K.Madsen,L.D. Marks,WIEN2k: an APW+lo program for calculating the properties of solids, J. Chem. Phys. 152 (2020),074101, https://doi.org/10.1063/1.5143061.

[31] J.P. Perdew, K. Burke, M. Ernzerhof, Generalized gradient approximation made simple. Physical review letters 77 (18) (1996) 3865.

[32] P. Perdew, K. Burke, M. Ernzerhof, Generalized gradient approximation made simple, Phys. Rev. Lett. 77 (1996) 3865, https://doi.org/10.1103/PhysRevLett.77.3865..

[33] R. W. G. Wyckoff, Crystal Structures, 2nd ed., Vol. 1(John Wiley & Sons, (1963)..

[34] Abdulkareem, A. Nawzad M. I. Bahaa, and A. S. Sarkawt. "A first principle investigation of the non-synthesized cubic perovskite LiGeX3 (X= I, Br, and Cl)." Materials Science in Semiconductor Processing 131 (2021): 105858..

[35] T. Katsura, Y. Tange, A simple derivation of the Birch–Murnaghan equations of state (EOSs) and comparison with EOSs derived from other definitions of finite strain, Minerals 9(2019)745, https://doi.org/10.3390/min9120745.

[36] I.N. Frantsevich, F. F. Voronov S.A. Bokuta. Handbook of elastic constants and elastic moduli of metals and nonmetals. Kiev: Naukova Dumka; 1983.

[37] V. G. Tyuterev, & N. Vast. Murnaghan's equation of state for the electronic ground state energy. Computational materials science, 38(2), 350-353. (2006), https://doi.org/10.1016/j.commatsci.2005.08.012.

[38] F. Mouhat F-X. Coudert. Necessary and sufficient elastic stability conditions in various crystal systems. Phys Rev B. 2014;90:224104.

[39] J.Wang and Y. Zhou, Phys. Rev. B 69, 214111 (2004)..

[40] Max Born, On the stability of crystal lattices. I. Mathematical Proceedings of the Cambridge Philosophical Society, 36, pp 160172(1940), DOI:10.1017/S0305004100017138..

[41] Y. O. Ciftci, & M. Evecen. First principle study of structural, electronic, mechanical, dynamic and optical properties of half-Heusler compound LiScSi under pressure. Phase Transit. 91, 1206–1222 (2018)..

[42] F. Herman."Theoretical investigation of the electronic energy band structure of solids." Reviews of Moder 4 Physics 30.1 (1958): 102..

[43] J. Musil, F. Kunc, H. Zeman, H. Polakova, Relationships between hardness, Young's modulus and elastic recovery in hard nanocomposite coatings, Surf. Coating. Technol. 154 (2–3) (2002) 304–313, https://doi.org/10.1016/S0257-8972(01)01714 5.

[44] A.M. Shawahni, M.S. Abu-Jafar, R.T. Jaradat, T. Ouahrani, R. Khenata, A. A. Mousa, K.F. Ilaiwi, Structural, elastic, electronic and optical properties of SrTMO3 (TM= Rh, Zr) compounds: insights from FP-LAPW study, Materials 11 (10) (2018)2057,, https://doi.org/10.3390/ma11102057.

[45] R. Hill, The elastic behaviour of a crystalline aggregate, Proc. Phys. Soc. 65 (5)(1952) 349–354, https://doi.org/10.1088/0370-1298/65/5/307.

[46] A. Reuss, Berechnung der fließgrenze von mischkristallen auf grund der plastizitätsbedingung für einkristalle, Z. Angew. Math. Mech. 9 (1929) 49–58.

[47] S. F. Pugh. XCII. Relations between the elastic moduli and the plastic properties of polycrystalline pure metals. The London, Edinburgh, and Dublin Philosophical Magazine and Journal of Science, 45(367), 823-843. (1954), https://doi.org/10.1080/14786440808520496.

[48] G. Wang, Y. Li. Z. Jiang, X. Chong, & J. Feng. Balance between strength and ductility of dilute Fe2B by high-throughput first-principles calculations. Ceramics International, 47(4), 4758-4768. (2021), https://doi.org/10.1016/j.ceramint.2020.10.045.

[49] H. Bouafia, S. Hiadsi, B. Abidri, A. Akriche, L. Ghalouci, B. Sahli. Structural, elastic, electronic and thermodynamic properties of KTaO3 and NaTaO3: Ab initio investigations. Computational Materials Science, 75(), 1–8. (2013)., doi:10.1016/j.commatsci.2013.03.030.

[50] X. Zhu, S.G. Louie, Quasiparticle band structure of thirteen semiconductors and insulators, Phys. Rev. B 43 (17) (1991) 14142,.

[51] A. P. Nayak, S. Bhattacharyya, J. Zhu, J. Liu, X. Wu, T. Pandey, ... & J. F. Lin. Pressure-induced semiconducting to metallic transition in multilayered molybdenum disulphide. Nature communications, 5(1), 1-9 (2014).

[52] M. Radjai, A. Bouhemadou, D. Maouche, Structural, Elastic, Electronic and Optical,

Properties of the Half-Heusler ScPtSb and YPtSb Compounds under Pressure, 2021 arXiv preprint arXiv:2112.09940.

[53] Gray, L. Harold. "The absorption of penetrating radiation." Proceedings of the Royal Society of London. Series A, Containing Papers of a Mathematical and Physical Character 122.790 (1929): 647-668..

[54] S. Hasegawa."Reflection high-energy electron diffraction."Characterization of Materials, 97 (2012): 1925 1938.